EMA-C 90181

FINAL REPORT

PRECIPITATION AND AIR FLOW (PRAI) PROJECT

and

DOPPLER RADAR DATA PROCESSING (DOPDATE) PROJECT

(1 January 1988 - 31 December 1990)

A report to the Water Research Commission

Project leaders:

G HELD
A M GOMES

PRETORIA
NOVEMBER 1990

WRC Report No. WRC 223/1/91
ISBN 1 874858 17 9

KEYWORDS: Radar, Doppler radar, rainfall, thunderstorms, precipitation, air flow, hailstorms, thermodynamics, equivalent potential temperature, Area-Time-Integral, early storm stages, cell mergers, South Africa.

EXECUTIVE SUMMARY

The Division of Earth, Marine and Atmospheric Science and Technology, EMATEK, (formerly National Physical Research Laboratory) of the CSIR has been intensely involved in precipitation studies since the late fifties, although originally mainly in the field of laboratory investigations. However, in 1970, an S-band (10 cm) weather radar was bought and has been continuously in operation during the rainy seasons since 1971. Not only has a comprehensive knowledge of precipitation patterns on the Highveld been accumulated, but members of the research team also gained considerable insight into mechanisms of thunderstorms. However, it was realised some years ago that, in order to fully understand the mechanisms of precipitation formation, including that of hail storms, one has to have detailed measurements of the three-dimensional air flow pattern in and around a storm. It was therefore decided to modify the S-band radar at Houtkoppen to operate in Doppler mode. Many storms were thus observed since the 1987/88 rainy season and a good data base of precipitation versus airflow inside storms was built up (digital Doppler radar records). Results which demonstrate the usefulness of single-Doppler radar observations have already been presented in previous reports and some more sophisticated applications based on radial velocity measurements are being presented in this report (cf. Section 2.2). Nevertheless, it was realised all along, that a single Doppler radar is only the first step towards a multiple Doppler radar facility which is the only means to actually observe by radar, and then calculate the three-dimensional air flow pattern inside a thunderstorm. For this purpose, two standard C-band radars had been purchased and were subsequently modified to also operate in Doppler mode. It was planned to have them already operational for the 1989/90 season, but this did unfortunately not materialise due to unforeseen circumstances which are explained in more detail in Section 1 of this report. Therefore, during the past year emphasis was put on the analysis of single-Doppler radar data and the various applications of such observations.

This report presents a summary of achievements during the three-year *Precipitation and Airflow (PRAI) Project* and the one-year *Doppler Radar Data Processing (DOPDATE) Project*.

The objectives of both projects can briefly be summarised as follows:

The original proposal for the three-year PRAI project was aimed at providing supplementary information on precipitation processes on the Highveld for on-going weather modification research projects. It had been realised that accurate measurement of total areal rainfall is of prime importance for precipitation enhancement projects. It was therefore proposed to establish relationships between the spatial distribution of precipitation within clouds and the internal air flow in thunderstorms; between the surface precipitation (rain and hail) patterns and the three-dimensional air flow in storms; and finally between rainfall intensities as measured by rain gauges and the reflectivity recorded by radar. It was also proposed to verify or reject the hypothesis of accumulation zones above the main updraught region and to *possibly* identify storm systems which have a good potential for producing rain on the ground, but are inefficient in their mechanism and would therefore be more suitable for cloud seeding operations than naturally efficient clouds. During the second year the research proposal was expanded to include detailed studies of raindrop-size distributions and Z-R relationships in an attempt to improve the accuracy of radar measurements of areal rainfall. In line with this objective was also the investigation of the V-ATI (Volume x Area-Time-Integral) of radar reflectivity.

The WRC also approved further funds for additional analysis work under the project name DOPDATE, which was to run concurrently with the PRAI project during 1990. The emphasis of the new project was on the selection and analysis of convective clouds at a very early stage in their life cycle, in order to verify and *possibly quantify* the daughter-cell and feeder-cell cloud merging concepts of storm mechanisms on the Highveld. The joint execution of both projects resulted in a drastic improvement of the sensitivity of the Houtkoppen S-band radar; also the other two C-band radars were to have come on line during the 1989/90 rainy season; the CRAY computer programs should be verified and tested and the EVAD (Extended Velocity-Azimuth Display) method should be investigated as a means for extracting maximum information from existing single-Doppler radar data.

The objectives as summarised above and in detailed annual Work Programmes which were approved by the Steering Committee, have by and large been achieved.

Thermodynamic and kinematic properties of Highveld storms

It became obvious from extensive literature studies that the relationship of buoyancy and wind shear is fundamentally important in defining storm structure. Therefore, the convective available potential energy (CAPE), which is a function of the potential temperature of an air parcel rising moist adiabatically and the environmental potential temperature, has been calculated for Highveld storms, using the Irene (Pretoria) 12 GMT sounding. In further developments, the bulk Richardson number (Ri), which is a function of CAPE and the wind shear (speed) between low and middle levels of the atmosphere, has been calculated. Storm form three seasons (85/86, 86/87, 87/88) were classified according to CAPE and Ri and the results are presented diagrammatically in Section 2.1. Highveld values of CAPE ranged from 800 to 4800 $m^2.s^{-2}$, representing typical values of convective energy available to develop convection. Ri values were found to be less characteristic on the Highveld, viz. rather low (10 to 40), and are only useful for storm classification purposes if used in conjunction with CAPE. The vast majority of storms fell into the multicell category. No definite supercell storm was found according to the classification criteria.

Kinematic properties of the wind field can be derived from single-Doppler radar observations in widespread homogeneous precipitation. In principle, the horizontal wind speed and direction can be determined by measuring the radial velocity as a function of the azimuth at a constant elevation angle (VAD = Velocity Azimuth Display). Even the divergence of the horizontal wind can be calculated, but inhomogeneities in the particle fall speed can lead to significant errors. Therefore, Srivastava's extended VAD (EVAD) method was applied to a Highveld storm. The basic assumption for EVAD is that the divergence and particle fall speed are horizontally uniform and thus only a function of height. Therefore, the limitation of the VAD method to small elevation angles is eliminated and the divergence can be calculated throughout the complete volume scan.

The storm selected as a test case (21 November 1987) was part of a large squall line with strong convective activity at the leading edge, but fairly homogeneous stratiform precipitation behind it. A radius of 25 km was chosen for the imaginary EVAD circle in order to avoid patchy radar echoes. Vertical profiles of the horizontal wind divergence and vertical velocity were calculated for six complete volume scans. The magnitudes of the wind speed ranged from 3-6 $m.s^{-1}$ in the lower and middle levels, increasing to 18 $m.s^{-1}$ at higher levels. Strong convergence was found below 2,5 km (maximum of $4 \times 10^{-4}s^{-1}$) while the maximum divergence ($4 \times 10^{-4}s^{-1}$) was found at about 5,5 km AGL. Typical updraught and downdraught values were 25 $cm.s^{-1}$ with maxima up to 1 $m.s^{-1}$. The results are presented in the form of time-height graphs.

Doppler radar observations can also be used to estimate the precipitation rate and efficiency by integrating the mass continuity equation vertically, using VAD-derived divergence values. This was done for the test storm during a 28-minute period, yielding a total rainfall of 2,9 mm. Compared with rain gauge measurements at Jan Smuts Airport, which is actually just outside the 25 km radius, the VAD method estimated 8% less rain than the gauge, resulting in a slight over-estimation of the "precipitation efficiency" for the period of analysis.

Although all these findings must be regarded as preliminary, subject to many more test results, the versatility of observations made using only one Doppler radar has clearly been demonstrated.

Raindrop size distributions and Z-R relationships

The importance of studying drop size distributions (DSDs) is related to a number of aspects of thunderstorm research. DSD studies are particularly important in radar-measurement of rainfall, as variability in DSDs causes significant variability in rainfall rate (R) and radar reflectivity factor (Z). DSDs in convective rainfall over the Transvaal Highveld were measured using a raindrop disdrometer. A paramaterisation technique was used to quantify temporal variability in DSDs. The parameterisation technique is based on the assumption that DSDs can be represented by an exponential distribution which in turn, can be represented by N_o, the intercept value and Λ, the slope of the distribution. DSD variability will thus be reflected in N_o and Λ.

Comparisons between N_o, Λ and rainfall rate showed that convective storm systems over the Transvaal Highveld are characterised by drop-sorting (sedimentation) and drop break-up effects. These effects lead to large drop dominance in the initial DSDs of convective rain followed by an influx of small drops in the later stages of the storm. Stratiform rain was characterised by a pattern of small drop dominance in the spectrum from the onset of rain. DSD variations were also compared to variations in radar reflectivity factor. Within an individual storm, the radar reflectivity factor was seen to be both greater and less than the rainfall rate in response to changes in the DSD. A summary of the entire season's data showed that underestimation or overestimation of rainfall rate using an average Z-R relationship is a function of changes in the drop size distribution and not, primarily, in rainfall rate.

The Area-Time-Integral method of radar-rainfall measurement

Radar measurement of rainfall, although seen by many as the solution to the problem of areal and temporal measurement of rainfall, is not straight forward. The problems include variability in the Z-R relationship as well as changes in precipitation from the height at which it is measured to the ground. If the area of the radar echo is integrated over time and compared with radar-estimated rainfall volume, a strong correlation is seen to exist. It is this principle that is utilised in the Area-Time-Integral (ATI) method of volumetric rainfall measurement by radar. The ATI method has been proposed as a means of measuring rainfall using radar which to a large extent overcomes the above-mentioned problems.

Three different methods of computing ATI values are discussed in determining an appropriate Volume versus Area-Time-Integral (V-ATI) relationship for convective storms over the Transvaal Highveld. Computing ATI from the hourly average echo area gave the lowest measurement error. On the basis of this, a V-ATI relationship of the form $V=3,06(ATI)^{1,14}$ was computed where V is in units of $km^2.mm$ and ATI in units of $km^2.h$. In order to enhance operational applications of the ATI method a "scan by scan" integration technique was also calculated. This gave a V-ATI relationship of the form $V=0,04(ATI)^{1,18}$ where V is in units of $km^2.mm$ and ATI in units of $km^2.min$ ($V = 2,4(ATI)^{1,18}$ when ATI is in units of $km^2.h$). Average rainfall rates for convective storms over the Transvaal Highveld calculated using a V-ATI relationship were seen to be higher than those for other parts of the world, but this is in keeping with characteristics of South African storms discussed by other authors.

Daughter cells and cloud seeding

The main goal of this study is to identify the principal mechanism for new cell generation in South African clouds which are suitable for cloud seeding activities, as cloud growth patterns may have a major impact on the effective placement of seeding material in all the cells of a storm case (Changnon *et al.*, 1975). It is also important to understand cloud merger processes for proper evaluation of seeding effects. This short pilot project is a survey of several case studies and includes a discussion which integrates previous research and methodology.

The information needed at this time is on the relative frequency of feeder type mergers compared to daughter type mergers, as the former can be expected to maximise the efficient use of seeding material (as recycling is possible), while in the latter it is minimised and additional seeding may be necessary to treat all cells of a single dynamic entity. The key feature to be identified now is whether the major new cells are essentially separate from the older cells or replace them in the same relative position in the moving storm system. Thus, the new cell locations (relative to the initial cell) must be monitored over time in the presence of storm translation. Consequently, the proper definition of daughter and feeder cells is one of the main interests of this pilot study. Therefore, high resolution temporal and spatial radar images were required, and a lengthy introduction included.

Early storm development and cloud mergers: a single Doppler radar case study

A detailed, three-dimensional case study of an isolated, and for the Highveld, typical multicellular storm illustrates very clearly the various mechanisms of cloud merging, cell development and regeneration, which sustain such storms for hours while they are traversing the Highveld. The case study is based on single Doppler radar observations of a storm which occurred on 27 April 1987 between the West Rand and Pretoria. Radial velocities of the air flow inside the storm were carefully analysed and, whenever possible, interpreted in terms of updraughts or downdraughts. The study identified two main mechanisms:

Daughter-cell merging situation.
A new cell had developed rapidly between 5 and 8 km AGL some 3-4 km northeast of a mature cell. As the new cell grew and intensified, the radial air flow was increasing significantly, indicating an updraught tilted away from the old cell. The two cells then merged into one complex by rapid expansion and intensification within a period of about 10 minutes. Seven minutes later, the original cell had been totally incorporated into the new structure and could no longer be identified.

Feeder-cell merging situation.
Three very small cells of 1-2 km in diameter have been observed, forming some 4-5 km north of mature echoes in an area of strong convergence within a period of about five minutes. It is noteworthy that the cell which had formed later than and between the existing two, was the one to have developed to full maturity, by entraining the flanking cells quite rapidly. This process took less than six minutes. Once this cell had established itself as the survivor, it grew rapidly in height, area and intensity and moved together with its mother cell for a period of about 18 minutes. It eventually merged into the mother storm, but always remained identifiable during its whole life cycle of less than 25 minutes.

A *slightly different mechanism* of a feeder-cell merging situation was observed in parallel to the above case. A new cell had developed aloft on the perimeter of an existing storm, rapidly growing in intensity and volume. Within a matter of five to seven minutes it had been totally incorporated in the leading edge of the old storm aloft, thus dramatically enhancing its anvil and tilt of the echo core.

It is noteworthy that these different cell merging mechanisms can occur sequentially or simultaneously during the same storm situation on one particular day. The main difference between daughter-cell and feeder-cell merging situations appears to be the reflectivity factor, and thus the cell intensity, which is much greater in the case of daughter-cell mergers than in feeder-cell merging situations (the feeder-cell is generally $\leq$40 dBZ).

Case studies of this nature are very time consuming, as can be seen from the fact that a total of approximately 420 PPI plots and 600 vertical cross-sections formed the basis of the analysis of a storm period lasting less than one hour! It is therefore impossible, at this stage, to estimate the relative frequency of the various storm merger situations.

It has also become very obvious that, in order to study storm or cell merger situations, one must have the three-dimensional reflectivity and air flow pattern available for making useful inferences. The latter should actually be derived from dual or triple Doppler radar observations rather than inferred from single Doppler radar observations.

However, both types of merger mechanisms are very important for cloud-seeding experiments as the reaction to the introduction of seeding material might yield different results depending on the merger type.

Processing of Doppler radar data

Although it was initially envisaged that at least two Doppler radars (S-band at Houtkoppen and C-band at CSIR) would be operational during the 1989/90 season, this did, unfortunately, not materialise. Only the S-band radar at Houtkoppen was operated routinely, while test runs were made with the C-band radar on the CSIR campus. The reasons for this were manifold, and are discussed in detail in Section 7. During the course of many test runs, several other difficulties had to be overcome which resulted from some of the hardware modifications. Therefore, no useful data could be collected using more than one Doppler radar until March 1991.

However, the difficulties outlined above did certainly not deter from completing the implementation of the CRAY programs on the CSIR's VM mainframe computer and their final testing.

In order to analyse radar data with the NCAR programs, two major steps have to be executed, viz. 'SPRINT' (Sorted Position Radar Interpolation) and 'CEDRIC' (Cartesian Space data processor). 'SPRINT' is designed to interpolate volumetric radar space measurements collected at constant elevation angles to a regularly spaced three-dimensional Cartesian grid. 'CEDRIC' is used for the reduction and analysis of single and multiple Doppler radar volumes in Cartesian space.

After implementation of 'SPRINT', it was found that the Universal Radar Data Format required more storage space on the VM mainframe computer than could be allocated. It was therefore decided to modify the input format of our radar data in order to facilitate speedy processing. All sections of 'SPRINT' and 'CEDRIC' have been thoroughly tested with Houtkoppen's single Doppler radar data and typical examples of the output from 'SPRINT' are shown.

A storm which was observed on 4 March 1991 by both the Houtkoppen and Pretoria Doppler radar, has been selected as one of two test cases for dual Doppler analysis. Results from the preparation of the data sets for such an analysis are included. The three-dimensional air flow pattern, based on one dual Doppler radar volume scan, is shown for a storm which was observed on 26 March 1991 and which was more suitable for synthesis than the one from 4 March 1991. CAPPIs with the reflectivity and the horizontal airflow, as well as vertical cross sections showing up- and downdraughts, are included in the report.

General Conclusions

A vast amount of radar data and related meteorological observations have been processed in order to achieve the goals set for both the PRAI and DOPDATE projects. The results which emerged from the many sub-projects are very encouraging and in some cases even quite exciting. There are a number of aspects which are in urgent need of continued attention, such as obtaining at least one complete season of dual or triple Doppler radar observations for climatological investigations, a more quantitative study of cloud merger processes, the application of single-Doppler radar observations for estimating precipitation efficiencies and certain hardware improvements. Reasons and proposed avenues for such further investigations have been addressed in detail in Section 8 (Conclusions and Recommendations).

However, it is felt that it would be a tragic event if such a research project would have to be terminated due to a lack of funds for maintaining the multiple Doppler radar facility, which is an absolutely unique asset in South African precipitation research.

Following the recommendations of the *Workshop on Rainfall Stimulation Research in South Africa* (Berg-en-Dal Conference Centre, Kruger National Park, 21-23 August 1989) which was attended by all leading scientists in the field of cloud physics in South Africa and by four overseas experts, *all* available resources, both in manpower and hardware, should be coordinated in a National Research Project, in order to obtain the optimal benefit from such a unique set-up.

Since the CSIR multiple Doppler radar facility is still the only one in South Africa which deploys S- and C-band Doppler radars for thunderstorm research, it seems only logical to maintain such a unique asset, especially now, since the first dual Doppler radar observations have become available. This had also been emphasized by the overseas consultants on many occasions.

FOREWORD

A first draft of this report had been prepared for the Water Research Commission during November 1990. Since then a few sections were added and others improved in order to submit a completely up-to-date version as a final report on both, the *Precipitation and Air Flow (PRAI) Project* and the *Doppler Radar Data Processing (DOPDATE) Project*.

G Held

A M Gomes

Pretoria

March 1991

CONTENTS

1. INTRODUCTION

The Division of Earth, Marine and Atmospheric Sciences and Technology, EMATEK, (formerly National Physical Research Laboratory) of the CSIR has been intensely involved in precipitation studies since the late fifties, although originally mainly in the field of laboratory investigations. However, in 1970, an S-band (10 cm) weather radar was bought and has been continuously in operation during the rainy seasons since 1971. Not only has a comprehensive knowledge of precipitation patterns on the Highveld been accumulated, but members of the research team also gained considerable insight into mechanisms of thunderstorms. However, it was realised some years ago that, in order to fully understand the mechanisms of precipitation formation, including that of hail storms, one has to have detailed measurements of the three-dimensional air flow pattern in and around a storm. The only way to adequately measure air flow inside a storm is by means of at least two Doppler radars, since aircraft can only provide spot measurements in space and time, besides the dangers of penetrating tall convective clouds.

It is EMATEK's aim to continue the study of these processes in clouds. An important point is that synthesis of available data revealed the crucial dependence of hail formation on the air flow patterns inside clouds (Held, 1982). Knowledge and full understanding of the mechanisms of thunderstorms on the Highveld, viz., the relationship between precipitation, either in the form of raindrops or hailstones, and airflow is extremely important for weather modification projects as well as for cloud modellers.

In order to measure air flow inside clouds remotely, modifications were performed to change the Mitsubishi radar at Houtkoppen to operate in the Doppler mode. The CSIR's radar facility was successfully operated during the 1987/88 rainy season (Dicks *et al.*, 1987). Many storms were observed and a good data base of precipitation versus air flow inside storms was collected and stored for subsequent analysis.

Considering severe storm types that occur on the Highveld, the squall line is the one which is characterised by its widespread areal coverage. Most of them are very efficient in producing rain and hail over large areas, but are less frequent than isolated or scattered storms.

In the first progress report of the Precipitation and Airflow Project (PRAI) for the Water Research Commission (Gomes and Held, 1988), severe storm occurrence over the Transvaal Highveld was described. The descriptions, based on coherent as well as Doppler radar data, included analyses of two squall line systems that traversed the Pretoria-Witwatersrand area in November 1987. Several severe thunderstorms occurred in the Pretoria-Witwatersrand area resulting in hail damage and flooding. From the 12-day period chosen for the analysis, from 9 to 20 November, two particular days have been discussed (10 and 19) associated with the passage of a squall line during the late afternoon in the first case and early in the evening in the second one. The characteristic thermodynamic structure of the troposphere and its modification after the passage of the disturbance is highlighted through equivalent potential temperature profiles obtained from Irene upper air sounding data. The analysis, particularly of the radial velocity fields as observed by the Doppler radar, indicated the tendency for storms of this type to exhibit well organised mesoscale features in the mature stage of development. The thermodynamic environment in the form of θ_e profiles in which these storms developed was also considered. The substantial change in θ_e at low levels was highlighted.

Following the recommendations at the end of the first year, a motivation for a second scientist to help with analysis and interpretation of the vast volume of available radar data had been favourably considered by the Water Research Commission. Thus, Mr S O'Beirne, who already had previous experience with the analysis of our radar data, could be appointed with effect from 2 January 1989. This made it possible not only to substantially increase the volume of radar observations being studied in detail, but also to commence with the V x ATI (Volume x Area-Time-Integral) analysis of radar reflectivities as proposed in the work programme for the second year (Gomes *et al.*, 1989).

Unfortunately, bad luck struck the S-band radar at Houtkoppen during the 1988/89 rainy season: right at the beginning of the season the co-axial magnetron began to arc and had to be replaced. Since the spare magnetron was slightly larger than the previously used Varian magnetron, hardware modifications in the transmitter cabinet had to be made before installation which took considerable time. Good radar data were obtained from 8 November 1988 until 4 December 1988, when a direct lightning strike severely damaged most of the electronic circuit boards. Repair work took more than three months by which time the rainy season was almost over and only a few very light storms could be observed. These unexpected problems in turn delayed the schedule for converting the Enterprise C-band radars to Doppler mode considerably since all available manpower had to be utilised for repair work.

Following the recommendations of the Berg-en-Dal Workshop on rainfall stimulation research (21-23 August 1989, informal minutes, WRC, 1990, p28) the sensitivity and resolution of the CSIR's Houtkoppen radar (S-band) was drastically improved from the beginning of the 1989/90 rainfall season. This was achieved by firstly removing the range-correction circuitry from the hardware and then applying range-correction in the software at the processing stage. This increased the sensitivity from 23 dBZ to approximately -10 dBZ. Secondly, the resolution of reflectivity measurements was increased from 16 levels of 3,3 dB intervals (4-bit data-recording format) to 256 levels of 0,25 dB intervals (8-bit data-recording format). Although all storm observations during the 1989/90 season were made in this format, the data could unfortunately not be processed for analysis yet, because the initial data acquisition was made on 800 bpi magnetic tapes, the only data logging system available at Houtkoppen then, while the Central Computer Facility at the CSIR had decommissioned the 800 bpi magnetic tape drive on its mainframe computers. This necessitated the change-over from 800 to 1600 bpi tape drive facilities at Houtkoppen, which had to be executed within the man-power constraints for re-writing the data acquisition programme. Once this was achieved, a copying procedure was written for the new computer which facilitated copying of 800 bpi tapes from the old HP2100 computer to the new HP A400 computer using a 1600 bpi tape drive. The re-written tapes are currently being copied into the CSIR mainframe computer for further processing and archiving.

Also, during the 1989/90 season, the Pretoria C-band Doppler radar had been commissioned, but unfortunately serious interfacing problems were encountered between the hardware output from the modified EEC C-band radar and the Hewlett-Packard A600 computer which proved to be just too slow on some of its peripherals to accommodate the data stream in its entirety. In order to remedy the problems, certain hardware modifications and streamlining of the data acquisition program (which had been subcontracted to a private consultant) had to be undertaken. During the course of many test runs, several other difficulties had to be overcome which resulted from these latest modifications. Therefore, no data could be collected using more than one Doppler radar during the past and current rainy season. However, a few dual Doppler storm records were obtained during March 1991. A very preliminary test case is included in this report. The NCAR programs for processing multiple Doppler radar data, which have already been implemented and are currently being tested on the CSIR's VM mainframe computer are being utilised for the analysis.

1.1 REFERENCES

DICKS D, HODSON M C, HELD G and NEISHLOS H, 1987. Initial results from the newly-developed CSIR Doppler pulse-pair processor. *Abstracts of the 4th Annual Conference of the South African Society for Atmospheric Sciences*, 13-14 October 1987, Pretoria, 27.

GOMES A M and HELD G, 1988. *First progress report: Precipitation and Airflow (PRAI) Project*. CSIR Report EMA-C 8885, Pretoria, 18pp.

GOMES A M, O'BEIRNE S and HELD G, 1989. *Second progress report: Precipitation and Airflow (PRAI) Project*. CSIR Report EMA-C 89126, Pretoria, 42pp.

HELD G, 1982. Comparison of radar observations of a devastating hailstorm and a cloudburst at Jan Smuts Airport. E M Agee ad T Asai (Eds), in *Cloud Dynamics*, 273-284.

WATER RESEARCH COMMISSION, 1990. *Minutes of the Review Workshop on Rainfall Stimulation Research in South Africa*. Berg-en-Dal Conference Centre, Kruger National Park, 21-23 August 1989, 41pp.

2. THERMODYNAMIC AND KINEMATIC PROPERTIES OF HIGHVELD STORMS

Ana Maria Gomes

2.1 CONVECTIVE AVAILABLE POTENTIAL ENERGY (CAPE) OF HIGHVELD STORMS

Cataloguing storm types and representative soundings provides observational evidence on the distribution of storm type as a function of the environment. Modelling represents a powerful way of examining the influence of environmental conditions on the type of storm likely to develop. An additional benefit of modelling is the opportunity to diagnose model fields to describe the relevant physical processes better. By varying conditions and observing the resultant storm type, it is possible to build a conceptual model of a storm type. It may be possible to distinguish between storm types based upon inherent dynamical differences, rather than what might be a superficial difference in appearance.

From the simulations of Moncrieff and Miller (1976), Weisman and Klemp (1982) and others, it is clear that the relationship of buoyancy and shear is fundamentally important in defining storm structure. This is valid for convection ranging from isolated single cells to complex storms such as squall lines. The basic storm structure seems to be controlled by the vertical distributions of buoyancy and winds. Following Moncrieff and Green (1972), convective available potential energy (CAPE) can be written as equation (1):

$$\mathrm{CAPE} = g \int \frac{\theta(z) - \overline{\theta}(z)}{\overline{\theta}(z)}\, dz \qquad (1)$$

where $\theta(z)$ is the potential temperature of a parcel rising moist adiabatically, and $\overline{\theta}(z)$ is the environmental potential temperature. The limits of integration extend through the levels where the parcel temperature exceeds the environmental temperature. Weisman and Klemp (1982) examined the types of storms that formed when the initial conditions in a homogeneous environment were varied. The available energy was varied from 1000 to 3500 $m.s^{-2}$, and the one-dimensional low-level vertical wind shears ranged from 0 to 0,008 s^{-1}. Through this range, many of the different types of storms that are observed in nature were simulated. They also defined a parameter, a bulk Richardson Number similar to that of Moncrieff and Green (1972), given by

$$Ri = \frac{CAPE}{2\ \overline{u}^2} \qquad (2)$$

where CAPE has been defined in Equation (1) and $\overline{u}^2$ represents a difference between the environmental wind speeds at low and middle levels.

Weisman and Klemp (1986) have demonstrated through numerical simulation studies that different storm structures evolve from different environments. The rotation of the wind shear vector with height preferentially promotes the severity of right- or left-moving storms and can differentiate between fundamental storm types. Rotation of the shear vector with height is stressed, because it is easily possible to have curvature or turning of the wind vector with height but have undirectional shear. With adequate buoyancy, these conditions lead to the long-lived, steady state, and often severe storm structures. In stratifying their numerical modelling results, Weisman and Klemp (1982, 1984) found that storms of the long-lived multicellular type were favoured in environments having moderate thermodynamic instability and large vertical shear; a combination that produces relatively low values of Ri. They suggest that for $10<Ri<40$, supercell development is favoured, whereas multicell growth is favoured for higher Ri values.

Following the ideas discussed above, values of CAPE and Ri that would be representative of Transvaal Highveld storms were calculated using 12 GMT soundings from the Irene upper air station during the 85/86, 86/87 and 87/88 seasons. Results are presented in Figure 2.1 for CAPE values as a function of the number of storms which occurred during each season. Values of CAPE range from 800 to 4800 $m^2.s^{-2}$, representing the typical values of convective energy available to develop convection.

A scatter diagram of CAPE values and vertical wind shear values is shown in Figure 2.2, where one can see a large spread of the values, representing conditions of relatively low shear combined with significant convective energy available for convection, and moderate to low CAPE with low to moderate vertical shear. Also interesting is Figure 2.3, where values of the bulk parameter Richardson Number (Ri) are shown for three seasons, compared with the model classification given by Weisman and Klemp (1982).

The storms in the present study varied greatly in size and intensity but in terms of a classification scheme, the storm type was not very diverse. All of the storms exhibited multicellular characteristics during some part of their lifetimes, and none exhibited features that would place them solidly in the supercell category. Although the range in vertical wind shear was comparatively large [1 to 6 (x $10^{-3}s^{-1}$)], weak to moderate instability lead to Ri values that were on the low side (10 to 40); a range typically associated with storms of the supercell type, provided sufficient buoyancy exists. In these cases, our low Ri are more a manifestation of low CAPE values (<1100 $m^2.s^{-2}$) than of strong vertical shear. At this point of the analysis it is opportune to call attention to comparisons of typical values for storms observed in the USA with the ones occurring on the Highveld. Ri values can be used for classification of storm structure, but only in conjunction with the associated CAPE and shear values.

2.2 DETERMINATION OF KINEMATIC PROPERTIES OF THE WIND FIELD USING SINGLE-DOPPLER RADAR

2.2.1 The VAD Method

Lhermitte and Atlas (1961) showed that, in a situation of widespread homogeneous precipitation, the horizontal wind speed and direction can be determined by measuring the radial velocity V as a function of the azimuth at a constant elevation angle (the so-called VAD or Velocity Azimuth Display). Caton (1963) showed that the divergence of the horizontal wind may be calculated from VAD observations.

Browning and Wexler (1968) showed that the information of the horizontal wind also may be obtained from VAD data and they presented a systematic derivation of the VAD analysis method. Their main results will be summarised in this section.

The radial component of the particle velocity is given by

$$V = (u \sin \beta + v \cos \beta) \cos \alpha + w \sin \alpha \qquad (1)$$

where β is the azimuth angle measured clockwise from the north, α is the elevation angle, and u, v, w are the components of the particle velocity along the x-(eastward), y-(northward) and z-(upward) axes, respectively. If for a given range gate

1. u, v, w do not change during the observation period

2. u, v are linear functions of x and y, and

3. w is independent of the position over the VAD circle, then Equation (1) may be rewritten as:

$$V = a_0 + a_1 \sin\beta + b_1 \cos\beta + a_2 \sin 2\beta + b_2 \cos 2\beta \qquad (2)$$

where

$$a_0 = \mathrm{DIV} \frac{r \cos\alpha}{2} + w \sin\alpha \qquad (3)$$

$$a_1 = u_0 \cos\alpha \qquad (4)$$

$$b_1 = v_0 \cos\alpha \qquad (5)$$

Here, DIV is the divergence of the horizontal wind, and u_0 and v_0 are the values of u and v at the centre of the VAD circle, with radius r. The coefficients a_2 and b_2 are related to the deformation of the horizontal wind. In widespread precipitation, the vertical velocity of precipitation is essentially due to the terminal fall speed V_T, i.e.

$$W = w - V_T \sim - V_T$$

hence Equation (3) may be rewritten as

$$a_0 = DIV \frac{r \cos\alpha}{2} - V_T . \sin\alpha \qquad (6)$$

In order to determine the parameters of the wind field, one takes the radial velocity V for a given range over the VAD circle, and then determines the coefficients a_0, a_1, a_2, b_1 and b_2 by Fourier analysis or least-squares fitting procedures. From the coefficients, a_1 and b_1, the horizontal wind speed and direction can be computed. However, the divergence of the horizontal wind can be determined from a_0 only if V_T is known or the elevation angle is so small that the term $V_T . \sin\alpha$ can be neglected in Equation (6). According to Browning and Wexler (1968), inhomogeneities in the particle fall speed can lead to errors in the determination of DIV. For these reasons, Browning and Wexler recommended that, for the determination of DIV, α should be kept small viz. $\leq 9°$ for rain and 27° for snow. Obviously, the upper limit for α would also depend on the accuracy desired in the determination of DIV.

Srivastava *et al.* (1986) proposed a modified VAD method as a way to overcome these limitations, the so-called extended VAD (EVAD) method.

Their extension of the VAD method pivots on a transformation of Equation (6) to read

$$\frac{2a_0}{r \cos\alpha} = DIV - 2 V_T \frac{h}{r^2} \qquad (7)$$

where h is the height corresponding to the horizontal range and elevation angle α. Their basic assumption is that the DIV and V_T are functions of the height only, i.e. they are horizontally uniform. Consider the VAD scans for many paired values of range and elevation angle such that the resulting VAD circles lie in a narrow interval of height over which the DIV and V_T may be regarded constant in height as well. If these conditions are satisfied, then a plot of $2a_0/(r \cos\alpha)$ versus h/r^2 for these VAD scans, should be a straight line according to Equation (7). Conversely, if the plot is a straight line, it is likely that the conditions mentioned above are satisfied. Both the DIV and V_T may be determined from the intercept and the slope of the straight line obtained by least-squares fit to the data. Their extension of the VAD method does not require knowledge of the particle fall speed or restriction of the scans to low elevation angles. On the contrary, it is important for the success of the method that h/r^2, or in other words the elevation angle, should have a sufficient range of variation to enable a proper fit of the data to Equation (7).

When the extended VAD method was compared with deviations of the VAD method proposed by others, it was found that the EVAD has certain advantages over the other methods. First, in the EVAD method u and v are calculated for each VAD circle at different elevation angles representing a narrow height interval. Therefore, the homogeneity and steadiness of the wind field can be checked. Secondly the error of fit of $2a/(r \cos\alpha)$ against h/r^2, by linear regression, provides a built-in test of the validity of some of the assumptions of the EVAD method, namely, the uniformity of W and DIV in the horizontal. Thirdly, and most important, the EVAD method uses the radial velocity data over complete circles, which means that the a_0 determined by a full circle of radial velocity data is related to the average DIV over the circle by Equation (6), even if the velocity field is not linear, provided that V is representative of the average fall velocity within the circumference of the VAD circle. In other words, Equation (6) is not adversely affected by irregular variations in DIV and V when a full circle of data is used.

2.2.2 Preliminary Results of the Extended VAD (EVAD) Analysis

The technique of retrieving kinematic parameters using single-Doppler data, described above, has been implemented and the storm that occurred on 21 November 1987 was selected for EVAD analysis because of its characteristic widespread precipitation.

This squall line was first monitored by the Houtkoppen radar at 14:38 when it was approximately 110 km south-southwest of the radar site. By 16:07, the storm began to traverse the hail-reporting network. Hailfalls were reported in the East Rand and the northern suburbs of Johannesburg. Precipitation measured ranged between 13,2 mm at Bapsfontein, southeast of Pretoria, and 63 mm at Krugersdorp on the West Rand (O'Beirne, 1988). During the next two hours, an extensive trailing stratiform region could be observed (Figure 2.4). The radar was completely embedded in the region of stratiform precipitation, which appeared fairly homogeneous on the PPI reflectivity picture.

From Figure 2.4, one can also see the convective leading edge of the squall line exhibiting cores of 60 dBZ at approximately 45 km north-northeast of the radar. Also to be seen in this Figure is the imaginary EVAD circle of 25 km radius. The VAD analysis was then limited to range gates within a horizontal distance of up to 25 km from the radar, thus avoiding patchy VAD circles.

Vertical profiles of the horizontal wind, divergence and vertical velocity were obtained using the EVAD (Extended Velocity Azimuth Display) method.

The VAD data of the Houtkoppen radar consisted of six sets of complete scans at elevation angles ranging from 1,9 to 50,5 degrees. The range gate spacing was 300 m and the average between successive azimuths was about 1,0 degree. Unfortunately, no data was collected at vertical incidence for this particular storm.

As a first step in the analysis, the radial velocity was reformatted. The reformatting was done by elevation angle and range gate number, after which the velocity data for a complete VAD circle could be conveniently accessed by range gate and elevation angle.

Next, the Doppler velocities for a given VAD circle were fitted according to Equation (2) by a least-squares method and the coefficients a_0, b_1 and b_2 determined. The standard error of the fit was calculated. Each of the Doppler velocities was then re-examined and those that differed from the first by more than twice the standard deviation, were flagged. A second fit was then performed, excluding the flagged velocities or outliers in the distribution.

As mentioned before, the VAD analysis was limited to range gates within a horizontal distance of 25 km from the radar. Upwards of 2500 data points associated with VAD circles for each set of scans were analysed. The resultant set of values consisting of the coefficients a_0, a_1, a_2 and b_2, the error of fit, and other parameters, were arranged by elevation and horizontal range. These data were then classified into height intervals, averaging 500 m in depth.

The coefficients a_1 and b_1 were used to determine the horizontal winds. A linear least-squares fit was then performed, as suggested by Equation 7. The standard error of the fit was determined to locate and reject spurious values of a_0. The final fit yielded values of the DIV as a function of the height.

2.2.3 Profiles of Horizontal Wind Speed and Wind Direction

Profiles of horizontal wind speed and wind direction obtained from the VAD analysis are shown in Figures 2.5 and 2.6. The time-height profile of wind direction, Figure 2.6, shows that in the lower levels, the air flow was predominantly from northeast, veering to southeast and then to southwest at higher levels. In other words, taking into account the movement of the squall line as a whole towards the northeast at an average speed of 35 $km.h^{-1}$, we have a relative front-to-rear flow in the lower levels with a compensating rear-to-front flow in the upper levels relative to the squall line.

The magnitudes of the wind speed range from 3 to 6 $m.s^{-1}$ in the lower and middle levels, increasing to 18 $m.s^{-1}$ at higher levels.

2.2.4 Divergence of the Horizontal Wind

A time-height plot of divergence constructed from six EVAD scans is shown in Figure 2.7. From this Figure, the alternating layers of divergence and convergence can be identified throughout the depth of the EVAD volume.

Below 2,5 km height, the wind shows a strong convergent field having a maximum convergence of about 4 x $10^{-4}s^{-1}$ at 1,0 km AGL. This convergent pattern is alternated with a divergent flow above it. Meanwhile, the mid-level divergent layer increased in thickness and in intensity, showing a strong divergent wind field with a maximum divergence of about 4 x $10^{-4}s^{-1}$ at about 5,5 km height. The upper-level divergent layer persisted throughout the time of the analysis, but it was somewhat weaker at a later stage.

2.2.5 Vertical Air Velocity

The vertical air velocity was determined by numerical integration of the anelastic continuity equation

$$DIV + \partial(\rho w)/\partial Z = 0 \qquad (8)$$

The vertical air velocity is shown in Figure 2.8. Basically, the vertical velocity profile is dominated by mesoscale upward motion during the first five minutes of the analysis and then characterised by downward motions afterwards. The mesoscale downdraught was also well defined, with a depth of about 7 km, indicating its presence over the entire layer and continued to the surface. Typical updraught and downdraught values were 25 $cm.s^{-1}$ with peak values near 1 $m.s^{-1}$ during the period of observation.

2.2.6 Precipitation and Precipitation Efficiency Derived from Single-Doppler Radar

Wilson *et al.* (1981) have examined the use of Doppler radar for the estimation of precipitation rates and efficiencies in stratiform rain situations. Using the divergence values obtained from the VAD method, the mass continuity equation is integrated vertically to obtain the vertical velocity profile. From the vertical velocity and saturation mixing ratio profiles, the height-integrated condensation rate is obtained. The accuracy of this technique to estimate condensation rates is obviously closely related to the accuracy of the vertical velocity profiles. Theoretical precipitation amounts can then be calculated using the equation for the condensation rate.

The condensation rate in the vertical column of air above the radar is assumed to be equal to the precipitation rate (R)

$$R = \int_{\text{Cloud base}}^{\text{Cloud top}} \rho(Z)\ w(Z)\ \frac{dm}{dZ}\ dZ \qquad (9)$$

where m is the saturated mixing ratio with respect to ice or water, which ever is appropriate.

In this case the theoretical VAD-derived rainfall rate is actually an average for a 25 km radius around the radar.

In their study, Wilson *et al.* (1981) have shown very promising results of precipitation and precipitation efficiencies derived from the VAD technique. Since divergence can be shown to be the most error-prone derivable kinematic property, the close correspondence between rain gauge and VAD-derived rainfall rates gives a high degree of confidence in the VAD method. Hobbs *et al.* (1980) have reported a wide range of precipitation efficiencies for western Washington rainstorms. They reported an efficiency of at least 80% in a similar wide cold frontal rain band as described in this case study.

Following a similar approach, condensation rates have been calculated for the storm on 21 November 1987 during the period of 17:27 to 17:55. The results presented in Figure 2.9 illustrate the use of the technique. From the divergence field one can see the evident low-level (0-2 km) convergence responsible for the increase in vertical velocity and consequently the condensation rate also being concentrated at low and middle levels, reaching a maximum at about 2 km AGL.

In addition, the precipitation rate at ground level was obtained by assuming an equilibrium between condensate production and sedimentation of precipitation, which will be referred to as VAD estimated precipitation. Unfortunately, no rain gauge data within a radius of 25 km of the radar was available and the only information that could be used for the calculation was the accumulated hourly rainfall for Jan Smuts Airport, which is 5 km outside the VAD circle in the east-southeast. The VAD derived rainfall for the period 17:27 to 17:55 is shown in Figure 2.10 a, which gives a total of 2,9 mm during a period of 28 minutes. Based on this result, and extrapolating for a one-hour period, the resultant rainfall rate would be 6,2 mm. If the rainfall accumulated during the period of 17:00 to 18:00, 6,7 mm (Figure 2.10b) is used to compare the rate of GAUGE/VAD, the result shows that the VAD during this period estimated 8% less rain than the gauge, resulting in a "precipitation efficiency" of 108% for the period of the analysis.

Obviously, the aim of this exercise is to illustrate that this technique can be used in the calculation of precipitation and precipitation efficiency, which in turn does not exclude other available techniques. Besides, this is certainly not the most ideal case study; because of the scanning cycles the vertical resolution was not as good as for cases described in the literature. However, the VAD technique has been shown to be a very powerful tool for measuring kinematic features of the wind field. The extension of this technique to estimate condensation rate and precipitation rate appears reasonably good, but the accuracy must be checked against the actual rainfall measurements which are not available at this stage of the analysis.

Provided care is taken to obtain an accurate estimate of the surface precipitation of the VAD cylinder, this technique should provide accurate estimates of precipitation efficiency on the mesoscale.

2.3 REFERENCES

BROWNING K A and WEXLER, 1968. A determination of kinematic properties of a wind field using Doppler radar. *J. Appl. Meteorol.*, 7, 105-113.

CATON P G F, 1963. The measurement of wind and convergence by Doppler radar. *Proc. 10th Conference Radar Meteorology*, Washington DC, Amer. Meteor. Soc., 290-296

HOBBS P V, MATEJKA T J, HERZEGH P H, LOCATELLI J D and HOUSE R A Jr, 1980. The mesoscale and microscale structure and organization of clouds and precipitation in mid-latitude cyclones. I: A case study of a cold front. *J. Atmos. Sci.*, 37, 568-596.

LHERMITTE, R M and ATLAS D, 1961. Precipitation motion by pulse-Doppler radar. *Preprints, 9th Conference on Radar Meteorology*, (Norman, Okla), AMS, Boston, 218-223.

MONCRIEFF M W and GREEN J S A, 1972. The propagation and transfer properties of steady convective overturning in shear. *Quart. J. Roy. Meteor. Soc.*, 98, 336-352.

O'BEIRNE S, 1988. *A case-study of a squall-line storm over the Transvaal Highveld.* Unpublished Honours Project, University of the Witwatersrand, Johannesburg, 31.

SRIVASTAVA R C, MATEJKA T J and LORELLO T J, 1986. Doppler radar study of the trailing anvil region associated with a squall line. *J. Atmos. Sci.*, 43, 356-377.

WEISMAN, M L and KLEMP J B, 1982. The dependence of numerically simulated convective storms on vertical wind shear and buoyancy. *Mon. Weath. Rev.*, 110, 504-520.

WEISMAN, M L and KLEMP J B, 1984. The structure and classification of numerically simulated convective storms in directionally varying wind shears. *Mon. Weath. Rev.*, 112, 2479-2498.

WILSON J, CARBONE R and RAMSAY B, 1981. Precipitation and precipitation efficiencies derived from single Doppler radar. *Preprint 20th Conference on Radar Meteorology*, Nov 30 - Dec 3, Boston, Mass., American Meteorological Society, 461-468.

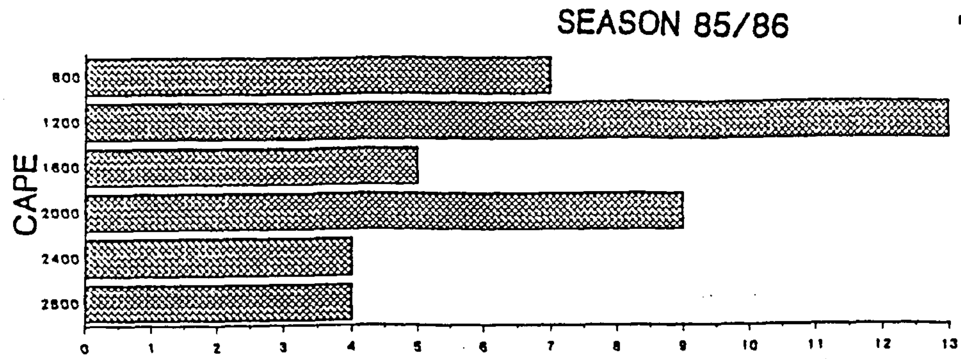

FREQ	CUM. FREQ	PERCENT	CUM. PERCENT
7	7	16.67	16.67
13	20	30.95	47.62
5	25	11.90	59.52
9	34	21.43	80.95
4	38	9.52	90.48
4	42	9.52	100.00

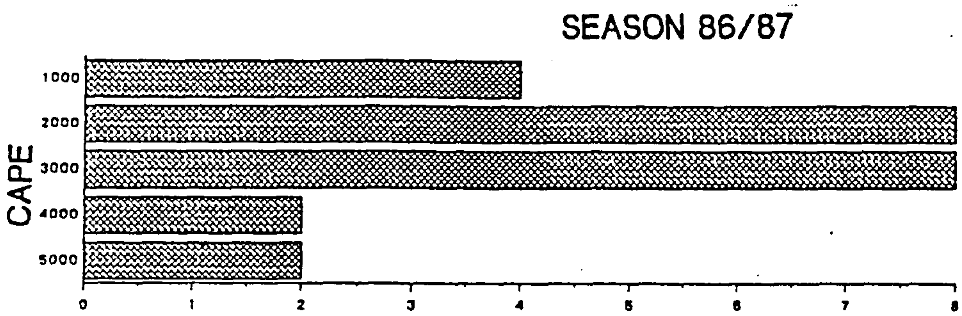

FREQ	CUM. FREQ	PERCENT	CUM. PERCENT
4	4	16.67	16.67
8	12	33.33	50.00
8	20	33.33	83.33
2	22	8.33	91.67
2	24	8.33	100.00

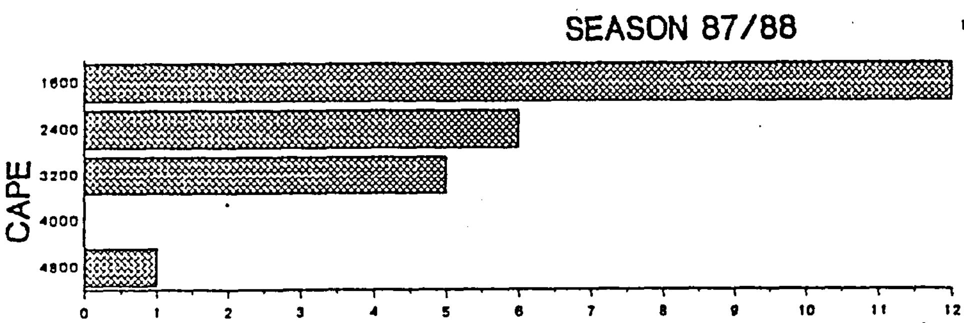

FREQ	CUM. FREQ	PERCENT	CUM. PERCENT
12	12	50.00	50.00
6	18	25.00	75.00
5	23	20.83	95.83
0	23	0.00	95.83
1	24	4.17	100.00

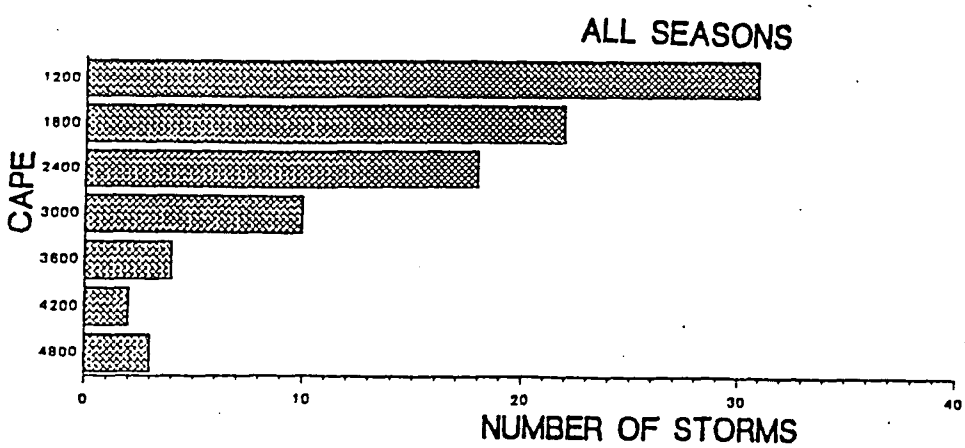

FREQ	CUM. FREQ	PERCENT	CUM. PERCENT
31	31	34.44	34.44
22	53	24.44	58.89
18	71	20.00	78.89
10	81	11.11	90.00
4	85	4.44	94.44
2	87	2.22	96.67
3	90	3.33	100.00

Figure 2.1: Frequency distribution of convective available potential energy (CAPE - $m^2.s^{-2}$) during the seasons 85/86, 86/87, 87/88 and for all three seasons.

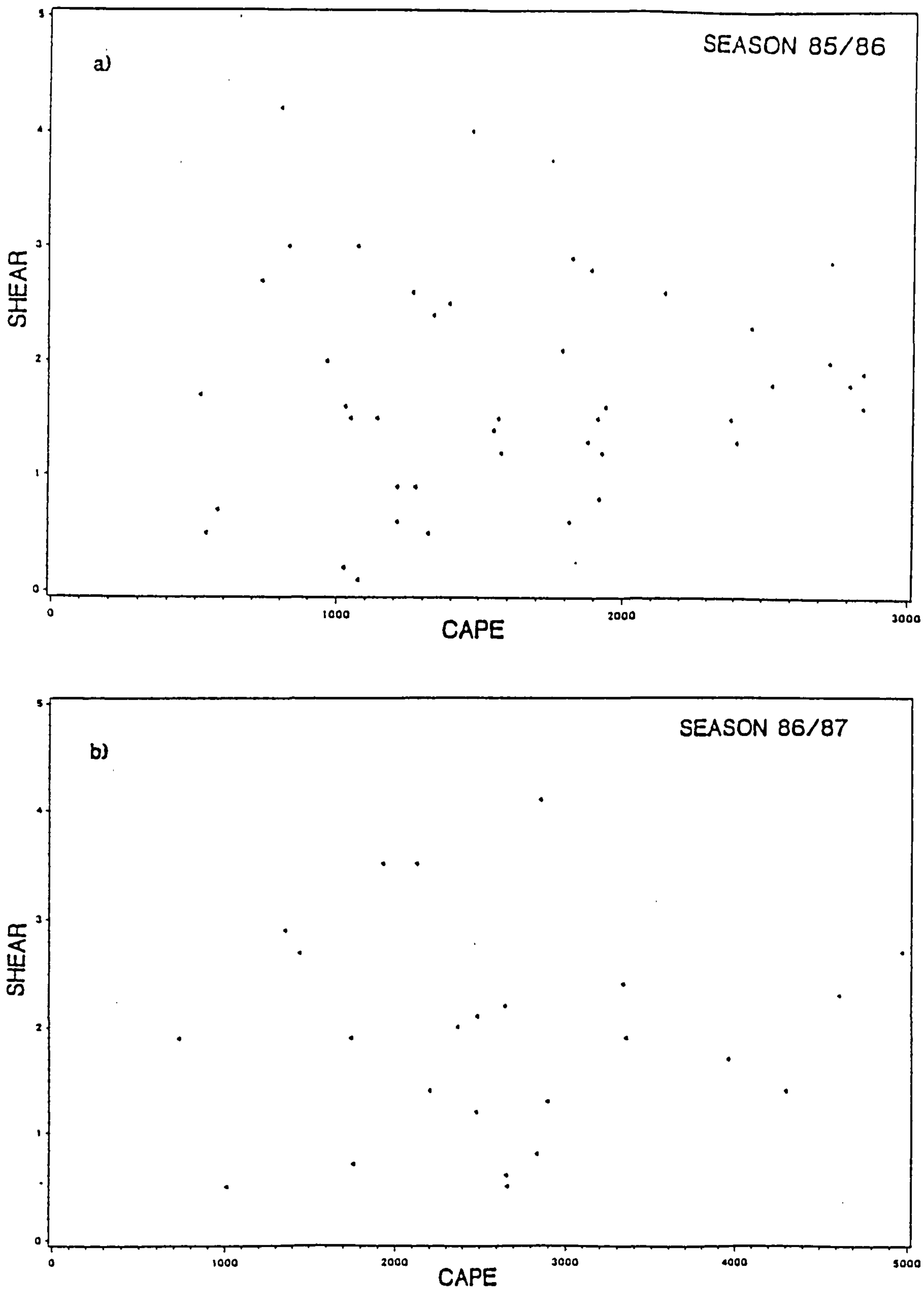

Figure 2.2: Scatter diagram of CAPE ($m^2.s^{-2}$) versus vertical wind shear ($10^{-3}.s^{-1}$).
a) season 85/86, b) season 86/87

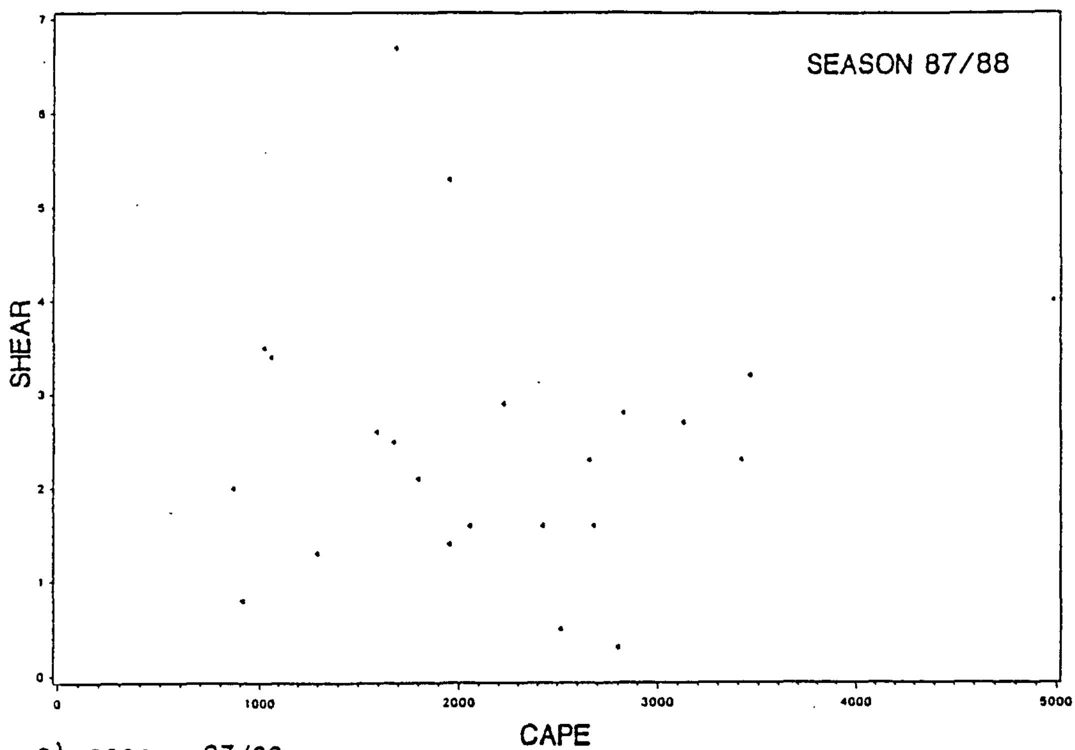

Figure 2.2: c) season 87/88.

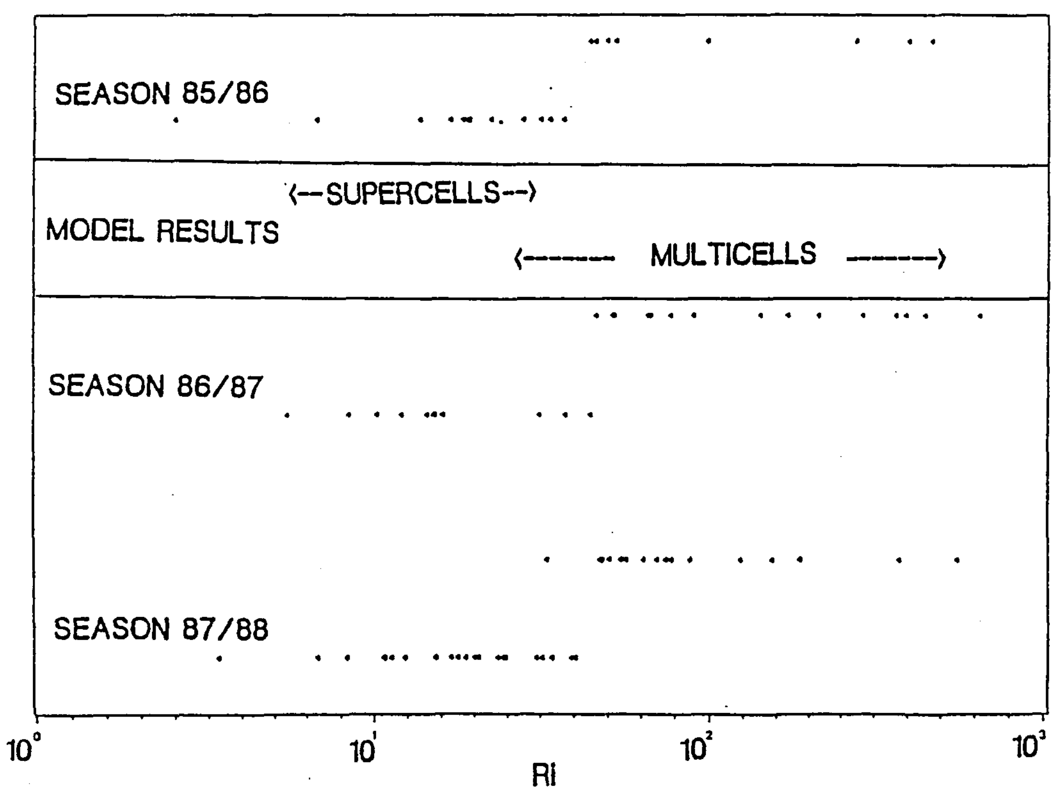

Figure 2.3: Values for Richardson Number (Ri) for seasons 85/86, 86/87 and 87/88 compared with the classification model given by Weisman and Klemp (1982).

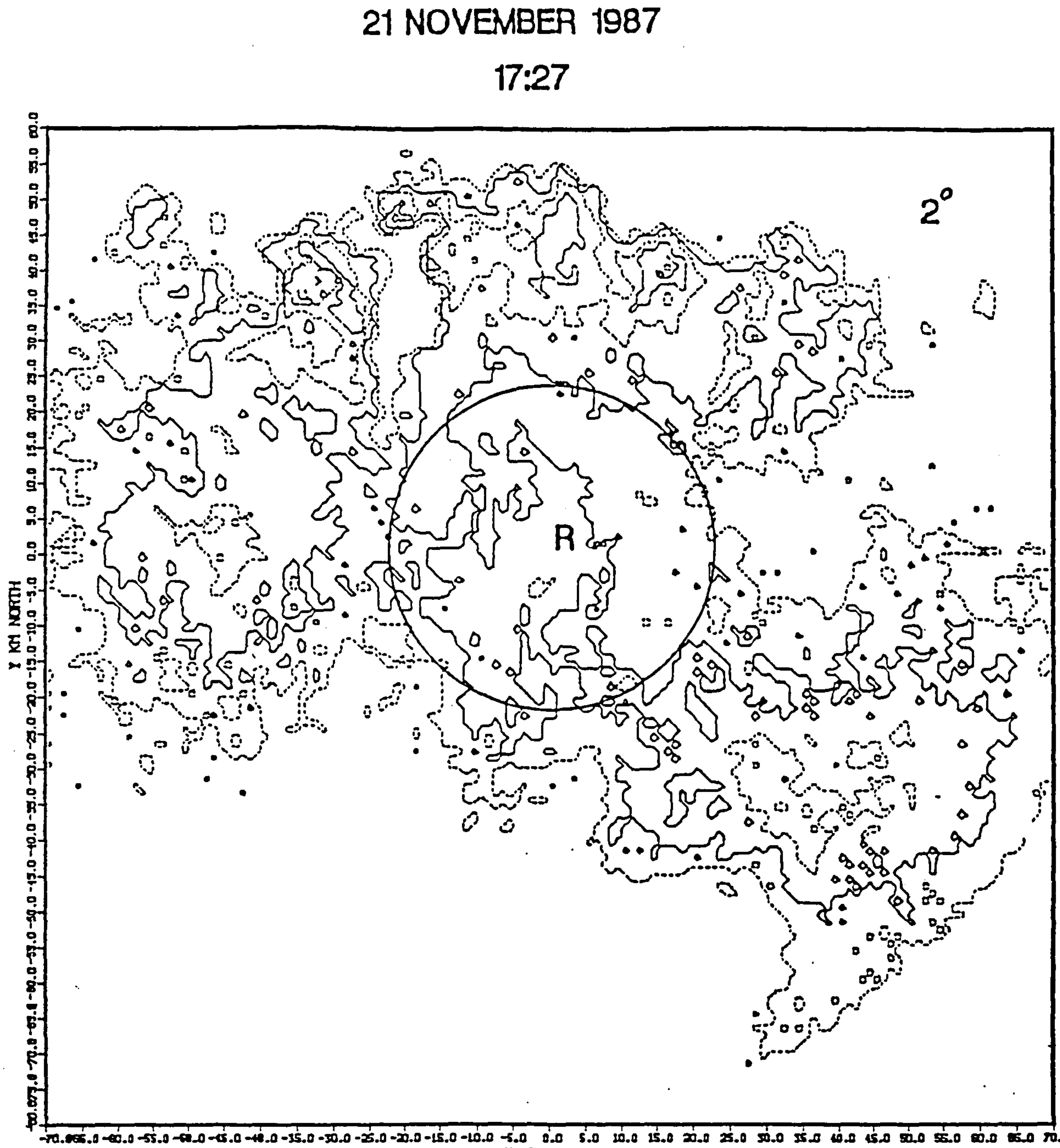

Figure 2.4: PPI reflectivity for 21 November 1987 at 17:27, showing the imaginary EVAD circle of 25 km considered for the analysis. Reflectivity contours are 23,3; 30; 40; 50 and ≥60 dBZ.

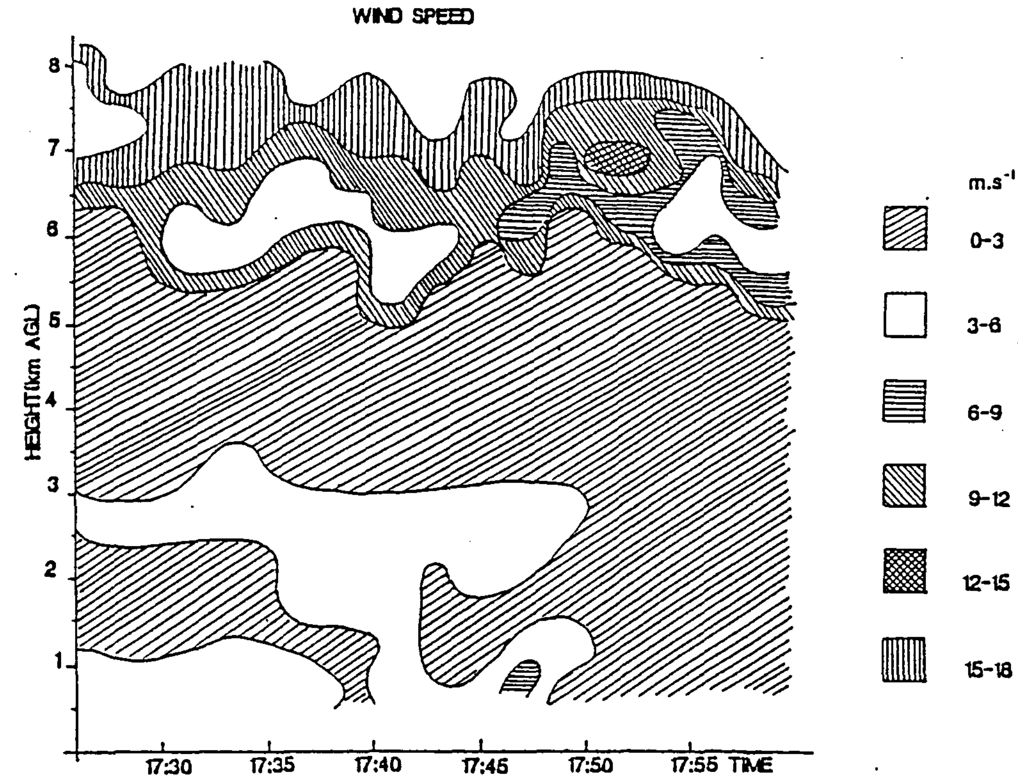

Figure 2.5: Vertical profile of horizontal wind speed (m.s^{-1}), for the 21 November 1987 storm.

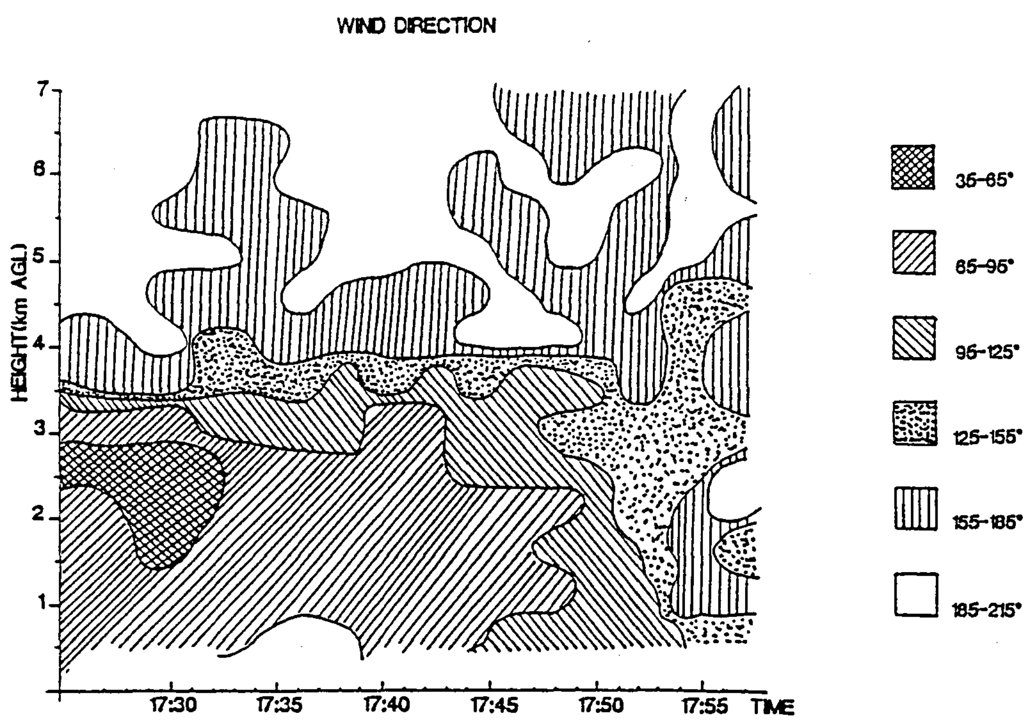

Figure 2.6: Vertical profile of wind direction (degrees), for the 21 November 1987 storm.

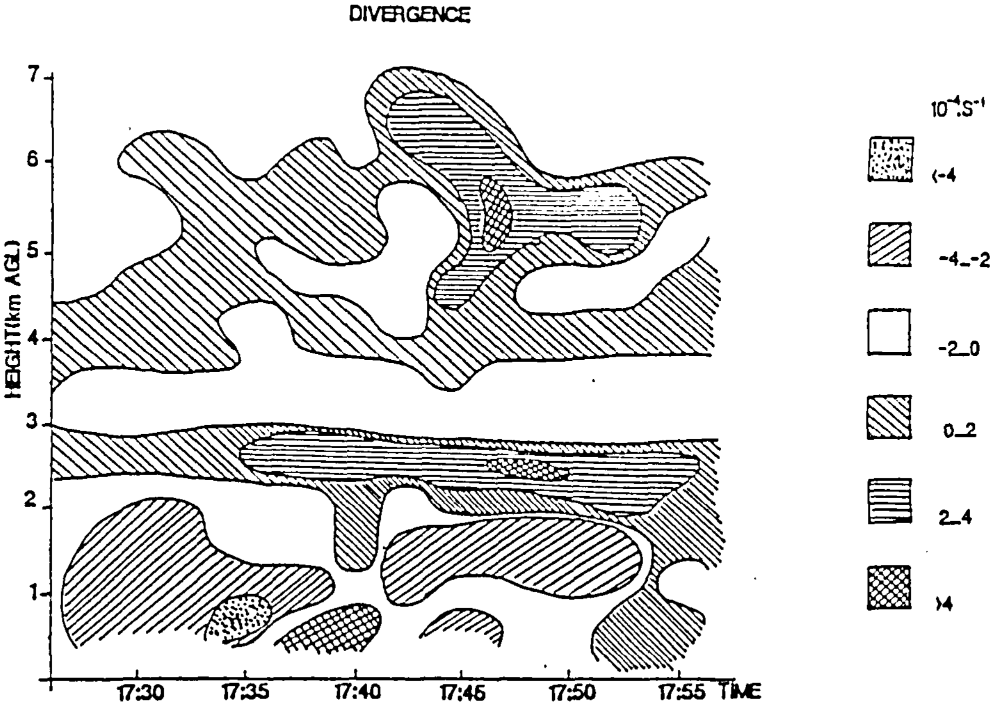

Figure 2.7: Vertical profile of divergence ($10^{-4}.s^{-1}$), for the 21 November 1987 storm.

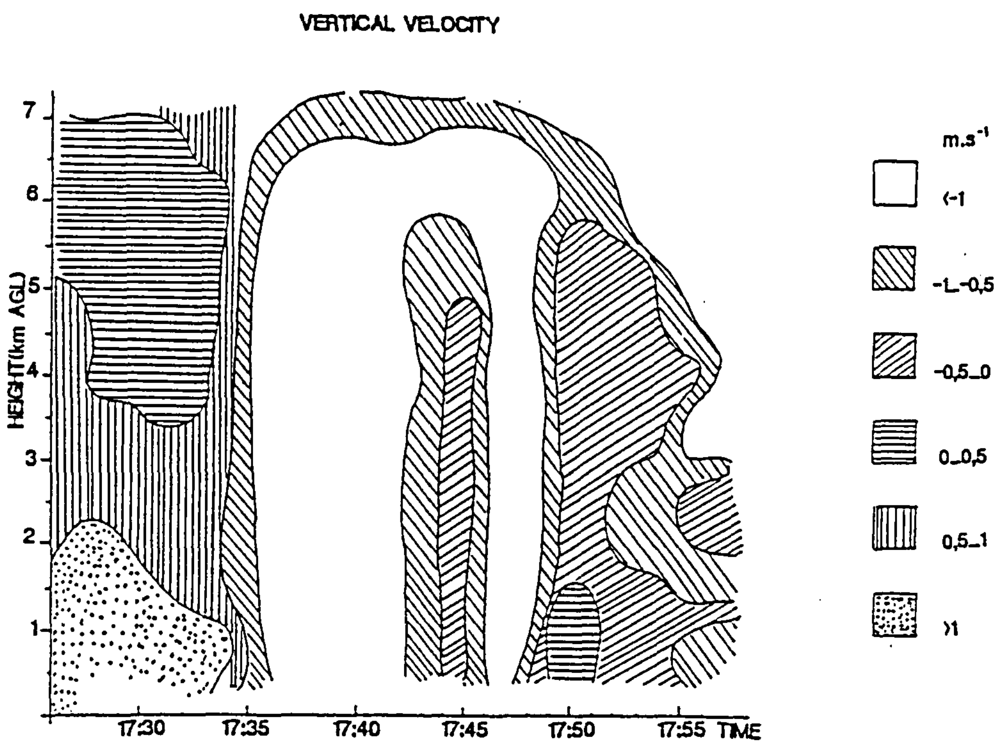

Figure 2.8: Vertical profile of vertical air velocity ($m.s^{-1}$), for the 21 November 1987 storm.

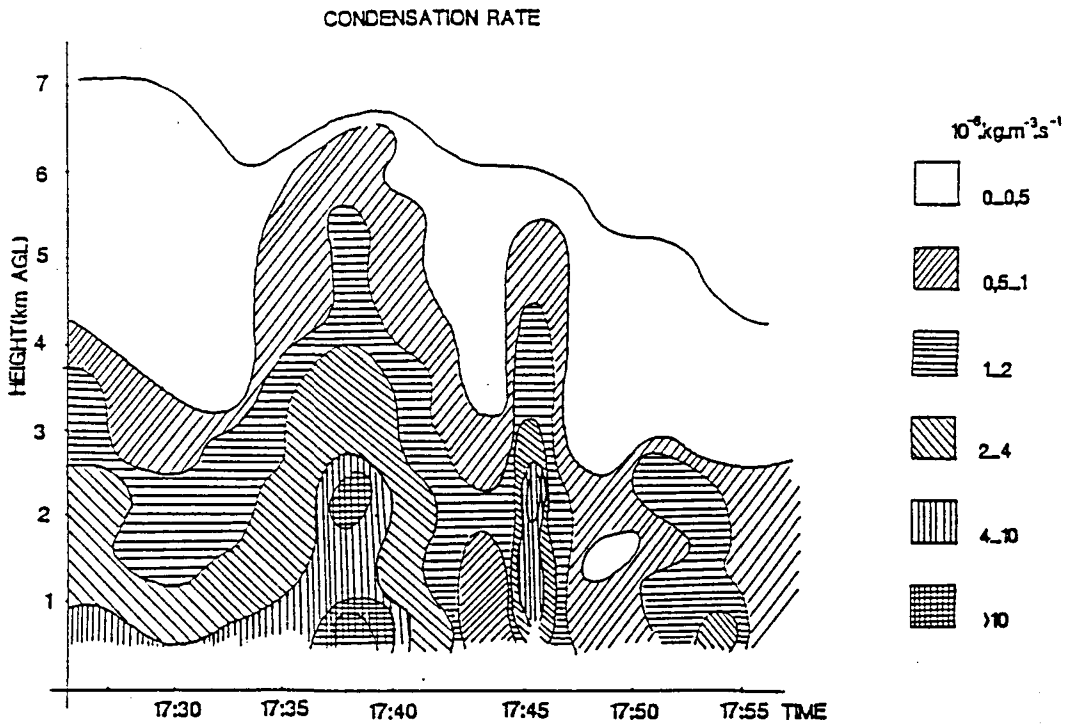

Figure 2.9: Vertical profile of condensation rate (10^{-6}.kg.m^{-3}.s^{-1}), for the 21 November 1987 storm.

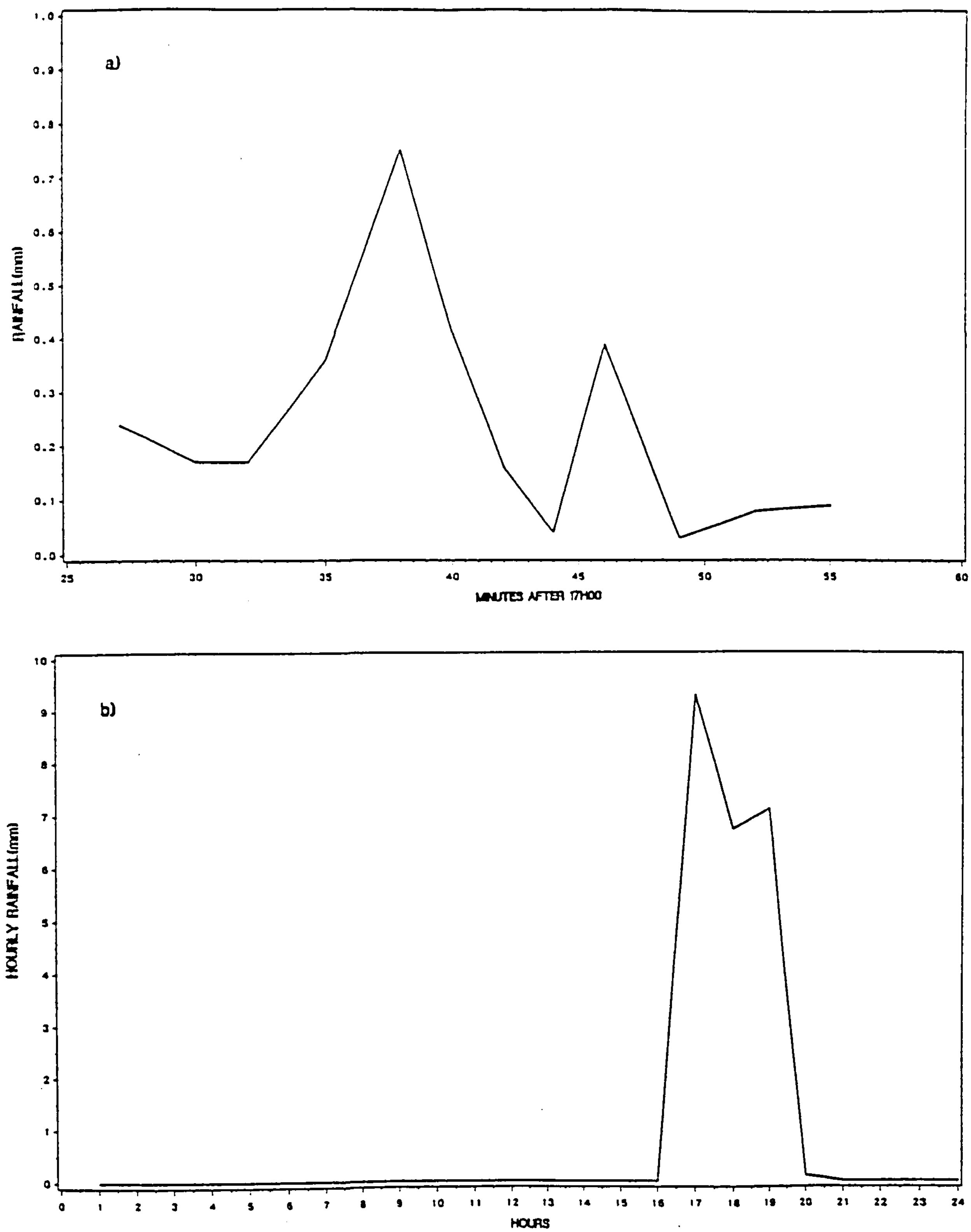

Figure 2.10: a) VAD derived rainfall during 17:27 and 17:55 on 21 November 1987.
b) Hourly rainfall at Jan Smuts Airport on 21 November 1987, which is located about 5 km outside the VAD circle in the east-southeast.

3. RAINDROP SIZE DISTRIBUTIONS AND Z-R RELATIONSHIPS

Sean O'Beirne

3.1 BACKGROUND

The study of drop size distributions (DSD) in rainfalls has a wide range of applications in the field of meteorology. Studies of changes in DSDs may hold important clues in understanding the processes of raindrop evolution. Quantifying pollutant scavenging and the erosional effects of drop impacts on soils requires detailed knowledge of DSDs (Zawadzki and de Agostinho Antonio, 1988). DSD studies having received the most research attention, however, have been those relating DSDs to radar reflectivity in order to realise accurate radar-measurement of rainfall. Indeed, radar reflectivity factor (Z), liquid water content (M) and rainfall rate (R) are all direct functions of a given DSD (Doviak and Zrnic, 1984). Improvements in accuracy of radar-measured rainfall are still dependent on a better understanding of DSDs (Hodson, 1986).

Studies of DSDs have utilised a variety of measurement approaches, from analysis of coloured prints left on dyed absorbant paper (Marshall and Palmer, 1948), through raindrop cameras (Fujiwara, 1965) to electromechanical devices such as spectropluviometers (Donnadieu, 1980) and disdrometers (Joss and Waldvogel, 1967). In addition a number of DSD studies have been based on data from vertically-pointing Doppler radars (Sekhon and Srivastava, 1971; Pasqualucci, 1976; Hodson, 1986). All these studies have pointed to a considerable degree of temporal variation of raindrop spectra which can be related to various physical processes such as drop-sorting, aggregation, coalescence and drop break-up (Joss and Waldvogel, 1988). The variations in raindrop spectra also have a profound influence on rain rates and the reflectivity factor. In the course of this section drop-size distributions measured during the 1989/1990 rainfall season and their implications for radar-measurement of rainfall will be presented.

3.2 THEORY

Although Wiesner (1895) made one of the first known sets of DSD measurements, the work of Marshall and Palmer (1948) has received widest acclaim as seminal work in the field. Using dyed filter paper to measure the distribution of raindrops with size, they proposed a general relation of the form

$$N_D = N_o e^{-\Lambda D} \qquad (1)$$

where D is the raindrop diameter, N_D is the number of drops of diameter between D and D+dD, N_o is the value of N_D for $D = 0$, and Λ is an empirically determined coefficient of rain intensity (Battan, 1973). In addition Marshall and Palmer (1948) found that N_o was a constant and equal to 0,08 cm^{-4} and that

$$\Lambda = 4{,}1R^{-0{,}21}$$

where R is rainfall rate in $mm.h^{-1}$ and Λ in cm^{-1}.

The general applicability of such a relationship was criticised by Mason and Andrews (1960) who showed that while the M-P distribution was suitably representative of DSDs in warm frontal rain, coalescence showers had DSDs that were entirely different.

DSDs measured at the ground were somewhat restrictive in application and attention became increasingly focused on comparisons between DSDs measured at ground level compared with the initial spectra aloft. The importance of DSDs aloft, besides being in the area likely to be measured by radar, had the potential to offer valuable clues as to factors influencing the evolution of raindrop spectra. An initial exponential DSD for example, with a large negative slope would be substantially modified by the effects of coalescence, accretion and evaporation whereas only small changes would be evident in an initial DSD of relatively small negative slope (Hardy, 1963). Hardy concluded that spectra observed at the ground must develop from a distribution aloft having fewer smaller drops and more larger drops than indicated by an M-P distribution.

Srivastava (1967) argued that an M-P distribution would change only slowly during fall and that narrow distributions would rapidly tend towards an exponential distribution. On the basis of this evidence he concluded that the exponential shape of a DSD is due to the coalescence process. The effects of drop break-up were included in subsequent work in which equilibrium distributions were shown to be the result of a balance between drop growth and drop disintegration processes. These equilibrium distributions would be realised more rapidly in situations of higher liquid water content, but it was unlikely that they would be realised in natural conditions of liquid water content and fall distance (Srivastava, 1971). Srivastava noted furthermore that observed distributions were distinctly steeper and limited to smaller sizes than the computed distributions, implying that other processes besides break-up and coalescence were responsible for shaping DSDs, but the omission of factors such as the effects of collisional break-up and condensation may also have played a part.

Making use of a vertically-pointing Doppler radar, Sekhon and Srivastava (1971) measured DSDs at heights below the 0°C-level. Most of the size distributions were found to be well approximated by an exponential distribution but with a steeper curve than that of M-P. Of the conclusions they drew the most profound was that N_0 in fact increases with increasing rain rate and is thus not constant. Joss and Waldvogel (1974) confirmed this finding using ground-based disdrometer measurements and pointing out that the pattern of temporal variation of N_0 may often exhibit a "jump" which appeared to indicate a change in rainfall regime from continuous to convective rain or vice versa.

Young (1975) expanded on the work of Srivastava by improving the computations of the condensation and break-up treatments as well as including the activation of cloud condensation nuclei (CCN). Young utilised two conceptually different models namely "collisional break-up" and "spontaneous disintegration". The spontaneous disintegration model generated an even flatter curve than that produced by Srivastava (1971) leading Young to conclude that it was unlikely that spontaneous break-up was the sole agent in shaping DSDs. The collisional break-up model on the other hand produced a "steady state" spectrum, exponential in form and in fair agreement with M-P. List and Gillespie (1976) modelled DSD evolution in still air assuming warm rain processes. They used only collisional break-up data to produce spectra which had virtually no drops larger than 2,5 mm in diameter but with high concentrations of smaller drops. On the basis of these results List and Gillespie (1976) concluded that the existence of large drops could be solely attributed to ice-phase precipitation mechanisms. Srivastava (1978) in formulating equations by which evolving DSDs could be paramaterised, showed that collisional break-up dominates over spontaneous break-up when the initial number concentrations (N_D) of small drops is within the commonly observed range. When N_D was some two orders of magnitude lower, spontaneous break-up was seen to play a significant role in shaping the observed DSDs.

Carbone and Nelson (1978) using airborne optical spectrometer measurements, together with 3 and 10 cm radars, showed that the temporal evolution of DSDs at cloud base is dominated by updraught sorting (sedimentation) effects where smaller drops do not have sufficient terminal velocity to fall through cloud base. Sedimentation leads to higher numbers of large drops and lower number densities of small drops during the cloud-growth stage. During this stage number densities are typically one order of magnitude lower than M-P at the 1 mm diameter size. During dissipation, drop spectra assume M-P characteristics but rarely achieve comparably high concentrations of small drops or comparably low concentrations of large drops. The agreement found between their own results and those of Srivastava (1971; 1978), suggests that the spontaneous break-up process may be important for rainfall rates in excess of 30 $mm.h^{-1}$ when liquid water content values are greater than 1 $g.m^{-3}$. High variability of drop-spectra precludes the reliable use of conventional radar rainfall (Z-R) estimation techniques in convective precipitation unless some allowance is made for spatial and temporal change. On intensely studied storm days where large quantities of precipitation were produced, early radar echoes resulted from both liquid and ice-phase processes. In particular the question arises as to whether an ensemble of drops will evolve to a unique equilibrium if given enough time. Carbone and Nelson (1978) argued that the findings of their work cast doubt on the concept of a unique equilibrium in the presence of strong vertical air motions.

Hodson (1986) using a vertically pointing Doppler radar as well as data from Pasqualucci (1982a; 1982b) showed that the M-P distribution is entirely inappropriate for rain rates exceeding 25 $mm.h^{-1}$. At rain rates exceeding 25 $mm.h^{-1}$ the slope of the distribution, Λ, will tend towards a constant value between 2,1 and 2,3 mm^{-1}. A Z-R relationship computed from these values gives Z=939R and indicates that attenuation is also proportional to rain rate when the vertical wind velocity is nil. When the rain rate is greater than 25 $mm.h^{-1}$, the M-P distribution applies for drops greater than 3 to 3,5 mm in diameter, but larger drops have decreasing values of Λ arising from drop break-up. Drop break-up data from Low and List (1982) indicate that a large number of drops in the 3 to 3,5 mm size range are generated by drop break-up effects.

Srivastava's (1971) idea of equilibrium drop size distributions, in which drop growth effects were balanced out by drop disintegration effects received considerable attention in the 1980's. Srivastava found that natural levels of liquid water content would not allow realisation of equilibrium in the time or fall distance normally available. List *et al.* (1987) agreed with this claim showing model results of equilibrium DSDs to be trimodal with peaks at drop diameters of 0,268, 0,790 and 1,760 mm. Equilibrium distributions were shown to take time to evolve especially at rain rates of less than 10 $mm.h^{-1}$. In natural, steady rain spectra deviations from equilibria are indicative of a number of features. These features include not yet developed equilibria, changes in rain processes with height and whether rain origin is related to warm or cold cloud processes (List *et al.*, 1987). Using a time-dependent rain shaft model and assuming a M-P distribution with a rain rate of 50 $mm.h^{-1}$, List *et al.* showed that the largest drops would reach the ground first with the onset of rain. As more drops appear the drop spectrum widens rapidly as a result of collisional drop break-up. At high rain rates equilibrium is reached after some 3 km of fall. Results of the model runs showed that small drops measured at the ground do not originate at cloud base but occur rather as a result of collisional break-up effects amongst the larger drops during their fall. Although this specific work was based on assumptions pertaining to warm rain processes, List *et al.*, argued that the results may also represent cold cloud processes where warm rain develops parallel to the ice particles. List (1988) showed that any DSD will develop with time into an equilibrium DSD regardless of the initial spectrum. All equilibrium distributions have the same shape with observed differences being related to a factor proportional to rain rate.

3.3 INSTRUMENTATION

Drop-size distributions were measured using a Joss-Waldvogel raindrop disdrometer (Joss and Waldvogel, 1967) which was operated on the roof of the Atmos Building within the CSIR campus. The principle of operation of the disdrometer is that a voltage is induced into a sensing coil by the downward displacement of a styrofoam body. This signal is amplified and applied to another coil within the transducer to counteract the movement of the body and return it to its rest position (Figure 3.1). Thus, the instrument retains a high recovery rate and is capable of measuring several hundred drops a second (Waldvogel, 1974; Kinnel, 1976). The disdrometer was housed in a polystyrene-lined box to dampen extraneous noise from the drops hitting the roof and covered with foam rubber to prevent splashing effects. The disdrometer was operated in close proximity to a tipping-bucket rain gauge allowing appraisal of the disdrometer in measuring rainfall. Unfortunately some teething troubles with installing the disdrometer meant that continuous measurement was only effected from the end of November. The disdrometer was subsequently operational for the duration of the 1989/1990 rainfall season.

Rainfall totals measured using the disdrometer compared reasonably well with totals measured using the tipping-bucket rain gauge with a mean difference between the two instruments for 26 rain episodes of -0,097 mm. Significant departures for individual rain episodes are apparent, however, of which underestimates by the disdrometer during periods of high rain rate are most significant (Figure 3.2). The underestimation appears to be related to an instrument deficiency in that smaller drops are not always registered during high rain rates due to instrument dead-time. Various authors have reported this problem including Joss and Gori (1978) and List (1988). List in particular compared DSDs measured by disdrometer with those measured using a laser spectrometer. Small drops measured by the spectrometer were not recorded by the disdrometer in high rainfall rates. The deficiency should not detract too much from the usefulness of the instrument. Although rain rates may be underestimated on some occasions, calculation of the reflectivity factor will not be significantly affected by drops of less than 1 mm in diameter.

3.4 Z-R RELATIONSHIPS

There are a number of ways by which average DSD patterns can be represented. Of these the most widely used remains an average Z-R relationship. Radar reflectivity factor (Z) is given by the summation of the sixth power of drop diameters

$$Z = \int_0^\infty N_D D^6 dD \tag{2}$$

and is expressed in units of $mm^6.mm^{-3}$. Rainfall rate is given by

$$R = \frac{\pi}{6}\int_0^\infty N_D D^3 Vt_D dD \tag{3}$$

assuming the terminal velocity of drops (Vt) is constant (Wilson and Brandes, 1979). The relationship between Z and R is usually expressed in an empirically-determined equation of the form

$$Z = aR^b \tag{4}$$

with values of a and b most commonly following those proposed by Marshall and Palmer (1948), viz. a = 200 and b = 1,6. Using the above equations to determine values of Z and R from the disdrometer data, a least squares regression fit with coefficients a = 300 and b = 1,4 was computed (Figure 3.3).

The general applicability of an average Z-R relationship has received criticism from as far back as 1965, however, when Fujiwara (1965) using a drop size camera indicated the need for different Z-R relationships for different rain types. Wide-ranging values for the coefficients a and b have been mooted from all over the world. Not only do Z-R relationships differ from place to place but also from storm to storm in the same place and even during the same storm event. Z-R variability is probably best summarised by the much-quoted example of Battan (1973) having documented over 65 different Z-R relationships. Carbone and Nelson (1978) showed that it was necessary to use different Z-R relationships depending on whether the storm was growing or dissipating and Hodson (1986) contended that the widely used M-P relationship is inappropriate at rainfall rates which exceed 25 $mm.h^{-1}$.

Significant Z-R variability is evident in convective storms over the Transvaal Highveld. By computing Z-R relationships for individual rain episodes during the 1989/1990 rainfall season, wide ranging values of the coefficients a and b are seen to exist (Figure 3.4). A series of Z-R relationship calculations at 5 $mm.h^{-1}$ intervals indicated that 25 $mm.h^{-1}$ is in fact a threshold above which the Z-R relationship differs significantly from the Z-R for all rainfall rates. A Z-R relationship of the form $Z = 638\ R^{1.28}$ was thus calculated for rain rates exceeding 25 $mm.h^{-1}$ on the Transvaal Highveld (Figure 3.5). Hodson's (1986) Z-R relationship for rain rates exceeding 25 $mm.h^{-1}$ is $Z = 939\ R$. Hodson based his Z-R computation on the assumption that the slope of the DSD, Λ, will become constant at 2,2 mm^{-1} in rain rates exceeding 25 $mm.h^{-1}$. A scatter plot of the relationship between rain rate and Λ determined from DSDs measured by disdrometer (Figure 3.6) indicates that although there is a definite trend towards a constant value of Λ, the constancy is only realised at rainfall rates exceeding 100 $mm.h^{-1}$ as Willis and Tattleman (1989) also suggest. In addition, Hodson shows how Pasqualucci's (1982a; 1982b) data from a vertically pointing Doppler radar indicates a constant value of Λ for liquid water content values exceeding 1,2 $g.m^{-3}$. A scatter plot of the relationship between liquid water content and lambda determined from the disdrometer data shows a similar pattern (Figure 3.7).

3.5 DROP SIZE DISTRIBUTIONS

Marshall and Palmer's (1948) investigation of the distribution of raindrops with size was based on time-averaged DSDs. Average DSDs for individual rain episodes over the Transvaal Highveld as measured by the disdrometer tend to be flatter than M-P curves with fewer small drops and more large drops (Figure 3.8). The temporal variation of DSDs is not represented in either a time-averaged DSD or an average Z-R relationship, however. The extent of the temporal variability of DSDs is clearly evident in a three-dimensional drop size distribution field (Figure 3.9). In order to quantify temporal variability in drop size spectra, Waldvogel's (1974) parameterisation method was used. Waldvogel based his technique on the assumption that a DSD averaged over one minute would be adequately described by an exponential distribution. The exponential distribution could be described in turn by the intercept value, N_o, and the slope, Λ. N_o and Λ are obtained by substituting for the number of drops N_D (Eqn. 1) in the equations for calculating liquid water content (W) and radar reflectivity factor (Z) as follows:

$$W = \frac{\pi}{6}\int_0^\infty N_D D^3 dD = \frac{\pi}{6} N_o \int_0^\infty e^{-\Lambda D} D^3 dD \tag{4}$$

$$Z = \int_0^\infty N_D D^6 dD = N_o \int_0^\infty e^{-\Lambda D} D^6 dD \tag{5}$$

N_o and Λ can now be calculated from Eqs. (4) and (5)

$$N_o = \frac{1}{\pi}\left(\frac{6!}{\pi}\right)^{4/3}\left(\frac{W}{Z}\right)^{4/3} W = 446\left(\frac{W}{Z}\right)^{4/3} W \tag{6}$$

$$\Lambda = \left(\frac{6!}{\pi}\right)^{1/3}\left(\frac{W}{Z}\right)^{1/3} = 6,12\left(\frac{W}{Z}\right)^{1/3} \tag{7}$$

Changes in rain rate, liquid water content and radar reflectivity factor can then be related to changes in the drop size spectra. In Figure 3.10, N_o, Λ and rain rate have been plotted as functions of time. At 16:30 (marked "a" in Figure 3.10), a pattern of moderately decreasing values of N_o and a considerable decrease in Λ are associated with a significant increase in rainfall rate. A flat slope and a low intercept value imply that the DSD is dominated by large drops with relatively few smaller drops. Such a pattern is similar to patterns derived from theoretical studies such as those of List (1988) who used a time dependent rain shaft model to show that the cloud base spectrum would be significantly modified by drop-sorting (sedimentation) effects. Drop sorting is the process by which only large drops have sufficient terminal velocity to fall through an updraught. The resultant DSD at ground level would thus be characterised by an initial scattering of large drops. As the numbers of the large drops increase, smaller drops would begin to appear in the spectra. These small drops would originate as a result of collisional break-up effects, rather than having originated at cloud base. Such a pattern can be seen at 16:35 (marked "b" in Figure 3.10) where an increase in the numbers of small drops is evidenced by a significant increase in N_0 and a moderate increase in Λ.

The effect is even more pronounced in a storm of 22 December 1989 at 18:18 (Figure 3.11). There is an initial, parallel decrease in N_0 and Λ. Both increase marginally in conjunction with a slight decrease in rainfall rate before Λ decreases again while N_0 remains relatively low as the rainfall rate increases. Between 18:24 and 18:25 (marked "a" in Figure 3.11), N_0 exhibits a "jump" similar to that described by Waldvogel (1974), of slightly more than one order of magnitude. At the same time Λ steepens and rainfall rate continues to increase. Λ subsequently decreases and the rainfall rate peak of 46,5 $mm.h^{-1}$ coincides with high values of N_0 and low values of Λ (marked "b" in Figure 3.11). Stratiform rain on the other hand, without significant drop-sorting effects shows an entirely different pattern. On 4 March 1990 a convective storm system passed over the disdrometer site trailing an extensive region of stratiform rain. Rain fell intermittently for some 6 hours. After an initial downpour with the passing of the leading edge of the storm, rain had stopped falling by 21:59 and very gradually began to fall again after 22:00. The parallel increase in N_0 and Λ implies that drop size spectra had no large drops (marked "a" in Figure 3.12). The pattern prevails for about 10 minutes before decreases in both N_0 and Λ indicate an influx of large drops (marked "b" in Figure 3.12). Whether the influx of large drops is related to processes of rain drop evolution at cloud base or whether they have arisen from drop coalescence effects cannot be resolved.

In order to consider the effects of changing drop spectra on rain rate and reflectivity factor, the storm of 8 December 1989 is once again considered. In Figure 3.13b, the variation of the rain rate with time is compared with that of the reflectivity factor. Radar reflectivity exceeds rain rate at "a" whereas rain rate exceeds radar reflectivity at "b" and at "c". At "d" radar reflectivity changes from exceeding rain rate to underestimating rain rate in response to a changing DSD while rain rate remains reasonably constant.

Individual analyses are restrictive to an extent in considering seasonal patterns and trends. Values of Z and R were thus plotted as functions of N_0 and Λ in order to summarise the relationship between changes in DSD and changes in rain rate and radar reflectivity (Figure 3.14). Of particular interest is the wide range of possible DSD spectra for each of the four groups of rain rate. Each plot is further divided into two groups of four blocks. The solid lines indicate seasonal median values of N_0 and Λ. Median values were decided on as the most likely representation of an equilibrium DSD in which drop growth effects are balanced out by drop disintegration effects (Srivastava, 1971; Zawadzki and de Agostinho Antonio, 1986; List, 1988). The dashed lines indicate median values for the individual rain episodes. In the case of 4 March 1990 (Figure 3.14c), in which initial convective activity was followed by a prolonged period of stratiform rain, the median values are very close to equilibrium. Both 8 December and 22 December 1989 have much flatter median slopes implying greater numbers of large drops and the likelihood that smaller drops evident in the spectrum occurred as a result of drop break-up effects.

Data from the entire season was subsequently summarised in this way. A variety of combinations of N_0 and Λ are evident from individual analyses and therefore all possible combinations were considered. These combinations are summarised in Table 3.1.

Table 3.1: Possible combinations of N_o and Λ and related characteristics of the DSD

N_0	Λ	Characteristics of the distribution
Median	Median	Equilibrium distribution
Median	Above median	Few large drops. Possible drop break-up effects
Median	Below median	More large drops. Drop coalescence and/or large drops originating at cloud base
Above median	Median	Higher numbers of drops across the spectrum High rain rates
Above median	Above median	Large numbers of small drops. Considerable drop break-up effects
Above median	Below median	Higher numbers of drops across the spectrum, but with relatively more larger drops
Below median	Median	Few drops across the entire spectrum
Below median	Above median	No large drops. Few small drops
Below median	Below median	Scattering of larger drops. Drop-sorting or coalescence effects

Each of the categories from Table 3.1 was incorporated into the N_o - Λ plot by adding the 25 and 75% quartiles from the entire data set. The divisions were then labelled A1 to D4 (Figure 3.15). Divisions within the quartiles (i.e. C1 to C4, B1 to B4, D2, D3, A2 and A3) are interpreted as the equilibrium values referred to in Table 3.1. Block A1 would thus represent below median values of N_o and below median values of Λ whereas block D1 would represent above median values of N_o with below median values of Λ. For each of the 16 blocks, rainfall rate measured by disdrometer was compared to rain rate as computed using the average Z-R relationship. The results are summarised in Table 3.2. It can be seen from the table that the maximum rain rate in block A1 was overestimated by the average Z-R relationship by about 55%. The maximum rain rate on this occasion was 116 $mm.h^{-1}$. In block D1 on the other hand, the maximum rain rate of 196 $mm.h^{-1}$ was underestimated by 36% using the average Z-R relationship. Similarly in blocks A4 to D3 in which similar rain rates were measured, the average Z-R relationship can both overestimate and underestimate the rain rate depending on the drop-size distribution.

Table 3.2: Differences between rain rate as measured and rain rate computed using an average Z-R relationship of $Z = 300\ R^{1.41}$

		1	% contribution *	2	% contribution	3	% contribution	4	% contribution
A	Mean	11,24%	13,2	-16,67%	9,6	-17,65%	9,3	-16,67%	4,9
	Min	-74,00%		-71,43%		-75,00%		-50,00%	
	Max	-54,69%		-25,12%		-18,33%		-15,79%	
B	Mean	24,00%	7,6	-3,75%	6,9	4,00%	6,8	8,33%	3,5
	Min	-65,00%		-24,19%		-9,09%		-8,33%	
	Max	-40,80%		-6,41%		9,09%		11,90%	
C	Mean	26,06%	3,9	19,77%	6,6	23,26%	7,0	24,00%	3,0
	Min	-4,23%		3,82%		10,20%		8,33%	
	Max	-12,92%		21,40%		23,22%		28,87%	
D	Mean	36,66%	2,3	39,64%	5,0	44,67%	7,6	47,77%	2,8
	Min	19,89%		25,73%		28,71%		32,79%	
	Max	36,19%		46,39%		53,63%		57,24%	

* refers to the percentage of values in each sector.
\+ indicates that measured rain rate is greater than the calculated one.
\- indicates that measured rain rate is less than the calculated one.

3.6 CONCLUSIONS

In the course of this section raindrop size distributions as measured at ground level using a raindrop disdrometer were discussed. An average Z-R relation of the form $Z=300R^{1.4}$ was calculated. The considerable degree to which DSDs may vary over time was highlighted and the effects of changing DSDs on rain rate and radar reflectivity factor were considered. Variations in DSDs were shown to cause both underestimation and overestimation of rain rate when using an average Z-R relation at both high and low rain rates depending on the shape of the drop spectra.

The results must be seen in the context of the limitation of this study. These include the fact that data from only one season was utilised in the study and that only ground-based measurements were considered. The degree to which DSD variability at the ground reflects that at cloud base needs more detailed investigation. The results do give some ideas though as to the sort of processes that act upon DSDs and how these effects are likely to influence the accuracy of radar-measured rainfall. What is clear from the results is that an average Z-R relation, although fundamental to radar-rainfall measurement should not be used without regard to the processes mentioned above.

3.7 REFERENCES

BATTAN L J, 1973. *Radar Observations of the Atmosphere*, University of Chicago, Chicago.

CARBONE R E and NELSON L D, 1978. The evolution of raindrop spectra in warm-based convective storms as observed and numerically modelled, *J. Atmos. Sci.*, 35, 2302-2314.

DONNADIEU G, 1980. Comparison of results obtained with the VIDIAZ spectropluviometer and the Joss-Waldvogel raindrop disdrometer in "rain of a thundery type", *J. Appl. Meteor.*, 19, 593-597.

DOVIAK R J and ZRNIC D S, 1984. *Doppler Radar and Weather Observations*, Academic Press, Orlando.

HARDY K R, 1963. The development of raindrop size distributions and implications related to the physics of precipitation, *J. Atmos. Sci.*, 20, 299-312.

HODSON M C, 1986. Raindrop size distributions, *J. Climate Appl. Meteor.*, 25, 1070-1074.

FUJIWARA M, 1965. Raindrop size distributions from individual storms, *J. Atmos. Sci.*, 22, 585-591.

JOSS J and GORI E G, 1978. Shapes of raindrop size distributions, *J. Appl. Meteor.*, 17, 1054-1061.

JOSS J and WALDVOGEL A, 1967. Ein Spektrograph fur Niederschlagstropfen mit automatischer Auswertung, *Pure Appl. Geophysics*, 68, 682-688.

JOSS J and WALDVOGEL A, 1988. Precipitation measurement and hydrology, in ed Atlas, D, *Radar in Meteorology*, Amer. Meteor. Soc., Boston, 557-606.

KINNEL P I A, 1976. Some observations of the Joss-Waldvogel rainfall disdrometer, *J. Appl. Meteor.*, 15, 499-502.

LIST R, 1988. A linear radar reflectivity-rainrate relationship for steady tropical rain, *J. Atmos. Sci.*, 45, 3564-3572.

LIST R and GILLESPIE J R, 1976. Evolution of raindrop spectra with collision-induced break-up, *J. Atmos. Sci.*, 33, 2007-2013.

LIST R, DONALDSON N R and STEWART R E, 1987. Temporal evolution of drop spectra to collisional equilibrium in steady and pulsating rain, *J. Atmos. Sci.*, 44, 362-372.

MARSHALL J S and PALMER W McK, 1948. The distribution of raindrops with size, *J. Meteor.*, 5, 165-166.

MASON B J and ANDREWS J B, 1960. Drop size distributions for various types of rain, *Quart. J. Roy. Meteor. Soc.*, 86, 346-353.

PASQUALUCCI F, 1975. Low altitude Doppler radar measurements of precipitation at vertical incidence, *16th Radar Meteorology Conf.*, Houston, American Meteorological Society, 415-420.

PASQUALUCCI, F 1982a. Drop size distribution measurements in convective storms with a vertically pointing 35 GHz Doppler radar. Multi-Parameter measurement of precipitation, *U.R.S.I. Open Symposium*, Bournmouth, U.K., U.R.S.I. and I.E.E., 139-144.

PASQUALUCCI F, 1982b. The variation of drop size distribution in convective storms: A comparison between theory and measurement, *Geophys. Res. Lett*, 9, 839-841.

SEKHON R S and SRIVASTAVA R C. 1970. Doppler radar observations of drop-size distributions in a thunderstorm, *J. Atmos. Sci.*, 28, 983-994.

SRIVASTAVA R C, 1967. On the role of coalescence between raindrops in shaping their size distribution, *J. Atmos. Sci.*, 24, 287-292.

SRIVASTAVA R C, 1971. Size distributions of raindrops generated by their break-up and coalescence, *J. Atmos. Sci.*, 28, 410-415.

SRIVASTAVA R C, 1978. Parameterisation of raindrop size distributions, *J. Atmos. Sci.*, 35, 108-117.

WALDVOGEL A, 1974. The N_o jump of raindrop spectra, *J. Atmos. Sci.*, 31, 1067-1078.

WIESNER J, 1895. Beitrage zur Kenntnis des tropischen Regens, *Bericht Math. Nat.Kl.*, Wien, 104.

WILLIS P T and TATTLEMAN P, 1989. Drop-size distributions associated with intense rainfall, *J. Appl. Meteor.*, 28, 3-15.

WILSON J W and BRANDES E A, 1979. Radar measurement of rainfall - a summary. *Bull. Amer. Meteor. Soc.*, 60, 1048-1058.

YOUNG K C, 1975. The evolution of drop spectra due to condensation, coalescence and break-up, *J. Atmos. Sci.*, 32, 965-973.

ZAWADZKI,I and DE AGOSTINHO ANTONIO M, 1988. Equilibrium raindrop size distributions in tropical rain, *J. Atmos. Sci.*, 45, 3452-3459.

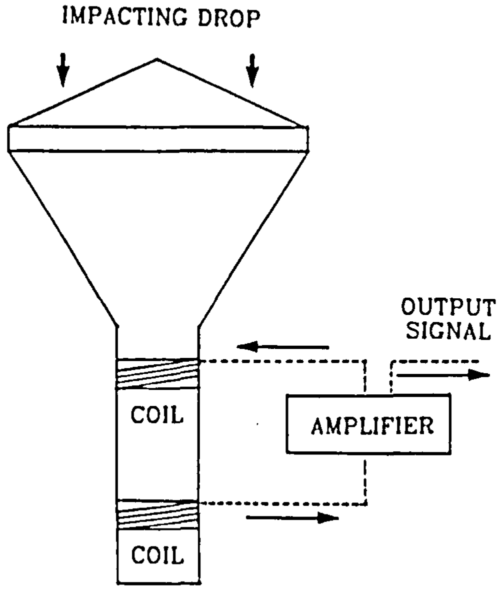

Figure 3.1: Schematic illustration of the principle of operation of the raindrop disdrometer.

Please note that in the following figures the variables R, Z, N_D and N_0 are plotted against logarithmic axes. All other variables are plotted against linear axes.

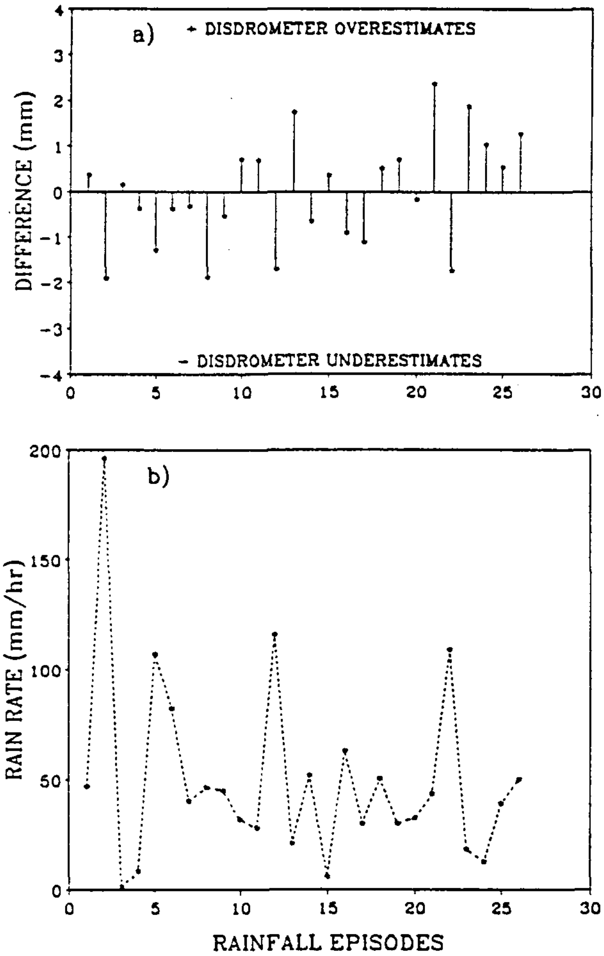

Figure 3.2: a) Differences between rain totals measured by disdrometer and those measured by tipping-bucket rain gauge for 26 consecutively numbered rain episodes during the 1989/90 rainfall season.
b) Maximum rainfall rates per minute for the rain episodes used in the above gauge/disdrometer comparison.

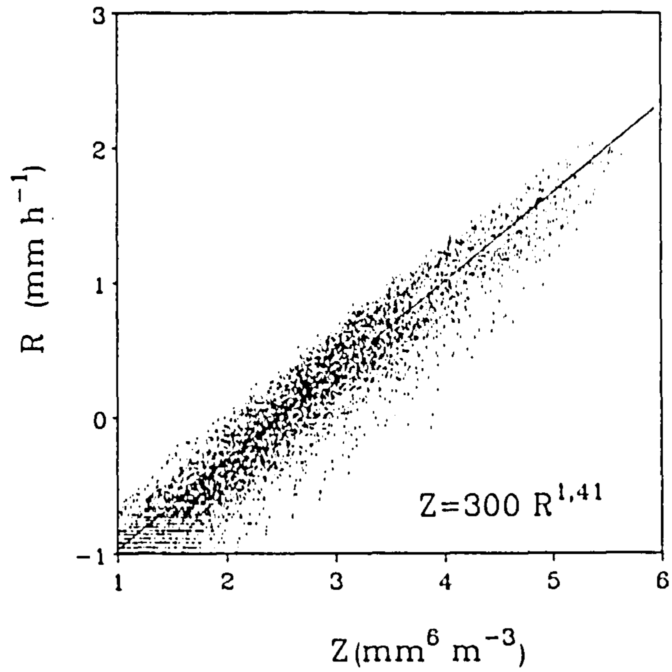

Figure 3.3: Scatter plot of the relationship between Z and R computed from disdrometer data recorded in Pretoria during the 1989/90 season.

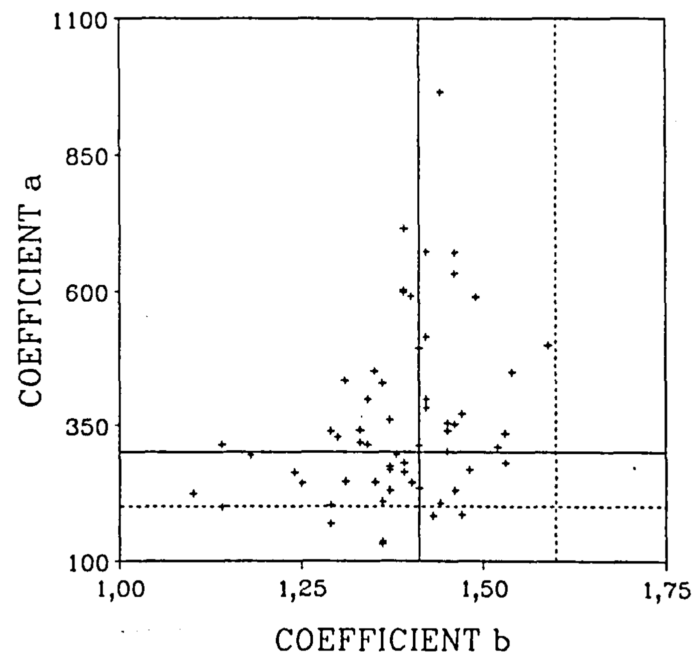

Figure 3.4: Distribution of coefficients a and b in the relationship $Z=aR^b$ calculated from individual rain episodes between November 1989 and May 1990.

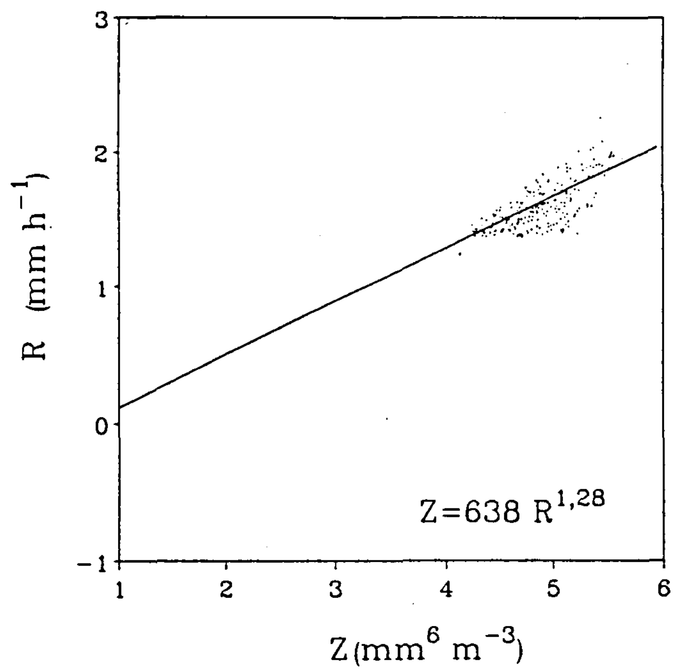

Figure 3.5: Scatter plot of the relationship between Z and R computed from disdrometer data for rain rates exceeding 25 mm.h^{-1}.

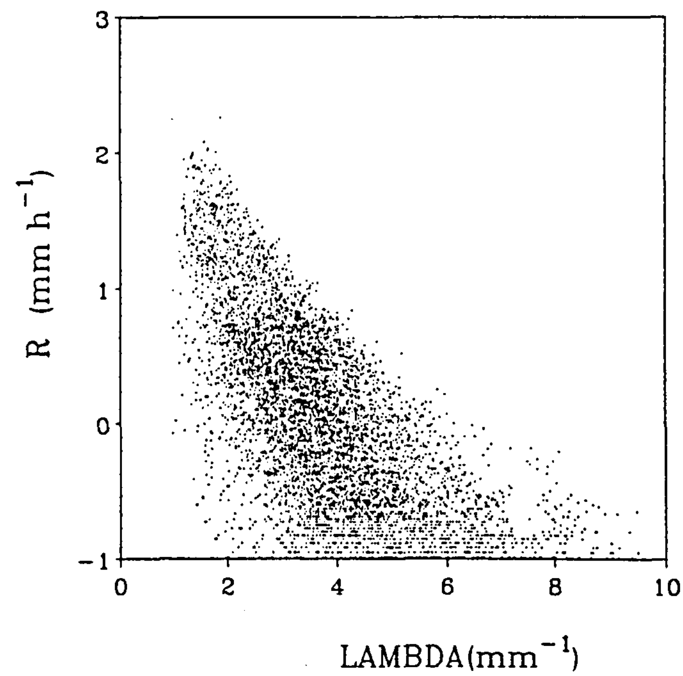

Figure 3.6: Scatter plot of the relationship between Λ and R computed from disdrometer data for the entire 1989/90 season.

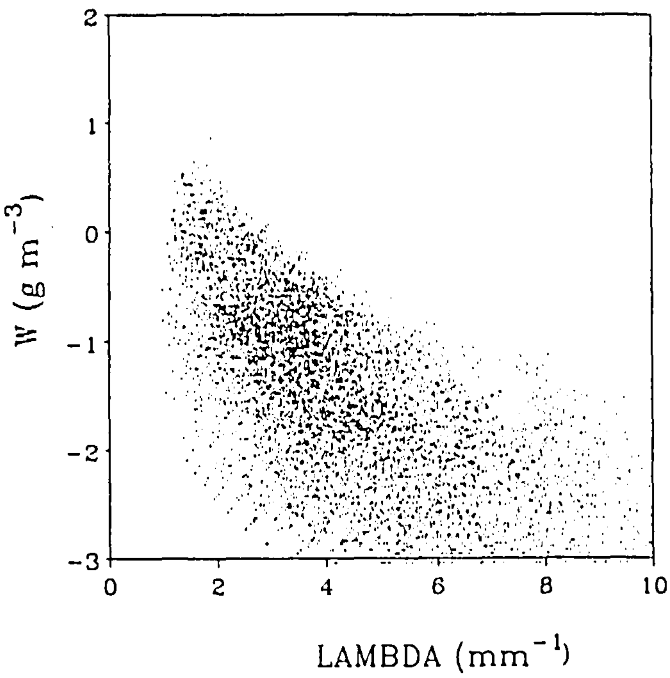

Figure 3.7: Scatter plot of the relationship between Λ and liquid water content computed from the disdrometer data for the entire 1989/90 season.

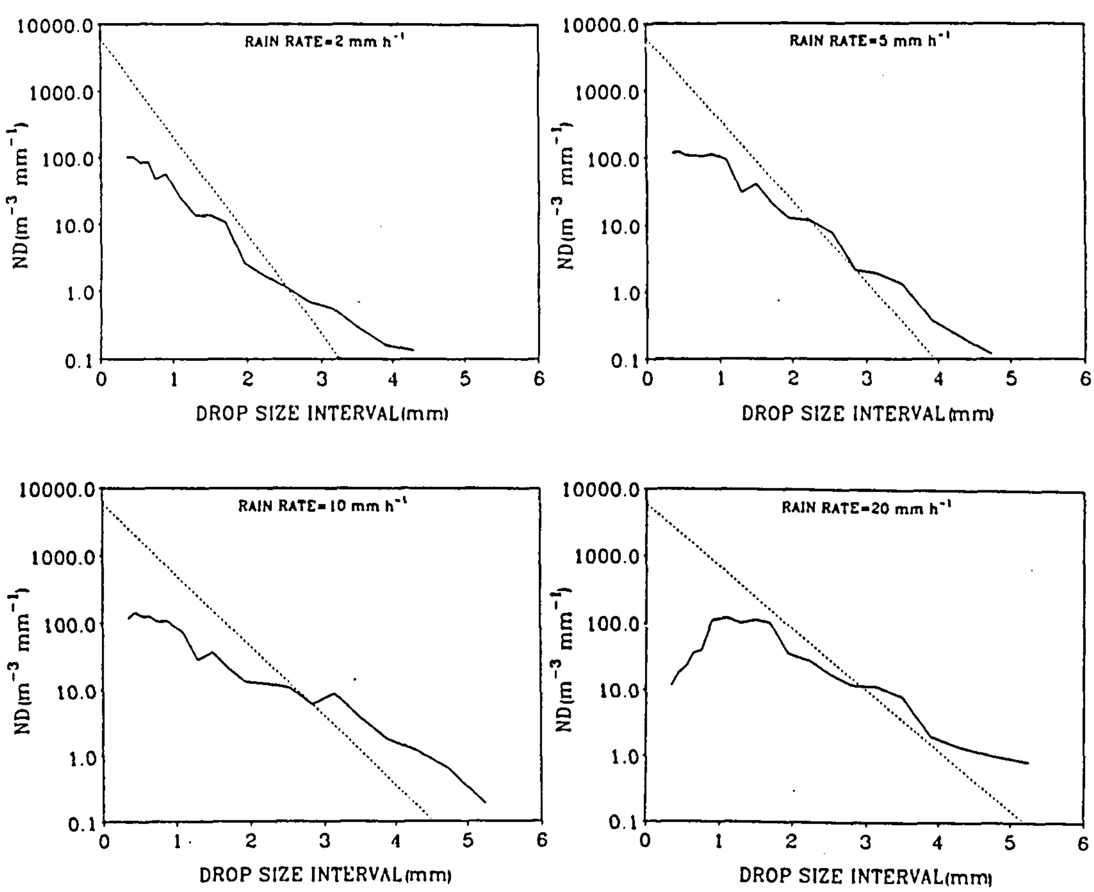

Figure 3.8: Plots of drop size distributions for rain events with differing average rain rates (solid lines), compared with Marshall and Palmer (1948) (dashed lines).

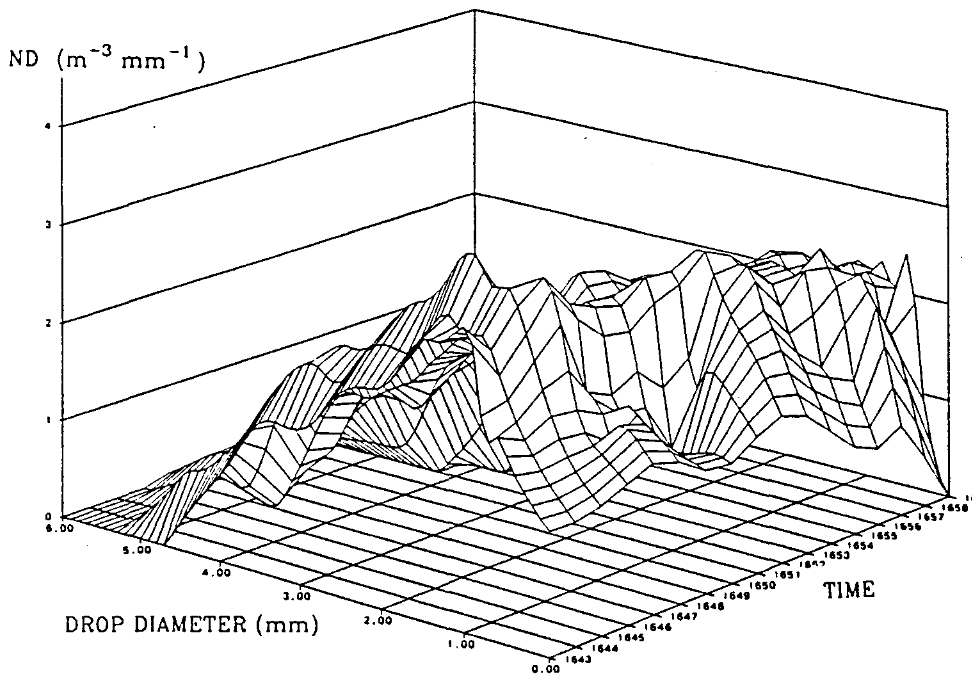

Figure 3.9: Three-dimensional drop size distribution field from 16:43 to 16:49 on 8 December 1989.

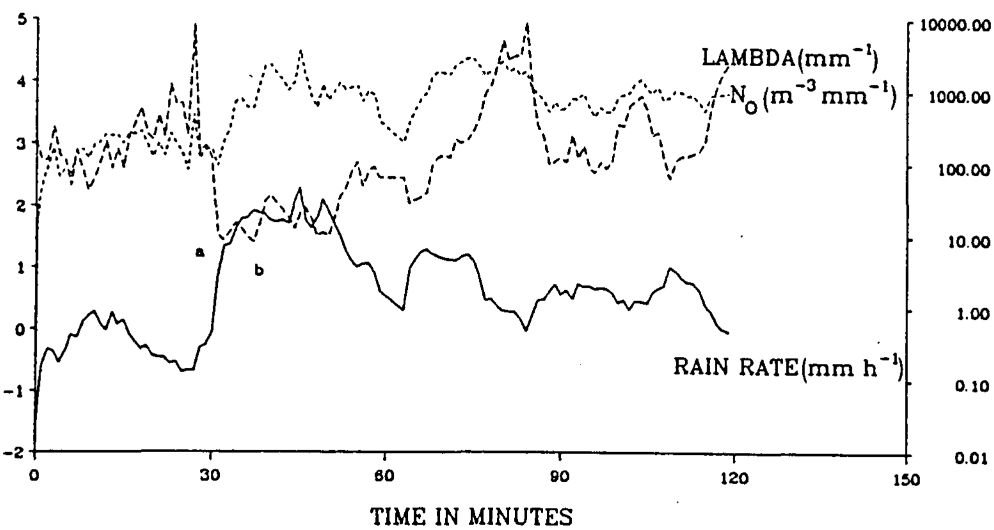

Figure 3.10: N_o, Λ and rain rate plotted as functions of time for 8 December 1989, 16:00 to 17:59. N_o and rain rate are plotted against a log scale on the right hand axis, Λ against a linear scale on the left hand axis. The letters a and b denote points of interest discussed in the text.

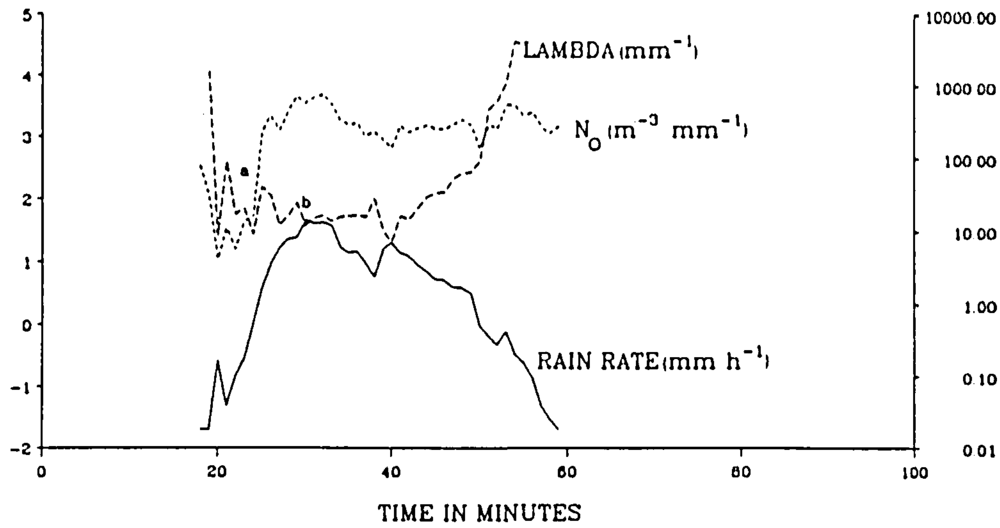

Figure 3.11: N_o, Λ and rain rate plotted as functions of time for 22 December 1989, 18:18 to 18:59. N_o and rain rate are plotted against a log scale on the right hand axis, Λ against a linear scale on the left hand axis. The letters a and b denote points of interest discussed in the text.

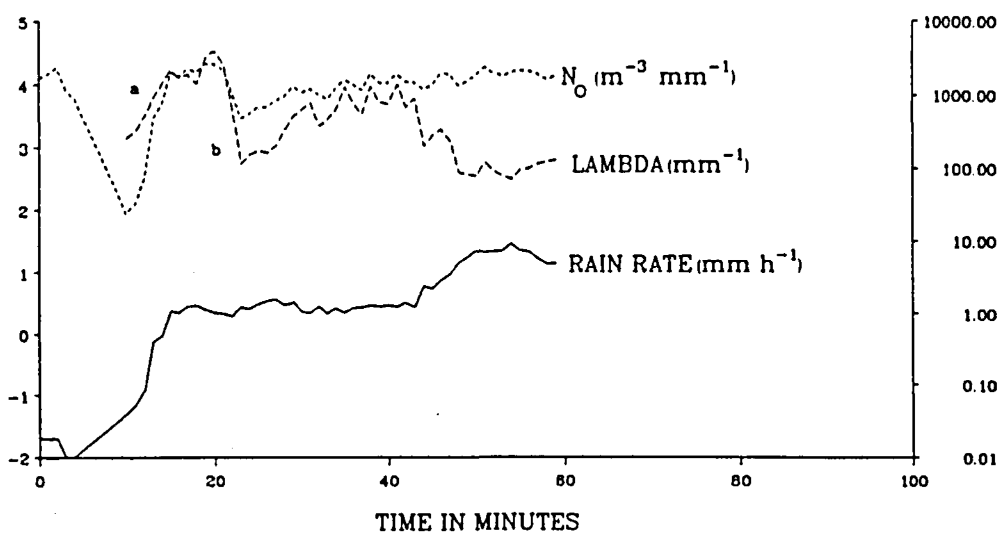

Figure 3.12: N_o, Λ and rain rate plotted as functions of time for 4 March 1990, 22:00 to 22:59. N_o and rain rate are plotted against a log scale on the right hand axis, Λ against a linear scale on the left hand axis. The letters a and b denote points of interest discussed in the text.

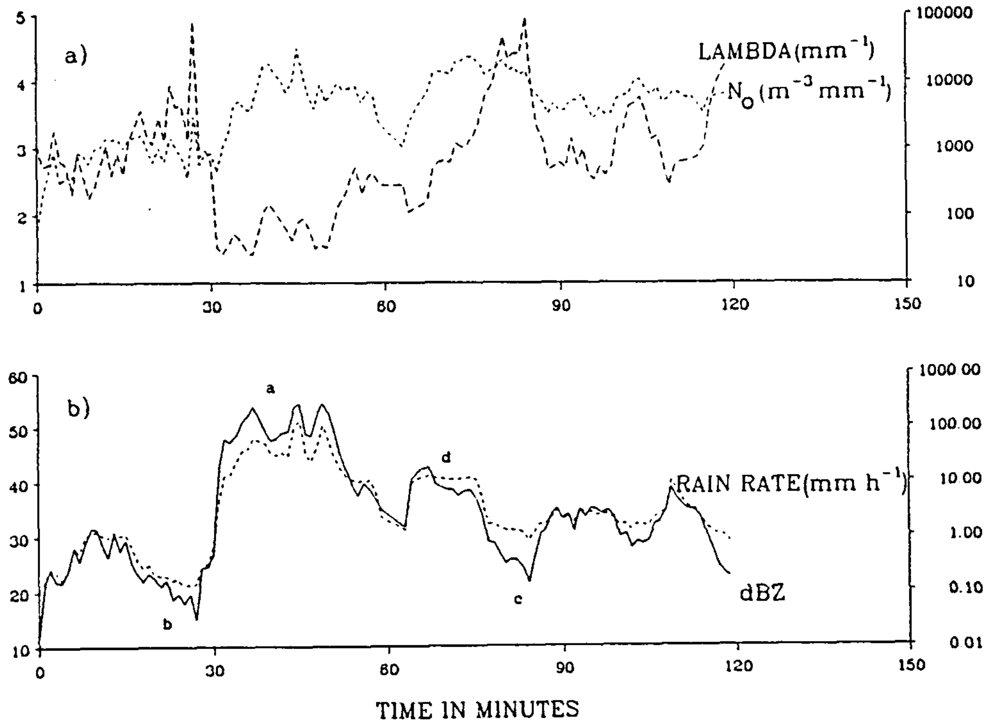

Figure 3.13: a) N_o and lambda plotted as functions of time for 8 December 1989, 16:00 to 17:59.
b) Rain rate and radar reflectivity factor for the same period. The letters a,b,c and d denote points of interest discussed in the text.

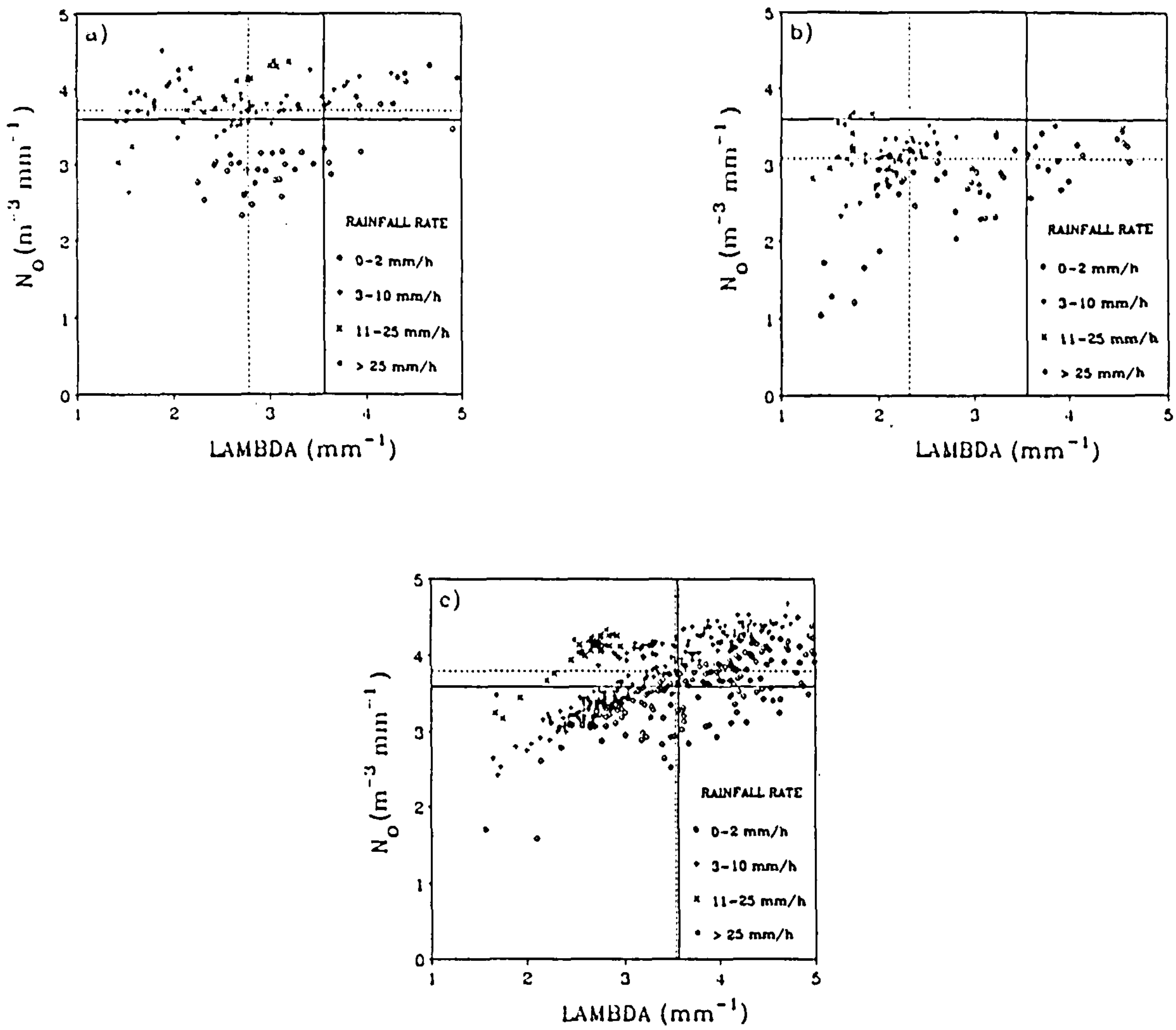

Figure 3.14: Rain rate as a function of N_o and Λ. Solid lines indicate median values for the entire season, dashed lines median values for the individual rain episode.
a) 8 December 1989, 16:00 to 17:59
b) 22 December 1989, 18:06 to 21:20
c) 4 March 1990, 19:14 to 05:21.

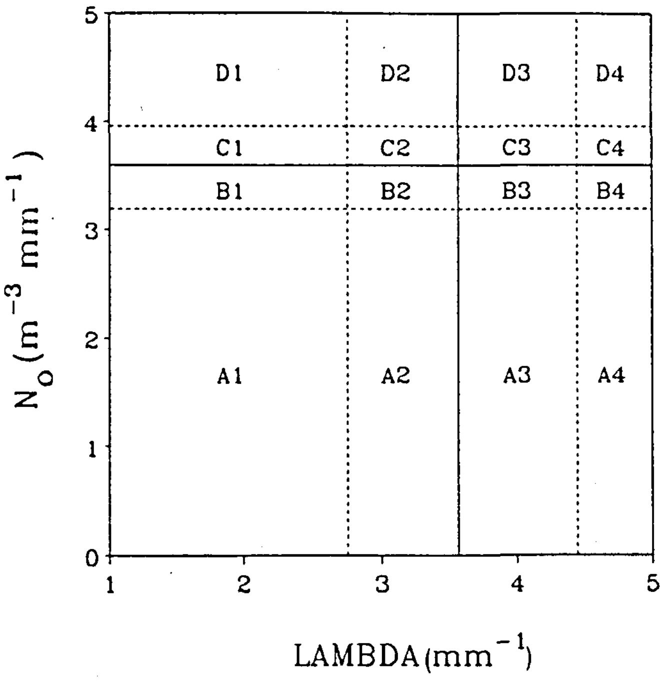

Figure 3.15: All possible combinations of N_o and Λ for rainfall rates exceeding 0,01 $mm.h^{-1}$. Solid lines indicate the median values, dashed lines the 25 and 75% quartiles respectively.

4. THE AREA-TIME-INTEGRAL METHOD OF RADAR-RAINFALL MEASUREMENT

Sean O'Beirne

4.1 BACKGROUND

The use of weather radar in measuring rainfall has a number of advantages over a rain gauge network. Firstly, as the equivalent of an infinitely dense rain gauge network, a 360° sweep of the radar accurately maps the areal extent of differing rainfall intensities within a precipitation field and secondly, rain information is assimilated in real-time. In an area such as the Transvaal Highveld where convective rain systems produce precipitation highly variable in space and time, radar measurement of rainfall becomes a necessity. Radar cannot be used to measure rainfall rate directly. However, the backscattered energy from varying raindrop distributions is measured and then related to rain rate. Inaccuracies in radar-measured rainfall thus may arise from variations in the Z-R relationship (see previous Section) or from anomalous propagation of the radar signal (Wilson and Brandes, 1979). In addition, precipitation may change considerably from the height of the radar beam to the ground (Austin, 1981).

The Area-Time-Integral (ATI) method of volumetric rainfall measurement has been proposed as a means of circumventing many of the above-mentioned problems (Doneaud, *et al.*, 1981; 1984a; 1988). The method is based on the principle that rain volume is dependant to a greater degree on storm area than on rainfall rate because the distribution of rainfall rates from one convective storm to the next is quite similar (Lopez, *et al.*, 1983) i.e. the probability density function (p.d.f.) of rainfall rates from one storm to the next is essentially constant (Atlas, *et al.*, 1990). In the previous progress report (Gomes *et al.*, 1989) the ATI technique was briefly examined and some preliminary results for convective storm systems over the Transvaal Highveld were presented. These results were based on hourly integrations over a 1° longitude by 0,5° latitude grid square and were used to suggest that a reflectivity threshold of 26,6 dBZ would be suitable for ATI computations over the Transvaal Highveld. For the purposes of the present report, an alternative method of defining the area over which to integrate echo area was used. This was simply to include all the echo area within a 100 km radius of the radar in the case of standard radar data and a 75 km radius in the case of data recorded in Doppler mode due to range limitations for short pulse operation. In the course of this Section, several different methods of determining a V-ATI relationship will be investigated in order to find an optimal relationship suitable for use in convective rainfall measurement by radar in storm systems over the Transvaal Highveld.

4.2 THEORY

The background to radar-measurement of rainfall and the ATI method in particular was reviewed in the previous progress report (Gomes *et al.*, 1989). Some of the more important aspects of that review are repeated here for continuity's sake.

The ATI technique of volumetric rainfall measurement is based on the relationship between storm size and rainfall volume in convective storm systems. Rain volume V over an area A during time t is given by

$$V = \int_t^{\infty}\int_A^{\infty} R\,da\,dt \tag{1}$$

Assuming rainfall rate R to be constant Eqn. 1 could be rewritten as

$$V = R \int_t^{\infty}\int_A^{\infty} da\,dt \tag{2}$$

It is the double integral that is referred to as ATI, a value which may be approximated for by summation i.e.

$$ATI = \int_t^{\infty}\int_A^{\infty} da\,dt \simeq \sum_{i=1}^{\infty} A_i \Delta t_j \tag{3}$$

An important part of the calculation of the ATI is determining an appropriate reflectivity threshold. Echo below this threshold is then not included in the ATI. There are a number of factors that need to be considered in selecting an appropriate threshold value. A threshold value set too high would exclude echo area that is significant in terms of precipitation produced. On the other hand, a threshold set too low would include echo area that is unlikely to produce significant amounts of precipitation (Doneaud, *et al.*, 1984a). This latter point is also important in reducing the need for an evaporation correction between the height of the radar beam and the ground (Doneaud, *et al.*, 1981). It was the determination of a suitable reflectivity threshold for ATI calculations on the Transvaal Highveld that was discussed in the 1989 progress report. An improvement in the correlation coefficient between ATI and radar-estimated rainfall volume was noted from the 23,3 dBZ to the 26,6 dBZ threshold. In addition Doneaud, *et al.*, (1981; 1984a) selected a 25 dBZ threshold in their ATI computations. On the - basis of the above mentioned considerations, a reflectivity threshold of 26,6 dBZ was considered suitable for ATI computation on the Transvaal Highveld.

Using an appropriate reflectivity threshold radar-estimated rain volume can be related to ATI in a power-law of the general form

$$V=K(ATI)^{b} \qquad (4)$$

where K and b are coefficients determined by the regression analysis. The average rain rate $\overline{R}$ in $mm.h^{-1}$ can then be ascertained from the ratio of the ATI in $km^2.h$ to the rain volume in $km^2.mm$. From Eqn. 2

$$\overline{R}=V/(ATI) \qquad (5)$$

By substituting (4) into (5)

$$\overline{R}=K(ATI)^{b-1} \qquad (6)$$

As the ATI decreases with increasing threshold value, the value of K must increase in order to maintain the volumetric rain accumulation (Doneaud, *et al.*, 1984a; Atlas, *et al.*, 1990).

4.3 DATA

Data used in the present study were obtained from an S-Band weather radar situated at Houtkoppen. Characteristics of the radar are to be found in the first progress report on the Precipitation and Airflow (PRAI) Project (Gomes and Held, 1988). Radar data in plan-position-indicator (PPI) format was used at minimum elevation angle (approximately 2°). Any echo area within a 100 km radius of the radar in the case of standard radar data and 75 km when the radar was operated in Doppler mode was included in the area integrations. A computer program was used to calculate the areas of echo clusters for different reflectivity thresholds (i.e. 23,3 dBZ; 26,6 dBZ; 30,0 dBZ and 33,3 dBZ). The corresponding rain volume for each echo area was computed using a Z-R relationship of $Z=300R^{1,41}$ which was calculated from data measured by the raindrop disdrometer. Data from the 1987/1988 and the 1988/1989 rainfall seasons, some 29 storm days in total, was used in the analysis.

4.4 RESULTS OF V-ATI CALCULATIONS FOR THE TRANSVAAL HIGHVELD

Pioneering work on V-ATI relationships was done by Doneaud, *et al.* (1981). Using data from convective storm systems over North Dakota, they proposed two alternative methods of computing a V-ATI relationship. The first of these was to use the maximum echo coverage of any one scan for each hour and the second to use the average echo coverage for each hour. Doneaud *et al.* (1981) found that the maximum echo coverage method had a better correlation coefficient (r=0,91) than the average echo coverage method (r=0,86) when regressed against radar-estimated rainfall volume, and therefore the former was recommended as the better approach. Regression parameters for radar-estimated rain volume versus ATI for the maximum echo coverage approach and the average echo area for convective storms over the Transvaal Highveld are given in Table 4.1 and Table 4.2, respectively.

In the case of the maximum echo area coverage, the highest correlation coefficient is evident at the 23,3 dBZ threshold. The correlation coefficient decreases from 23,3 to 26,6 dBZ and then increases marginally to the 33,3 dBZ threshold. On the strength of the correlation coefficient,

Table 4.1: Radar-estimated rain volume versus ATI regression parameters for differing reflectivity thresholds. RERV and ATI are calculated from maximum hourly echoes.

Threshold values in dBZ	23,3	26,6	30,0	33,3
Equivalent rainfall rate ($Z=300R^{1,41}$) in $mm.h^{-1}$	0,79	1,35	2,35	3,83
Coefficient K	3,27	10,04	11,85	14,28
Exponent b	1,15	1,03	1,05	1,07
Correlation coefficient	0,95	0,91	0,92	0,93
Log standard error of the estimate	0,13	0,17	0,15	0,14
Average rain rate calculated from the V-ATI relationship	9,58	12,40	16,58	22,30

Table 4.2: Radar-estimated rain volume versus ATI regression parameters for differing reflectivity thresholds. RERV and ATI are calculated from hourly echo area averages.

Threshold values in dBZ	23,3	26,6	30,0	33,3
Threshold rainfall rate ($Z=300R^{1,41}$) in $mm.h^{-1}$	0,79	1,35	2,35	3,83
Coefficient K	3,06	8,13	10,21	12,23
Exponent b	1,14	1,05	1,06	1,08
Correlation coefficient	0,96	0,93	0,94	0,94
Log standard error of the estimate	0,11	0,14	0,12	0,14
Average rain rate calculated from the V-ATI relationship	7,95	10,80	13,44	19,69

23,3 dBZ would appear to be a suitable reflectivity threshold and therefore for the maximum echo area method a V-ATI relationship of the form $V=3{,}27(ATI)^{1,15}$ at the 23,3 dBZ threshold appears to be most suitable (Figure 4.1). The fact that the exponent b exceeds 1 agrees with intuitive reasoning that larger storms are likely to have higher average rain rates.

When V-ATI relationships were calculated using hourly echo area averages a pattern of decreasing correlation coefficients with increasing threshold is evident. The higher correlation coefficient in the case of hourly echo area averages ($r=0,96$) and the lower standard error of the estimate ($s=0,11$) implies that this technique is possibly more accurate than the hourly maximum area technique. The average rain rates included in the tables were calculated using Eqn. 6 in which the average value of ATI for the various reflectivity thresholds was used as ATI value in the calculation. It is clear that the average rain rates generated by the V-ATI relationship will ultimately govern both the choice of reflectivity threshold and the most suitable method of V-ATI computation. There are a number of facets of the average rain rates in the tables that need consideration.

The V-ATI relationship computed by Doneaud *et al.* (1984a), using a 25 dBZ threshold, gave an average rainfall rate for convective storm systems over North Dakota of 4,0 $mm.h^{-1}$ (Doneaud *et al.*, 1984b) with a standard deviation of 1,55 $mm.h^{-1}$. However, Doneaud *et al.* (1984b) found a 20% increase in average rainfall rate in a subsequent, wetter rainfall season. Although a single disdrometer is unlikely to be a satisfactory gauge of average rainfall rates for an entire region, average rainfall rates calculated from the disdrometer data gave some interesting results. An average rainfall rate of 4,4 $mm.h^{-1}$ was calculated for the 1989/1990 rainfall season. More interesting was the fact that average rain rates of 7,3 $mm.h^{-1}$, 8,9 $mm.h^{-1}$, 11,3 $mm.h^{-1}$ and 15,1 $mm.h^{-1}$ were calculated when each of the four equivalent rain rate thresholds in the V-ATI computations were used. These are seen to be quite similar to the rain rates computed using the V-ATI relationships. The similarity in average rain rates from disdrometer data and those calculated from an average V-ATI relationship would appear to suggest that the assumption of constant p.d.f. of rainfall rate implicit in the ATI method is reasonable. The results also appear to indicate that even the minimum threshold of 23,3 dBZ may in fact overestimate the average rainfall rate. Clearly these conclusions would need better verification but they do provide interesting avenues of investigation.

It is also interesting to note that the values of the coefficient K computed in the V-ATI relationship for the Transvaal Highveld are very similar to those computed by Doneaud *et al.* (1984a). The V-ATI relationship that he finally proposed for convective storms over North Dakota was of the form $V=3,7(ATI)^{1,08}$. The fact that the average rainfall rates for the Transvaal Highveld were higher than those for North Dakota is definitely attributable to the moderately steeper slopes of the V-ATI relationships for the Transvaal Highveld. Rosenfield and Gagin (1989) compared characteristics of convective storm systems for Israel with those over South Africa in order to identify factors influencing the total rainfall yield from these systems. One of their findings was the relationship between rainfall volume and the absolute humidity at cloud base. They found that increases in the absolute humidity at cloud base were proportional to increases in the rain volume to the power of 1,2 in Israel and 1,69 in South Africa. They suggested that the precipitation efficiency of continental storms increases with increasing cloud base temperature and that convective storm systems over South Africa frequently exhibit cloud base temperatures of 12-15°.

In a similar vein Rosenfield *et al.* (1990) determined instantaneous area average rain rates by measuring the ratio of the area of rain intensity above a given threshold to the total echo area ($F<\tau>$) and comparing it to the areal rain intensity (R). The point is not to dwell on the method but merely to consider the fact that a comparison of $R-F<\tau>$ relationships between South Africa, Texas, Australia (Darwin) and data from the GATE experiment showed the steepest $R-F<\tau>$ slope for convective storms over South Africa. Rosenfield *et al.* (1990) also showed that in areas where warm rain processes are dominant, there will be an increased frequency of small showers characterised by light rainfall. Kraus and Bruintjies (1985) showed that convective rain over central South Africa is initiated through ice-phase mechanisms with no evidence of any significant warm rain processes. Mather and Parsons (1990) computed a V-ATI relationship of the form $V=5,90(ATI)^{1,1}$ for convective storms over the eastern escarpment, a relationship indicating still higher average rain rates.

The above evidence suggests that higher average rain rates given by V-ATI relationships for convective storm systems over the Transvaal Highveld are not unreasonable. Disdrometer data suggests that average rainfall rates closer to 4,5 $mm.h^{-1}$ would be better approximations but it must be pointed out that the latter part of the 1989/1990 rainfall season was characterised by a number of episodes of sustained stratiform rain. Nonetheless, the average rainfall rate of 7,95 $mm.h^{-1}$ in the case of the hourly echo averages (23,3 dBZ threshold) appears to be a more realistic value than the 9,58 $mm.h^{-1}$ in the case of the hourly echo area maximums. In addition, the higher correlation coefficient and lower standard error of the estimate deem the hourly echo area average method the more accurate. This would suggest that a V-ATI relationship of the form $V=3,06(ATI)^{1,14}$ is most appropriate to the Transvaal Highveld (Figure 4.2). Although the threshold used is now lower than that initially proposed, it is relevant to consider a conclusion drawn by Rogers (1989) in calculating a suitable average rain rate to be used in a rain storm model. Rogers concluded that thresholds of greater than 25 dBZ in the ATI technique would not be appropriate because of the increasing dependence of average rain rate on the maximum rain rate as higher thresholds are used to define the echo area.

An obvious shortfall of the hourly average echo area method is that a minimum tracking time of one hour would be needed before volumetric rainfall totals could be estimated. This inhibits the operational versatility which is cited as the main advantage of the ATI technique. It was decided therefore to calculate a V-ATI relationship based on scan-by-scan integrations. The regression parameters are summarised in Table 4.3. When consulting the table it must be borne in mind that the coefficient K has been calculated from ATI in units of $km^2.min$. Although the correlation coefficient for the scan-by-scan integration techniques is slightly less (r=0,94) than the hourly echo average method, the average rainfall rate of 8,14 $mm.h^{-1}$ still appears to be a reasonable value. Proper verification of the rainfall rate still needs to be done but the results suggest that a V-ATI relationship of the form $V=0,04(ATI)^{1,18}$ (Figure 4.3) would be most appropriate when using a scan-by-scan integration technique of computing V-ATI for convective storm systems over the Transvaal Highveld.

Table 4.3: Radar-estimated rain volume versus ATI regression parameters for differing reflectivity thresholds. RERV and ATI are calculated from scan-by-scan integrations.

Threshold values in dBZ	23,3	26,6	30,0	33,3
Threshold rainfall rate ($Z=300R^{1,41}$) in $mm.h^{-1}$	0,79	1,35	2,35	3,83
Coefficient K	0,04	0,06	0,09	0,14
Exponent b	1,18	1,16	1,15	1,13
Correlation coefficient	0,94	0,96	0,97	0,97
Log standard error of the estimate	0,04	0,03	0,02	0,02
Average rain rate calculated from the V-ATI relationship	8,14	10,23	13,66	19,00

4.5 CONCLUSIONS

In the course of this section the Area-Time-Integral (ATI) method of volumetric rainfall measurements was considered. Three different methods for determining a Volume versus Area-Time-Integral (V-ATI) relationship were considered. Of these the hourly average area method was deemed to be the most accurate. Although the V-ATI relationship computed using this method appeared to give average rainfall rates that appeared high, consideration of other literature showed that higher average rainfall rates are not unusual for convective storms over South Africa. Operational aspects of the ATI technique of volumetric rainfall measurement meant computing a V-ATI relationship that can be used on individual scans. Although the V-ATI relationship calculated required verification, they do appear to indicate that the ATI technique is an operationally viable means of radar measurement of rainfall.

4.6 REFERENCES

ATLAS D, ROSENFIELD D and SHORT D A, 1990. The estimation of convective rainfall by area integrals 1. The theoretical and empirical basis. *J. Geoph. Res.*, 95, 2153-2160.

DONEAUD A A, SMITH P L, DENNIS A S and SENGUPTA S, 1981. A simple method for estimating convective rain volume over an area. *Water Resour. Res.*, 17, 1976-1682.

DONEAUD A A, IONESCU-NISCOV S, PRIEGNITZ and SMITH P L, 1984a. The area-time integral as an indicator for convective rain volumes. *J. Climate Appl. Meteor.*, 23, 555-561.

DONEAUD A A, IONESCU-NISCOV S and MILLER J R (Jnr), 1984b. Convective rain rates and their evolution during storms in a semiarid climate. *Mon. Wea. Rev.*, 112, 1602-1612.

DONEAUD A A, MAKARAU A and JOHNSON L R, 1988. A modified ATI technique for nowcasting convective rain volumes over areas. *J. Appl. Meteor.*, 27, 491-502.

GOMES A M and HELD G, 1988. *First Progress report: Precipitation and Airflow (PRAI) Project*. CSIR Report EMA-C 8885, Pretoria, 18pp.

GOMES A M, O'BEIRNE S and HELD G, 1989. *Second Progress report: Precipitation and Airflow (PRAI) Project*. CSIR Report EMA-C 89126, Pretoria, 42pp.

KRAUSS T W and BRUINTJIES R T, 1985. Physical properties of summertime convective clouds in the Bethlehem region of South Africa. *Preprints, Fourth WMO Conference on Weather Modification*, Honolulu, World Meteor. Org., 251-254.

LOPEZ R E, THOMAS J, BLANCHARD D O and HOLLE R L, 1983. Estimation of rainfall over an extended region using only measurements of the area covered by radar echoes. Paper presented at 21st Conference on Radar Meteorology, Am. Meteorol. Soc., Edmonton, Alberta, Canada, Sept. 19-23.

MATHER G K and PARSONS R, 1990. Radar measurements of rainfall - the area method. Paper presented at the Seventh Annual Conference of the South African Society for Atmospheric Sciences, Pretoria, Oct. 22 & 23.

ROGERS R R, 1989. Average rain rate in a model rain storm, *Proceedings, 24th Conference on Radar Meteorology*, Miami, American Meteorological Society, 652-653.

ROSENFIELD D and GAGIN A, 1989. Factors governing the total rainfall yield from continental convective clouds. *J. Appl. Meteor.*, 28, 1015-1030.

ROSENFIELD D, ATLAS D and SHORT D A, 1990. The estimation of convective rainfall by area integrals 2. The height-area rainfall threshold (HART) method. *J. Geoph. Res.*, 95, 2161-2176.

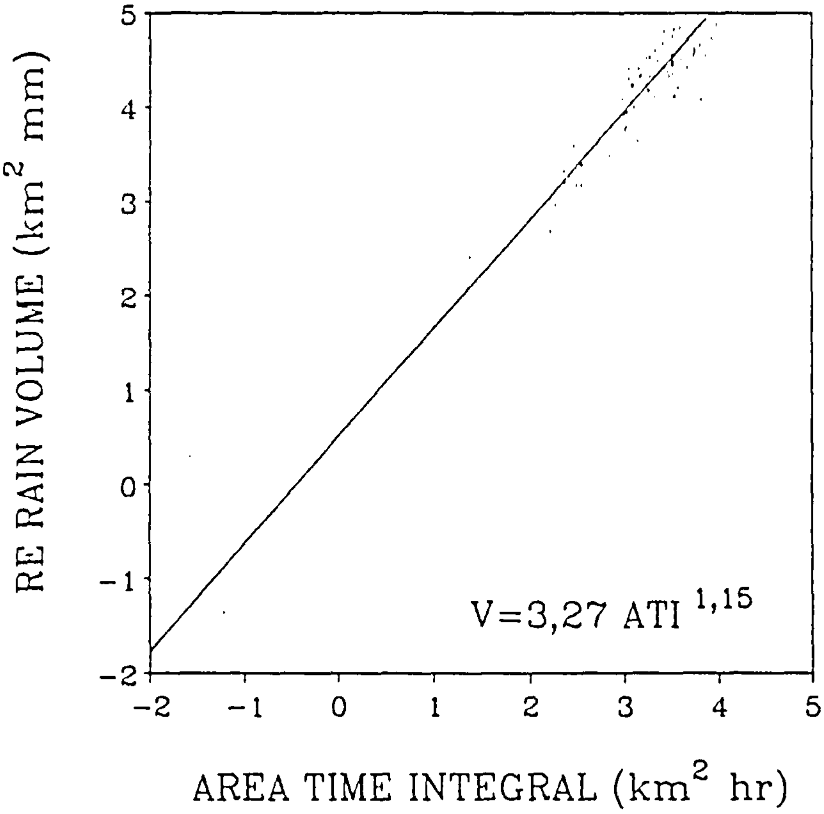

Figure 4.1 Scatter plot of the V-ATI relationship for convective storms over the Transvaal Highveld using the maximum hourly echo coverage method. The reflectivity threshold is 23,3 dBZ.

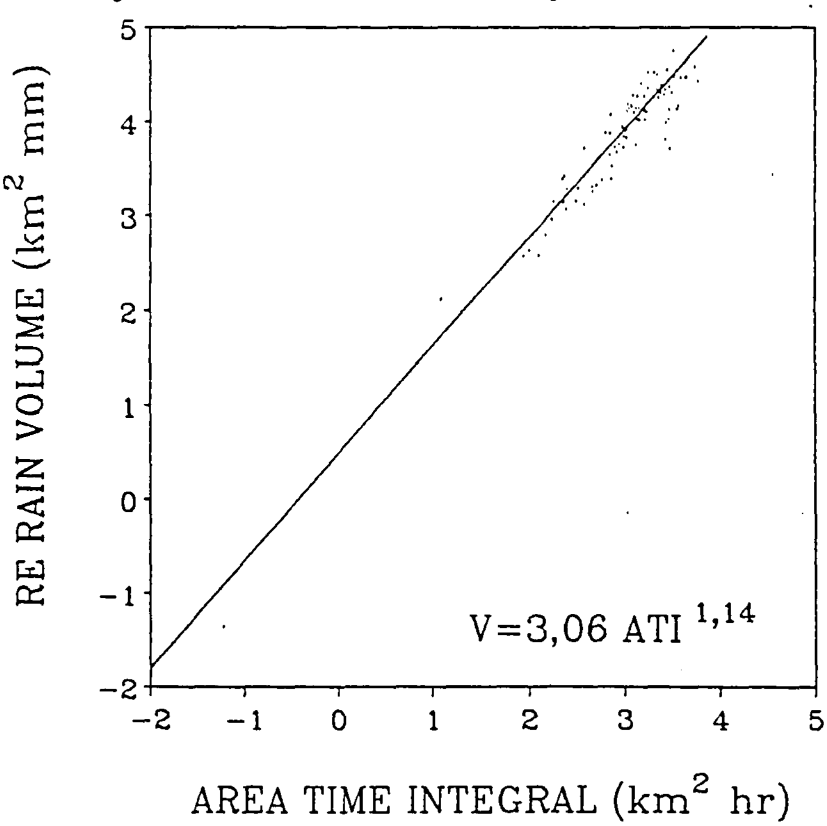

Figure 4.2 Scatter plot of the V-ATI relationship for convective storms over the Transvaal Highveld using the hourly average echo coverage method. The reflectivity threshold is 23,3 dBZ.

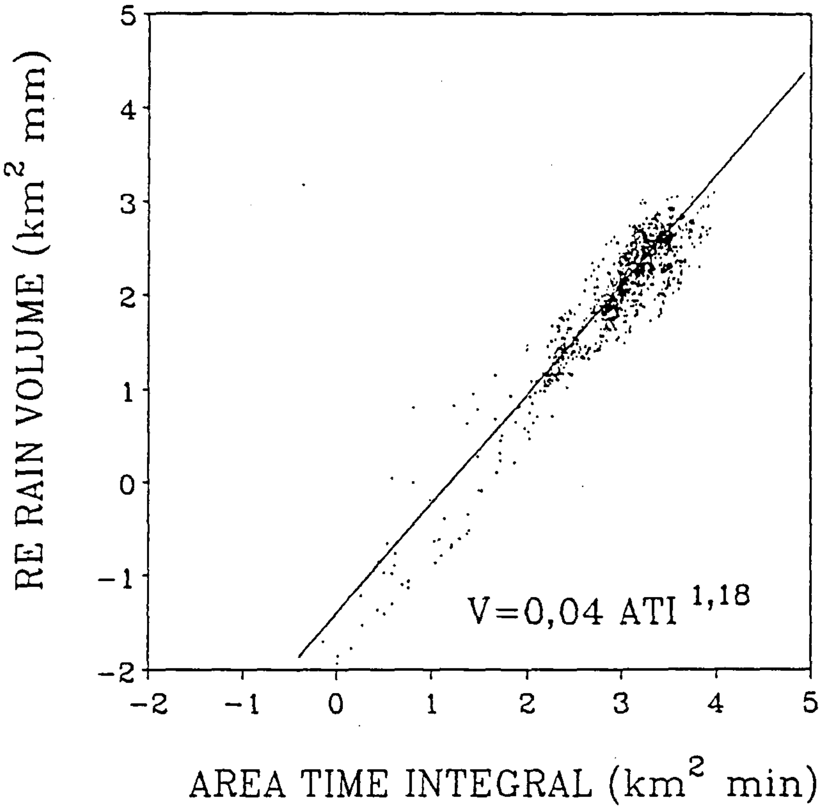

Figure 4.3 Scatter plot of the V-ATI relationship for convective storms over the Transvaal Highveld using a scan-by-scan integration technique. The reflectivity threshold is 23,3 dBZ.

5. DAUGHTER CELLS AND CLOUD SEEDING

Ronald C Grosh

5.1. BACKGROUND

Rain stimulation research in South Africa is expected to continue for a long time, as a water shortage is clearly developing in response to the pressure of population growth and the accompanying development of support industries. Rain stimulation research faces a variety of technical and practical problems which must be solved before an operational cloud seeding program can be expected to provide optimum results (e.g. Changnon *et al.*, 1975). In this Chapter, the way in which the characteristics of cloud regeneration mechanisms might affect the scientific and logistical considerations of a rain stimulation project utilising airborne dispersion of glaciogenic seeding material, are broadly discussed. Radar observations of multicellular storm growth provide the main basis for this discussion, as this type of storm has been the main focus of the promising Programme for Atmospheric Water Supply, PAWS (CSIR/CloudQuest, 1990).

Multi-cellular storms have been found to be suitable candidates for rain stimulation experiments in the eastern part of South Africa, both from the operational and scientific viewpoints. Towers on the edge of relatively isolated multiple cellular storms have been successfully penetrated repeatedly by the sturdy aircraft employed for seeding (a Learjet) with a negligible rate of failure to penetrate due to pilot judgement of overly severe convection. More importantly, early seeding results based on three years of data (approximately 85 cases) have been positive, on average, with radar observations indicating both statistically significant <u>and</u> physically logical rain enhancements following randomized seeding of growing turrets at the -10°C level with dry ice (CSIR/CloudQuest, 1990). Unfortunately, these storms are not the heaviest rain producers and the hydrologic significance of seeding them has yet to be quantified. Studies by Carte and Held (1978) of storm occurrences on the South African Highveld have shown that, although squall lines and similar well organised convective systems clearly will produce more rain on a case by case basis, they are naturally efficient, relatively infrequent (7% of storm days) and dangerous to penetrate as well. Fortunately, isolated thunderstorms occur on about 39% of Highveld storm days with scattered storms occurring on the other 54% of these days. Multi-cellular storms occur frequently (72%) on days with scattered storms, but less frequently on days with isolated storms. Nevertheless, multi-cellular storms are the dominate storm type on more than half of the storm days over the Witwatersrand region (Carte and Held, 1978). Thus, a large selection of cases is potentially available for modification.

Areal rain stimulation projects utilising set ground networks of a given areal extent may have severe logistic problems if large numbers of cells are present and must be treated for long periods. Some of the writer's previous research in this area was directed towards providing logistical information to be used for planning seeding logistics under a given type of weather situation (strong convection-hail) over a 5000 km^2 network in central Illinois (Changnon *et al.*, 1975). For example, it was found that, on average, five or six 40 dBZ radar cells would require treatment at one time and that (maximum gain) echoes would exist over the network for five and six hours with large (diameter ≈100 km) storms needing to be circumnavigated in that warm humid climate. However, the South African rain research is not yet in the network phase. Thus, the characteristics of individual cloud systems are examined without regard to a surface network. It is the building blocks of clouds that are of most interest here, but not just for logistic reasons. The characteristics of multicellular cloud mergers are of scientific importance as well, since natural cloud growth mechanisms will affect weather modification efforts.

5.1.1 Observational cloud merger studies

The most extensive cloud merger studies are all based on radar observations, primarily low elevation angle scans. Westcott (1977) examined 600 echoes on three summer days in Florida, Lopez (1976) analysed 6000 echoes from six tropical cloud clusters north-east of Barbados, and Houze and Cheng (1977) tracked 2000 GATE echoes using this procedure. However, the vertical radar structure of merging storm echoes has been analysed much less frequently, two studies in Illinois are discussed here (Changnon 1976, Grosh 1978a).

Westcott found that merged echoes were 5 (first order mergers) to 30 times (second order - or subsequent - mergers) larger in area than single echoes and produced 10 to 100 times as much rain. However, Lopez found that smaller echoes tended to grow as a result of merger, but that some initially large echo pairs would decrease in size after merging. A further scale dependence was quantified by Houze and Cheng. Only 5% of echoes smaller than 100 km^2 merged, but larger storms (up to 1000 km^2 and 10 000 km^2) were more likely to form by merger (22% and 59%, respectively). Changnon found that all 190 convective storm echoes he examined from a 19 day study period grew vertically after merging. About half of the mergers occurred during the first quarter of echo life time. Grosh studied the full three dimensional structure of six merging echoes and used radar and rain gauges to determine the rain flux from the echo areas over a dense surface network. Merged echoes were larger and produced more rain than unmerged echoes. However, feeder type merging dominated the small sample and impressive echo growth did <u>not</u> follow merging.

Gomes *et al.* (1989) report a cloud merger observed in South Africa by Doppler radar. In this case new cloud clusters were found to develop ahead of the large (30 km length) main cell, probably in the convergent area caused by its cold air outflow. In this case, the merging of two large storms was also observed to coincide with hail and heavy rain at the ground.

New cells tend to form near expected inflow regions, on the equatorward side (approximately 50%) and leading edge (approximately 25%), of multicellular storms on the Highveld (Carte and Held, 1978). This result compares reasonably well with the results of the American Thunderstorm Project (Beyers and Braham, 1949) where the distance dependency of new cell formation was also described (e.g. new cells are very likely to form between cells less than 10 km apart, but 11 times less likely when separated by over 14,5 km (Figure 5.1).

5.1.2 Feeder cells

Examples of storms with more organised inflow regions have been discussed by Dennis *et al.* (1970). Based on 22 Great Plains (USA) severe storms, they found that feeder cells formed close to the main cell (within 2 km) and rapidly merged. Large and steady severe storms had feeder cells forming in a line along the right rear flank (northern hemisphere). The feeder cell could become the main core of the storm in some cases. A related type of storm in the more humid Midwest (USA) has been described by Grosh (1978b), and Grice and Maddox (1984) state that these severe quasi-stationary rain storms occur frequently in other climates as well. In these last cases, the merging cell merges directly with the older core and becomes the dominant tower (Figure 5.2). These storms have some similarities with the more steady supercell storms which appear to evolve beyond this stage due to a slightly different environment. Supercell storms occur rarely in the mid latitude climates where they were discovered, and there was only one report of a supercell-like storm in the first seven years of the CSIR radar programme (Carte, 1981). Thus, they will be encountered infrequently and, because of their severity, would be avoided as a seeding target in any case.

5.1.3 Daughter cells

On the other hand, Chisholm and Renick (1972) have described the daughter cell type of repeating merger mechanism whereby a new cell appearing to the near right rear (northern hemisphere) grows to become the dominant cell as the older parent cloud fades *next* to them (Figure 5.3). This case is thought to minimise the effective spreading of seeding material compared with the feeder case where the new cells actually move into the same region the older parent cell occupies.

5.1.4 Weak evolution

In organised cases with reasonably proximal merging cells, Foote and Frank (1983) have applied the term "weak evolution" to distinguish cases in between the multicell model (where cores never merge, similar to the daughter cell case, for example) and the steady supercell model. If the updraught diameter (D) is small relative to the distance (L) between significant updraughts, the case can be categorised as multi-cellular (separate cores). When L is small compared with D, the supercell term is more appropriate. When L is intermediate, convection may approach the single supercell state more closely than the multiple cell case, but individual cell cores though merged can still be distinguished and convection is noticeably less steady (Figure 5.4). Obviously, some feeder cell storms have strong similarities to the weak evolution case, such as in the case of the quasi-stationary rain system.

5.1.5 Cloud model studies

Several groups have studied cloud mergers with numerical models (Orville *et al.*, 1980; Cheng, 1989; Turpeinen, 1982; Wilkens *et al.*, 1976; Hill, 1974; Wilhelmson and Chen, 1982; Farley and Orville, 1986). The models have a distinct advantage over the standard merger observation technique (radar) in that the nature of the merger can be more accurately described, e.g. there is no longer a need to speculate as to whether updraughts have merged along with rain areas, the model calculations can tell all. Wilkens *et al.* (1976) studied the most basic elements of cloud merging, thermals. Their 2-D model output revealed an important fundamental result; if the positive buoyancy fields of adjacent thermals mostly overlapped, the thermals would merge. Also, as expected, if the buoyancy fields did not overlap, merging did not follow, and, furthermore, the vertical motions damped.

Moving up to cells with scale of several kilometres, Hill (1974) described the formation of a storm which drew in smaller cells. After merger, the smaller storms developed *within* the larger circulation. At about the same scale Orville *et al.* (1980) studied mergers between feeder and mature type clouds with a 2-D model and found that mergers only occur if the clouds are in different growth stages and are sufficiently close to each other. In the output, pressure gradients were observed to occur which drove smaller cells (4 km diameter) toward the main cell (7 km).

Three-dimensional models have shown how two updraughts might merge (a dynamic merger) via the new updraught of the bridge cloud forming between the two initial clouds which first connect via "echo (rain) merger" (Turpeinen, 1982).

Also, a study of hailstorm feeder clouds was undertaken by Cheng (1989) via a 2-D model with high resolution. Ambient air flow and/or low-level cold outflows induced by evaporation led to wind shear generated gravity waves and the development of nearby feeder cloud formations. Moisture distribution was also found to play an important role in the development of the waves and clouds. The calculated cloud separations agreed with observations. New cells were found to form over or just behind the cold outflow boundary of previous cells (Wilhelmson and Chen, 1982; Farley and Orville, 1986). Also, Thorpe *et al.* (1980) and Droegemeir and Wilhelmson (1987) modelled the thunderstorm outflows and found they behave as cold density currents.

5.1.6 The nature of echo merging

Although there have been many studies of echo merging, some of the most basic features of merging are not well understood because of instrumental shortcomings (Westcott, 1984). In particular, when a rain area is observed to merge with another echo area observed by ordinary radar, it is not possible to specify whether the updraughts have merged as well. Obviously, this may have great impact on the dispersal of seeding material, not to mention storm dynamics. For example, the larger diameter of combined updraughts may increase their protection from entrainment and thereby lead to considerably enhanced storm energetics. Also, the role of larger scale dynamics in the merger process is usually poorly specified. Thus, the true cause of the subsequent cloud intensification and growth which is often observed (and is the reason for much of the interest in mergers) remains quite obscure. That is, what is more important to the post merger intensification, the local interaction of cloud elements or the larger scale forcing? Although the nature of larger scale forcing is unlikely to be resolved for some time, Doppler radar (Westcott and Kennedy, 1989) and/or in situ aircraft observations of updraught state and location (Malkus, 1954) have the potential for supplying some of the information necessary to clarify these issues. However, neither these observations nor cloud models are available to the present study. Although multiple level radar observations could be utilized to monitor some aspects of the dynamic state of the merging clouds, in the present study single level PPI observations were found to be adequate to support the conclusions.

5.2 DATA

CSIR archives of digital data from the S-band Houtkoppen radar covers about 10 years. This data bank served as the primary source of information for the merger study, primarily because of the convenient and relatively advanced in-house data display programs available at CSIR where the study was to be performed. Multiple cellular storm cases were selected from days with relatively isolated convection, as determined from the archive of occasional polaroid photographs of the PPl display on storm days as observed by the CSIR radar at Houtkoppen. Based on the PAWS results, special attention was focused on isolated multi-cellular storms during days with 40 dBZ echoes, warm cloud bases (cloud-base temperature >5°C) and moderate instability (ΔT at 500 hPa >0°C).

5.2.1 Sample size

Six selected multiple cellular merged storms from three days in 1987 were tracked on the radar imagery for this study, 3 November (1 storm), 16 November (4 storms) and 2 December (1 storm). The storms were chosen primarily because of their merged or multiple-cellular nature, and *relatively* isolated locations. Severe storms (producing hail) and those near the radar ground clutter pattern were avoided. Although the sample of storms used here is small, a wide range of cloud conditions were covered, including warm and cool bases and strong and weak translation (Table 5.1).

5.2.2 Synoptic and mesoscale conditions

However, on all three days the synoptic pressure patterns giving rise to the multiple cellular storms were rather similar (see Figures 5.5a, b and c). A trough was observed over the heart of the country and high pressure dominated the west coast with a high pressure centre also observed north of Maputo on either the east coast or some eastern inland location. The contour pattern was the most confused on 3 November 1987, as low pressure also extended from the south coast up to the northeast coast and the eastern high pressure centre was displaced inland. Noontime, upper-level winds at Irene were generally from the west-southwest on all three days.

However, only on 3 November 1987 were no northerly-component wind being reported near or below cloud base (Figure 5.5d). Peak winds were observed at 200 hPa and were 21 to 32 $m.s^{-1}$, with the weakest jet also occurring on 3 November 1987. Thus, single cell storms were not expected on these days, but multicell storms were clearly favoured and on the two days with distinct directional shear, the possibility of severe weather needed to be considered as these hodographs are approaching the supercell profiles described by Chisholm and Renick (1972). Cloud bases were moderate to warm and the atmosphere unstable (Table 5.1). On all three days, cloud top heights for boundary layer parcels (60 hPa averaging depth) could rise to above 200 hPa (about 12,4 km) and about 6 km above the seeding level at -10°C (Figures 5.5e, f and g).

Table 5.1. Atmospheric and cloud conditions over Irene at noon on the three study days in 1987 (60 hPa averaging depth).

Variables	3 Nov	16 Nov	2 Dec
1. Cloud Base Temp (°C)	9,5	6,7	13,0
2. 500 hPa Buoyancy (°C)	5,5	3,0	5,0
3. 1÷2	1,7	2,2	2,6
4. Mixing Ratio (g/kg)	11,0	9,4	12,9
5. Convective Temperature (°C)	29,5	30,4	27,5
6. Speedshear to jet peak (s^{-1})	$1,7*10^{-3}$	$2,1*10^{-3}$	$2,8*10^{-3}$
7. Cell Speed ($km.h^{-1}$)	~15	~50	~20

16 November 1987 was the day with the coldest cloud bases, while 2 December 1987 had the warmest cloud bases, the largest subcloud moisture content, and the greatest windshear.

5.3 MERGER CRITERIA

The following criteria were applied in analysing the radar observations.

i. Duration: any contact.

ii. Initial cell separation: all detectable separations (23 dBZ threshold was used).

iii. Size: multi-cellular storms were the main focus of attention, especially semi-isolated cases. Well organised storms (squall lines and heavy storms) are not the primary interest. 40 dBZ echoes were also required. At Nelspruit the horizontal extent of the multi-cellular storms passing the PAWS seeding criteria averaged at about 50 km^2 with peak areas being 117 km^2. Storm-top heights should also be able to reach the -10°C level (seeding level).

OTHER MONITORED CHARACTERISTICS

i. Wind, stability, cloud base temperature.

ii. Cell motion versus system motion.

iii. Storm orientation.

iv. Type of merger:
- a) Feeder versus daughter cells (versus weak evolution).
- b) Differential cell motion.
- c) Expansion merging.
- d) Bridging between pre-existing cells.
- [e) Updraught/downdraught merging as well as rain areas (in ideal conditions).]

5.4 ANALYSES

5.4.1 3 November 1987

On 3 November 1987 small, widely scattered echoes began to form after about 13:00 SAST (South African Standard Time). By 16:00 storms were beginning to show clearly multicellular form and were distributed in randomly located clusters about the Houtkoppen radar. Continued echo growth then followed, but the overall echo pattern remained essentially random until about 18:00 when some of the multiple cellular storms appeared to be forming a broad scattered line approximately 90 km north of Houtkoppen. A self propagating storm (echo C) which generated several new cells on its downwind edge was tracked using contoured plots of the digital radar data.

The digital radar data starting at 15:21 was examined. A more or less 60 km long line extended from the radar toward the southwest and there was also a large area of randomly distributed storm echoes centred about 30 km to the south. These two storm areas are not analysed here because they were associated with ground clutter contamination and known severe weather reports (hail).

At about 16:30, a rapidly growing and intense (50 dBZ) new echo (C) developed about 65 km northwest of the Houtkoppen radar and about 30 km from the northern end of the linear echo (Figure 5.6a). At about this time, two major new echoes (B and C) had appeared near an earlier cell (A) at the end of the line. Echoes A and B died shortly after this time. However, storm C went through a major growth phase and was still being tracked at the end of the examined data an hour and a half later. Thus, it was chosen for analysis.

Storm C quickly developed a small new 40 dBZ intensity centre, C2 (Figure 5.6b, 16:38) near the appendage sprouting northeastwards at 16:32 (Figure 5.6a). This was in turn quickly enveloped by the expanding 40 dBZ contour of the initial core C (Figure 5.6c, 16:41).

By 16:53 (the next available image, Figure 5.6d) three new 50 dBZ intensity centres had formed near the earlier bulges about the three leading edges of echo C (Figure 5.6c) and surrounded the old core which was still maintaining a 50 dBZ contour as well. However, the old core quickly dissipated as the three new 50 dBZ centres grew rapidly in area (Figure 5.6e, 16:59).

The forward cell (C4) appears to have become by far the dominant cell, e.g., at 17:19 (after some missing scans; Figure 5.6f) the other cells were greatly reduced in intensity.

Forward propagation continued as contiguous new 50 dBZ cells sprang to life, first to the right (C6; Figure 5.6f, 17:19) and then to the left (Figure 5.6g, 17:30) of the general echo motion.

Finally, the last two cells appeared to have merged through the expansion of the 40 dBZ contour as the cells themselves weakened (17:35; Figure 5.6h).

5.4.2 16 November 1987

On 16 November, several moderate sized (approximately 20 km in diameter) convective complexes occurred about the Houtkoppen radar site. At times the storms showed some evidence of an overall linear alignment pattern, but in general the situation was best described as a disorganised area of squalls. In the late afternoon, several storms approached the radar from the west-northwest. Four storms that could be easily tracked (i.e. not confused with ground targets) were studied.

The 16th November was the day with the strongest low-level (below 700 mb) winds, especially for northerly components. Thus, at the start of the radar data (15:41) examined for this day an intense (50 dBZ) nearly 50 km long linear cell approximately 50 km to the southwest of the radar was observed to be moving at about 50 $km.h^{-1}$ toward the east-southeast. This system appears to have consisted of two primary convective areas originally, with the more northerly cell probably developing as the southerly component maximized its intensity (Figures 5.7a and b).

This echo couplet appeared to be moving in parallel with a line which was very close to the radar and probably contaminated by ground return. Further convective developments to the north of the couplet were becoming apparent by 16:00 as several small cells started to appear and grow while the north cell (B) began to maximize its low-level rain flux (Figures 5.7b and c). However, another smaller associated echo couplet (C-D) a few kilometres to the south of cell A (Figure 5.7a) was also growing during this time and other new cells appeared nearby as well. At 16:18 the echo couplet A-B merged with the weaker southern echo couplet C-D apparently as a result of the expansion of C-D. Differential motion relative to the larger A-B couplet appears to have been non-existent (although a precise determination of the translation speed of evolving storms is rarely possible).

The cluster of five or so closely spaced echoes trailing to the immediate north of the merged system (A-B-C-D) at 16:00 will be referred to here as M-N-O-P-Q (Figure 5.7b). Some of these echoes also merged by expansion, first the weaker couplet M and N (Figure 5.7c) and then 10 minutes later the stronger cells O-P-Q (Figure 5.7d). The echo cores maintain their separation distances during this period. Two notable additional echoes form during this period (16:08-16:18), R and S. Echoes M, N and O dissipate during the next half hour (Figure 5.7f). However, M-N never merged with O-P-Q. Echo S pulsates between one and two cores during most of its lifetime, but then merged to the rear of P-Q by 16:49 just as the complex moved into heavy ground clutter (Figure 5.7h). Once again, differential storm speed is not the merger mechanism. The echoes S and P bridged at 16:49 with the core centres in about the same relative location they were in at 16:18.

Storm R grew rapidly. It was about 15 km long by 16:08 (Figure 5.7c), and based on its shape probably consisted of three major towers or cells at that time, although there is no separation in the 30 dBZ contour. This storm also moved rapidly (40 to 50 $km.h^{-1}$) eastward. By 16:18 (Figure 5.7d) it had a 50 dBZ core which was 4 km long and it was rapidly producing contiguous new cells along its north and south edges. The new northern convection (Rn) quickly developed a large (6 km diameter) clearly separate 50 dBZ centre (16:26, Figure 5.7e) as the consolidated southern core shrunk. At this time, a separate new cell (R3) can be seen about 3 km to the northwest of the northern core. This new cell and another separate cell, R4, to its northwest (Figure 5.7g) also rapidly grew and merged with the parent cell (Rn) (Figure 5.7h). The rapid intensification of the new convection (R4) was probably related to strong outflow from (Rn) which was just passing its intensity peak, and from R3 which had already started a rapid decline from its peak of 50 dBZ at 16:43. This storm provides the closest approach to the classical daughter cell example of Chisholm and Renick (1972), reproduced in Figure 3.

5.4.3 2 December 1987

On 2 December, an echo system which grew by a mechanism that appeared similar to the well-known 'daughter cell' pattern (Chisholm and Renick,

1972) was observed approxiamtely 50 km north-northwest of the Houtkoppen radar.

This system occurred between two older irregularly shaped lines of echoes. The longer line was about 200 km long and located some 90 km south of the radar. The shorter line (approximately 80 km long) was about 90 km to the west and nearly perpendicular to the west end of the longer line. As time passed, these two features became more cluster-like. The daughter cell variant developed between these more established systems about 40 km from the nearest echoes to the south.

Starting at about 15:54, radar observations were made of the newer convection. There were four main cells associated with the new daughter type system (Figure 5.8a). Three of the cells had intensities above 40 dBZ. The most intense of these was the cell furthest to the east (cell A), which intensified to more than 50 dBZ by 16:00 and had a diameter of about 10 km (Figure 5.8b). The somewhat larger cell to its north (cell B) was more complex and had a double core. The four cells were separated by about 5 km or less between cells.

These cells remained separate at the 23 dBZ level for about 10 minutes more and then at 16:04, shortly after the peak rain from cell A, the two northernmost cells merged at the 23 dBZ level as an area of weak echo bridged the gap between them (Figure 5.8c). Within nine minutes all four cells were linked at the lowest intensity level (23 dBZ), and by 16:20 (Figure 5.8d) a linear configuration was emerging along the northwest side of the complex from the alignment of the northernmost cell (B) with the two cells furthest to the west and the considerable expansion and thereby merging of their 30 dBZ core areas. 50 dBZ intensities were observed at two locations along the line, as well as in cell A. Cell A diminished soon after its peak rainout and the linear pattern to the north became dominant (Figure 5.8e). The complete system was in an advanced state of decay by 17:00.

Thus, a southern hemisphere version of the classic daughter cell merging seems to be occurring around 16:20. Actually, existing echoes are merging via expansion. Nevertheless, the intensification of the line after the peak rain from cell A indicates that its outflow air may have contributed to the enhancement of the new line. Since this is not the feeder cell pattern (there is little relative motion of the cells and there is also no sign of overwhelming growth by any of the cell cores), it is probably best to associate the expansion type of merging with the daughter cell pattern, as the central cores appear to remain relatively independent throughout the process and would all have to be treated separately by a seeding aircraft.

5.5 CONCLUSIONS

The merged cloud systems described in this study had dimensions of about 25 to 50 km (23 dBZ contour). Typical 40 dBZ cells were up to 5 to 15 km long, with 50 dBZ cores being roughly half that size. Thus, these storms are large but still likely treatment candidates. It also seems likely that up to four cells may often be present at about the same time in a multicellular system in the process of developing and more contiguous cells may appear later on during continued propagation.

Based on virtually all the storms studied here, it is quite clear that a very common type of echo pattern in multicell storms is for sequential cells to appear near each other but with cores (and towers) which do not merge. Instead, they remain remote at nearly constant spatial separations and echo merging is achieved primarily via the expansion of the weaker echo periphery of the discrete cells. Furthermore, over 20 years of experience with storm observations suggest that the expansion pattern is one of the most, if not the most, frequent types of cloud merging. Nearby cells may exist independently or may be initiated and/or influenced by the downdraughts or pressure pulses from neighbouring cells, but the actual mechanism of the cells linking together is related to the cells proximity rather than some explosive strongly interactive dynamic mechanism and thus, the merging often occurs in a relatively benign fashion. If isolated multiple cellular storms are to be focused on for the rain stimulation research activities, this type of merging will be encountered quite frequently. Expanding systems are probably not as likely to be hazardous for penetrating aircraft as those systems merging via mechanisms involving strong relative cell motions or the rapid systematic self generating propagation and incorporation of new cells. Nevertheless, expanding storm systems will still be relatively difficult to treat for rain stimulation purposes, as the storms may still be quite intense, and each cell must be treated individually.

5.6 REFERENCES

BEYERS H R and BRAHAM R R Jr, 1949. *The Thunderstorm: Report on The Thunderstorm Project*. US Government Printing Office, Washington DC, 287pp.

CARTE A, 1981. Morphology of persistent storms in the Transvaal on 16/17 October 1978. *Atmos. Phys.*, 54, 86-100.

CARTE A and HELD G, 1978. Variability of hailstorms on the South African plateau. *J. Appl. Meteor.*, 17, 365-373.

CHANGNON S A Jr, MORGAN G M, ACHTEMEIR G L, TOWERY N G and GROSH R C, 1975. Design of an experiment to suppress hail project for Illinois. *J. Appl. Meteor.*, 14, 771-782.

CHANGNON S A Jr, 1976. Effects of urban areas and echo merging on radar echo behaviour. *J. Appl. Meteor.*, 15, 561-570

CHENG L, 1989. Numerical simulations of hailstorm feeder-cloud initiation. *Atmos. Ocean.*, 27, 279-305.

CHISHOLM A J and RENICK J H, 1972. The kinematics of multicell and supercell Alberta hailstorms. *Contribution to 6th Annual Conference of the Canadian Meteorological Society*, Toronto, 24-31.

CSIR/CLOUDQUEST, 1990. *Programme for Atmospheric Water Supply. Phase 2, 1987-1989, Volume 1: Executive Summary*. WRC Report No. 133/5/90, Pretoria, 8pp.

DENNIS A S, SCHOCK C A and KOSCIELSKI A, 1970. Characteristics of hailstorms in western South Dakota. *J.Appl. Meteor.*, 9, 127-135.

FARLEY R D and ORVILLE H D, 1986. Numerical modelling of hailstorms and hailstone growth. Part 1: Preliminary model verification and sensitivity test. *J. Clim. Appl. Meteor.*, 21, 2014-2035.

FOOTE G B and FRANK H W, 1983. Case study of a hailstorm in Colorado. Part III: Airflow from triple Doppler measurements. *J. Atmos.Sci.*, 40, 686-707.

GOMES A M, O'BEIRNE S and HELD G, 1989. *Second Progress Report: Precipitation and Air Flow (PRAI) Project*. CSIR, Pretoria, 42pp.

GRICE G K and MADDOX R A, 1984. Radar signatures associated with heavy rains. *Preprints: 22nd Conference on Radar Meteorology*, AMS, Boston, 182-187.

GROSH R C,1978a. Lightning and precipitation in the life history of isolated thunderstorms. *Preprints: Conference on Cloud Physics and Atmospheric Electricity*, AMS Boston, 617-624.

GROSH, R C, 1978b. A local severe rainstorm. *Preprints: Flash Floods Conference*, AMS,Boston, 70-79.

HILL G E, 1974. Factors controlling the size and spacing of cumulus clouds as revealed by numerical experiments. *J. Atmos. Sci.*, 31, 646-673.

HOUZE R A, Jr and CHENG C P, 1977. Radar characteristics of tropical convection observed during GATE. Mean properties and trends over the summer season. *Mon. Wea. Rev.*, 105, 964-980.

LOPEZ R E, 1976. Radar characteristics of the cloud populations of tropical disturbances in the northwest Atlantic. *Mon. Wea. Rev.*, 104, 268-283.

MALKUS J S, 1954. Some results of a trade-cumulus cloud investigation. *J. Meteor.*, 11, 220-237.

ORVILLE H D, KUO H, FARLEY R D and HWANG C S, 1980. Numerical simulation of cloud interactions. *J. Rech. Atmos.*, 14, 499-516.

PRESTON-WHYTE R A and TYSON P D, 1988. *The Atmosphere and Weather of Southern Africa*. Oxford U. Press., Cape Town.

TURPEINEN O, 1982. Cloud interactions and merging on day 261 of GATE. *Mon. Wea. Rev.*, 110, 1238-1254.

WESTCOTT N E, 1977. Radar characteristics of south Florida convective rainfall. *Proceedings, Sixth Conference on Planned and Inadvertent Weather Modification*. Champaign-Urbana, Ill. 10-13 October 1977, AMS, Boston, 190-191.

WESTCOTT N E, 1984. A historical perspective on cloud mergers. *Bull. Amer. Meteor. Soc.*, 65, 219-226.

WESTCOTT N E and KENNEDY P C, 1989. Cell development and merger in an Illinois thunderstorm observed by Doppler radar. *J. Atmos. Sci.*, 46, 117-131.

WILHELMSON R B and CHEN C S, 1982. A simulation of the development of successive cells along a cold outflow boundary. *J. Atmos. Sci.*, 39, 1466-1483.

WILKENS E M, SASAKI Y K, GERBER G E and CHAPLIN W H Jr, 1976. Numerical simulation of the lateral interactions between buoyant clouds. *J. Atmos. Sci.*, 33, 1321-1329.

01/28c/sgg

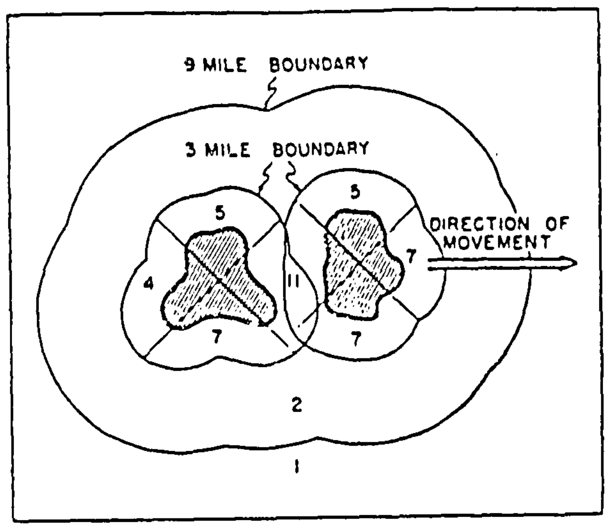

Figure 5.1 The relative probability for the formation of new thunderstorm cells in the vicinity of parent cells (northern hemisphere). The hatched areas represent the PPI radar echoes from the parent cells and the irregular closed curves represent the limits of the 3- and 9-mile (4,8 and 14,5 km) zones surrounding the echoes. The numbers indicate the relative probability of new echo (cells) formation in the zones and quadrants with the probability outside the 9-mile (14,5 km) zone being considered as unity. (After Byers and Braham, 1949; Westcott, 1984.)

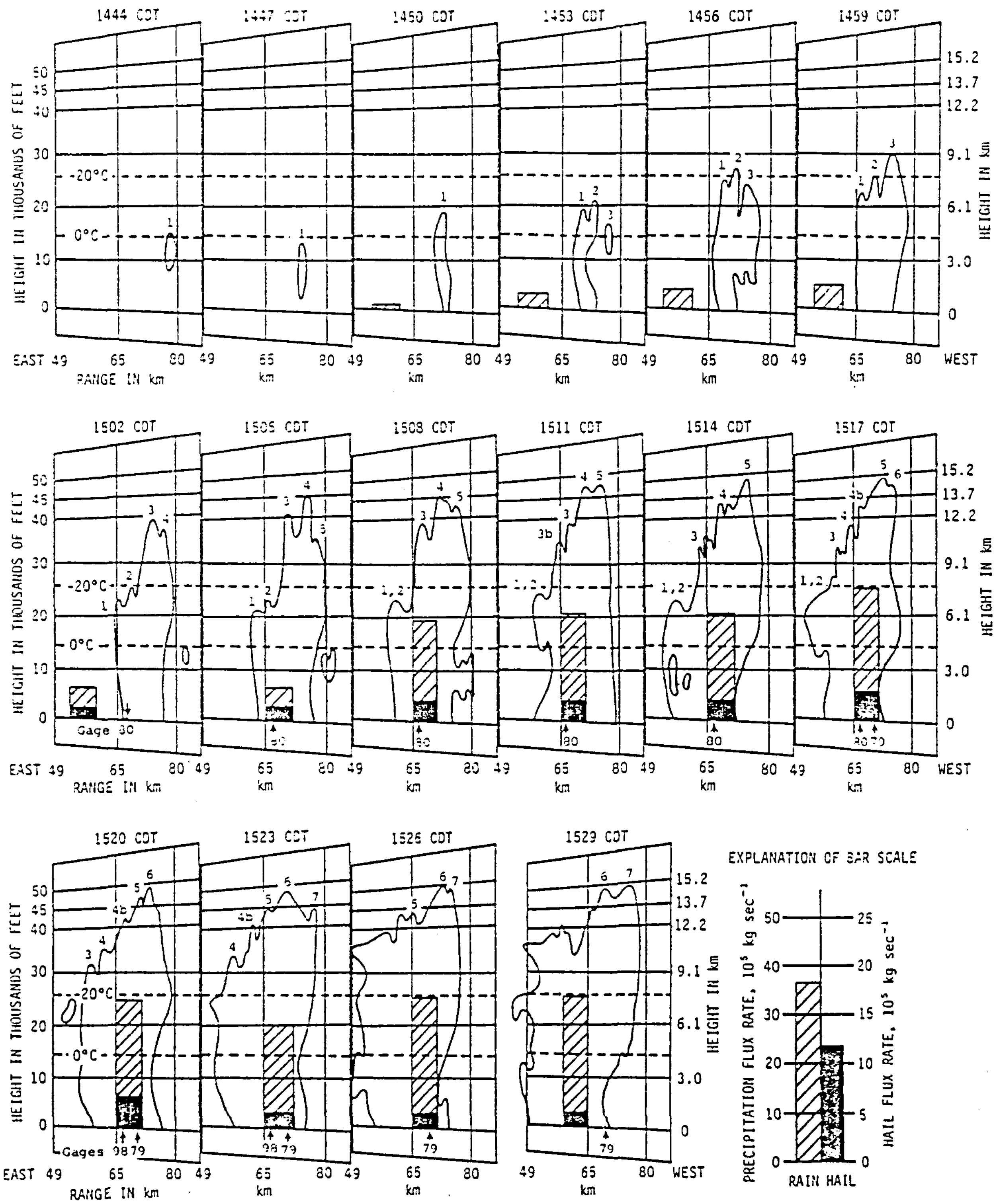

Figure 5.2 Feeder cells overtaking earlier cells and becoming the dominant cell in a heavy Illinois rain storm. (After Grosh, 1978b.)

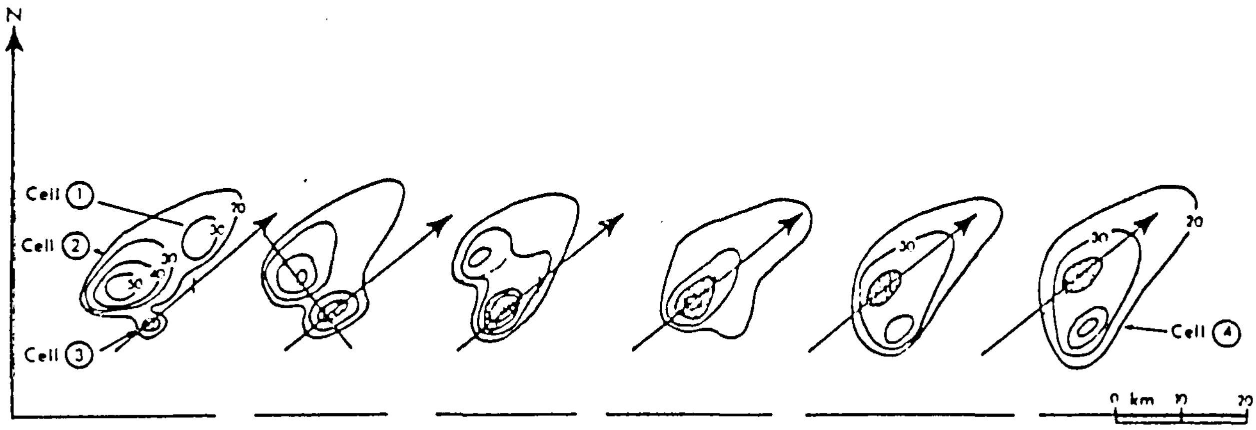

Figure 5.3 Schematic PPIs of evolution of multicellular Canadian storm over 21 minute period. (After Chisholm and Renick, 1972.)

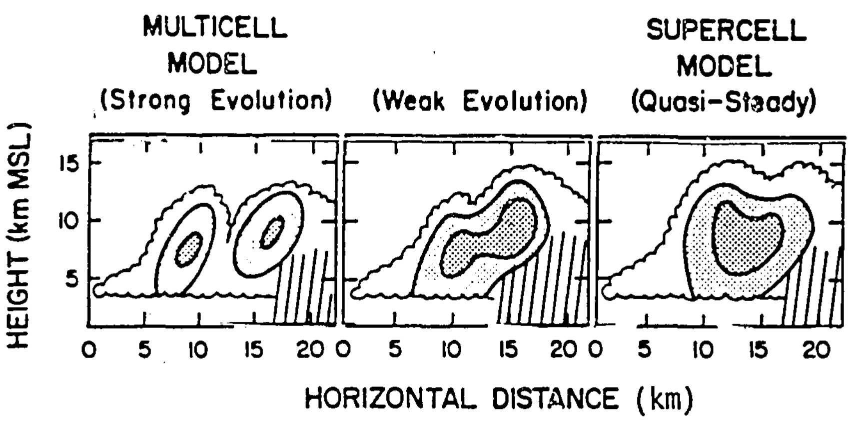

Figure 5.4 Schematic depiction of "weak evolution" of updrafts as seen in comparison with the structural difference between strongly evolved and steady storms. Contour lines represent 5 and 15 mps isotachs. (After Foote and Frank, 1983.)

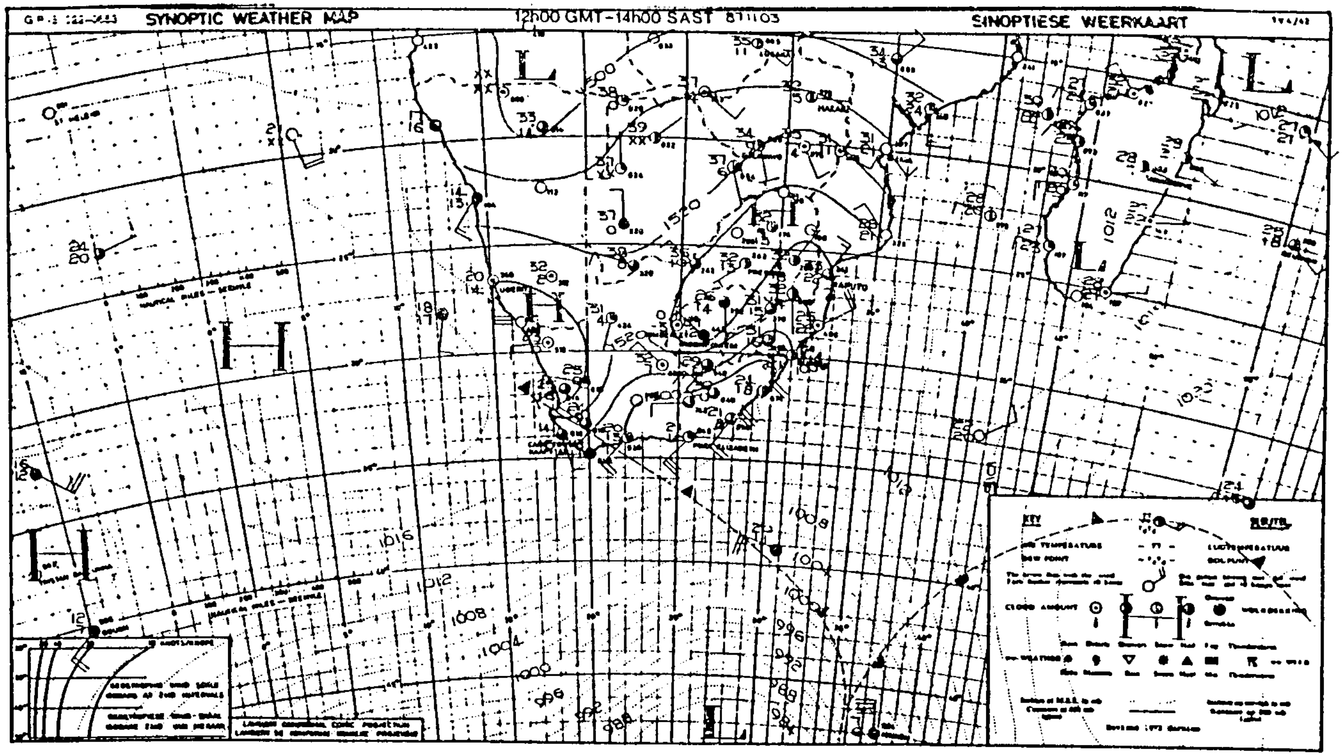

Figure 5.5a Synoptic weather chart for 3 November, 1987 (SA Weather Bureau).

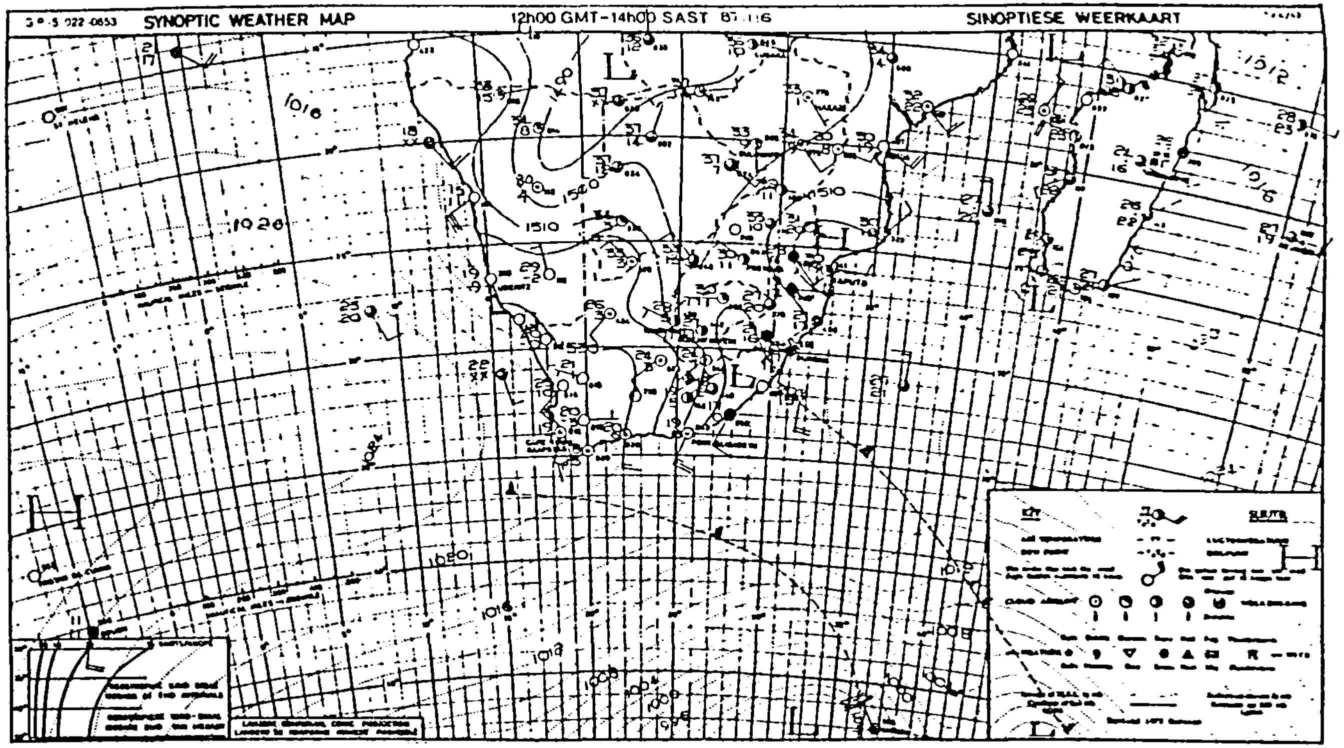

Figure 5.5b Synoptic weather chart for 16 November 1987 (SA Weather Bureau).

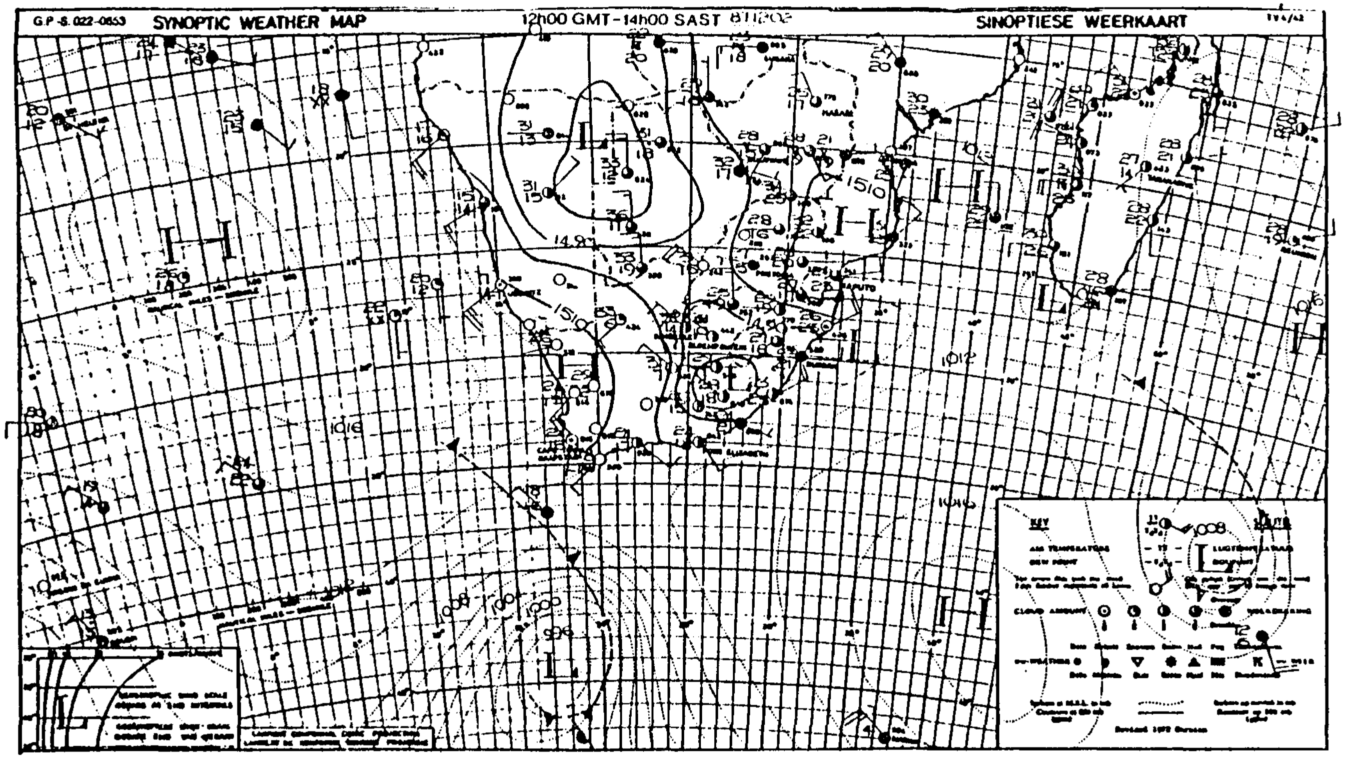

Figure 5.5c Synoptic weather chart for 2 December 1987 (SA Weather Bureau).

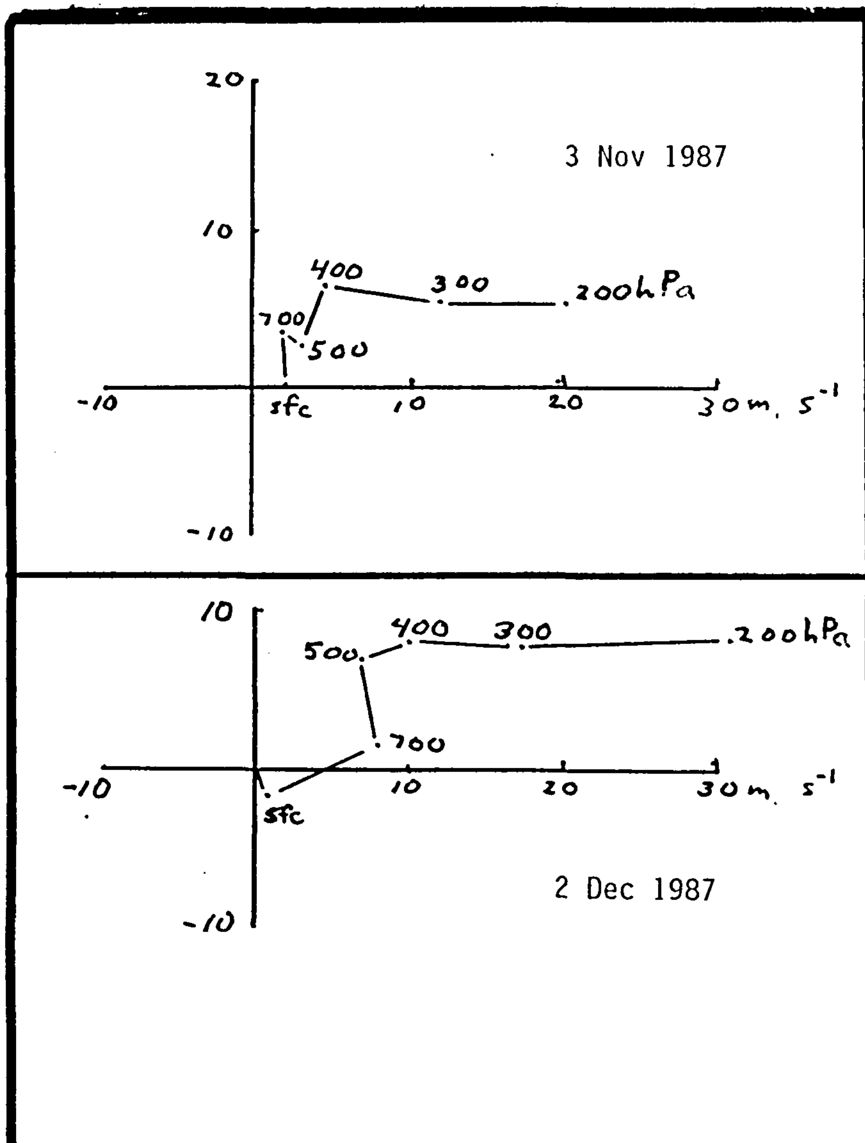

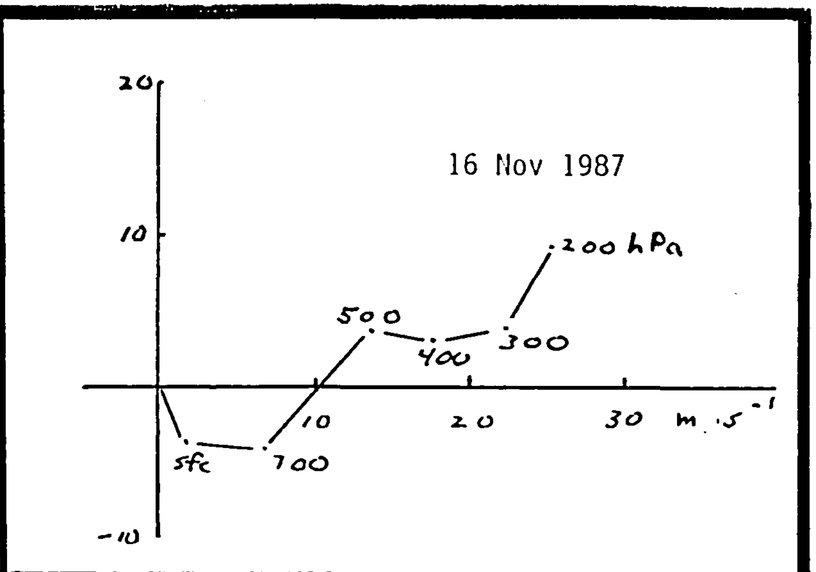

Figure 5.5d Irene hodographs for noon (13:30) on the study days.

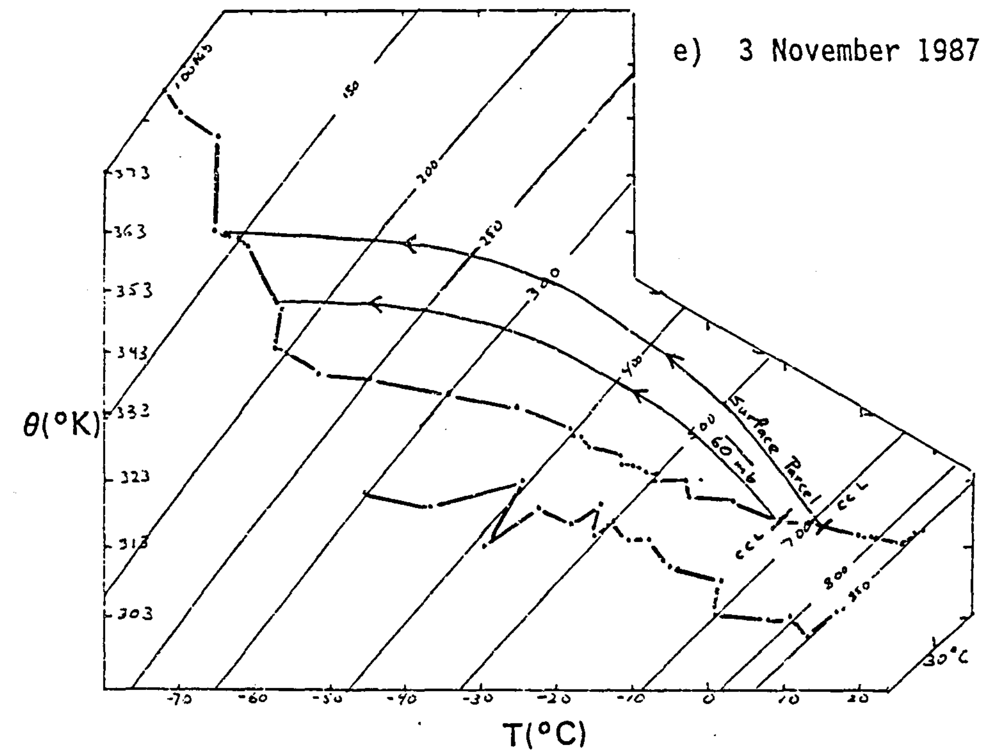

Figures 5.5e, f and g Noon soundings from Irene for the three study days. Thermodynamic "trajectories" are for surface conditions and a surface layer 60 hPa deep.

g) 2 December 1987

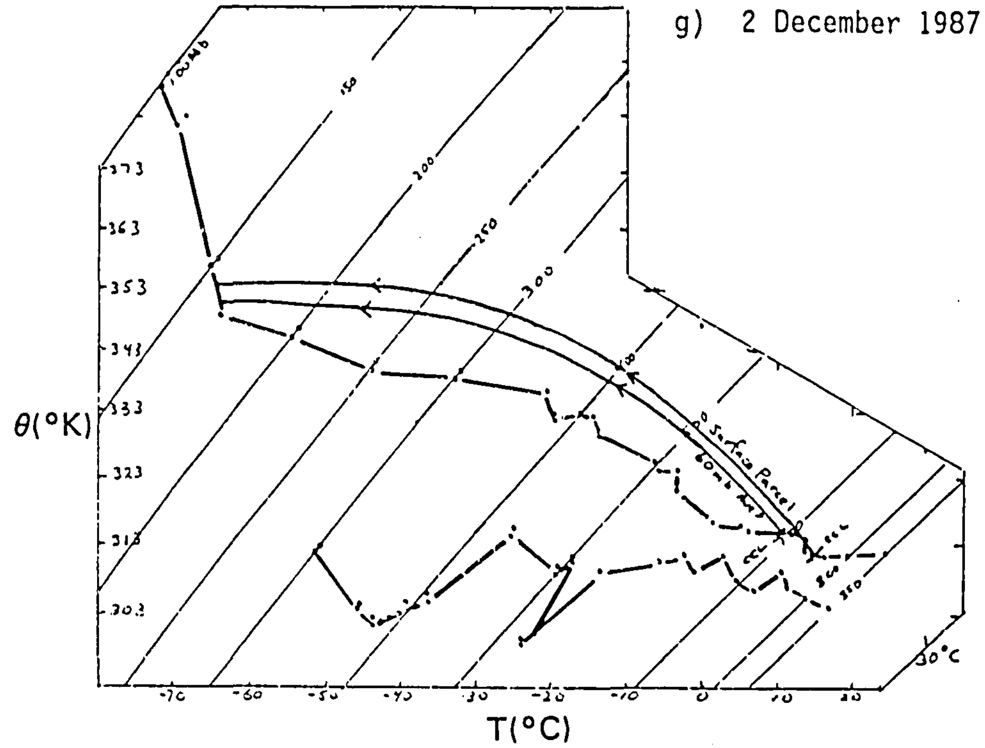

f) 16 November 1987

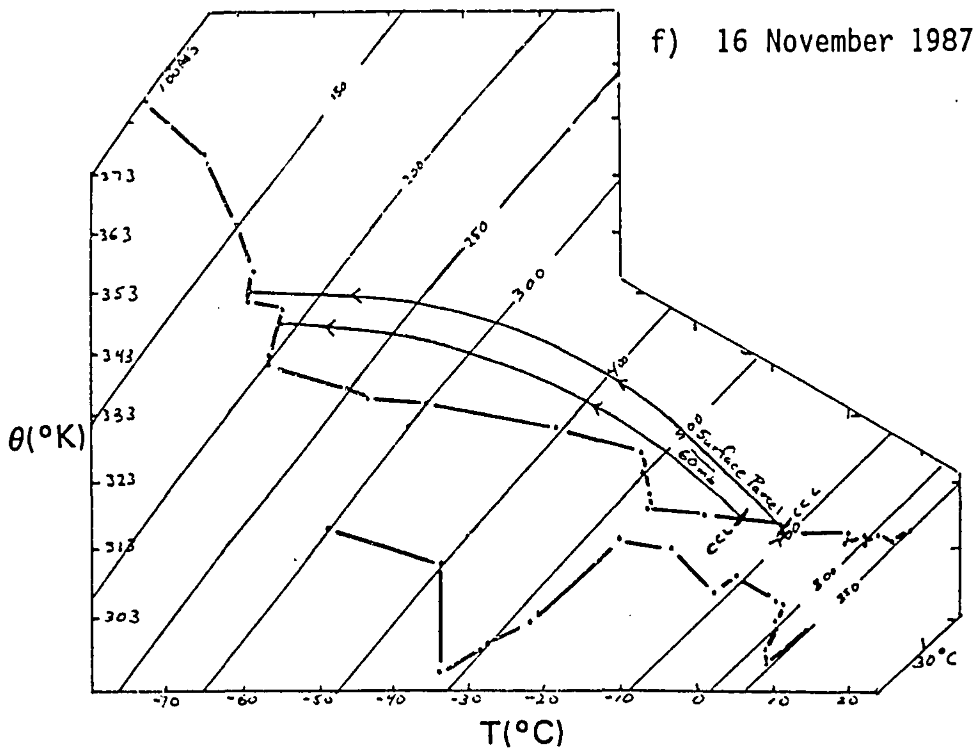

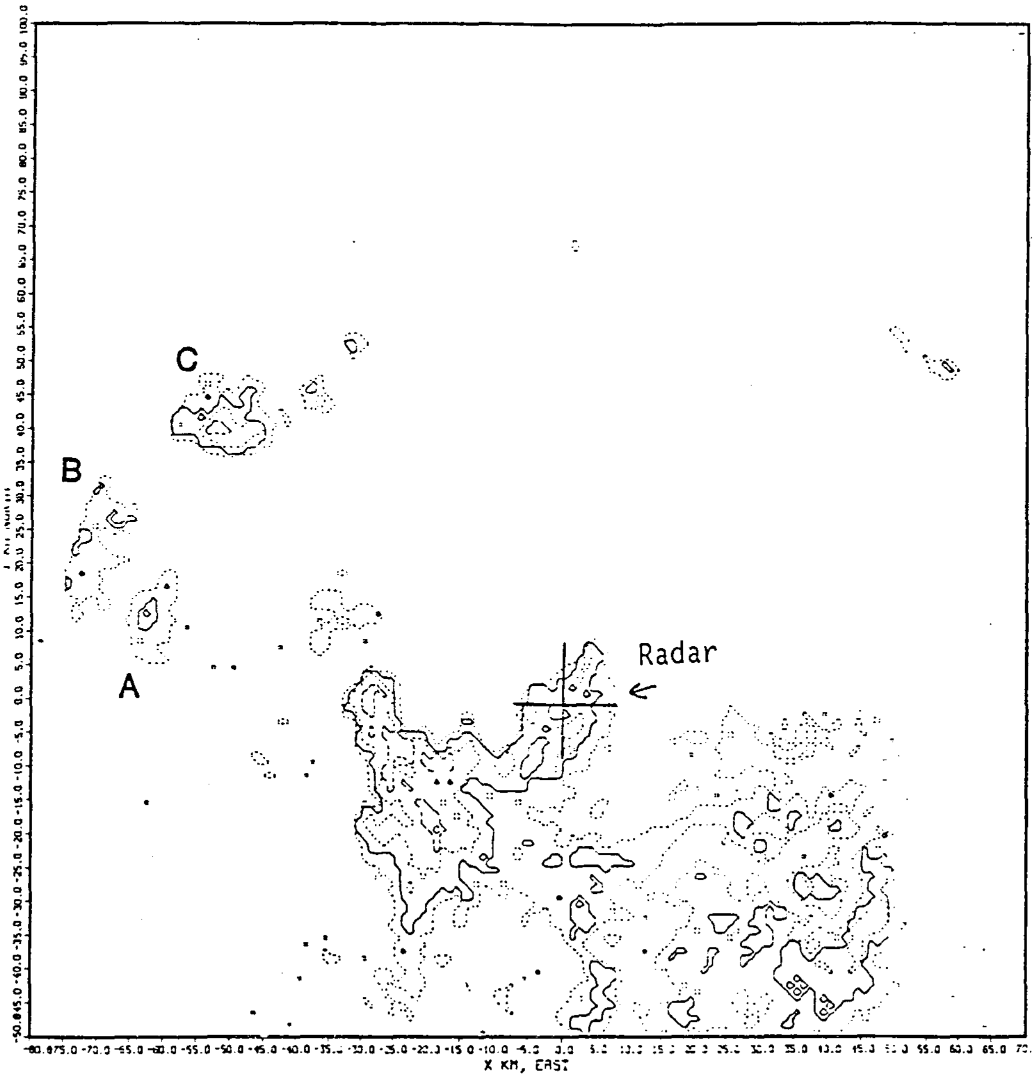

Figure 5.6 Radar PPI images for 3 November 1987 (antenna elevation 5°). Contours depict 23, 30, 40 and 50 dBZ intensities.
a) 16:32 SAST.

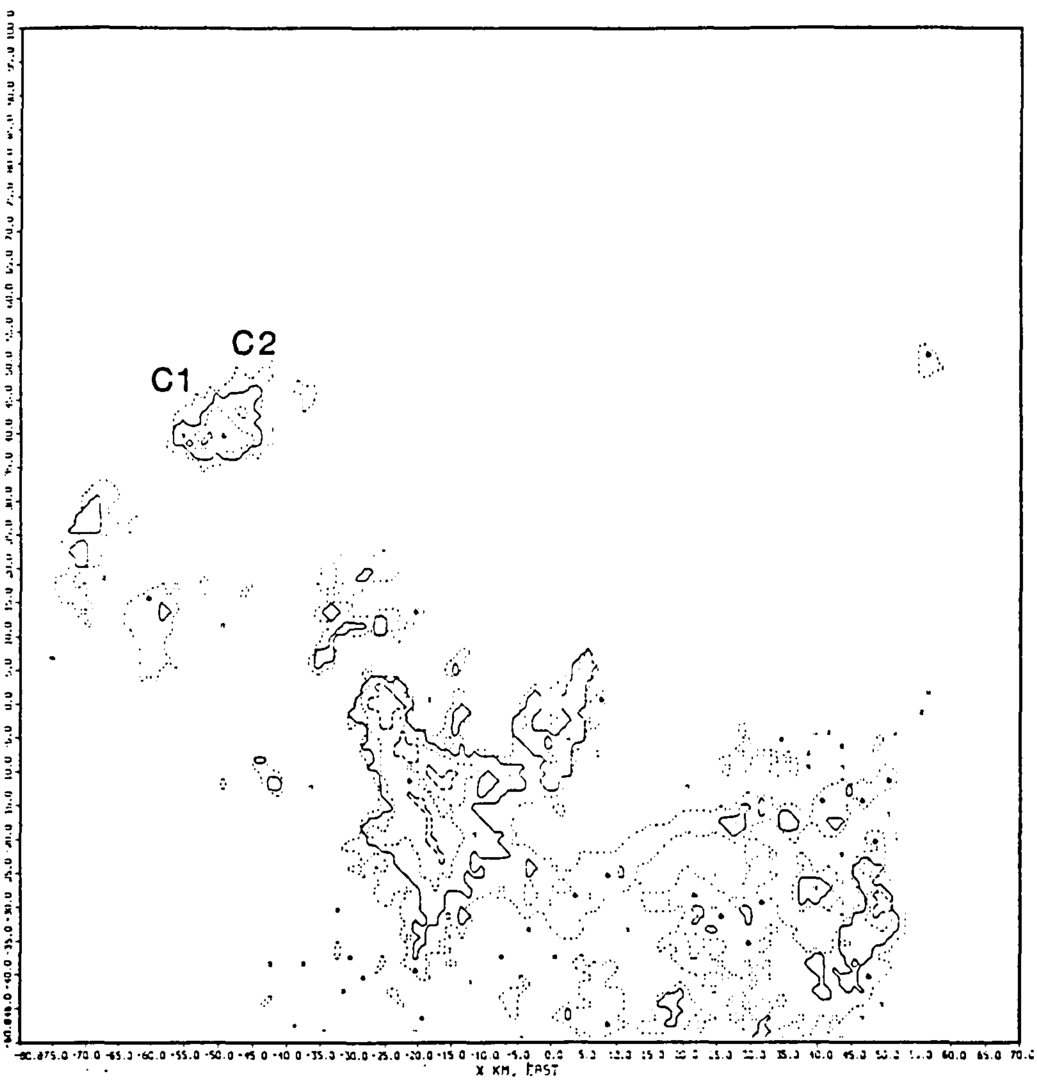

Figure 5.6b 16:38

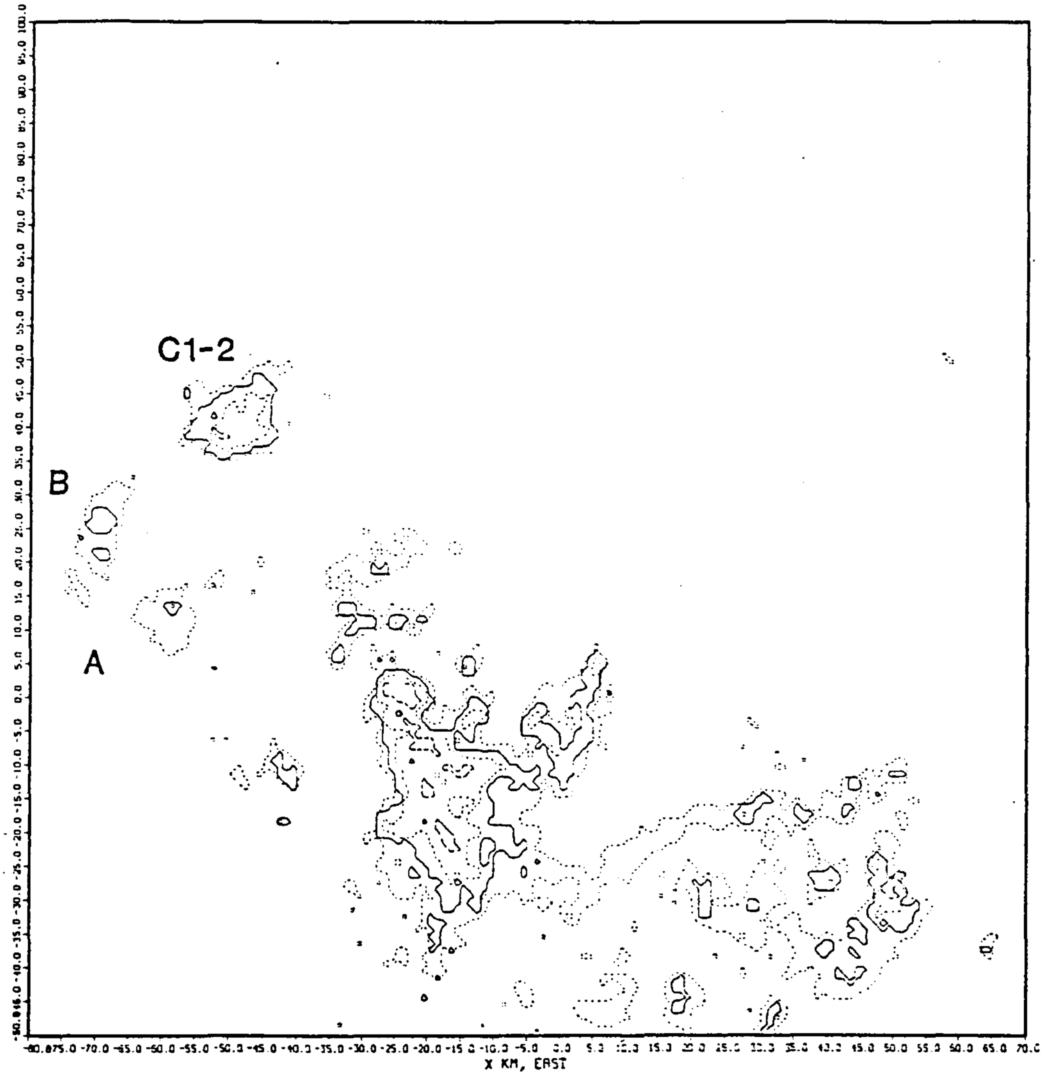

Figure 5.6c 16:41

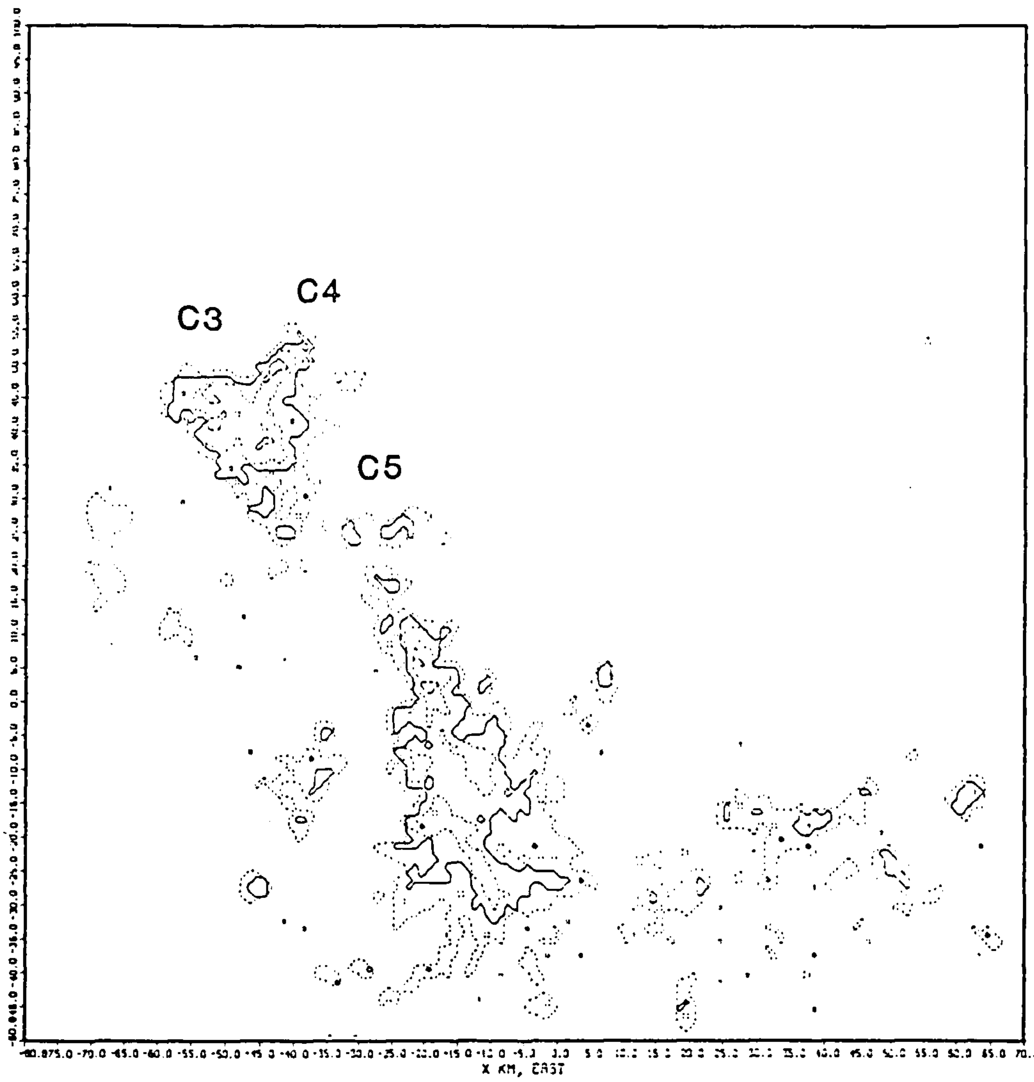

Figure 5.6d 16:53

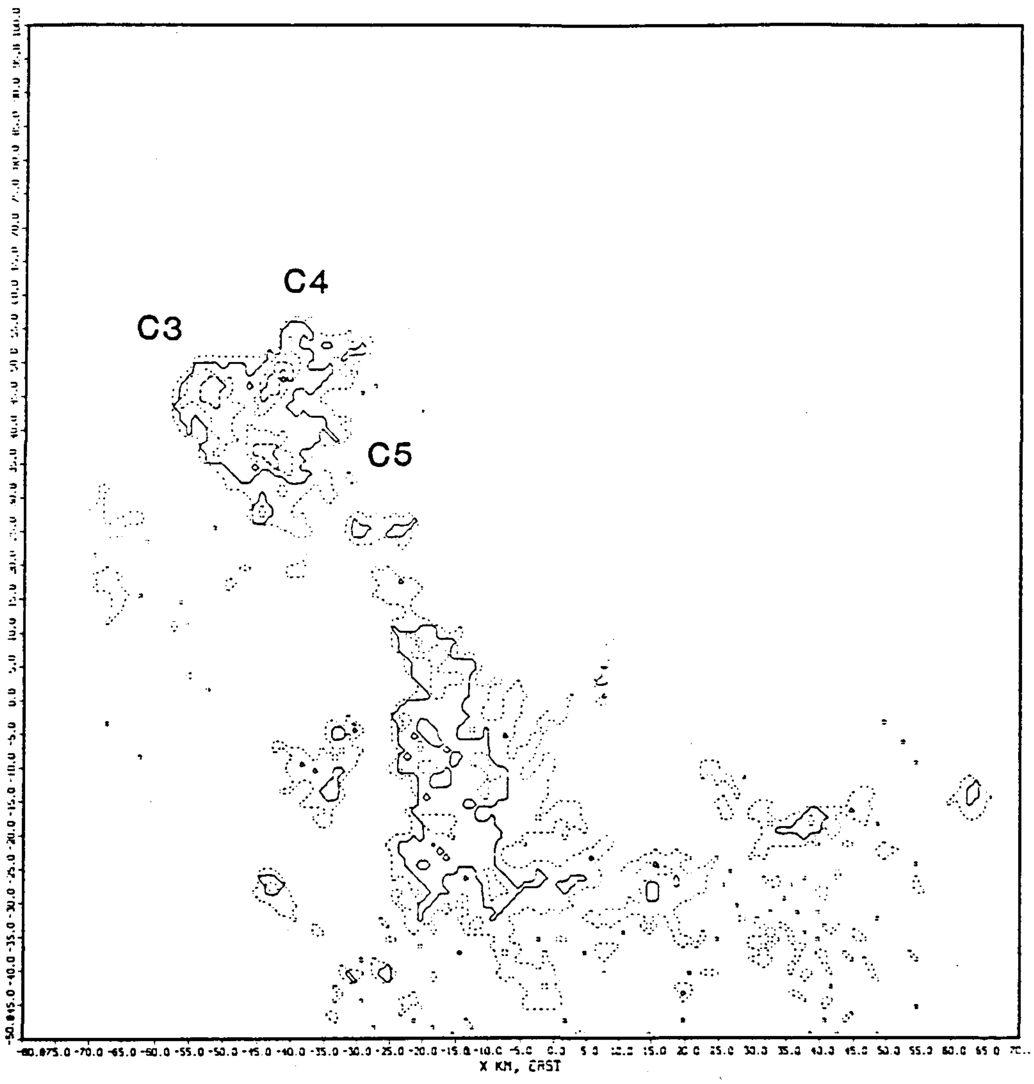

Figure 5.6e 16:59

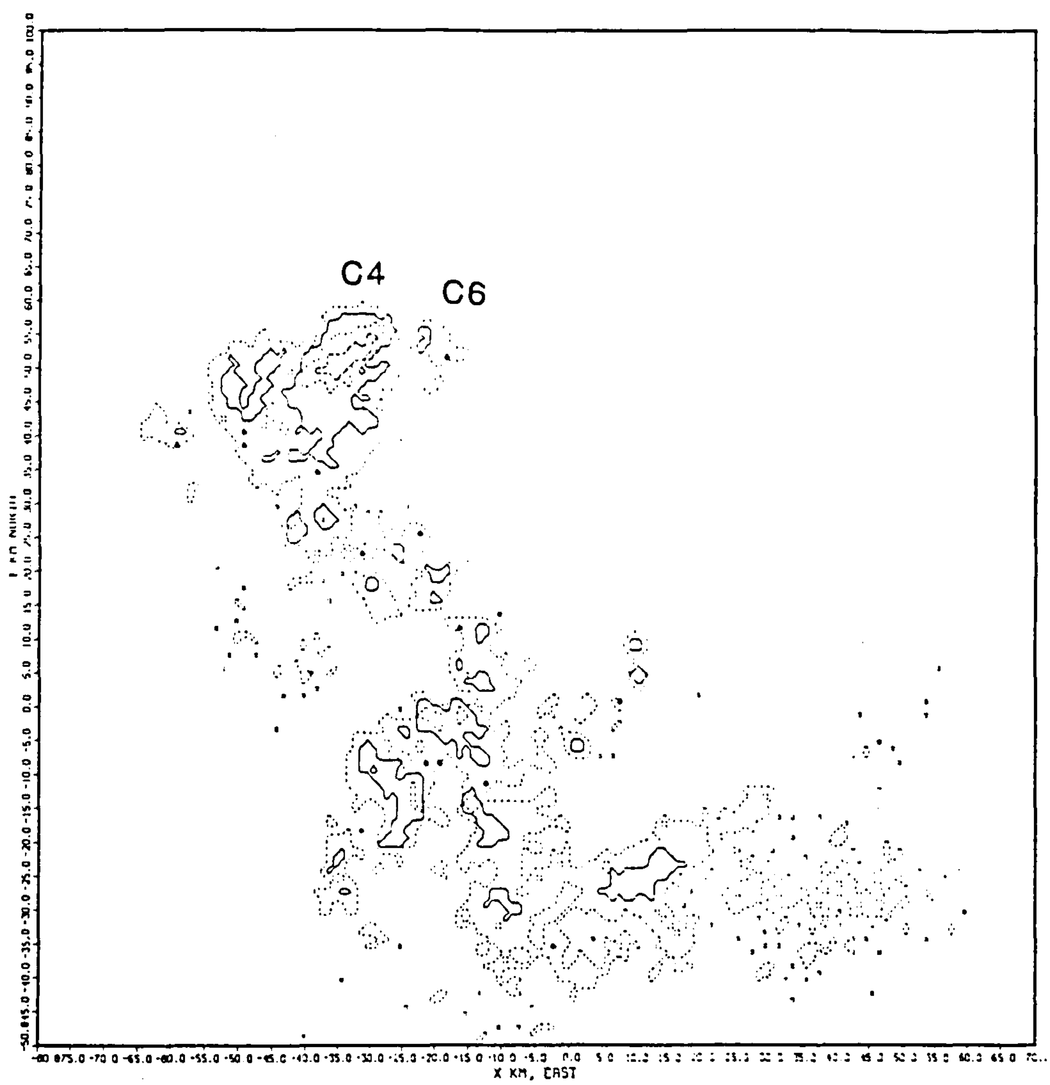

Figure 5.6f 17:19

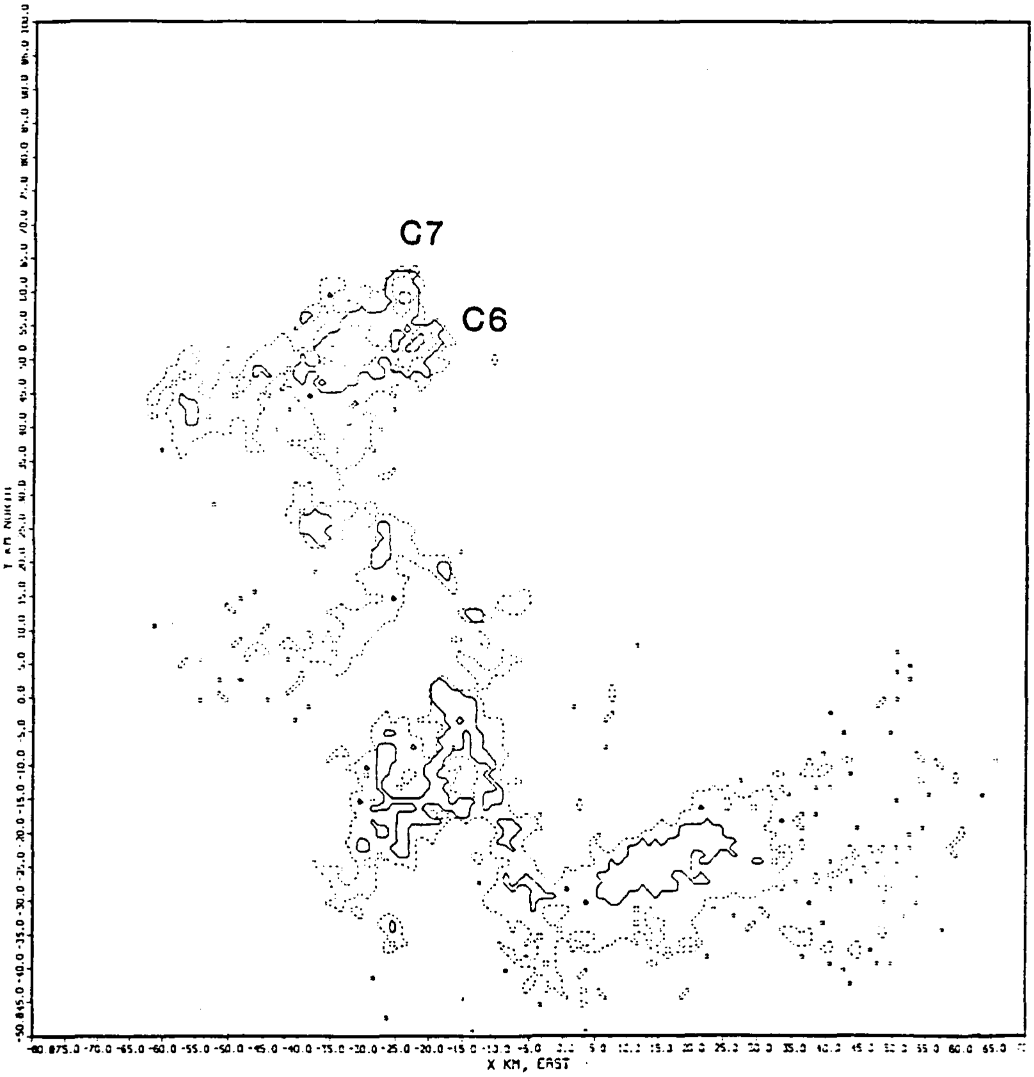

Figure 5.6g 17:30

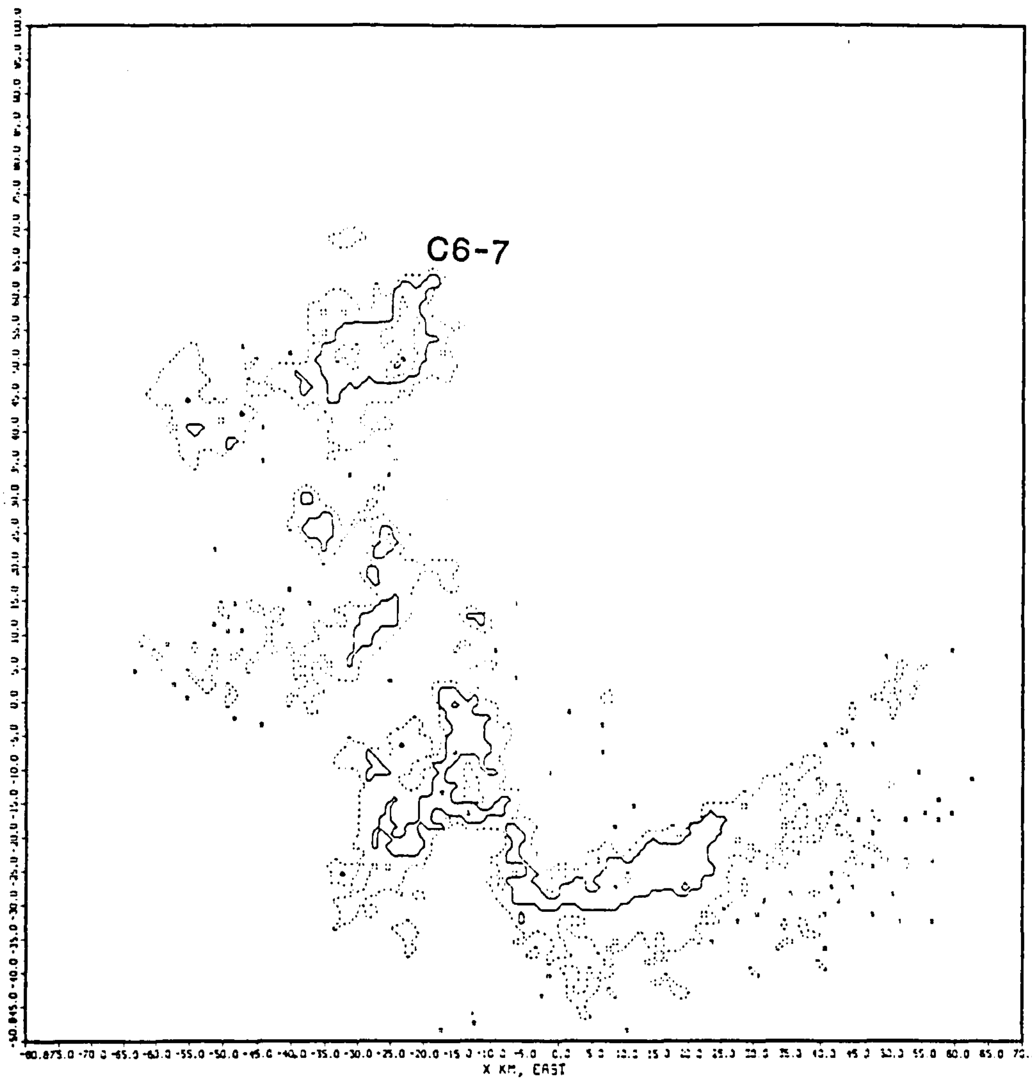

Figure 5.6h 17:35

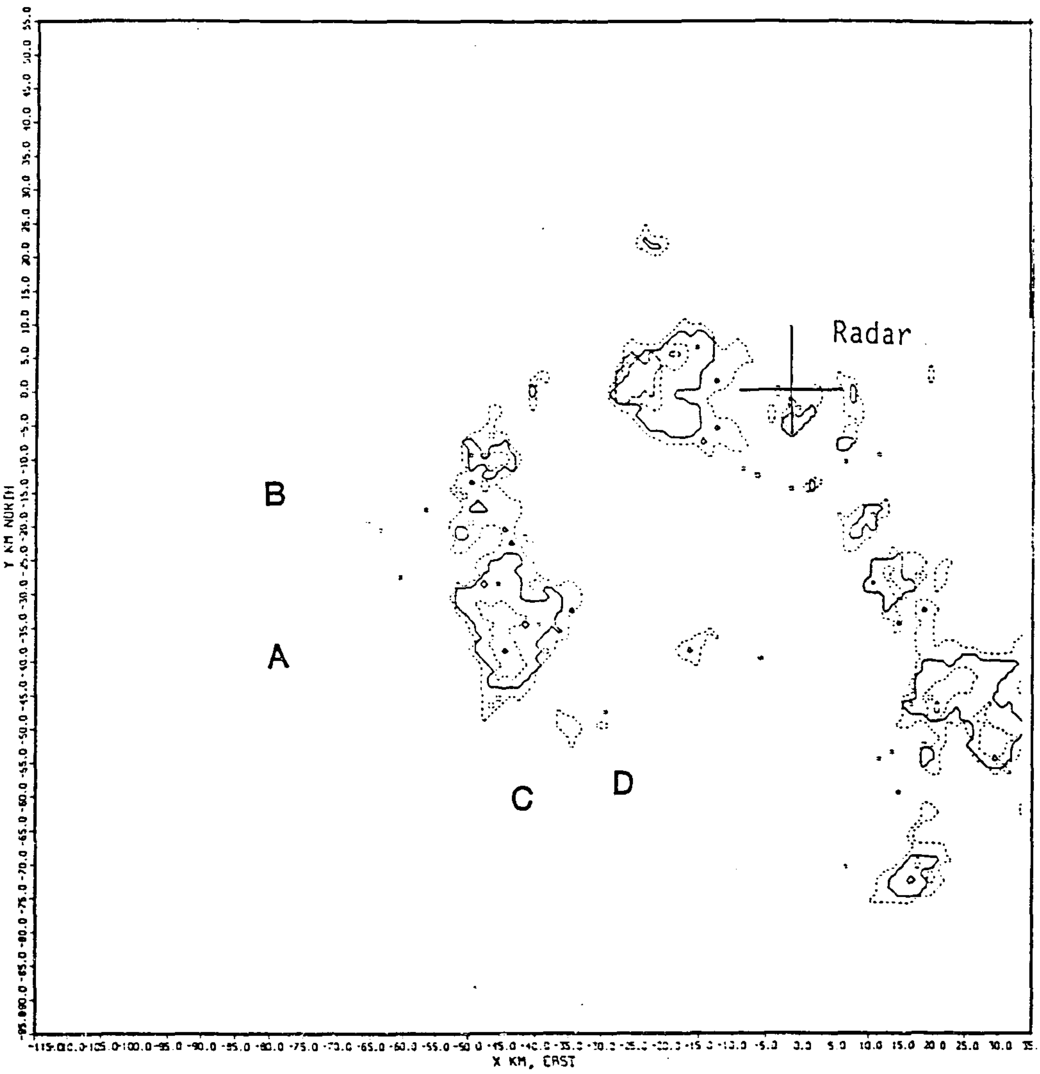

Figure 5.7 Radar PPI images for 16 November 1987 (antenna elevation 2°). Contours depict 23, 30, 40 and 50 dBZ intensities.
a) 15:41 SAST.

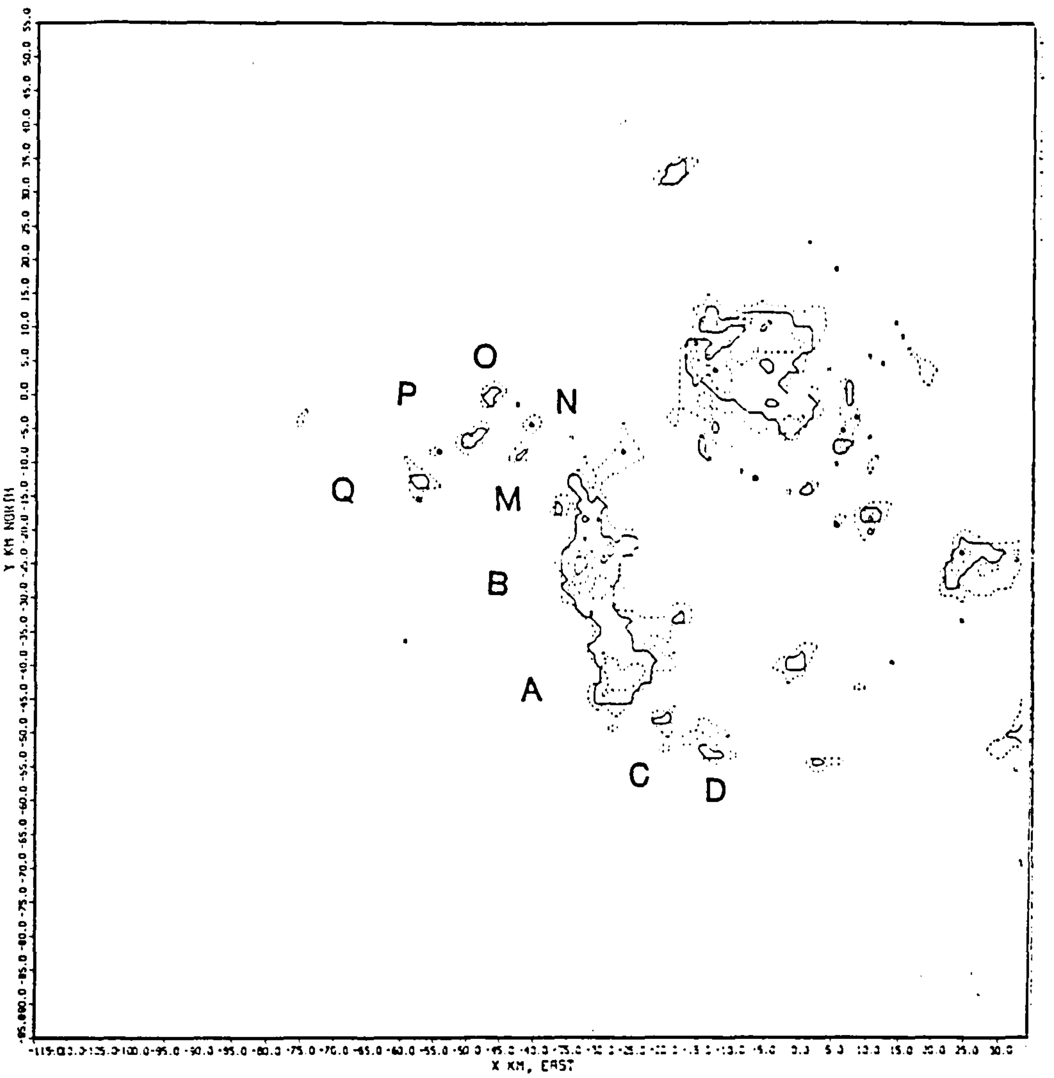

Figure 5.7b 16:00

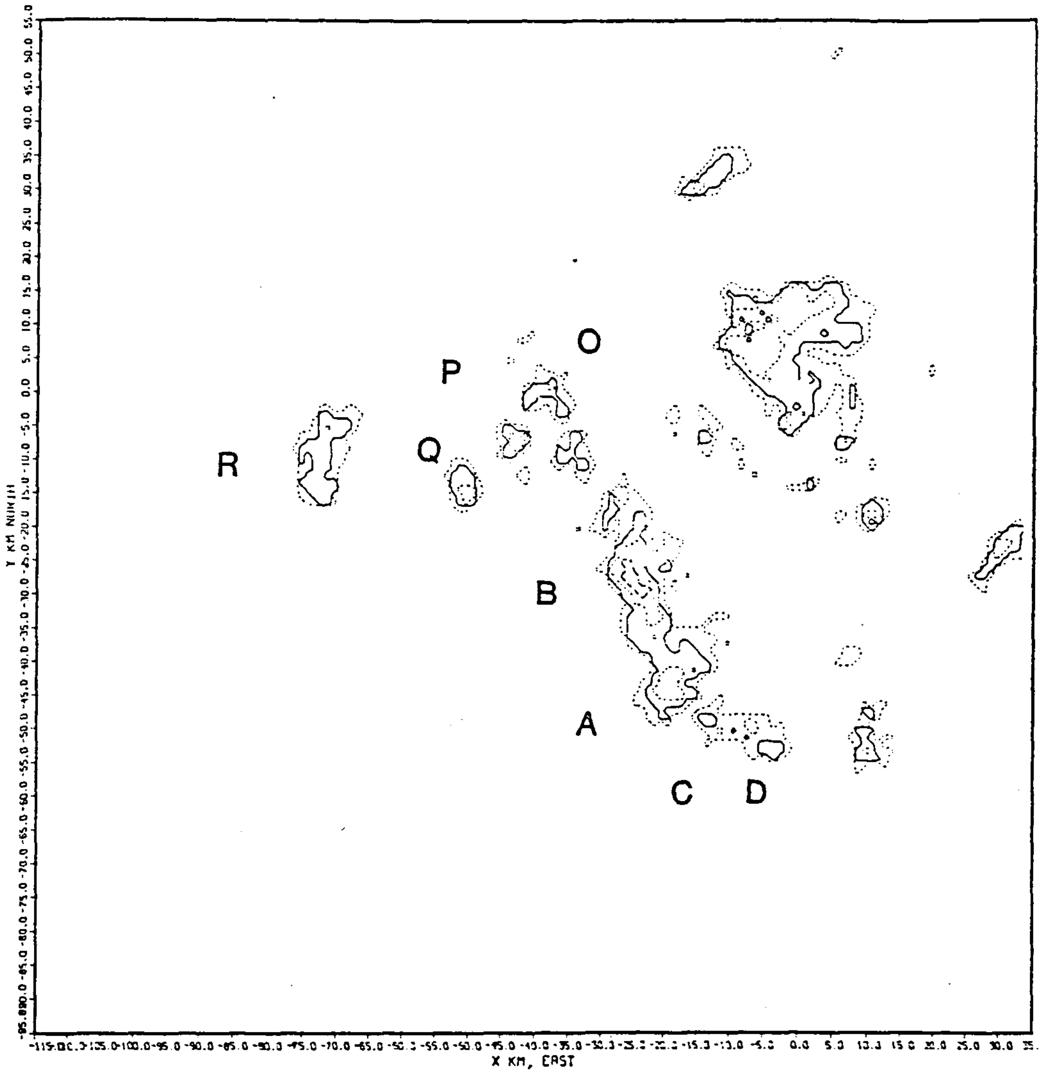

Figure 5.7c 16:08

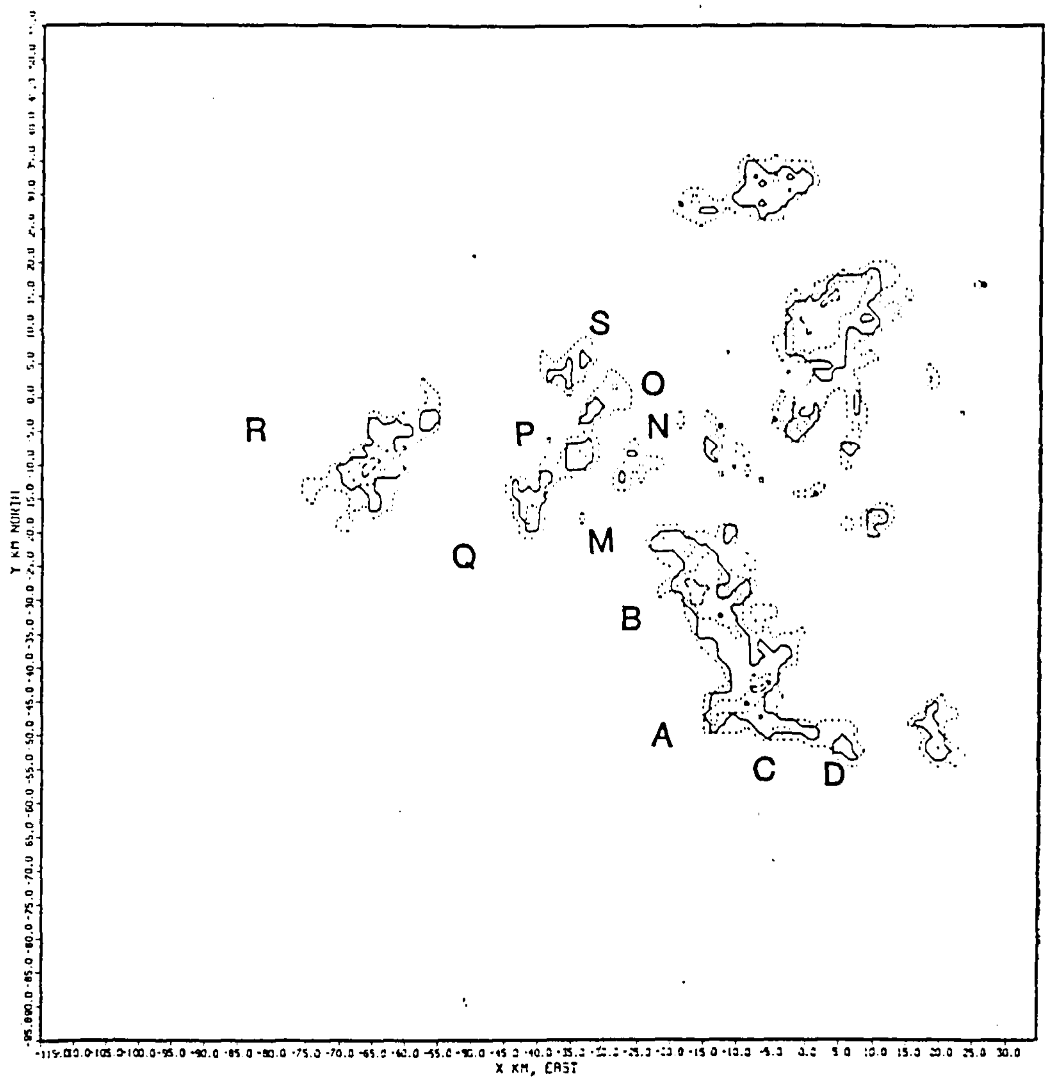

Figure 5.7d 16:18

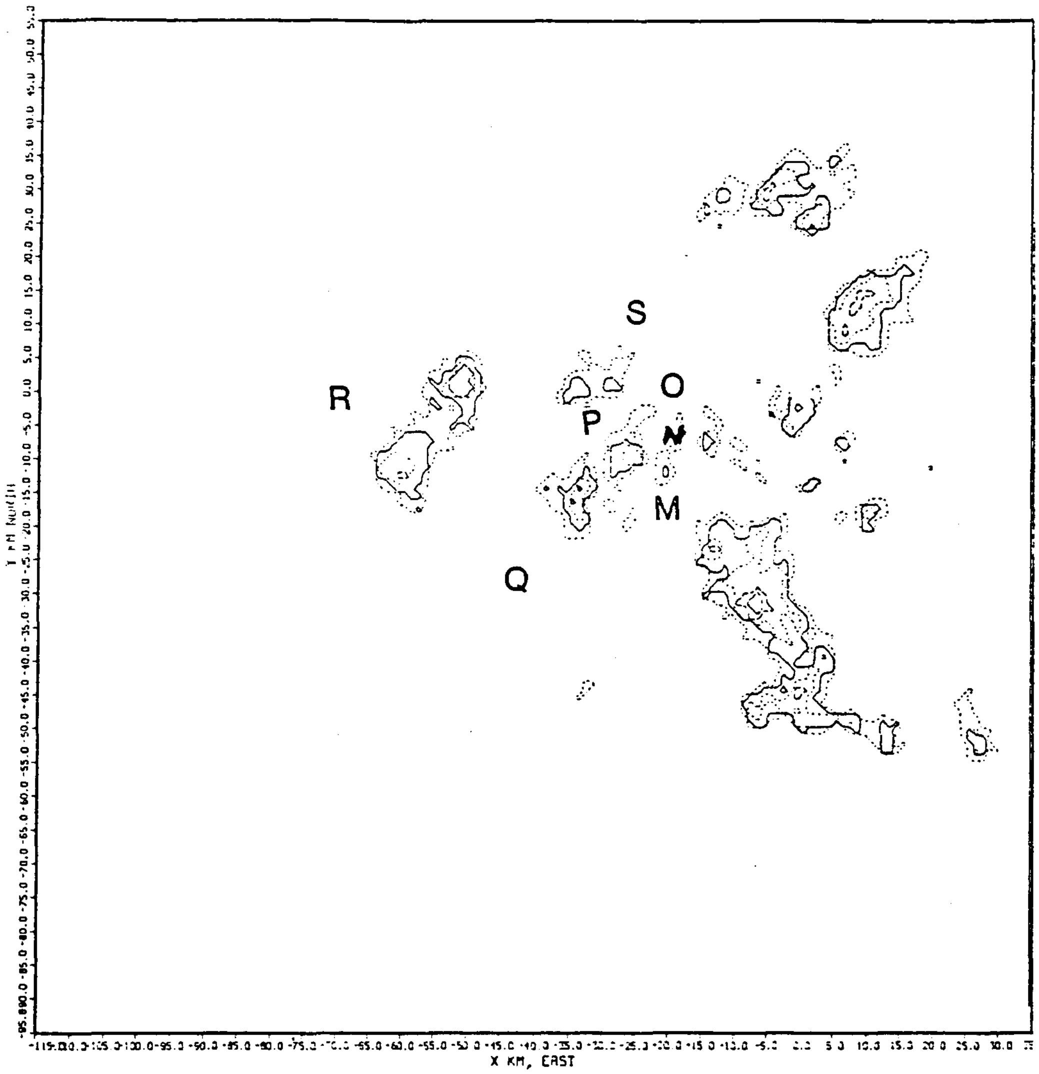

Figure 5.7e 16:26

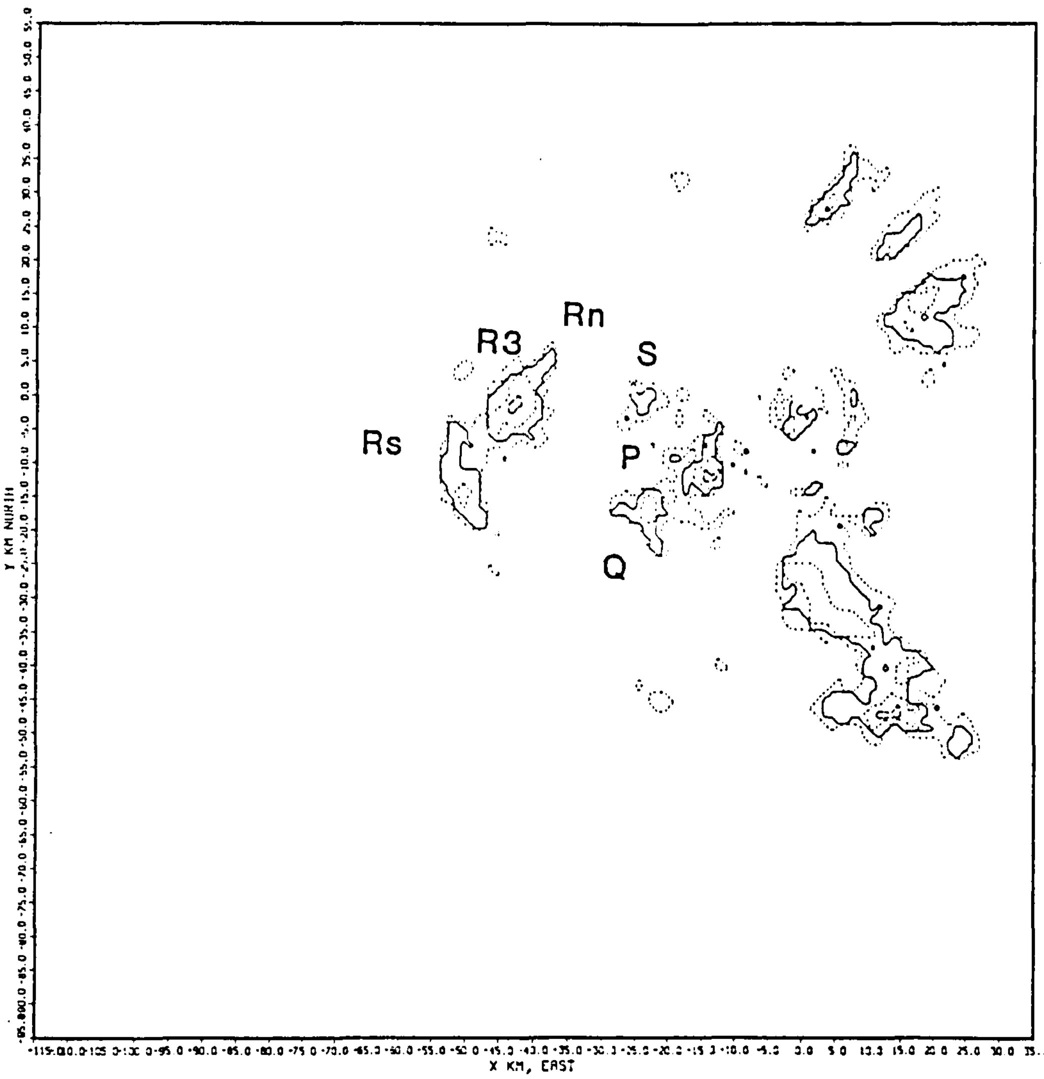

Figure 5.7f 16:39

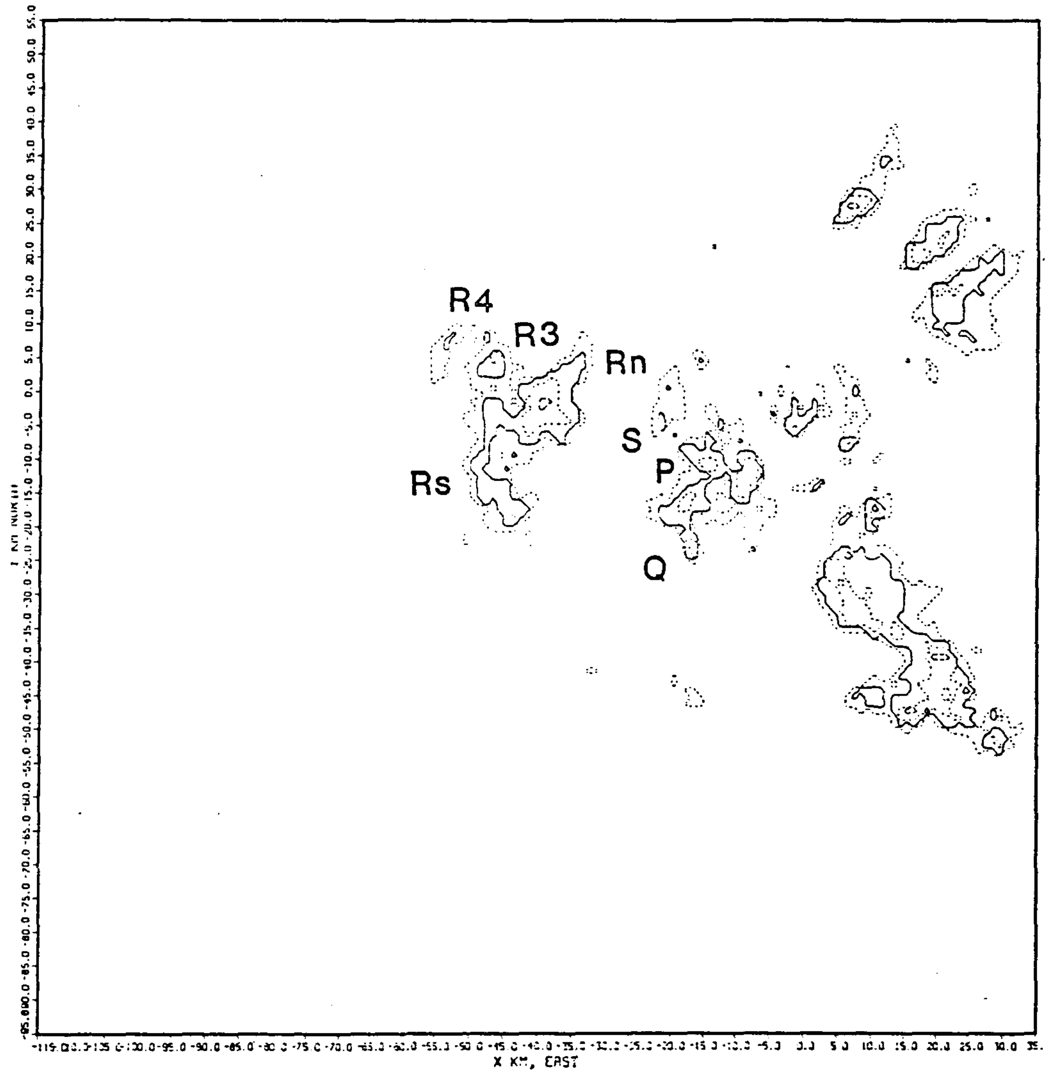

Figure 5.7g 16:43

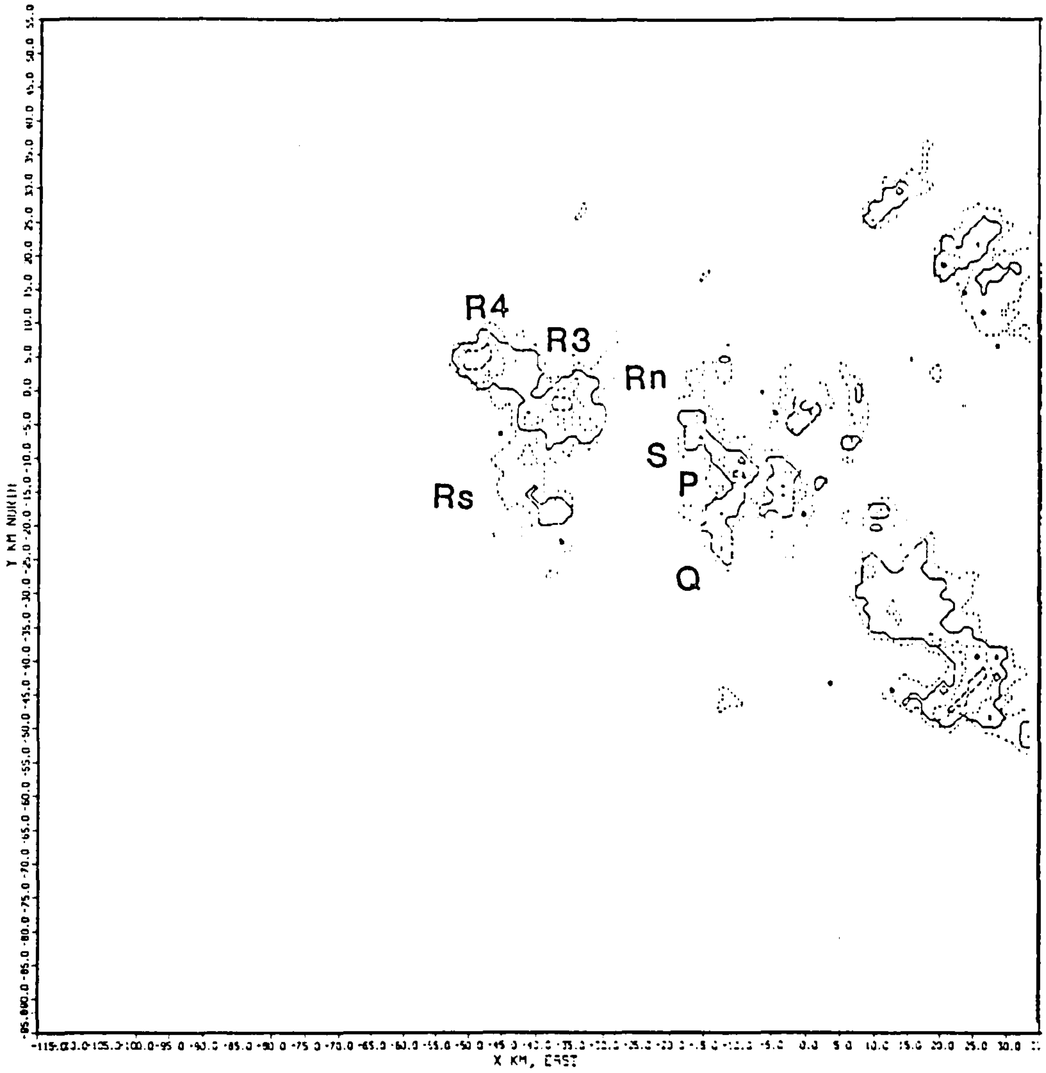

Figure 5.7h 16:49

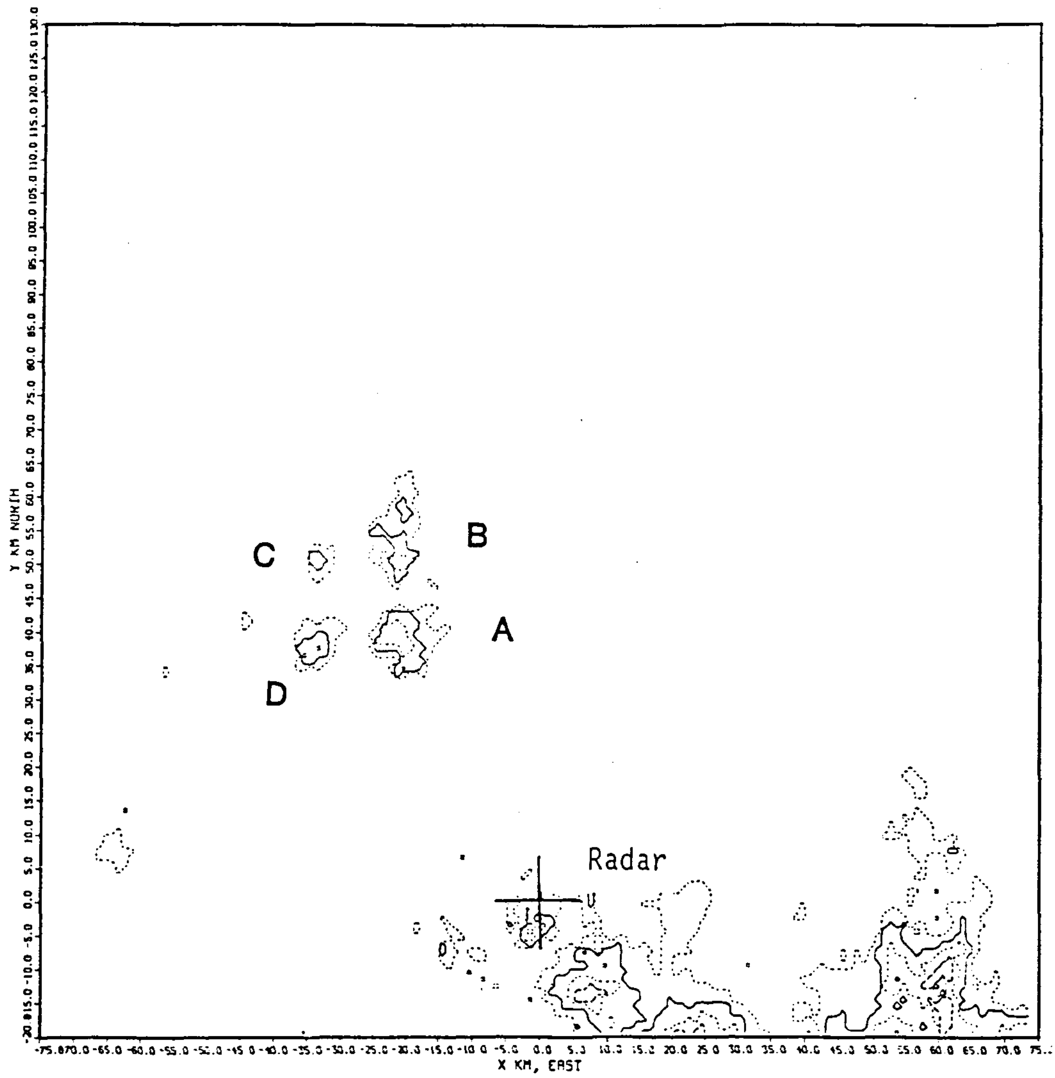

Figure 5.8 Radar PPI images for 2 December 1987 (antenna elevation 2°). Contours depict 23, 30, 40 and 50 dBZ intensities. a) 15:54 SAST.

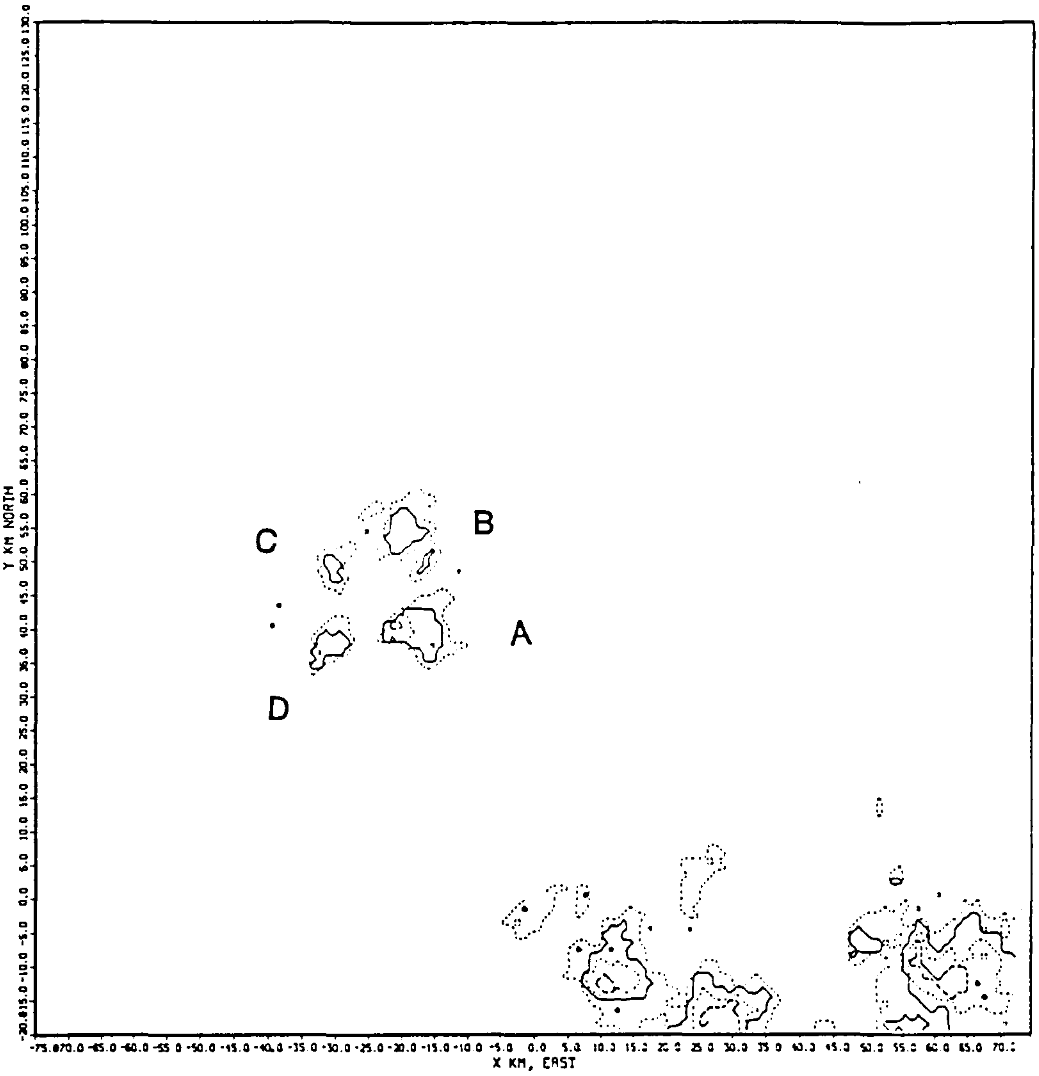

Figure 5.8b 16:01

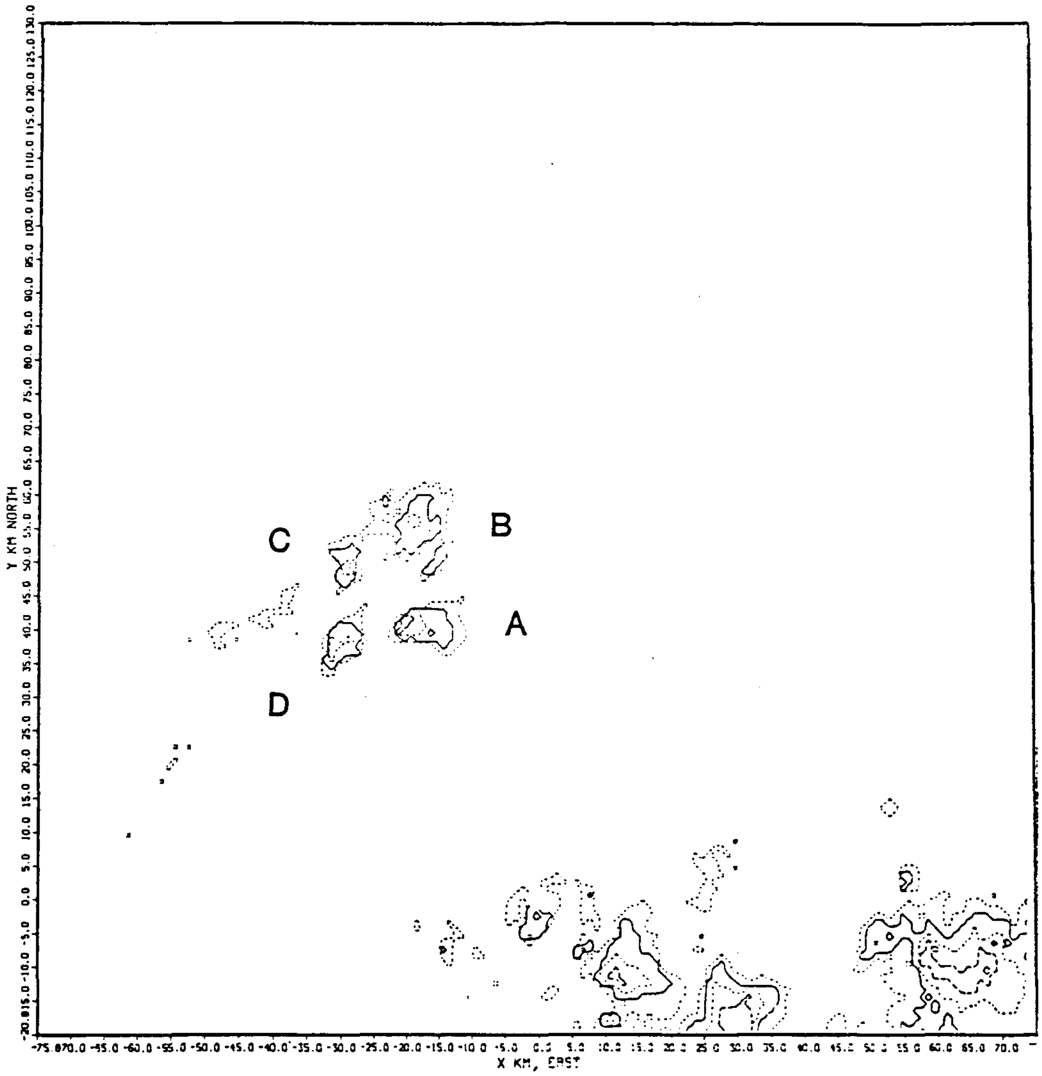

Figure 5.8c 16:04

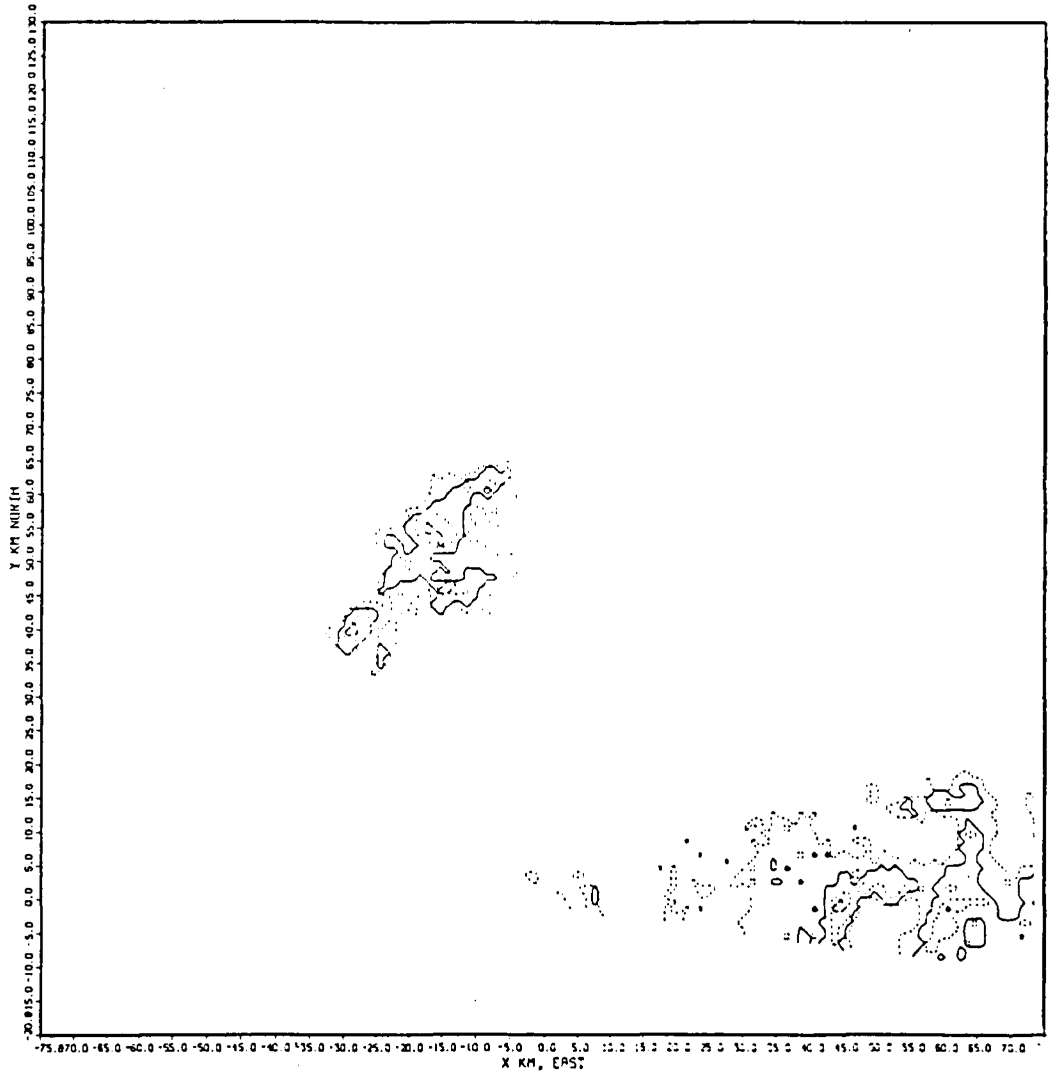

Figure 5.8d 16:20

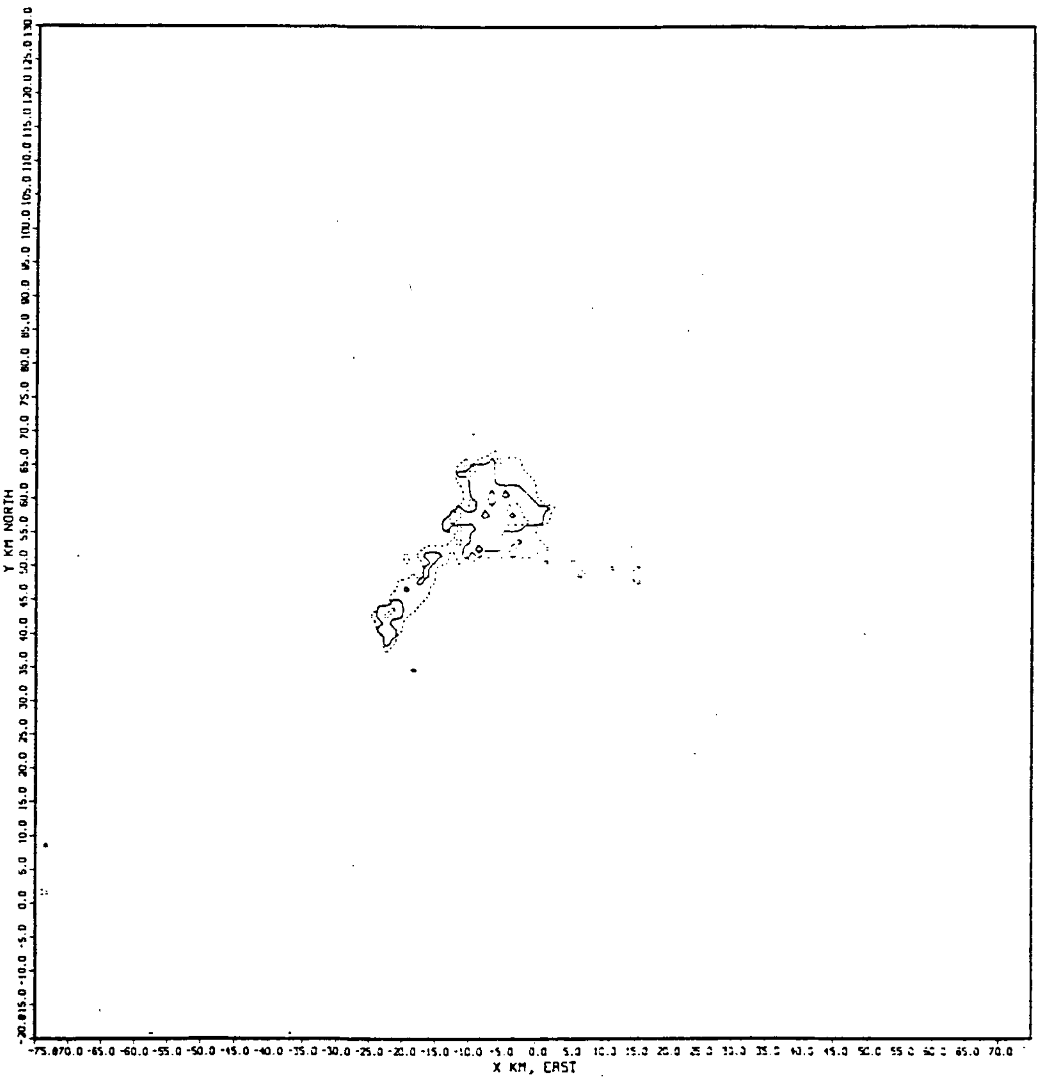

Figure 5.8e 16:39

6. EARLY STORM DEVELOPMENT AND CLOUD MERGERS: A SINGLE-DOPPLER RADAR CASE STUDY

Gerhard Held and Dawid J deV Swanepoel

The purpose of this study is to highlight the complexity of cell development and subsequent merging with either the parent storm (feeder-cloud mechanism) or with a quasi-independent cell (daughter-cell concept) by studying detailed radar reflectivity and radial air flow patterns in an isolated multicellular storm on the Transvaal Highveld.

The importance of cell mergers for successful cloud seeding experiments or operations, as well as for efficient cloud modelling has already been discussed in a lengthy introduction to the previous Section. Also, results from investigations of various cloud-merger mechanisms in other parts of the world have been dealt with in a brief literature study in Section 5. However, in order to put the findings of this detailed case study into proper perspective, it is thought that the most relevant research results from North America should be reiterated briefly.

Dennis *et al.*, (1970) described the feeder-cloud mechanism very neatly for a relatively large sample of hailstorms which were observed in western South Dakota. The term "feeder-cloud" was first used by Goyer *et al.* (1966) during a study of persistent hailstorms. According to Dennis *et al.* (1970) most of their case studies showed that new growth tended to be on the western or southwestern flank of storms, i.e. on the trailing edge of typical eastward-moving storms. The inflow region was often marked by lines of cumulus ("feeder") clouds which grew rapidly into new cells as they merged into the "mother storm". However, they also reported occasional cases where the inflow was on the southern or southeastern side of the storms, but in both cases the inflow region was on the equatorward side of the storms, which agrees well with findings from Highveld storms (Carte and Held, 1978), although in South Africa, the new development is more commonly found near the leading edge of the storms.

Cheng and Rogers (1988) also linked the occurrence of feeder clouds to the formation of hail. In their study of Alberta hailstorms, they found that feeder clouds formed approximately in a line parallel to the vertical ambient wind shear near cloud base level. The spacings between feeder clouds were almost equal and estimated to be 3 km and eventually manifested as distinct hail streak events at the surface. The persistent location of feeder clouds was speculated to be the result of interaction between the inflow and the low-level outflow of the storm.

The importance of the "weak-echo-region" (WER) was first stressed by Browning and Donaldson (1963). The existence of this echo-free region within the storm was attributed by them to adiabatic concentrations of water in the form of rather small cloud droplets which, owing to the high velocities within the core of the updraught, would not have sufficient time to attain radar-detectable sizes. Chisholm and Renick (1972) reported that combined radar, aircraft and photo observations have shown conclusively that cloud-filled WERs observed by radar are accompanied by extensive, smooth, uniform updraughts at cloud base of the order of 4 to 6 $m.s^{-1}$. Thus, the observation of a WER in a radar echo would indicate a major updraught into this particular storm.

The daughter-cell merging situation has been described by Chisholm and Renick (1972) for multicellular hailstorms occurring in Alberta. They found that new radar cells develop from cloud towers 3 to 5 km in diameter in a preferred region on the RH storm flank (i.e. equatorward side). The newly formed cell does not move into the storm complex, but rather grows rapidly and becomes the storm centre. Meanwhile, the original cell begins to decay while another new cell forms.

A slightly different concept of cell mergers was described recently by Westcott and Kennedy (1989) which is especially important for the current study because it relates to a non-severe thunderstorm. Two different cases of mergers are discussed, one of which is based on differential cell motion when one cell is decreasing in intensity while the other one is increasing. The second case is thought to be more relevant for our particular case study, because the development of a new cell between two existing cells produced the merger. Periods of significant intercell flow at 4 km coincided with the times when the mid-level reflectivity band linking the cell cores showed rapid intensification. Westcott and Kennedy (1989) suggested that the intercell flow is a result of radial outflow observed at heights above the maximum updraught level in the actively growing echoes. The strengthening of the reflectivity bridge may have been the result of both particle transfer and environmental modification due to radial outflow.

Before embarking on the detailed case study, it should be stressed that the above findings strictly apply to severe or hail-producing storms observed in the northern hemisphere. Only Westcott and Kennedy (1989) analysed a non-severe storm. Thus, significant deviations from those results might have to be expected, since Carte and Held (1978) already stressed the different behaviour pattern of thunderstorms occurring on the South African Highveld.

6.1 **THE STORM IN GENERAL** (27 April 1987)

The atmosphere over the interior, especially over the central, eastern and northern parts of the subcontinent was quite unstable (Figure 6.1) on 27 April 1987, with an upper level trough being undercut by a relatively strong High ridging in from the Indian Ocean across almost the entire subcontinent (Figure 6.2). Such conditions are very conducive for the development of thunderstorms on the Highveld.

A great variety of single and multicellular thunderstorms developed during the early afternoon in a band extending from about 120 km west of the radar to about 150 km east of it, with a width (north - south extent) of between 60 km in the west and 120 km in the east. The larger storm complexes occurred over the eastern Transvaal Highveld and the Witwatersrand region. The storm band as a whole moved slowly in a northerly direction.

An isolated, and for the Highveld, typical multicellular storm (Carte and Held, 1978) which had developed at 14:45 between 5 and 10 km southeast of the radar was chosen for the study. It moved at an average speed of 32 $km.h^{-1}$ to the northeast and consisted of a minimum of two cells at any time during its life cycle of two hours, with new cells developing on the left flank, while the storm decayed on the right flank (Figure 6.3). Individual cells moved at speeds of up to 40 $km.h^{-1}$. The storm reached maximum intensity between 15:24 and 15:38. Echo tops reached up to 12 km AGL and maximum reflectivities were 60 to 63,3 dBZ. At 15:39, radial velocities of 21 $m.s^{-1}$ were observed at 9 km AGL (PPI elevation 18°) in the updraught core. Six minutes later grape-size hail fell on the ground at which time the reflectivity near ground level increased to 66,6 dBZ.

For the purpose of studying the very early stages of storm development and the related radial velocity field, emphasis was put on the best resolution of the lower range of reflectivities. Therefore, all cross-sections depicting merger situations are contoured for 23,3, 30, 33,3, 36,6 and 40 dBZ, since a maximum of five different contours can be plotted at any one time. Three separate plots were made of every PPI in the volume scan in order to resolve all 15 levels from 23,3 to $\geq$60 dBZ at 3,3 dBZ intervals. However, due to a capacity problem of the VM mainframe computer, reflectivity contours from 50 dBZ upwards may have been plotted incorrectly at this stage (the problem will be rectified as soon as possible), but actual values can be verified by means of B-scans. The radial velocity field has not been corrected for storm movement, hence no actual speeds are quoted from the plots. The maximum unambiguous velocity is 25 $m.s^{-1}$. The length of the arrow indicating the direction and magnitude of the radial velocity at a particular point is proportional to the speed (see Figure 6.4: the arrow shown in the key corresponds to 25 $m.s^{-1}$; an arrow of half this length would thus represent 12,5 $m.s^{-1}$).

A total of approximately 420 PPI plots and 600 vertical cross-sections were generated for the storm period from 14:43 to 15:31 during which merger situations were studied.

6.2 EXAMPLE OF A DAUGHTER-CELL MERGING SITUATION

The first volume scan considered in this analysis was from 14:43:04 to 14:45:29, covering elevation angles between 2° and 22°. The radial air flow was almost exclusively towards the radar. No signs of new cell development in the vicinity of the storm could be found on any of the PPIs. However, clear evidence of a new cell is seen on the 18° PPI of the subsequent volume scan. The vertical cross-section through the storm shows that the cell had obviously developed very rapidly between 5 and 8 km AGL and 3-4 km to the northeast of the mature cell, with a maximum reflectivity of 33,3 dBZ at 6,4 km (Figure 6.4). The radial air flow is noteworthy in so far as it was light to moderate and away from the radar in the new cell (18°), whereas it was in the opposing direction in the old storm.

During the next volume scan, new development can also be seen just east of the mature cell, but being part of it and only in the lower levels (up to 8°). The radial flow in the mature cell is still towards the radar, while it is outwards in both regions of development. The new cell had grown significantly and also intensified as can be seen from the set of vertical cross-sections in Figure 6.5, which are parallel to each other and spaced at 1 km intervals. A slight bridging between the two cells can be seen above 6 km AGL at very low reflectivity levels (<26,6 dBZ). Figure 6.6 shows that the new cell had further grown and intensified and also moved away from the older cell, although still linked at low reflectivity aloft. It's precipitation still had not reached ground level. The radial air flow was increasing significantly with height from 8° to 18° elevation, indicating an updraught tilted away from the old cell. Precipitation from the new cell reached the ground at 14:55 (Figure 6.7). Airflow at the 2° elevation indicated strong convergence in the region of the new cell, while the radial component of the air flow at the old cell was now pointing away from the radar. Aloft, it was diverging in the old cell (5°-18° elevation), but in the new cell, radial flow was away from the radar, and still strongly increasing in speed with height, but slightly decreasing above 10 km AGL. It is noteworthy that the link between the old and the new cell had intensified slightly (26,6 dBZ) in some areas as can be seen from the 18° PPI and the cross-sections.

The volume scan commencing at 14:57:59 (Figure 6.8a) illustrates very nicely how two mature cells merge into one storm complex by expansion and intensification of radar reflectivities aloft. The 2° PPI indicates a

3 km separation of the 23,3° dBZ contour between the cells (5 km for 30 dBZ). The centres of the echo cores are approximately 11 km apart. The maximum reflectivity reached just more than 50 dBZ in the old cell, but was slightly above 53,3 dBZ in the new cell and was in both cases in the lower part of the echo (3-4 km AGL). It is noteworthy, that the 23,3 dBZ contours were just fusing on the 8° PPI with a predominantly outward air flow, except in the region where the bridging takes place. The 12° PPI shows that even the 30 dBZ contour has now merged. The air flow was still predominantly outwards, but a small convergence zone can be seen on the eastern flank of the new cell indicative of strong entrainment into the storm (the actual speeds would be much bigger since the cell was moving in an eastward direction and thus its speed would have to be *added* to the opposing radial component). A similar convergence was also observed on the 5° PPI. The 18° PPI showed a totally merged single cell with strong radially outward flow except in the centre where a small convergence area is observed. This volume scan is best documented by sets of west - east and north - south oriented, parallel vertical cross-sections (Figures 6.8b,c). The cross-section from southwest to northeast through the slowly collapsing old cell, the linking "accumulation zone" aloft and the new cell is probably the most characteristic picture of what is actually happening. Since this section is almost tangential, no inferences about the air flow in this plane can be made on the basis of the radial velocity components. However, it is quite safe to assume that a reasonably strong updraught is required to suspend the large volume of rainwater between about 4 and 6,5 km AGL between the two cells. This could be indicative of a possible mechanism how the old cell becomes entrained into the new one.

The next volume scan started at about 15:01 (Figure 6.9a). The 2° elevation PPI did not reveal any significant features, but the 23,3 dBZ contours of the two cells were now only 1,5 km apart (30 dBZ - 3 km). Strong convergence can be seen at the eastern edge of the old cell, while the new cell is characterised by radial outwards flow, except on the northeastern flank where there is an indication of light convergence. On the 5° PPI (not shown) the 23,3 dBZ contour is already merged between the two cells and the 30 dBZ is only 2 km apart; the radial flow pattern is mostly away from the radar. On the 8° PPI the 30 dBZ is still not joined, but the intensity of the new cell is already ≥50 dBZ while the old cell gradually decreases (maximum about 33,3 dBZ). The radial flow is still mostly outwards, except in the merging zone where there is a bit of convergence (southern part) as well as divergence (northern part). The next PPI at 12° shows only one cell with significant convergence on the southern flank and some divergence in the centre. In general, the radial speeds are light to moderate. The 18° PPI is unfortunately incomplete (not shown), but does indicate a strong shear of the radial component in the southern half of the new cell. The 25° PPI shows that the new cell (maximum 36,6 dBZ) and another nearby storm are coming quite close to each other. In both cases, one can see diverging radial air flow in the most intense cores. Strong flow towards the northern flank of the left storm can be observed, but this will be discussed in the next section on the first echo study. The last scan was at 35° elevation (not shown) and basically indicates a general outward flow from the left storm, especially strong on the northern flank. Figure 6.9b shows west - east cross-sections at one 1 km spacing (the base lines are indicated in Figure 6.9a). Strong convergence can be seen on the 8° and 12° PPI above an area which appears echo-free on the lower elevations (Figure 6.9a). The west - east cross-sections show very clearly how this then leads to a merger aloft. South - north sections through the same complexes (Figure 6.9b) show the development of first echoes some 6 km north of the older cells. Their history, however, will be discussed in the next section. The total merging of the original old and new cells is depicted in two southwest - northeast sections (right hand side of Figure 6.9c). The narrowing of the gap below the accumulated precipitation aloft can be seen very clearly. The old cell is now almost depleted. This process of final merging continues during the next volume scan which is not shown here. The final act can be seen in the scan commencing at 15:06 (Figure 6.10a) where the old cell is basically gone. Only a relatively insignificant 30 dBZ contour on the 2° PPI indicates where its remnant is. There is nothing left of it on the 5° PPI. The air flow in this region is very weak and generally away from the radar. All its former energy has obviously been absorbed into the new cell through the merging process aloft. Vertical sections 2 and 3 in Figure 6.10c depict the storm after the merging had been complete.

6.3 EXAMPLE OF A FEEDER-CELL MERGING SITUATION

The first time that an early echo near the multicellular storm, which was chosen as study object, was detected during the volume scan commencing at about 14:58 (Figure 6.8a). On the 12° PPI, only an area of about 1 x 1 km was covered by FE1 at that stage, but strong radial flow outwards was already noticed. It was about 5 km north of the parent echo. It is also noteworthy that the Doppler velocities indicated the presence of the echo on the 8° PPI, while the reflectivity was obviously too low and too patchy to produce a contoured echo. However, it can be seen in the B-scan as a very weak echo.

At about 15:01 (Figure 6.9a) FE1 can now be seen on the 5° PPI scan covering an area of about 2 x 1 km some 4-5 km north of other echoes and in an area of strong convergence, as one would expect. It should be pointed out that the radial air flow pattern on the 2° PPI was rather confused. Another first echo, FE2, was observed on the 8° PPI, about 6 km east of FE1, covering an area of 1 x 1 km and displaying strong outward flow. FE1 was approximately 3 x 1,5 km large with light inward flow. Both echoes were still observed on the 12° PPI, FE1 being 1 x 1 km with weak outward flow and FE2 2 x 3 km with divergence on the southeastern flank. The position of both echoes (FE1 and FE2) relative to the mother storm can be seen nicely in cross-sections 4 and 8, respectively, in Figure 6.9c.

The following volume scan (15:03:33 to 15:05:41) shows FE1 and FE2 in almost the same positions as in the previous scans. Only FE2 has slightly grown in size and intensified to 27 dBZ (8° PPI). However, a new cell, FE3, appeared between the original first echoes, extending from 3 to 6 km AGL, with a very small core of $\geq$27 dBZ. The radial velocities indicated an outward flow at all levels, mostly very light, except in the vicinity of the small cores of FE2 and FE3 where it was slightly stronger. It can be speculated that these first echoes are induced by a downdraught flowing from the mother storm in a northerly direction.

The next volume scan (15:06:22 to 15:08:16) depicted in Figure 6.10 seems to indicate fierce competition amongst the various first echoes, and the first one to have become radar-detectable need not necessarily be the one which has better chances to develop. FE1 has by now totally disappeared, while FE2 has grown significantly to about 4 x 3 km (5° PPI) with the 26,6 dBZ contour extending right down to ground level (Figure 6.10a). The air flow was light to moderate away from the radar at all levels. FE3 has also grown and intensified, but more at higher levels (12° and 18°, Figure 6.10b) than FE2, which can also be seen in the vertical sections in Figure 6.10c (cross-sections 7 and 5). The radial air flow in FE3 was mostly towards the radar and fairly strong up to 12° elevation. This led to a strong shear zone between FE2 and FE3 which can be seen on the 5° radial flow pattern. Also noteworthy is the shear on the northern flank of the mother storm, clearly visible on the 8° and 12° PPI. The 18° elevation scan is of particular interest because it shows the echo core of FE3 (30 dBZ between 5 and 6 km AGL; also see cross-section 7 in Figure 6.10c) and a strong outward flow in the radial velocity field. This created a very strong shear of the radial air flow with height between the 12° and 18° scans. FE3 does not appear on the 25° PPI any more; however, there is still a strong shear zone along the northern flank of the mother storm, extending up to 35° elevation (>10 km AGL).

Another interesting feature of this volume scan is brought to light in cross-sections 17 and 18 (Figure 6.10c) where the sudden development of a new cell in the immediate vicinity of an existing storm becomes evident. This storm, designated B, is east of the previously described mother storm (see cross-section 14). There was no sign in the previous volume scan of new development in this region. The core is centred around 8 km AGL and already has a reflectivity of 37 dBZ. A relatively strong convergence of radial velocities in this region is evident on the 12° PPI. Strong radial outflow can be seen on the 18° flow pattern, most likely being indicative of a northeastwards tilted updraught.

It had already been mentioned above that FE1 had ceased to exist, and that FE3 appears to have the better survival chances. This is confirmed by the observations of the next volume scan, starting at 15:09. FE2 only appears on the lowest two PPIs (2° and 5°) and has, in fact, already merged with FE3 (Figure 6.11a, 2° PPI). The radial air flow in both echoes is relatively weak and outwards, but its strength increases rapidly with height in FE3 and reaches a maximum where the reflectivity also indicates the echo core, viz. 12° and 18° elevation (>30 dBZ). As can be seen from the vertical sections in Figure 6.11b, the mother echo is strongly tilted towards the north (sections 6 to 8; left side) and northeast (sections 6 and 7; right side). Also shown in these sections is the beginning of a weak-echo-region (WER) on the northern flank of the mother storm, where FE3 tends to merge into the anvil (cross-section 9).

The radial air flow pattern in the mother storm (A) is quite noteworthy. Although it is generally outwards from the radar and moderate on all scans, the variation in strength along the northwestern flank is remarkable. A very strong component towards northeast can be seen on the lowest two scans (2° and 5°, Figure 6.11a) most likely indicating a strong downdraught. Above it, the radial velocities decrease significantly (8° and 12° elevation), but thereafter they increase rapidly with height (18° to 35°, Figure 6.11a), suggesting an overlying, strong updraught blowing into the anvil on the northern flank of the storm and capable of supporting large quantities of precipitation in this region. This would also explain the strong tilt of the northern echo depicted in Figure 6.11b.

Another interesting feature of this volume scan is the rapid entrainment of the newly developed cell, indicated in the previous volume scan, into storm B as shown in the south - north section no. 18 in Figure 6.11b. The radial velocities reached a maximum on the 18° PPI with a very strong eastward component in the central and southern portion of the echo.

The next volume scan commenced at 15:11:43. It is noteworthy that already on the 2° PPI the 23,3 dBZ contour of FE3 is shown to be linked to the mother storm (Figure 6.12a). Although FE3 can be identified as a separate entity on all scans, the vertical sections in Figure 6.12b indicate the already beginning entrainment into the mother storm at several levels. FE3 reached maximum reflectivity (37 dBZ) between 4 and 5 km AGL (see section 9 in Figure 6.12b). This section also indicates rapid intensification and expansion of the anvil on the northern flank of the mother storm. The radial air flow pattern in FE3 is still similar to the one in the previous volume scan. Noteworthy, however, are the extremely strong radial velocities in the mother storm on the 35° PPI, indicative of major developments aloft. The top of the storm is approximately 12 km AGL. The weak echo region underneath the vigorously growing anvil is clearly visible in the west-southwest - east-northeast section (no. 7) in Figure 6.12b. According to Browning and Donaldson (1963) and Chisholm and Renick (1972) a strong updraught can be anticipated in this region.

It is interesting to note that storms A and B are rather close together and linked by lower-intensity reflectivity-contours (generally 26,6 dBZ up to 12° elevation and 30 dBZ on 18° PPI). However, they do not appear to interfere with each other or show signs of a possible merger. Two cores of eastwards pointing radial velocity maxima in storm B can be distinguished on the 18° PPI (Figure 6.12a), resulting in a relatively strong tilt of its echo core into the same direction. The development aloft on the northern flank of storm B can still be distinguished clearly (sections 19 to 21 in Figure 6.12b). It is characterised by a light, converging air flow pattern on the 12° and 18° scans (Figure 6.12a).

FE3 is still steadily growing, both in size and intensity as shown in the following volume scan (15:14:23 to 15:16:43). It can be seen from the 2° PPI that FE3 now is about 5 km in diameter and the 30 dBZ contour has reached ground level (Figure 6.13a). The air flow is very weak away from the radar. The 5° PPI is extremely interesting in this case because of the air flow pattern, which indicates convergence where FE3 is progressively being entrained or merged with its mother echo. Also, the reflectivity has exceeded 36,6 dBZ which is reaching up to the 35° PPI (Figure 6.13a). The next scan at 8° elevation shows that the radial air flow was outward again and quite weak. Only from 18° upwards did the air flow again become stronger, reaching maximum radial velocities towards northeast on the 35° PPI. This is obviously the same updraught core already mentioned in the discussion of the previous volume scan (see north - south section no. 7 in Figure 6.13b). The west-southwest - east-northeast section discussed earlier has not changed much and still indicates a strong tilt of the echo towards northeast and an underlying

WER. The rapidly northwards expanding and intensifying anvil of storm A can also be seen in the west - east cross-sections 3 to 7. Storm B also has a significant anvil on its northern flank. The cell which developed aloft on its northern boundary has now been completely entrained in the main storm (B) and is hardly noticeable in the south - north section 23 in Figure 6.13b.

FE3 is continuing to expand, especially in the mid-levels (5° and 8° elevation) with the 36,6 dBZ contour extending to ground level as shown by the volume scan of 15:17. Maximum reflectivities are increasing steadily, viz. 43,3 dBZ on 5° PPI and 40 dBZ on 8°. From 12° elevation upwards FE3 becomes more and more incorporated into its mother echo (Figure 6.14a). The radial air flow pattern of FE3 is relatively weak and outwards directed in all levels. The convergence zone has not been detected in these scans. The mother storm (A) has moderate outwards directed radial air flow at all levels. Vertical cross-sections from west to east at 2 km intervals (Figure 6.14b) show the core of FE3 (cross-section 3), and going southwards, they also show the anvils of storms A and B which have intensified to such an extent that these storms have actually merged aloft (sections 7 to 11). The radial air flow in this region was quite strong towards the east. The section 8 (southwest - northeast) still indicates a very strong tilt of storm A towards northeast with an underlying WER. South - north sections (11A and 12A) illustrate the merging of FE3 into its mother echo.

The next volume scan (15:19:35 to 15:21:33) does not differ significantly from the previous one in both the reflectivity and air flow patterns, and is therefore not discussed in detail here. The tilt and the strongly developed anvil remain a very characteristic feature of storm A and FE3. Although the storm complex as a whole is steadily moving towards northeast, the relative positions of A and FE3 remain more or less the same throughout the intensification process. Very much the same applies to the subsequent volume scan (15:22:17 to 15:24:13). However, there are definite indications that FE3 and storm A have reached the early stages of dissipation. This is manifested in an increase of reflectivity near ground level (at 2° FE3 has 40-43 dBZ) while the height of the 26,6 dBZ contour of FE3 has dropped to below 4 km AGL. This is illustrated in

Figure 6.15a (2° PPI) and Figure 6.15b (section 13, south - north). The radial velocities have dropped significantly with the exception of two regions indicated on the 18° PPI. Three vertical sections from southwest - northeast and one from west to east through these regions show clearly that these are areas where development aloft is still very active, thus regenerating the storm complex while the older cells are collapsing. The new development aloft appears to be generated by the mechanism described in the previous Section (Chapter 6.2).

This gradual process of decay and regeneration between or near existing storms continues during the next three volume scans until the old storms and cells have virtually disappeared or were replaced by new ones by 15:30. As discussed in section 6.1, the storm complex continued to move in a northeasterly direction for another 75 minutes.

6.4 CONCLUSIONS

The detailed, three-dimensional case study of an isolated, and for the Highveld, typical multicellular storm illustrates very clearly the various mechanisms of cloud merging, cell development and regeneration, which sustain such storms for hours while they are traversing the Highveld. Since this case study is based on observations made before the 1989/90 season, the resolution of the reflectivity was only in steps of 3,3 dB with a lower threshold of 23,3 dBZ. (The more recent observations from the past two seasons could be resolved to fractions of a dB, but time was insufficient to incorporate such data.) However, in view of the results achieved in this Section, it is thought that the resolution of the reflectivity factor was sufficient for an initial investigation. Radial velocities of the air flow inside the storm were also carefully analysed and, whenever possible, interpreted in terms of updraughts or downdraughts.

Two main mechanisms were identified:

i) Daughter-cell merging situation.

A new cell had developed rapidly between 5 and 8 km AGL some 3-4 km northeast of a mature cell. As the new cell grew and intensified, the radial air flow was increasing significantly, indicating an updraught tilted away from the old cell. The two cells then merged into one complex by rapid expansion and intensification within a period of about 10 minutes. Seven minutes later, the original cell had been totally incorporated into the new structure and could no longer be identified.

ii) Feeder-cell merging situation.

Three very small cells of 1-2 km in diameter have been observed forming some 4-5 km north of mature echoes in an area of strong convergence within a period of about five minutes. It is noteworthy that the cell which had formed later than and between the existing two was the one to have developed to full maturity, by entraining the flanking cells quite rapidly. This process took less than six minutes. Once this cell had established itself as the survivor, it grew rapidly in height, area and intensity and moved together with its mother cell for a period of about 18 minutes. It eventually merged into the mother storm, but always remained identifiable during its whole life cycle of less than 25 minutes.

A *slightly different mechanism* of a feeder-cell merging situation was observed in parallel to the above case. A new cell had developed aloft on the perimeter of an existing storm rapidly growing in intensity and volume. Within a matter of five to seven minutes it had been totally incorporated in the leading edge of the old storm aloft, thus dramatically enhancing its anvil and tilt of the echo core.

It is noteworthy that these different cell merging mechanisms can occur sequentially or simultaneously during the same storm situation on one particular day. The main difference between daughter-cell and feeder-cell merging situations appears to be the reflectivity factor, and thus the cell intensity, which is much greater in the case of daughter-cell mergers than in feeder-cell merging situations (the feeder-cell is generally $\leq$40 dBZ). It should also be pointed out that features of all cell-merging mechanisms discussed in the introduction to this Section (Dennis *et al.*, 1970; Cheng and Rogers, 1988; Chisholm and Renick, 1972; Westcott and Kennedy, 1989) could be detected at one or other stage of the analysis.

Case studies of this nature are very time consuming, as can be seen from the fact that a total of approximately 420 PPI plots and 600 vertical cross-sections formed the basis of the analysis of a storm period lasting less than one hour! It is therefore impossible, at this stage, to estimate the relative frequency of the various storm merger situations.

It has also become very obvious that, in order to study storm or cell merger situations, one must have the three-dimensional reflectivity and air flow pattern available for making useful inferences. The latter should actually be derived from dual or triple Doppler radar observations rather than inferred from single Doppler radar observations, a fact which had also been stated by Cheng and Rogers (1988).

However, both types of merger mechanisms are very important for cloud-seeding experiments as the reaction to the introduction of seeding material might yield different results depending on the merger type.

6.5 REFERENCES

BROWNING K A and DONALDSON R J, 1963. Airflow and structure of a tornadic storm. *J. Atmos. Sci.*, 20, 535-545.

CARTE A E and HELD G, 1978. Variability of hailstorms on the South African plateau. *J. Appl. Meteor.*, 17, 365-373.

CHENG L and ROGERS D C, 1988. Hailfalls and hailstorm feeder clouds - an Alberta case study. *J. Atmos. Sci.*, 45, 3533-3545.

CHISHOLM A J and RENICK J H, 1972. The kinematics of multicell and supercell Alberta hailstorms. *Proceedings, 6th Annual Conference of the Canadian Meteoroloical Society*, Toronto, 24-31.

DENNIS A S, SHOCK C A and KOSCIELSKI A, 1970. Characteristics of hailstorms of western South Dakota. *J. Appl. Meteor.*, 9, 127-135.

GOYER G G, HOWELL W E, SCHAEFER V J, SCHLEUSNER R A and SQUIRES P, 1966. Project Hailswath. *Bull. Amer. Meteor. Soc.*, 47, 805-809.

WESTCOTT N E and KENNEDY P C, 1989. Cell development and merger in an Illinois thunderstorm observed by Doppler radar. *J. Atmos. Sci.*, 46, 117-131.

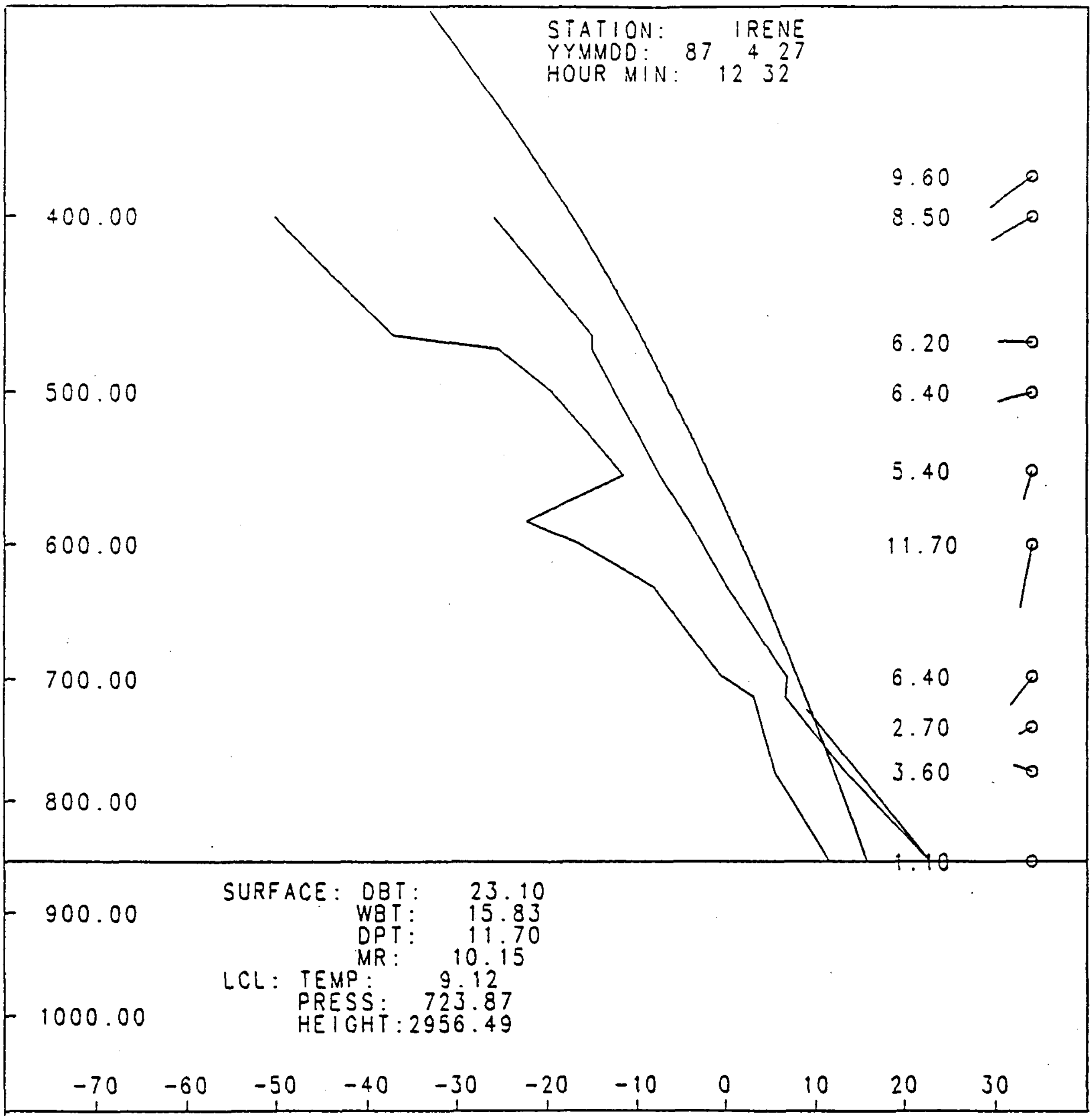

Figure 6.1: Midday (13:30 SAST) sounding from Irene (Pretoria) on 27 April 1987 (Stueve diagram).

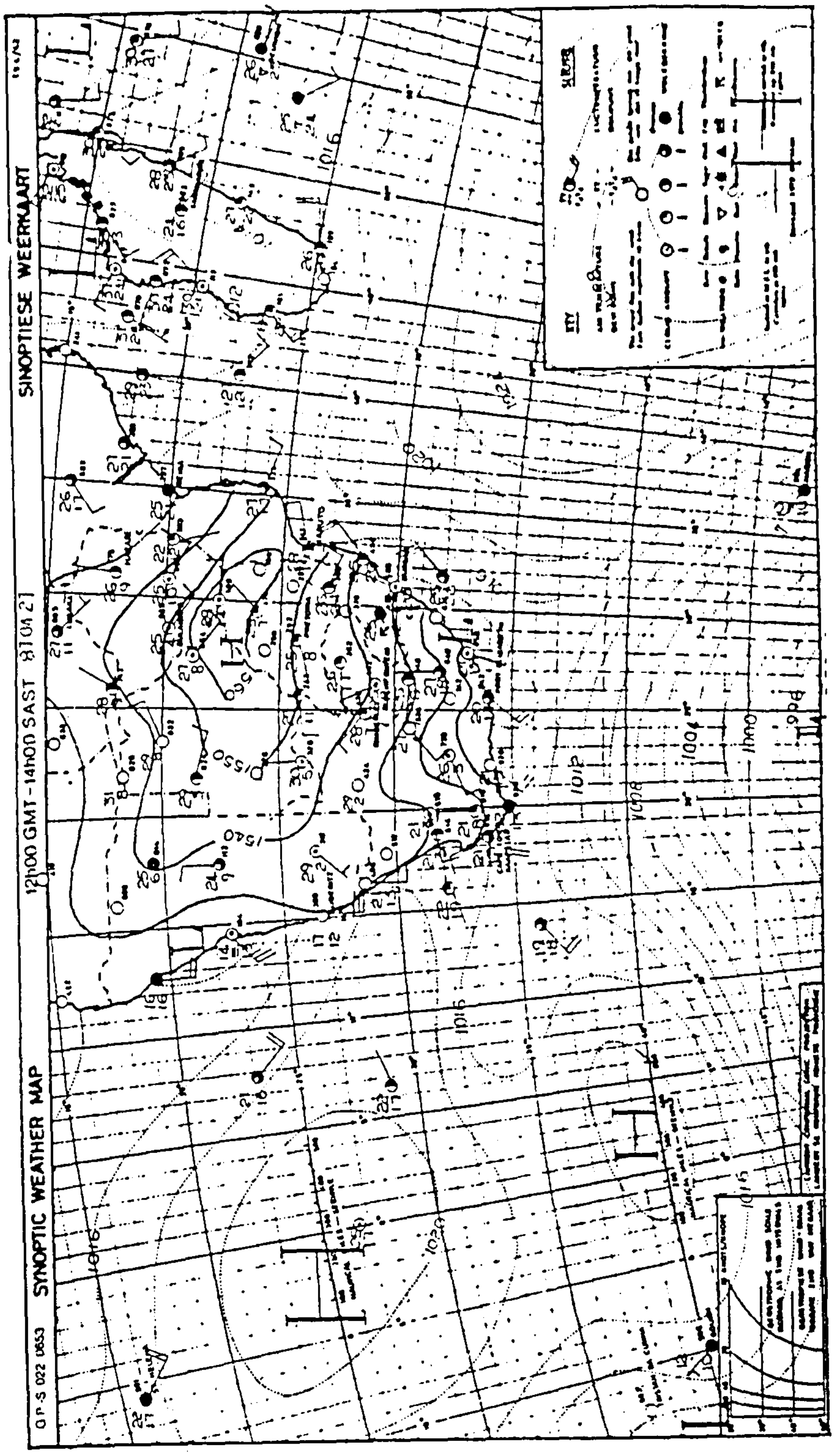

Figure 6.2: Synoptic weather map on 27 April 1987, 14:00, showing sea-level isobars (dotted) and 850 hPa contours over the continent (South African Weather Bureau).

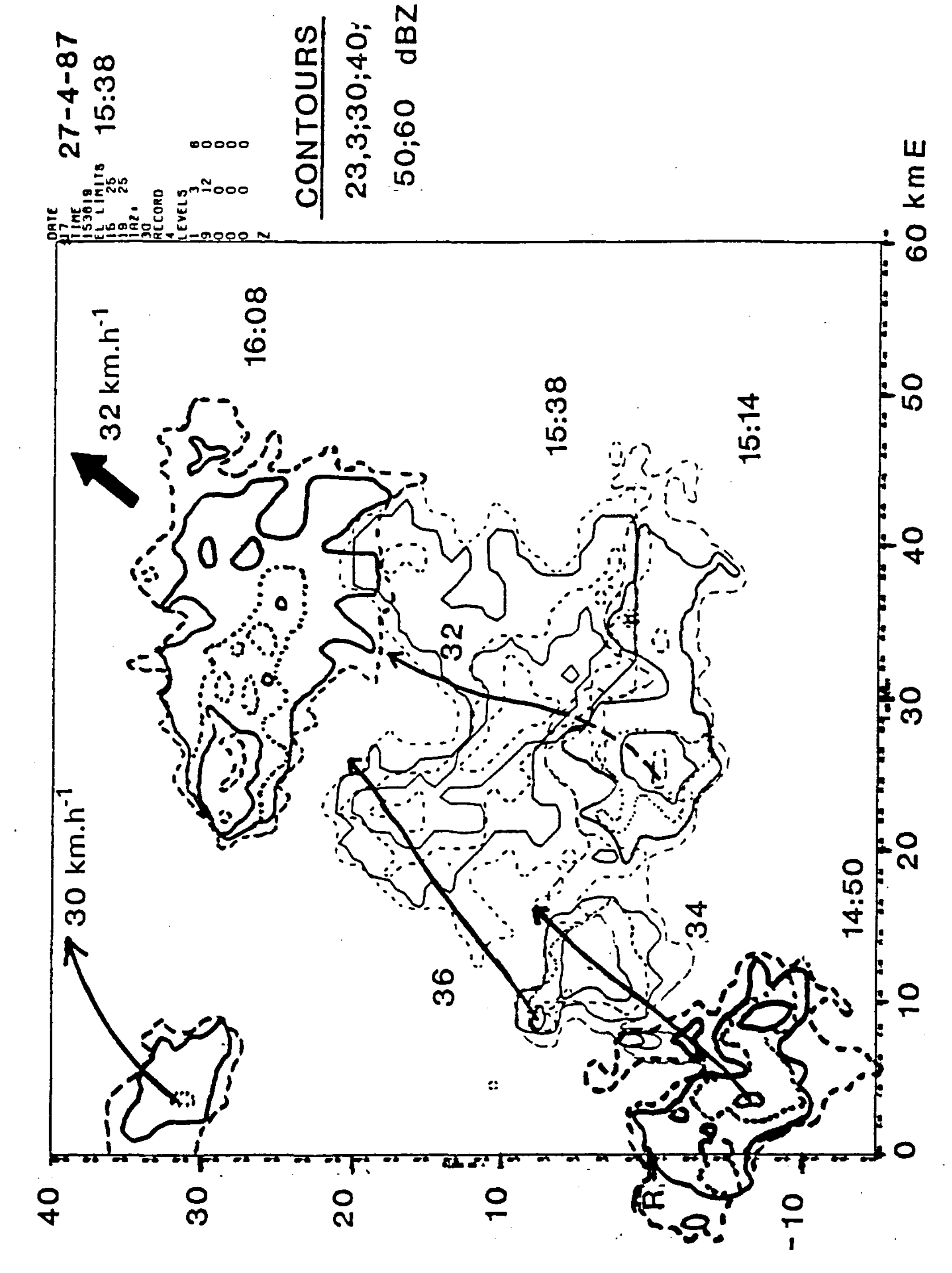

Figure 6.3: The multicellular storm of 27 April 1987 and its movement depicted at four different times. The position of the Houtkoppen radar is marked R.

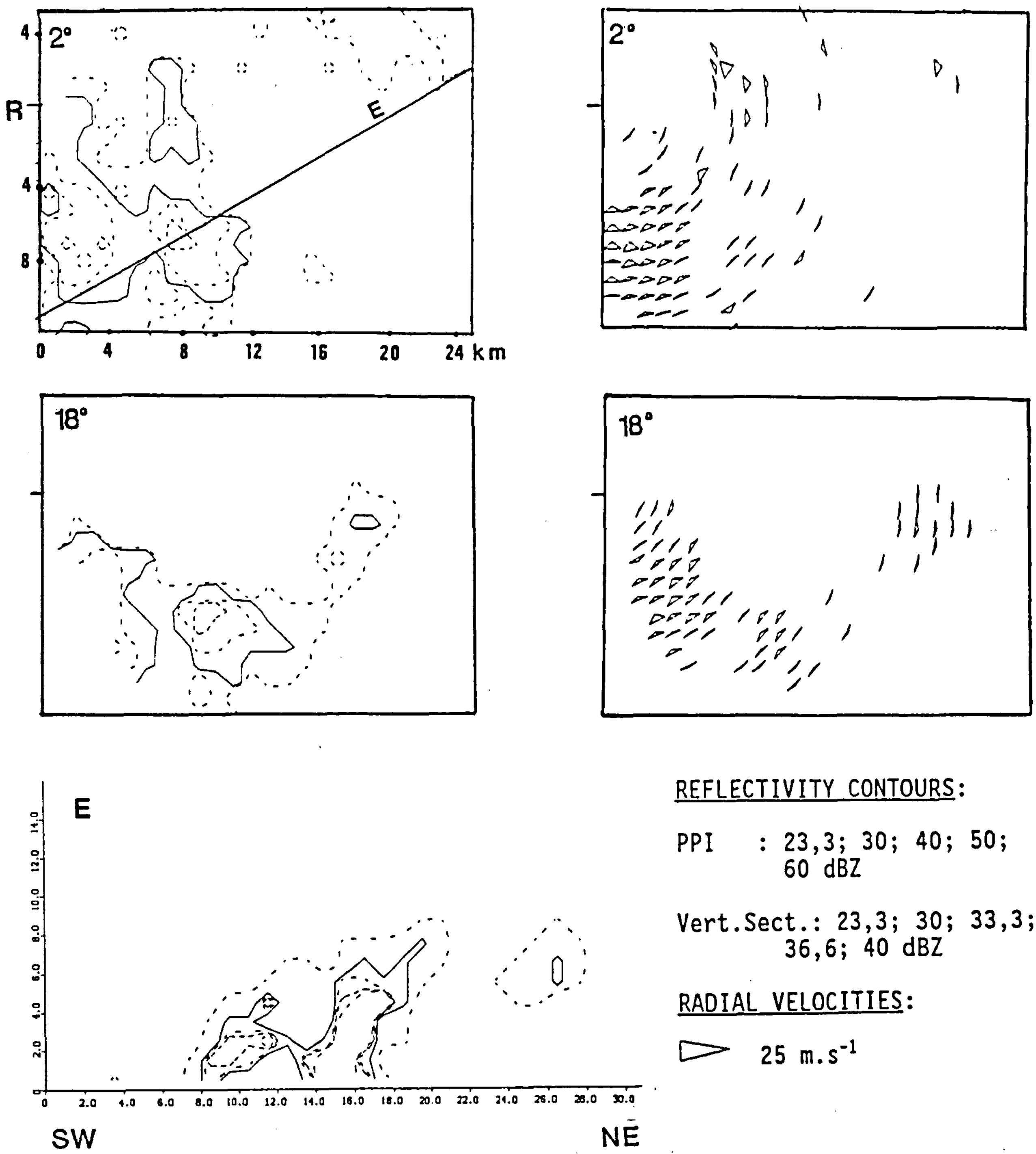

REFLECTIVITY CONTOURS:

PPI : 23,3; 30; 40; 50; 60 dBZ

Vert.Sect.: 23,3; 30; 33,3; 36,6; 40 dBZ

RADIAL VELOCITIES:

25 m.s^{-1}

Figure 6.4: 14:46:48 - 14:48:30, showing the first echo of new development northeast of a mature storm (horizontal distance and height of vertical sections are indicated in km).

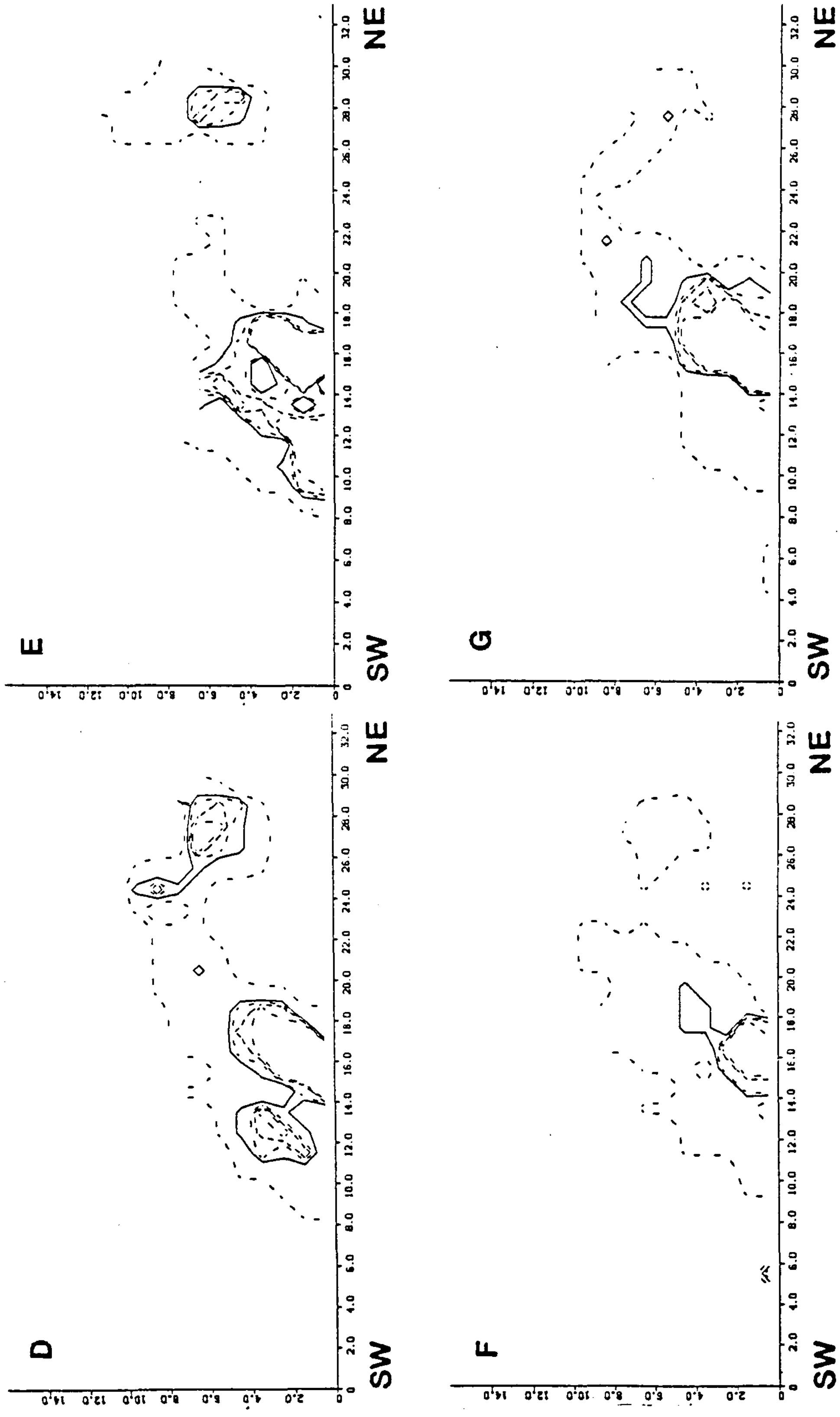

Figure 6.5: 14:49:38 - 14:51:59. Vertical cross-section, E, is along the same base line as in Figure 6.4. The base line for D is 1 km to the northwest, while F and G are 1 km apart to the southeast and all are parallel to E.

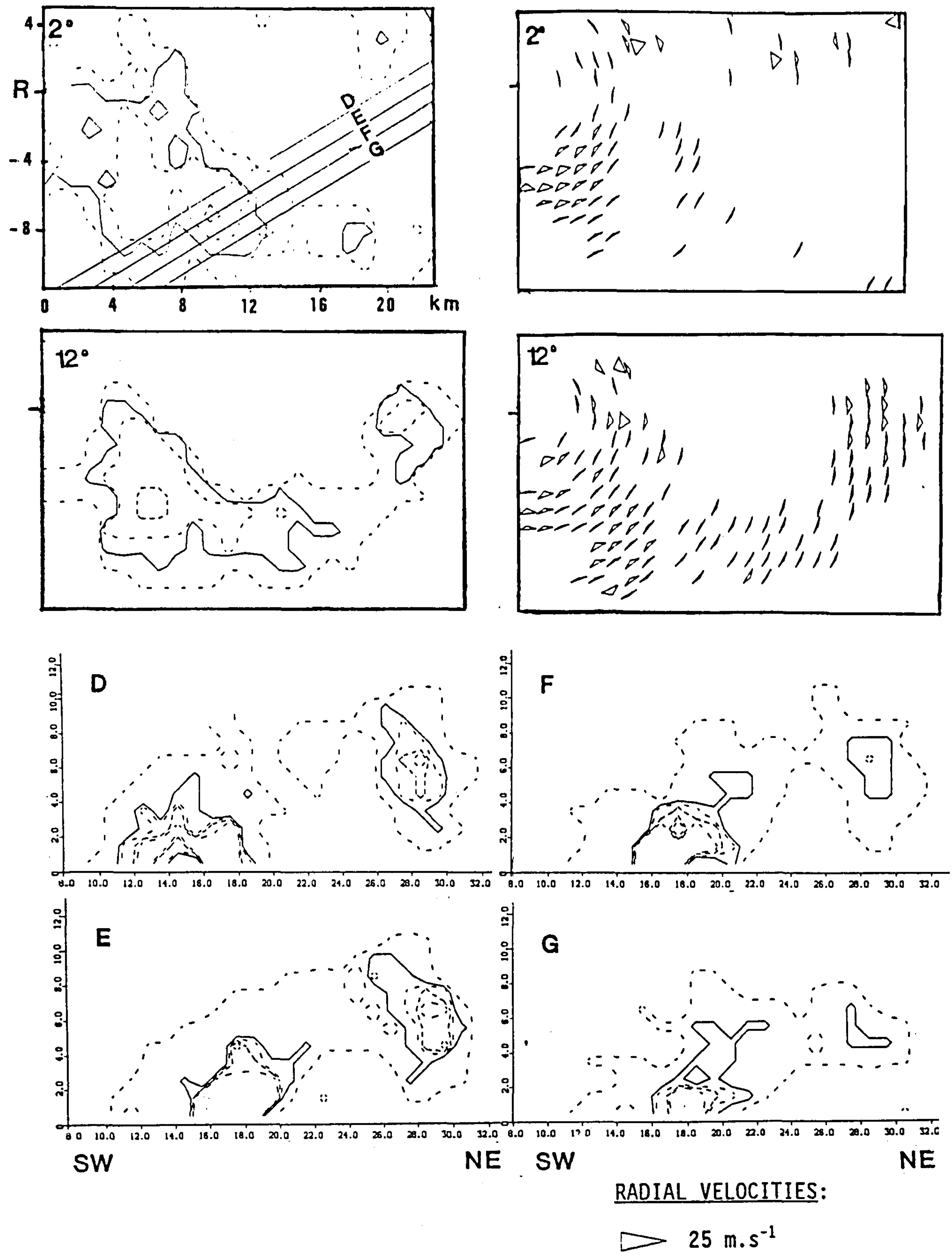

Figure 6.6: 14:52:29 - 14:54:43 (see Figure 6.4 for key).

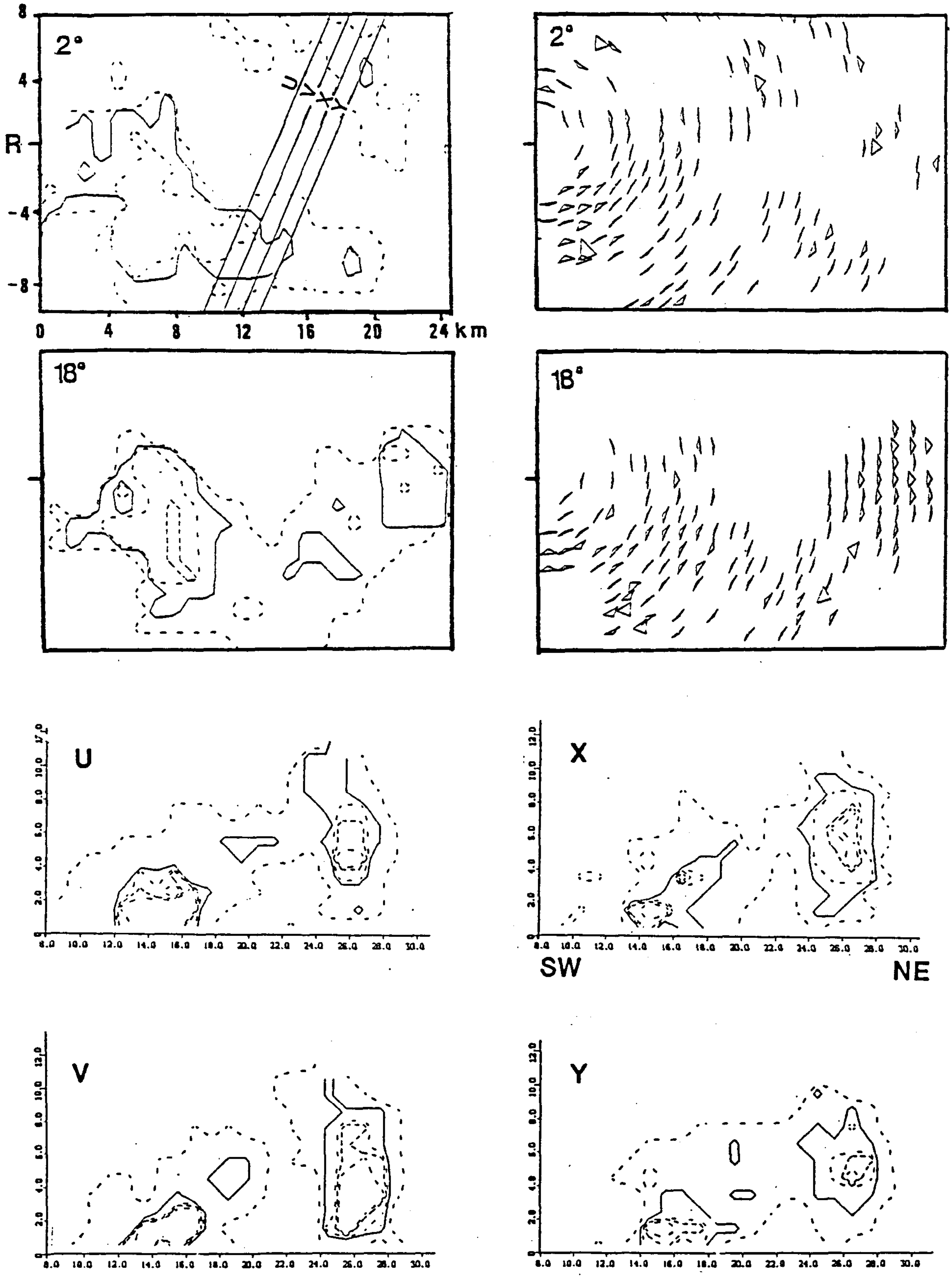

Figure 6.7: 14:55:23 - 14:57:20 (see Figure 6.6 for key).

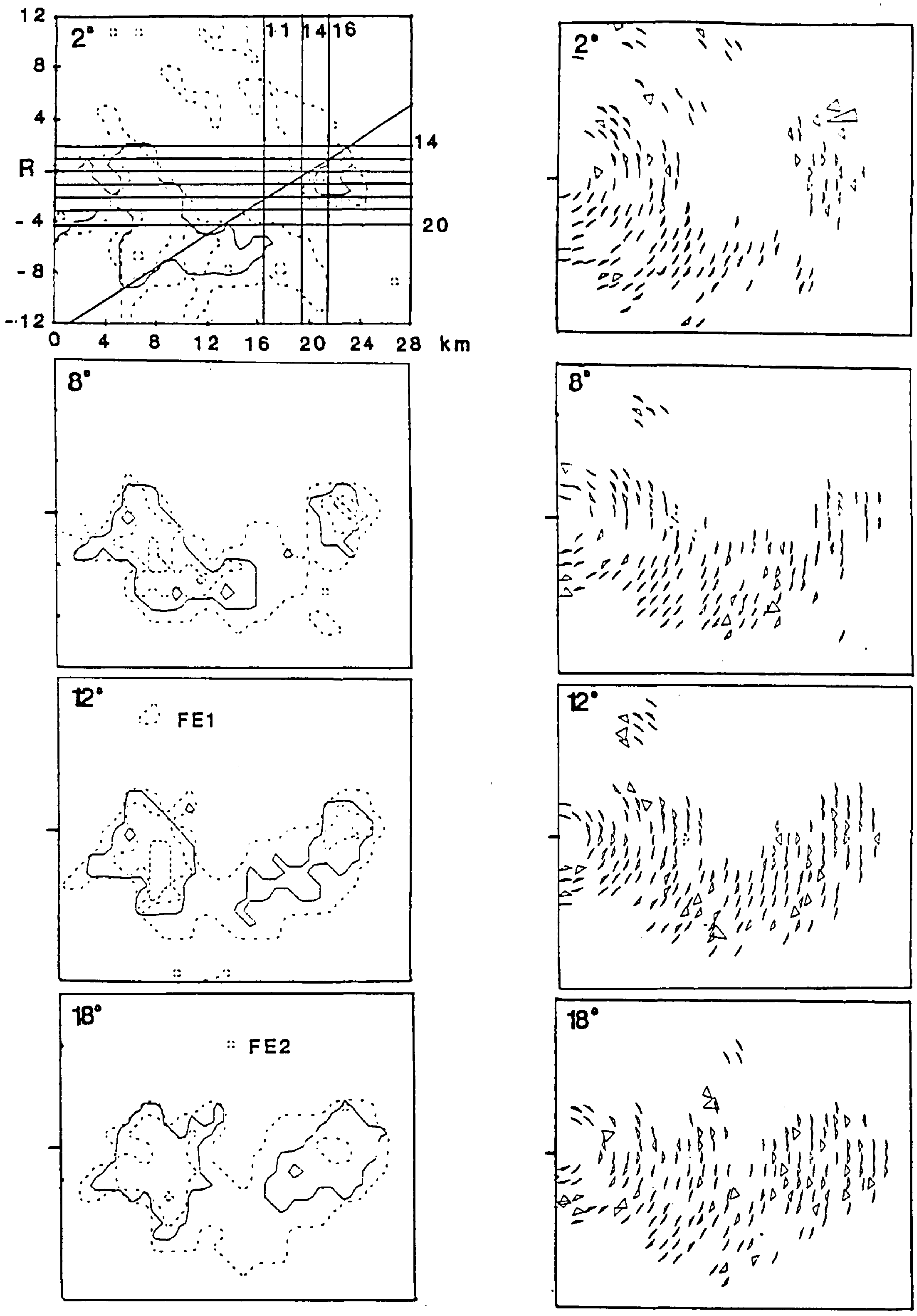

Figure 6.8a: 14:57:59 - 15:00:00. PPI contours and radial velocity field (see Figure 6.10a for key).

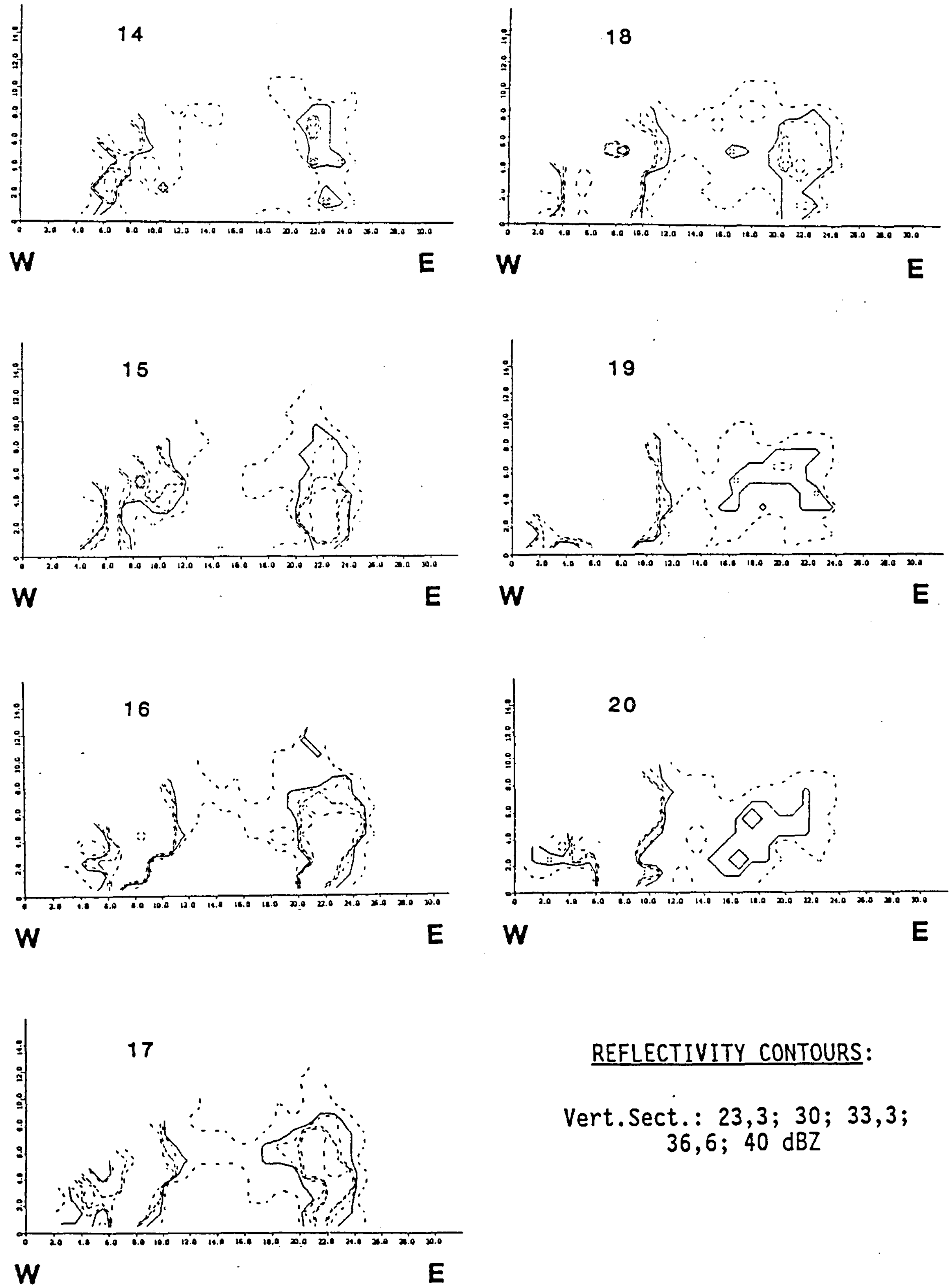

REFLECTIVITY CONTOURS:

Vert.Sect.: 23,3; 30; 33,3; 36,6; 40 dBZ

Figure 6.8b: 14:57:59 - 15:00:00. West - east vertical sections at 1 km spacing along base lines 14-20 marked in Figure 6.8a.

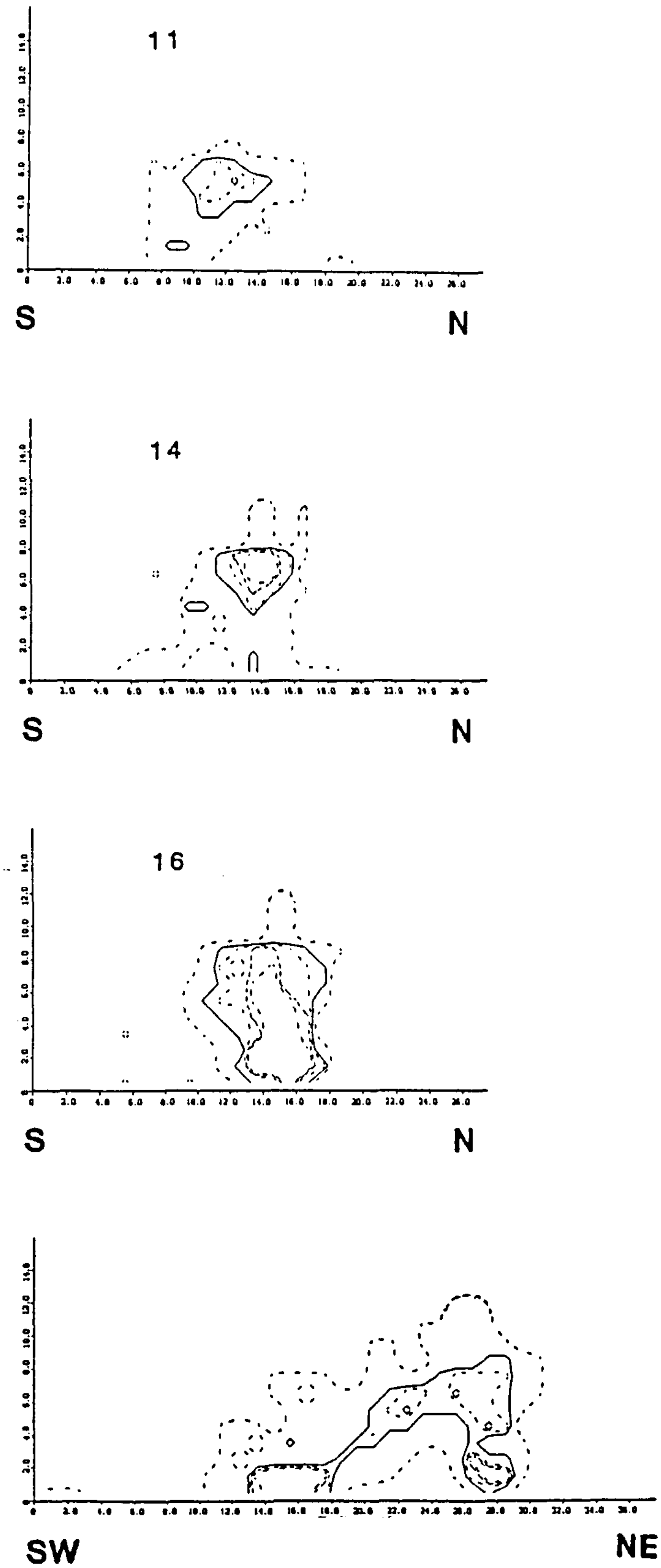

REFLECTIVITY CONTOURS:

Vert.Sect.: 23,3; 30; 33,3;
36,6; 40 dBZ

Figure 6.8c: 14:57:59 - 15:00:00. South - north and southwest - northeast vertical sections along base lines marked in Figure 6.8a.

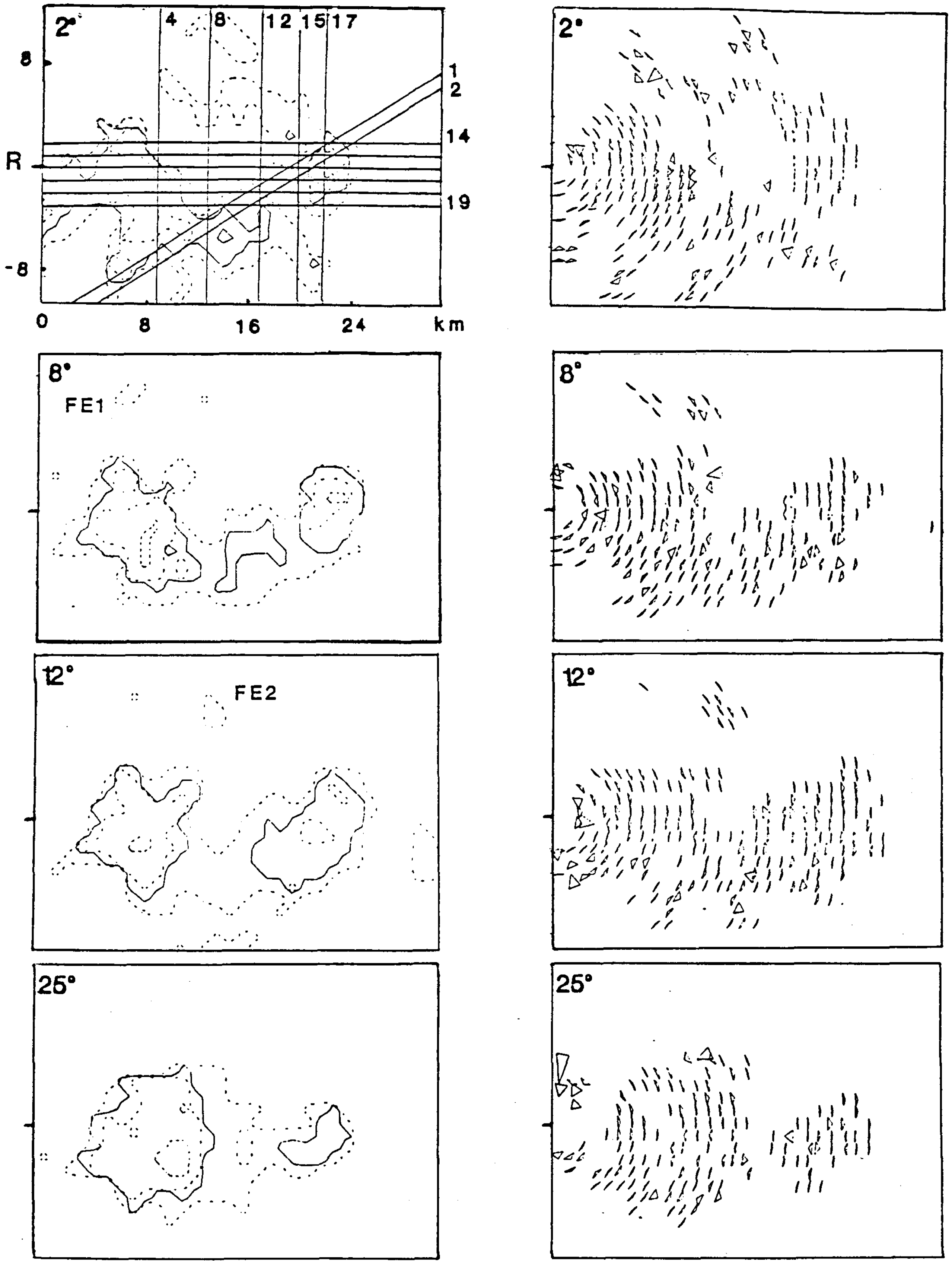

Figure 6.9a: 15:00:52 - 15:03:05. PPI contours and radial velocity field (see Figure 6.10a for key).

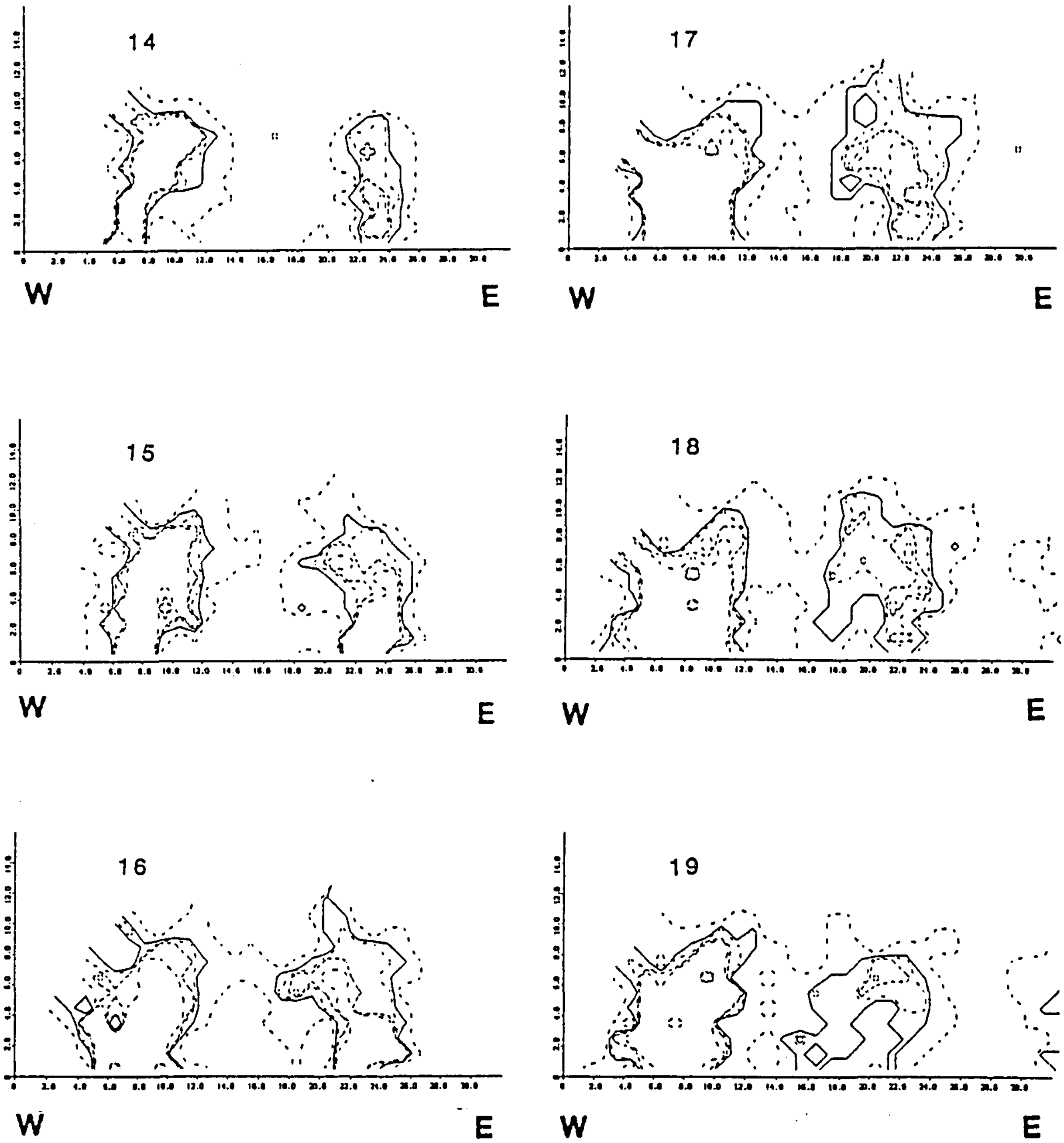

REFLECTIVITY CONTOURS:

Vert.Sect.: 23,3; 30; 33,3;
36,6; 40 dBZ

Figure 6.9b: 15:00:52 - 15:03:05. West - east vertical sections at 1 km spacing along base lines 14-19 marked in Figure 6.9a.

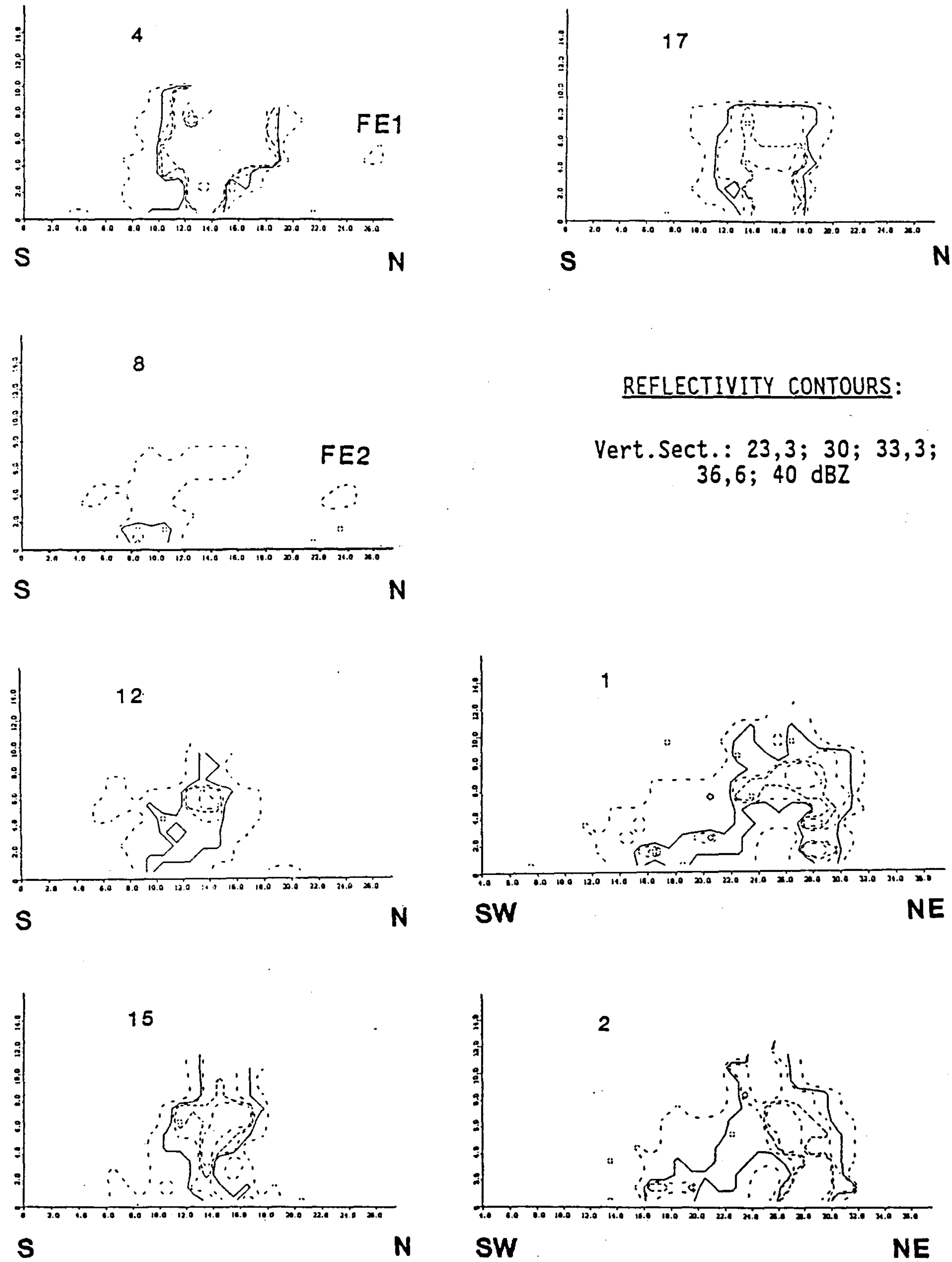

Figure 6.9c: 15:00:52 - 15:03:05. South - north and southwest - northeast vertical sections along base lines marked in Figure 6.9a.

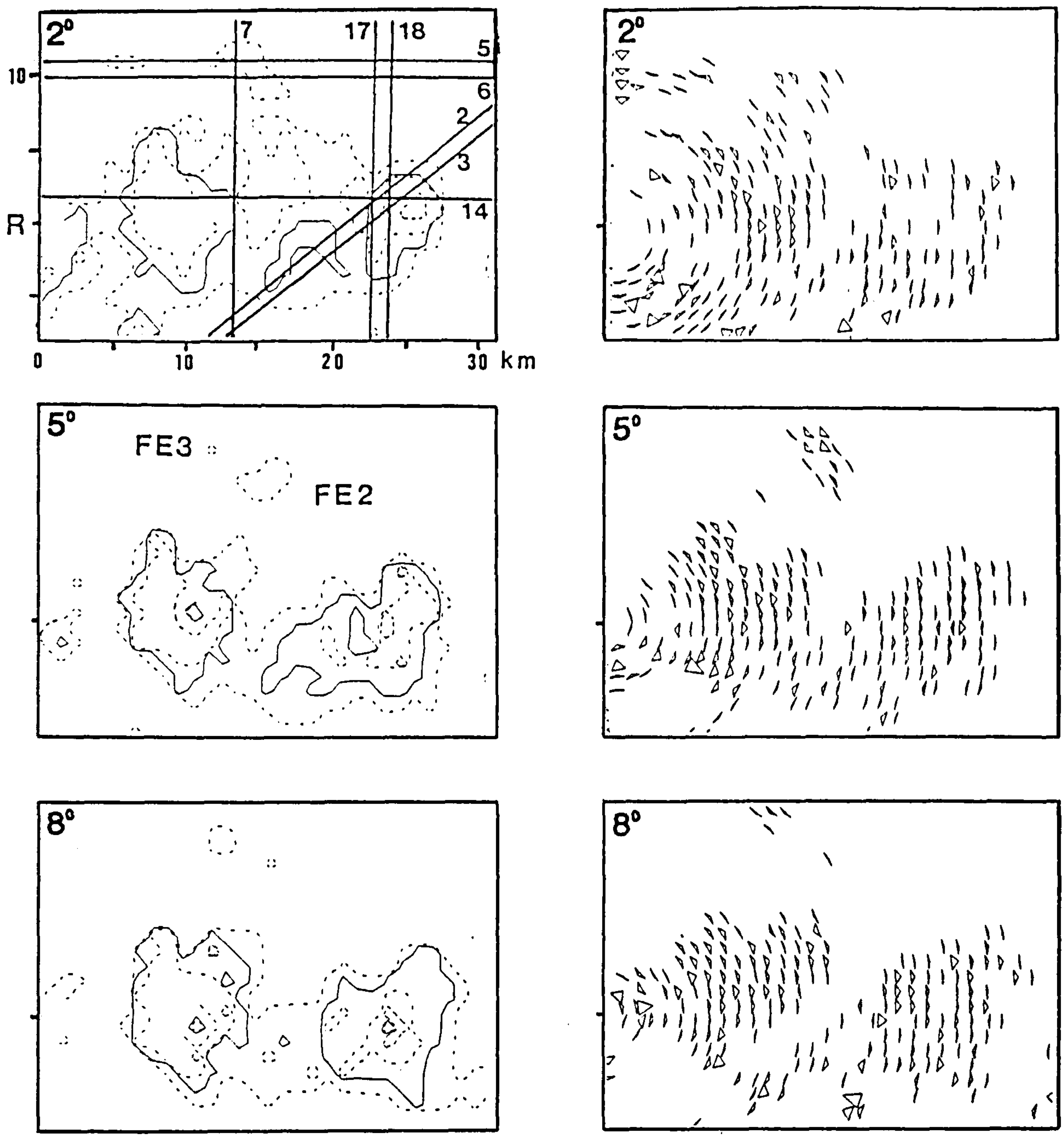

REFLECTIVITY CONTOURS:

PPI : 23,3; 30; 40; 50; 60 dBZ

Vert.Sect.: 23,3; 30; 33,3; 36,6; 40 dBZ

RADIAL VELOCITIES:

25 $m.s^{-1}$

Figure 6.10a: 15:06:22 - 15:08:16. PPI contours and corresponding radial velocity fields (2° to 8° elevation).

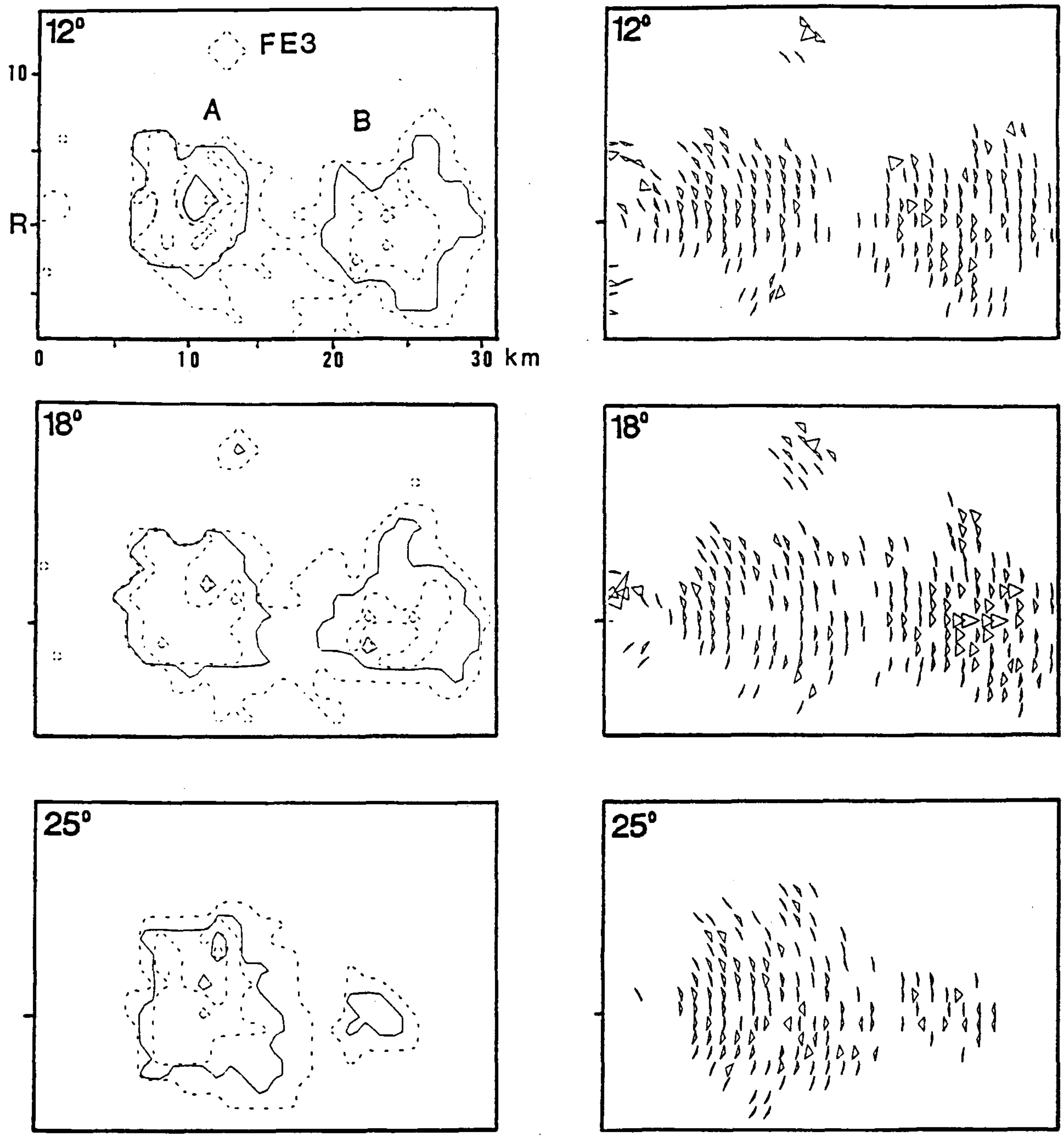

REFLECTIVITY CONTOURS:

PPI : 23,3; 30; 40; 50; 60 dBZ

Vert.Sect.: 23,3; 30; 33,3; 36,6; 40 dBZ

RADIAL VELOCITIES:

25 m.s^{-1}

Figure 6.10b: 15:06:22 - 15:08:16. PPI contours and corresponding radial velocity fields (12° to 25° elevation).

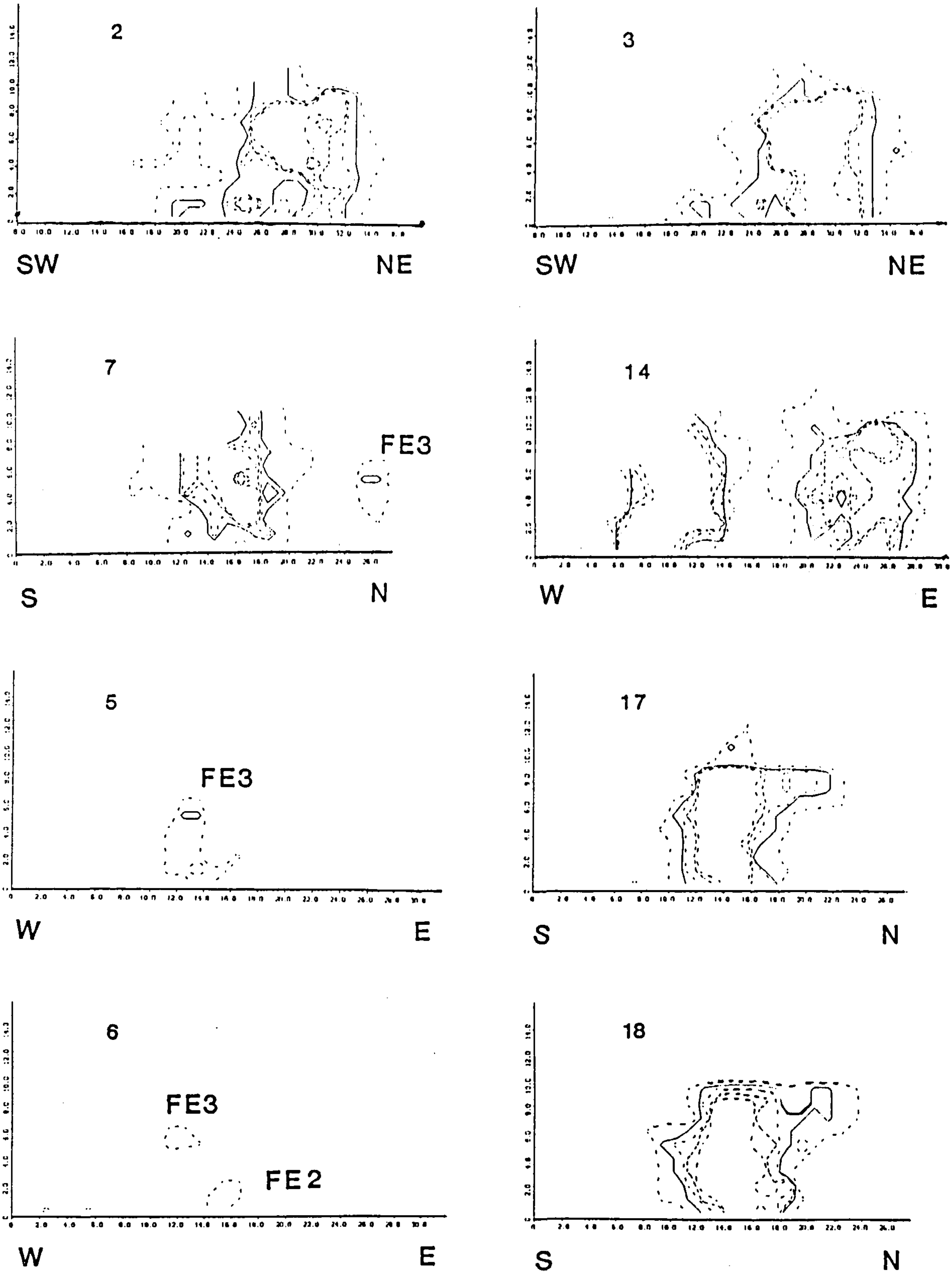

Figure 6.10c: Vertical sections along base lines marked in Figure 6.10a.

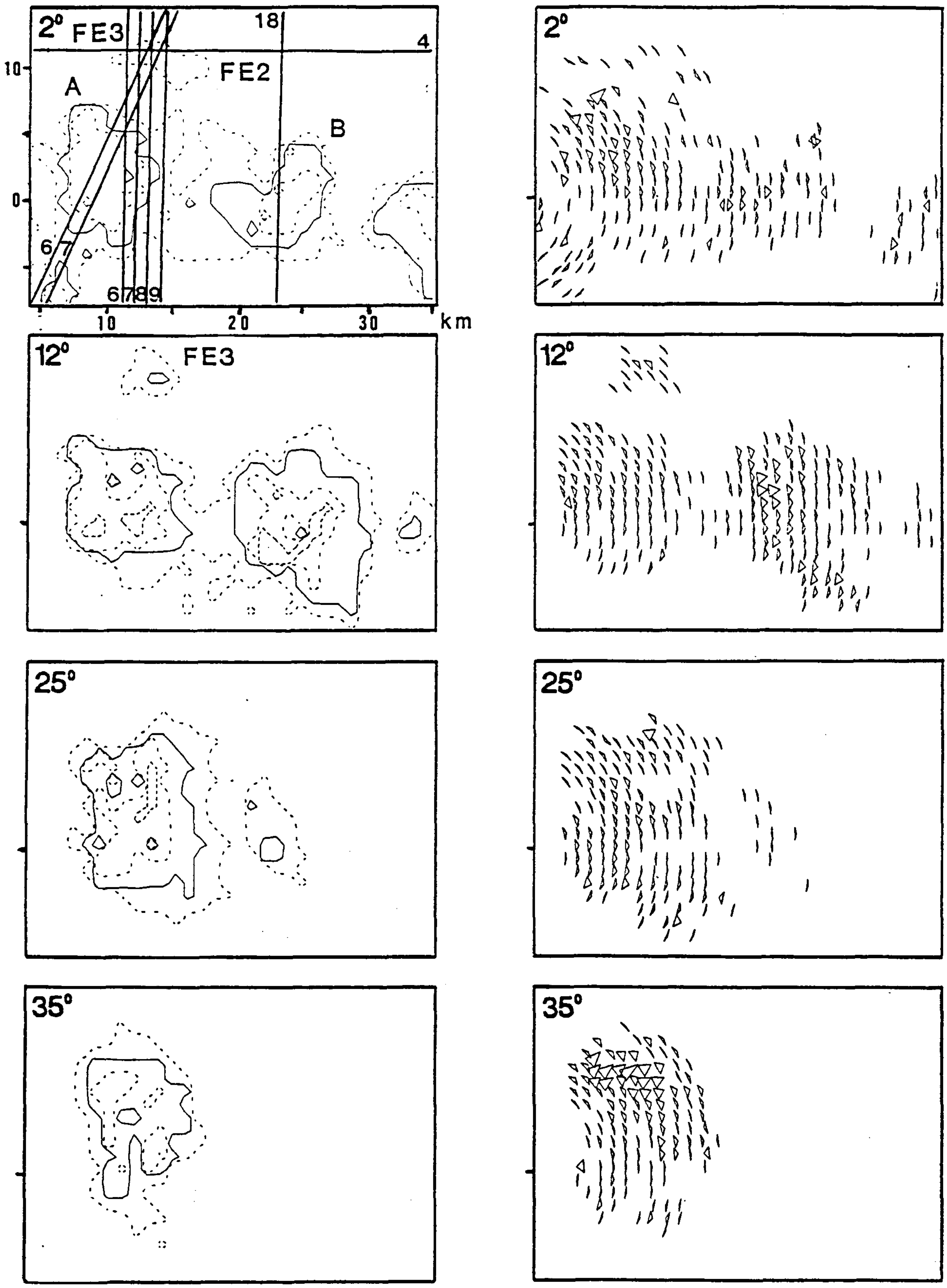

Figure 6.11a: 15:09:02 - 15:11:03. PPI contours and radial velocity field (see Figure 6.10a for key).

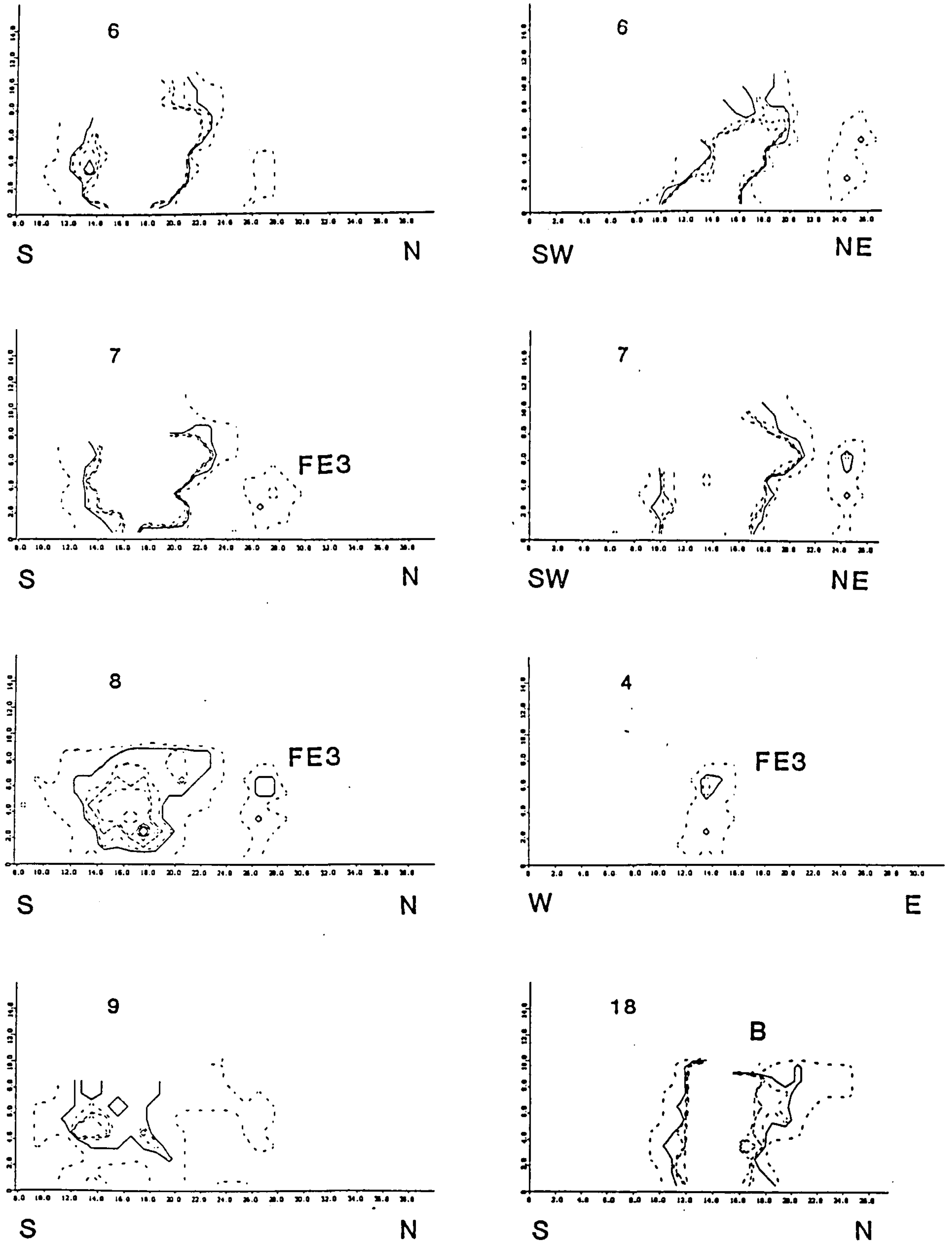

Figure 6.11b: 15:09:02 - 15:11:03. Vertical cross-sections along base lines shown in Figure 6.11a (see Figure 6.10a for key).

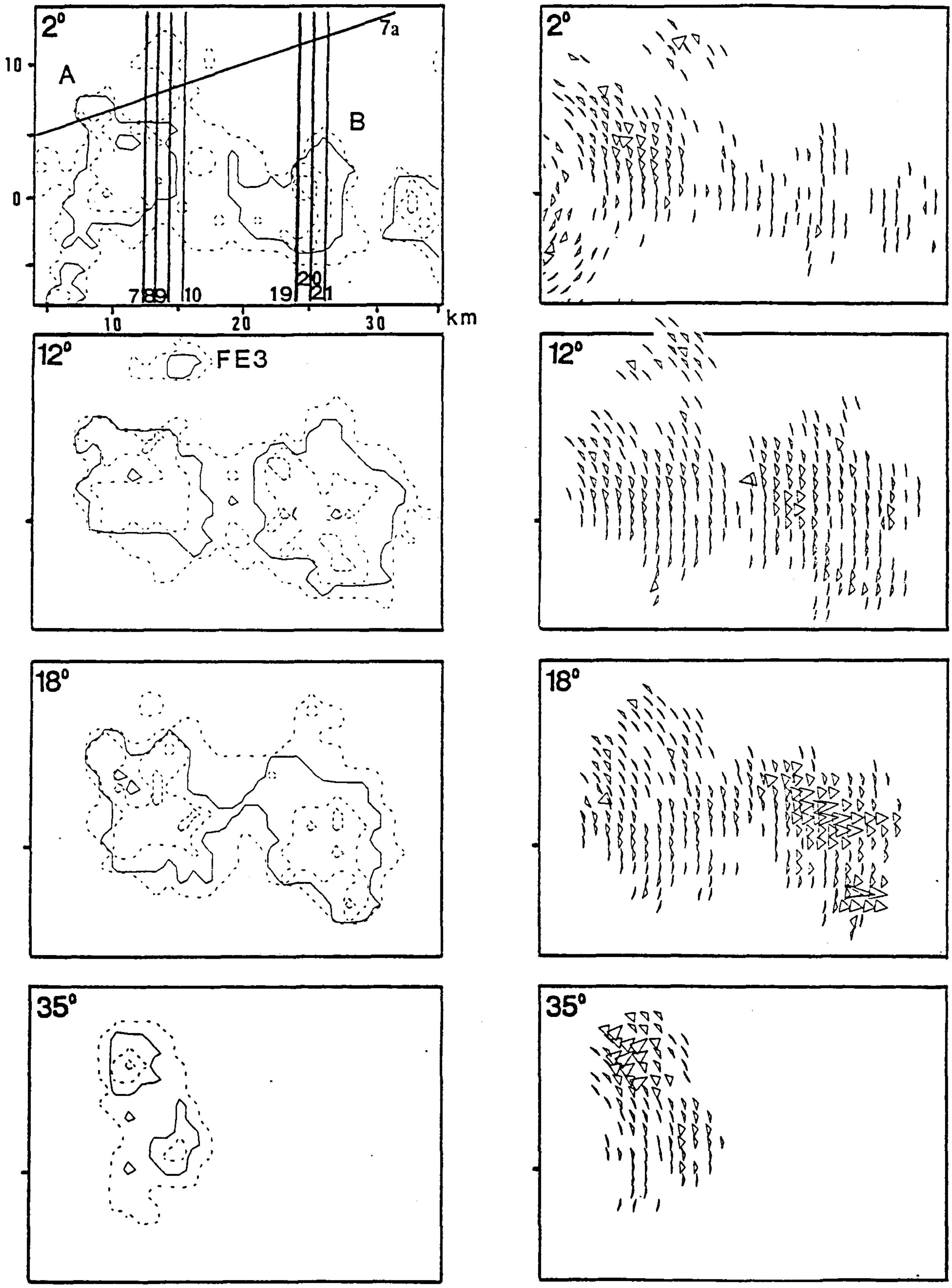

Figure 6.12a: 15:11:43 - 15:13:43. PPI contours and radial velocity field (see Figure 6.10a for key).

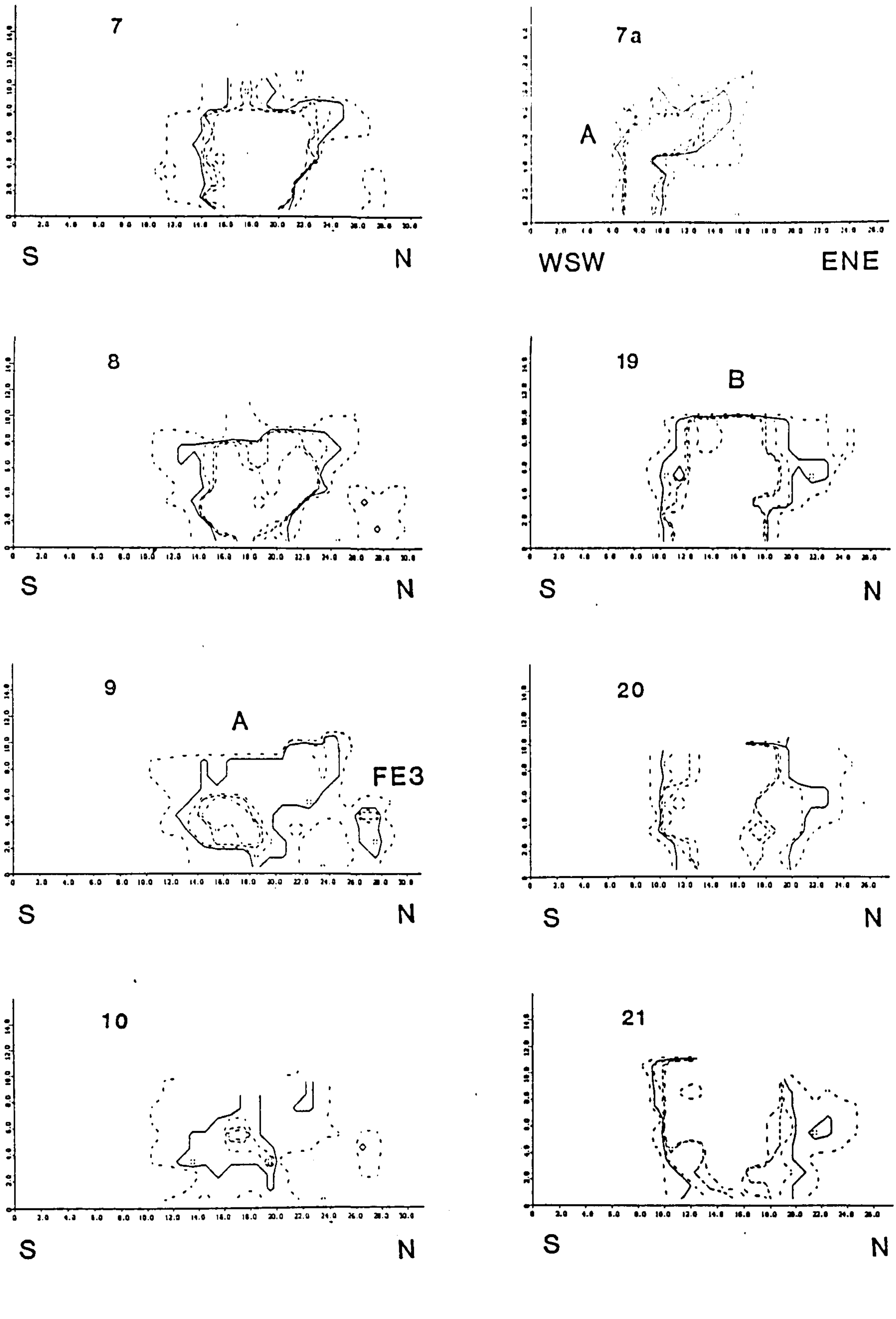

Figure 6.12b: 15:11:43 - 15:13:43. Vertical cross-sections along base lines shown in Figure 6.12a (see Figure 6.10a for key).

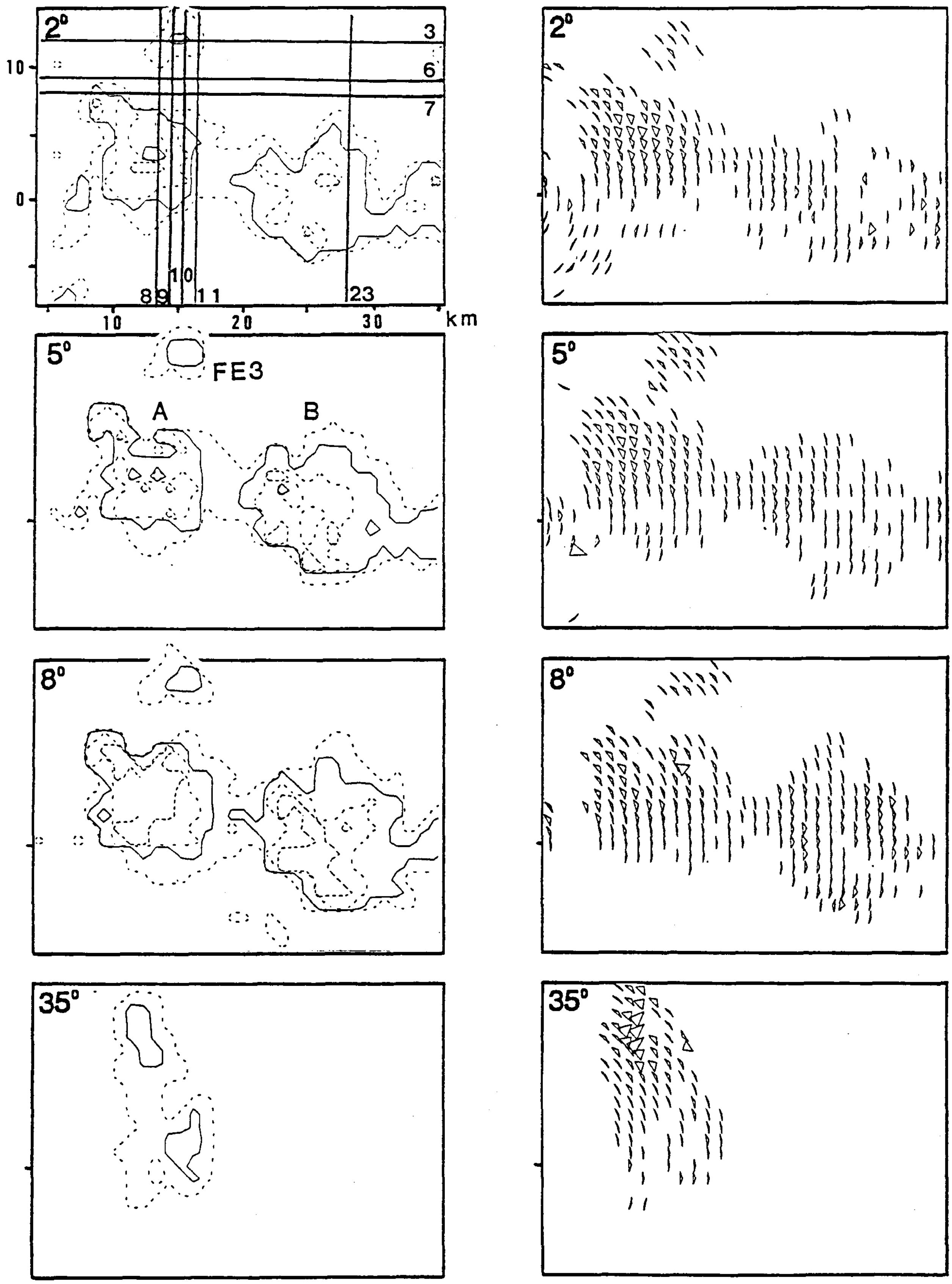

Figure 6.13a: 15:14:23 - 15:16:43. PPI contours and radial velocity field (see Figure 6.10a for key).

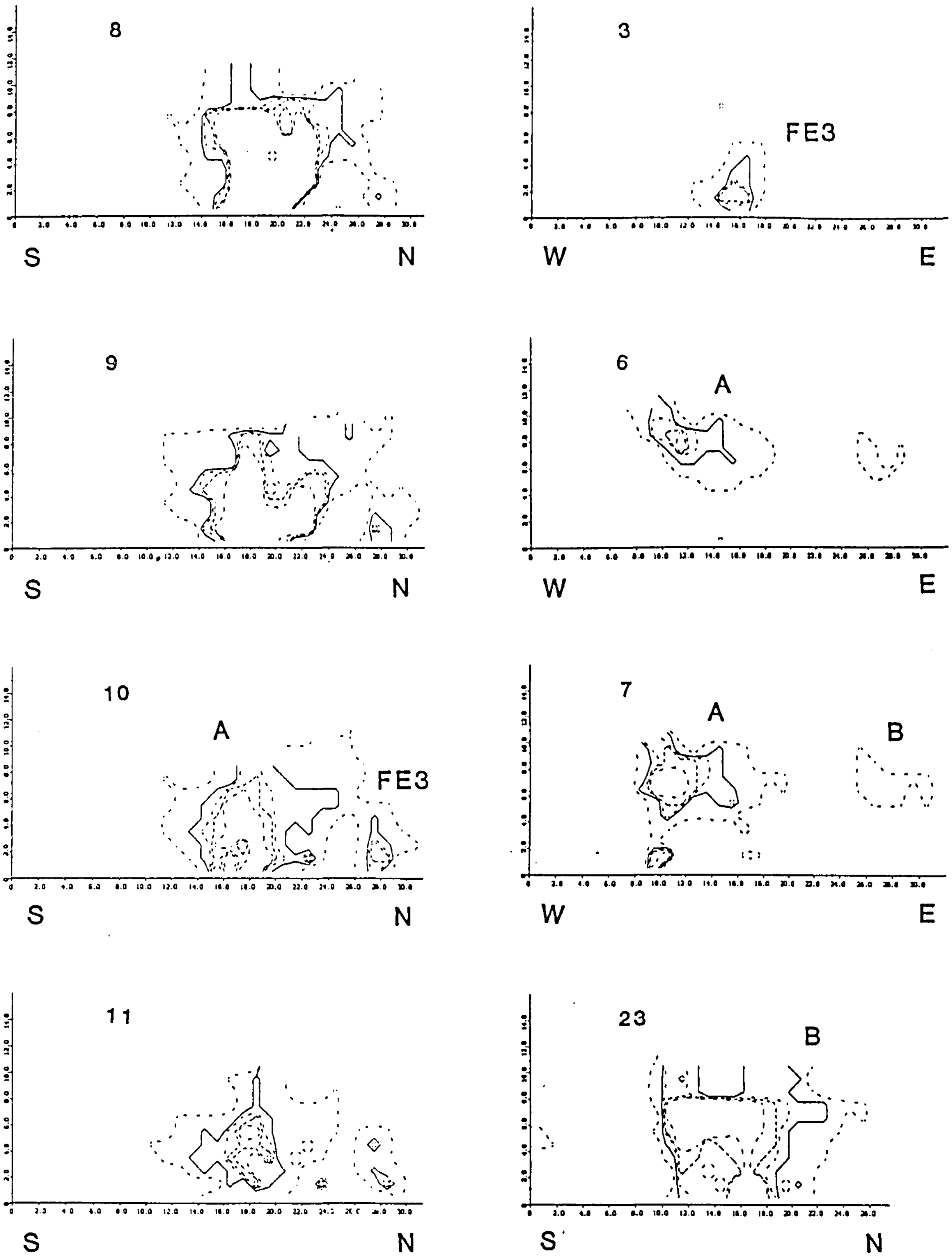

Figure 6.13b: 15:14:23 - 15:16:43. Vertical cross-sections along base lines shown in Figure 6.13a (see Figure 6.10a for key).

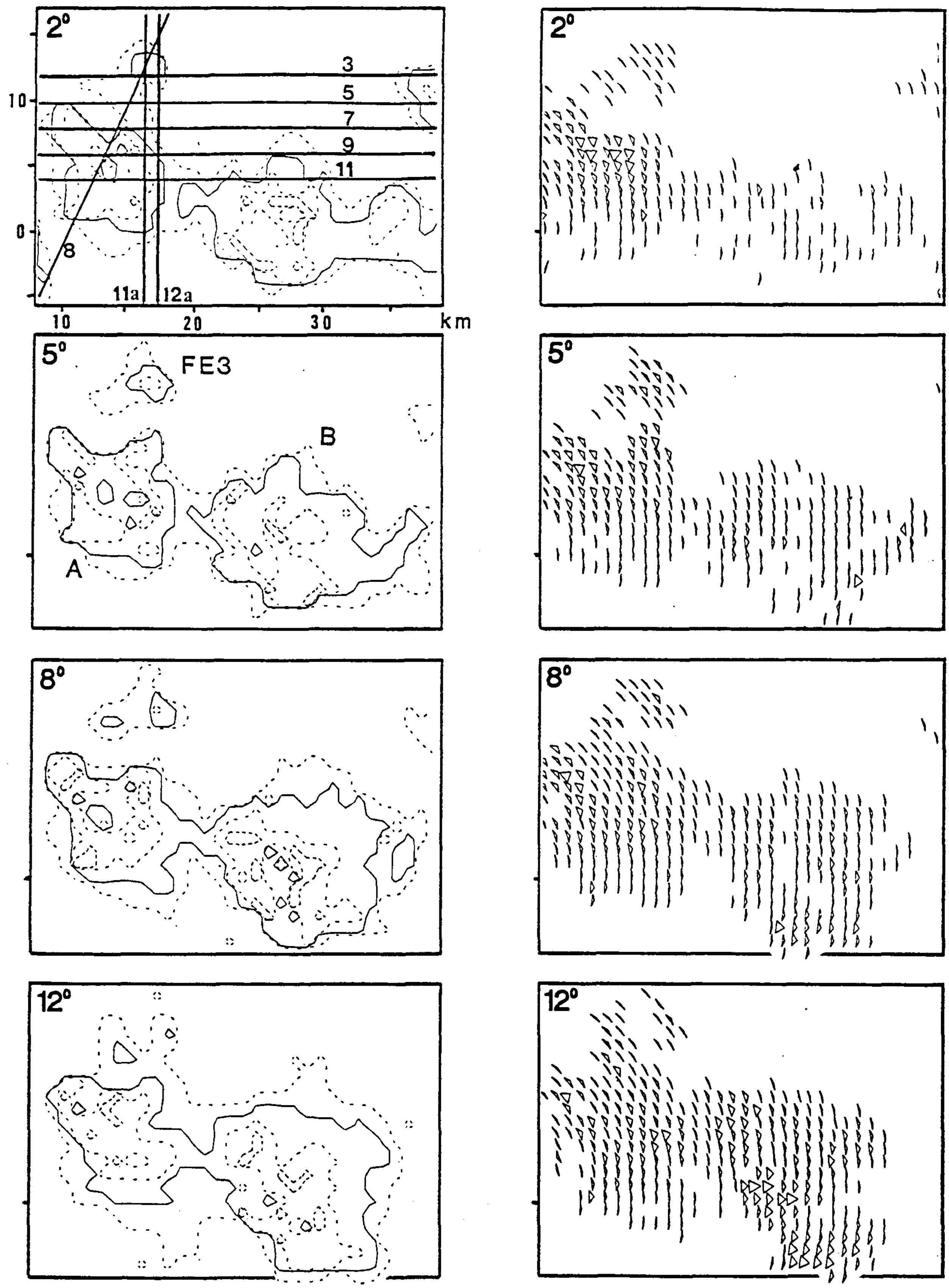

Figure 6.14a: 15:17:03 - 15:18:54. PPI contours and radial velocity field (see Figure 6.10a for key).

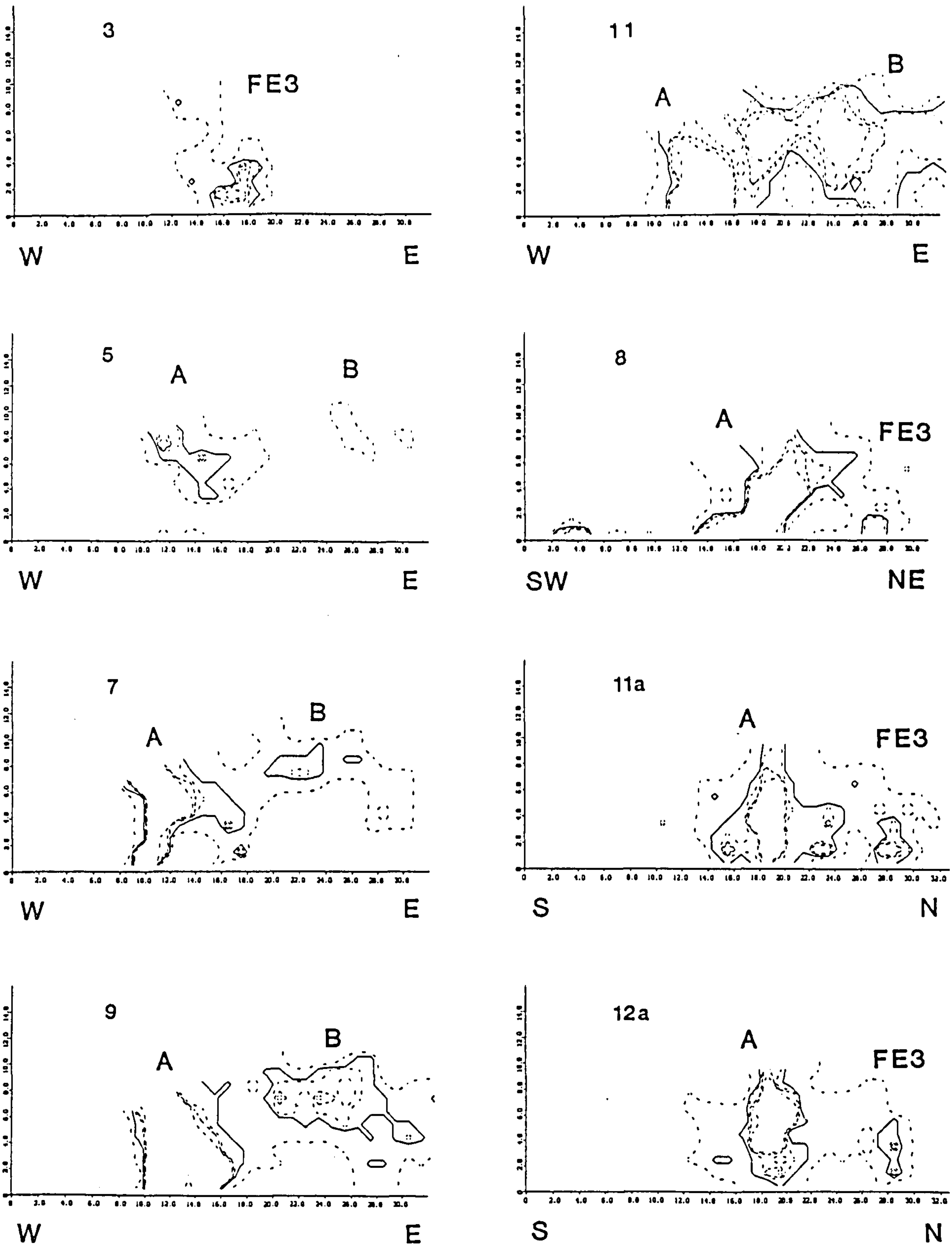

Figure 6.14b: 15:17:03 - 15:18:54. Vertical cross-sections along base lines shown in Figure 6.13a (see Figure 6.10a for key).

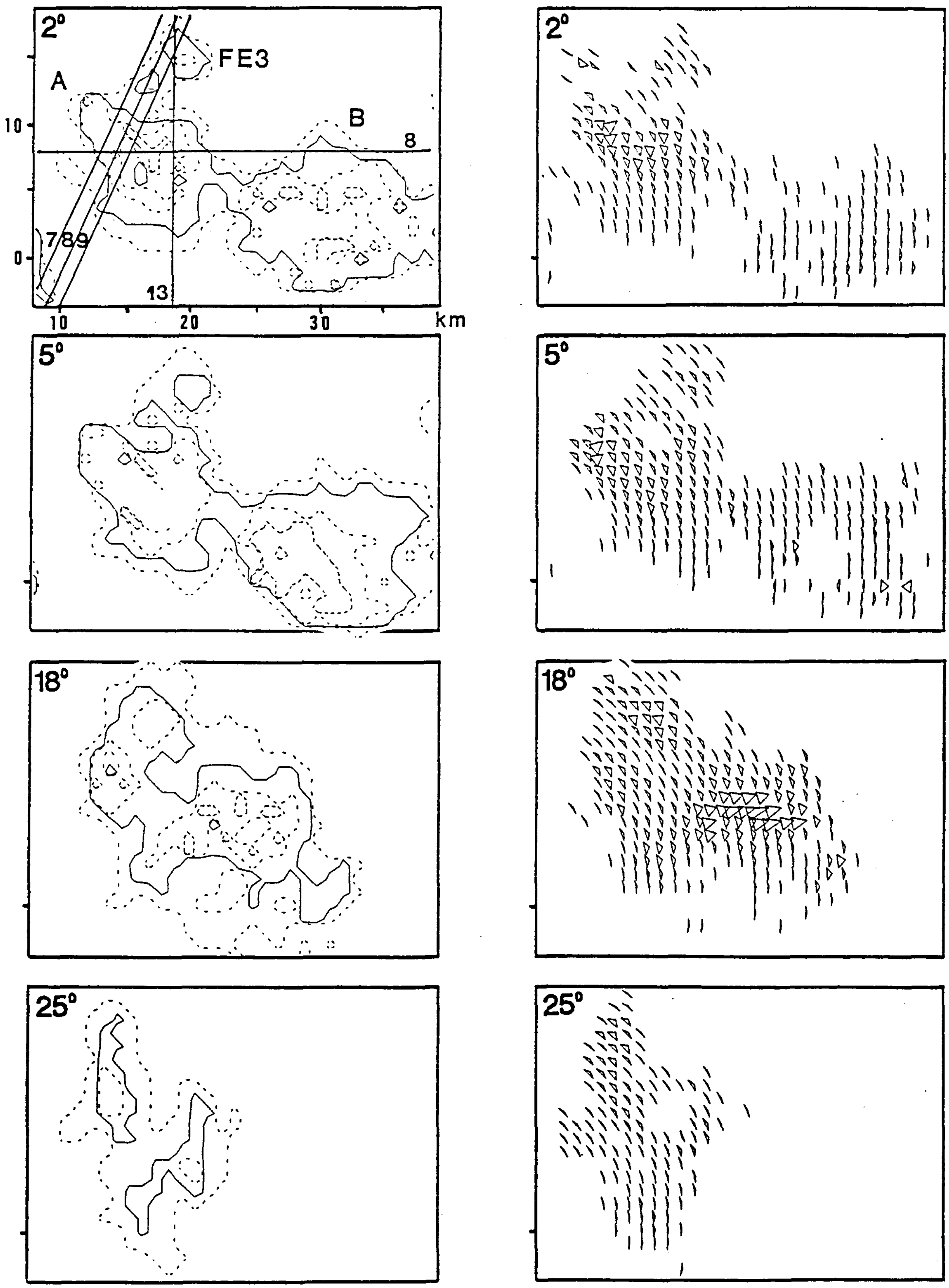

Figure 6.15a: 15:22:17 - 15:24:13. PPI contours and radial velocity field (see Figure 6.10a for key).

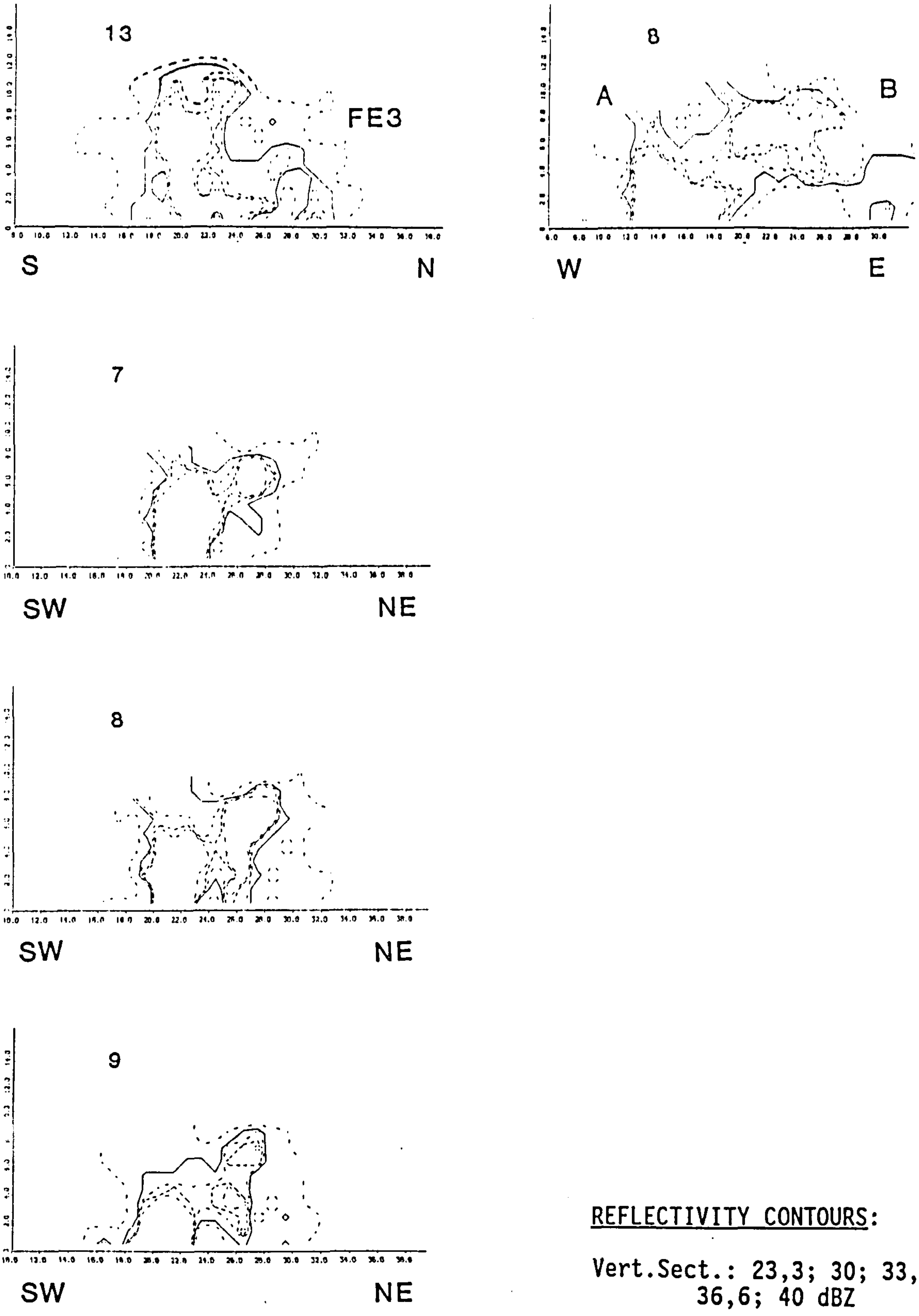

REFLECTIVITY CONTOURS:

Vert.Sect.: 23,3; 30; 33,3; 36,6; 40 dBZ

Figure 6.15b: 15:22:17 - 15:24:13. Vertical cross-sections along base lines shown in Figure 6.13a (see Figure 6.10a for key).

7. PROCESSING OF DOPPLER RADAR DATA

Gerhard Held and Ana Maria Gomes

Although it was initially envisaged that at least two Doppler radars (S-band at Houtkoppen and C-band at CSIR) would be operational during the 1989/90 season, this did, unfortunately, not materialise. Only the S-band radar at Houtkoppen was operated routinely, while test runs were made with the C-band radar on the CSIR campus. The reasons for this were manifold, but can mostly be traced back to interfacing problems between the hardware output from the modified EEC C-band radar and the Hewlett-Packard A600 computer which proved to be just too slow on some of its peripherals to accommodate the data stream in its entirety. In order to remedy the problems, certain hardware modifications and streamlining of the data acquisition program (which had been subcontracted to a private consultant) had to be undertaken. During the course of many test runs, several other difficulties had to be overcome which resulted from these latest modifications. Therefore, no useful data could be collected using more than one Doppler radar until March 1991.

However, the difficulties outlined above did certainly not deter from completing the implementation of the CRAY programs on the CSIR's VM mainframe computer and their final testing. These programs to process radar data from multiple Doppler radars were initially obtained through the courtesy of Dr Jay Miller from the National Center for Atmospheric Research (NCAR) where they ran on a CRAY 1-A supercomputer. EMATEK, at its own expense, subcontracted a specialist group from DATATEK to convert these programs and implement them on the VM mainframe computer. Final testing and fine tuning of the input data was then undertaken within the framework of the "DOPDATE" project as indicated in the Work Programme approved by the WRC for 1990.

In order to analyse radar data with the NCAR programs, two major steps have to be executed, viz. 'SPRINT' (Sorted Position Radar Interpolation) and 'CEDRIC' (Cartesian Space data processor). 'SPRINT' is designed to interpolate volumetric radar space measurements collected at constant elevation angles to a regularly spaced three-dimensional Cartesian grid

(Mohr *et al.*, 1981). 'CEDRIC' is used for the reduction and analysis of single and multiple Doppler radar volumes in Cartesian space. It provides a wide variety of commands for data manipulation coupled with significantly enhanced display capabilities (Mohr, 1985). The full capabilities of both program suites have been described in great detail by Mohr *et al.* (1981), Miller *et al.* (1986) and Mohr *et al.* (1986). Copies of these three papers are included in Appendix B.

After implementation of 'SPRINT', it was found that the Universal Radar Data Format, as specified by Barnes (1980), required more storage space on the VM mainframe computer than could be allocated. It was therefore decided to modify the input format of our radar data in order to facilitate speedy processing.

7.1 ANALYSIS OF SINGLE-DOPPLER RADAR OBSERVATIONS

All sections of 'SPRINT' and 'CEDRIC' have been thoroughly tested with Houtkoppen's single Doppler radar data. Typical examples of the output from 'SPRINT' are shown in Figures 7.1a, b, c, and d.

Now that 'SPRINT' has provided the matrix of reflectivity and radial velocity data, 'CEDRIC' will perform any analysis of these volume scans as required, including automatic (or specified) unfolding of radial velocities, remapping of data for vertical cross-sections, statistical analysis of data, filling of gaps in the data set, compensation of velocities for storm motion and algebraic manipulation of multi-dimensional Cartesian fields. A histogram indicating frequencies of specific reflectivities within a complete volume scan is shown in Figure 7.2. CAPPIS at 3 km AGL for the same volume scan display the radar reflectivity (Figure 7.3) and rainfall rate (Figure 7.4), respectively.

7.2 PRELIMINARY ANALYSIS OF DUAL DOPPLER RADAR OBSERVATIONS

On 4 March 1991, the first promising observation of a storm with both, Pretoria and Houtkoppen radars, was obtained. After a preliminary study of records from each radar individually was done, it was decided to analyse a small storm consisting of two cells and located approximately 25 km from both radars (Figure 7.5a). The single-Doppler radial velocity and reflectivity data were independently converted to a three-dimensional Cartesian coordinate system by SPRINT, using a successive linear interpolation algorithm described by Mohr and Vaughan (1979) and Mohr *et al.* (1981). The regular volume containing data in this case covers 80 x 50 km in the horizontal and 7,2 km in the vertical. The spacing of grid points was 1,0 km in the horizontal and 0,5 km in the vertical.

Preliminary single-Doppler analysis of records from both, Houtkoppen and Pretoria, has been completed and the dual Doppler analysis for the period 15:56:16 to 15:59:05 should be available soon. The three-dimensional wind field will be computed using the CEDRIC analysis package, developed at NCAR (Mohr *et al.*, 1986). The CEDRIC analysis scheme solves the three-dimensional wind field iteratively, utilising the geometrical relationships among the single-Doppler velocities measured by each radar, the Cartesian wind components and the location in space, and the vertical integration of the anelastic continuity equation.

The CAPPIs in Figure 7.5a have been generated for increments of 0,5 km in height, but only every other one is shown in the Figure. The maximum reflectivity value in each CAPPI is indicated by X and its value printed just above the key on the righthand side. Figure 7.5b shows the 5,2 km MSL CAPPI with the radial wind vectors. The strong divergence in cell A at this level, and actually extending from 4,7 to 6,2 km, is noteworthy.

Davis-Jones (1979) has noted from experience that a minimum beam intersection angle (difference in azimuth of the two radars when they are scanning identical volumes) of 30° is usually necessary for qualitatively reasonable dual Doppler analyses. This particular storm which occurred on 4 March 1991 seems, at a first approach, to be suitable for dual analysis, because it falls within the range mentioned above. Figure 7.6 shows the position of both radars. The full circles indicate the maximum range for each radar when operated in Doppler mode. The dashed circles outline the area for optimal dual Doppler radar observations. An even more suitable, isolated storm was observed on 26 March 1991 and the dual-Doppler observations have been used to demonstrate the application and versatility of the CRAY programs for synthesizing the storm and for calculating the three-dimensional air flow within it.

This particular storm initially consisted of several small cells between 7 and 27 km northeast of the Houtkoppen radar (12:37) as shown in Figure 7.7. These cells merged within a period of less than 20 minutes into one multi-cellular complex which moved from 210° at an average speed of 9,9 $m.s^{-1}$. It reached its peak intensity (> 50 dBZ) at approximately 13:14. This volume scan was therefore chosen for a detailed dual-Doppler analysis. The complex continued to move towards northeast but gradually dropped in intensity and decreased in size from 13:35 onwards (Figure 7.7).

The volume scan from 13:13:08 to 13:15:10 was then processed by SPRINT and CEDRIC with a horizontal grid of 1 km and a vertical resolution of 0,5 km. The CAPPIs showing the reflectivity contours from the Houtkoppen radar and the related horizontal wind field from 2,8 to 8,3 km MSL are depicted in Figures 7.8 and 7.9. Vertical cross sections along the baselines shown in Figure 7.8 show the reflectivity pattern with height and the air flow in terms of up- and downdraughts. Figure 7.10 shows vertical sections along south - north and west - east baselines. Figure 7.11a and b depict vertical sections along baselines from southwest to northeast and northwest to southeast, respectively. These sections were constructed by first rotating the storm around a new origin ("REMAPPING" facility) so that the new X-axis is pointing towards 146° from true north.

This is the very first time that the actual three-dimensional air flow has been observed in a South African thunderstorm and presented graphically in terms of up- and downdraughts related to the reflectivity pattern.

7.3 REFERENCES

BARNES S C, 1980. Report on a meeting to establish a common Doppler radar exchange format. *Bull. Amer. Meteor. Soc.*, 61, 1401-1404.

DAVIS-JONES R P, 1979. Dual-Doppler radar coverage area as a function of measurement accuracy and spatial resolution. *J. Appl. Meteor.*, 18, 1229-1233.

MILLER L J, MOHR C G and WEINHEIMER A J, 1986. The simple rectification to Cartesian space of folded radial velocities from Doppler radar sampling. *J. of Atmos. and Oceanic Techn.*, 3, 162-174.

MOHR C G, 1985. SPRINT - Sorted Position Radar Interpolation. User's Manual.

MOHR C G and VAUGHAN R L, 1979. An economical procedure for Cartesian interpolation and display of reflectivity factor data in three-dimensional space. *J. Appl. Meteor.*, 28, 661-670.

MOHR C G, MILLER L J and VAUGHAN R L, 1981. An interactive software package for the rectification of radar data to three-dimensional Cartesian coordinates. *Preprints of 20th Conference on Radar Meteorology*, Boston, Amer. Meteor. Soc., 690-695.

MOHR C G, MILLER L J, VAUGHAN R L and FRANK H W, 1986. The merger of mesoscale data sets into a common Cartesian format for efficient and systematic analysis. *J. of Atmos. and Oceanic Techn.*, 3, 143-161.

```
SUMMARY OF INPUT COMMAND
------- -- ----- -------

                        UNIT NUMBER:    21
                          TAPE NAME: RAD52
                        REWIND TAPE: NO
                NUMBER FILES TO SKIP:     0
                    EXPERIMENT NAME: MULDOP
                         RADAR NAME: HOUT


>>>>>GRID    -40.     0.     -20.     10.     1.     2.     10.     1.                <<<<<

     SUMMARY OF CARTESIAN COMMAND
     ------- -- --------- -------

     CARTESIAN COORDINATE SYSTEM SPECIFICATIONS:

      AXIS      MINIMUM (KM)      MAXIMUM (KM)      DELTA (KM)     NO. OF PTS.
      ----      ------------      ------------      ----------     -----------

       X           -40.00              0.00            1.00             41
       Y           -20.00             10.00            1.00             31
       Z             2.00             10.00            1.00              9

      AXIS ORDER IS   X  Y  Z
      ANGLE OF THE X-AXIS RELATIVE TO NORTH:   90.0 DEGREES
      (X,Y)  AXES ARE SPECIFIED RELATIVE TO:  (0.00,0.00)

>>>>>PROCESS     20. 171349. 172123.                                               <<<<<

     SUMMARY OF PROCESS COMMAND
     ------- -- ------- -------

                          DATE (YYMMDD):      20
               BEGINNING TIME (HHMMSS): 171349
                  ENDING TIME (HHMMSS): 172123
     SPECIAL VOLUME PROCESSING PERFORMED:  NONE
   ELEVATION SCANS WILL BE DETERMINED BY: SWEEP NUMBER

++++++++++++++++++++++++++++++++++++++++++++++++++++++++++++++++++++++++++++++++++++++++++++++++++++++++++++++

        VOLUME FOUND   -   DAY :    20        BEGINNING TIME : 171349
```

SCAN NO	SCAN DIR	ELEVATION FIXED	ELEVATION MIN	ELEVATION MAX	ELEVATION MEAN	AZIMUTH BEG	AZIMUTH END	SPACING MIN	SPACING MAX	SPACING MEAN	BEAMS GOOD	BEAMS BAD
1	1	2.00	1.89	1.89	1.89	152.2	78.6	1.00	1.50	1.24	523	0
2	1	5.00	5.19	5.19	5.19	165.5	79.1	1.00	1.50	1.24	512	0
3	1	6.00	6.19	6.19	6.19	103.7	77.2	1.09	1.41	1.24	560	0
4	1	12.00	12.19	12.19	12.19	200.4	79.8	1.09	1.41	1.24	484	0
5	1	18.00	13.19	13.19	18.19	204.0	55.8	1.09	2.41	1.25	460	0
6	1	25.00	25.19	25.19	25.19	229.1	37.3	1.09	1.41	1.24	425	0
7	1	35.00	35.30	35.30	35.30	205.2	19.0	1.09	1.41	1.24	430	0
8	1	50.00	50.30	50.30	50.30	271.1	21.0	1.09	1.41	1.25	377	0

Figure 7.1a: Extracts from input commands and statistics of volume scan.

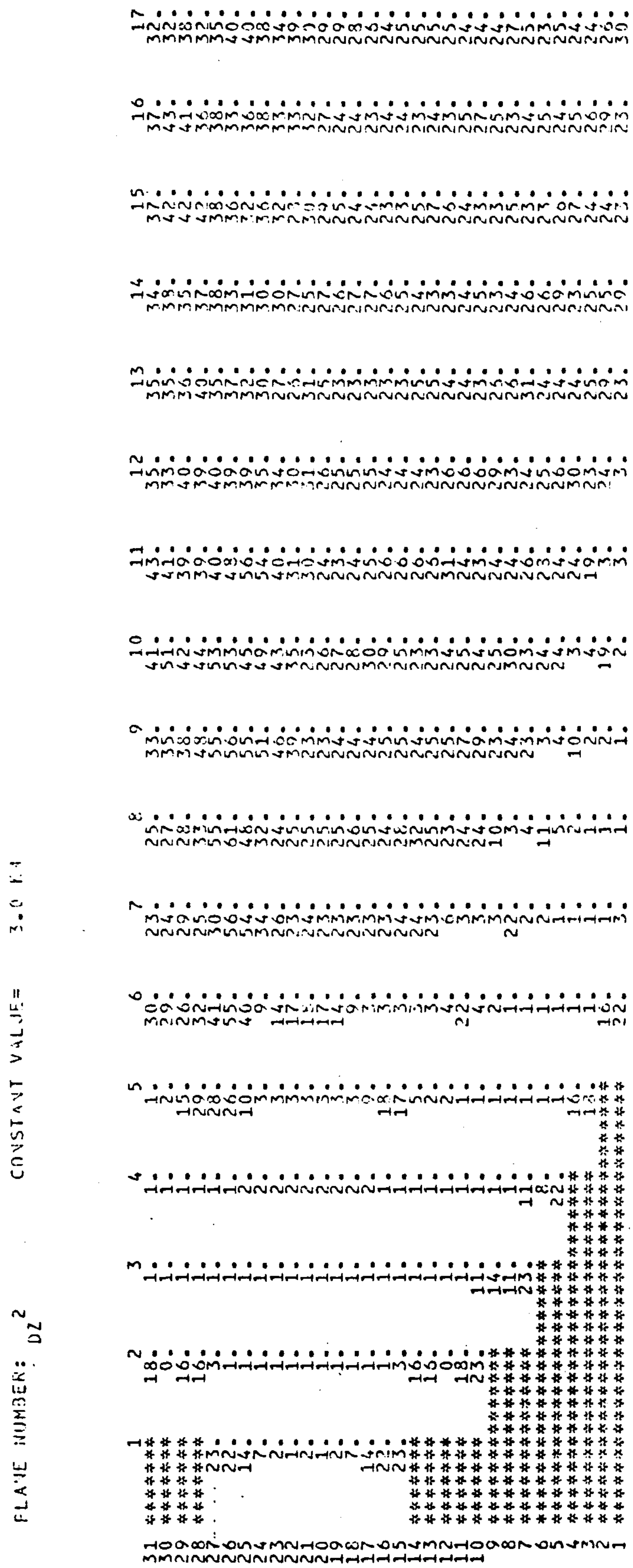

Figure 7.1b Radar reflectivity (dBZ) for CAPPI at 3,0 km AGL (only part of picture). The spacing of grid points is 1 km for both the x and y axis.

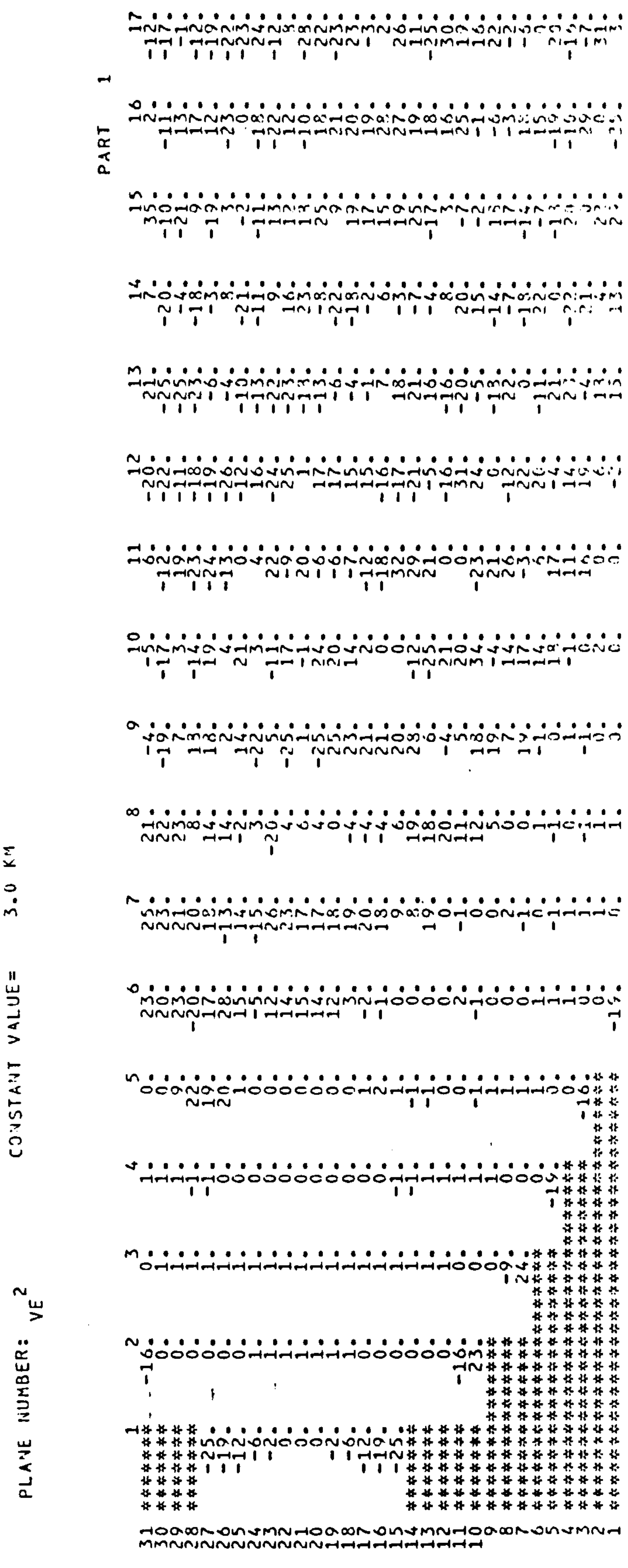

Figure 7.1c Velocity field $(m.s^{-1})$ for the CAPPI shown in Figure 7.1b

PLANE NUMBER: QU^2 CONSTANT VALUE= 3.0 KM

PART 1

	1	2	3	4	5	6	7	8	9	10	11	12	13	14	15	16	17
31	*******	61.	31.	32.	44.	15.	89.	99.	-81.	-13.	53.	3.	58.	68.	5.	-10.	10.
30	*******	61.	54.	24.	100.	15.	100.	48.	31.	-18.	1.	53.	-4.	8.	-51.	-28.	54.
29	*******	62.	54.	-49.	-12.	68.	100.	1.	-97.	-30.	29.	69.	48.	-25.	2.	15.	15.
28	*******	68.	46.	-49.	83.	27.	67.	30.	46.	-14.	35.	32.	81.	15.	6.	2.	30.
27	21.	68.	32.	44.	66.	-23.	49.	-7.	51.	-7.	-11.	58.	1.	-53.	-10.	-13.	2.
26	61.	31.	32.	44.	36.	32.	48.	30.	34.	9.	-16.	-35.	23.	52.	-16.	29.	-32.
25	61.	31.	24.	100.	-28.	41.	14.	-48.	65.	50.	-33.	-17.	18.	61.	94.	-75.	57.
24	61.	54.	24.	100.	39.	-11.	-47.	-63.	-9.	-38.	23.	-7.	27.	49.	13.	23.	3.
23	61.	54.	24.	100.	100.	17.	34.	40.	50.	46.	17.	49.	-14.	-16.	69.	75.	13.
22	62.	54.	24.	63.	100.	17.	63.	-80.	90.	-33.	42.	-19.	-20.	6.	-18.	-22.	28.
21	62.	54.	24.	63.	100.	17.	96.	-52.	-70.	-39.	49.	55.	73.	43.	10.	-75.	55.
20	62.	54.	24.	63.	100.	17.	96.	-52.	87.	14.	-52.	49.	27.	-14.	40.	29.	79.
19	61.	54.	24.	100.	100.	17.	91.	-52.	87.	14.	-54.	54.	47.	14.	20.	97.	41.
18	61.	54.	24.	100.	39.	-40.	91.	31.	87.	14.	36.	54.	47.	42.	100.	98.	95.
17	61.	31.	24.	100.	39.	45.	91.	31.	95.	-56.	36.	1.	47.	-79.	54.	22.	-42.
16	61.	31.	32.	44.	39.	45.	47.	31.	95.	101.	19.	6.	59.	-3.	54.	48.	-113.
15	21.	63.	32.	44.	-32.	45.	47.	-54.	43.	101.	19.	38.	97.	-3.	47.	41.	30.
14	*******	68.	46.	-49.	-32.	100.	29.	96.	23.	43.	35.	37.	97.	47.	89.	100.	39.
13	*******	62.	54.	-49.	63.	100.	17.	96.	-52.	87.	14.	-54.	54.	47.	42.	54.	26.
12	*******	61.	54.	24.	100.	39.	-40.	91.	31.	95.	101.	36.	6.	59.	-3.	47.	40.
11	*******	61.	31.	32.	44.	39.	45.	47.	-54.	43.	43.	19.	33.	97.	47.	39.	100.
10	*******	-43.	68.	46.	-49.	-32.	100.	29.	96.	22.	87.	14.	-54.	54.	47.	-79.	54.
9	*******	*******	62.	54.	24.	63.	100.	-40.	91.	31.	95.	101.	19.	38.	97.	47.	89.
8	*******	*******	61.	31.	32.	44.	39.	45.	47.	45.	23.	43.	36.	-54.	54.	47.	-79.
7	*******	*******	-43.	68.	45.	-49.	63.	100.	17.	96.	-52.	87.	-56.	19.	33.	97.	47.
6	*******	*******	*******	62.	54.	24.	100.	39.	45.	47.	-54.	43.	43.	34.	-54.	54.	47.
5	*******	*******	*******	61.	31.	32.	44.	-32.	100.	29.	65.	71.	95.	101.	17.	38.	97.
4	*******	*******	*******	*******	62.	54.	24.	100.	39.	45.	47.	45.	23.	43.	14.	36.	6.
3	*******	*******	*******	*******	61.	31.	37.	44.	-32.	100.	17.	91.	31.	95.	43.	35.	-54.
2	*******	*******	*******	*******	*******	62.	54.	24.	100.	39.	45.	29.	96.	-52.	37.	101.	19.
1	*******	*******	*******	*******	*******	61.	68.	46.	-49.	63.	100.	45.	47.	45.	23.	37.	-55.

Figure 7.1d Quality field (percent) for the CAPPI shown in Figure 7.1b Data points with percentages between -60,0 and 60,0 should be carefully examined before accepting or discarding these data.

```
DZ           XY KM        MEAN      STDV       N     I1    I2    J1    J2          MIN      MAX
             VOLUME       26.31     9.24     3729     1    31     1     4          0.4      60.8
         HISTOGRAM       (SCALED BY    1.00)       1479 BAD POINTS
(         .      0.00):                                                                     0.00
(     0.00,      5.00): ***                                                                 3.33
(     5.00,     10.00): ***                                                                 3.49
(    10.00,     15.00): **                                                                  1.56
(    15.00,     20.00): **                                                                  1.58
(    20.00,     25.00): ******************************************                         41.65
(    25.00,     30.00): **************************                                         25.85
(    30.00,     35.00): *********                                                           8.88
(    35.00,     40.00): ******                                                              6.01
(    40.00,     45.00): ***                                                                 3.22
(    45.00,     50.00): **                                                                  2.23
(    50.00,     55.00): **                                                                  1.80
(    55.00,     60.00):                                                                     0.40
(    60.00,     65.00):                                                                     0.03
(    65.00,     70.00):                                                                     0.00
(    70.00,     75.00):                                                                     0.00
(    75.00,     80.00):                                                                     0.00
(    80.00,     85.00):                                                                     0.00
(    85.00,     90.00):                                                                     0.00
(    90.00,     95.00):                                                                     0.00
(    95.00,      +    ):                                                                    0.00
       INTERVALS        ....+....+....+....+....+....+....+....+....+                       PER
                           5%  10%  15%  20%  25%  30%  35%  40%  45%                       CENT
```

Figure 7.2 Frequency distribution of reflectivity values within the volume scan on 16 November 1987, 17:13:49 - 17:16:17, generated by 'CEDRIC'.

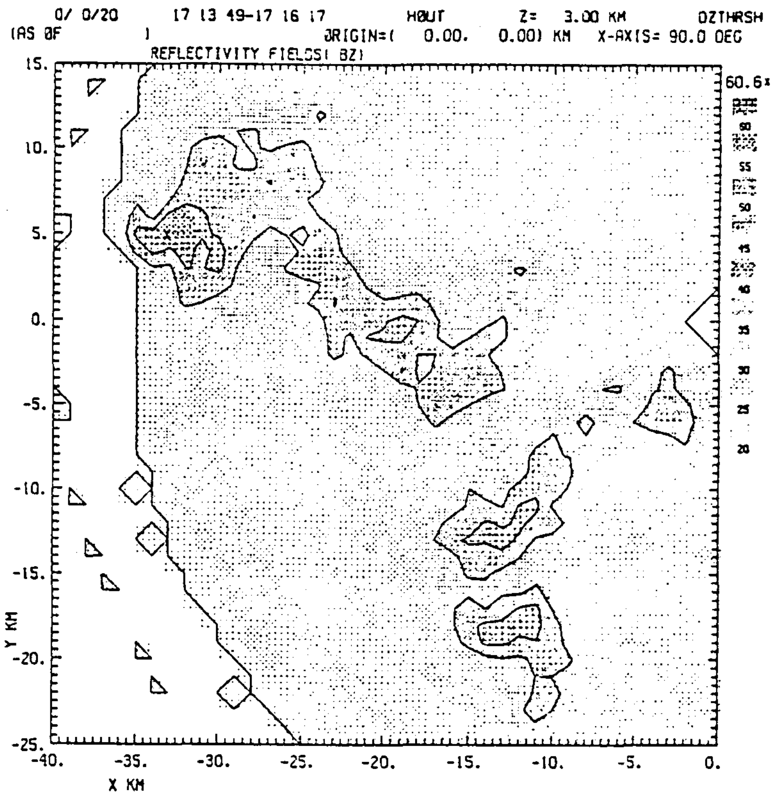

Figure 7.3 CAPPI at 3 km AGL showing radar reflectivities (dbZ) for part of the volume scan on 16 November 1987, 17:13:49 - 17:16:17, generated by 'CEDRIC'.

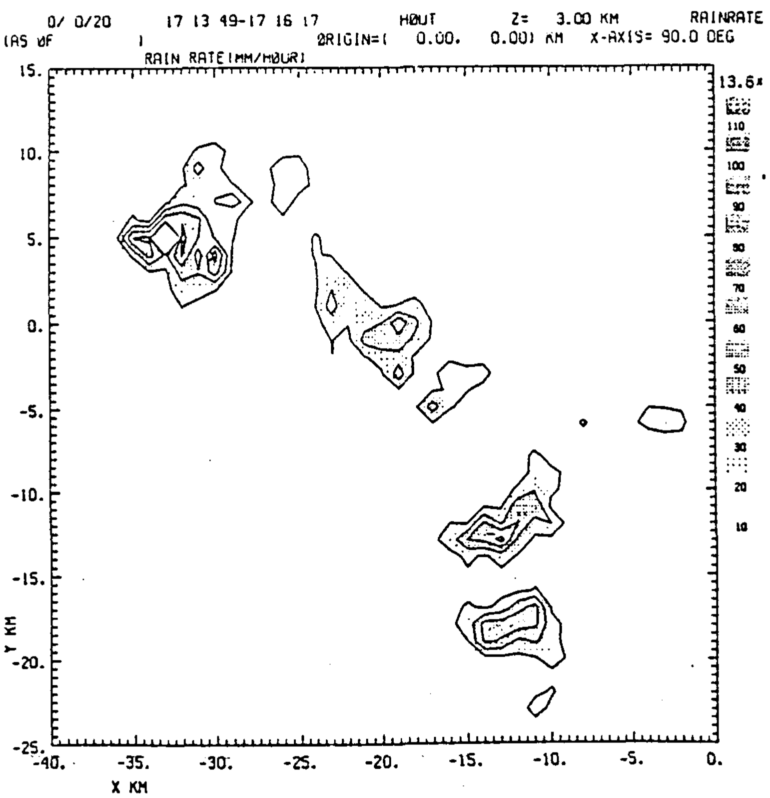

Figure 7.4 Rainfall rates ($mm.h^{-1}$) for above CAPPI, also generated by 'CEDRIC'.

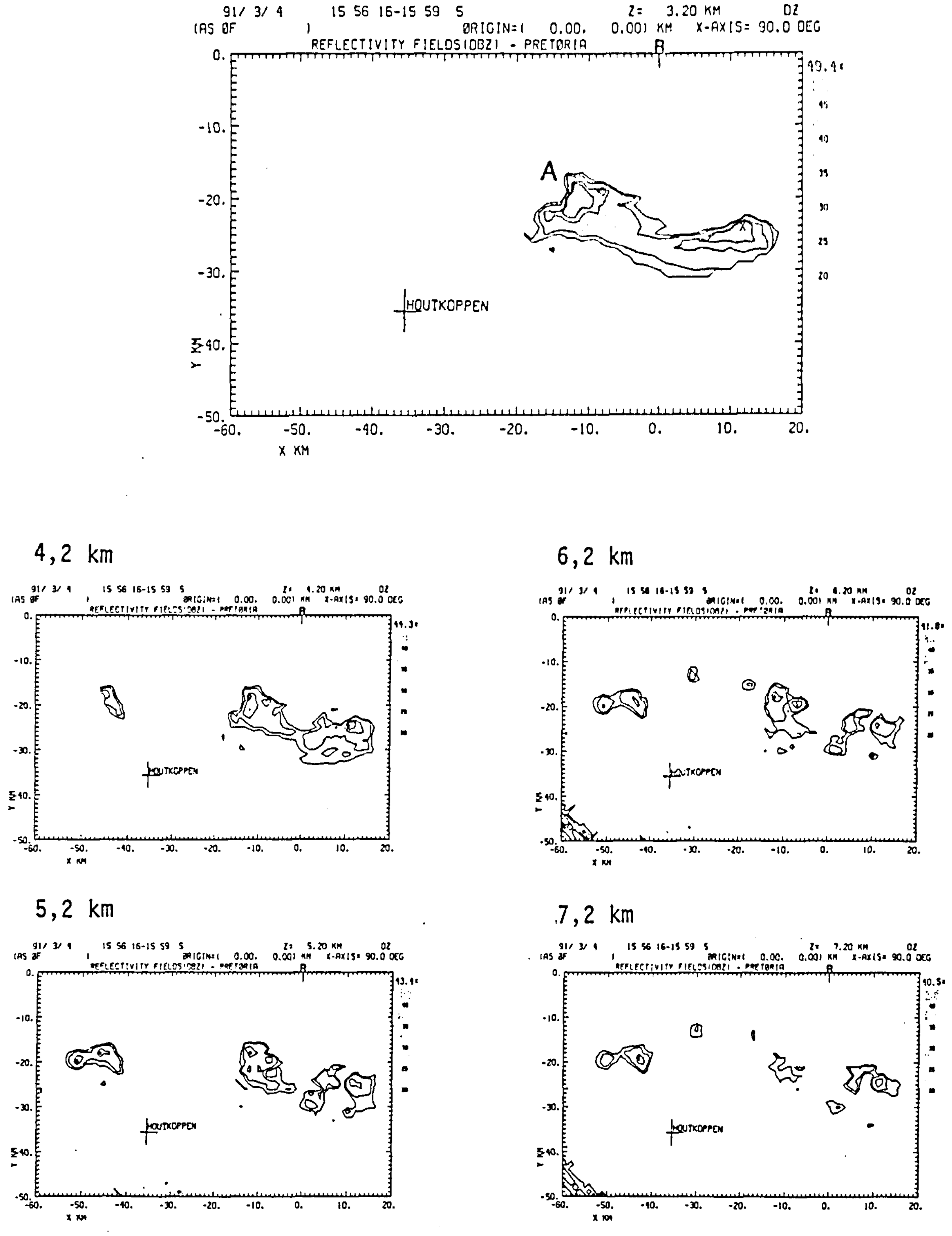

Figure 7.5a: CAPPIs generated by SPRINT and plotted by CEDRIC, showing reflectivity contours in dBZ of a storm observed by the Pretoria Doppler radar on 4 March 1991 at 15:56 at 3,2 km, 4,2 km, 5,2 km, 6,2 km and 7,2 km MSL (outer contour is 20 dBZ, contour interval is 5 dB, scale in km relative to the Pretoria radar R).

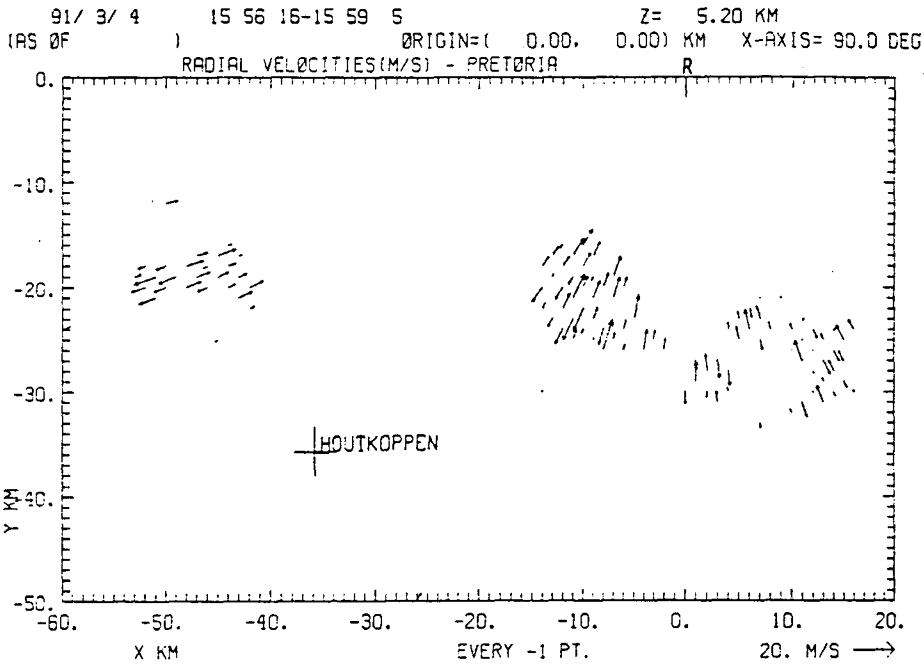

Figure 7.5b: CAPPI at 5,2 km MSL showing radial wind vectors for the same scan as in Figure 7.5a.

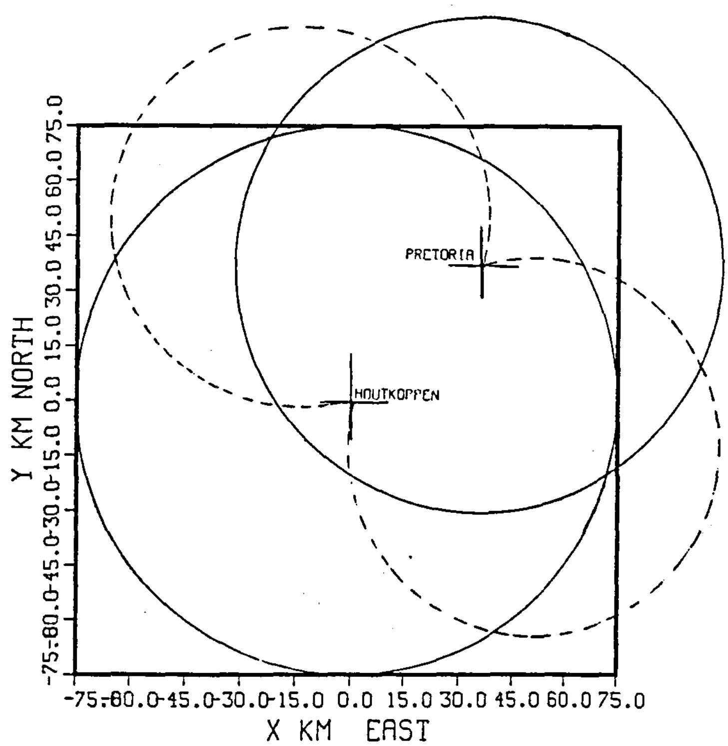

Figure 7.6: Maximum range of Doppler radars at Houtkoppen and Pretoria (full circles) and area of optimal dual Doppler radar coverage (dashed line).

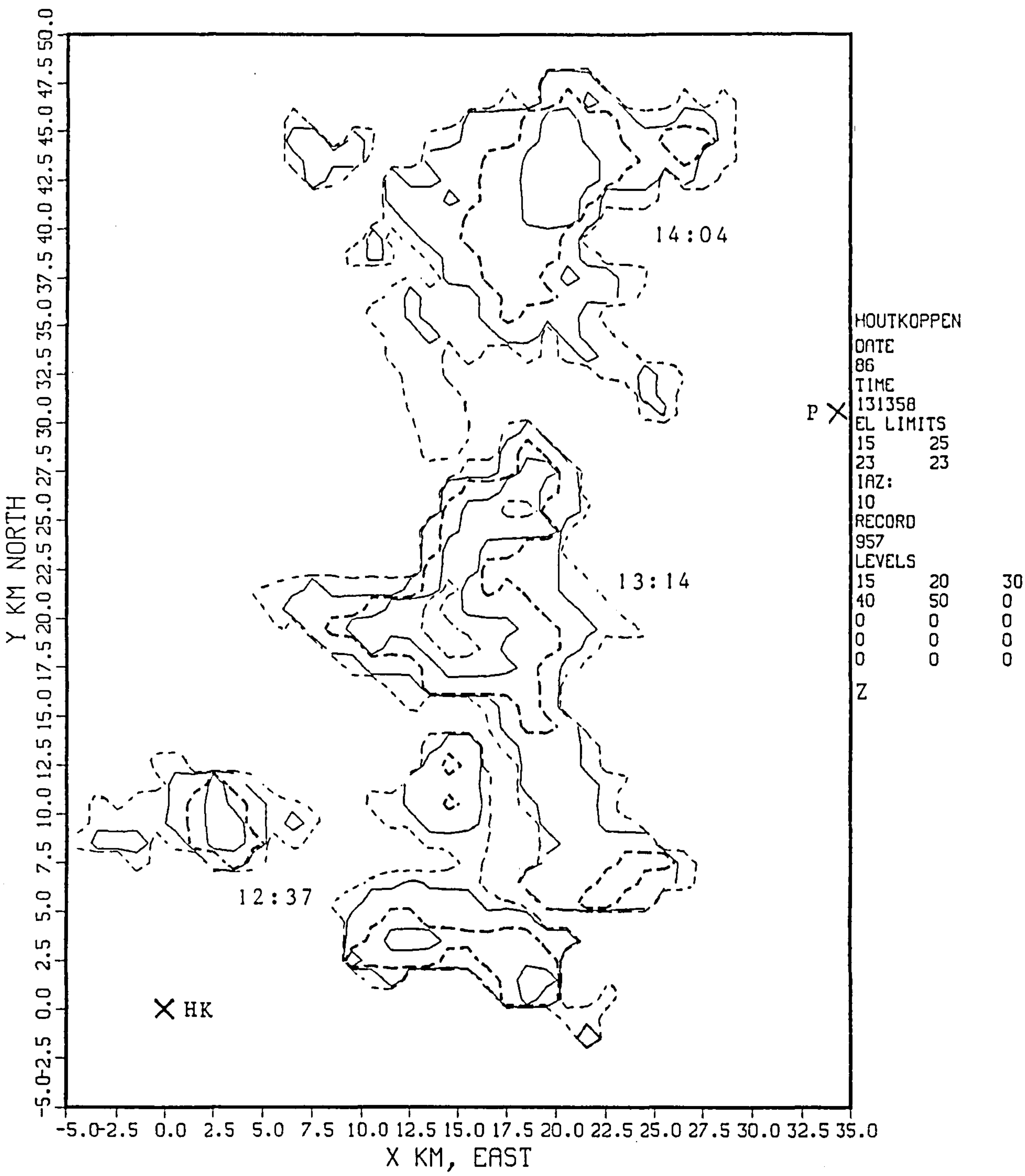

Figure 7.7: Schematic history of an isolated multi-cellular storm on 26 March 1991, based on 2° elevation PPIs as recorded at Houtkoppen. Reflectivity contours are 15, 20, 30, 40 and ≥ 50 dBZ, using the conventional CSIR PPI plotting routines. The positions of the radars are marked HK (Houtkoppen) and P (Pretoria).

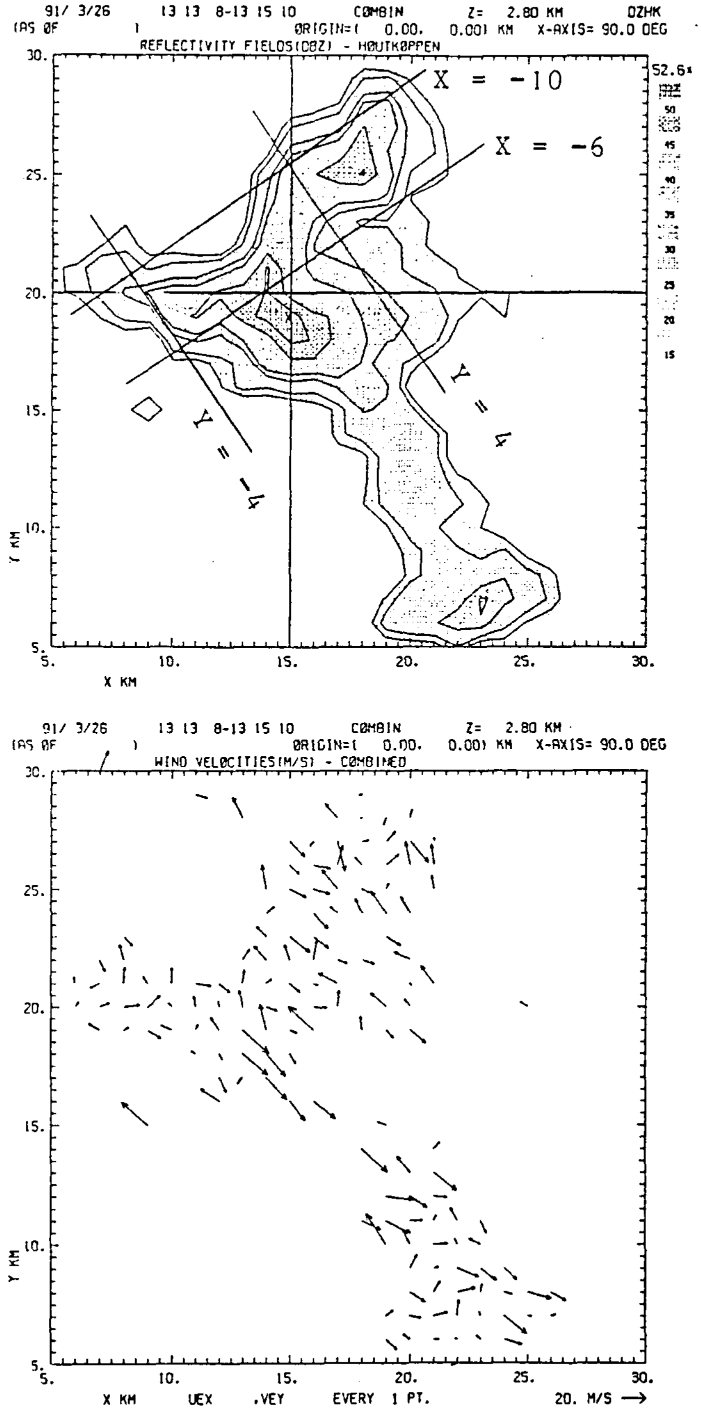

Figure 7.8: CAPPI at 2,8 km MSL (approximately 1,3 km AGL) of the storm on 26 March 1991 calculated by CEDRIC from a volume scan between 13:13:08 and 13:15:10.

Top: reflectivity contours in dBZ, intervals of 5 dB, observed by Houtkoppen radar.

Bottom: horizontal wind velocity field in $m.s^{-1}$ synthesized from Houtkoppen and Pretoria Doppler radar observations.

The scale of these plots is the same as in Figure 7.7. The baselines of the vertical cross-sections are indicated.

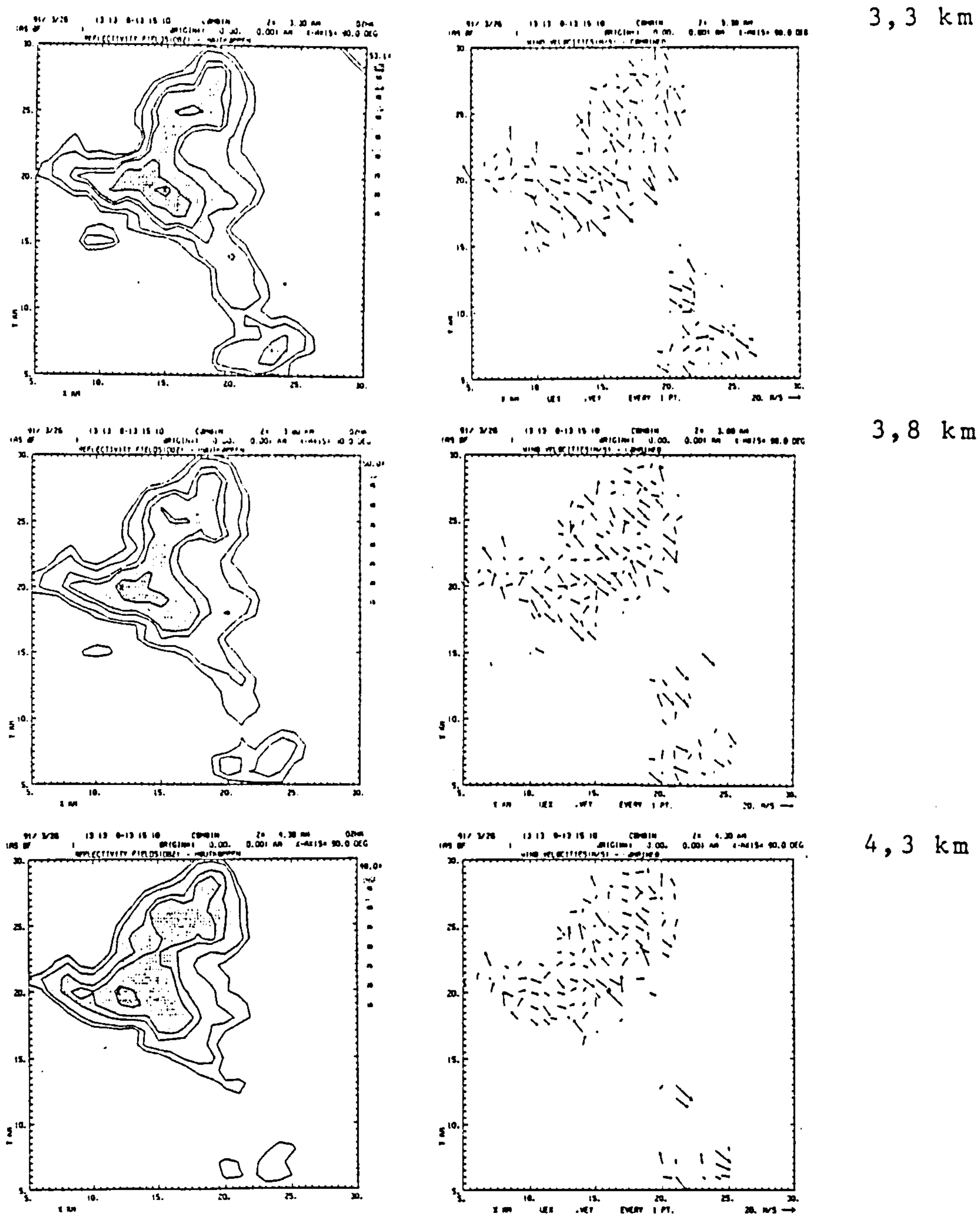

Figure 7.9: CAPPIs of the storm on 26 March 1991 (volume scan 13:13:08 - 13:15:10) at 500 m height intervals, showing reflectivity and horizontal air flow patterns.

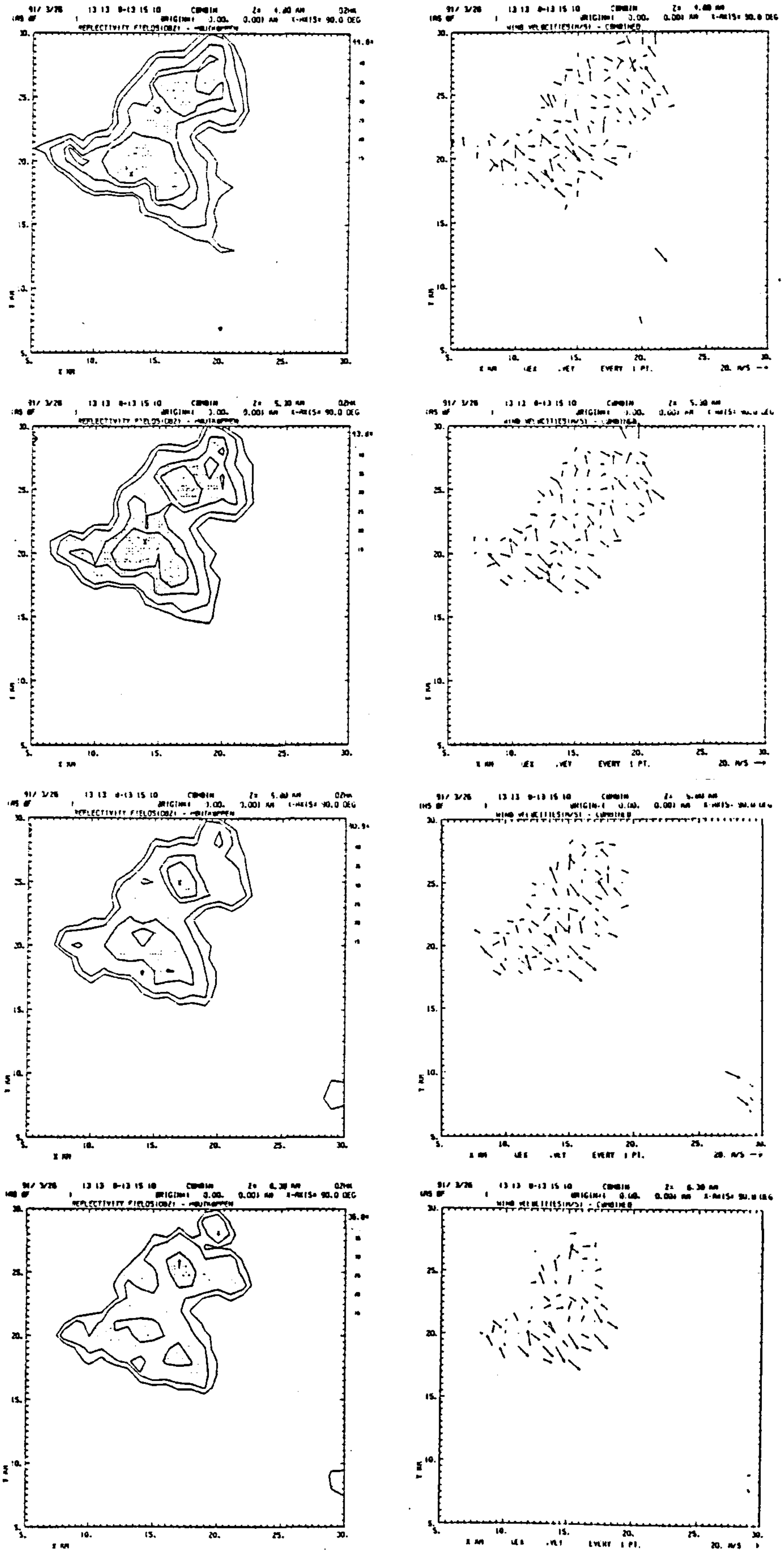

4,8 km

5,3 km

5,8 km

6,3 km

Figure 7.9: Continued

6,8 km

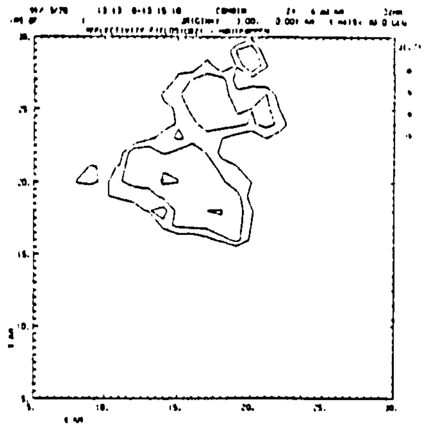

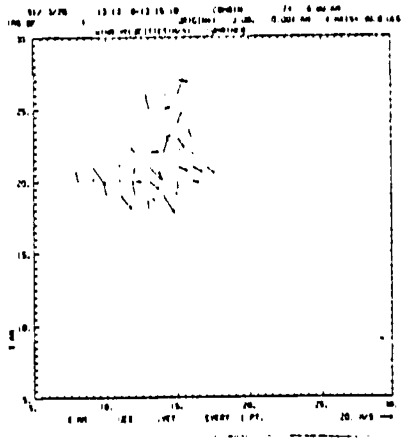

7,3 km

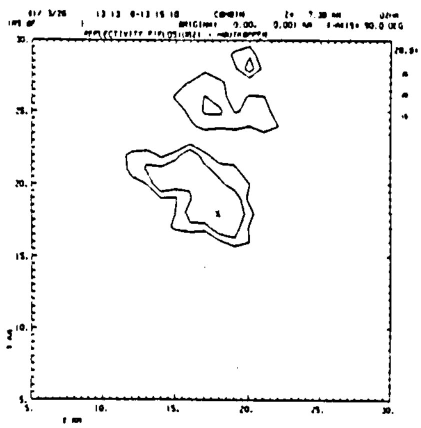

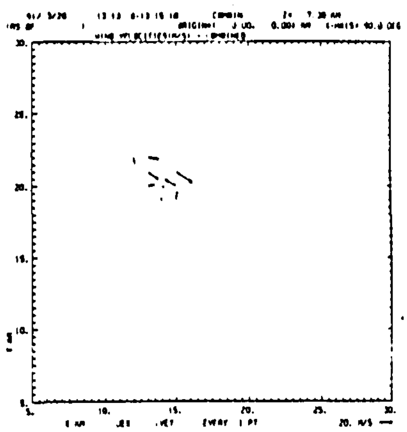

7,8 km

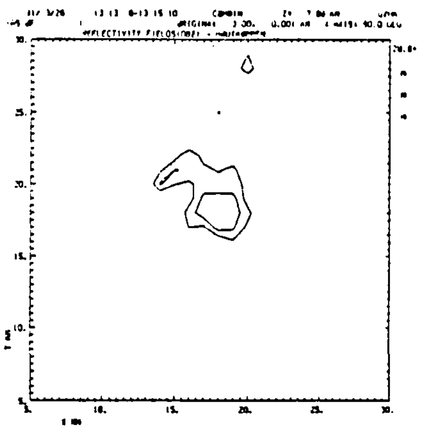

The air flow could not be calculated at this level because the echo is on the baseline between the two radars and therefore only spurious values are generated.

8,3 km

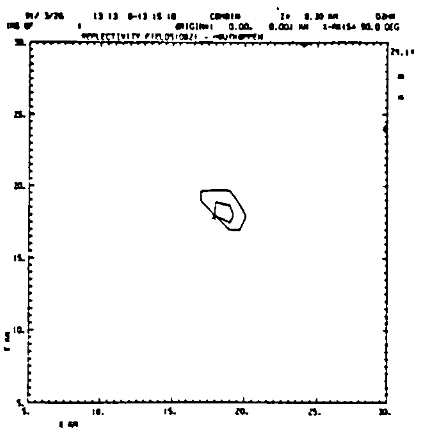

The air flow could not be calculated at this level because the echo is on the baseline between the two radars and therefore only spurious values are generated.

Figure 7.9: Continued

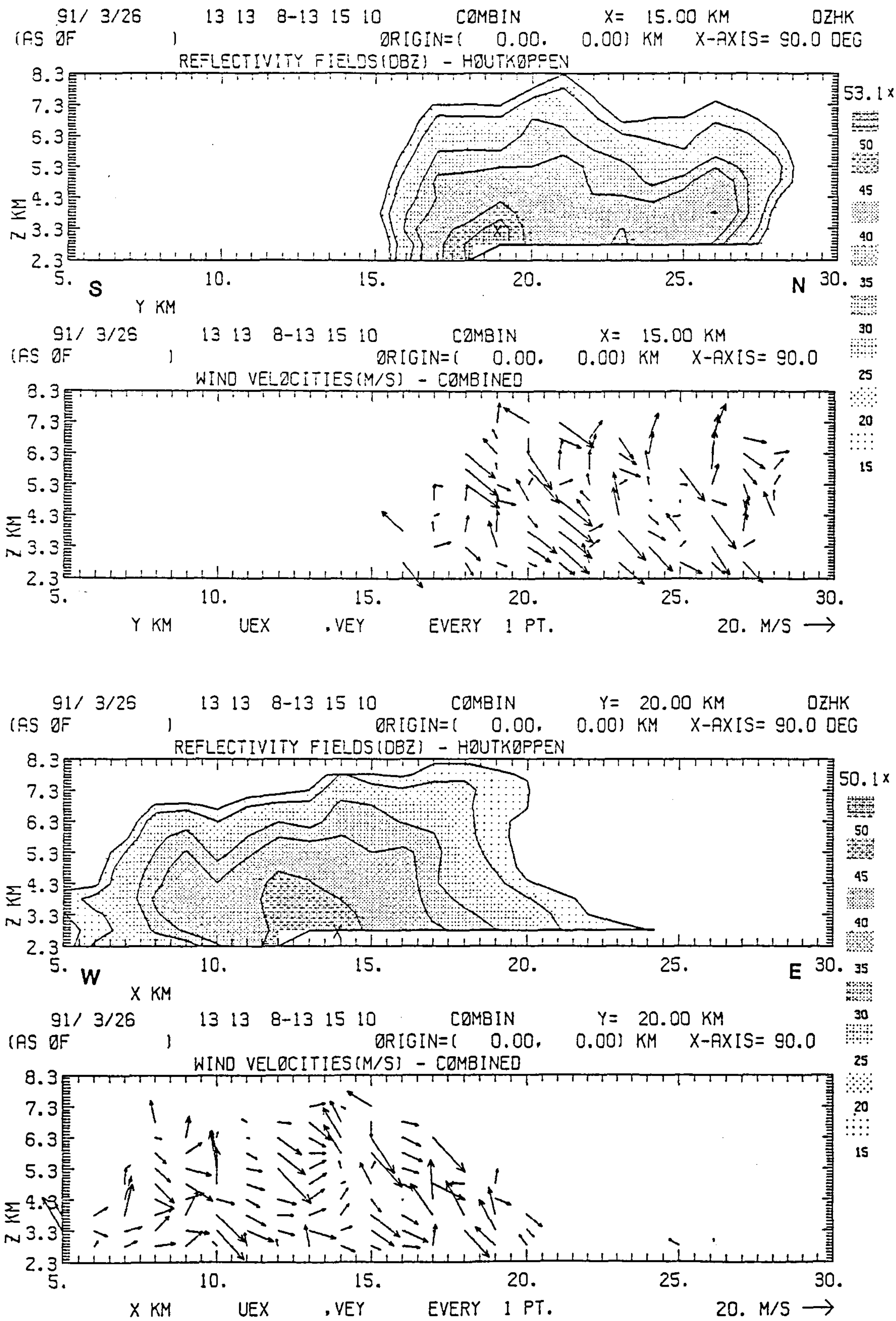

Figure 7.10: Vertical cross-sections through the storm shown in Figure 7.9 along baselines from south to north and west to east (see Figure 7.8 for exact position of baselines).

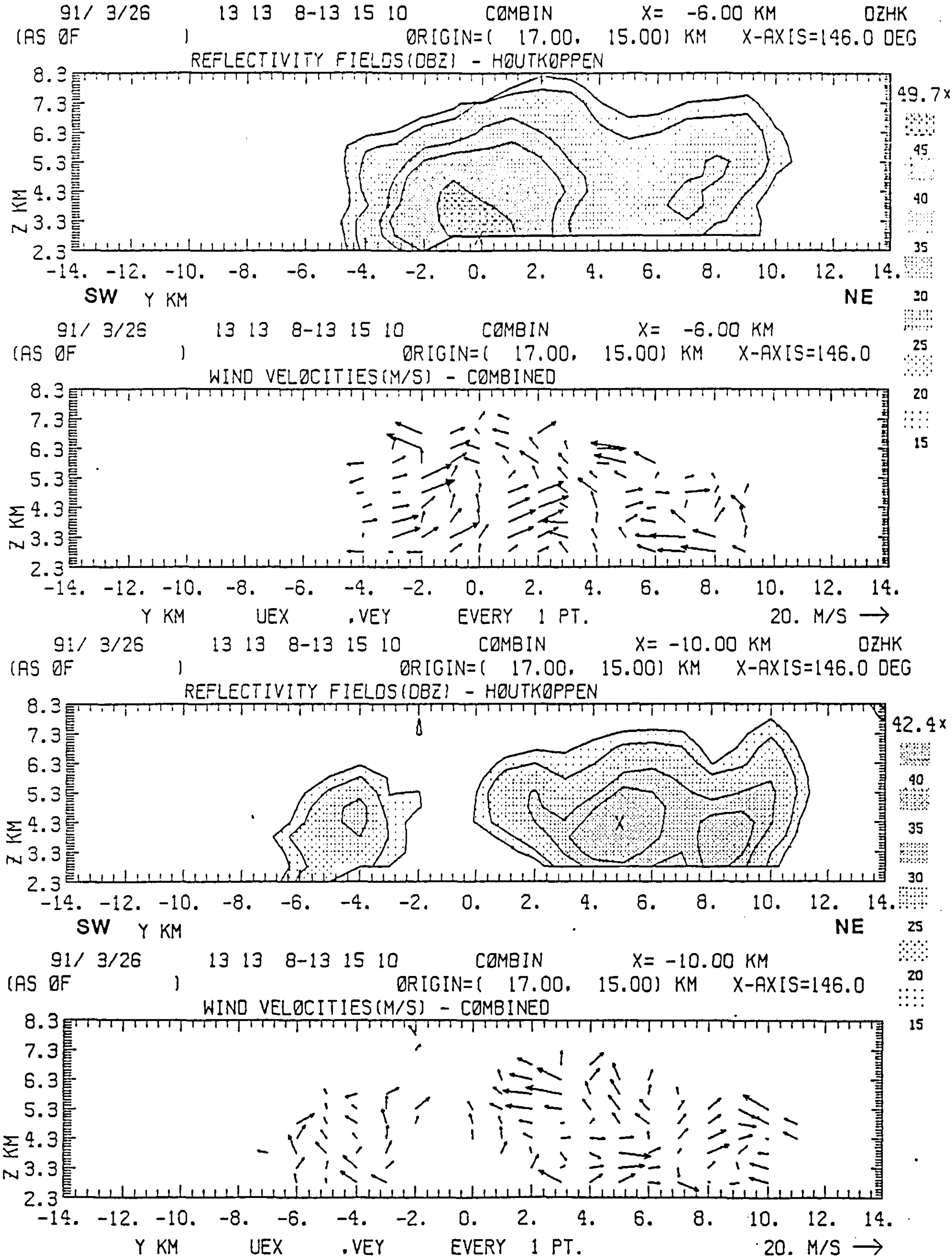

Figure 7.11a: Vertical cross-sections through the storm shown in Figure 7.9 along baselines from southwest to northeast (see Figure 7.8 for exact position of baselines).

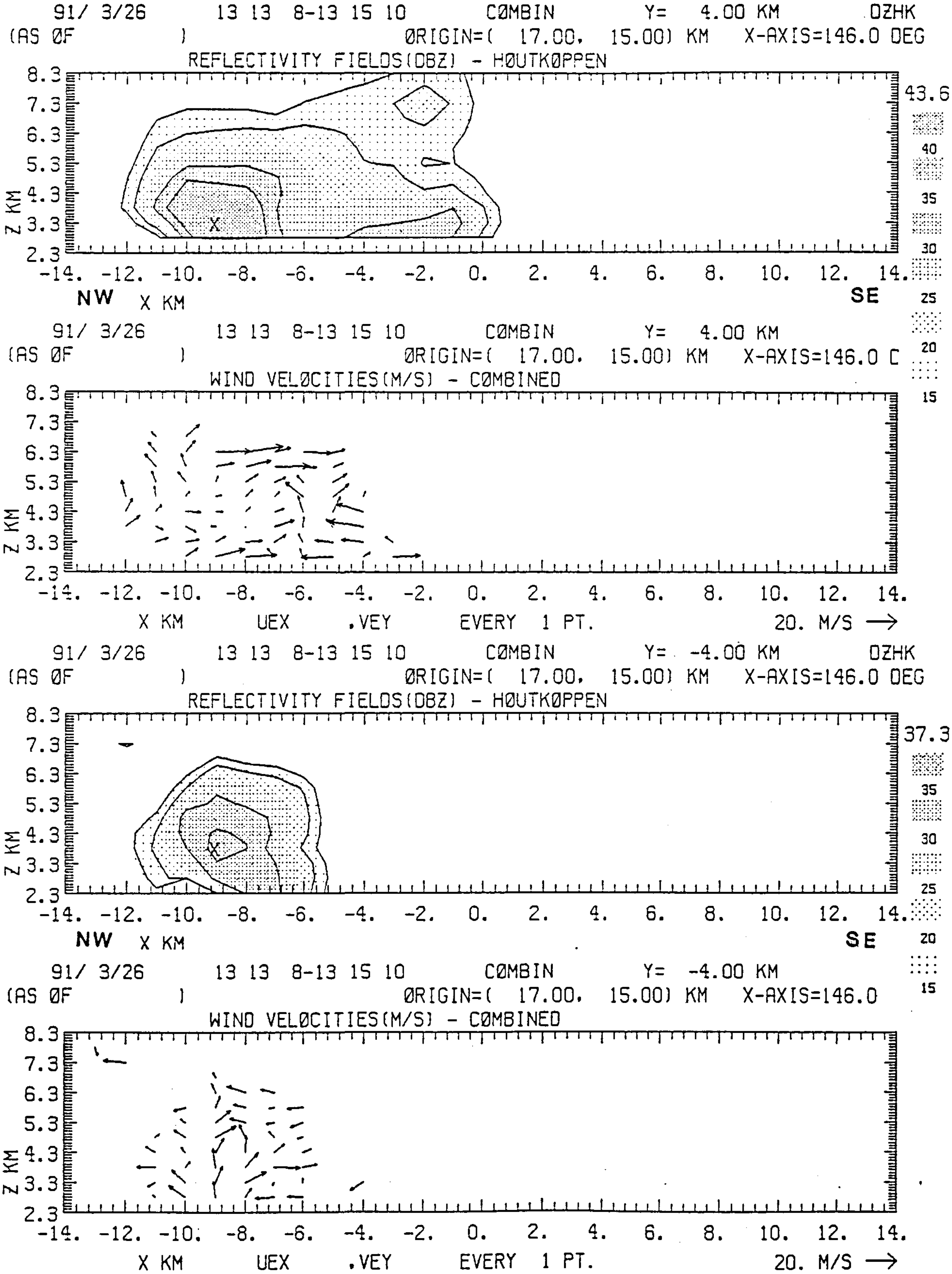

Figure 7.11b: Vertical cross-sections through the storm shown in Figure 7.9 along baselines from northwest to southeast (see Figure 7.8 for exact position of baselines).

8. CONCLUSIONS AND RECOMMENDATIONS

This Section is not intended to repeat any of the conclusions already made by the respective authors at the end of every Section, but rather to highlight the most significant findings on which the recommendations are based.

The original proposal for the three-year PRAI project was aimed at providing supplementary information on precipitation processes on the Highveld for on-going weather modification research projects which are being sponsored by the Water Research Commission (WRC) and the South African Weather Bureau. It had been realised that accurate measurement of total areal rainfall is of prime importance for precipitation enhancement projects. It was therefore proposed to establish relationships between:

- the spatial distribution of precipitation within clouds and the internal air flow in thunderstorms,

- the surface precipitation (rain and hail) patterns and the three-dimensional air flow in storms,

- rainfall intensities as measured by rain gauges and the reflectivity recorded by radar.

It was also proposed to verify or reject the hypothesis of accumulation zones above the main updraught region and to *possibly* identify storm systems which have a good potential for producing rain on the ground, but are inefficient in their mechanism and would therefore be more suitable for cloud seeding operations than naturally efficient clouds.

A request to appoint an additional climatologist for the second and third year of the PRAI project was approved by the WRC. Thus, the research proposal could be expanded to include detailed studies of raindrop-size distributions and Z-R relationships in an attempt to improve the accuracy of radar measurements of areal rainfall. In line with this objective was also the investigation of the V-ATI (Volume x Area-Time-Integral) of radar reflectivity. These research objectives were focused even sharper at the end of the second year, based on results achieved thus far, as well as on recommendations of the *Workshop on Rainfall Stimulation Research in South Africa*, which was held during August 1989.

The WRC also approved further funds for additional analysis work under the project name DOPDATE, which was to run concurrently with the PRAI project during 1990. The emphasis of the new project was on the selection and analysis of convective clouds at a very early stage in their life cycle, in order to verify and *possibly quantify* the daughter-cell and feeder-cell cloud merging concepts of storm mechanisms on the Highveld.

The joint execution of both projects resulted in a drastic improvement of the sensitivity of the Houtkoppen S-band radar; also the other two C-band radars were to have come on line during the 1989/90 rainy season; the CRAY computer programs should be verified and tested and the EVAD (Extended Velocity-Azimuth Display) method should be investigated as a means for extracting maximum information from existing single-Doppler radar data.

The objectives as summarised above and in detailed annual Work Programmes which were approved by the Steering Committee, have by and large been achieved. Unfortunately, the implementation of the multiple Doppler radar facility was delayed significantly, due to unforeseen reasons stated in Section 1 of this report. However, the facility is now operational (since February 1991) and examples of the horizontal and vertical air flow in an isolated storm have been included in this report in order to demonstrate the application and versatility of the CRAY programs which were adapated and installed on the CSIR VM mainframe computer.

For completeness of this final report it seems appropriate to extract some of the conclusions from the previous annual progress reports (Gomes and Held, 1988; Gomes, O'Beirne and Held, 1989; see Section 1 for full references).

In the first preliminary report, Gomes and Held (1988) presented a review of the characteristics related to severe weather phenomena with special emphasis on squall lines. These mesoscale systems have been found to be very effective in producing rain. The attention had been focused on observations made during the 1987/88 season. A 12-day period during November 1987 was investigated when several severe storms occurred (9 to

20 November 1987). Conserved parameters like the equivalent potential temperature were selected to represent the thermodynamic structure of the atmosphere, which is modified by large-scale downdraughts after the passage of a disturbance. Two particular days within the period (10 and 19 November 1987) were chosen for detailed analysis, because, on the first day, storms were very effective rain producers, while on the second severe hail storms occurred.

The similarities in the two storms which occurred during November 1987, with other case studies from earlier years could be emphasized as far as the multicellular structure is concerned and the penetration into the tropopause on one of the days. Certainly the key answer resides in the structure of the internal air flow characteristics of each particular storm. Considering differences and similarities between the two storms (10 and 19 November 1987) one could designate the apparent semi-stationary nature with individual cells moving at about the same speed as the complex as a whole in the first case and individual cells moving twice as fast as the complex in the second. Echo tops reached great heights in both cases, but they only penetrated the tropopause on 19 November. Maximum reflectivities during approximately 20 minutes were between 67 and 69 dBZ during the most intense phase of the storm on 10 November (Figure 8.1). At that stage the ascending core and subsequent descending core are observed in intense downdraught regions (Figure 8.2). Radar reflectivities of 67 dBZ were present in the storm on 19 November which were very persistent in time, filled a large volume and were of great vertical extent, indicating the presence of strong updraughts in the cloud, which can be highlighted by examining the corresponding radial velocity fields (Figures 8.3a and b).

Only minor differences in the three-dimensional radar reflectivity pattern were found between the two storm systems. The basic difference seems to reside in their air flow structure as can be seen from the resultant radial velocity fields recorded by the Doppler radar. Although these findings were preliminary, the potential to use Doppler radar to identify efficient rain producing systems and severe weather has been clearly demonstrated.

In the second Progress Report (Gomes *et al.*, 1989) more insight into the behaviour of storms has been gained by expanding the number of case studies that include Doppler radar data. Although generalisations concerning the exact patterns of air flow would have been premature, it was becoming increasingly obvious that answers to key issues concerning the structure and dynamics of thunderstorm development are to be found in the internal flow patterns of each particular storm.

The case study of 7 January 1988 presented by Gomes *et al.* (1989) exhibits some type of organisation during its mature stage, where rotation represented by some symmetry in the radial velocity field through the core of the storm suggests the presence of strong updraughts. This is in accordance with observations reported from North America.

If signatures of the radial velocity field observed in the storm of 19 November 1987 are compared with those for the 7 January 1988 storm, some significant differences in the air flow structure can be identified. On 19 November 1987, the presence of couplets of opposing radial velocities aligned azimuthally suggests a meso-cyclone signature not observed in the storm on 7 January 1988 (Figures 8.4 and 8.5). The first one did produce severe hail while no hailfall but good rain was reported from the second one while traversing the hail-reporting network.

The study of the storm that occurred on 27 December 1987 indicated that a relationship exists between air flow and dynamic interaction between storm cells and cloud complexes. The importance of such dynamic interaction is not to be overlooked, particularly in the light of the fact that the merging of the large multicellular complexes coincided with hail and heavy rainfall at the ground. The importance of understanding air flow conditions that lead to the development of feeder clouds is related to the ways in which these cells may contribute to the enhanced vigour of the storm system. The possibility of a synergistic effect as a result of the merging of the two multicellular complexes or of the incorporation of a feeder cell into the main cloud complex cannot be discounted.

Highlights from the third year of investigations are:

- Results achieved with applying the EVAD (Extended Velocity-Azimuth Display) method to derive precipitation efficiency from single-Doppler radar observations (Section 2.2 in this report).

- The investigation of raindrop size distributions and Z-R relationships, which showed that, based on the entire season's data, underestimation or overestimation of rainfall rate using an average Z-R relationship is a function of changes in the drop size distribution and not in rainfall rate (Section 3 in this report).

- Results based on the V-ATI (Volume versus Area-Time-Integral) which showed that average rainfall rates for convective storms over the Transvaal Highveld calculated using a V-ATI relationship were seen to be higher than those for other parts of the world but this is in keeping with characteristics of South African storms (Section 4 in this report).

- Preliminary findings from detailed case studies of storm merger mechanisms in South Africa, with special emphasis of reflectivity and air flow patterns in daughter-cell and feeder-cell merger situations (Sections 5 and 6 in this report).

Based on the findings of both the PRAI and the DOPDATE projects, the following recommendations are made:

■ Following the recommendations of the *Workshop on Rainfall Stimulation Research in South Africa* (Berg-en-Dal Conference Centre, Kruger National Park, 21-23 August 1989) which was attended by all leading scientists in the field of cloud physics in South Africa and by four overseas experts, all available resources, both in manpower and hardware, should be coordinated in a National Research Project, in order to obtain the optimal benefit from such a unique set-up.

- Since the CSIR multiple Doppler radar facility is still the only one in South Africa which deploys S- and C-band Doppler radars for thunderstorm research, it seems only logical to maintain such a unique asset, especially now, since the first dual Doppler radar observations have become available. This had also been emphasized by the overseas consultants on many occasions.

  However, the CSIR cannot carry the full burden of maintaining and further developing the three Doppler radars without external support from either Government Departments or the Water Research Commission.

- At least one complete season of good dual or triple Doppler radar observations should be available to perform some important climatological investigations such as the frequency of occurrence of certain cloud merger situations in South Africa and their mechanisms and impact on rain stimulation efforts (e.g. daugher-cell versus feeder-cell cloud merger). A better understanding of the early cloud stages and of rapidly forming accumulation zones above a weak-echo-region would be equally important for cloud seeding experiments.

- Various improvements to the radar facility would be of great advantage, e.g.:

  - Addition of a polarisation facility for the detection of ice-phase precipitation aloft.

  - Real-time display of radial velocities at least at the Houtkoppen S-band radar.

- EVAD (Extended Velocity-Azimuth Display) method, based on a typical example, has been shown to be a suitable tool to derive precipitation efficiency from good single-Doppler radar observations of stratiform-type rainfall. Special scanning cycles should be incorporated in a Doppler radar research project in order to obtain a more representative sample of different synoptic situations conducive to uniform precipitation patterns from storms for which EVAD was applied to calculate precipitation estimates and efficiencies (more rain gauges, longer observational periods and a better time resolution would be required for fine-tuning EVAD in South African precipitation systems).

- Finally, it should be borne in mind that the above recommendations only address the most important issues, either in principle or in more detail for larger research components. There are numerous less spectacular suggestions inherent in the various individual conclusions contained in this report which should certainly not be neglected.

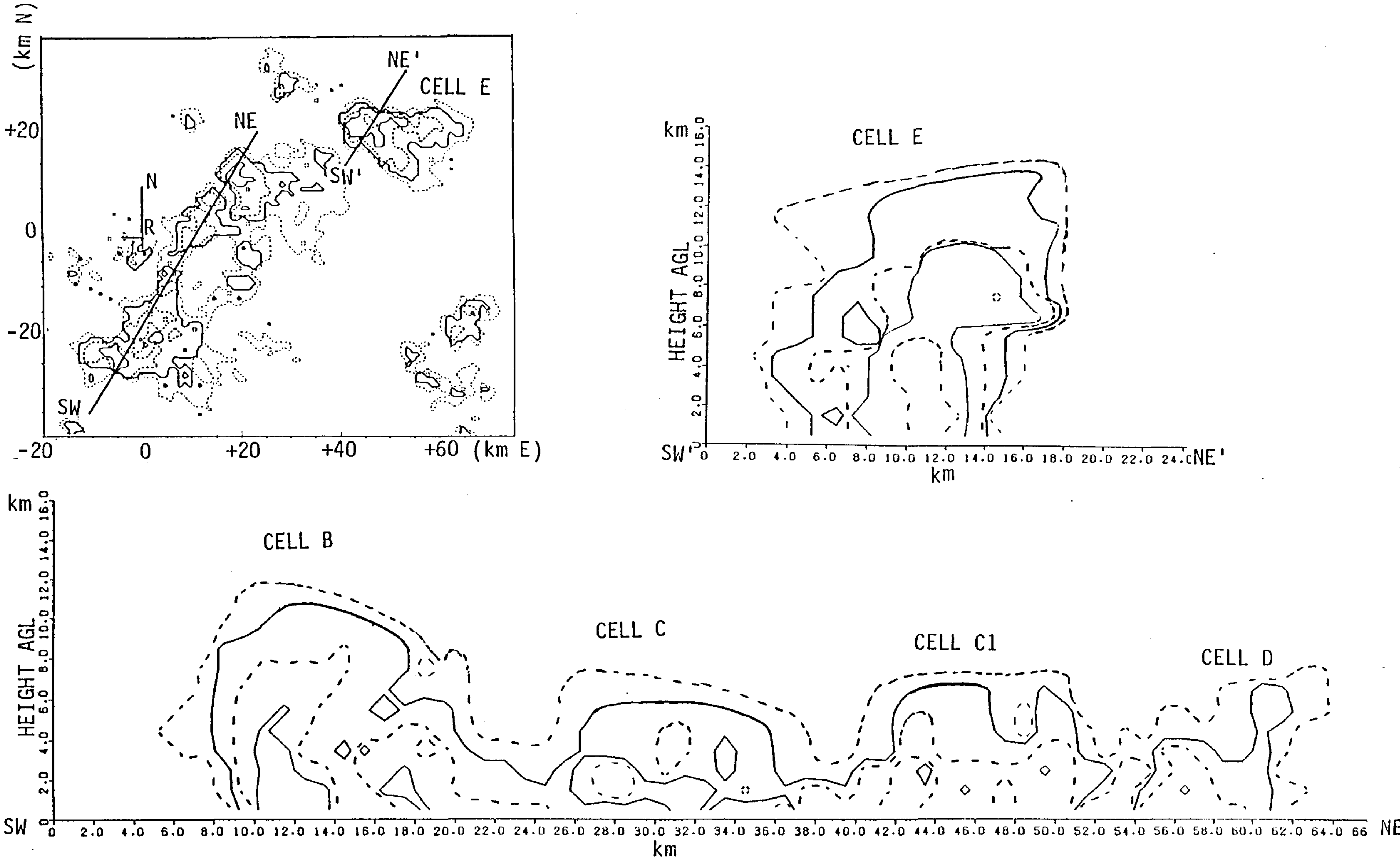

Figure 8.1: Computer plots of the squall line on 10 November 1987, 15h13. Top left: 2° PPI. Top right: Vertical cross-section through cell E from SW to NE as shown in the 2° PPI. Bottom: Vertical cross- section through the main storm as indicated by the base line.

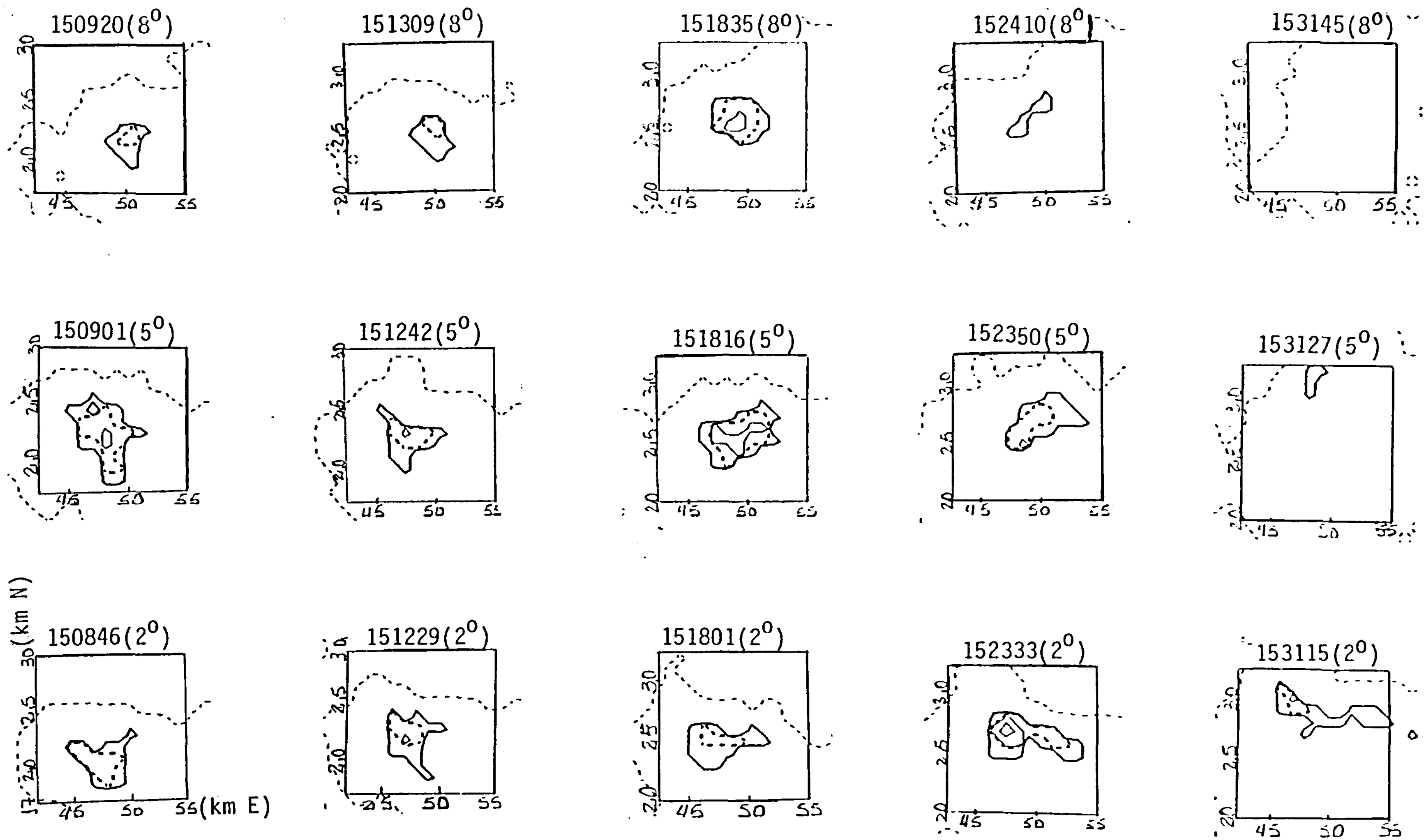

Figure 8.2: Radar signature associated with a downburst at the ground. Times in h:m:s; radar contours: 23, 47, 50, 53, 57 dBZ.

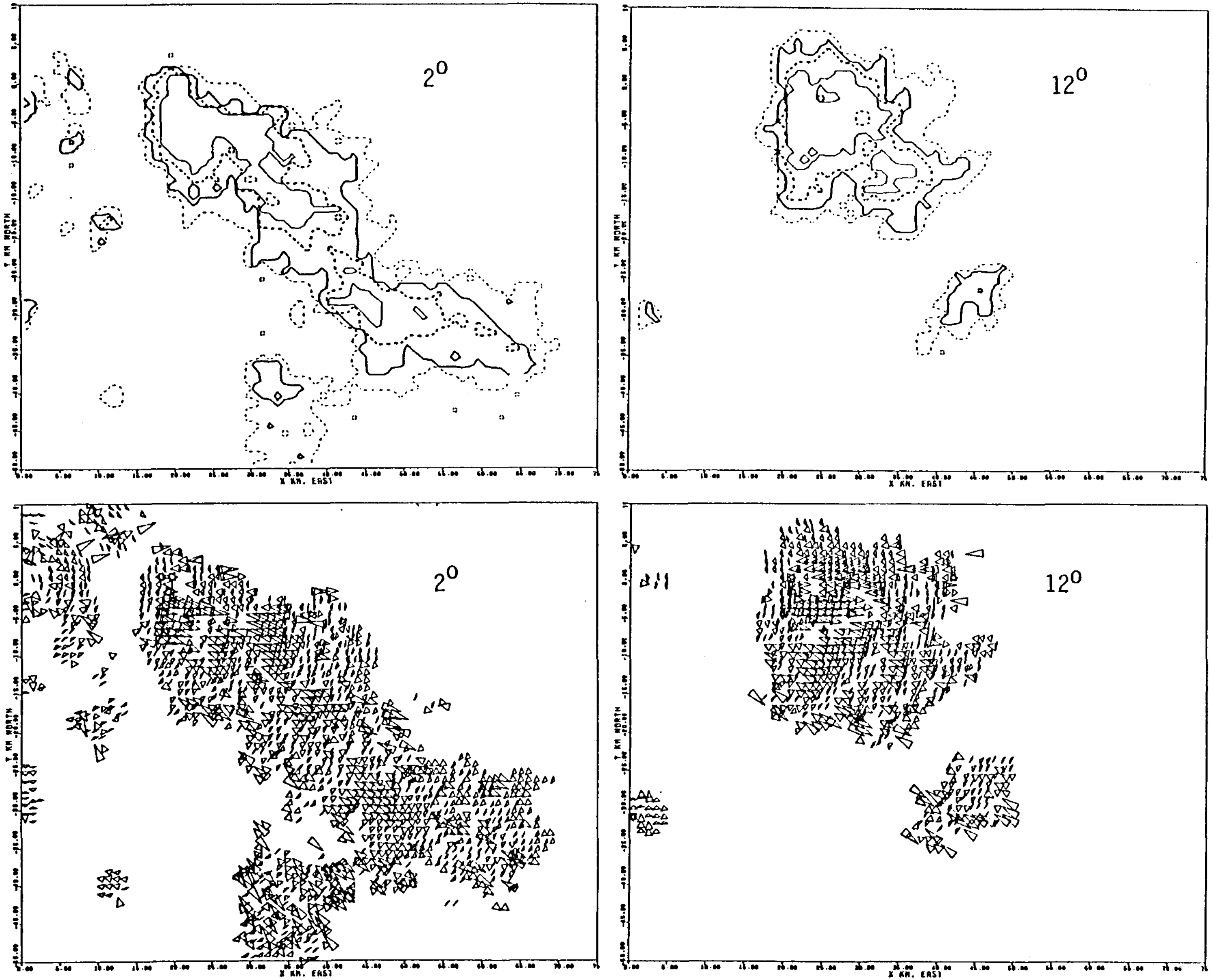

Figure 8.3a: 19 November 1987, 19h42: Radar reflectivity and airflow pattern at 2° and 12° elevation.

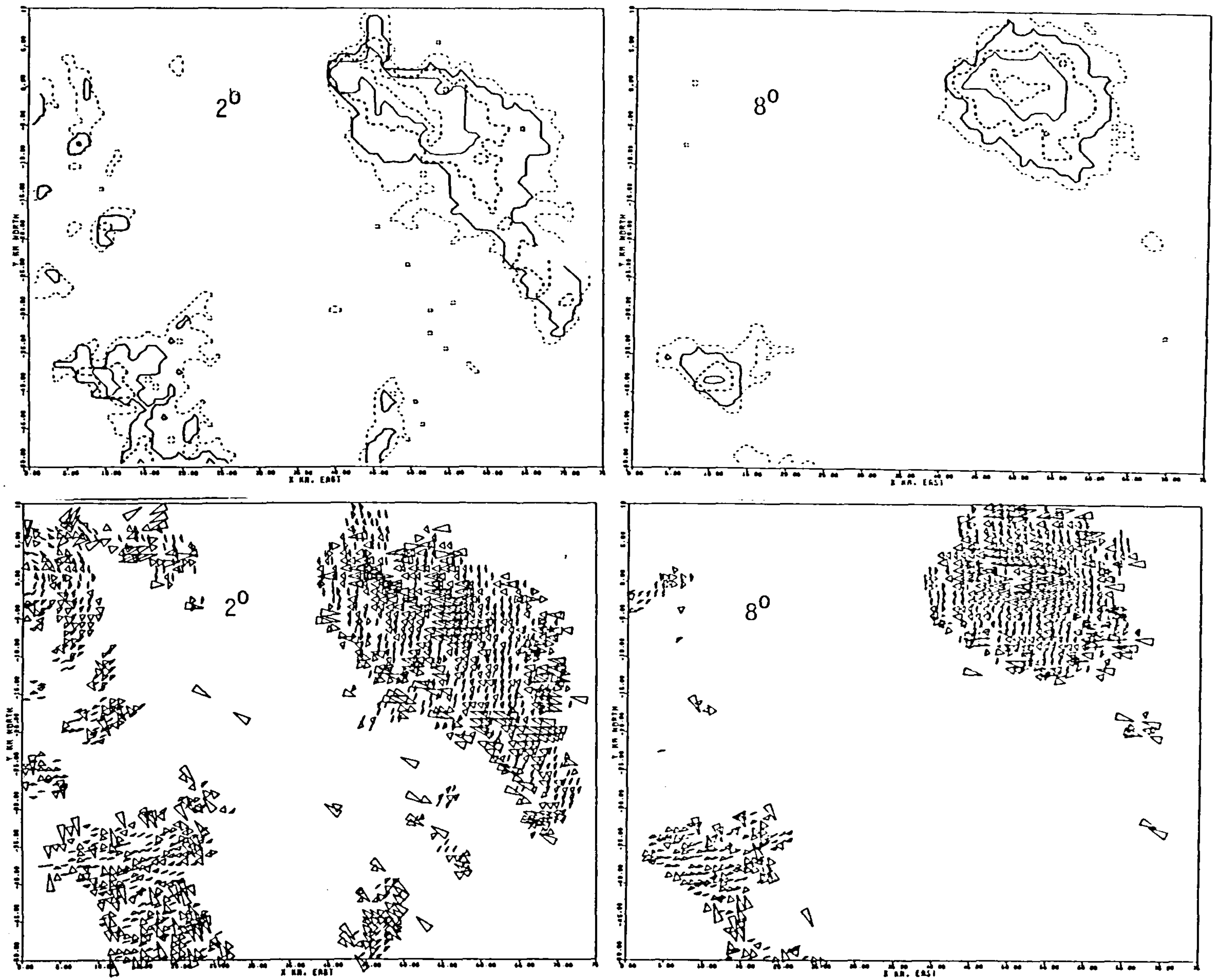

Figure 8.3b: 19 November 1987, 20h06: Radar reflectivity and airflow pattern at 2° and 8° elevation.

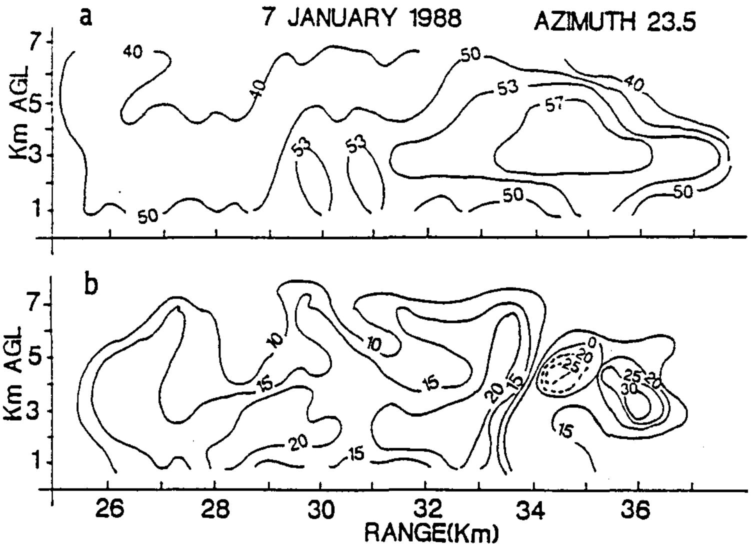

Figure 8.4: 7 January 1988, 22:05. RHI (Range Height Indicator) through azimuth 23,5°
(a) reflectivity contours in dBZ
(b) Doppler velocities in $m.s^{-1}$ (dashed lines: radial velocities away from the radar; solid lines: towards radar).

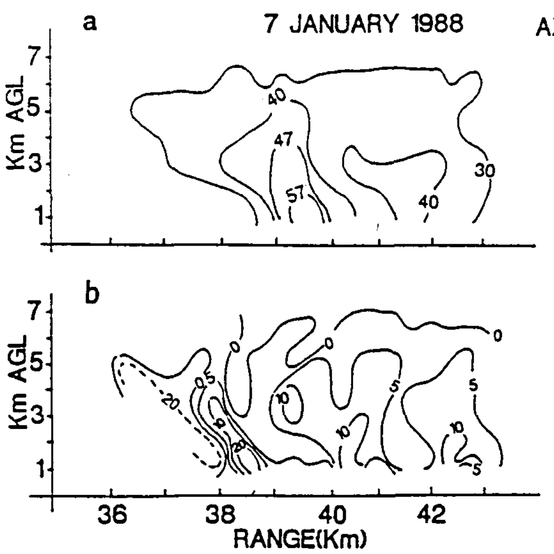

Figure 8.5: 7 January 1988, 22:27. RHI (Range Height Indicator) through azimuth 23,5°
(a) reflectivity contours in dBZ
(b) Doppler velocities in $m.s^{-1}$ (dashed lines: radial velocities away from the radar; solid lines: towards radar).

9. ACKNOWLEDGEMENTS

The *Precipitation and Air Flow (PRAI) Project* and the *Doppler Radar Data Processing (DOPDATE) Project* were financially supported by the Water Research Commission. However, research could not have been conducted without the vital support of the operational side of the project (hardware maintenance and data acquisition) by the CSIR Executive under the project MULDOP.

The staff of the radar facility provided the tools and the observations for the above research projects and their important contribution and dedication is gratefully acknowledged. A special word of thanks should go to Messrs M C Hodson, D J Dicks and G du Plessis for maintenance, development and radar observations.

Dr L J Miller of the National Center for Atmospheric Research in Boulder provided copies of the original CRAY programs, SPRINT and CEDRIC, which were then implemented on the CSIR's VM mainframe computer. He is sincerely acknowledged for this valuable contribution towards Doppler radar research in South Africa. Mrs E E Jacobs and Mrs R de Villiers are acknowledged for implementing the CRAY programs on the VM mainframe computer and for their assistance with the verification of these programs. Also, the staff of the CSIR Computer Centre is thanked for their patience and assistance in processing radar data tapes during the duration of the projects.

Certain meteorological data, mostly radiosonde observations, were supplied by the South African Weather Bureau and Mr J A Koch is thanked for his friendly assistance.

Miss Y Hong and Mrs L M Boatwright are thanked for assisting with the preparation of figures and the final report. The mammoth task of typing the manuscript was professionally handled by Mrs S G Good, who is wholeheartedly thanked for her part in completing this report.

10. APPENDIX A

Paper presented at the Sixth Brazilian Meteorological Congress, 19-24 November 1990, Salvador, Bahia, Brazil.

Proceedings of the 6th Brazilian Meteorological Congress.
19-24 November 1990.
Salvador-Bahia, Brazil
pp820-825

STRUCTURE OF A CONVECTIVE STORM ON THE SOUTH AFRICAN HIGHVELD BASED ON SINGLE-DOPPLER RADAR ANALYSIS

A M Gomes and G Held

Atmospheric Processes & Management Advice, EMATEK, CSIR
P O Box 395, PRETORIA 0001, South Africa

1. INTRODUCTION

The occurrence of deep convection in central and northeastern regions of South Africa is often accompanied by hail, producing extensive agricultural damage (Carte, 1977). Deep convective situations provide the major portion of rainfall on the South African plateau which is about 1500 m above MSL. The life cycle and dynamic characteristics of severe storm systems over the Transvaal Highveld have been studied extensively by Held (1982), Held and Carte (1979) and Held and van den Berg (1977), where mechanisms leading to the development of deep convection are highlighted, and the need for knowledge of the internal air flow structure of such storms is stressed.

The S-band radar is positioned approximately 22 km north-northwest of the centre of Johannesburg and 45 km southwest of Pretoria. Modifications to the radar and a locally developed pulse-pair processor allow the remote measurement of air flow inside clouds since 1987.

Considering severe storm types that occur on the Highveld, the squall line is the one which is characterised by its widespread areal coverage. Most squall lines are very efficient in producing rain and hail over large areas, but are significantly less frequent than isolated or scattered storms (Carte and Held, 1978). Analysis of two squall line systems that traversed the Johannesburg-Pretoria area in November 1987 (Gomes and Held, 1988) showed that the radial velocity field, as observed by the Doppler radar, exhibited well organised mesoscale features, such as couplets of radial velocities, indicative of strong convergence. Smull and Houze (1985, 1987) and Rutledge *et al.* (1988) focused their interpretation of single-Doppler radar images on the two-dimensional flow structure shown in RHI presentations of the squall line.

They indicated the presence of kinematic structures connecting the development of a trailing rain region to the leading convective rain band; there is a front to rear system relative flow aloft, overlying a rear to front flow which, in turn, overlies a rearward flow at low levels. These ideas are used in the interpretation of the case study presented in this paper. However, the precipitation system presented here, which occurred on 7 January 1988, does not show the development of a trailing rain region, because of its predominantly convective character.

2. VERTICAL STRUCTURE OF THE ATMOSPHERE PRIOR TO STORM DEVELOPMENT

Vertical profiles of the thermodynamic variables and the wind hodograph were obtained from radiosonde ascents made just south of Pretoria (Irene) at 12 GMT.

The vertical wind profile from the midday sounding (approximately six hours before the storm had passed through the radar surveillance area) showed that the subcloud winds were northeasterly, backing with height to westerly at cloud base, then to southwesterly in the mid-troposphere and thereafter veering to west-northwesterly remaining fairly constant in direction. The wind shear in the cloud layer, extending from 3.2 to 9.6 km MSL is $2.3 \times 10^{-3}s^{-1}$ with considerable directional shear in the lower levels.

Profiles of the potential temperature (θ), equivalent potential temperature (θ_e) and saturated equivalent potential temperature (θ_{es}) (Figure 1) show an atmosphere with high surface temperatures (θ_e and θ_{es}). A positive lapse rate of θ_e and θ_{es} below 3 km indicates that this layer was potentially and conditionally unstable. A shallow stable layer is found between 3 and 3.5 km. From there up to 5 km θ_e is relatively low, so evaporative cooling and downdraught formation are favoured in this layer (Riehl, 1969; Zipser, 1977). The 0°C level was located near 4.5 km MSL.

3. RESULTS AND DISCUSSION OF THE 7 JANUARY 1988 STORM

The discussion of the evolution of the 7 January 1988 storm is based on a series of PPI's. Radar echoes from 20:30 to 22:40 SAST (South African Standard Time) have shown intense convective activity spread throughout the 75 km range of the Doppler radar. The analysis concentrates on a period during which the major storm was approximately 20 km southwest of the radar, where isolated storms began to show a more organised structure. Like most of the storms occurring in this area, this one was also multicellular in structure. By 21:10, there were basically three major clusters located near the central area and to the east of the radar. During the following 25 minutes, the northern and eastern cells were moving southwards and westwards respectively, merging with the storm located southwest of the radar. By 21:46, a well-defined line of precipitation, approximately 60 km long and 25 km wide, could be observed. During this period, the system was already in its mature phase, with a well-developed leading convective rainband propagating northeastwards at an average speed of 30 $km.h^{-1}$. After 22:11, one could observe an interesting feature, where shallow cells began to appear in the northeastern part of the storm, probably as a result of the downdraught, undercutting and lifting the air ahead. Radar reflectivities and radial components of the air flow at 22:27 are shown in Figure 2a and b. Downdraughts penetrate the inflowing air, splitting and lifting it to the level of free convection and, in so doing, creating a new updraught region forward of the old cell (Wallace and Hobbs, 1977). By approximately 22:38, the area had been totally filled with precipitation.

Figure 2c illustrates the multicellular nature of the storm in a vertical cross-section along the line A-AA. It can be seen that the echo in the leading convective band extended to a height of 15 km AGL, with maximum reflectivities between 50 and 60 dBz. Also important to notice is the overhang on its northwestern flank together with a weak-echo-region (WER) most probably indicating the position of the updraught. The most striking aspect of the radial velocity images is the dominant flow towards the radar (Figure 2b). The radial velocities are much larger, 25-30 $m.s^{-1}$, in the area enclosed by the most intense reflectivity values. It is rather a complex pattern to physically interpret. The small wedge of radial flow velocities away from the radar in the northwestern part of the storm complex indicates most probably aliasing of velocities. The extensive area of relatively low radial velocities towards the radar in the southern rear of the storm (Figure 2b) could be interpreted in two ways. It could be a low velocity region, or it may be a region where the wind is almost tangential to the radar which would also result in small radial components of the velocity. Figures 3a and b show Z (reflectivity) and V (radial velocity) respectively, in cross-sections along the 23.5° azimuth in a plane, more or less in the direction of the storm movement. Storm overhang and strong reflectivity gradients on the leading edge suggest strong inflow into the storm. At 22:05 (Figure 3a) the dominant flow from low levels up to 7 km has a large positive component, with local extremes of up to 20 $m.s^{-1}$ maintained until it reached the core represented by the maximum values of reflectivity, where a sharper tilt was observed at a range of 33 to 37 km. Vertical cross-sections of the reflectivity and radial flow velocities at 22:27 (Figure 3b) illustrate a similar structure to that shown previously for 22:05. However, the air flow was somewhat weaker and the maximum radial velocities had descended to the lowest 2 km, following the collapse of the core.

It might be premature to draw conclusions at this stage of the analysis. However, radial convergence in the mid-levels appears to be characteristic during the stage of maximum storm intensity, indicative of organised updraught areas.

4. ACKNOWLEDGEMENTS

This research project was partially supported by the Water Research Commission. The radar operators are thanked for their dedication in collecting the Doppler radar data, and the South African Weather Bureau is acknowledged for making the radiosonde observations available.

5. REFERENCES

CARTE A E, 1977. Hail damage to agriculture and its prevention. South African Journal of Science, 73, 327-330.
CARTE A E and HELD G, 1978. Variability of hailstorms on the South African Plateau. J. of Appl. Met., 17, 365-373.
GOMES A M and HELD G, 1988. First progress report: Precipitation and air flow (PRAI) project. CSIR Report EMA-C 8885, Pretoria, 32pp.
HELD G, 1982. Comparison of radar observations of a devastating hailstorm and a cloud burst at Jan Smuts Airport. E M Agee and T Asai (eds), in Cloud Dynamics, Reidel Publ. Co., Dordrecht, 273-284.
HELD G and CARTE A E, 1979. Hailstorms in the Transvaal during January 1985. S A Geogr. J., 61, 128-142.
HELD G and VAN DEN BERG H J C, 1977. A pre-frontal squall line on 14 November 1975. Arch. Met. Geoph. Biokl., 26, 361-379.
RIEHL H, 1969. Some aspects of cumulonimbus convection in relation to tropical weather systems. Bull. Amer. Met. Soc., 30, 587-595.
SMULL G F and HOUZE R A, Jr, 1985. A mid-latitude squall line with a trailing region of stratiform rain: Radar and satellite observations. Mon. Wea. Rev., 113, 117-133.
SMULL G F and HOUZE R A, Jr, 1987. Dual-Doppler radar analysis of mid-latitude squall line with a trailing region of stratiform rain. J. Atmos. Sci., 44, 2128-2148.
RUTLEDGE S A, HOUZE R A, Jr, BIGGERSTAFF M I and MATEJKA T, 1988. The Oklahoma-Kansas mesoscale convective system of 10-11 June 1985: Precipitation structure and single-Doppler radar analysis. Mon. Wea. Rev., 116, 1409-1430.
WALLACE J M and HOBBS P V, 1977. Atmospheric science, an introductory survey. Academic Press, New York, (Chapter 5).
ZIPSER E J, 1969. The role of organized unsaturated convective downdrafts in the structure and rapid decay of an equatorial disturbance. J. Appl. Meteor., 8, 799-814.

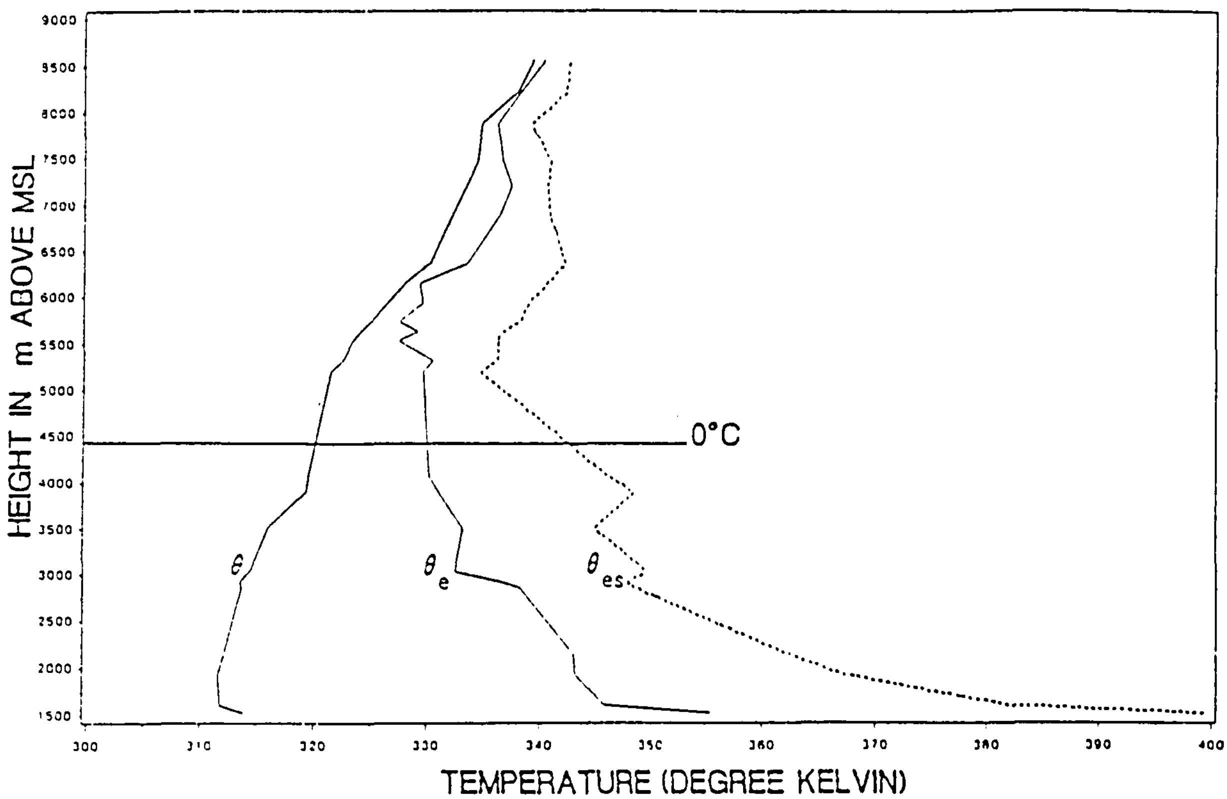

Figure 1: Vertical profiles of the potential temperature (θ), the equivalent potential temperature (θ_e) and the saturated equivalent potential temperature (θ_{es}) at Irene on 7 January 1988, 12:00 GMT.

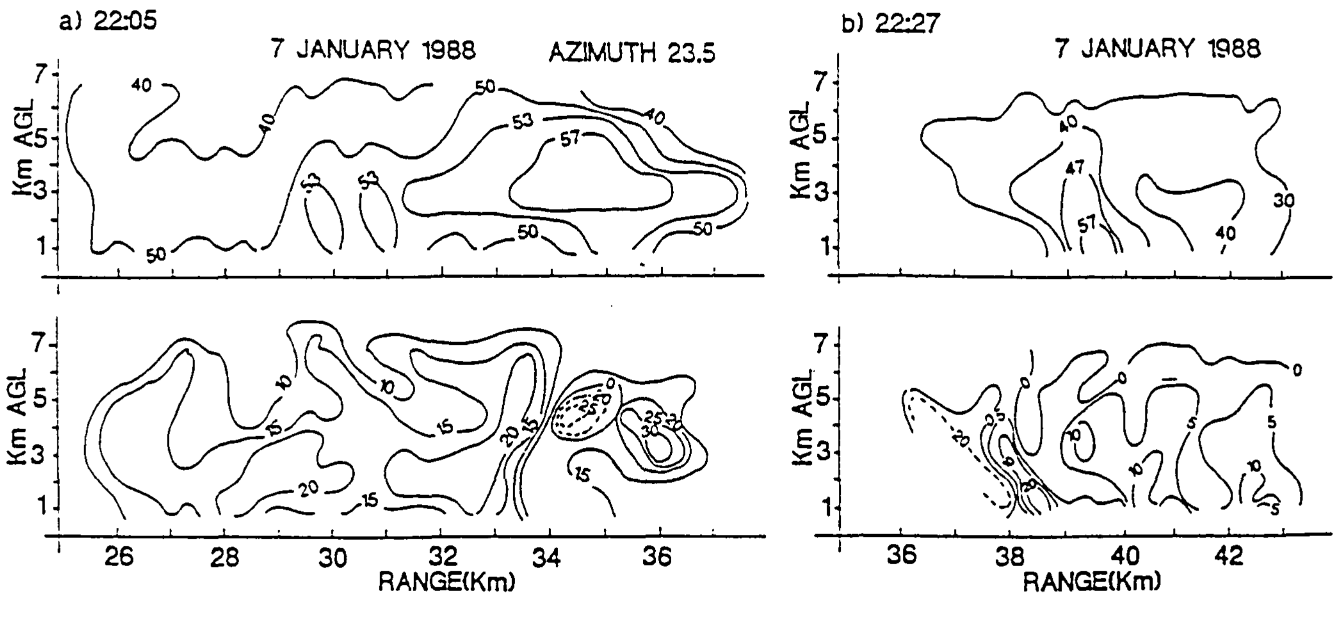

FIGURE 3: 7 January 1988. RHI (Range Height Indicator) section through azimuth 23.5°, indicating reflectivity contours in dBz (top) and Doppler velocities in $m.s^{-1}$ (bottom; dashed lines: radial velocities away from the radar, viz. negative velocities; solid lines: towards the radar, viz. positive velocities).

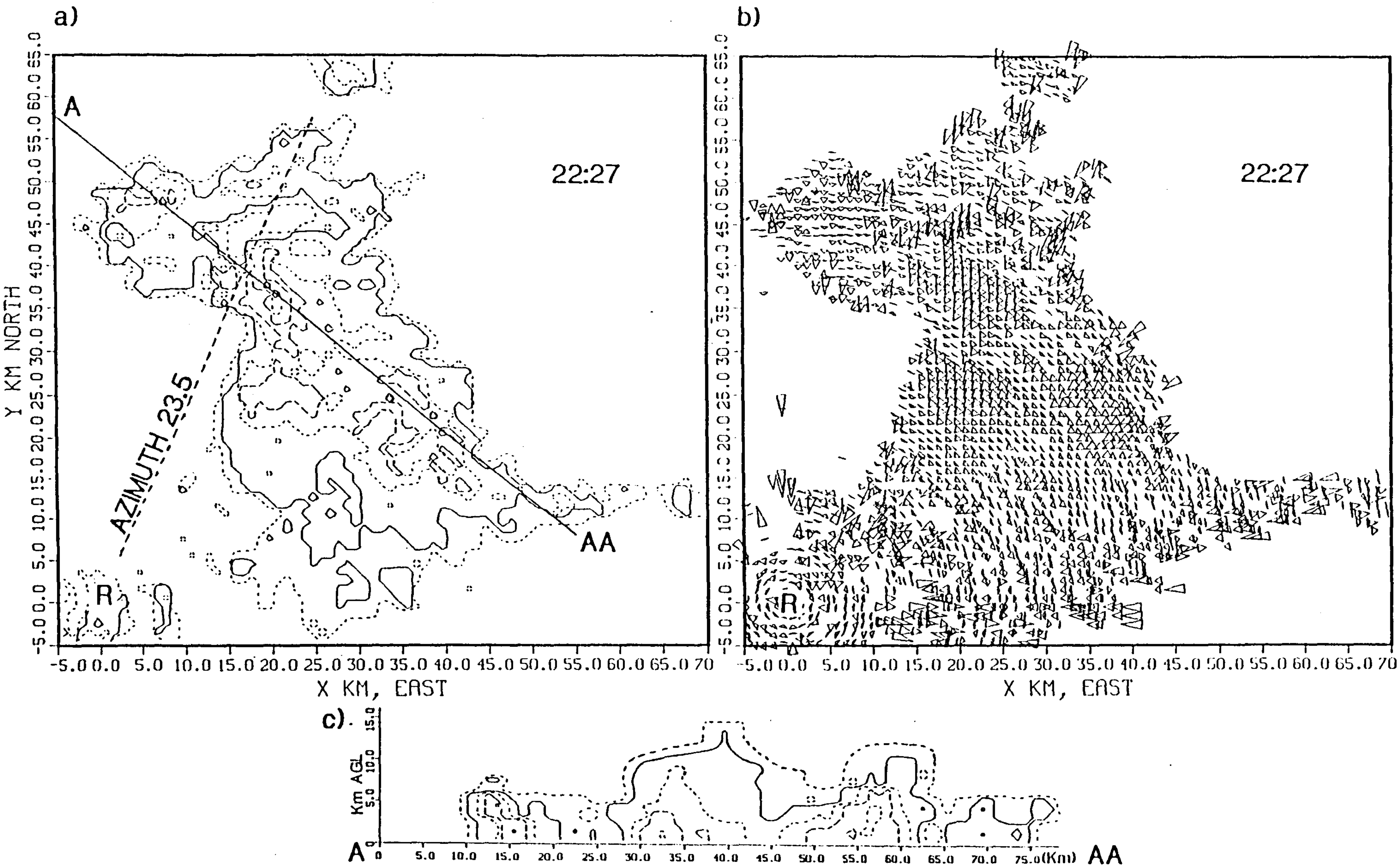

Figure 2: 7 January 1988. (a) PPI plot at 2° elevation (reflectivity contours: 23, 30, 40, 50, 60 dBz).
(b) Radial air flow pattern at 2° elevation.
(c) Vertical cross-section along the line A-AA.

11. APPENDIX B

Copies of publications describing the application of the programs 'SPRINT' and 'CEDRIC' for multiple Doppler radar analysis.

MILLER L J, MOHR C G and WEINHEIMER A J, 1986. The simple rectification to Cartesian space of folded radial velocities from Doppler radar sampling. *J. of Atmos. and Oceanic Techn.*, 3, 162-174.

MOHR C G, MILLER L J and VAUGHAN R L, 1981. An interactive software package for the rectification of radar data to three-dimensional Cartesian coordinates. *Preprints of 20th Conference on Radar Meteorology*, Boston, Amer. Meteor. Soc., 690-695.

MOHR C G, MILLER L J, VAUGHAN R L and FRANK H W, 1986. The merger of mesoscale data sets into a common Cartesian format for efficient and systematic analyses. *J. of Atmos. and Oceanic Techn.*, 3, 143-161.

appen/28c/sgg

Reprinted from JOURNAL OF ATMOSPHERIC AND OCEANIC TECHNOLOGY, Vol. 3, No. 1, March 1986
American Meteorological Society

The Simple Rectification to Cartesian Space of Folded Radial Velocities from Doppler Radar Sampling

L. JAY MILLER, CARL G. MOHR AND ANDREW J. WEINHEIMER

The Simple Rectification to Cartesian Space of Folded Radial Velocities from Doppler Radar Sampling*

L. JAY MILLER, CARL G. MOHR AND ANDREW J. WEINHEIMER

*National Center for Atmospheric Research*** Boulder, CO 80307

(Manuscript received 5 September 1984, in final form 8 July 1985)

ABSTRACT

Periodic sampling of the Doppler radar return signal at the pulse repetition frequency causes measured velocities to be ambiguous (folded) when true meteorological velocities along the radial direction exceed the Nyquist or folding value. Furthermore, mean radial velocity estimates become more uncertain as the spatial variability of velocity increases or the returned signal strength decreases. These data have conventionally been prepared for such uses as multiple-Doppler radar wind synthesis by unfolding and editing them in the sampling domain (range-azimuth-elevation spherical coordinates).

An alternative method of locally (to the output grid point) unfolding the *unedited* radial velocities during their linear interpolation to a regular Cartesian grid is presented. The method preserves the spatial discontinuities of order twice the Nyquist value associated with velocity folding. A nondimensional velocity quality parameter is also computed which serves to identify interpolated values that contain too much variance to be reliable. Editing of radar data is thereby postponed until all radar data are mapped to the analysis coordinate system. This allows for iterative global unfolding and multiple-Doppler synthesis of complicated convective storm flow patterns. The resolution of folding in such flow fields may require more information than is usually available from single radar radial velocity fields in spherical coordinates. Further, the amount of data that must be subsequently manipulated is reduced about ten-fold in the process of interpolation.

1. Introduction

Radial velocities measured by Doppler radars are often interpolated to a regular (x, y, z) grid, especially when they are used in the multiple radar synthesis of three-dimensional wind fields. Although the processing of multiple radar data involves other steps such as the actual synthesis of three-dimensional winds using measurements from several viewing directions (e.g., Carbone et al., 1980), we have restricted this paper to the transformation of data from radar space to analysis space (interpolation), the removal of velocity ambiguities (unfolding), and the elimination of spurious values (thresholding). Common practice is to edit and unfold individual radar velocity measurements in the sampling space (range-azimuth-elevation; R, A, E) before interpolating them (e.g., Ray and Ziegler, 1977; Oye and Carbone, 1981). However, this step can be done after interpolation provided the remapping method preserves the statistical characteristics of the measured radial velocities and does not introduce any biases in the interpolated values. Two especially important characteristics are the spatial discontinuities associated with folding of the radial velocities due to periodic sampling at the pulse repetition rate and the randomness of velocities when the backscattered signal strength indicates that only noise is present.

Most radar systems use the covariance or "pulse-pair" technique (e.g., Zrnić, 1977) to estimate the power-weighted average radial velocity within pulse volumes at several range locations along the pointing direction. When only noise is present in the backscattered return, this technique should give mean radial velocities that are uniformly distributed from $-V_n$ to V_n (the Nyquist co-interval) where V_n is the folding or Nyquist velocity. Unknown biases in the radial velocity processor can sometimes corrupt the noise distribution, but it is usually nearly uniform with a few preferential estimates occasionally occurring.

When the magnitude of the true meteorological radial velocity within a pulse volume exceeds V_n, sampling the return signal at the pulse repetition rate will cause estimates of Doppler velocity to be ambiguous or folded (e.g., Doviak et al., 1978). When this happens an integer multiple of twice the Nyquist velocity must be added to the measured pulse-volume average value to remove this ambiguity (Ray and Zeigler, 1977). Folding therefore represents an artificial and identifi-

* An earlier version of this paper appeared in the *Preprints of the 21st Radar Meteorology Conference*, Edmonton, Alberta, Canada, Sept. 1983, sponsored by the American Meteorological Society.

** The National Center for Atmospheric Research is sponsored by the National Science Foundation.

able spatial discontinuity of order $2V_n$ in the radial velocity. If the discontinuity is not handled properly when aliased data are transformed to a regular *xyz*-grid, the velocity estimates cannot be correctly unfolded after interpolation.

The three-dimensional interpolation scheme developed by Mohr and Vaughan (1979) has been modified to include range averaging and local velocity unfolding. They determined the grid point value by a three-dimensional linear interpolation of eight measured values from two consecutive range locations along the four beams (two azimuths from each of two elevation scans) surrounding the grid point. All these data are usually obtained within 10–15 s (30–40 s in extreme cases of large azimuthal sectors) even though the scan of the entire volume of interest may take 2–3 min. Radar data that contain ambiguous measurements can be interpolated with this method *without first unfolding them in radar sampling space* since the extension we propose preserves the original spatial discontinuities associated with folding. Further, this local unfolding technique applied to uniformly distributed noise estimates results in interpolated noise that remains nearly uniform with almost the same variability as the original distribution. The algorithm is discussed and the application of this procedure to a folded velocity field is presented. The advantages and cautions associated with this technique are also discussed.

2. Rectification of folded radial velocities

An example of radial velocities measured at an elevation angle of 9.5° by the NCAR/FOF (Field Observing Facility) CP-2 10-cm radar on 2 August during the 1981 Cooperative Convective Precipitation Experiment (CCOPE; Knight, 1982) in southeastern Mon-

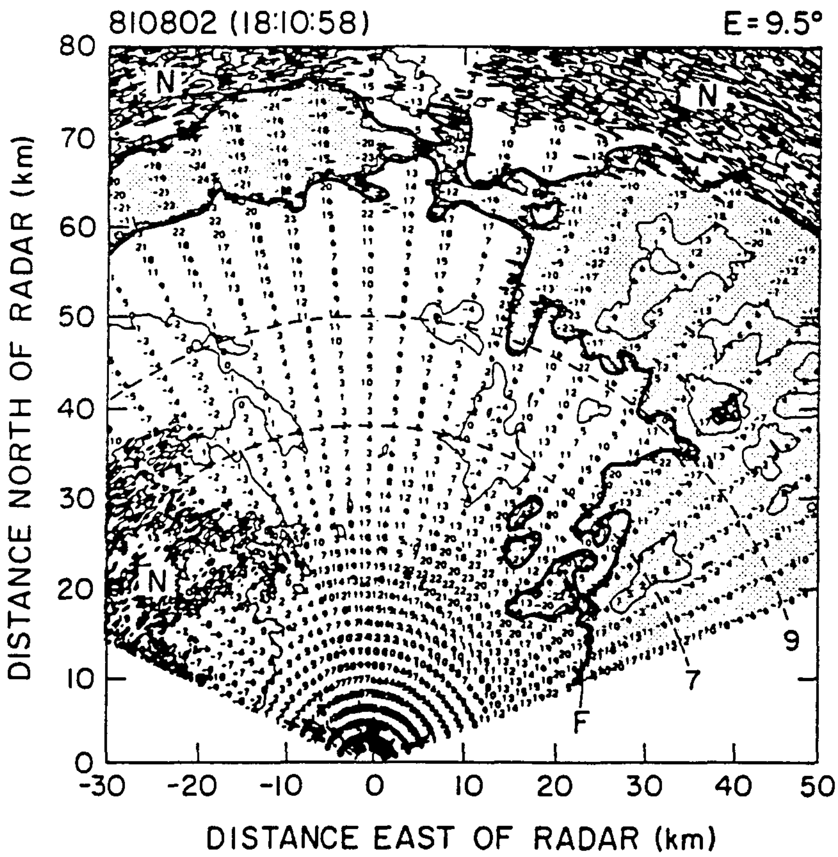

FIG. 1. Horizontal projection of measured radial velocities at an elevation angle of 9.5° from CP-2. These data were obtained on 2 August 1981 during the CCOPE field program in southeastern Montana. Numbers at every eighth gate along every sixth ray represent the magnitude of the radial velocity (positive values indicate motion away from the radar), with contours drawn at −25, 0 and 25 m s^{-1}. The bold line (F) indicates the position of the local discontinuity associated with folding. Regions of ambiguous or folded (about the Nyquist velocity of 25.6 m s^{-1}) velocities are shaded. Noisy estimates (N) exist to the northwest and also beyond about 70 km north of the radar. Ranges where the 7 and 9 km horizontal planes pass through this elevation surface are shown by dashed arcs.

tana is shown in Fig. 1. These data are part of the storm-volume scan from 1809:09 to 1812:32 (Mountain Daylight Time) that will be used to demonstrate the proposed technique. The storm was sampled every 200 m, 0.7° and 1° in range, azimuth, and elevation, respectively. The local discontinuity associated with folding is marked with a bold line. At locations away from the fold discontinuity the radial velocity field is again continuous, though perhaps ambiguous. Shaded regions in the figure contain ambiguous velocities while noise estimates exist beyond about 70 km to the north and in a patch northwest of the radar. Figure 2 shows these data after velocities have been unfolded in radar space using conventional methods (e.g., Oye and Carbone, 1981). In this example, noisy estimates (those mean values from low signal-to-noise power ratio regions or from broad velocity spectra) are retained though they could have been easily removed. In Section 4 we will compare interpolations of folded (Fig. 1) and unfolded (Fig. 2) values at 7 and 9 km (dashed arcs) to demonstrate that the same results can be obtained using the proposed alternative method.

Conventional editing and unfolding steps can be postponed until after interpolation so long as poor estimates of velocity and folding can still be identified. The idea is to designate a local velocity at each (x, y, z) point and to offset all velocities that affect this point so that they lie within the ambiguous velocity interval of this initial estimate prior to interpolation. This is done independently at each interpolation grid point and only represents a local resolution of velocity folding. Interpolated velocities which are folded must be subsequently de-aliased in Cartesian space using global techniques.

The true (unfolded) radial velocity U at a (R, A, E) measurement point is

$$U = V + \kappa V_a; \quad \kappa = 0, \pm 1, \pm 2, \cdots \qquad (1)$$

where V is the measured quantity which may be aliased and is subject to measurement error, $V_a = 2V_n$ is the ambiguous velocity interval, and κ is the integer factor needed to remove Nyquist folding ambiguities from V. When the measured velocity differs by more than V_n from the value expected at the grid point, the integer folding factor in Eq. (1) is nonzero and can be approximated by

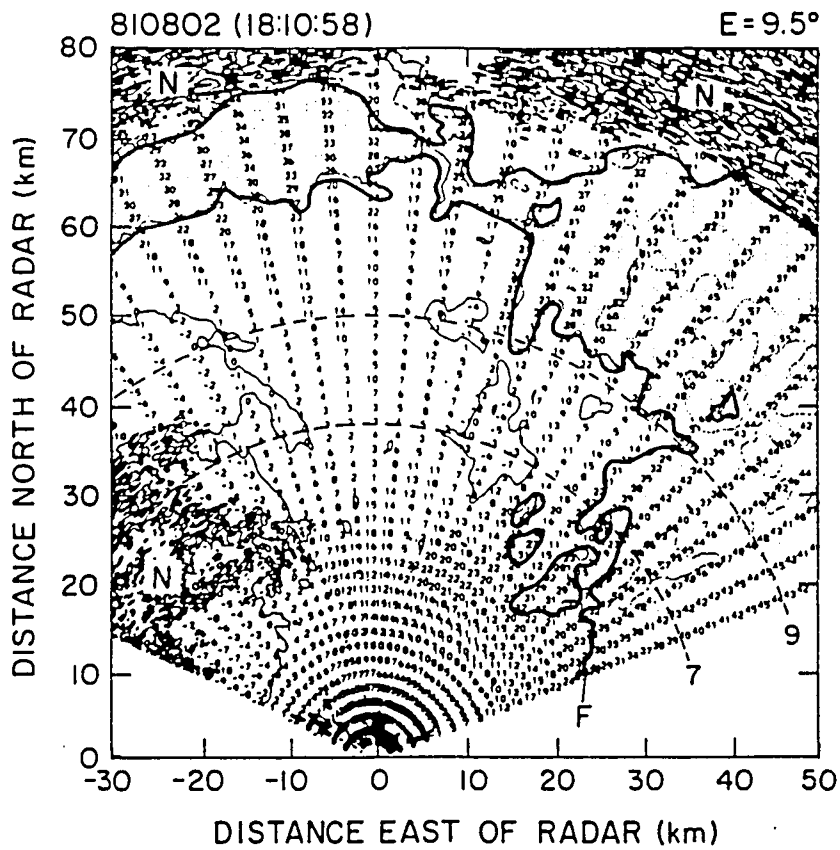

FIG. 2. Radial velocities shown in Fig. 1 after they have been unfolded in radar space. Areas where velocities have been de-aliased are shaded. An additional contour at 51.2 m s^{-1} has been added. This corresponds to the zero contour in the ambiguous zone in Fig. 1.

$$K = \frac{U_e - V}{V_a}, \tag{2a}$$

where U_e is a preliminary estimate of the true radial velocity (U) at the (x, y, z) point. The appropriate integer unfolding factor is determined by

$$\kappa = \begin{cases} \mathrm{INT}(K + 0.5), & \text{if} \quad K \geq 0 \\ \mathrm{INT}(K - 0.5), & \text{if} \quad K < 0, \end{cases} \tag{2b}$$

where INT represents truncation toward zero. The quantity U_e is arbitrarily set to one of the measured input values in the neighborhood of the (x, y, z) point, and the remaining contributing values are forced into the ambiguous velocity interval centered on U_e using Eqs. (1) and (2). Strictly this operation does not represent complete unfolding, but temporary removal of a discontinuity that would result in biased estimates when interpolation to grid points is performed. To completely unfold or de-alias the velocities, the addition or subtraction of another integer multiple of V_a may still be needed after interpolation. Henceforth, we will refer to the removal of the folding discontinuity within the population of input measurements contributing to the estimate at each (x, y, z) point as local unfolding or more simply as "unfolding."

Since U_e comes from the population of input samples which are contained within the Nyquist co-interval (unless they have been previously unfolded), the values of κ determined by Eq. (2) will be -1, 0, or $+1$. *It is assumed that no true velocity is more than V_n from the reference velocity.* This is equivalent to assuming that the largest possible physical gradients of radial velocity that can occur within the sampling cell surrounding the Cartesian grid point are $V_n/(M - 1)\Delta R$ in range, $V_n/R\Delta A \cos E$ in azimuth, and $V_n/R\Delta E$ in elevation, where ΔR, ΔA and ΔE are the respective sampling increments. The sampling cell consists of M range (R) gates and four adjacent beams, two in azimuth (A) and two in elevation (E). Spatial gradients across the sampling cell larger than these will cause the true radial velocities to be spread over more than one V_a interval, leading to the requirement that some values of κ exceed unity. In this event, which is uncommon provided the Nyquist velocity is large (about 25 m s^{-1}) and radar (R, A, E) sampling locations are closely spaced (less than about 1 km), the algorithm will obviously fail to interpolate an unbiased velocity value.

Radar velocity measurements from a range slab of thickness M gates centered at slant range R to the interpolation xyz-grid point are range-averaged to obtain estimates at each of four azimuth-elevation locations surrounding the xyz-grid point:

$$\hat{U}(A_j, E_k) = \sum_{m=1}^{M} U_m/M,$$

where the U_m have been "unfolded" according to Eqs. (1) and (2). This step is done to approximately equalize the sampling increments in the range and cross-beam directions and is not intended to represent complete filtering that may be required. The quantities A_j and E_k represent the respective azimuth and elevation angles of the beams. A caret denotes either range-averaged or xyz-grid values, and quantities without a caret represent either measured or "unfolded" velocities at radar sampling locations. The geometry of the angular sampling cell at the range of the xyz-grid point and interpolation are illustrated in Fig. 3. Following Mohr and Vaughan (1979), these range-averaged data are bilinearly interpolated using

$$\hat{U}(A, E) = \left(\frac{E_{k+1} - E}{\Delta E}\right) \times \left[\hat{U}_j\left(\frac{A_{j+1} - A}{\Delta A}\right) + \hat{U}_{j+1}\left(\frac{A - A_j}{\Delta A}\right)\right]_k + \left(\frac{E - E_k}{\Delta E}\right) \times \left[\hat{U}_j\left(\frac{A_{j+1} - A}{\Delta A}\right) + \hat{U}_{j+1}\left(\frac{A - A_j}{\Delta A}\right)\right]_{k+1}, \tag{3}$$

where $\Delta E = E_{k+1} - E_k$, $\Delta A = A_{j+1} - A_j$. The terms in brackets represent linear interpolations along azimuth at the k and $k + 1$ elevation levels. Combining Eqs. (1) and (3), in abbreviated form the "unfolded" and interpolated radial velocity becomes

$$\hat{U}(x, y, z) = \sum_{A,E} (wV)_{jk} + V_a \sum_{A,E} (w\kappa)_{jk}. \tag{4}$$

The first term on the right is the geometrically weighted sum of measured values, while the second term represents a weighted folding factor to correct for bias that would result if measured values were not locally unfolded before interpolation. The quantity w is the geometric weighting factor associated with each (A_j, E_k) location in Eq. (3). The values of κ in Eq. (4) are the

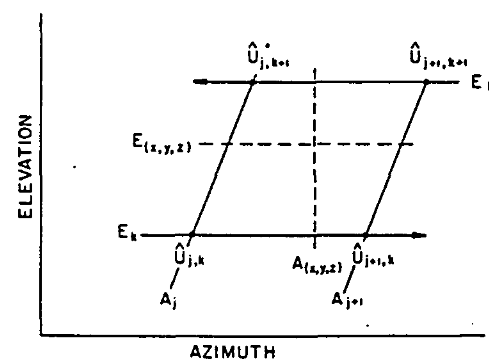

FIG. 3. The geometry of the sampling cell and bilinear interpolation along a constant range surface passing through the Cartesian grid point (x, y, z). The $\hat{U}_{jk}$ represent the averages of M range gate measurements centered at $R(x, y, z)$ and located at the four radar beams left and right, above and below the point $A(x, y, z)$, $E(x, y, z)$.

ones that must be used to remove the local discontinuity from the measured velocities.

The form of the weighting function to be used in Eq. (4) for interpolating radar information to a regular Cartesian grid is usually a matter of personal preference. We choose the linear weighting and range averaging presented in Eq. (3); other distance weighting schemes such as the Cressman method (e.g., Ray et al., 1975) could also be used. All such schemes assign a distance-weighted average value to the grid point, where the weight decreases rapidly as the distance from the grid point increases or else only estimates within some small radius of the grid point are used. It is not our intent to debate the virtues of all such schemes; however, if the method employed uses values only in proximity to the output grid point, the discontinuity associated with folding can be removed and then the weighting applied in the way we present. That is, they can be interpolated without prior radar-space editing.

Figure 4 illustrates the results of interpolating the folded radial velocity field (shown in Fig. 1) at two levels in the storm using the methodology that we propose. These horizontal planes at 7 (Fig. 4a) and 9 km (Fig. 4b) intersect the elevation plane in Fig. 1 at the dashed arcs. The boundary of folded radial velocities in the southeast portion of the grid is shown by a bold line, with shading indicating regions of ambiguous velocities as in Fig. 1. A zone of ambiguous velocities extends northward along the eastern portion of the grid as also seen in Fig. 1. The patch of noisy measurements northwest of the radar is also clearly replicated as evidenced by the many contours in the western portion of the domain. A time associated with each interpolation grid point is also obtained by applying the same linear interpolation scheme to the original observation times. In this way the multiple radar synthesis that includes advective corrections at Cartesian grid points as formulated by Gal-Chen (1982) can be utilized.

3. Quality of the interpolated velocities

Since the interpolation method is applied to all radar-measured velocities without prior editing, we need a way to determine the quality of the interpolated value. This measure can be used later in Cartesian space to reject unreliable velocities interpolated from radar measurements that are too noisy and to identify regions where local unfolding may have required a folding factor exceeding unity. When no signal is present covariance-measured radial velocities ideally have variance $\sigma_n^2 = V_n^2/3$, so that large local variability should tell us when interpolated values are coming from an input population dominated by noise. Further, large spatial gradients of the measured velocities should also lead to significant variability. When neither of these conditions exist, the spread of velocities should be much smaller. Thus we compare the sample variance var(U) of "unfolded" velocities to be used in the interpolation with the expected value of σ_n^2 for white noise to determine the reliability of the interpolated velocity. A nondimensional velocity quality parameter

$$Q(x, y, z) = 1 - \mathrm{var}(U)/\sigma_n^2 \tag{5}$$

is calculated. All measurements affecting a grid point estimate are locally unfolded using Eqs. (1) and (2) and then their corresponding variance var(U) is obtained.

The nondimensional velocity quality parameter Q is close to zero when all radial velocities are noise (see Appendix for the expected value and variance of Q when a noise population is unfolded), and it approaches unity as the spatial variability of the measured velocities decreases. Further, Q can become negative when the distribution of "unfolded" measurements is more clustered toward its extreme values with fewer estimates near the center velocity. The parameter Q reflects variability from measurement errors in individual velocities as well as large spatial gradients in the true radial velocity field surrounding the interpolated grid point. It is, therefore, a better measure of the acceptability of grid point estimates than is the magnitude of the covariance function which is often used to determine reliability of individual measurements contributing to the interpolated estimate. More importantly, Q can be computed for all radar systems in the same way. Systems that do not record the magnitude of the covariance function instead flag the velocity as good or bad at the time of measurement (e.g., the bad data flag bit used in the NCAR/FOF 5 and 10 cm radars). Unfortunately, such procedures do not allow the data-user to decide if these values are acceptable for his purposes.

An example of the actual behavior of Q in a noise-only environment was determined by interpolating radial velocities from NCAR's CP-2 radar. The transmitter was intermittent for a short time on 11 July 1981 during CCOPE so that noise-only data could be recorded while the antenna was rotating and the processing system was still operating. This provided recorded data at spatial resolution typically associated with normal probing of severe convective storms. The frequency distribution of Q for interpolation at one horizontal level is shown in Fig. 5 (solid line histogram). It roughly obeys a Gaussian law with a nearly zero mean value and standard deviation of about 0.3 so that interpolated (signal) velocities appear to be acceptable when $Q > 0.6$. This can be seen also in the distribution of Q when both signal and noise are present (Fig. 5, dashed line histogram). The values to the right of 0.6 are definitely associated with signal since a value of $Q = 0.8$ corresponds to var(U) = 43.7 m^2 s^{-2} with noise variance σ_n^2 = 218.4 m^2 s^{-2} for this case. (The Nyquist velocity was 25.6 m s^{-1}).

A histogram of noise input velocities from a volume scan on 2 August 1981 (Fig. 1) is shown in Fig. 6a. The percent of the total number of values (3194) appearing

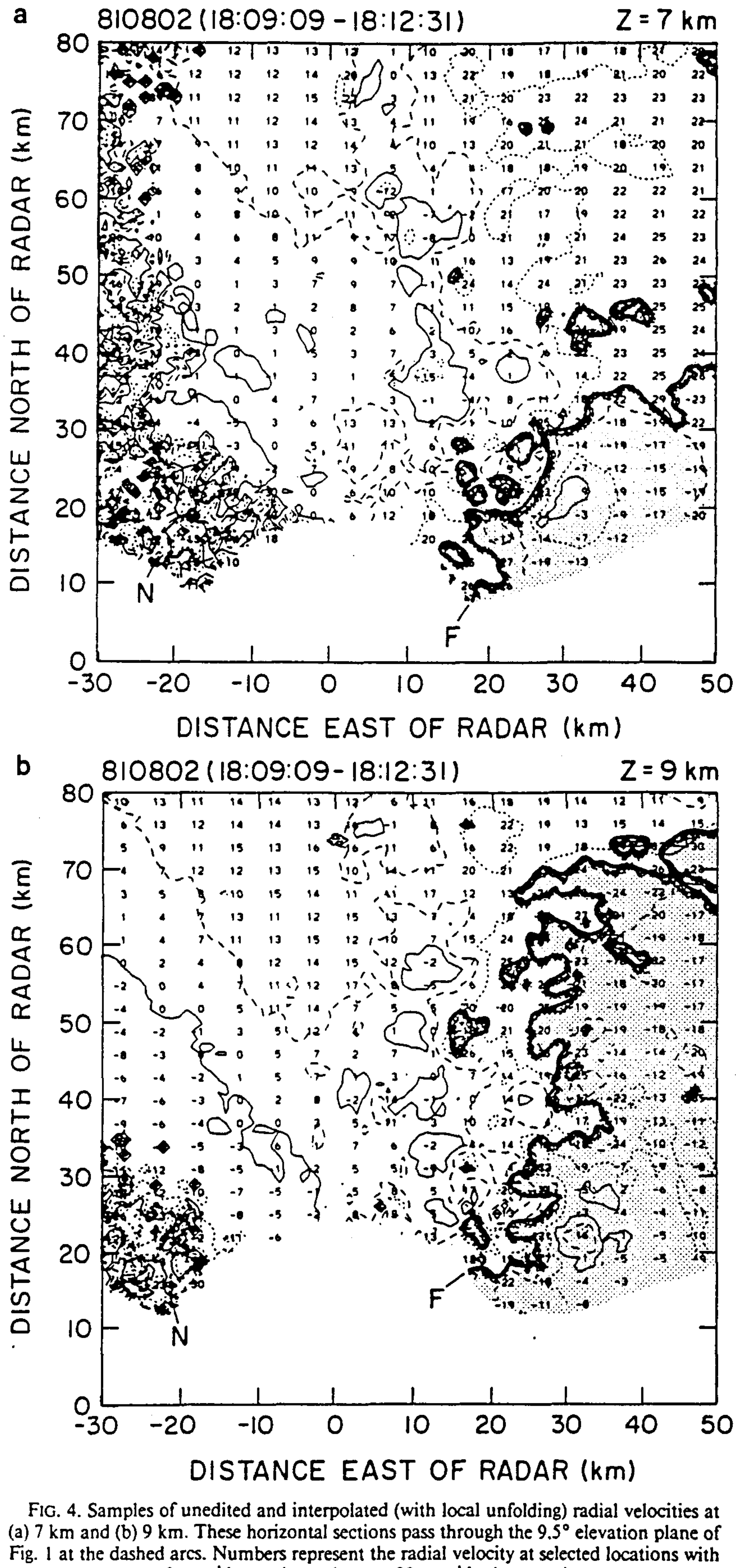

FIG. 4. Samples of unedited and interpolated (with local unfolding) radial velocities at (a) 7 km and (b) 9 km. These horizontal sections pass through the 9.5° elevation plane of Fig. 1 at the dashed arcs. Numbers represent the radial velocity at selected locations with contours drawn at 10 m s^{-1} intervals starting at -30 m s^{-1} in the repeating pattern: dashed, short-dashed and solid. The zero contour is solid. The bold line (F) marks the position of the local discontinuity caused by folding. The regions of ambiguous (folded) velocities are shaded. Noisy velocities (N) exist along the western portion of the grid.

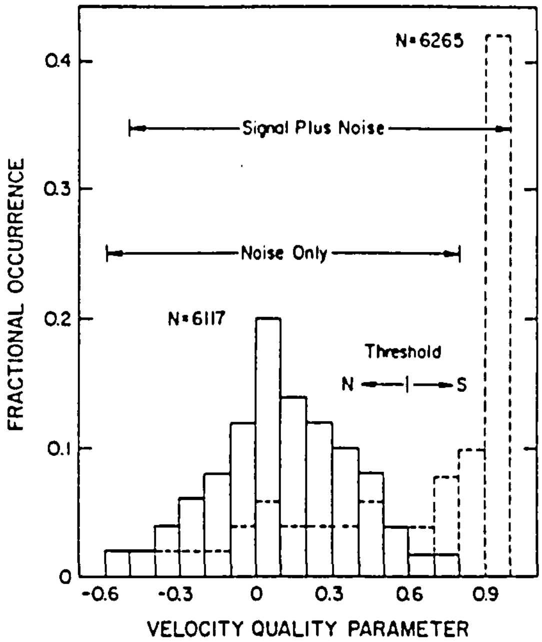

FIG. 5. Frequency distributions of velocity quality parameter for interpolated noise-only (solid) and signal-plus-noise (dashed) radial velocity fields. The numbers of values at this horizontal level (6 km above mean sea level) used to determine the distributions were 6117 and 6265, respectively. A value of 0.6 appears to adequately separate noise from signal.

in each of the bins of width 2 m s^{-1} is represented by the ordinate. The distribution is nearly uniform with sample mean of 0.01 m s^{-1} and standard deviation of 14.51 m s^{-1}, compared to theoretical values of 0.0 and 14.78 m s^{-1}, respectively. The distribution of interpolated (with local unfolding) velocities corresponding to the noise-only input velocities in Fig. 6a is shown in Fig. 6b. Since the reference velocity used for local unfolding is itself equally likely to occur anywhere within the ambiguous velocity interval, the effect of interpolation with unfolding is to create local Gaussian populations having an expected value of U_e and conditional variance equal to that of $\hat{U}$ for a given U_e. The distribution of $\hat{U}$ is then a convolution of this (relatively narrow) Gaussian with the original uniform distribution (Rohatgi, 1976). The tendency for more values to be concentrated near zero is mostly a result of convolving a Gaussian distribution whose width depends on the number of original measurements used in the interpolation with the *actual* distribution of velocities coming from the radar processor.

If no local unfolding were invoked the distribution of velocities would look like the one shown in Fig. 6c. If the radial velocities come from statistically similar populations having zero mean and equal variance $\sigma_n{}^2$, the variance of the grid point estimate is

$$\sigma^2(\hat{U}) = \sigma_n{}^2 \frac{\sum w_{jk}^2}{M},$$

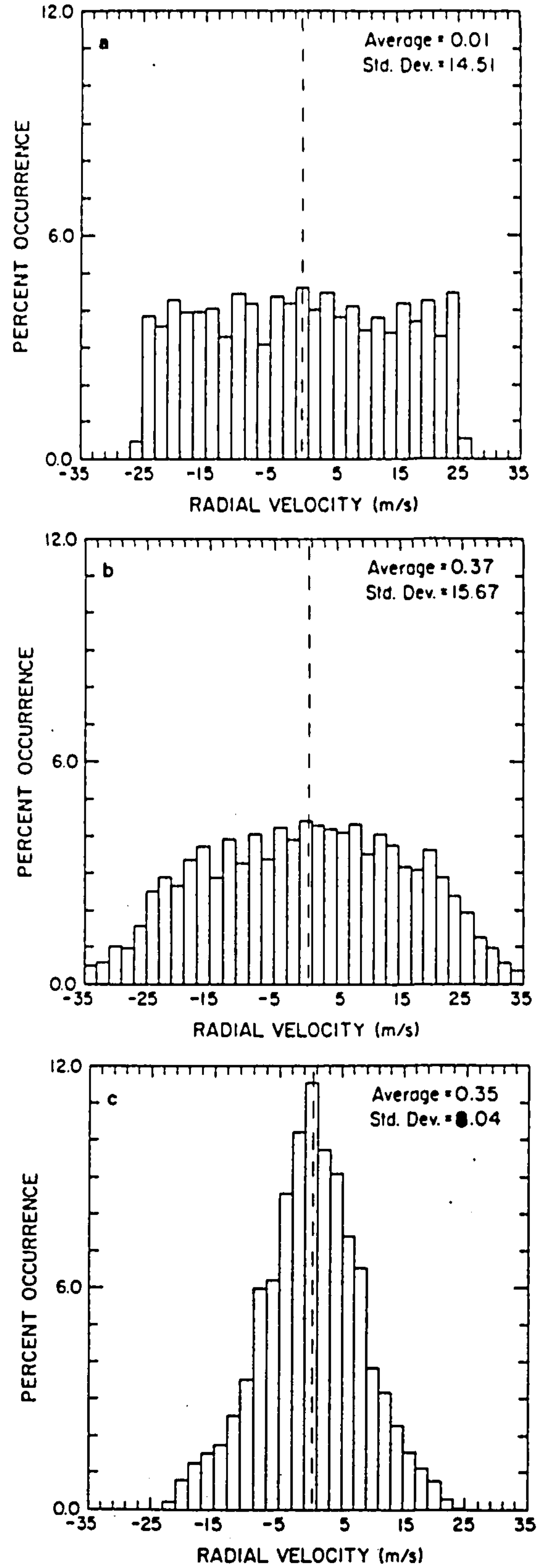

FIG. 6. Frequency distributions of radial velocities for "noise-only" (i.e., Q less than 0.5) portions of the 2 August radar scan volume presented in Figs. 1, 2 and 4: (a) input, (b) interpolated with local unfolding, and (c) interpolated without local unfolding. The average

where the quantities w_{jk} are the geometric weighting factors in Eq. (3). If the grid point should happen to coincide with an original sample location, all the weights except one are zero. If, however, the grid point is equidistant from all four sample locations (see Fig. 3), the sum of squares of weights is 0.25. Since all values of A, E are equally likely to occur, the expected value of $\Sigma\ w_{jk}^2$ is its areal average of 4/9. Three gates were used so the expected variance is $0.15\sigma_n^2$ or a standard deviation of 5.7 m s^{-1} compared to the observed value of 8.04 m s^{-1} (Fig. 6c). As can be seen the distribution of interpolated (with local unfolding, Fig. 6b) noise-only measurements is clearly "noiselike" and is similar to the one found in radar space (Fig. 6a). The importance of the local unfolding is further evidenced by noting the character of the contours in the western portion of Fig. 4a and contrasting that with what would happen if no local unfolding were invoked during interpolation (Fig. 6c). Some of the chaotic character would be lost.

4. Comparison with conventional methods

All radial velocities except noisy ones (as determined by the bad data flag bit) were carefully unfolded in radar space and then interpolated using the linear method with three-gate smoothing, but with no additional local unfolding. Examples of these data are shown in Fig. 7. Shaded regions in the eastern portion of the grid where velocities were originally ambiguous are now unfolded. Noisy estimates in the western portion were interpolated with local unfolding to replicate the effects discussed in Section 3.

For comparison, unedited original measurements such as those shown in Fig. 1 were interpolated with local unfolding and then unfolded in Cartesian space (Fig. 8), using global techniques described by Mohr and Miller (1983). These data were also thresholded on the velocity quality parameter ($Q > 0.6$) to eliminate the noisy portion. At grid locations outside regions of noise the average difference between velocity estimates derived by conventional methods and our method was 0.05 m s^{-1} with a standard deviation of only 0.11 m s^{-1}.

To further substantiate this equality of methods, we constructed several scatter plots to show point-by-point comparisons of velocities derived by conventional methods with those obtained by the proposed method. The following radial velocity fields were created:

- VGUF—velocities were unfolded in radar space and then interpolated with no additional unfolding,
- VNUF—unedited velocities were interpolated with local unfolding,
- VLUF—the field VNUF was unfolded in Cartesian space,
- VBIA—unedited velocities were interpolated without local unfolding,
- VGTH—the field VGUF was thresholded on Q, and
- VLTH—the field VLUF was thresholded on Q.

Figure 9a shows a scatter plot of the conventional method velocity (VGUF) along the abscissa versus the interpolated with local unfolding velocity (VNUF). There are two regression lines of VNUF that are offset by V_a = 51.2 m s^{-1} above and below (or right and left of) the one-to-one line. These represent values that need to be unfolded in Cartesian space, while values along the one-to-one line were never ambiguous in the first place. These velocities (VNUF) are shown in Fig. 9b after unfolding has been accomplished in Cartesian space. The few points that do not lie along the one-to-one line are from the noisy regions, as seen in Fig. 9c where these values have been eliminated by thresholding on Q. Note the small improvement in the correlation coefficient from r = 0.998 in Fig. 9b to r = 1.000 in Fig. 9c indicating that both methods are producing identical results in regions of usable data.

Contrast these results with the ones in Fig. 10 where unedited velocities were interpolated without local unfolding. The shaded area indicates regions where velocities cannot be unfolded by the addition or subtraction of any integer multiple of the ambiguous velocity. This is further demonstrated in Fig. 11 where these biased velocities (VBIA) are plotted against the conventional-method velocities (VGUF). The vertical scatter of VBIA near the Nyquist velocity typifies the amount of bias that occurred. The large scatter near the negative Nyquist is also from biasing as well as from noisy values. Although the bias in these velocities cannot be removed, all these interpolated velocity values can be eliminated by thresholding on the velocity quality parameter computed using unedited input measurements.

5. Concluding remarks

We have discussed a way of rectifying folded velocity measurements taken in radar sampling space to regular (x, y, z) analysis space. These locally unfolded and interpolated velocities can then be globally unfolded using techniques described by Mohr and Miller (1983). Noisy data are eliminated and remaining velocities are unfolded using the interactive software package CEDRIC (Mohr and Miller, 1983). This procedure has been shown to give results identical to those using more conventional approaches.

Two main advantages of not editing radial velocities until after interpolation are 1) the amount of radar data that must be subsequently manipulated is reduced by a factor of ten to twenty; and 2) all the data from

value is marked by a vertical dashed line. Each bin of width 2 m s^{-1} designates the percent of all velocities (total of 3194) that occurred within the bin. The average value and standard deviation of the distribution is shown in the upper right hand corner.

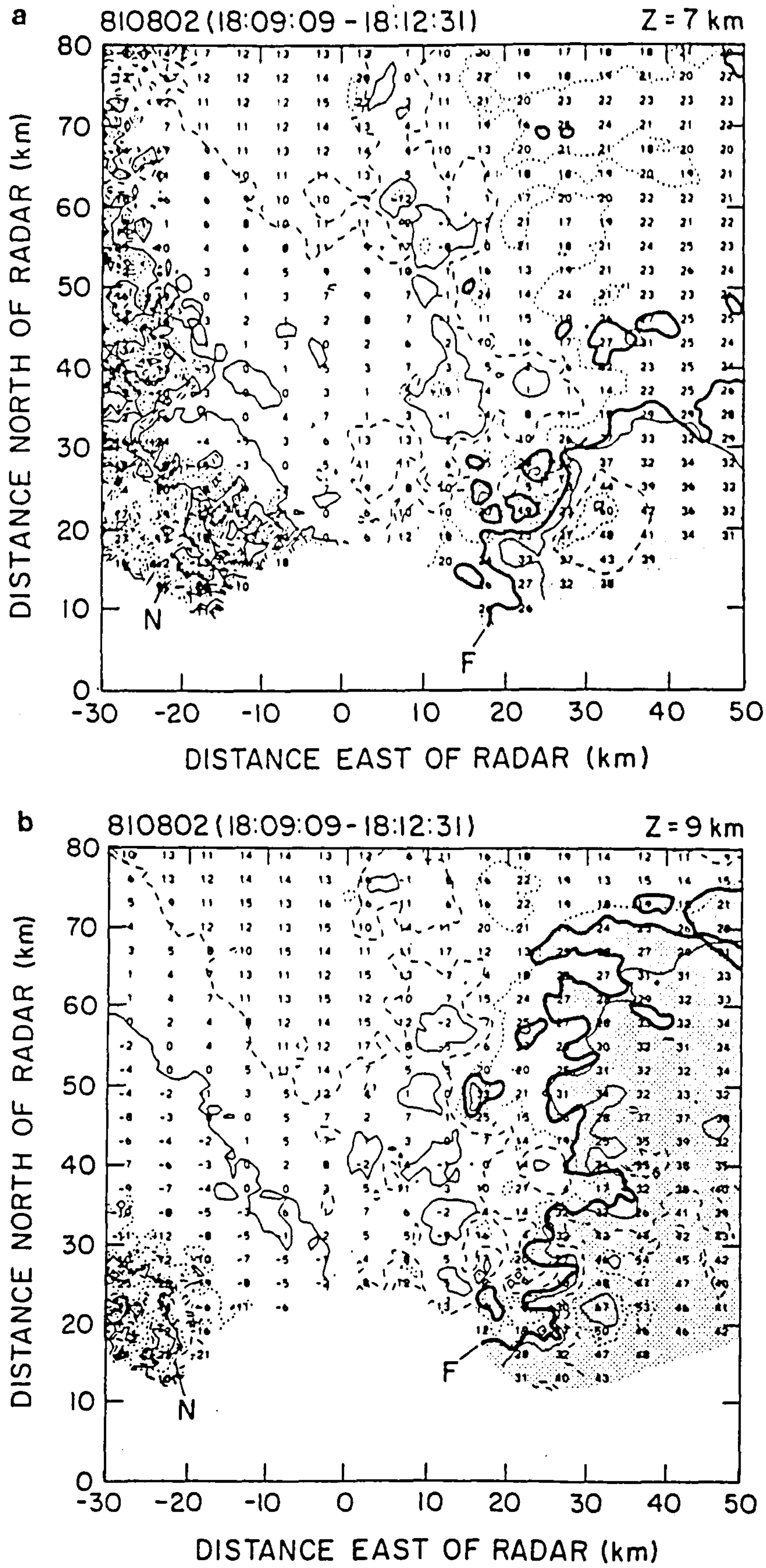

FIG. 7. Radial velocities at (a) 7 and (b) 9 km that were unfolded in radar space before they were interpolated. This format is identical to that given in Fig. 4. Additional contours are drawn at 30 m s^{-1} (solid), 40 m s^{-1} (dashed), 50 m s^{-1} (short-dashed), and 60 m s^{-1} (solid).

a

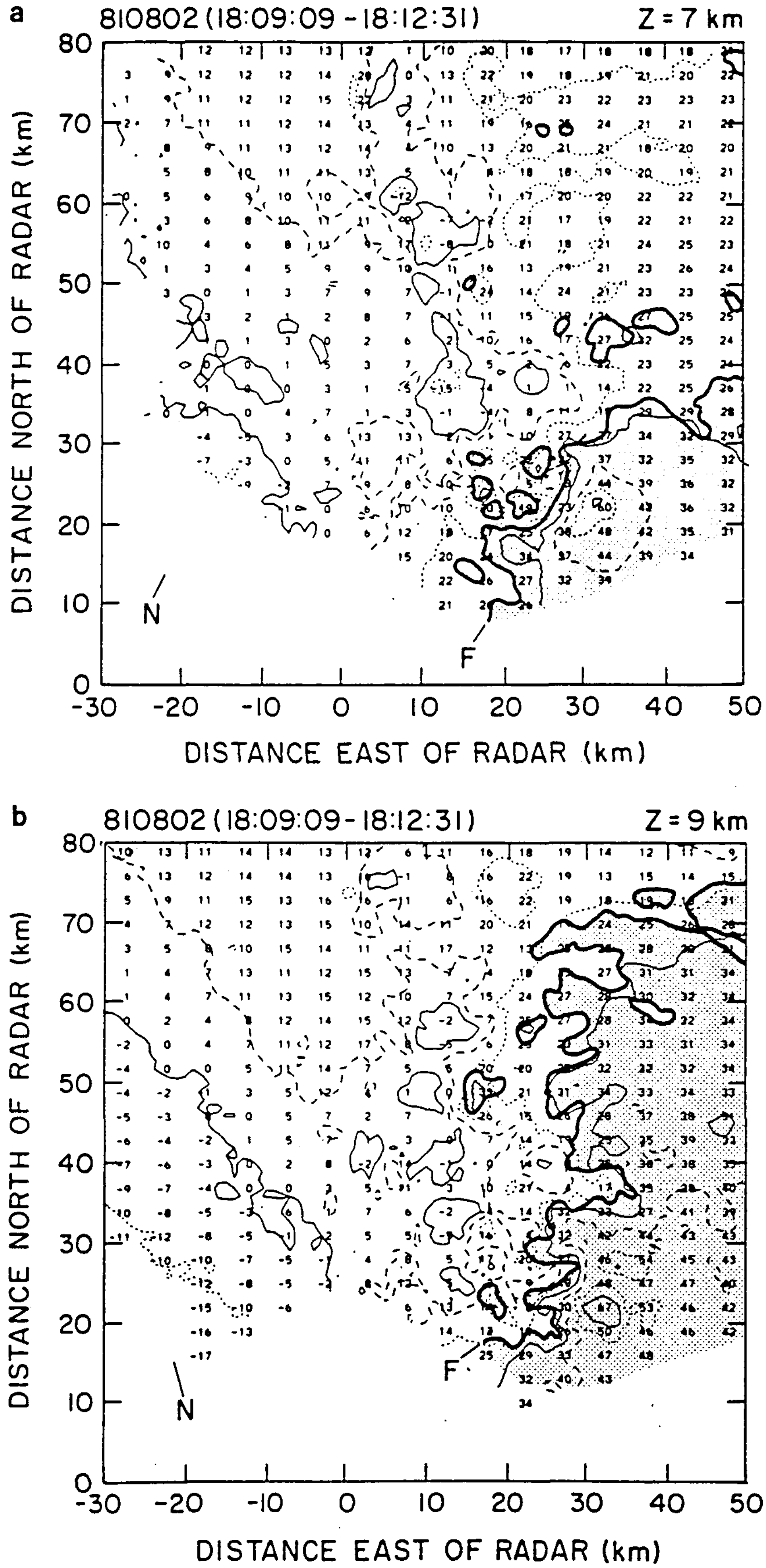

b

FIG. 8. Interpolated (with local unfolding) velocities shown in Fig. 4 that were unfolded in Cartesian space and thresholded on the quality parameter (Q greater than 0.6). Additional contours have been added as in Fig. 7. Compare these fields with those in Fig. 7.

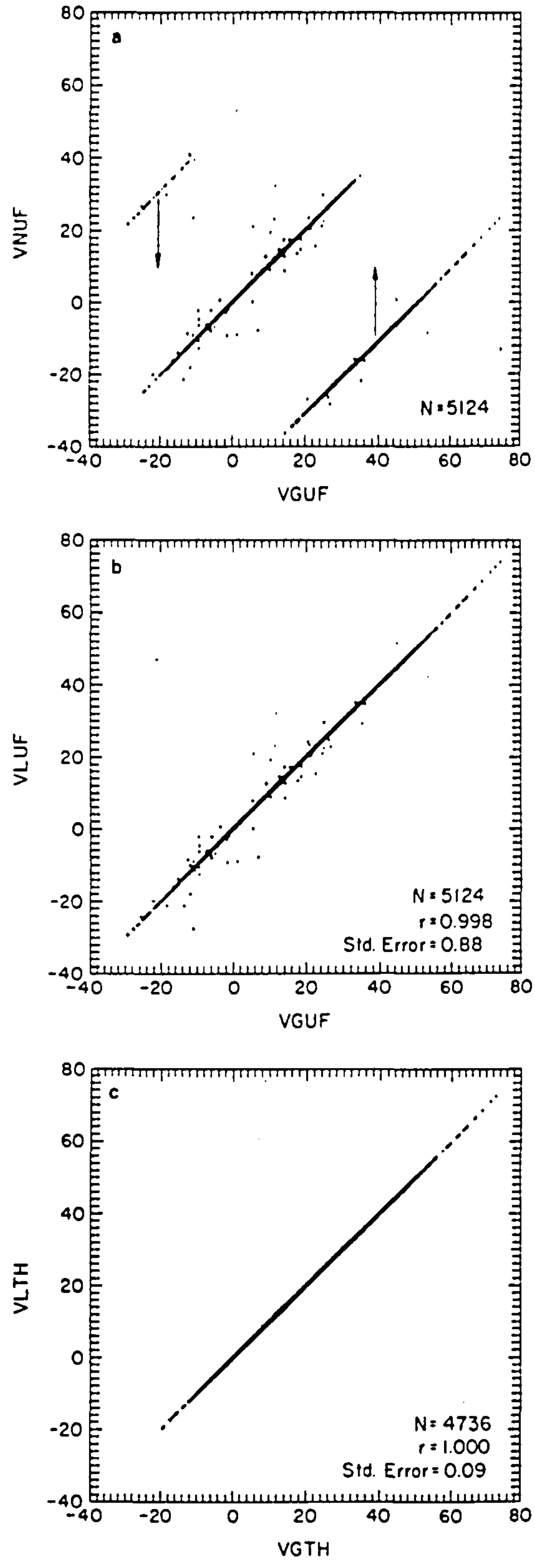

FIG. 9. Scatter plots of radial velocities that were unfolded in radar space and then interpolated (VGUF) versus (a) VNUF—locally unfolded during interpolation and (b) VLUF—unfolded VNUF in Cartesian space. The directions of movement of (VGUF, VNUF) pairs when VNUF is unfolded are marked by arrows in (a). VGTH was produced by thresholding VGUF on the velocity quality parameter and is plotted versus (c) VLTH—thresholded VLUF on quality parameter. The number of points (N), linear regression coefficient (r), and standard error [defined as $\sigma_y(1 - r^2)^{1/2}$, where σ_y is the ordinate] are marked in the lower right-hand corner.

different radars are located at common grid points, thereby facilitating interactive global unfolding and multiple radar wind synthesis attempts of difficult cases. When adjacent true velocity values differ by more than twice the Nyquist velocity, the local unfolding-interpolation scheme will fail to interpolate a correct grid point estimate. Application of Eqs. (1) and (2) would give a folding factor of one, rather than the required two or more. The interpolated value would therefore be incorrect.

For a large severe storm there may be as many as 500–1000 range gates per beam, 100–200 beams per elevation sweep and 15–20 sweeps per storm volume or about 1–4 × 10^6 original sampling points per storm volume. These are typically interpolated to about 100 × 100 grid points at 15–18 vertical levels, or 1.5–1.8 (×10^5) values. Large radar data bases such as the one from the CCOPE Doppler radar network can be written to mass storage devices (e.g., the terabit memory system at NCAR) where they can be processed using a batch version of this interpolation procedure (Mohr et al., 1981) on the CRAY-1A computer. Most of these radar measurements can be interpolated without prior radar-space editing and written to tape for transport to smaller machines such as a VAX 11/780 computer where the results can be edited and synthesized in Cartesian analysis space. This means that about one-tenth as many magnetic tapes must be handled, and most if not all of the data needed for a case study can reside on disk in the smaller machine.

Many times there is insufficient information available from a single radar to unambiguously unfold all the measured velocities. If the computation-intensive step of interpolation does not have to be repeated, preliminary unfolding and synthesis can be attempted. Incompatibilities between radars will usually show up as physically impossible resultant vector winds so that the offending values of radial velocity can then be unfolded in a different way and resynthesized. Furthermore, since most meteorologists are more accustomed to working with data on constant height surfaces rather than constant elevation angle surfaces (radar spherical coordinates), Cartesian space is a more comfortable framework for manipulating the data base and arriving at believable results. Measurements can be transformed without radar space editing in most cases so that the majority of the data processing can be delayed until all radar estimates are organized onto a common (for all radars) grid where editing is less tedious and time-consuming.

Acknowledgments. The authors acknowledge the diligent efforts of the NCAR Field Observing Facility

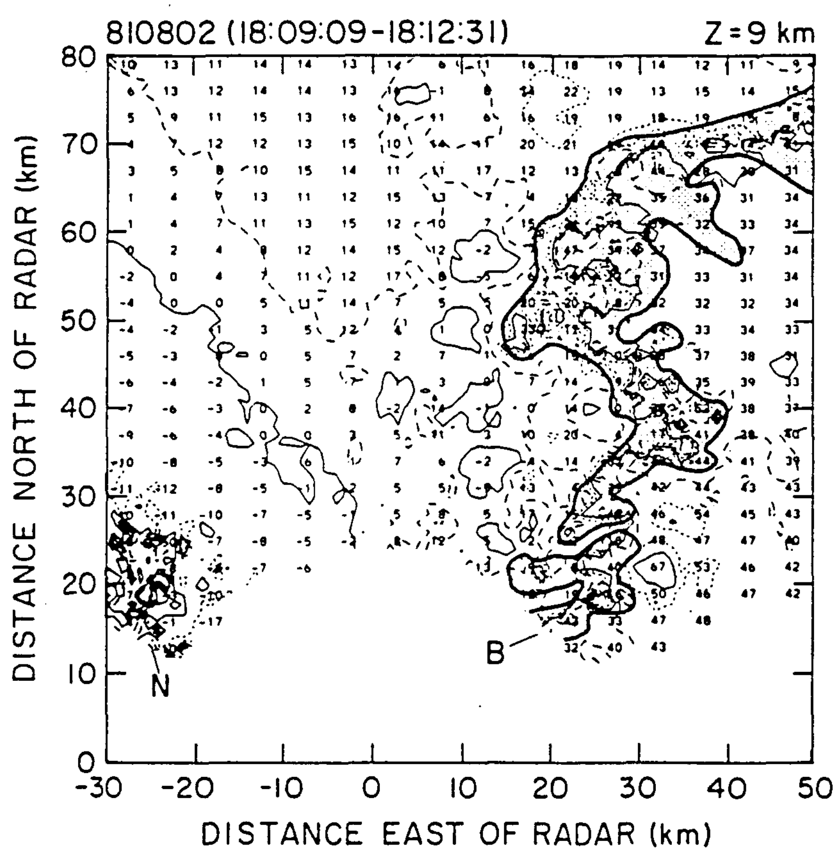

FIG. 10. Biased velocities that result when unedited and folded velocities are interpolated without invoking the local unfold algorithm. These data were then unfolded using the velocities in Fig. 7b as references. The shaded region surrounding the fold discontinuity contains biased velocities; that is, they cannot be unfolded to agree with Fig. 7b by the addition or subtraction of integer multiples of the ambiguous velocity, V_a.

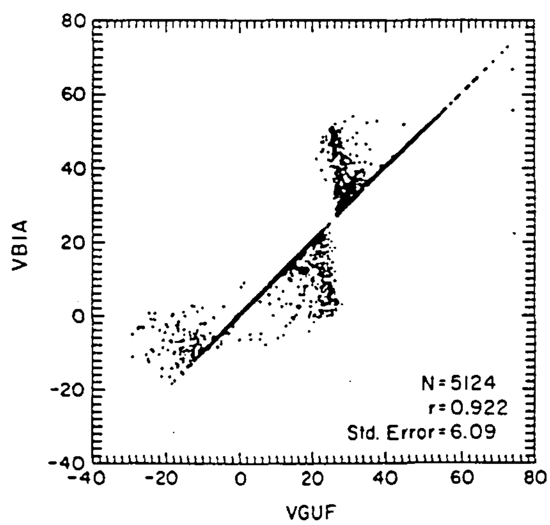

FIG. 11. As in Fig. 9 except VGUF versus VBIA— biased velocities of Fig. 10. This scatter plot clearly shows biasing in the grid point estimates that cannot be removed. However, those values that are biased can be eliminated from the dataset by thresholding on the velocity quality parameter.

technical staff in the maintenance and operation of the CP-2 radar. The success of the CCOPE experiment would not have been possible without the dedication of these technicians and engineers.

APPENDIX

Behavior of the Variance and Nondimensional Velocity Quality Parameter

In this appendix we consider the behavior of the variance [var(U)] and nondimensional velocity quality parameter (Q) in Eq. (5) when all radial velocity measurements are random noise. This is of fundamental importance since we calculate these statistics at each grid point and use their values to discriminate against interpolated velocities coming from regions of noise. The applicability of this exercise is limited, however, by the extent to which the pulse-pair processor is not ideal and does not yield a uniform distribution of output velocities in noise.

When no return signal is present, covariance-determined velocities will ideally be distributed uniformly from $-V_n$ to V_n, and thus will have a zero mean and variance $\sigma_n^2 = V_n^2/3$. However, the unfolding of such a distribution to a reference velocity that is a sample from the population results in a variance somewhat smaller than σ_n^2. The velocity notation used in the main body of the paper is retained: at radar sampling locations V_i and U_i represent measured and unfolded velocities, respectively. The local mean value of the unfolded velocities is

$$\bar{U} = \frac{\sum U_i}{I}, \tag{A1}$$

with variance [Z = var(U) in Eq. (5)]

$$Z = \frac{\sum (U_i - \bar{U})^2}{I - 1}. \tag{A2}$$

The expected value of Z for a uniform noise distribution is derived from the conditional probability density for the unfolded velocities U_i, given that a reference velocity $V_1 = v_1$ has been chosen. For $i \neq 1$, the U_i will be uniformly distributed over a range of $2V_n$ centered at v_1. The conditional probability density of the $U_i (i \neq 1)$ is

$$p_{U_i|V_1}(u_i|v_1) = \begin{cases} \dfrac{1}{2V_n}, & v_1 - V_n < u_i < v_1 + V_n \\ 0, & \text{otherwise.} \end{cases} \tag{A3}$$

Further, for $i = 1$ the unfolded velocity will certainly be v_1, given that $V_1 = v_1$:

$$p_{U_1|V_1}(u_1|v_1) = \delta(u_1 - v_1), \tag{A4}$$

where δ is the Dirac delta function. The conditional expectation or mean of each of the U_i is v_1:

$$E_c[U_i] = \int du_i u_i p_{U_i|V_1}(u_i|v_1) \\ = v_1. \tag{A5}$$

The conditional expectation of Z may be expressed in terms of the conditional variances of the U_i given by

$$E_c[(U_i - v_1)^2] = \begin{cases} \sigma_n^2, & i \neq 1 \\ 0, & i = 1. \end{cases} \tag{A6}$$

Then by taking steps identical to those in the derivation of the expected value of a sample variance (e.g., Bendat and Piersol, 1971), it follows that

$$E_c[Z] = \frac{I - 1}{I} \sigma_n^2. \tag{A7}$$

(This Z is actually not a sample estimate of variance in the usual sense, because the values of U_i do not constitute a random sample of a single random variable, U_1 being distributed differently than the other U_i.) From the definition of the velocity quality parameter in Eq. (5), the expected value of Q becomes

$$E_c[Q] = 1 - E_c[Z]/\sigma_n^2 \\ = \frac{1}{I}. \tag{A8}$$

This will be near zero for most practical choices of I (I = 12 for 3-gate range averaging).

In order to distinguish between signal and noise using the parameter Q, it is important that the variance of Q in noise not be too large. Otherwise, a significant number of values of Q in noise, which are expected to be near zero, may actually be near unity, as they are for signal. The conditional variance of Q, var$_c[Q]$, may be shown to be

$$\text{var}_c[Q] = \frac{4}{5(I - 1)}\left(1 + \frac{1}{2I} - \frac{4}{I^2}\right) \\ \approx \frac{4}{5I}. \tag{A9}$$

This indicates that the reliability of Q as a discriminator against noise is increased by increasing the number of samples I going into each grid point estimate.

REFERENCES

Bendat, J. S., and A. G. Piersol, 1971: *Random Data: Analysis and Measurement Procedures*, Wiley-Interscience, 407 pp.

Carbone, R. E., F. I. Harris, P. H. Hildebrand, R. A. Kropfli, L. J. Miller, W. Moniger, R. G. Strauch, R. J. Doviak, K. W. Johnson, S. P. Nelson, P. S. Ray and M. Gilet, 1980: The multiple Doppler radar workshop, November 1979. *Bull. Amer. Meteor. Soc.*, **61**, 1169–1203.

Doviak, R. J., D. Sirmans, D. Zrnić and G. B. Walker, 1978: Considerations for pulse-Doppler radar observations of severe thunderstorms. *J. Appl. Meteor.*, **17**, 189–205.

Gal-Chen, Tzvi, 1982: Errors in fixed and moving frames of references: Applications for conventional and Doppler radar analysis. *J. Atmos. Sci.*, **39**, 2279–2300.

Knight, C. A. (Ed.), 1982: The Cooperative Convective Precipitation Experiment (CCOPE), 18 May–7 August 1981. *Bull. Amer. Meteor. Soc.*, **63**, 386–398.

Mohr, C. G., and L. J. Miller, 1983: CEDRIC—A software package for Cartesian space editing, synthesis and display of radar fields under interactive control. *Preprints, 21st Conf. on Radar Meteorology*, Boston, Amer. Meteor. Soc., 569–574.

——, and R. L. Vaughan, 1979: An economical procedure for Cartesian interpolation and display of reflectivity factor data in three-dimensional space. *J. Appl. Meteor.*, **18**, 661–670.

——, L. J. Miller and R. L. Vaughan, 1981: An interactive software package for the rectification of radar data to three-dimensional Cartesian coordinates. *Preprints, 20th Conf. on Radar Meteorology*, Boston, Amer. Meteor. Soc., 690–695.

Oye, R., and R. Carbone, 1981: Interactive Doppler editing software. *Preprints, 20th Conf. on Radar Meteorology*, Boston, Amer. Meteor. Soc., 683–689.

Ray, P. S., and C. Ziegler, 1977: De-aliasing first-moment Doppler estimates. *J. Appl. Meteor.*, **16**, 563–564.

———, R. J. Doviak, G. B. Walker, D. Sirmans, J. Carter and B. Bumgarner, 1975: Dual-Doppler observations of a tornadic storm. *J. Appl. Meteor.*, **14**, 1521–1530.

Rohatgi, V. K., 1976: *An Introduction to Probability Theory and Mathematical Statistics*, Wiley and Sons, 684 pp.

Zrnić, D. S., 1977: Spectral moment estimates from correlated pulse pairs. *IEEE Trans. Aero. Elec. Sys.*, **AES-13**, 344–354.

AN INTERACTIVE SOFTWARE PACKAGE FOR THE RECTIFICATION OF RADAR DATA TO THREE-DIMENSIONAL CARTESIAN COORDINATES

C. G. Mohr, L. J. Miller and R. L. Vaughan
National Center for Atmospheric Research*
Boulder, Colorado 80307

1. INTRODUCTION

Interactive mini-computer systems have become an indispensable medium for the acquisition, editing, display, and archival of digital radar data. The usefullness of interactive systems in an operational environment is well documented (see Silver and Geotis, 1976) and today most research radar processors incorporate a minicomputer as a major component in the acquisition system. In the laboratory environment, there exists a number of post-processing facilities which have been designed for the editing and display of archived data sets. Interactive systems at Alberta (Ramsden *et al.*, 1976), Air Force Geophysics Laboratory (Glover, 1980), and at the National Center for Atmospheric Research (Brown and Borgogno, 1980) have all proven themselves to be indispensable for the initial reduction and interpretation of digital radar data.

In forecasting developments for the 1980's Serafin and Lhermitte (1980) anticipated the evolution of even more elaborate interactive systems that would provide all the functions necessary for the synthesis and display of vector wind fields from multiple Doppler radars. As a modest step toward that goal we, at NCAR, have developed an interactive software package for the rectification of digital radar fields to a three-dimensional Cartesian coordinate system.

Aside from the obvious necessity for transforming multiple Doppler velocities to common coordinates, there are numerous advantages to be gained by replicating radar fields onto a regular Cartesian grid. The resultant data structure contains fewer data points, is easier to manipulate, facilitates the construction of more meaningful displays, and lends itself more readily to interpretation.

2. INTERACTIVE VS. BATCH INTERPOLATION

It is reasonable to question whether there are any advantages to be gained by implementing the task of Cartesian rectification as an interactive function. Characteristically, it is a time comsuming I/O intensive process best performed on a large general purpose computer. However, as experience has shown, this transformation is also a highly parameterized and occasionally unpredictable procedure often requiring numerous trial and error iterations before the radar data is satisfactorily replicated in Cartesian coordinates.

Unknowns to be resolved prior to final interpolation include 1) size, resolution, placement and orientation of the Cartesian grid; 2) identification of "noise" and how it should be handled; 3) fields to rectify and their attendent idiosyncrasies (i.e., Z vs. dBZ, velocity fields and the folding problem); and 4) the selection of an appropriate method for interpolation.

Consequently, there is an obvious need for observing the results of a particular interpolation in a timely fashion so that potential errors can be avoided prior to the archival of a permanent output file.

3. GENERAL OUTLINE OF THE SYSTEM

3.1 Hardware

The interactive package was developed for use on the Digital Equipment Corporation VAX family of minicomputers. The particular configuration upon which this package has been implemented is a VAX 11/780 processor with 2-160 megabyte disk drives, two magnetic tape transports and a 300 line per minute matrix printer with graphics capabilities. Users have access to the machine through a variety of alphanumeric and vector graphics terminals located in a common area. Although digital imaging hardware with color capability could certainly be supported it is not a requirement in this system.

Burgess *et al.* (1976) have shown that even in an operational environment, concise displays of Doppler data are possible without the need for sophisticated digital imaging equipment. For this reason, and in the interests of portability, we have taken some care not to inexorably link the interactive software in any way to specialized hardware or system-dependent features.

3.2 Software

As indicated in the previous section, emphasis was placed on making the basic software package portable from one system to another. It is written according to FORTRAN-77 standards and with the exception of the NCAR graphics software

* The National Center for Atmospheric Research is sponsored by the National Science Foundation.

(documented by Wright, 1978), the package does not require any resident or system-dependent routines.

All data structures and buffers are parameterized in the main program so that the package can be configured according to the size and nature of the radar data as well as the computer system upon which it is run. Program speed depends on a variety of factors including characteristics of the input data, buffer sizes, number of fields, and machine load. Nevertheless, a conservative timing estimate can be obtained based upon the number of grid locations in the Cartesian coordinate system by using 30,000 points per minute as a reference.

3.3 System Configuration

Figure 1 illustrates the major hardware and software components of the interactive Cartesian rectification system. Data flow paths indicate the relational structure among these components.

Transfer of data between magnetic tape and disk storage is handled by a separate program designed to process tapes generated in the common Doppler radar data exchange format. (See Barnes, 1980, for the specifications of this format.) Cartesian coordinate data is written to output

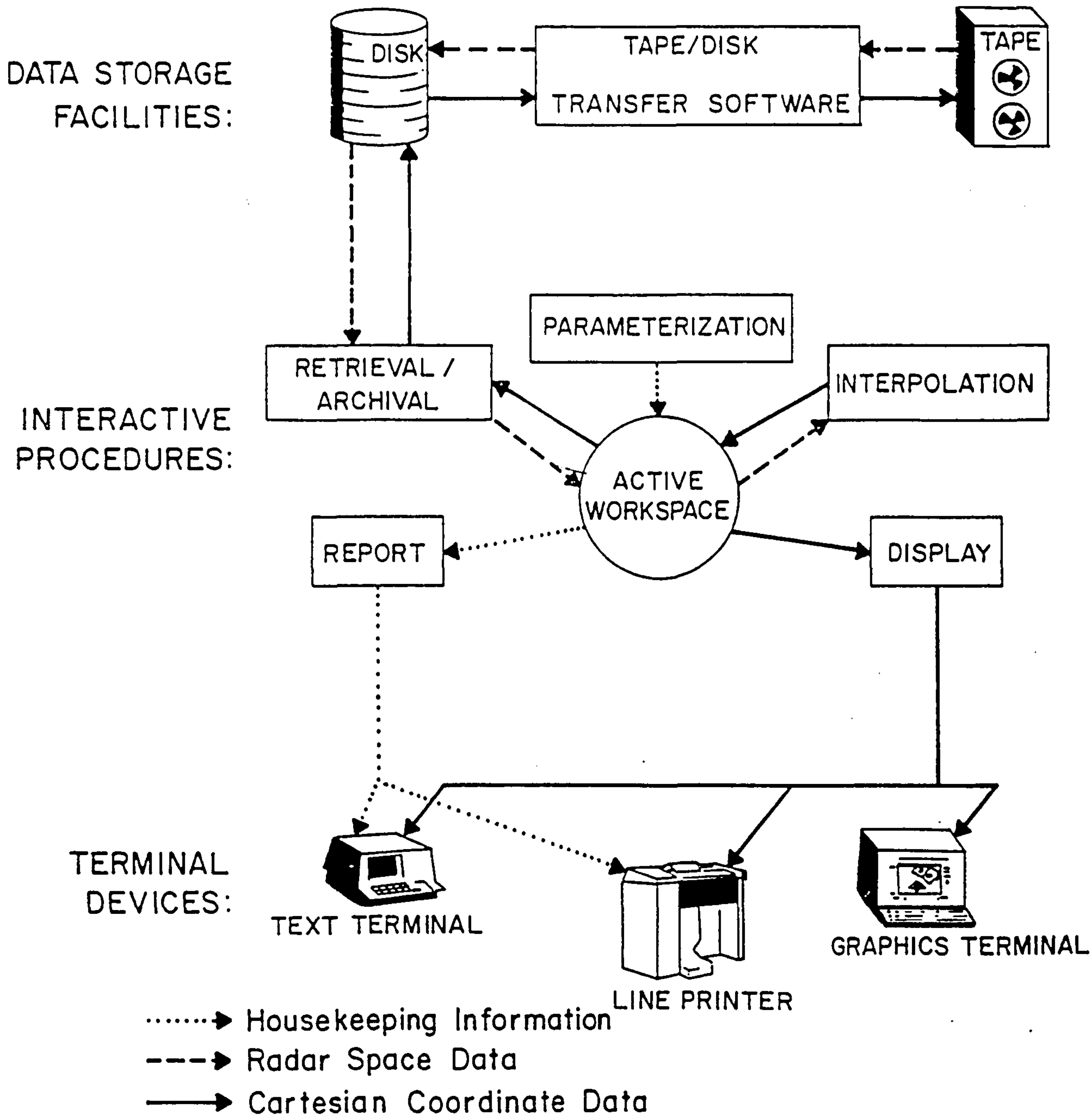

Fig. 1. Major hardware and software components of the interactive Cartesian rectification system. Relationships among components are indicated by data flow paths.

tapes in a standard format used within NCAR that is compatible with the batch mode Multiple Doppler Radar Analysis System (MUDRAS) described by Kohn *et al.*, 1978.

Interactive command procedures available to the user fall into five general categories:

1) Retrieval/archival of radar space and Cartesian data to and from disk;
2) Parameterization of the Cartesian coordinate system and rectification method;
3) Initiation of the actual interpolation;
4) Report on current parameterization and input/output data structures; and
5) Display by means of alphanumeric products and vector graphics.

Reports may be sent to either the text terminal at which the user is situated, a line printer, or both. Alphanumeric displays are disposed of similarly. If terminal devices with graphics capabilities are available, plots may be generated.

4. INTERACTIVE COMMANDS DESCRIPTION

4.1 Retrieval/Archival Commands

INPUT: This command connects a radar space data set residing on disk to the active workspace. It permits the user to process data from more than one radar without having to re-enter the program.

VOLUME: This command selects an input volume scan from the connected radar space data set and activates it for input to the interpolation procedure.

MUDRAS: Once an acceptable Cartesian output volume has been generated (it may be one of several trial and error iterations), this command archives the result on disk storage as a permanent data set.

4.2 Parameterization Commands

CARTESIAN: This command allows the user to specify the characteristics of the destination Cartesian coordinate system. Size, resolution, orientation and placement are all defined by the user. In addition, the axis to be held constant (i.e., Z, Y, or X) and the spatial units of the axes (i.e., kilometers, miles, feet, etc.) may also be selected. The Cartesian grid may consist of up to 64 levels, each containing a maximum of 16,000 points.

METHOD: This command specifies the constraints under which the radar space data is to be converted to a Cartesian coordinate system. The purpose of the rectification procedure is to replicate the radar fields in X, Y, Z space with a minimum of alteration. Mueller (1977) has observed that small scale features, exemplified by high reflectivity gradients, appear less often as the sampling volume increases. Analogous results can be expected when "sampling down" to the Cartesian grid. For this reason we have elected to use as small a sample volume as possible in our rectification method; namely the volume defined by the eight original values surrounding each Cartesian location in space.

Figure 2 illustrates this sample volume and the basic method employed for Cartesian rectification. Wherever possible, bilinear interpolation is performed at the projection point on each of 2 successive elevation planes. A final estimate at the Cartesian location is computed using the interpolated values at the projection points. Mohr and Vaughan (1979) have shown this to be an effective method when applied to reflectivity data from severe storms. Miller and Strauch (1974) and Pytlowany *et al.* (1979) have also successfully employed similar interpolation procedures in the conversion of radar space data to CAPPI planes.

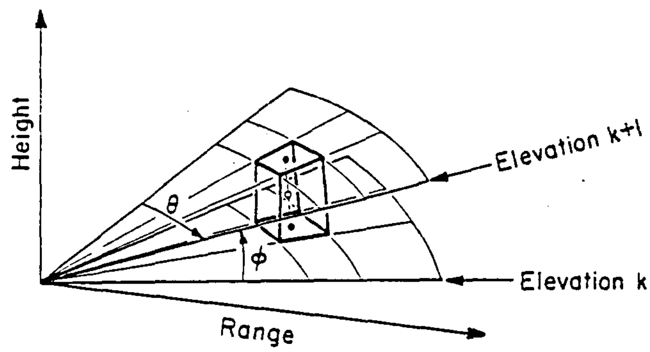

Fig. 2. Illustration of sampling volume used for Cartesian rectification. Volume is defined by the eight adjacent radar space samples surrounding a Cartesian location in space. Solid dots indicate projection points of the Cartesian grid location (shown as an open dot) on consecutive elevation scan planes k and k+1.

Within the framework outlined above, any one of three rectification methods may be specified:

1) *Closest point,* which selects the original radar value nearest the destination Cartesian location as the best estimate;

2) *Successive bilinear interpolation,* (described earlier); or

3) *Hybrid interpolation* whereby method 2 is performed whenever all eight values satisfy user-defined threshold criteria; otherwise the closest point (method 1) is selected. This hybrid method ensures that "noisy" data is replicated without significant alteration in weak signal regions.

When methods 2 or 3 are employed the user is asked to designate a threshold field and a minimum value upon which the validity of data points in all fields can be determined. For all methods, thresholds may also be set for each rectified field prior to output.

As mentioned earlier, certain problems are encountered when attempting to rectify reflectivity and velocity data. With respect to reflectivity data, some analysts choose to interpolate the intensity field while others prefer the computations to be performed on the logarithmic quantities dBM and/or dBZ. All three field types are recognized by the software and options exist for deriving dBM from intensity and dBZ from dBM after rectification has been completed.

Rectification of unedited velocity data is, of course, compounded by the aliasing problem. Potential ambiguities in the rectified velocity field estimates are avoided by ensuring that all eight radar values are in the same unambiguous nyquist velocity interval prior to interpolation. This optional de-aliasing technique is similar to the one described by Ray and Ziegler (1979) in which all velocities within a specified region are folded into the same interval according to some reference velocity. In our implementation the region consists of the eight points defining the three-dimensional sampling volume and the radial velocity value associated with the strongest returned power among the eight points is used as a reference. Should it become necessary, de-aliasing of rectified estimates can be subsequently performed in Cartesian space without compromising the original radial velocity data.

4.3 Interpolation Command

The *INTERPOLATION* command transforms the data contained in the radar space volume to the designated Cartesian coordinate system according to the constraints specified by the user in the *METHOD* command. It may be invoked at any time provided that all relevant data structures and parameterization have been previously defined. That being the case, the user is able to make minor adjustments to the parameterization followed by re-interpolation until a satisfactory result is obtained. By the same token, once the proper parameterization has been established for a particular radar volume, subsequent rectification of similar cases may proceed without delay.

This command invokes a one-pass algorithm through the original radar data based upon the retrieval strategy prescribed by Mohr and Vaughan (1980). The current implementation has been modified to accommodate 360 degree scanning as well as Cartesian coordinate systems in which the radar position is embedded. There are no limits on the size of the input data set and a maximum of 10 radar fields may be processed at a time.

4.4 Report Command

The function of the *REPORT* command is to supply general information upon request and to maintain a permanent record of activity during an interactive session. Figure 3 contains an example of hard copy output generated for a single volume by the *REPORT* command. Summaries of the radar space data set, the Cartesian output file and the method employed for rectification all appear in this report. The insertion of user-supplied comments is also illustrated.

Although not included in this example, parameterization of the Cartesian coordinate system and header information associated with any archived data sets may also be examined. Any report which the user wishes to retain may be diverted to a permanent text file for future reference.

4.5 Display Command

Figure 4 contains examples of output generated by the DISPLAY command. These display products fall into two distinct categories.

4.5.1 Symbolic displays

Symbolic displays represent the data by means of alphanumeric symbols and are designed for use with inexpensive text terminals and line printers.

Whenever a symbolic display cannot be viewed completely within the area provided by a particular terminal, the display is automatically subdivided according to the characteristics of the device.

```
RADAR (.RAD)  VOLUME HEADER      PINTST
  DATE: 78/ 7/28        TIME: 14: 9: 2--14:10:32      PTS/RECORD:  304
  TAPE: E1677     RADAR: NOAA-C     PROGRAM: PULSIN.8     PROJECT: PINTST
  NO. OF FIELDS:  3

  FIELD NAME     SCALE FACTOR
     VEL             100
     VAR             100
     DBI             100

  RADAR HEIGHT (KMSL):   1.500
  GATES/SCAN: 120   FIRST GATE (KM): 21.000     GATE SPACING (KM):  0.300
  NYQUIST VELOCITY (M/S): 16.10

  SCAN SUMMARY
   SCAN      ELEVATION      DIRECTION  (+1: CW, -1:CCW)
    1          0.50            -1
    2          1.50             1
    3          2.50            -1
    4          3.50             1
    5          4.50            -1
    6          5.50             1

INTERPOLATION METHOD SUMMARY

  METHOD:  DOPPLER HYBRID WITH OPTIONAL VELOCITY UNFOLDING

  INPUT FIELDS
   NO.   NAME      SCALE FACTOR      INTERPOLATE     RESET VALUE     FOLDING
    1     VE          100.0             YES                          FOLDED
    2     SW          100.0             YES
    3     DI          100.0             YES

  OUTPUT FIELDS
   NO.   NAME      SCALE FACTOR      INTERPOLATION   RESET VALUE     FOLDING
    1     VE          100.0             DIRECT                       UNFOLDED
    2     DZ          100.0             DERIVED          0.00
    3     SW          100.0             DIRECT

  THRESHOLDING
   FIELD: DI         MINIMUM ACCEPTABLE VALUE:    5.00
   NYQUIST (M/S):    16.10

CARTESIAN (.CAR)  VOLUME HEADER     TPOC            INTERPOLATION METHOD: 3
  DATE: 78/ 7/28       TIME: 14: 9: 2--14:10:32     PTS/RECORD:  512
  TAPE: E1677     RADAR: NOAA-C     PROGRAM: TERPOC.1     PROJECT: PINTST
  NO. OF FIELDS:  3
  FIELD NAME      SCALE FACTOR
   VE                 100
   DZ                 100
   SW                 100

  AXIS      MINIMUM (KM)      MAXIMUM (KM)      DELTA (KM)     NO. OF PTS.
   X          -45.00             -5.00            0.50             81
   Y          -30.00             10.00            0.50             81
   Z            2.00             10.00            1.00              9

     AXIS ORDER IS   X  Y  Z

  RADAR HEIGHT (KMSL):   1.500



  (X,Y) LOCATION OF THE RADAR (KM): (   0.00,   0.00)
  ANGLE OF X-AXIS REL. TO NORTH:   90.00


    *****   THIS IS AN EXAMPLE OF USER SUPPLIED TEXT   *****

    THE PRECEEDING INFORMATION IS A REPORT ON ...
      1- INPUT VOLUME IN RADAR SPACE,
      2- INTERPOLATION METHOD PARAMETERIZATION, AND
      3- CARTESIAN SPACE OUTPUT FILE.

            - END OF MESSAGE -
```

Fig. 3. Summary of an interpolated volume as generated by the REPORT command. Information regarding the input data set, Cartesian output file and transformation criteria are presented in this report.

When a text terminal is used, an interrupt (awaiting user response) is initiated after the generation of each subsection, so that the information remains frozen on the screen until it is no longer needed. Similar subsectioning, determined by the maximum number of characters per line, is performed without interruption when displays are disposed to a line printer.

Three symbolic products are currently available:

1) *Digital Display* - Fig. 4a is a digital display of reflectivity data from a 41 x 41 CAPPI plane. The number of digits is selectable and any datum which cannot be properly encoded according to the number of digits specified is represented instead by its sign.

2) *Coded Display* - Fig. 4b is a coded display of the same CAPPI. Individual symbols for each reflectivity estimate are generated according to a user-controlled symbol table. As in the previous display, periods indicate Cartesian estimates below threshold or for which no data exists.

3) *Statistical Summary* - Fig. 4d contains reflectivity field statistics for

a.

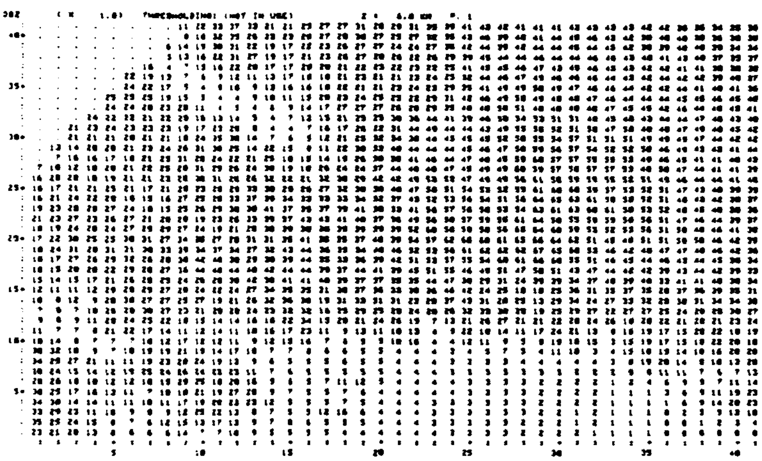

b.

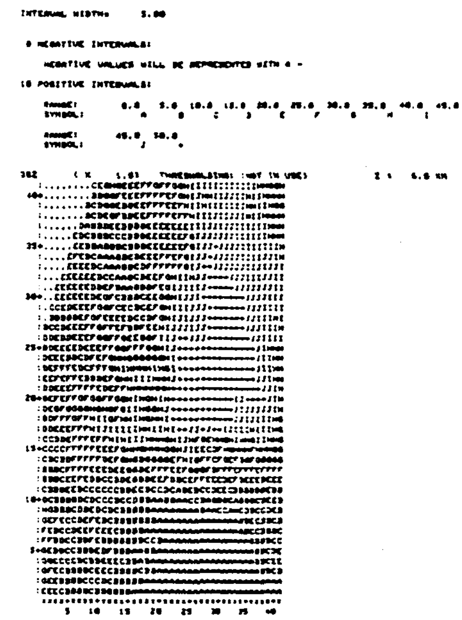

c.

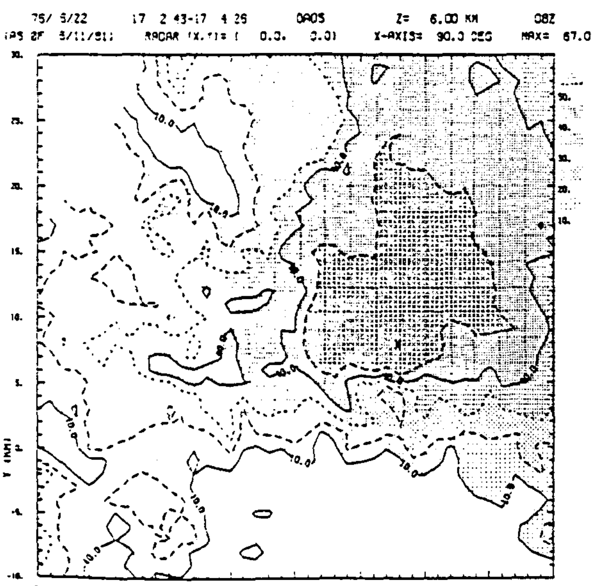

d.

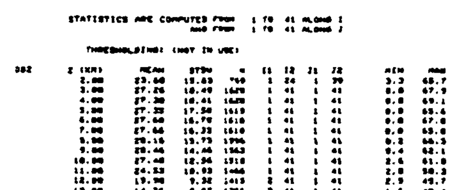

Fig. 4. Sample products generated by the DISPLAY command. In these examples the reflectivity field (dBZ) from a 41 by 41 CAPPI at 6 km is shown. Figure 4a contains a digital display of dBZ values. Periods indicate Cartesian locations below threshold or for which no data exists. Figure 4b contains a coded display, 4c contains a contour/grayscale plot and 4d contains a statistical summary for the entire volume. Annotation describes these displays in further detail.

every CAPPI in the volume. Statistics may be generated for any or all planes and radar fields.

For all presentations, the user is permitted to specify regions of interest and threshold criteria. Whenever digital and coded displays are produced, scaling factors may also be employed.

4.5.2. Graphics displays

These products can only be generated on terminal devices with graphics capabilities. Figure 4c contains a contour/grayscale plot of the same CAPPI presented in the digital and coded displays. Contour levels and grayscale tones may be generated separately or, as in this example, in conjunction with one another. Options permit the selection of a viewing window, contour levels, and annotation features.

More sophisticated displays, such as perspective illustrations of the data, have not been incorporated into the rectification software. Although the effort required to do so would be minimal, it is felt that such products best belong in a separate package designed specifically for the manipulation and display of archived data sets.

5. SUMMARY

The Cartesian rectification package has been operating experimentally for approximately six months. During that time a variety of modifications and embellishments (most of which are described in this manuscript) have been incorporated into the software. As discussed earlier, it is primarily intended for use in the reduction of Doppler radar data. The utility of this software will be examined in the fall of 1981 when it will be enlisted in the analysis of radar data collected during the 1981 CCOPE[1] field season. This interactive package has been developed as a supplement to the batch processing facilities already available on the large NCAR computers through the existing MUDRAS software.

Future plans call for the implementation of an interactive synthesis program and eventually the development of analysis software capable of editing, manipulating, and displaying Cartesian fields interactively. Throughout this effort we shall have a unique opportunity to examine which, if any, radar analysis functions should be performed in batch mode on a large computer and which, if any, belong in an interactive environment.

6. ACKNOWLEDGMENTS

The authors wish to acknowledge the efforts of Ray Bovet in establishing and maintaining the excellent facilities available on the MRS/VAX 11/780 which were used to develop and test the software. We also wish to acknowledge Karen Miller (CSD/NCAR) for her software support in the development of the tape to disk transfer programs and the report generator. Finally we wish to commend Will Garcia for his figure drafting and Carol Brown and Sue Stippich for preparing the manuscript.

[1] CCOPE is an acronym for the Cooperative Convective Precipitation Experiment conducted near Miles City, Montana, during the summer of 1981.

7. REFERENCES

Barnes, S. L., 1980: Report on a meeting to establish a common Doppler radar data exchange format. *Bull. Amer. Meteor. Soc.*, *61*, 1401-1404.

Brown, B. C., and V. F. Borgogno, 1980: A laboratory radar display system. *Preprints 19th Conf. on Radar Meteorology*, Miami Beach, Amer. Meteor. Soc., 272-285.

Burgess, D. W., L. D. Hennington, R. J. Doviak and P. S. Ray, 1976: Multimoment Doppler display for severe storm identification. *J. Appl. Meteor.*, *15*, 1302-1306.

Glover, K. M., 1980: On the automation of weather radar information for air and ground operations. *Preprints 19th Conf. on Radar Meteorology*, Miami Beach, Amer. Meteor. Soc., 118-124.

Kohn, N. M., A. L. Johnston and C. G. Mohr, 1978: MUDRAS - Multiple Doppler radar analysis system. *NOAA Tech. Memo. ERL/WPL-35*, Wave Propagation Laboratory, Boulder, 170 pp.

Miller, L. J., and R. G. Strauch, 1974: A dual-Doppler radar method for the determination of wind velocities within precipitation weather systems. *Remote Sens. Environ.*, *3*, 219-235.

Mohr, C. G., and R. L. Vaughan, 1979: An economical procedure for Cartesian interpolation and display of reflectivity factor data in three-dimensional space. *J. Appl. Meteor.*, *18*, 661-670.

_____ and _____, 1980: A proposed algorithm for the real-time interpolation of reflectivity factor data in three-dimensional space. *Preprints 19th Conf. on Radar Meteorology*, Miami Beach, Amer. Meteor. Soc., 294-300.

Mueller, E. A., 1977: Statistics of high radar reflectivity gradients. *J. Appl. Meteor.*, *16*, 511-513.

Pytlowany, P. J., F. P. Richards and M. D. Hudlow, 1979: GATE radar CAPPI derivation for three-dimensional reflectivity analysis. *NOAA Tech. Memo. EDIS-27*, Environmental Data and Information Service, Washington, D. C., 28 pp.

Ramsden, J., M. R. Johnson, R. G. Humphries and B. L. Barge, 1976: Interactive computer-generated displays of radar data. *Preprints 17th Conf. on Radar Meteorology*, Seattle, Amer. Meteor. Soc., 468-473.

Ray, P. S., and C. Ziegler, 1977: De-aliasing first-moment Doppler estimates. *J. Appl. Meteor.*, *16*, 563-564.

Serafin, R. J., and R. M. Lhermitte, 1980: Meteorological radar developments in the 1980's. *Prep. 19th Conf. on Radar Meteor.*, Miami Beach, Amer. Meteor. Soc., 679-685.

Wright, T., 1978: NCAR Graphics software (Fourth Preliminary Edition). Prepared by the Atmospheric Technology Division of the National Center for Atmospheric Research, Boulder, Colorado.

Reprinted from JOURNAL OF ATMOSPHERIC AND OCEANIC TECHNOLOGY, Vol. 3, No. 1, March 1986
American Meteorological Society

The Merger of Mesoscale Datasets into a Common Cartesian Format for Efficient and Systematic Analyses

CARL G. MOHR, L. JAY MILLER, ROBIN L. VAUGHAN AND HAROLD W. FRANK

National Center for Atmospheric Research, Boulder, CO 80307*

(Manuscript received 3 March 1985, in final form 8 July 1985)

ABSTRACT

During the 1981 summer season within a 70 000 km^2 area surrounding Miles City, Montana, researchers from approximately twenty institutions participated in the Cooperative Convective Precipitation Experiment (CCOPE). The measurements collected during this project comprise one of the most comprehensive datasets ever acquired in and around individual convective storms on the high plains of North America. Principal data systems utilized during CCOPE included 8 ground-based radars (7 of which had Doppler capability), 12 instrumented research aircraft, and a network of 123 surface stations.

A major data processing goal has been to combine these independently acquired mesoscale measurements into a numerical description of observed atmospheric conditions at any point in time. Using the CCOPE data archive as an example, this paper describes the procedures used to reduce these high resolution observations to a common spatial and temporal framework. The final product is a digital description of the environment similar to that employed by most modelers—a three-dimensional Cartesian coordinate system containing fields that represent the instantaneous state of the atmosphere at discrete times across the period of interest. A software package designed to facilitate the construction and analysis of these composite data structures will also be discussed.

1. Introduction

One of the fundamental purposes of the Cooperative Convective Precipitation Experiment (CCOPE) was to assemble a comprehensive dataset on convective clouds using the fullest possible array of available meteorological measurement systems. Efforts were focused on acquiring and later reconstructing complete descriptions of the atmospheric conditions related to three phases of thunderstorm activity: prestorm, early storm, and mature storm. During the three-month period of operation, approximately 300 billion bits worth of information were recorded on computer tape for later reduction and analysis. A complete summary of the 1981 CCOPE field program along with a list of all the organizations and individuals responsible for the various instrument systems is provided by Knight (1982).

The challenge from a data processing standpoint was to reduce this large body of measurements as efficiently as possible and to make it accessible for analysis by any and all participants. A considerable number of software systems have been developed for the purpose of compositing meteorological observations. Most are designed to be used interactively on minicomputers and each can be identified with respect to some area of specialization. PROFS (Reynolds, 1982) assimilates real-time information for use in regional-scale forecasting; McIdas III (Suomi et al., 1983) and GEMPAK (desJardins and Petersen, 1985) provide excellent facilities for the analysis of conventional and satellite measurements; PCDS (Treinish and Ray, 1985) processes climatological datasets; and RADPAK (Heymsfield et al., 1983) contains highly accurate algorithms for remapping satellite data and edited radar observations to common display coordinates.

The procedures and software described in this article have been developed for use in a batch environment and their primary purpose is to reduce high resolution measurements from different field observation systems to a large multidimensional data structure (>100 000 grid locations). The batch computing environment at NCAR consists of two Cray-1A processors, an AMPEX terabit mass storage device, and a Dicomed camera system with 4096^2 resolution. This environment is ideal for processing data from mesoscale field experiments such as CCOPE for the following reasons:

Accessibility. A large segment of the atmospheric community has access to the computing facilities at NCAR and all the datasets and programs are readily available on the system.

Computing power. The vectorizing architecture and speed of the Cray-1A processor permits the use of multidimensional editing and analysis algorithms that cannot be supported on smaller machines.

Throughput. Multiple datasets representing hours of observations can be analyzed by a single job.

* The National Center for Atmospheric Research is sponsored by the National Science Foundation.

Hard copy capability. Publication quality displays can be produced in large quantities quickly and inexpensively.

The algorithms utilized for reducing and analyzing these field measurements are, for the most part, well known and are documented in the literature. Our strategy has been to organize them together in a fashion so that major decisions regarding the final form of the composite storm description can be postponed until reports from all sources have been converted to Cartesian coordinates. By way of illustration, a unified digital description of a mature storm observed during CCOPE on 1 August 1981 at 1640 local time will be constructed from independent Doppler radar, aircraft, and surface instrument network (i.e., mesonet) measurements. A software package called CEDRIC that contains a comprehensive set of analysis tools for manipulating the information in these data structures will also be discussed.

2. Data collection and archival

The successful reconstruction of a mesoscale event from multiple data sources is directly related to how well the information is organized. Analysis efforts in the past have been needlessly complicated by the diversity of formats produced by independent instrument systems. In recognition of this problem common archive formats for Doppler radar and mesonet observations were informally adopted by the meteorological community at the beginning of the decade (Barnes, 1980). These formats were utilized in CCOPE, and as a direct result we were able to avoid costly reformatting and maintenance of redundant software systems for those datasets. Similar benefits were realized for the set of airborne measurements through the use of generalized input routines.

Figure 1 contains a schematic diagram depicting a typical CCOPE mature storm study and the roles of the principal data systems in the investigation. A detailed summary of the entire archive along with the technical specifications of each system can be found in the 1981 CCOPE Data Inventory (1982).

a. Radar

Seven Doppler radars participated in coordinated scanning of the target volume while an eighth conventional radar maintained surveillance over the entire region. Each Doppler radar recorded reflectivity and radial velocity and, at two of the sites, dual wavelength reflectivity measurements were acquired at wavelengths of 10 and 3 cm. Approximately 2–4 min were required to scan a mature storm, and during that time each radar collected upwards of one million individual pulse volume samples. The life cycle of most storms was embodied in 10–20 of these coordinated three-dimensional scans. In accordance with the CCOPE operations

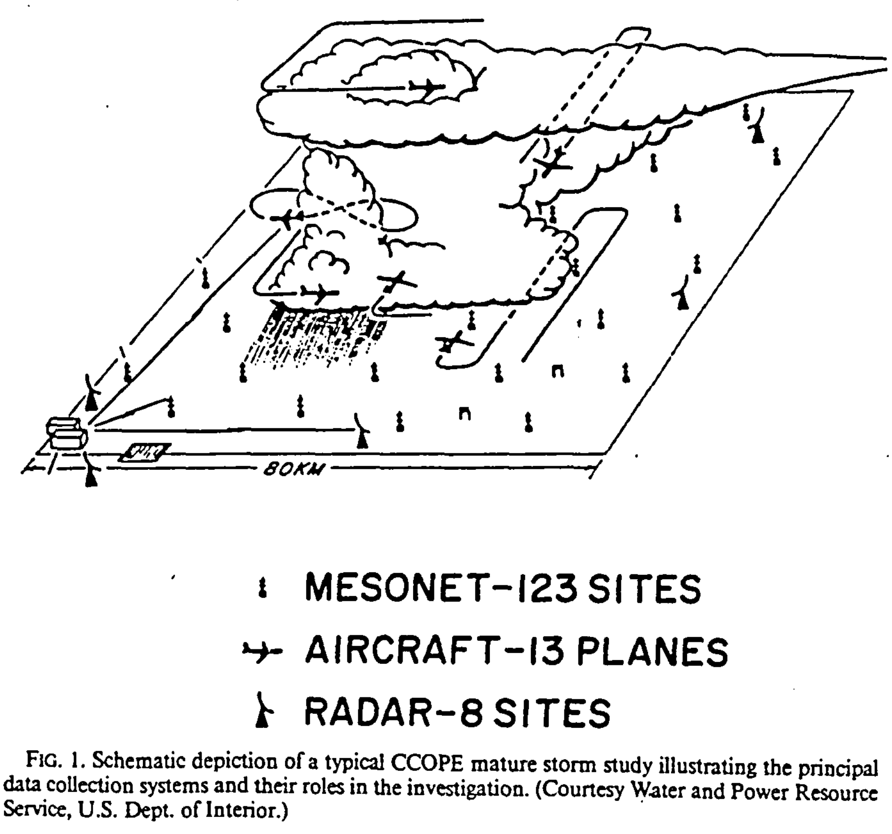

FIG. 1. Schematic depiction of a typical CCOPE mature storm study illustrating the principal data collection systems and their roles in the investigation. (Courtesy Water and Power Resource Service, U.S. Dept. of Interior.)

plan (1981), the organizations responsible for the individual radars provided their data in the common Doppler radar exchange format described by Barnes (1980). An obvious benefit of this requirement was that it shifted the burden of reformatting from the analysts to the suppliers of the data. As a result, the problems associated with imposing a logical structure onto the volume scans were solved by those persons who were best equipped to deal with the idiosyncrasies of their respective datasets. In general, this "universal radar format" is an excellent medium for the archival and exchange of radar space information. Although inconsistencies were later detected in some of the tapes, appropriate corrections could usually be made in the access software. Only on rare occasions was it necessary to rewrite any of the original archive tapes.

b. *Aircraft*

As many as 12 instrumented aircraft ranging from a motorless Schweizer 2-32 sailplane to a multi-engine Convair 990 jet collected in situ measurements throughout various regions of the thunderstorm. Typical missions included coordinated updraft mapping near cloud-base (propeller-driven aircraft), penetrations into developing cloud turrets (propeller and sailplane), and systematic probing of the storm top and surrounding environment (jet aircraft). Independent onboard data acquisition and display systems generated digital time series of pressure, temperature, moisture, wind, and hydrometeor occurrences along with related navigational information. These reports were recorded directly onto magnetic tape at a basic rate of one sample per second. The duration of most research flights was from two to four hours.

The aircraft data base, like the radar data base, consisted of reduced and calibrated measurements archived on magnetic tapes that were provided by the same institutions that collected the data. Since no "common format" existed for aircraft data, the programs that read these tapes had to be made flexible enough to accommodate time series reports from any source. The program best exemplifying this particular approach is the GENPRO processor (Lackman and Friesen, 1983) which was used to generate standard plots of common parameters for all participating aircraft.

c. *Mesonet*

A fixed network of 123 automated surface stations was deployed over a region 120 km on a side. Ninety-six of these stations (PROBE)[1] were spaced at 20 km intervals over the entire area while 27 sites (PAM)[2] were nested within the larger array at 7 km intervals in a more densely-spaced network whose dimensions were 60 by 50 km. The PROBE system telemetered 5 min averages of pressure, temperature, moisture, and wind via satellite to a central computer in Denver, Colorado where the reports were transferred to magnetic tape for subsequent processing. PAM stations transmitted similar information at 1-min resolution via radio link to a nearby communications center, which was responsible for real-time display and archival of the measurements. Except for an occasional instrument failure, both systems operated 24 hours a day.

Magnetic tapes containing measurements from the PROBE (5 min) and PAM (1 min) networks were provided separately in the common mesonet exchange format. By agreement no editing was performed on these archive datasets other than to identify events associated with instrument malfunctions. Data from the two networks were reassembled on the mass storage system at NCAR and reports from all 123 sites were subsequently calibrated using systematic procedures developed by Wade and Engle (1985).

The existence of common formats (radar and mesonet) and the design of flexible input algorithms (aircraft) meant that only one access routine was needed to read any or all reports from a given dataset. As a result, basic archival tasks specific to each system such as intercomparison of independent instruments, incorporation of improved calibrations, and the generation of standard graphic products were all greatly simplified. For example, if an additional display of airborne measurements was requested, the changes only had to be made in a single program instead of a dozen (one per aircraft) potentially different places! Similar savings in software development and maintenance costs were realized for the radar and mesonet systems.

3. Building the composite data structure

Once well-calibrated, internally consistent, and complete datasets have been constructed for each of the systems, the reports can be remapped to Cartesian coordinates. Identified with each grid location are all available meteorological parameters, or fields, describing the atmospheric parcel that it represents in space and time. Fields of interest include pressure, temperature, moisture, reflectivity, and the (u, v, w) components of the vector signifying the instantaneous motion of the parcel. The advantages of this destination data structure are obvious. It is simple enough so that fields from any measurement system can be incorporated and the data at any location can be readily accessed, manipulated, altered, and displayed.

Figure 2 illustrates our data processing scheme. Reports from the radar, aircraft, and mesonet datasets are converted to the destination Cartesian coordinate structure using specialized interpolation routines called SPRINT, ACANAL, and SMANAL, respectively.

---

[1] Portable Remote OBservations of the Environment system operated by the Montana Department of Natural Resources and Conservation.

[2] Portable Automated Mesonet system operated by the Atmospheric Technology Division of the National Center for Atmospheric Research.

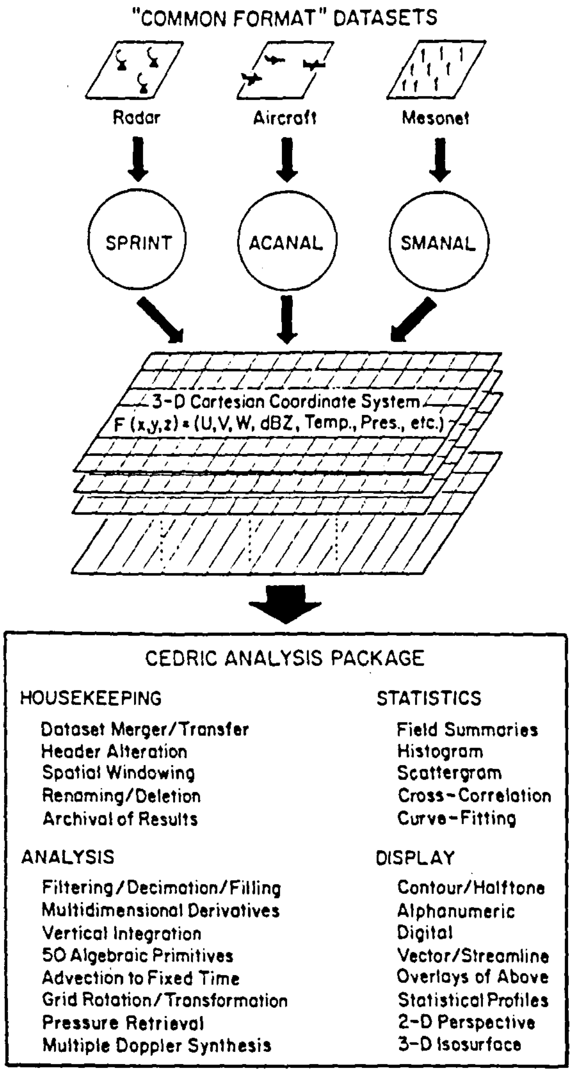

FIG. 2. Processing diagram illustrating the flow of information from the common format datasets to the multi-parameter Cartesian coordinate structure. Specialized transformations specific to each dataset perform the remapping. Additional manipulation of the Cartesian space reports is conducted using CEDRIC.

These remapping procedures utilize existing techniques and have been designed to provide the user with a broad range of options for preconditioning the input reports, parameterizing the transformations, and examining the interpolated fields. Researchers may freely manipulate these options in order to generate gridded products that satisfy their personal preferences and scientific requirements. Unlike some software systems (e.g., Koch et al., 1983) no constraints are imposed on the selection of values affecting either the weighting function or the placement and resolution of the output grid.

Each interpolation procedure is also capable of transferring input reports without alteration to the nearest destination Cartesian grid location. This additional capability has proven useful for making point comparisons of independent observations such as radar parameters versus in situ aircraft measurements. These kinds of studies and other analyses are performed on the resultant Cartesian data structures using the CEDRIC (Custom Editing and Display of Reduced Information in Cartesian Space) software package.

a. Radar

Ground-based radar measurements are converted to a three-dimensional Cartesian coordinate system by SPRINT, using a successive linear interpolation algorithm described by Mohr and Vaughan (1979) and Mohr et al. (1981). Each field selected for interpolation is independently converted using original radar measurements from the four beams (two on either side, above and below) surrounding each destination Cartesian location in space. This procedure is illustrated in Fig. 3. The open dot indicates a destination grid point. Solid dots appear at its projection point along an arc of constant range on adjacent elevation planes k and $k + 1$. Radar space input reports are denoted by the corners of the box. Estimates at each projection point are computed using bilinear interpolation—first along range and second across azimuth. A final linear interpolation is performed along elevation using the estimates at these projection points in order to produce a resultant value at the Cartesian location.

Whenever there is an insufficient number of reliable (that is, not flagged as missing or "bad") radar space values to perform a bilinear interpolation at the projection point on an elevation plane, the closest input report whether it be "good" or "bad" is selected instead. If either or both elevation planes have been assigned a closest point value, the Cartesian location will receive its final estimate from the nearer of the two. This is done to ensure that "noisy" data are replicated without significant alteration in the weak signal regions, particularly along the edges of the storm.

When using this hybrid technique, the user must specify a maximum distance past which a "closest" point value should not be trusted as being represen-

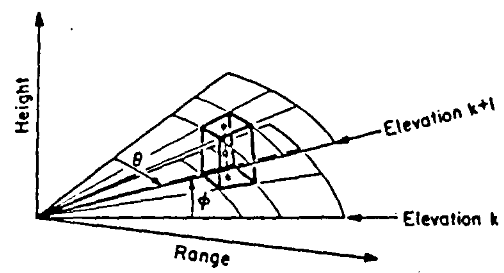

FIG. 3. Illustration of sampling volume used for Cartesian transformation of radar data. Volume is defined by the eight adjacent radar space samples surrounding a Cartesian location in space. Solid dots indicate projection points of the Cartesian grid location (shown as an open dot) on consecutive elevation scan planes k and $k + 1$. The quantity θ is the angular direction along azimuth and Φ is the elevation angle above the horizon (after Mohr et al., 1981).

tative. If this distance is exceeded along any one axis (range, azimuth, or elevation), the Cartesian location will be flagged as missing. The user may also attempt to equalize the spatial resolution in the range and azimuth directions by requesting that a fixed number of gates be averaged along each beam. Certain field types receive specialized treatment in SPRINT:

1) *Velocity.* The finite interval over which a uniformly pulsed Doppler radar measures radial velocities is from $-V_n$ to $+V_n$ where V_n is the Nyquist velocity expressed as a function of the pulse repetition frequency (PRF) and transmitted wavelength (λ):

$$V_n = (\mathrm{PRF})\lambda/4. \quad (1)$$

Whenever the true velocity exceeds the magnitude of the Nyquist value for a given radar the measured velocity is ambiguous or "folded." Velocity fields are conventionally unfolded one elevation plane at a time in radar space using, for example, the interactive Doppler editing software (IDES) developed by Oye and Carbone (1981). An alternative technique proposed by Miller et al. (1985) demonstrates how unfolding can instead be performed in Cartesian space provided that the input velocities contributing to the estimate at each grid location are forced into the same unambiguous Nyquist interval during the interpolation. SPRINT has been designed to support either approach.

2) *Quality.* Whenever a velocity field is interpolated, SPRINT generates a corresponding field called QUAL that contains a measure of the quality of the Cartesian space velocity estimates. This nondimensional parameter is derived at every grid location using:

$$Q(x, y, z) = 1 - \mathrm{var}(U)/(V_n^2/3) \quad (2)$$

where var(U) is the spatial variance of the unfolded input velocities contributing to the estimate. The discriminating properties of Q are described by Miller et al. (1985).

3) dBZ and dBM. Fields whose estimates are in logarithmic units may be optionally converted to linear units before any calculations are performed. If no reflectivity (dBZ) field is present, it may be derived from the received power (dBM).

4) *Time.* SPRINT does not adjust for storm motion when it remaps radar space reports to Cartesian coordinates. Instead, the time in seconds relative to the beginning of the scan is calculated from the header information associated with the four beams surrounding each Cartesian grid location and saved as an additional parameter in a field called TIME. The presence of this field enables us to interpolate observations from the individual radars without having to deal with the problem of storm advection at this step of the data reduction. Although some accuracy is lost (the four beams contributing to each grid estimate may be as much as 15 s apart), advecting in Cartesian space offers more flexibility in the later stages of the analysis, particularly when determining which analysis time and combination of radars produces the most representative wind field.

SPRINT provides a description of the input and output characteristics of every volume that it processes along with a statistical summary of the interpolated fields.

b. *Aircraft*

Aircraft measurements acquired at a constant altitude are remapped by ACANAL to a two-dimensional Cartesian grid that is structurally compatible with the synthesized radar observations. Complete details of the procedure are given in Fankhauser et al. (1985). An important region of the storm that contains insufficient reflectors to be adequately observed using radar is the inflow sector just below cloud base. Constant altitude flight patterns designed to map this region were flown every 15 to 20 min by one or more research aircraft. Figure 4a contains the ground-relative track flown by an instrumented Beechcraft Queen Air (304D) during a 16 min period of inflow observation on 1 August 1981. The symbol (+) is plotted at 12-s intervals along the track. Circles appear every whole minute. In order to generate an instantaneous picture of the region under investigation, it is necessary to select a fixed analysis time (1640 MDT) and to reposition each 1-s input report either forward or backward in space with respect to the moving storm. The result of this time normalization using the observed storm motion of 263° at 8.3 m s^{-1} is given in Fig. 4b. Vectors emanating from the repositioned track denote direction and speed of the ground-relative horizontal (u, v) winds measured by the aircraft.

Given an airplane ground speed of ~80 m s^{-1}, the spatial separation of the 1-s reports is approximately 80 m. Information at this resolution is considerably denser than both the intertrack distances (2.5 km) and the typical spacing of the Cartesian grid locations (1 km). These differences are resolved by applying a low pass filter to the time series of all original measurements and extracting the filtered samples at intervals consistent with those larger scales for input to the interpolation algorithm. In this case a 12-s interval was chosen which corresponds to a distance of ~1 km. The locations of these input reports are denoted by the (+) symbols appearing in Fig. 4a, b.

The Barnes objective analysis scheme (Barnes 1964; 1973) is utilized for interpolating the irregularly spaced input values to Cartesian coordinates. The weight assigned to an input datum at distance D from a specific grid location is given by the exponential function:

$$W = \exp[\ln(c)(D^2/R^2)], \quad (3)$$

where R is a user-selectable "radius-of-influence" at which W is equal to c. All input values are weighted

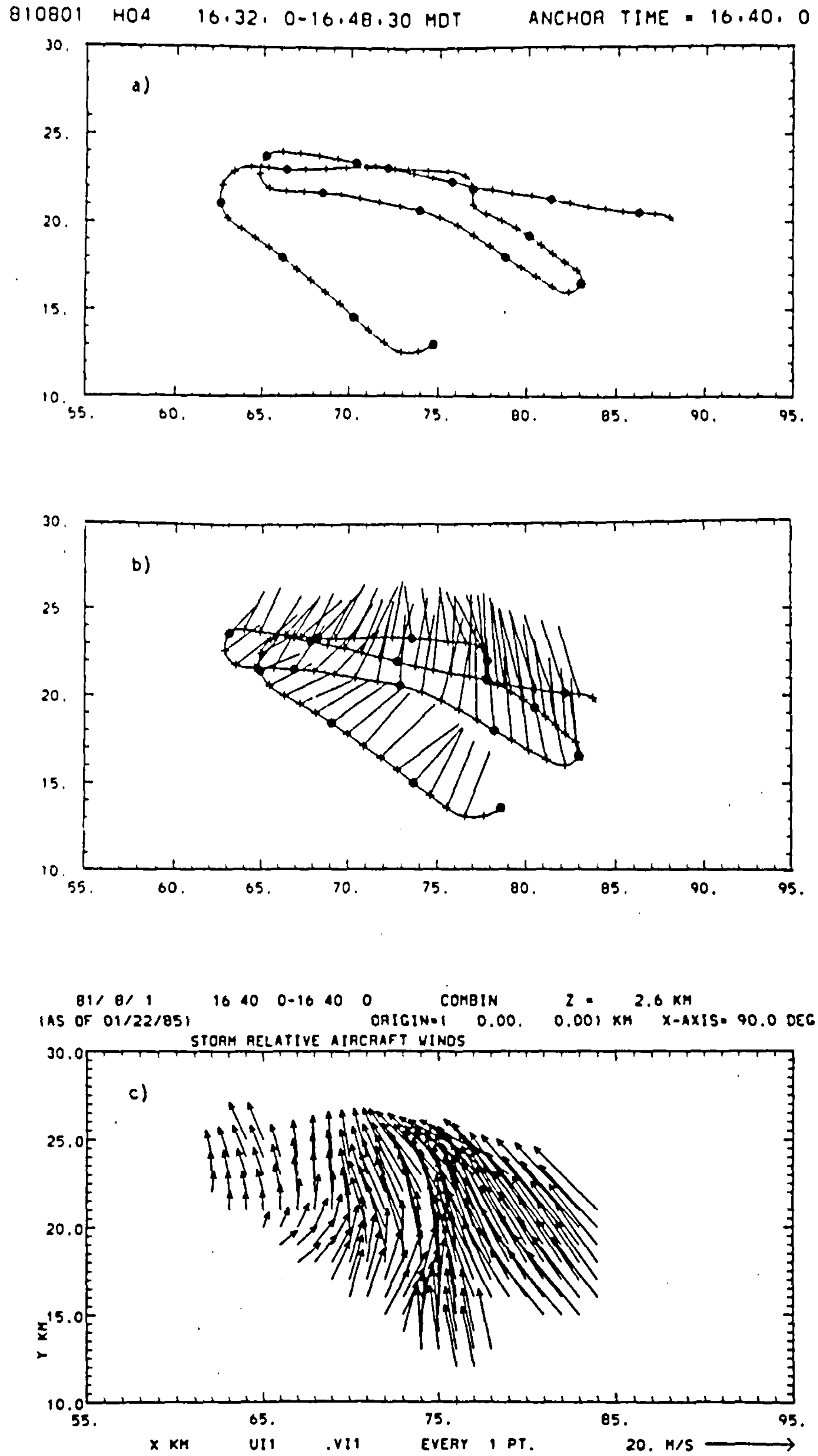

FIG. 4. (a) Ground relative flight track for NCAR Queenair Hiplex-4 (H04) flown near cloudbase (2.6 km MSL) in the inflow sector of a large thunderstorm on 1 August 1981 during the indicated time period. Track begins at (x, y) grid location (75, 13). Circles indicate 1 min positions. (b) Flight track in (a) repositioned with respect to observed storm motion of 263° at 8.3 m s^{-1} and an analysis time of 1640 MDT. Horizontal wind vectors plotted at 12 s intervals along the track are ground relative and are scaled so that 5 km = 20 m s^{-1}. (c) Storm relative horizontal airflow interpolated to a 1-km resolution grid using input from (b) and subtracting out the storm motion. Reference vector appears at lower right. Axes are labeled in km relative to the primary research radar, CP-2, located near Miles City, Montana (after Fankhauser et al., 1985).

using this relationship and the resultant normalized estimate is assigned to the grid location. The constant c has been set to 0.1 so that R uniquely determines the shape of the function. Using simulated data fields Caracena et al. (1984) have shown that the ideal value for λ_0 in the generalized Gaussian weighting function

$$W = \exp[-D^2/\lambda_0^2] \tag{4}$$

can be determined by:

$$\lambda_0 = 1.366\Delta X,$$

where ΔX is the spacing of the input reports. Accounting for the natural logarithm of 0.1 which we have incorporated into our formulation, this result translates to an optimal value of $R \approx 0.9\Delta X$ in Eq. (3). Since the distance between input reports is almost never uniform, the coarsest spatial resolution in any direction through the advected data generally determines our choice of ΔX and subsequently R as well. Another user-selectable parameter is the number of iterative improvement passes to apply to the grid of interpolated estimates. Each pass reduces the difference between the original input values and their Cartesian space counterparts by applying the same remapping function to the current set of residuals.

The resultant horizontal wind field is illustrated in Fig. 4c. An influence radius of 3 km with 5 iterative passes was used to perform the remapping, and storm relative vectors have been computed by subtracting the storm motion vector from the interpolated (u, v) components. Interpolated fields that are routinely produced from constant altitude aircraft observations include the components of air motion (u, v, w), pressure, temperature, and mixing ratio. Display products generated by ACANAL include profiles of the input time series (filtered and unfiltered) as well as two-dimensional plots (as in Fig. 4) of the constant altitude observations before and after interpolation.

c. *Mesonet*

Surface mesonet reports are remapped by SMANAL to a structurally compatible two-dimensional Cartesian grid in another region of the storm where the radar cannot provide accurate meteorological observations—near the ground. The mesonet input dataset consists of average values from all 123 sites at a uniform resolution of 5 minutes. Figure 5a contains a map showing every operational station inside a 90 by 90 km section of the surface network on 1 August 1981. Data from these sites are to be interpolated to a Cartesian grid with 1 km spacing whose boundaries are delineated by the dashed box in the center of the figure. Figure 5b shows the relocated horizontal wind measurements that are used as input to the remapping. In order to increase the number of input measurements and to preserve any transient features in the airflow that happen to be situated between stations at the analysis time (1640 MDT), provisions are made for the inclusion of as many as six additional off-time reports. This advective procedure is similar to that prescribed by Barnes (1973) where the relative weight of the relocated reports may, at the analyst's discretion, be lessened as a function of time. In the example shown, fully-weighted observations from 1635 and 1645 MDT have been displaced downstream and upstream respectively according to the same observed storm motion (from 263° at 8.3 m s^{-1}) used to reposition the aircraft track.

The same formulation (Eq. 3) that was utilized for interpolating the aircraft observations is also applied to the input surface mesonet reports. Optional variations that are available to the analyst for dealing with the unevenly-spaced network include:

(i) specifying two different radii-of-influence—one for the PROBE network and the other for the more densely spaced region embedded within it;

(ii) designating a minimum and maximum radius-of-influence and permitting the algorithm to compute a value between the two at each individual grid location based upon the spatial distribution of the surrounding input reports; and

(iii) removing all the PAM sites from the interpolation in order to work with a network of stations (PROBE) that is uniformly spaced.

For the remapping demonstrated in Fig. 5, all sites were included and a fixed radius of 25 km with two iterative passes was used in order to maintain uniform resolution across the entire output grid. Although there is a considerable loss of detail in the western half of the network, the position of the storm in our example required that we compromise the analysis with this seemingly large radius-of-influence so that the surface observations could be remapped to the area shown without any distortion effects in the data sparse regions. The results of interpolating the horizontal wind field (depicted in Fig. 5b) and subtracting out the storm motion vector are presented in Fig. 5c. Every third vector is plotted. The pressure, temperature, and moisture fields are routinely generated in a similar fashion. The surface topography field shown in Fig. 5d is constructed using a bilinear interpolation method, which ensures that the height above sea level at a given (x, y) location will be identical on all output grids created by the program. Displays produced by SMANAL include the preceding figures as well as contour plots and statistical summaries of the interpolated fields.

All of the software described in this section has been developed for use in batch mode on the Cray-1A computer system at NCAR. Two of the programs, SPRINT and CEDRIC, have also been adapted for interactive use on Digital Equipment Corporation VAX minicomputers with VMS operating systems. User guides are available containing all the necessary information for understanding and running these programs, including sample decks and dataset descriptions. The lo-

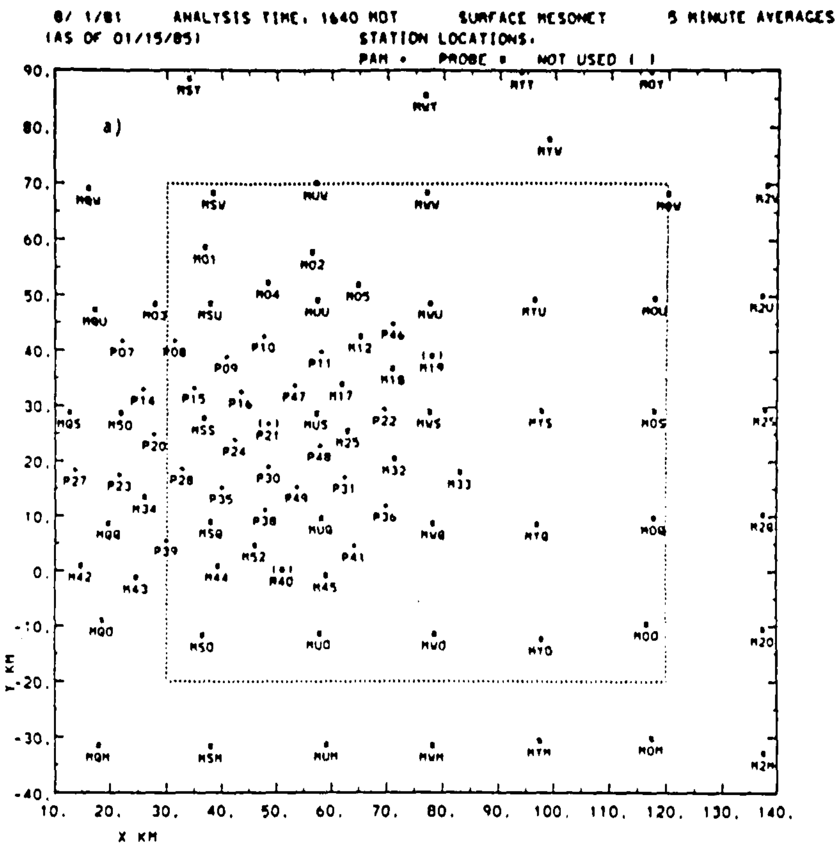
8/ 1/81 ANALYSIS TIME, 1640 MDT SURFACE MESONET 5 MINUTE AVERAGES
(AS OF 01/15/85)
STATION LOCATIONS:
PAM • PROBE * NOT USED ( )
a)
Y KM
X KM

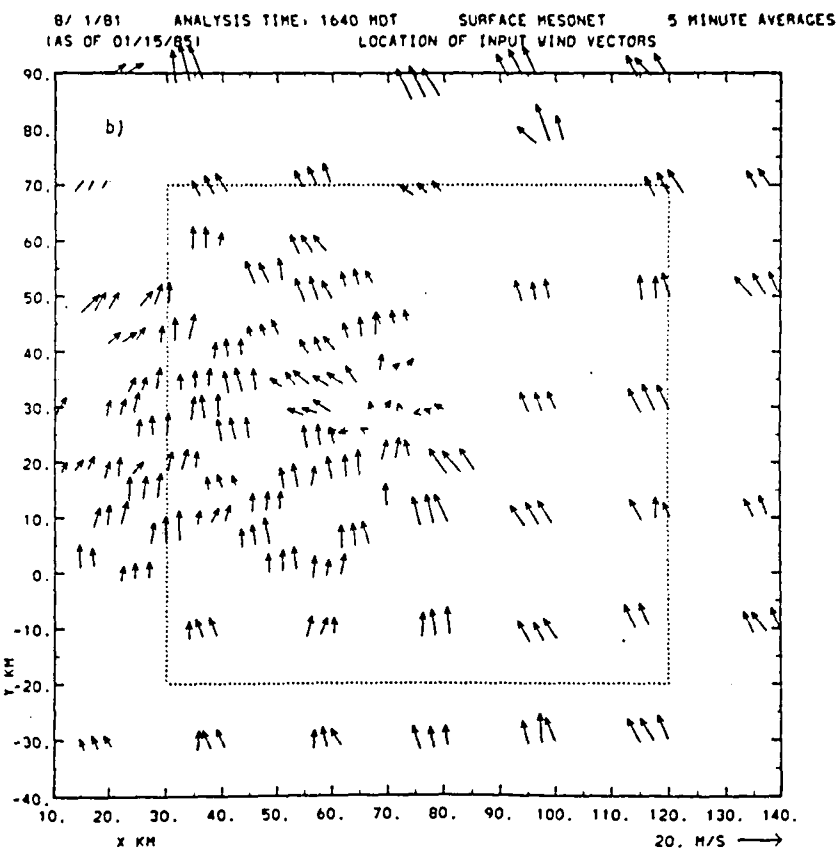
8/ 1/81 ANALYSIS TIME, 1640 MDT SURFACE MESONET 5 MINUTE AVERAGES
(AS OF 01/15/85)
LOCATION OF INPUT WIND VECTORS
b)
Y KM
X KM
20. M/S

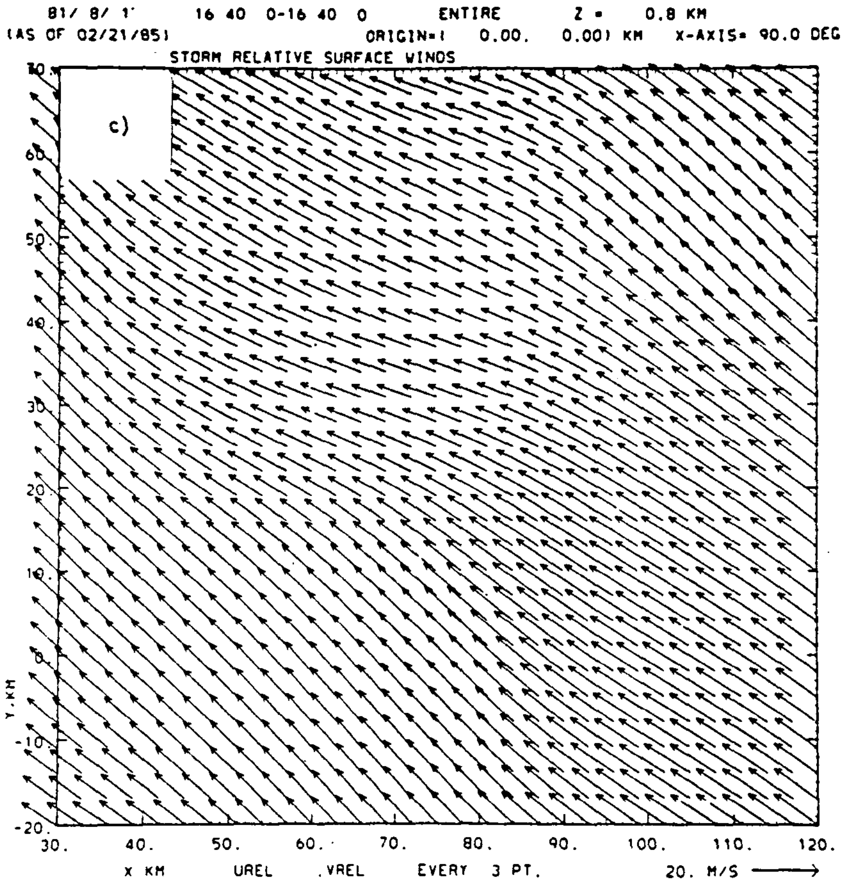
81/ 8/ 1 16 40 0-16 40 0 ENTIRE Z = 0.8 KM
(AS OF 02/21/85) ORIGIN=(0.00, 0.00) KM X-AXIS= 90.0 DEG
STORM RELATIVE SURFACE WINDS
c)
Y KM
X KM UREL , VREL EVERY 3 PT.
20. M/S

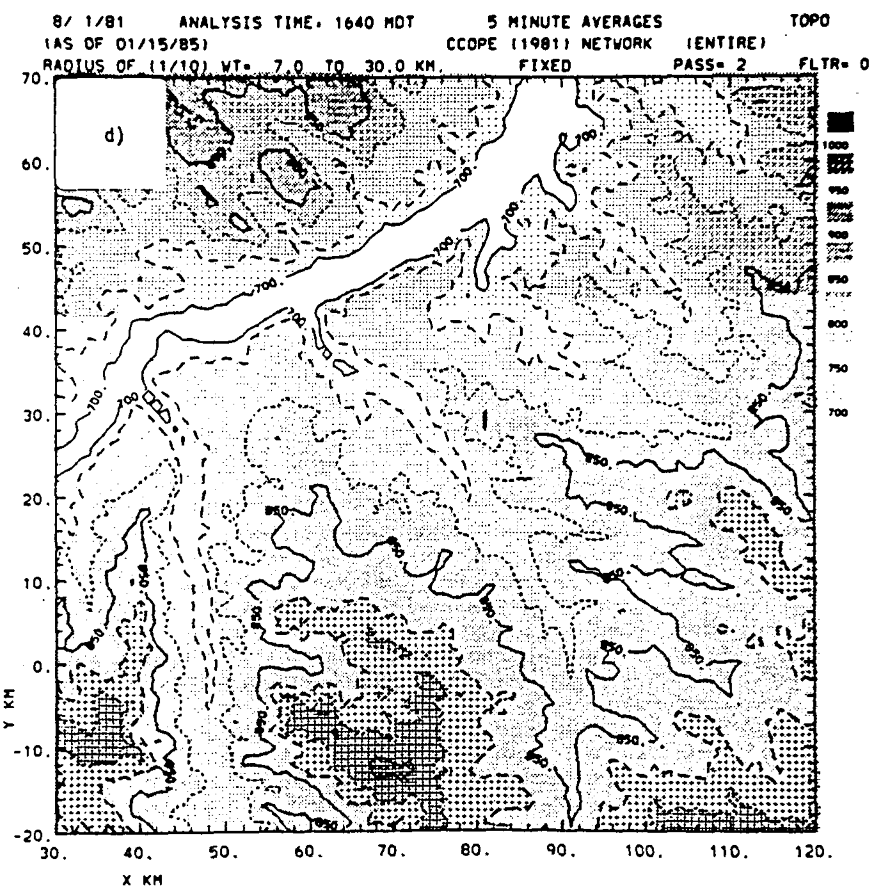
8/ 1/81 ANALYSIS TIME, 1640 MDT 5 MINUTE AVERAGES TOPO
(AS OF 01/15/85) CCOPE (1981) NETWORK (ENTIRE)
RADIUS OF (1/10) WT= 7.0 TO 30.0 KM, FIXED PASS= 2 FLTR= 0
d)
Y KM
X KM

cation, size, axes spacings, and contents of the Cartesian coordinate system may be arbitrarily defined by the user as long as the subsequent dimensions of the structure do not exceed (127 × 127 × 63) and that it does not contain more than 25 interpolated fields.

4. Analyzing the composite data structure

The CEDRIC analysis package contains a comprehensive set of commands for combining, editing, analyzing, and displaying the interpolated data fields. Many of the concepts embodied in CEDRIC had their origins in the MUDRAS (Multiple Doppler Radar Analysis System) software developed by Kohn et al. (1978). Virtually all of the operations are multidimensional and may be performed on any subset of the data with either the x, y, or z coordinate held fixed. Results can be archived at any stage of the analysis.

In the early stages of analysis when an overall strategy is still being developed for investigating an unfamiliar dataset, the interactive version of the program can be an invaluable aid. However, once the strategy has been established it becomes far more expedient to move from the minicomputer to a large batch processing environment. This is particularly true when dealing with datasets from CCOPE and other large mesoscale field experiments where the sheer bulk of information readily overwhelms the capacity of anything less than a supercomputer such as the Cray-1A at NCAR and its supporting facilities. With this in mind, our discussion of CEDRIC proceeds in the context of a batch environment where the data processing functions described below are most often used.

The batch mode command syntax of CEDRIC was designed to be as simple as possible. Commands consist of 80 character card image formats beginning with a keyword starting in column 1. Each card image is divided into 10 (8-col) groups referred to as P1 through P10. The keyword always occupies P1. Groups P2–P10 contain parameters relevant to the command. Commands are processed in the order in which they appear and may be repeated as often as desired. Default values (given in the user documentation) are used whenever a required parameter is left blank or if the information supplied is erroneous.

Any sequence of CEDRIC commands which must be repeated more than once during a run can be defined as a separate entity and subsequently executed using a single statement. Symbolic names can be used in place of the parameters in these command sequences and replaced with appropriate values just prior to execution. This facilitates the construction of commonly utilized procedures which, with a few minor alterations, can operate on multiple datasets in the same run. User-supplied comments may appear anywhere in the deck so long as they are bracketed by special delimiting statements. This construct is particularly useful for temporarily de-activating certain procedures without having to remove them from the command stream.

The remainder of this section contains a description of the principal functions available to the analyst in the CEDRIC software.

a. Retrieval and archival of Cartesian datasets

CEDRIC reads an existing Cartesian dataset from some external medium (disk, tape, or mass store) into the active workspace where the contents of the dataset can be altered and displayed. The active workspace takes on the spatial characteristics of the input volume most recently acquired unless the destination coordinates have been predefined by the user. Whenever a predefined Cartesian structure exists the input dataset is mapped to the user-specified coordinates so long as the two systems have grid locations in common. Missing data flags are supplied at destination locations that do not exist in the input volume and transferred reports that have no home in the target coordinates are discarded. After a Cartesian volume has been read into the active workspace, additional fields may be brought in from other datasets residing on external media. It is through the use of these procedures that complementary observations from the aircraft and mesonet systems are merged together with the Doppler radar products. Once the active workspace has been established, a three-dimensional rectangular region may be designated through which all reports will be accessed. This permits all algebraic operations to be performed on a subsection of the current (x, y, z) grid without disturbing the surrounding values and for displays to be generated on any coordinate background. The contents of the active workspace may be written to external storage in the same standard format as the input datasets at any stage of the analysis.

FIG. 5. (a) Surface mesonet sites contributing input measurements to the Cartesian space remapping on 1 August 1981 at an analysis time of 1640 MDT. Crosses and asterisks mark the locations of PAM and PROBE sites, respectively.
(b) Input horizontal wind reports from 1635, 1640, and 1645 recording times repositioned with respect to storm motion of 263° at 8.3 m s^{-1}.
(c) Storm relative horizontal winds interpolated to a 1-km grid with storm motion removed. Boundaries of this grid correspond to the dashed box shown in the interiors of (a) and (b).
(d) Surface topography in meters MSL mapped to the same 1 km grid as depicted in (c). Contours are drawn every 50 m and computer generated gray-scale shading has been added for emphasis. The Yellowstone River Valley appears as the unshaded region in white. Coordinate origin is the same as in the aircraft remapping (Fig. 4).

b. Filtering and data filling

Two-dimensional spatial filtering may be performed along any axis using either fixed weights over a local (3 × 3) region, a scale-telescoped filter developed by Leise (1981) or a linear least-squares approximation over a selectable ($n \times n$) region of influence (Bevington, 1969). Regions of missing data in observed fields would, if ignored, prevent the use of many routine analysis functions—filtering included. This situation can be remedied by replacing the missing values in a plane (either temporarily or permanently) using one of two available techniques. Leise's data filling algorithm (1981) is generally used to extend the entire dataset globally while the constrained local area linear least-squares approximation is better suited to the elimination of isolated data voids surrounded by good reports. Facilities also exist that allow the user to decimate data fields containing questionable reports. Outlyers are identified and removed from the field depending upon their deviation from the mean value of either a global or a local population.

c. Algebraic manipulation

By far the most popular and powerful analysis tool, the algebraic manipulation command (FUNCTION), enables users to construct customized algorithms for manipulating and altering data fields. The printer-file report given in Fig. 6 illustrates the use of this facility. Statements furnished by the analyst are delineated by angle brackets (⟩⟩⟩⟩⟩). The initial directive invokes the FUNCTION command and contains two parameters. The first (Z) specifies that the z-axis is to be held fixed, and the second (WINDOW) confines the calculations to a previously defined subset of the full (x, y, z) structure. Following this directive the program displays the requested axis configuration, the remaining user-supplied FUNCTION statements, and the spatial dimensions of the current subset region or "editing window." In this example three algebraic operations are grouped together to combine a pair of existing data fields in the following manner:

1) Aircraft (W-AIRC) and radar (W-RADAR) vertical velocity estimates are averaged together wherever both exist to produce a temporary field called W-MEAN;

2) A preliminary composite field (W-COMP) is then constructed by taking the average values from W-MEAN wherever they exist and filling in with the values from W-AIRC otherwise;

3) Finally, the radar estimates are blended in with the existing values of W-COMP to produce the combined vertical velocity field, W-STORM.

Information presented in the bottom portion of the figure verifies the successful execution of these operations and the addition of W-STORM to the active workspace. Similar operations are used to construct

```
>>>>>FUNCTION                                          Z      WINDOW <<<<<

AXIS CONFIGURATION:                      +
                                       Y +
                        Z (FIXED)        +++
                                          X

>>>>>        W-MEAN  T       +       W-AIRC  W-RADAR 0.5     0.5
>>>>>        W-COMP  T       ORELSE  W-MEAN  W-AIRC
>>>>>        W-STORM P       ORELSE  W-COMP  W-RADAR
>>>>>END

EDITING WINDOW LOOKS LIKE THIS:
                 INDICES                        DISTANCES
AXIS  POSN.    MIN     MAX            MIN      MAX     UNITS
  X     1       1       51            55.0     105.0    KM
  Y     2       1       51             0.0      50.0    KM
  Z     3       4        4             2.6       2.6    KM

 0 CONSTANT FIELD PLANES W/INITIALIZATION INFO

FUNCTION STACK...

F (OUT)  TYPE    FUNCTION       F1       F2           C1      C2      C3     C4
W-MEAN   /T    C1*F1+C2*F2     W-AIRC   W-RADAR     0.500   0.500
W-COMP   /T    F1.ORELSE.F2    W-MEAN   W-AIRC
W-STORM  /P    F1.ORELSE.F2    W-COMP   W-RADAR

DIRECTION THROUGH THE Z-PLANES:  1
    W-STORM  WILL BE CREATED AND SAVED AS A PERMANENT EDIT FIELD SCALED BY   64

 7 EDIT FIELDS EXIST AT PRESENT:
    W-AIRC   W-STORM  DZ-CP2   DZ-CHILL W-RADAR  COUNT    WREL
```

FIG. 6. Sample CEDRIC output illustrating the use of the FUNCTION facility. Commands entered by the user are preceded by ⟩⟩⟩⟩⟩. Remaining text is generated by the program.

composite u and v component fields over the full volume of the storm. Customized functions that are frequently used in the analysis of mesoscale datasets include converting radar reflectivity to equivalent rainfall, adjusting vertical velocity estimates with variational schemes, and deriving the terms of the vorticity equation from the kinematic fields.

d. Velocity unfolding

Although radial velocity estimates may have already been unfolded in radar space prior to Cartesian transformation, areas containing ambiguities might not be evident until the data has been examined in horizontal and vertical cross-sections or until a preliminary air motion synthesis has been attempted. Returning to radar space to perform additional unfolding after these velocities have already been interpolated is an unnecessary and cumbersome step backwards. By comparison Cartesian space unfolding offers the following advantages:

- the number of velocity estimates is considerably smaller;
- automated unfolding procedures which take advantage of the orthogonality of the data structure can be used to produce an internally consistent three-dimensional velocity field; and
- the radial velocity field from any radar can be directly compared and brought into agreement with the other radars in the network before it is incorporated into an existing synthesis.

Ambiguous radial velocity measurements in Cartesian space can be corrected using any one of the following techniques:

Automatic 2-D unfolding. Questionable radial velocities are identified and temporarily removed based upon their deviation from the mean of a local ($n \times n$)

region surrounding each grid point. Estimates are generated at the missing locations using Leise's data extension algorithm and saved in a separate array. Suspect velocities are then unfolded using the corresponding estimates as their reference and returned to the original velocity field.

Automatic template unfolding. A template field containing reference velocities is specified and used as a "seed" to initiate the procedure at any designated horizontal or vertical plane. The radial velocities in that plane are unfolded using the corresponding values in the template field as a reference. The unfolded array is saved and subsequently data-filled for use as the template for unfolding the two adjacent planes. Once those planes have been processed, the point-by-point slope of the unfolded velocity field is also taken into account when generating the templates for the next pair of planes to be operated upon. This procedure continues outward in both directions until the entire windowed region has been unfolded.

Forced unfolding. All velocities within the designated spatial window and either inside or outside of an arbitrary velocity range are forced to be within the same Nyquist interval of a user-specified reference velocity.

Forced template unfolding. A template field is specified and the velocity information in it is used as a reference for unfolding the measurements in another velocity field at each corresponding location in the volume. One method of generating the template field for use with this scheme has been to resample the (u, v, W) components from an existing particle motion synthesis at the location of a radar which has not yet been included in that synthesis. The resultant field of computed radial velocities can then be used as a reference for unfolding the actual measurements from the radar. This technique has proven to be particularly useful for incorporating additional estimates from Doppler radars which have acquired their velocities under extreme conditions within a narrow Nyquist interval.

e. Coordinate transformation

Before any time or space transformations are performed in Cartesian coordinates, it is first necessary to determine the storm displacement from one time period to the next. This may be accomplished objectively using a procedure that computes the array of linear cross-correlation coefficients between the horizontal planes of a pair of fields which are lagged with respect to one another along each axis of the plane. When the fields being correlated contain identical quantities from two consecutive volumes and no substantial temporal evolution has occurred, the speed and direction of a moving phenomenon can be readily deduced. Once this information is available, commands can be invoked for remapping the data to a new user-specified coordinate system and for advecting reports with temporal inconsistencies to a common time-of-day.

The remapping procedure is generally used to relocate a sequence of volumes to storm-relative coordinates (translation) and for generating vertical sections along the direction of storm motion (rotation). The destination coordinate system must be identical to the old one along the z-axis but may vary in placement and orientation along the x and y axes. Bilinear interpolation is used to remap the reports in regions where the two structures intersect, elsewhere missing data flags are supplied.

Cartesian space reports can be advected to a common time-of-day position provided that every grid location has a discrete acquisition time associated with it. Acquisition times are expressed in seconds relative to the beginning time of the volume and may be either constant for all points, constant within each z-level, or unique to each grid location. In conjunction with a designated storm motion, these acquisition times are used to differentially advect the data within each horizontal level to locations consistent with a fixed reference time. Values are then redistributed to (x, y) grid points using the same bilinear method that is employed in the remapping. This advection scheme is also available as an automated feature in the multiple Doppler synthesis.

f. Air motion synthesis

This procedure combines radial velocity reports from as many as six ground based Doppler radars. Options also exist for incorporating airborne Doppler measurements into the synthesis and are discussed by Mueller and Hildebrand (1985). The orthogonal components of target motion are computed using a least-squares solution of the system of over-determined equations whenever four or more input values are available, an exact solution if three are present, and a dual-radar approximation of the horizontal winds if only two exist. The formulations used to derive these orthogonal components (u, v, W) from multiple Doppler measurements at each (x, y, z) location are provided by Ray et al. (1978).

Prior to synthesis, all incoming data fields are automatically advected in the manner described above with corrections made to the input radial velocities and the transformation coefficients as prescribed by Gal-Chen (1982). Different size datasets may be combined so long as their coordinate structures are compatible. A Cartesian space output volume is created that contains the following fields:

U, V, W	orthogonal components of target motion;
USTD, VSTD, WSTD	normalized standard deviation associated with the estimate of each component;
CT	bit map of the radars contributing usable radial veloc-

ities to the synthesis at each grid location.

In addition, any original data fields associated with the contributing radars may also be included.

After a Cartesian space volume has been constructed containing kinematic observations from all available sources, a field of vertical air motions (w) can be obtained either by subtracting out the particle fall speeds from W (using an empirical velocity-reflectivity relationship) or by integrating the equation of mass continuity in either an upward or downward direction along the z-axis. When this latter technique is employed, the horizontal divergence is calculated using a centered-differencing scheme and supplied as the integrand. Boundary conditions may be either a constant, a fraction of the integrand, or values taken from another field. The resultant set of vertical velocities can be subsequently adjusted to conform with independent aircraft and ground-based measurements using the facilities available in FUNCTION. In addition to these air motion applications, this procedure can also be used as a general integrator to compute, for example, the total water in the atmosphere above each (x, y) grid location.

g. *Pressure retrieval*

An estimate of the pressure perturbation field at every z-level can be obtained using an algorithm described by Gal-Chen and Hane (1981). This algorithm solves, in a least-squares sense, the momentum equations rewritten in the form:

$$\left.\begin{aligned} \partial P/dx &= F \\ \partial P/dy &= G \end{aligned}\right\} \tag{5}$$

where dx and dy are the grid spacings along the x and y axes respectively. The input fields, F and G, can be constructed from the composite wind components using the algebraic operators available in FUNCTION. The output field, P, contains an estimate of the difference between the pressure at every grid location and the mean value of the horizontal plane. Details regarding the methodology of pressure retrieval from observed kinematics are provided by Gal-Chen (1978).

5. Displaying the composite data structure

A diverse selection of printed and plotted outputs is available in CEDRIC for examining the data fields. Options permit the user to view any region of interest by specifying an arbitrary window prior to display. In addition, the axis to be held constant when generating two-dimensional products may be altered at any time and the Cartesian dataset will be accessed accordingly. Plotted displays are produced using a device-independent vector graphics package developed at NCAR by Wright (1978).

Figure 7 presents a summary of the header information associated with the Cartesian space dataset containing a description of the storm under investigation at 1640 MDT on 1 August 1981. The fields in this dataset are:

```
CEDRIC (.CED)  VOLUME HEADER                          HF7F07
 GENERAL INFORMATION...
  DATE:        8/ 1/81     SOURCE:   HF7L02     SCIENTIST: FRANK
  BEG TIME:   16:40: 0     RADAR:    COMBIN     SUBMITTER: FRANKH
  END TIME:   16:40: 0     PROGRAM:  CEDR.0     DATE RUN:  01/02/85
  VOL. NAME: COMPOS1       PROJECT:  CART       TIME RUN:  02:09:13
  SCAN MODE: CRT           TAPE:     HF7F07     SEQUENCE:  111007

 DATA CHARACTERISTICS...
  COMPUTER:        C1     RECS/FIELD:       1     PTS/FIELD:     2601
  BITS/DATUM:      16     RECS/PLANE:       5     NO. PLANES:      23
  BLOCK SIZE:    3200     RECS/VOLUME:    139     BAD DATA:    -32768
  WORDS/PLANE:    651     WORDS/FIELD:  14973     MAX FIELDS:      25

 FIELDS PRESENT:  5 ...
   NO.   NAME        SCALE FACTOR
    1    UREL             64
    2    VREL             64
    3    DZS(CP2)        100
    4    WDOP             64
    5    WAIR             64

 LANDMARKS PRESENT:  3     ( 2 RADAR) ...
   NO.   NAME       X (KM)     Y (KM)     Z (KM)
    1    ORIGIN      0.00       0.00      0.000
    2    CP-2        0.00       0.00      0.700
    3    CHIL       26.54      52.20      0.015

 ORIGIN  LATITUDE:      46 DEG    25 MIN    55.60 SEC
        LONGITUDE:     105 DEG    56 MIN    10.50 SEC

 CARTESIAN COORDINATE SYSTEM SPECIFICATIONS...
  AXIS     MINIMUM (KM)     MAXIMUM (KM)      DELTA (KM)    NO. OF PTS.
   X          55.00            105.00            1.00           51
   Y           0.00             50.00            1.00           51
   Z           0.00             14.00            0.60           23

  AXIS ORDER IS   X  Y  Z
  ANGLE OF THE X-AXIS RELATIVE TO NORTH:     90.00    DEG.
  (X,Y)  AXIS ARE SPECIFIED RELATIVE TO:  (   0.00,   0.00)
```

FIG. 7. Standard summary of the pertinent header information associated with each Cartesian space dataset. General information, data characteristics, fields, landmarks, and coordinate structure are all provided in this easy-to-read format whenever a dataset is transferred to or from the active workspace.

UREL, VREL	storm relative horizontal wind components;
DZS (CP2)	S-band reflectivity from the NCAR CP-2 radar;
WDOP	vertical component of target motion (including particle fall speeds);
WAIR	vertical air motion (excluding particle fall speeds).

The composite set of air motions (UREL, VREL, WAIR) were constructed from mesonet, aircraft, and Doppler radar measurements in the following manner. Wherever multiple radar observations were available (those regions where the reflectivity exceeded ~15 dBZ), UREL and VREL were derived from a storm relative synthesis using six Doppler radars. At ground level (0.8 km) horizontal winds were supplied by the surface mesonet remapping in section 3c. Aircraft remappings provided additional estimates of UREL and VREL at 2.6 and 8.0 km. Coincident data values were averaged and isolated voids in the UREL and VREL fields were eliminated using the least-squares data filling algorithm. Finally, with the exception of the surface reports, both fields were smoothed along all three axes using the Leise filter. The vertical air motion field, WAIR, was obtained by integrating the horizontal divergence (∂UREL/∂x + ∂VREL/∂y) along the z-axis and adjusting the estimates to satisfy the constraint that WAIR be equal to zero at the bottom and top of the domain.

a

STATISTICS ARE FROM (1 TO 51) (55.0 TO 105.0 KM) ALONG I
(1 TO 51) (0.0 TO 50.0 KM) ALONG J
(1 TO 23) (0.0 TO 14.0 KM) ALONG K

DZS(CP2) Z KM	MEAN	STDV	N	I1	I2	J1	J2	MIN	MAX
0.8	0.00	0.00	0	0	0	0	0	0.0	0.0
1.4	0.00	0.00	0	0	0	0	0	0.0	0.0
2.0	7.09	10.37	1095	6	34	1	40	-6.9	60.7
2.6	9.87	17.26	2213	6	51	1	50	-7.6	61.9
3.2	9.07	16.90	2257	6	51	1	50	-7.7	60.4
3.8	8.20	16.94	2254	6	51	1	50	-8.3	61.0
4.4	7.45	17.33	2254	6	51	1	50	-9.6	63.8
5.0	7.87	17.72	2252	6	51	1	50	-9.9	64.2
5.6	7.11	17.86	2252	6	51	1	50	-10.1	62.9
6.2	7.14	17.90	2253	6	51	1	50	-10.5	65.0
6.8	7.26	17.80	2256	6	51	1	50	-10.6	64.6
7.4	7.71	17.50	2241	5	51	1	50	-11.1	62.6
8.0	8.57	17.20	2212	5	51	1	50	-10.9	62.0
8.6	9.89	16.82	2177	5	51	1	50	-11.2	61.3
9.2	11.30	16.17	2190	5	51	1	50	-11.2	60.4
9.8	12.57	15.51	2227	5	51	1	50	-11.3	59.5
10.4	12.78	14.63	2270	5	51	1	50	-10.8	57.1
11.0	11.71	13.61	2299	5	51	1	50	-11.3	54.9
11.6	8.86	12.33	2309	5	51	1	50	-11.0	50.3
12.2	4.42	10.81	2309	5	51	1	50	-11.2	48.2
12.8	0.10	9.04	2272	5	51	1	50	-11.1	41.6
13.4	-2.54	7.29	2199	5	51	1	50	-10.6	38.0
14.0	-3.61	5.53	2182	5	51	1	50	-9.8	31.9
VOLUME	7.28	15.97	45893	5	51	1	50	-11.3	65.0

b

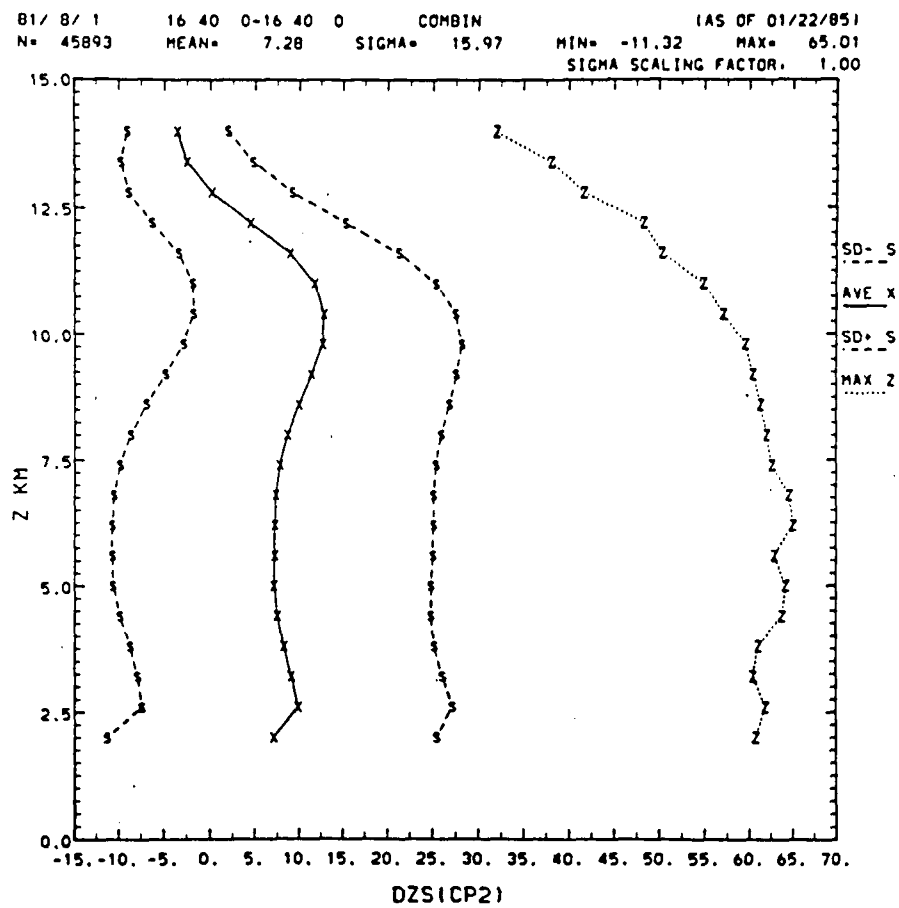

FIG. 8. Selected examples of statistical presentations available in CEDRIC:
(a) Statistics by plane and by volume in a tabular form for reflectivity field DZS (CP-2). Z-axis is held fixed. No data exists for levels below 2.0 km.
(b) Selected statistics from (a) plotted as a function of height. Mean value at each level, mean +/− sigma and maximum reflectivity are included in this display. Volume statistics are provided in the labeling at top of figure.

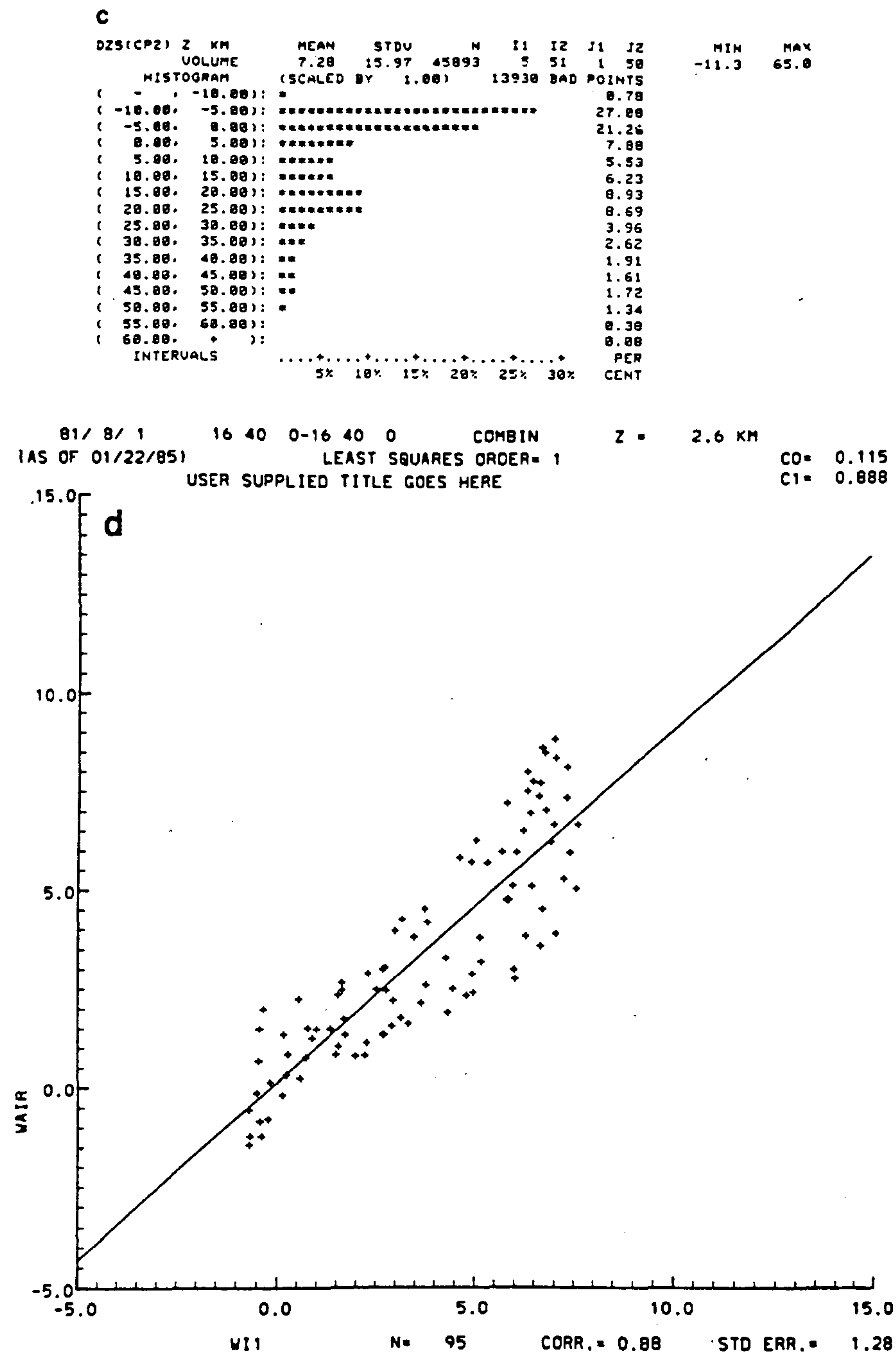

FIG. 8. (c) Frequency distribution of the entire volume of reflectivity values. Statistics for the population appear at the top. The term "bad points" refers to grid locations at which no reports were present.
(d) Scatter diagram of vertical air motion reports from Doppler analysis (WAIR) versus horizontal aircraft mapping (WI1) at height of 2.6 km. Equation of "best fit" line through the data is given at upper right. Number of pairs, correlation coefficient, and standard error of estimate appear below the horizontal axis.

As discussed earlier, the location of the analysis grid dictated the use of a large radius-of-influence in the surface mesonet remapping. Consequently, the wind patterns associated with the lowest level (0.8 km) have been preserved at larger scales than those retained in the Doppler radar and aircraft interpolations. Nevertheless, the surface data provided a sufficiently representative divergence field to enable us to use it as the lower boundary in the integration procedure. Had the storm been located above the dense network, surface observations would have been remapped at a resolution comparable to the other instrument systems and tech-

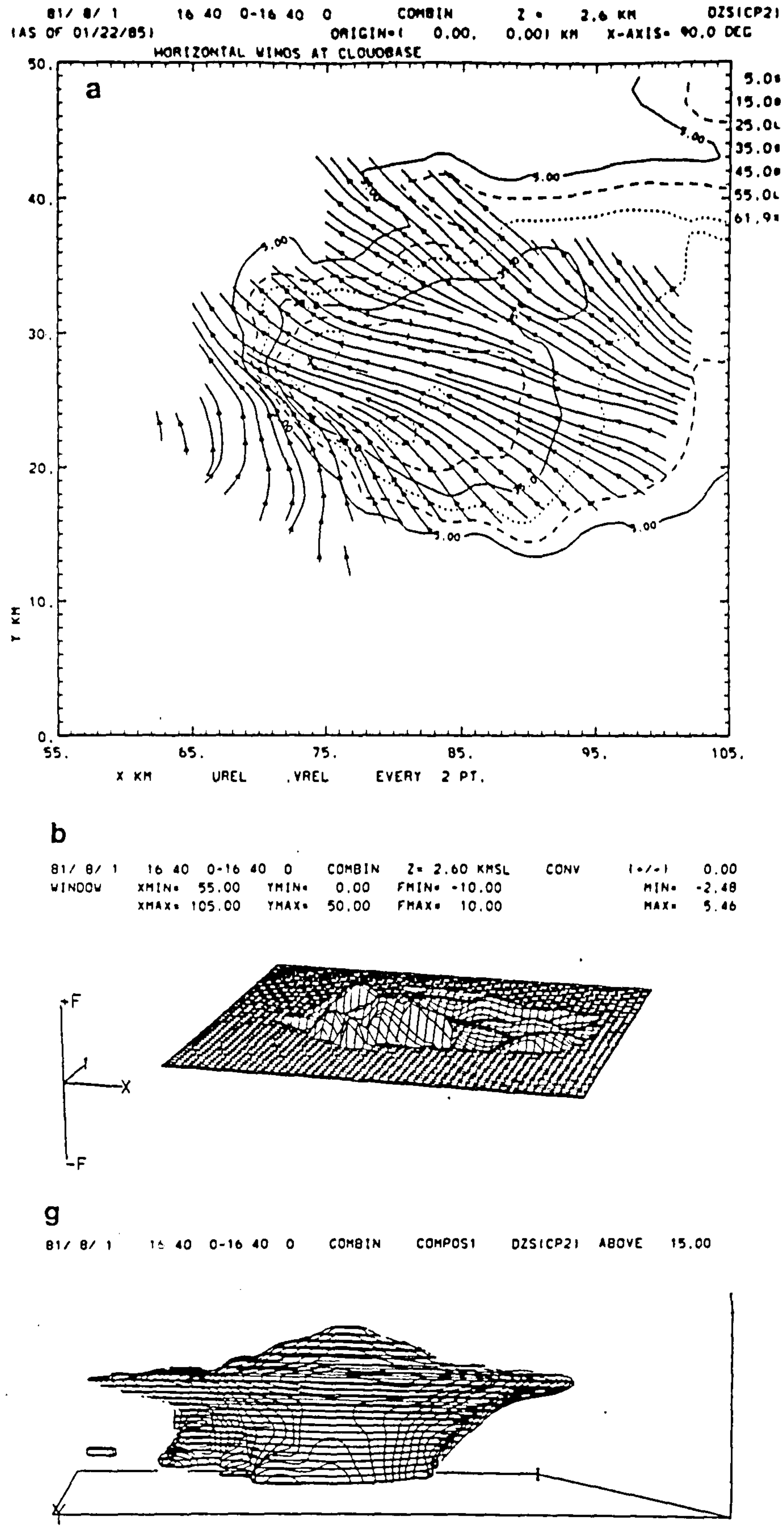

FIG. 9. Selected examples of two and three-dimensional displays produced by CEDRIC:

(a) Contoured reflectivity near cloudbase (2.6 km). Horizontal winds are depicted as streamlines in the overlay. Doppler winds have been extended at southwest flank using aircraft measurements.

(b) Two-dimensional perspective of the horizontal convergence using the winds shown in (a).

(g) Three-dimensional perspective of the entire reflectivity field DZS (CP-2). Values in excess of 15 dBZ are visible.

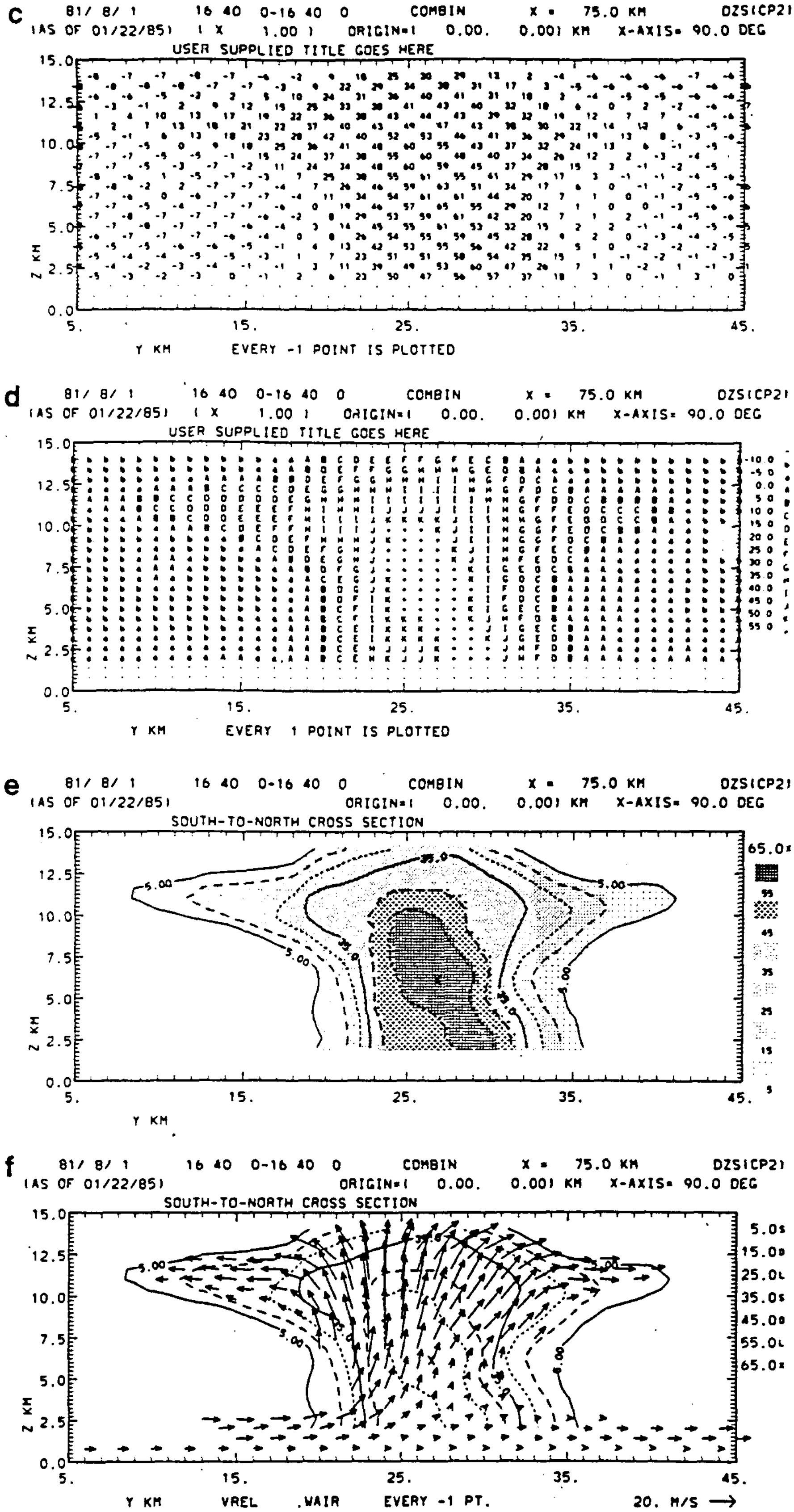

(c) Digital display of the reflectivities in a vertical south-to-north cross-section through the core of the storm.
(d) Coded display of the same reflectivity field and cross-section as in (c). User-specified reference table appears at right of figure.
(e) Contour plot with standard alternating dash pattern, line labeling, and termination of contours at missing data locations. Maximum value (65 dBZ) is indicated by an (X). Optional computer generated gray-scale shading has also been added.
(f) Simple contour plot with vectors depicting the composite air motion deduced from Doppler, aircraft, and mesonet observations included as an overlay. Reference vector is given at lower right.

niques incorporating the topography field in Fig. 5d could have been used to establish a more accurate lower boundary condition.

The resultant three-dimensional Cartesian space volume is the principal source for the displays presented in the remaining figures. Altitudes (z) are given in kilometers above sea level, x and y distances are in kilometers east and north with respect to the primary research radar CP-2. Figure 8 contains some examples of statistical products that are commonly used to examine the Cartesian space fields. Figure 8a is a tabular summary of the S-band reflectivity from CP-2, DZS (CP-2), at levels of constant altitude. The columns in this presentation are (from left to right): height of the cross-section, mean, standard deviation (σ), number of "good" estimates, the beginning and ending indices of the rectangular region surrounding the "good" estimates, and the minima and maxima of the population. Statistics over the entire volume are given in the last line. Figure 8b illustrates some statistical properties of the same field as plotted profiles. The four profiles included in this display are: mean $- \sigma$, mean, mean $+ \sigma$, and maximum value. User-specified symbols (S, X, and Z) corresponding to these profiles are digitized at the location of every z-level in the Cartesian volume. Figure 8c is a frequency distribution partitioned into intervals of 5 dBZ for the same reflectivity field. In this example, every report in the volume has been included. The term "bad points" refers to Cartesian grid locations for which no data are available. The percent contribution from each interval appears in the right-hand column of the display. Figure 8d is a scatter diagram of the vertical velocity field (WAIR) obtained by integrating the horizontal divergence versus vertical velocities at coincident locations (WI1) obtained from the constant altitude aircraft remapping presented earlier in section 3b. Correlation coefficient, standard error of estimate, and the equation of the least-squares line fit are included in the labeling. This particular comparison indicates that, within the context of the Cartesian space data structure, these independent estimates of vertical air motion are in satisfactory agreement.

Figure 9 demonstrates the facilities that exist for examining data fields in two and three dimensions. Figure 9a contains a contour plot of the reflectivity field at cloud base (2.6 km) with streamlines depicting the storm relative horizontal airflow superimposed. Horizontal winds measured by the cloud base aircraft (shown earlier in Fig. 4c) have been merged with Doppler results to extend the observations into the "echo free" inflow region at the southwest flank of the storm. Figure 9b is a perspective display of the convergence field (CONV) at the same altitude computed using the horizontal winds depicted in Fig. 9a. Viewing window and minimum–maximum values are provided in the titling.

Figures 9c through 9f present four different displays of the reflectivity field along a vertical cross section taken through the core of the storm at $x = 75$ km. In Fig. 9c the actual reflectivity values are digitized at their respective locations in the display. For purposes of readability the user has specified that every other point be plotted. Periods indicate grid locations for which no reports exist. In Fig. 9d each reflectivity value is represented by a symbol that has been assigned according to the user-defined table at the right. In this example positive reflectivities are denoted by capital letters; lower case letters are used for negative values. Reports in excess of the table limits are indicated by their signs (+ or −).

Figure 9e contains a contour plot of the data. Display characteristics over which the user has control include the levels to be contoured, line patterns and labels, designation of relative highs and lows, and whether or not contouring should be suppressed when values below threshold are encountered. The maximum value (65 dBZ) is indicated on the figure and in the labeling by an ×. Both this feature and the supplementary grayscale shading are optional.

Vectors depicting the storm relative airflow in the plane (VREL, WAIR) appear as an overlay in Fig. 9f. Winds beyond the boundary of the echo have been resolved using surface mesonet and low level aircraft observations. In general, any pair of the two-dimensional plot types illustrated in Figs. 9c through 9e may be combined together in a single display with either streamlines or vectors superimposed. The final display (Fig. 9g) is a three-dimensional isosurface plot of the total reflectivity surface in excess of 15 dBZ. This particular image has been generated with respect to a viewing angle directly west of the storm at a height of 10 km. Any field in the dataset can be depicted in a similar fashion.

6. Concluding remarks

This paper has presented an effective strategy for combining mesoscale observations from independent surface network, aircraft and radar data acquisition systems. The approach outlined has been successfully applied to the CCOPE data archive and as a result, information from any day of interest can be readily reduced to a common Cartesian coordinate system for analysis and display. Our experience with these procedures has led us to the following conclusions:

1) The common radar and mesonet formats save an enormous amount of data processing effort and should always be used for the exchange of such information after the completion of all field experiments. There should be similar formats for all major data collection systems.

2) Reports within each individual dataset should be carefully examined before any attempt is made to merge them with information from the other data systems. Although CEDRIC contains a full complement of tools for editing in Cartesian coordinates, problems such as poorly calibrated sensors, nonlinear biases and mislocated reports are best resolved before any time–space transformations or remappings are performed.

3) Provided that calibrated datasets are available and (x, y, z) space is the eventual destination, conversion to Cartesian coordinates at the earliest opportunity can significantly expedite the analysis effort. This is particularly true of radar measurements which, using proper precautions, can be processed almost entirely in an orthogonal coordinate system (Miller et al., 1985).

Now that established mechanisms exist for dealing with the high resolution datasets (radar, aircraft, and mesonet), we intend to focus our efforts toward incorporating as many of the remaining measurements as resources permit. Well-documented procedures exist for remapping rawinsonde (Fankhauser; 1969, 1974) and satellite observations (Hambrick and Phillips, 1980) to Cartesian coordinates. Time resolved cloud-to-ground lightning strokes (Orville and Rosentel, 1983) will most probably be assigned to the nearest grid locations in the lowest horizontal level. Plans also include the development of reformatting software to convert the output fields generated by mesoscale models to the CEDRIC format, thus enabling direct comparisons between observed and predicted conditions.

Acknowledgments. Mr. Thomas Engle (Cray Industries) deserves credit for setting up the CCOPE mesonet database on the mass storage system at NCAR. We also acknowledge the efforts of the part-time student programmers who have contributed either directly or indirectly to the success of this undertaking: Doug Rhoades (now with General Dynamics), Patti Cochran (now with GTE), Paul Poulsen (now with Ball Research), and Marta Oryshchyn and Jose Alvistur (still at NCAR). Special thanks also to Sudie Kelly for preparing the manuscript.

REFERENCES

Barnes, S. L., 1964: A technique for maximizing details in numerical weather map analysis. *J. Appl. Meteor.*, **3**, 396–409.

——, 1973: Mesoscale objective map analysis using weighted time-series observations. NOAA Tech. Memo. ERL NSSL-62, 60 pp. [NTIS COM-73-10781].

——, 1980: Report on a meeting to establish a common Doppler radar exchange format. *Bull. Amer. Meteor. Soc.*, **61**, 1401–1404.

Bevington, P. R., 1969: *Data Reduction and Error Analysis for the Physical Sciences.* McGraw-Hill, 336 pp.

Caracena, F., S. L. Barnes and C. L. Doswell, III, 1984: Weighting Function Parameters for Objective Interpolation of Meteorological Data. *Preprints, 10th Conf. on Weather Forecasting and Analysis,* Clearwater Beach, Amer. Meteor. Soc., 109–116.

CCOPE Operations Plan, 1981: Convective Storms Division, NCAR, 250 pp.

1981 CCOPE Data Inventory, 1982: Bureau of Reclamation, U.S. Dept of Interior Report, 451 pp.

desJardins, M. L., and R. A. Petersen, 1985: GEMPAK: A meteorological system for research and education. *Preprints, Int. Conf. on Interactive Information and Processing Systems for Meteorology, Oceanography, and Hydrology,* Los Angeles, Amer. Meteor. Soc., 313–319.

Fankhauser, J. C., 1969: Convective processes resolved by a mesoscale rawinsonde network. *J. Appl. Meteor.*, **8**, 778–798.

——, 1974: The derivation of consistent fields of wind and geopotential height from mesoscale rawinsonde data. *J. Appl. Meteor.*, **13**, 637–646.

——, C. J. Biter, C. G. Mohr and R. L. Vaughan, 1985: Objective analysis of constant altitude aircraft measurements in thunderstorm inflow regions. *J. Atmos. Ocean. Technol.*, **2**, 157–170.

Gal-Chen, T., 1978: A method for the initialization of the anelastic equations: Implications for matching models with observations. *Mon. Wea. Rev.*, **106**, 587–606.

——, 1982: Errors in fixed and moving frame of references: Applications for conventional and Doppler radar analysis. *J. Atmos. Sci.*, **39**, 2279–2300.

——, and C. E. Hane, 1981: Retrieving buoyancy and pressure fluctuations from Doppler radar observations: A status report. *Atmos. Technol.*, R. Carbone, Ed., Vol. 12, NCAR, 98–104.

Hambrick, L. N., and D. R. Phillips, 1980: Earth locating image data of spin-stabilized geosynchronous satelites. NOAA Tech. Memo. NESS III, 49 pp.

Heymsfield, G. M., K. K. Gnosh and L. C. Chen, 1983: An interactive system for compositing digital radar and satellite data. *J. Climate Appl. Meteor.*, **22**, 705–713.

Knight, C. A., 1982: The Cooperative Convective Precipitation Experiment (CCOPE), 18 May–7 August 1981. *Bull. Amer. Meteor. Soc.*, **63**, 386–398.

Koch, S. E., M. desJardins and P. J. Kocin, 1983: An interactive Barnes objective map analysis scheme for use with satellite and conventional data. *J. Climate Appl. Meteor.*, **22**, 1487–1503.

Kohn, N. M., A. L. Johnston and C. G. Mohr, 1978: MUDRAS—Multiple Doppler radar analysis system. NOAA Tech. Memo. ERL/WPL-35, Wave Propagation Lab, Boulder, 170 pp.

Lackman, R. L., and R. B. Friesen, 1983: General purpose data processing software for scientific data sets. *Preprints, Fifth Symposium Meteor. Observations and Instrumentation,* Toronto, Amer. Meteor. Soc., 231–238.

Leise, J. A., 1981: A multidimensional scale-telescoped filter and data extension package. NOAA Tech. Memo. ERL/WPL-82, Wave Propagation Lab, Boulder, 20 pp.

Miller, L. J., C. G. Mohr and A. J. Weinheimer, 1986: The simple rectification to Cartesian space of folded radial velocities from Doppler radar sampling. *J. Atmos. Oceanic Technol.*, **3**, 162–174.

Mohr, C. G., and R. L. Vaughan, 1979: An economical procedure for Cartesian interpolation and display of reflectivity factor data in three-dimensional space. *J. Appl. Meteor.*, **18**, 661–670.

——, L. J. Miller and R. L. Vaughan, 1981: An interactive software package for the rectification of radar data to three-dimensional Cartesian coordinates. *Preprints, 20th Conf. on Radar Meteor.*, Boston, Amer. Meteor. Soc., 690–695.

Mueller, C. M., and P. H. Hildebrand, 1985: Evaluation of meteorological airborne Doppler radar. Part II: Triple-Doppler analyses of air motions. *J. Atmos. Ocean. Technol.*, **2**, 381–392.

Orville, R. E., and E. Rosentel, 1983: Ground-strike lightning locations in CCOPE. *Trans. AGU*, **64**, 666.

Oye, R., and R. Carbone, 1981: Interactive Doppler editing software. *Preprints, 20th Conf. on Radar Meteorology,* Boston, Amer. Meteor. Soc., 683–689.

Ray, P. S., K. K. Wagner, K. W. Johnson, J. J. Stephens, W. C. Bumgarner and E. A. Mueller, 1978: Triple-Doppler observations of a convective storm. *J. Appl. Meteor.*, **17**, 1201–1212.

Reynolds, D. W., 1982: Prototype workstation for mesoscale forecasting. *Bull. Amer. Meteor. Soc.*, **64**, 264–273.

Suomi, V. E., R. Fox, S. S. Limaye and W. L. Smith, 1983: McIDAS III: A modern data access and analysis system. *J. Climate Appl. Meteor.*, **22**, 766–778.

Treinish, L. A., and S. N. Ray, 1985: An interactive information system to support climate research. *Preprints, Int. Conf. on Interactive Information and Processing Systems for Meteorology, Oceanography, and Hydrology,* Los Angeles, Amer. Meteor. Soc., 72–79.

Wade, C. G., and T. M. Engle, 1985: A technique for correcting humidity errors in mesometeorological data. *Proc., Int. Symp. on Moisture and Humidity: Its Measurement and Control in Science and Industry.* Washington, DC, Instrument Soc. Amer., 121–131.

Wright, T., 1978: *NCAR Graphics Software.* (4th preliminary ed.), Prepared by Atmospheric Technology Div., NCAR, Boulder.

MEV I G BUCHAN

VOORRAADOPNAME VAN BIBLIOTEEKBOEKE SOOS OP 31 MEI 1992

1979/12	Fowlers Modern English Usage
1979/14	Engles/Afrikaans Tegniese Woordeboek
1976/10	Bouwoordeboek English/Afrikaans - Afrikaans/English
1981/29a	Watertegnologieterme
1982/38	Tweetalige voorsetsel Woordeboek
1982/74	Afrikaanse woordelys en spelreëls
1982/8	German Dictionary
1982/7	Standard Methods for the examination of water and waste-water and supplement - 15th edition
1985/7	HAT verklarende handwoordeboek
1985/8+9	The Shorter Oxford English Dictionary (2 vol)
1985/13	Weerkunde & Hidrologie Woordeboek - Dic of Meteorology & Hydrology
1986/18	Editing Scientific Books and Journals
1987/10	Publication standards and Guidelines for Periodicals - D E Haag
1987/13	Nasionale Woordeboek - Afrikaanse verklaring De Villiers, Smuts, Eksteen en Gouws
1988/1	Dictionary of Scientific and Technical Terms - McGraw Hill 3rd Edition
1988/21	Dictionary of Troublesome words - Bill Bryson
1989/8	The Oxford Dictionary for writers and editors
1989/26	Afrikaans / Engelse Woordeboek - Reader's Digest
1991/1	Tweetalige Rekenaarwoordeboek - Bilinqual Computer Dic.

....

EMA-C 90181

FINAL REPORT

PRECIPITATION AND AIR FLOW (PRAI) PROJECT

and

DOPPLER RADAR DATA PROCESSING (DOPDATE) PROJECT

(1 January 1988 - 31 December 1990)

A report to the Water Research Commission

Project leaders:

G HELD
A M GOMES

PRETORIA
NOVEMBER 1990

WRC Report No. WRC 223/1/91
ISBN 1 874858 17 9

KEYWORDS: Radar, Doppler radar, rainfall, thunderstorms, precipitation, air flow, hailstorms, thermodynamics, equivalent potential temperature, Area-Time-Integral, early storm stages, cell mergers, South Africa.

EXECUTIVE SUMMARY

The Division of Earth, Marine and Atmospheric Science and Technology, EMATEK, (formerly National Physical Research Laboratory) of the CSIR has been intensely involved in precipitation studies since the late fifties, although originally mainly in the field of laboratory investigations. However, in 1970, an S-band (10 cm) weather radar was bought and has been continuously in operation during the rainy seasons since 1971. Not only has a comprehensive knowledge of precipitation patterns on the Highveld been accumulated, but members of the research team also gained considerable insight into mechanisms of thunderstorms. However, it was realised some years ago that, in order to fully understand the mechanisms of precipitation formation, including that of hail storms, one has to have detailed measurements of the three-dimensional air flow pattern in and around a storm. It was therefore decided to modify the S-band radar at Houtkoppen to operate in Doppler mode. Many storms were thus observed since the 1987/88 rainy season and a good data base of precipitation versus airflow inside storms was built up (digital Doppler radar records). Results which demonstrate the usefulness of single-Doppler radar observations have already been presented in previous reports and some more sophisticated applications based on radial velocity measurements are being presented in this report (cf. Section 2.2). Nevertheless, it was realised all along, that a single Doppler radar is only the first step towards a multiple Doppler radar facility which is the only means to actually observe by radar, and then calculate the three-dimensional air flow pattern inside a thunderstorm. For this purpose, two standard C-band radars had been purchased and were subsequently modified to also operate in Doppler mode. It was planned to have them already operational for the 1989/90 season, but this did unfortunately not materialise due to unforeseen circumstances which are explained in more detail in Section 1 of this report. Therefore, during the past year emphasis was put on the analysis of single-Doppler radar data and the various applications of such observations.

This report presents a summary of achievements during the three-year *Precipitation and Airflow (PRAI) Project* and the one-year *Doppler Radar Data Processing (DOPDATE) Project*.

The objectives of both projects can briefly be summarised as follows:

The original proposal for the three-year PRAI project was aimed at providing supplementary information on precipitation processes on the Highveld for on-going weather modification research projects. It had been realised that accurate measurement of total areal rainfall is of prime importance for precipitation enhancement projects. It was therefore proposed to establish relationships between the spatial distribution of precipitation within clouds and the internal air flow in thunderstorms; between the surface precipitation (rain and hail) patterns and the three-dimensional air flow in storms; and finally between rainfall intensities as measured by rain gauges and the reflectivity recorded by radar. It was also proposed to verify or reject the hypothesis of accumulation zones above the main updraught region and to *possibly* identify storm systems which have a good potential for producing rain on the ground, but are inefficient in their mechanism and would therefore be more suitable for cloud seeding operations than naturally efficient clouds. During the second year the research proposal was expanded to include detailed studies of raindrop-size distributions and Z-R relationships in an attempt to improve the accuracy of radar measurements of areal rainfall. In line with this objective was also the investigation of the V-ATI (Volume x Area-Time-Integral) of radar reflectivity.

The WRC also approved further funds for additional analysis work under the project name DOPDATE, which was to run concurrently with the PRAI project during 1990. The emphasis of the new project was on the selection and analysis of convective clouds at a very early stage in their life cycle, in order to verify and *possibly quantify* the daughter-cell and feeder-cell cloud merging concepts of storm mechanisms on the Highveld. The joint execution of both projects resulted in a drastic improvement of the sensitivity of the Houtkoppen S-band radar; also the other two C-band radars were to have come on line during the 1989/90 rainy season; the CRAY computer programs should be verified and tested and the EVAD (Extended Velocity-Azimuth Display) method should be investigated as a means for extracting maximum information from existing single-Doppler radar data.

The objectives as summarised above and in detailed annual Work Programmes which were approved by the Steering Committee, have by and large been achieved.

Thermodynamic and kinematic properties of Highveld storms

It became obvious from extensive literature studies that the relationship of buoyancy and wind shear is fundamentally important in defining storm structure. Therefore, the convective available potential energy (CAPE), which is a function of the potential temperature of an air parcel rising moist adiabatically and the environmental potential temperature, has been calculated for Highveld storms, using the Irene (Pretoria) 12 GMT sounding. In further developments, the bulk Richardson number (Ri), which is a function of CAPE and the wind shear (speed) between low and middle levels of the atmosphere, has been calculated. Storm form three seasons (85/86, 86/87, 87/88) were classified according to CAPE and Ri and the results are presented diagrammatically in Section 2.1. Highveld values of CAPE ranged from 800 to 4800 $m^2.s^{-2}$, representing typical values of convective energy available to develop convection. Ri values were found to be less characteristic on the Highveld, viz. rather low (10 to 40), and are only useful for storm classification purposes if used in conjunction with CAPE. The vast majority of storms fell into the multicell category. No definite supercell storm was found according to the classification criteria.

Kinematic properties of the wind field can be derived from single-Doppler radar observations in widespread homogeneous precipitation. In principle, the horizontal wind speed and direction can be determined by measuring the radial velocity as a function of the azimuth at a constant elevation angle (VAD = Velocity Azimuth Display). Even the divergence of the horizontal wind can be calculated, but inhomogeneities in the particle fall speed can lead to significant errors. Therefore, Srivastava's extended VAD (EVAD) method was applied to a Highveld storm. The basic assumption for EVAD is that the divergence and particle fall speed are horizontally uniform and thus only a function of height. Therefore, the limitation of the VAD method to small elevation angles is eliminated and the divergence can be calculated throughout the complete volume scan.

The storm selected as a test case (21 November 1987) was part of a large squall line with strong convective activity at the leading edge, but fairly homogeneous stratiform precipitation behind it. A radius of 25 km was chosen for the imaginary EVAD circle in order to avoid patchy radar echoes. Vertical profiles of the horizontal wind divergence and vertical velocity were calculated for six complete volume scans. The magnitudes of the wind speed ranged from 3-6 $m.s^{-1}$ in the lower and middle levels, increasing to 18 $m.s^{-1}$ at higher levels. Strong convergence was found below 2,5 km (maximum of $4 \times 10^{-4}s^{-1}$) while the maximum divergence ($4 \times 10^{-4}s^{-1}$) was found at about 5,5 km AGL. Typical updraught and downdraught values were 25 $cm.s^{-1}$ with maxima up to 1 $m.s^{-1}$. The results are presented in the form of time-height graphs.

Doppler radar observations can also be used to estimate the precipitation rate and efficiency by integrating the mass continuity equation vertically, using VAD-derived divergence values. This was done for the test storm during a 28-minute period, yielding a total rainfall of 2,9 mm. Compared with rain gauge measurements at Jan Smuts Airport, which is actually just outside the 25 km radius, the VAD method estimated 8% less rain than the gauge, resulting in a slight over-estimation of the "precipitation efficiency" for the period of analysis.

Although all these findings must be regarded as preliminary, subject to many more test results, the versatility of observations made using only one Doppler radar has clearly been demonstrated.

Raindrop size distributions and Z-R relationships

The importance of studying drop size distributions (DSDs) is related to a number of aspects of thunderstorm research. DSD studies are particularly important in radar-measurement of rainfall, as variability in DSDs causes significant variability in rainfall rate (R) and radar reflectivity factor (Z). DSDs in convective rainfall over the Transvaal Highveld were measured using a raindrop disdrometer. A paramaterisation technique was used to quantify temporal variability in DSDs. The parameterisation technique is based on the assumption that DSDs can be represented by an exponential distribution which in turn, can be represented by N_0, the intercept value and Λ, the slope of the distribution. DSD variability will thus be reflected in N_0 and Λ.

Comparisons between N_0, Λ and rainfall rate showed that convective storm systems over the Transvaal Highveld are characterised by drop-sorting (sedimentation) and drop break-up effects. These effects lead to large drop dominance in the initial DSDs of convective rain followed by an influx of small drops in the later stages of the storm. Stratiform rain was characterised by a pattern of small drop dominance in the spectrum from the onset of rain. DSD variations were also compared to variations in radar reflectivity factor. Within an individual storm, the radar reflectivity factor was seen to be both greater and less than the rainfall rate in response to changes in the DSD. A summary of the entire season's data showed that underestimation or overestimation of rainfall rate using an average Z-R relationship is a function of changes in the drop size distribution and not, primarily, in rainfall rate.

The Area-Time-Integral method of radar-rainfall measurement

Radar measurement of rainfall, although seen by many as the solution to the problem of areal and temporal measurement of rainfall, is not straight forward. The problems include variability in the Z-R relationship as well as changes in precipitation from the height at which it is measured to the ground. If the area of the radar echo is integrated over time and compared with radar-estimated rainfall volume, a strong correlation is seen to exist. It is this principle that is utilised in the Area-Time-Integral (ATI) method of volumetric rainfall measurement by radar. The ATI method has been proposed as a means of measuring rainfall using radar which to a large extent overcomes the above-mentioned problems.

Three different methods of computing ATI values are discussed in determining an appropriate Volume versus Area-Time-Integral (V-ATI) relationship for convective storms over the Transvaal Highveld. Computing ATI from the hourly average echo area gave the lowest measurement error. On the basis of this, a V-ATI relationship of the form $V=3,06(ATI)^{1,14}$ was computed where V is in units of $km^2.mm$ and ATI in units of $km^2.h$. In order to enhance operational applications of the ATI method a "scan by scan" integration technique was also calculated. This gave a V-ATI relationship of the form $V=0,04(ATI)^{1,18}$ where V is in units of $km^2.mm$ and ATI in units of $km^2.min$ ($V = 2,4(ATI)^{1,18}$ when ATI is in units of $km^2.h$). Average rainfall rates for convective storms over the Transvaal Highveld calculated using a V-ATI relationship were seen to be higher than those for other parts of the world, but this is in keeping with characteristics of South African storms discussed by other authors.

Daughter cells and cloud seeding

The main goal of this study is to identify the principal mechanism for new cell generation in South African clouds which are suitable for cloud seeding activities, as cloud growth patterns may have a major impact on the effective placement of seeding material in all the cells of a storm case (Changnon *et al.*, 1975). It is also important to understand cloud merger processes for proper evaluation of seeding effects. This short pilot project is a survey of several case studies and includes a discussion which integrates previous research and methodology.

The information needed at this time is on the relative frequency of feeder type mergers compared to daughter type mergers, as the former can be expected to maximise the efficient use of seeding material (as recycling is possible), while in the latter it is minimised and additional seeding may be necessary to treat all cells of a single dynamic entity. The key feature to be identified now is whether the major new cells are essentially separate from the older cells or replace them in the same relative position in the moving storm system. Thus, the new cell locations (relative to the initial cell) must be monitored over time in the presence of storm translation. Consequently, the proper definition of daughter and feeder cells is one of the main interests of this pilot study. Therefore, high resolution temporal and spatial radar images were required, and a lengthy introduction included.

Early storm development and cloud mergers: a single Doppler radar case study

A detailed, three-dimensional case study of an isolated, and for the Highveld, typical multicellular storm illustrates very clearly the various mechanisms of cloud merging, cell development and regeneration, which sustain such storms for hours while they are traversing the Highveld. The case study is based on single Doppler radar observations of a storm which occurred on 27 April 1987 between the West Rand and Pretoria. Radial velocities of the air flow inside the storm were carefully analysed and, whenever possible, interpreted in terms of updraughts or downdraughts. The study identified two main mechanisms:

Daughter-cell merging situation.
A new cell had developed rapidly between 5 and 8 km AGL some 3-4 km northeast of a mature cell. As the new cell grew and intensified, the radial air flow was increasing significantly, indicating an updraught tilted away from the old cell. The two cells then merged into one complex by rapid expansion and intensification within a period of about 10 minutes. Seven minutes later, the original cell had been totally incorporated into the new structure and could no longer be identified.

Feeder-cell merging situation.
Three very small cells of 1-2 km in diameter have been observed, forming some 4-5 km north of mature echoes in an area of strong convergence within a period of about five minutes. It is noteworthy that the cell which had formed later than and between the existing two, was the one to have developed to full maturity, by entraining the flanking cells quite rapidly. This process took less than six minutes. Once this cell had established itself as the survivor, it grew rapidly in height, area and intensity and moved together with its mother cell for a period of about 18 minutes. It eventually merged into the mother storm, but always remained identifiable during its whole life cycle of less than 25 minutes.

A *slightly different mechanism* of a feeder-cell merging situation was observed in parallel to the above case. A new cell had developed aloft on the perimeter of an existing storm, rapidly growing in intensity and volume. Within a matter of five to seven minutes it had been totally incorporated in the leading edge of the old storm aloft, thus dramatically enhancing its anvil and tilt of the echo core.

It is noteworthy that these different cell merging mechanisms can occur sequentially or simultaneously during the same storm situation on one particular day. The main difference between daughter-cell and feeder-cell merging situations appears to be the reflectivity factor, and thus the cell intensity, which is much greater in the case of daughter-cell mergers than in feeder-cell merging situations (the feeder-cell is generally $\leq$40 dBZ).

Case studies of this nature are very time consuming, as can be seen from the fact that a total of approximately 420 PPI plots and 600 vertical cross-sections formed the basis of the analysis of a storm period lasting less than one hour! It is therefore impossible, at this stage, to estimate the relative frequency of the various storm merger situations.

It has also become very obvious that, in order to study storm or cell merger situations, one must have the three-dimensional reflectivity and air flow pattern available for making useful inferences. The latter should actually be derived from dual or triple Doppler radar observations rather than inferred from single Doppler radar observations.

However, both types of merger mechanisms are very important for cloud-seeding experiments as the reaction to the introduction of seeding material might yield different results depending on the merger type.

Processing of Doppler radar data

Although it was initially envisaged that at least two Doppler radars (S-band at Houtkoppen and C-band at CSIR) would be operational during the 1989/90 season, this did, unfortunately, not materialise. Only the S-band radar at Houtkoppen was operated routinely, while test runs were made with the C-band radar on the CSIR campus. The reasons for this were manifold, and are discussed in detail in Section 7. During the course of many test runs, several other difficulties had to be overcome which resulted from some of the hardware modifications. Therefore, no useful data could be collected using more than one Doppler radar until March 1991.

However, the difficulties outlined above did certainly not deter from completing the implementation of the CRAY programs on the CSIR's VM mainframe computer and their final testing.

In order to analyse radar data with the NCAR programs, two major steps have to be executed, viz. 'SPRINT' (Sorted Position Radar Interpolation) and 'CEDRIC' (Cartesian Space data processor). 'SPRINT' is designed to interpolate volumetric radar space measurements collected at constant elevation angles to a regularly spaced three-dimensional Cartesian grid. 'CEDRIC' is used for the reduction and analysis of single and multiple Doppler radar volumes in Cartesian space.

After implementation of 'SPRINT', it was found that the Universal Radar Data Format required more storage space on the VM mainframe computer than could be allocated. It was therefore decided to modify the input format of our radar data in order to facilitate speedy processing. All sections of 'SPRINT' and 'CEDRIC' have been thoroughly tested with Houtkoppen's single Doppler radar data and typical examples of the output from 'SPRINT' are shown.

A storm which was observed on 4 March 1991 by both the Houtkoppen and Pretoria Doppler radar, has been selected as one of two test cases for dual Doppler analysis. Results from the preparation of the data sets for such an analysis are included. The three-dimensional air flow pattern, based on one dual Doppler radar volume scan, is shown for a storm which was observed on 26 March 1991 and which was more suitable for synthesis than the one from 4 March 1991. CAPPIs with the reflectivity and the horizontal airflow, as well as vertical cross sections showing up- and downdraughts, are included in the report.

General Conclusions

A vast amount of radar data and related meteorological observations have been processed in order to achieve the goals set for both the PRAI and DOPDATE projects. The results which emerged from the many sub-projects are very encouraging and in some cases even quite exciting. There are a number of aspects which are in urgent need of continued attention, such as obtaining at least one complete season of dual or triple Doppler radar observations for climatological investigations, a more quantitative study of cloud merger processes, the application of single-Doppler radar observations for estimating precipitation efficiencies and certain hardware improvements. Reasons and proposed avenues for such further investigations have been addressed in detail in Section 8 (Conclusions and Recommendations).

However, it is felt that it would be a tragic event if such a research project would have to be terminated due to a lack of funds for maintaining the multiple Doppler radar facility, which is an absolutely unique asset in South African precipitation research.

Following the recommendations of the *Workshop on Rainfall Stimulation Research in South Africa* (Berg-en-Dal Conference Centre, Kruger National Park, 21-23 August 1989) which was attended by all leading scientists in the field of cloud physics in South Africa and by four overseas experts, *all* available resources, both in manpower and hardware, should be coordinated in a National Research Project, in order to obtain the optimal benefit from such a unique set-up.

Since the CSIR multiple Doppler radar facility is still the only one in South Africa which deploys S- and C-band Doppler radars for thunderstorm research, it seems only logical to maintain such a unique asset, especially now, since the first dual Doppler radar observations have become available. This had also been emphasized by the overseas consultants on many occasions.

FOREWORD

A first draft of this report had been prepared for the Water Research Commission during November 1990. Since then a few sections were added and others improved in order to submit a completely up-to-date version as a final report on both, the *Precipitation and Air Flow (PRAI) Project* and the *Doppler Radar Data Processing (DOPDATE) Project*.

G Held

A M Gomes

Pretoria

March 1991

CONTENTS

1. INTRODUCTION

The Division of Earth, Marine and Atmospheric Sciences and Technology, EMATEK, (formerly National Physical Research Laboratory) of the CSIR has been intensely involved in precipitation studies since the late fifties, although originally mainly in the field of laboratory investigations. However, in 1970, an S-band (10 cm) weather radar was bought and has been continuously in operation during the rainy seasons since 1971. Not only has a comprehensive knowledge of precipitation patterns on the Highveld been accumulated, but members of the research team also gained considerable insight into mechanisms of thunderstorms. However, it was realised some years ago that, in order to fully understand the mechanisms of precipitation formation, including that of hail storms, one has to have detailed measurements of the three-dimensional air flow pattern in and around a storm. The only way to adequately measure air flow inside a storm is by means of at least two Doppler radars, since aircraft can only provide spot measurements in space and time, besides the dangers of penetrating tall convective clouds.

It is EMATEK's aim to continue the study of these processes in clouds. An important point is that synthesis of available data revealed the crucial dependence of hail formation on the air flow patterns inside clouds (Held, 1982). Knowledge and full understanding of the mechanisms of thunderstorms on the Highveld, viz., the relationship between precipitation, either in the form of raindrops or hailstones, and airflow is extremely important for weather modification projects as well as for cloud modellers.

In order to measure air flow inside clouds remotely, modifications were performed to change the Mitsubishi radar at Houtkoppen to operate in the Doppler mode. The CSIR's radar facility was successfully operated during the 1987/88 rainy season (Dicks *et al.*, 1987). Many storms were observed and a good data base of precipitation versus air flow inside storms was collected and stored for subsequent analysis.

Considering severe storm types that occur on the Highveld, the squall line is the one which is characterised by its widespread areal coverage. Most of them are very efficient in producing rain and hail over large areas, but are less frequent than isolated or scattered storms.

In the first progress report of the Precipitation and Airflow Project (PRAI) for the Water Research Commission (Gomes and Held, 1988), severe storm occurrence over the Transvaal Highveld was described. The descriptions, based on coherent as well as Doppler radar data, included analyses of two squall line systems that traversed the Pretoria-Witwatersrand area in November 1987. Several severe thunderstorms occurred in the Pretoria-Witwatersrand area resulting in hail damage and flooding. From the 12-day period chosen for the analysis, from 9 to 20 November, two particular days have been discussed (10 and 19) associated with the passage of a squall line during the late afternoon in the first case and early in the evening in the second one. The characteristic thermodynamic structure of the troposphere and its modification after the passage of the disturbance is highlighted through equivalent potential temperature profiles obtained from Irene upper air sounding data. The analysis, particularly of the radial velocity fields as observed by the Doppler radar, indicated the tendency for storms of this type to exhibit well organised mesoscale features in the mature stage of development. The thermodynamic environment in the form of θ_e profiles in which these storms developed was also considered. The substantial change in θ_e at low levels was highlighted.

Following the recommendations at the end of the first year, a motivation for a second scientist to help with analysis and interpretation of the vast volume of available radar data had been favourably considered by the Water Research Commission. Thus, Mr S O'Beirne, who already had previous experience with the analysis of our radar data, could be appointed with effect from 2 January 1989. This made it possible not only to substantially increase the volume of radar observations being studied in detail, but also to commence with the V x ATI (Volume x Area-Time-Integral) analysis of radar reflectivities as proposed in the work programme for the second year (Gomes *et al.*, 1989).

Unfortunately, bad luck struck the S-band radar at Houtkoppen during the 1988/89 rainy season: right at the beginning of the season the co-axial magnetron began to arc and had to be replaced. Since the spare magnetron was slightly larger than the previously used Varian magnetron, hardware modifications in the transmitter cabinet had to be made before installation which took considerable time. Good radar data were obtained from 8 November 1988 until 4 December 1988, when a direct lightning strike severely damaged most of the electronic circuit boards. Repair work took more than three months by which time the rainy season was almost over and only a few very light storms could be observed. These unexpected problems in turn delayed the schedule for converting the Enterprise C-band radars to Doppler mode considerably since all available manpower had to be utilised for repair work.

Following the recommendations of the Berg-en-Dal Workshop on rainfall stimulation research (21-23 August 1989, informal minutes, WRC, 1990, p28) the sensitivity and resolution of the CSIR's Houtkoppen radar (S-band) was drastically improved from the beginning of the 1989/90 rainfall season. This was achieved by firstly removing the range-correction circuitry from the hardware and then applying range-correction in the software at the processing stage. This increased the sensitivity from 23 dBZ to approximately -10 dBZ. Secondly, the resolution of reflectivity measurements was increased from 16 levels of 3,3 dB intervals (4-bit data-recording format) to 256 levels of 0,25 dB intervals (8-bit data-recording format). Although all storm observations during the 1989/90 season were made in this format, the data could unfortunately not be processed for analysis yet, because the initial data acquisition was made on 800 bpi magnetic tapes, the only data logging system available at Houtkoppen then, while the Central Computer Facility at the CSIR had decommissioned the 800 bpi magnetic tape drive on its mainframe computers. This necessitated the change-over from 800 to 1600 bpi tape drive facilities at Houtkoppen, which had to be executed within the man-power constraints for re-writing the data acquisition programme. Once this was achieved, a copying procedure was written for the new computer which facilitated copying of 800 bpi tapes from the old HP2100 computer to the new HP A400 computer using a 1600 bpi tape drive. The re-written tapes are currently being copied into the CSIR mainframe computer for further processing and archiving.

Also, during the 1989/90 season, the Pretoria C-band Doppler radar had been commissioned, but unfortunately serious interfacing problems were encountered between the hardware output from the modified EEC C-band radar and the Hewlett-Packard A600 computer which proved to be just too slow on some of its peripherals to accommodate the data stream in its entirety. In order to remedy the problems, certain hardware modifications and streamlining of the data acquisition program (which had been subcontracted to a private consultant) had to be undertaken. During the course of many test runs, several other difficulties had to be overcome which resulted from these latest modifications. Therefore, no data could be collected using more than one Doppler radar during the past and current rainy season. However, a few dual Doppler storm records were obtained during March 1991. A very preliminary test case is included in this report. The NCAR programs for processing multiple Doppler radar data, which have already been implemented and are currently being tested on the CSIR's VM mainframe computer are being utilised for the analysis.

1.1 REFERENCES

DICKS D, HODSON M C, HELD G and NEISHLOS H, 1987. Initial results from the newly-developed CSIR Doppler pulse-pair processor. *Abstracts of the 4th Annual Conference of the South African Society for Atmospheric Sciences*, 13-14 October 1987, Pretoria, 27.

GOMES A M and HELD G, 1988. *First progress report: Precipitation and Airflow (PRAI) Project*. CSIR Report EMA-C 8885, Pretoria, 18pp.

GOMES A M, O'BEIRNE S and HELD G, 1989. *Second progress report: Precipitation and Airflow (PRAI) Project*. CSIR Report EMA-C 89126, Pretoria, 42pp.

HELD G, 1982. Comparison of radar observations of a devastating hailstorm and a cloudburst at Jan Smuts Airport. E M Agee ad T Asai (Eds), in *Cloud Dynamics*, 273-284.

WATER RESEARCH COMMISSION, 1990. *Minutes of the Review Workshop on Rainfall Stimulation Research in South Africa*. Berg-en-Dal Conference Centre, Kruger National Park, 21-23 August 1989, 41pp.

2. THERMODYNAMIC AND KINEMATIC PROPERTIES OF HIGHVELD STORMS

Ana Maria Gomes

2.1 CONVECTIVE AVAILABLE POTENTIAL ENERGY (CAPE) OF HIGHVELD STORMS

Cataloguing storm types and representative soundings provides observational evidence on the distribution of storm type as a function of the environment. Modelling represents a powerful way of examining the influence of environmental conditions on the type of storm likely to develop. An additional benefit of modelling is the opportunity to diagnose model fields to describe the relevant physical processes better. By varying conditions and observing the resultant storm type, it is possible to build a conceptual model of a storm type. It may be possible to distinguish between storm types based upon inherent dynamical differences, rather than what might be a superficial difference in appearance.

From the simulations of Moncrieff and Miller (1976), Weisman and Klemp (1982) and others, it is clear that the relationship of buoyancy and shear is fundamentally important in defining storm structure. This is valid for convection ranging from isolated single cells to complex storms such as squall lines. The basic storm structure seems to be controlled by the vertical distributions of buoyancy and winds. Following Moncrieff and Green (1972), convective available potential energy (CAPE) can be written as equation (1):

$$\mathrm{CAPE} = g \int \frac{\theta(z) - \bar{\theta}(z)}{\bar{\theta}(z)} \, dz \qquad (1)$$

where $\theta(z)$ is the potential temperature of a parcel rising moist adiabatically, and $\bar{\theta}(z)$ is the environmental potential temperature. The limits of integration extend through the levels where the parcel temperature exceeds the environmental temperature. Weisman and Klemp (1982) examined the types of storms that formed when the initial conditions in a homogeneous environment were varied. The available energy was varied from 1000 to 3500 $m.s^{-2}$, and the one-dimensional low-level vertical wind shears ranged from 0 to 0,008 s^{-1}. Through this range, many of the different types of storms that are observed in nature were simulated. They also defined a parameter, a bulk Richardson Number similar to that of Moncrieff and Green (1972), given by

$$Ri = \frac{CAPE}{2\,\overline{u}^2} \qquad (2)$$

where CAPE has been defined in Equation (1) and $\overline{u}^2$ represents a difference between the environmental wind speeds at low and middle levels.

Weisman and Klemp (1986) have demonstrated through numerical simulation studies that different storm structures evolve from different environments. The rotation of the wind shear vector with height preferentially promotes the severity of right- or left-moving storms and can differentiate between fundamental storm types. Rotation of the shear vector with height is stressed, because it is easily possible to have curvature or turning of the wind vector with height but have undirectional shear. With adequate buoyancy, these conditions lead to the long-lived, steady state, and often severe storm structures. In stratifying their numerical modelling results, Weisman and Klemp (1982, 1984) found that storms of the long-lived multicellular type were favoured in environments having moderate thermodynamic instability and large vertical shear; a combination that produces relatively low values of Ri. They suggest that for $10<Ri<40$, supercell development is favoured, whereas multicell growth is favoured for higher Ri values.

Following the ideas discussed above, values of CAPE and Ri that would be representative of Transvaal Highveld storms were calculated using 12 GMT soundings from the Irene upper air station during the 85/86, 86/87 and 87/88 seasons. Results are presented in Figure 2.1 for CAPE values as a function of the number of storms which occurred during each season. Values of CAPE range from 800 to 4800 $m^2.s^{-2}$, representing the typical values of convective energy available to develop convection.

A scatter diagram of CAPE values and vertical wind shear values is shown in Figure 2.2, where one can see a large spread of the values, representing conditions of relatively low shear combined with significant convective energy available for convection, and moderate to low CAPE with low to moderate vertical shear. Also interesting is Figure 2.3, where values of the bulk parameter Richardson Number (Ri) are shown for three seasons, compared with the model classification given by Weisman and Klemp (1982).

The storms in the present study varied greatly in size and intensity but in terms of a classification scheme, the storm type was not very diverse. All of the storms exhibited multicellular characteristics during some part of their lifetimes, and none exhibited features that would place them solidly in the supercell category. Although the range in vertical wind shear was comparatively large [1 to 6 (x $10^{-3}s^{-1}$)], weak to moderate instability lead to Ri values that were on the low side (10 to 40); a range typically associated with storms of the supercell type, provided sufficient buoyancy exists. In these cases, our low Ri are more a manifestation of low CAPE values (<1100 $m^2.s^{-2}$) than of strong vertical shear. At this point of the analysis it is opportune to call attention to comparisons of typical values for storms observed in the USA with the ones occurring on the Highveld. Ri values can be used for classification of storm structure, but only in conjunction with the associated CAPE and shear values.

2.2 DETERMINATION OF KINEMATIC PROPERTIES OF THE WIND FIELD USING SINGLE-DOPPLER RADAR

2.2.1 The VAD Method

Lhermitte and Atlas (1961) showed that, in a situation of widespread homogeneous precipitation, the horizontal wind speed and direction can be determined by measuring the radial velocity V as a function of the azimuth at a constant elevation angle (the so-called VAD or Velocity Azimuth Display). Caton (1963) showed that the divergence of the horizontal wind may be calculated from VAD observations.

Browning and Wexler (1968) showed that the information of the horizontal wind also may be obtained from VAD data and they presented a systematic derivation of the VAD analysis method. Their main results will be summarised in this section.

The radial component of the particle velocity is given by

$$V = (u \sin \beta + v \cos \beta) \cos \alpha + w \sin \alpha \tag{1}$$

where β is the azimuth angle measured clockwise from the north, α is the elevation angle, and u, v, w are the components of the particle velocity along the x-(eastward), y-(northward) and z-(upward) axes, respectively. If for a given range gate

1. u, v, w do not change during the observation period

2. u, v are linear functions of x and y, and

3. w is independent of the position over the VAD circle, then Equation (1) may be rewritten as:

$$V = a_0 + a_1 \sin\beta + b_1 \cos\beta + a_2 \sin 2\beta + b_2 \cos 2\beta \tag{2}$$

where

$$a_0 = \mathrm{DIV} \frac{r \cos\alpha}{2} + w \sin\alpha \tag{3}$$

$$a_1 = u_0 \cos\alpha \tag{4}$$

$$b_1 = v_0 \cos\alpha \tag{5}$$

Here, DIV is the divergence of the horizontal wind, and u_0 and v_0 are the values of u and v at the centre of the VAD circle, with radius r. The coefficients a_2 and b_2 are related to the deformation of the horizontal wind. In widespread precipitation, the vertical velocity of precipitation is essentially due to the terminal fall speed V_T, i.e.

$$W = w - V_T \sim - V_T$$

hence Equation (3) may be rewritten as

$$a_0 = DIV \frac{r \cos\alpha}{2} - V_T.\sin\alpha \tag{6}$$

In order to determine the parameters of the wind field, one takes the radial velocity V for a given range over the VAD circle, and then determines the coefficients a_0, a_1, a_2, b_1 and b_2 by Fourier analysis or least-squares fitting procedures. From the coefficients, a_1 and b_1, the horizontal wind speed and direction can be computed. However, the divergence of the horizontal wind can be determined from a_0 only if V_T is known or the elevation angle is so small that the term $V_T.\sin\alpha$ can be neglected in Equation (6). According to Browning and Wexler (1968), inhomogeneities in the particle fall speed can lead to errors in the determination of DIV. For these reasons, Browning and Wexler recommended that, for the determination of DIV, α should be kept small viz. $\leq 9°$ for rain and 27° for snow. Obviously, the upper limit for α would also depend on the accuracy desired in the determination of DIV.

Srivastava *et al*. (1986) proposed a modified VAD method as a way to overcome these limitations, the so-called extended VAD (EVAD) method.

Their extension of the VAD method pivots on a transformation of Equation (6) to read

$$\frac{2a_0}{r \cos\alpha} = DIV - 2\, V_T \frac{h}{r^2} \tag{7}$$

where h is the height corresponding to the horizontal range and elevation angle α. Their basic assumption is that the DIV and V_T are functions of the height only, i.e. they are horizontally uniform. Consider the VAD scans for many paired values of range and elevation angle such that the resulting VAD circles lie in a narrow interval of height over which the DIV and V_T may be regarded constant in height as well. If these conditions are satisfied, then a plot of $2a_0/(r \cos\alpha)$ versus h/r^2 for these VAD scans, should be a straight line according to Equation (7). Conversely, if the plot is a straight line, it is likely that the conditions mentioned above are satisfied. Both the DIV and V_T may be determined from the intercept and the slope of the straight line obtained by least-squares fit to the data. Their extension of the VAD method does not require knowledge of the particle fall speed or restriction of the scans to low elevation angles. On the contrary, it is important for the success of the method that h/r^2, or in other words the elevation angle, should have a sufficient range of variation to enable a proper fit of the data to Equation (7).

When the extended VAD method was compared with deviations of the VAD method proposed by others, it was found that the EVAD has certain advantages over the other methods. First, in the EVAD method u and v are calculated for each VAD circle at different elevation angles representing a narrow height interval. Therefore, the homogeneity and steadiness of the wind field can be checked. Secondly the error of fit of $2a/(r \cos\alpha)$ against h/r^2, by linear regression, provides a built-in test of the validity of some of the assumptions of the EVAD method, namely, the uniformity of W and DIV in the horizontal. Thirdly, and most important, the EVAD method uses the radial velocity data over complete circles, which means that the a_0 determined by a full circle of radial velocity data is related to the average DIV over the circle by Equation (6), even if the velocity field is not linear, provided that V is representative of the average fall velocity within the circumference of the VAD circle. In other words, Equation (6) is not adversely affected by irregular variations in DIV and V when a full circle of data is used.

2.2.2 Preliminary Results of the Extended VAD (EVAD) Analysis

The technique of retrieving kinematic parameters using single-Doppler data, described above, has been implemented and the storm that occurred on 21 November 1987 was selected for EVAD analysis because of its characteristic widespread precipitation.

This squall line was first monitored by the Houtkoppen radar at 14:38 when it was approximately 110 km south-southwest of the radar site. By 16:07, the storm began to traverse the hail-reporting network. Hailfalls were reported in the East Rand and the northern suburbs of Johannesburg. Precipitation measured ranged between 13,2 mm at Bapsfontein, southeast of Pretoria, and 63 mm at Krugersdorp on the West Rand (O'Beirne, 1988). During the next two hours, an extensive trailing stratiform region could be observed (Figure 2.4). The radar was completely embedded in the region of stratiform precipitation, which appeared fairly homogeneous on the PPI reflectivity picture.

From Figure 2.4, one can also see the convective leading edge of the squall line exhibiting cores of 60 dBZ at approximately 45 km north-north-east of the radar. Also to be seen in this Figure is the imaginary EVAD circle of 25 km radius. The VAD analysis was then limited to range gates within a horizontal distance of up to 25 km from the radar, thus avoiding patchy VAD circles.

Vertical profiles of the horizontal wind, divergence and vertical velocity were obtained using the EVAD (Extended Velocity Azimuth Display) method.

The VAD data of the Houtkoppen radar consisted of six sets of complete scans at elevation angles ranging from 1,9 to 50,5 degrees. The range gate spacing was 300 m and the average between successive azimuths was about 1,0 degree. Unfortunately, no data was collected at vertical incidence for this particular storm.

As a first step in the analysis, the radial velocity was reformatted. The reformatting was done by elevation angle and range gate number, after which the velocity data for a complete VAD circle could be conveniently accessed by range gate and elevation angle.

Next, the Doppler velocities for a given VAD circle were fitted according to Equation (2) by a least-squares method and the coefficients a_0, b_1 and b_2 determined. The standard error of the fit was calculated. Each of the Doppler velocities was then re-examined and those that differed from the first by more than twice the standard deviation, were flagged. A second fit was then performed, excluding the flagged velocities or outliers in the distribution.

As mentioned before, the VAD analysis was limited to range gates within a horizontal distance of 25 km from the radar. Upwards of 2500 data points associated with VAD circles for each set of scans were analysed. The resultant set of values consisting of the coefficients a_0, a_1, a_2 and b_2, the error of fit, and other parameters, were arranged by elevation and horizontal range. These data were then classified into height intervals, averaging 500 m in depth.

The coefficients a_1 and b_1 were used to determine the horizontal winds. A linear least-squares fit was then performed, as suggested by Equation 7. The standard error of the fit was determined to locate and reject spurious values of a_0. The final fit yielded values of the DIV as a function of the height.

2.2.3 Profiles of Horizontal Wind Speed and Wind Direction

Profiles of horizontal wind speed and wind direction obtained from the VAD analysis are shown in Figures 2.5 and 2.6. The time-height profile of wind direction, Figure 2.6, shows that in the lower levels, the air flow was predominantly from northeast, veering to southeast and then to southwest at higher levels. In other words, taking into account the movement of the squall line as a whole towards the northeast at an average speed of 35 $km.h^{-1}$, we have a relative front-to-rear flow in the lower levels with a compensating rear-to-front flow in the upper levels relative to the squall line.

The magnitudes of the wind speed range from 3 to 6 $m.s^{-1}$ in the lower and middle levels, increasing to 18 $m.s^{-1}$ at higher levels.

2.2.4 Divergence of the Horizontal Wind

A time-height plot of divergence constructed from six EVAD scans is shown in Figure 2.7. From this Figure, the alternating layers of divergence and convergence can be identified throughout the depth of the EVAD volume.

Below 2,5 km height, the wind shows a strong convergent field having a maximum convergence of about 4 x $10^{-4}s^{-1}$ at 1,0 km AGL. This convergent pattern is alternated with a divergent flow above it. Meanwhile, the mid-level divergent layer increased in thickness and in intensity, showing a strong divergent wind field with a maximum divergence of about 4 x $10^{-4}s^{-1}$ at about 5,5 km height. The upper-level divergent layer persisted throughout the time of the analysis, but it was somewhat weaker at a later stage.

2.2.5 Vertical Air Velocity

The vertical air velocity was determined by numerical integration of the anelastic continuity equation

$$DIV + \partial(\rho w)/\partial Z = 0 \qquad (8)$$

The vertical air velocity is shown in Figure 2.8. Basically, the vertical velocity profile is dominated by mesoscale upward motion during the first five minutes of the analysis and then characterised by downward motions afterwards. The mesoscale downdraught was also well defined, with a depth of about 7 km, indicating its presence over the entire layer and continued to the surface. Typical updraught and downdraught values were 25 $cm.s^{-1}$ with peak values near 1 $m.s^{-1}$ during the period of observation.

2.2.6 Precipitation and Precipitation Efficiency Derived from Single-Doppler Radar

Wilson *et al.* (1981) have examined the use of Doppler radar for the estimation of precipitation rates and efficiencies in stratiform rain situations. Using the divergence values obtained from the VAD method, the mass continuity equation is integrated vertically to obtain the vertical velocity profile. From the vertical velocity and saturation mixing ratio profiles, the height-integrated condensation rate is obtained. The accuracy of this technique to estimate condensation rates is obviously closely related to the accuracy of the vertical velocity profiles. Theoretical precipitation amounts can then be calculated using the equation for the condensation rate.

The condensation rate in the vertical column of air above the radar is assumed to be equal to the precipitation rate (R)

$$R = \int_{\text{Cloud base}}^{\text{Cloud top}} \rho(Z)\ w(Z)\ \frac{dm}{dZ}\ dZ \qquad (9)$$

where m is the saturated mixing ratio with respect to ice or water, which ever is appropriate.

In this case the theoretical VAD-derived rainfall rate is actually an average for a 25 km radius around the radar.

In their study, Wilson *et al.* (1981) have shown very promising results of precipitation and precipitation efficiencies derived from the VAD technique. Since divergence can be shown to be the most error-prone derivable kinematic property, the close correspondence between rain gauge and VAD-derived rainfall rates gives a high degree of confidence in the VAD method. Hobbs *et al.* (1980) have reported a wide range of precipitation efficiencies for western Washington rainstorms. They reported an efficiency of at least 80% in a similar wide cold frontal rain band as described in this case study.

Following a similar approach, condensation rates have been calculated for the storm on 21 November 1987 during the period of 17:27 to 17:55. The results presented in Figure 2.9 illustrate the use of the technique. From the divergence field one can see the evident low-level (0-2 km) convergence responsible for the increase in vertical velocity and consequently the condensation rate also being concentrated at low and middle levels, reaching a maximum at about 2 km AGL.

In addition, the precipitation rate at ground level was obtained by assuming an equilibrium between condensate production and sedimentation of precipitation, which will be referred to as VAD estimated precipitation. Unfortunately, no rain gauge data within a radius of 25 km of the radar was available and the only information that could be used for the calculation was the accumulated hourly rainfall for Jan Smuts Airport, which is 5 km outside the VAD circle in the east-southeast. The VAD derived rainfall for the period 17:27 to 17:55 is shown in Figure 2.10 a, which gives a total of 2,9 mm during a period of 28 minutes. Based on this result, and extrapolating for a one-hour period, the resultant rainfall rate would be 6,2 mm. If the rainfall accumulated during the period of 17:00 to 18:00, 6,7 mm (Figure 2.10b) is used to compare the rate of GAUGE/VAD, the result shows that the VAD during this period estimated 8% less rain than the gauge, resulting in a "precipitation efficiency" of 108% for the period of the analysis.

Obviously, the aim of this exercise is to illustrate that this technique can be used in the calculation of precipitation and precipitation efficiency, which in turn does not exclude other available techniques. Besides, this is certainly not the most ideal case study; because of the scanning cycles the vertical resolution was not as good as for cases described in the literature. However, the VAD technique has been shown to be a very powerful tool for measuring kinematic features of the wind field. The extension of this technique to estimate condensation rate and precipitation rate appears reasonably good, but the accuracy must be checked against the actual rainfall measurements which are not available at this stage of the analysis.

Provided care is taken to obtain an accurate estimate of the surface precipitation of the VAD cylinder, this technique should provide accurate estimates of precipitation efficiency on the mesoscale.

2.3 REFERENCES

BROWNING K A and WEXLER, 1968. A determination of kinematic properties of a wind field using Doppler radar. *J. Appl. Meteorol.*, 7, 105-113.

CATON P G F, 1963. The measurement of wind and convergence by Doppler radar. *Proc. 10th Conference Radar Meteorology*, Washington DC, Amer. Meteor. Soc., 290-296

HOBBS P V, MATEJKA T J, HERZEGH P H, LOCATELLI J D and HOUSE R A Jr, 1980. The mesoscale and microscale structure and organization of clouds and precipitation in mid-latitude cyclones. I: A case study of a cold front. *J. Atmos. Sci.*, 37, 568-596.

LHERMITTE, R M and ATLAS D, 1961. Precipitation motion by pulse-Doppler radar. *Preprints, 9th Conference on Radar Meteorology*, (Norman, Okla), AMS, Boston, 218-223.

MONCRIEFF M W and GREEN J S A, 1972. The propagation and transfer properties of steady convective overturning in shear. *Quart. J. Roy. Meteor. Soc.*, 98, 336-352.

O'BEIRNE S, 1988. *A case-study of a squall-line storm over the Transvaal Highveld.* Unpublished Honours Project, University of the Witwatersrand, Johannesburg, 31.

SRIVASTAVA R C, MATEJKA T J and LORELLO T J, 1986. Doppler radar study of the trailing anvil region associated with a squall line. *J. Atmos. Sci.*, 43, 356-377.

WEISMAN, M L and KLEMP J B, 1982. The dependence of numerically simulated convective storms on vertical wind shear and buoyancy. *Mon. Weath. Rev.*, 110, 504-520.

WEISMAN, M L and KLEMP J B, 1984. The structure and classification of numerically simulated convective storms in directionally varying wind shears. *Mon. Weath. Rev.*, 112, 2479-2498.

WILSON J, CARBONE R and RAMSAY B, 1981. Precipitation and precipitation efficiencies derived from single Doppler radar. *Preprint 20th Conference on Radar Meteorology*, Nov 30 - Dec 3, Boston, Mass., American Meteorological Society, 461-468.

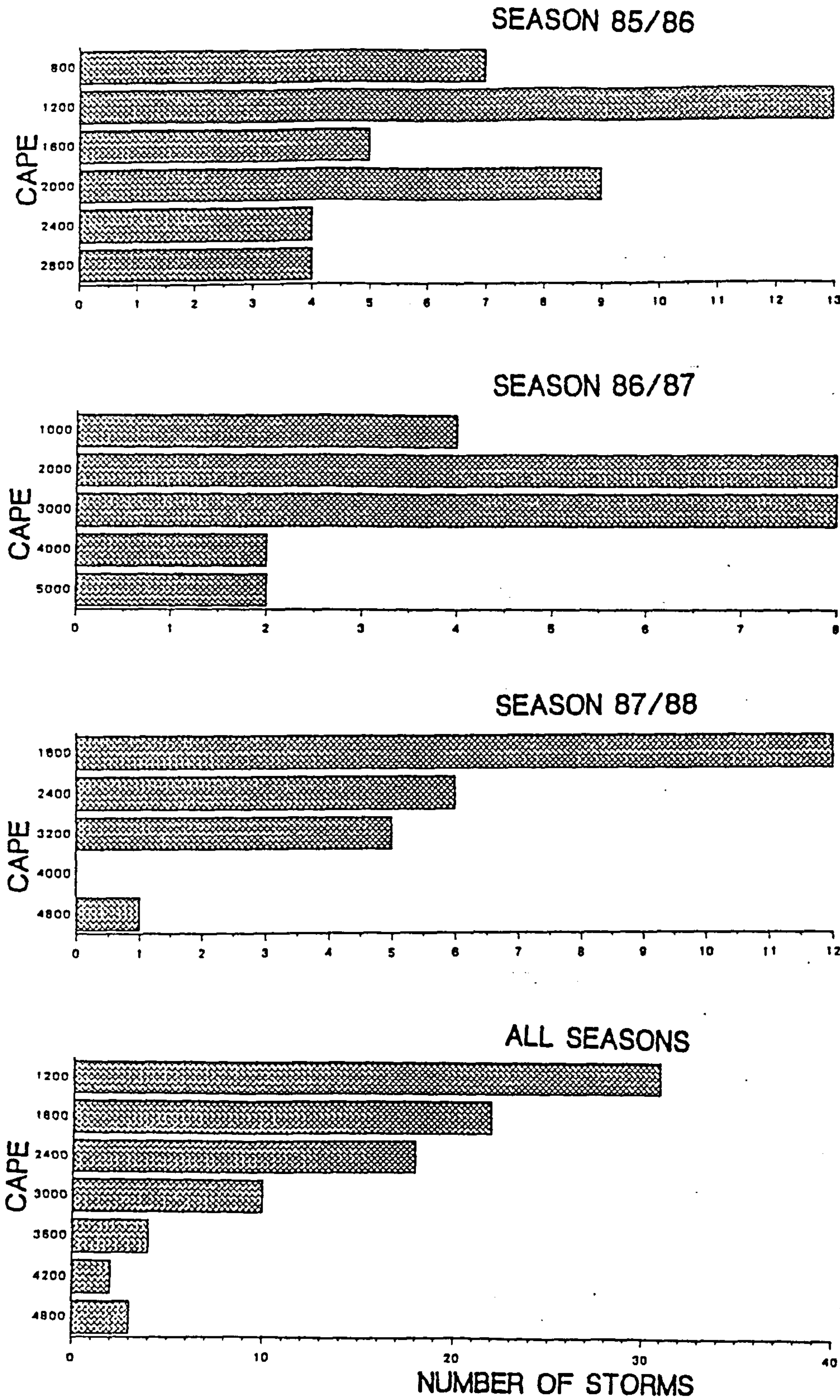

SEASON 85/86

FREQ	CUM. FREQ	PERCENT	CUM. PERCENT
7	7	16.67	16.67
13	20	30.95	47.62
5	25	11.90	59.52
9	34	21.43	80.95
4	38	9.52	90.48
4	42	9.52	100.00

SEASON 86/87

FREQ	CUM. FREQ	PERCENT	CUM. PERCENT
4	4	16.67	16.67
8	12	33.33	50.00
8	20	33.33	83.33
2	22	8.33	91.67
2	24	8.33	100.00

SEASON 87/88

FREQ	CUM. FREQ	PERCENT	CUM. PERCENT
12	12	50.00	50.00
6	18	25.00	75.00
5	23	20.83	95.83
0	23	0.00	95.83
1	24	4.17	100.00

ALL SEASONS

FREQ	CUM. FREQ	PERCENT	CUM. PERCENT
31	31	34.44	34.44
22	53	24.44	58.89
18	71	20.00	78.89
10	81	11.11	90.00
4	85	4.44	94.44
2	87	2.22	96.67
3	90	3.33	100.00

Figure 2.1: Frequency distribution of convective available potential energy (CAPE - $m^2.s^{-2}$) during the seasons 85/86, 86/87, 87/88 and for all three seasons.

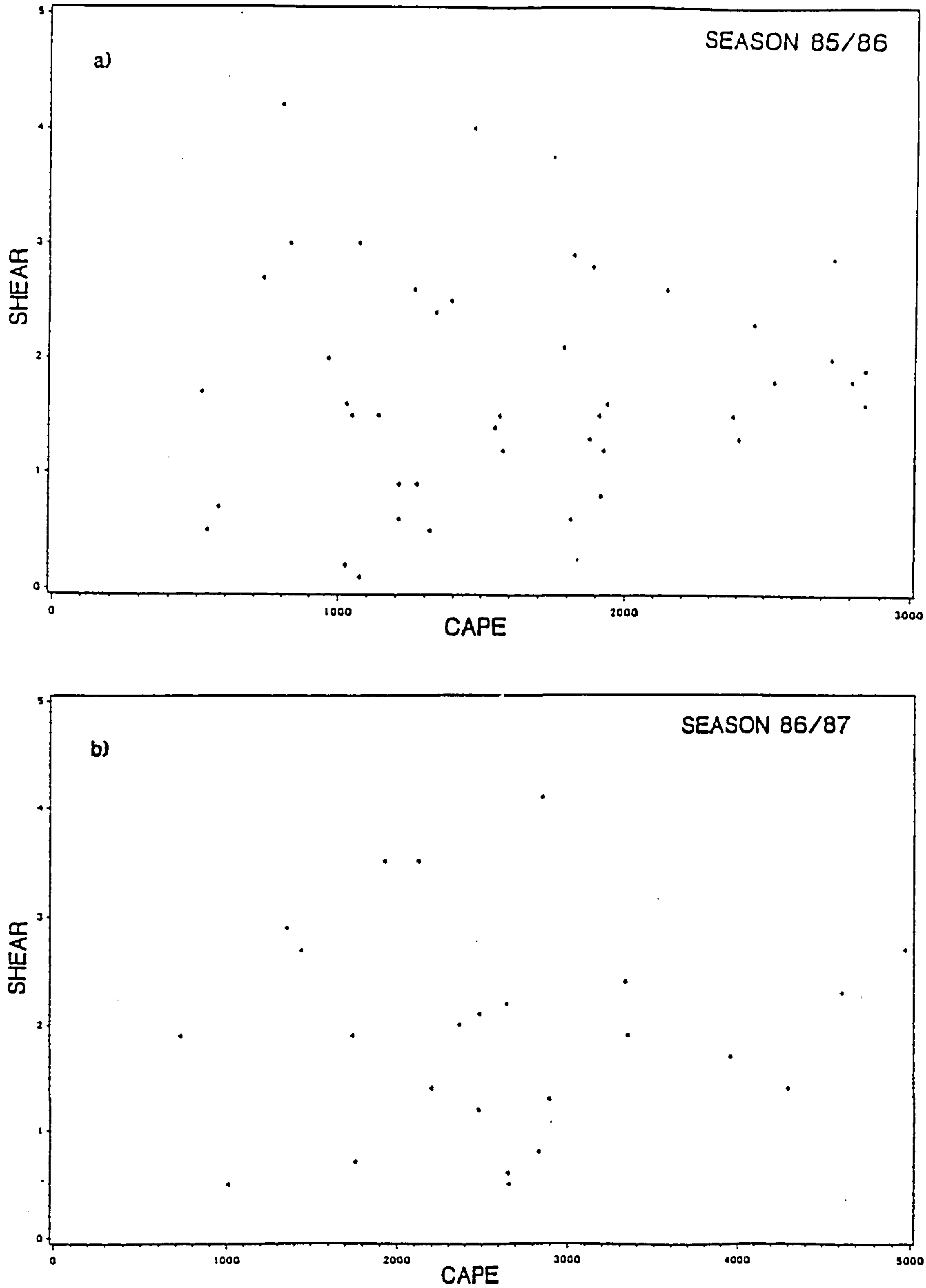

Figure 2.2: Scatter diagram of CAPE ($m^2.s^{-2}$) versus vertical wind shear ($10^{-3}.s^{-1}$).
a) season 85/86, b) season 86/87

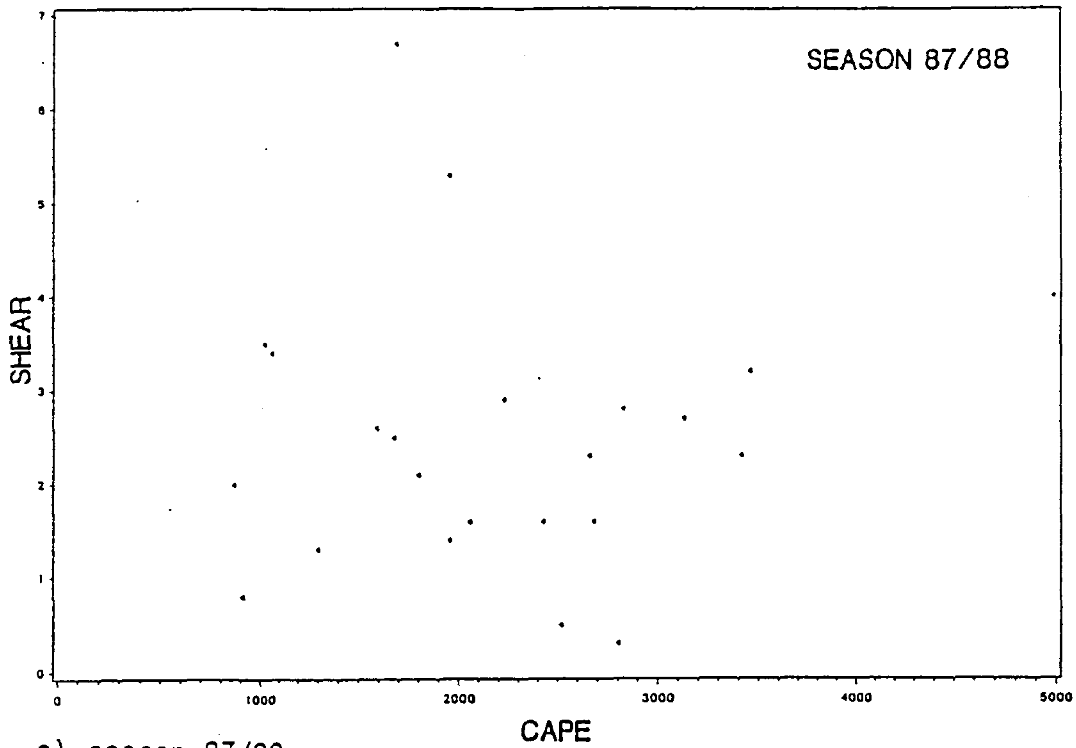

Figure 2.2: c) season 87/88.

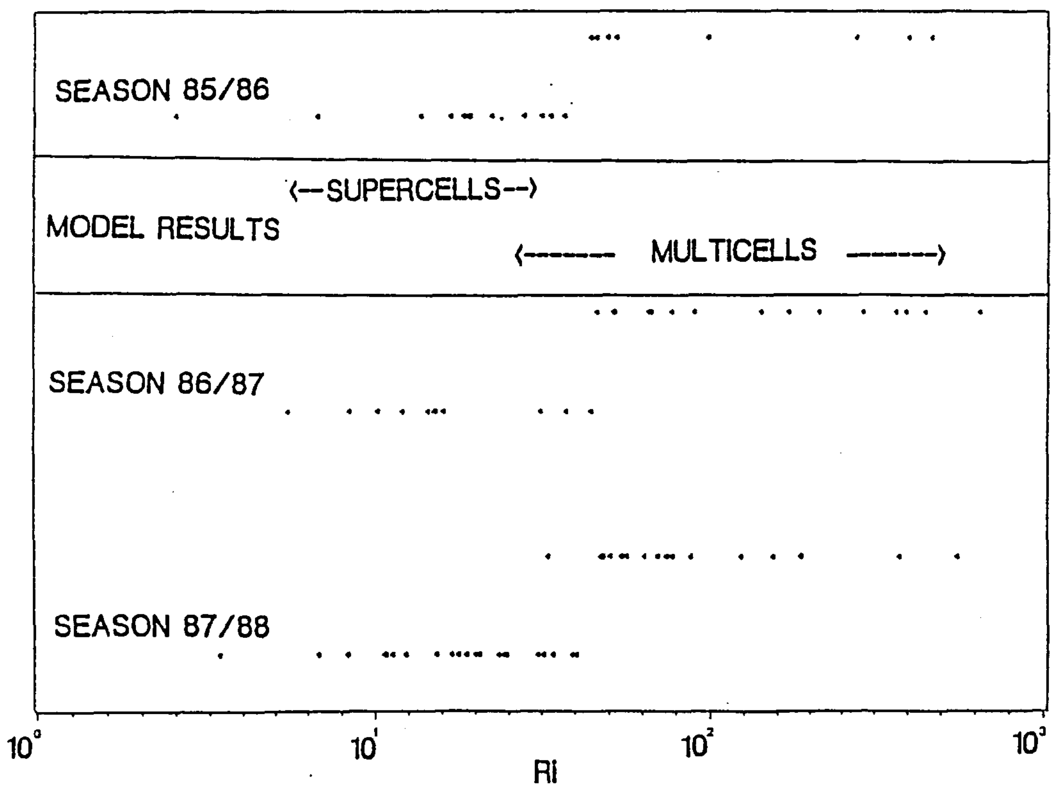

Figure 2.3: Values for Richardson Number (Ri) for seasons 85/86, 86/87 and 87/88 compared with the classification model given by Weisman and Klemp (1982).

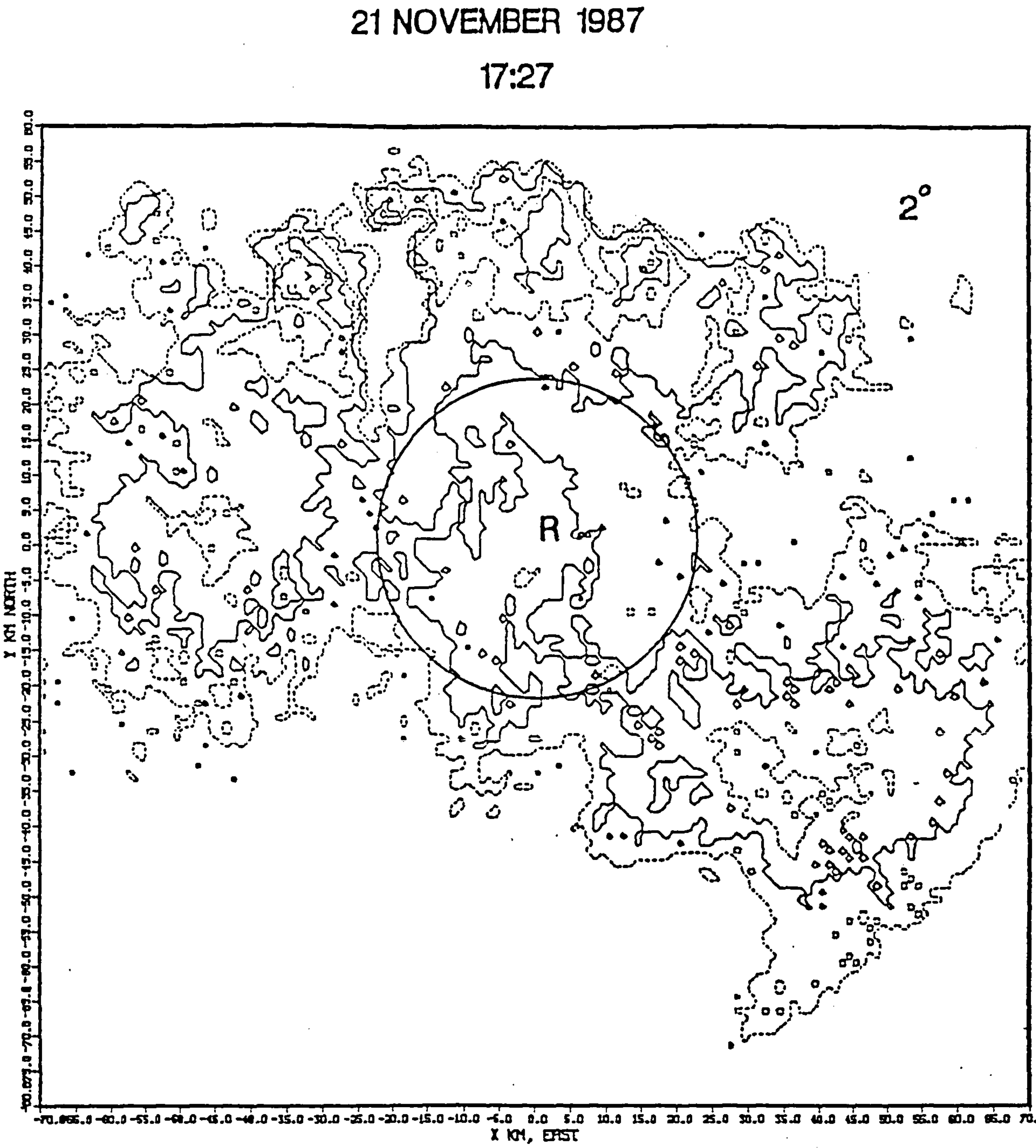

Figure 2.4: PPI reflectivity for 21 November 1987 at 17:27, showing the imaginary EVAD circle of 25 km considered for the analysis. Reflectivity contours are 23,3; 30; 40; 50 and $\geq$60 dBZ.

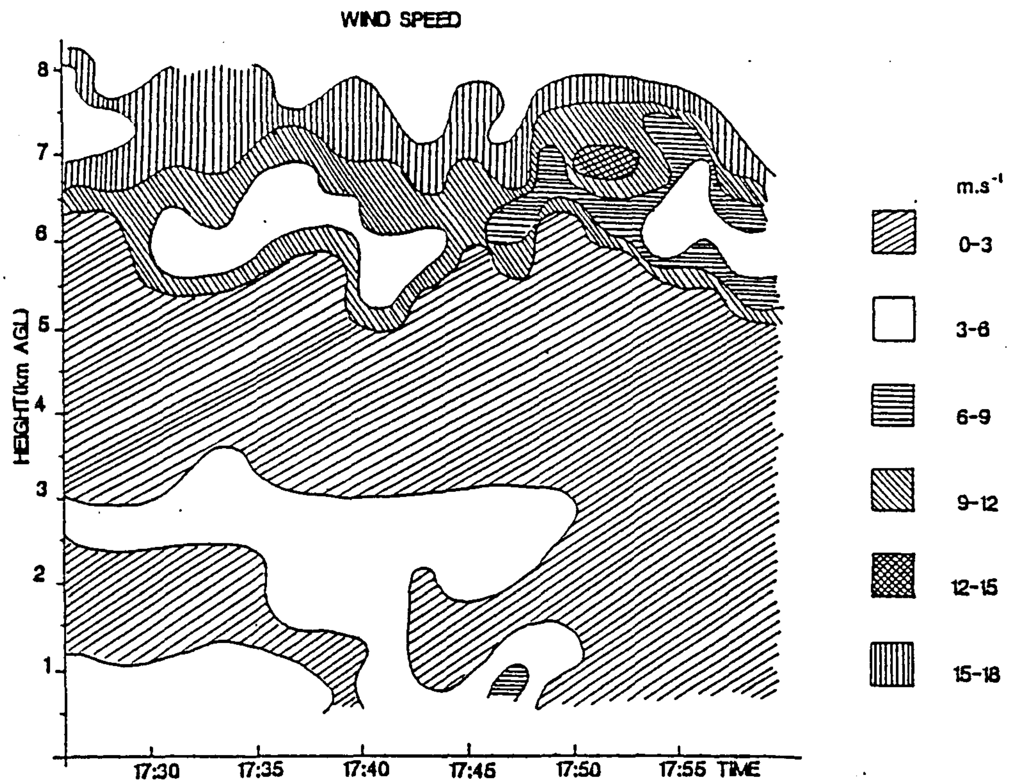

Figure 2.5: Vertical profile of horizontal wind speed ($m.s^{-1}$), for the 21 November 1987 storm.

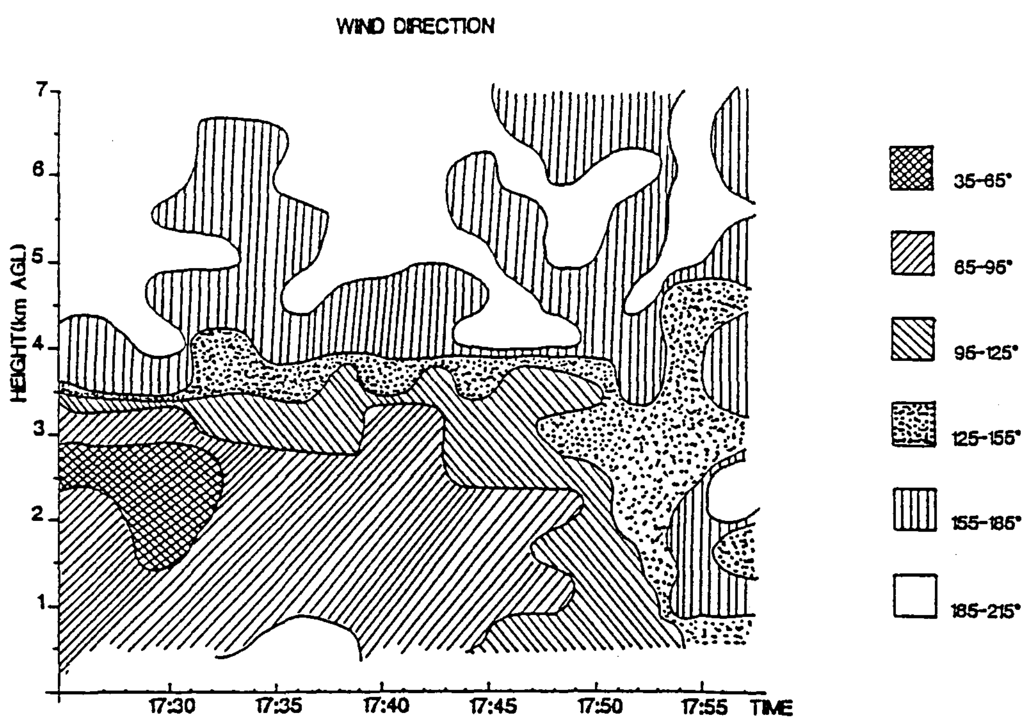

Figure 2.6: Vertical profile of wind direction (degrees), for the 21 November 1987 storm.

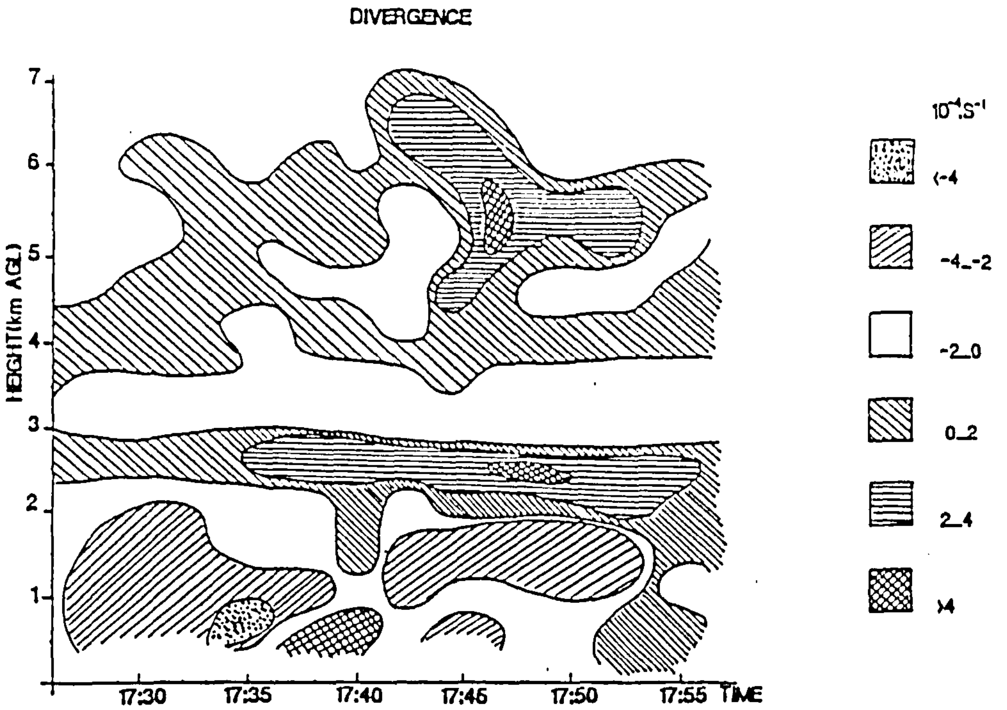

Figure 2.7: Vertical profile of divergence ($10^{-4}.s^{-1}$), for the 21 November 1987 storm.

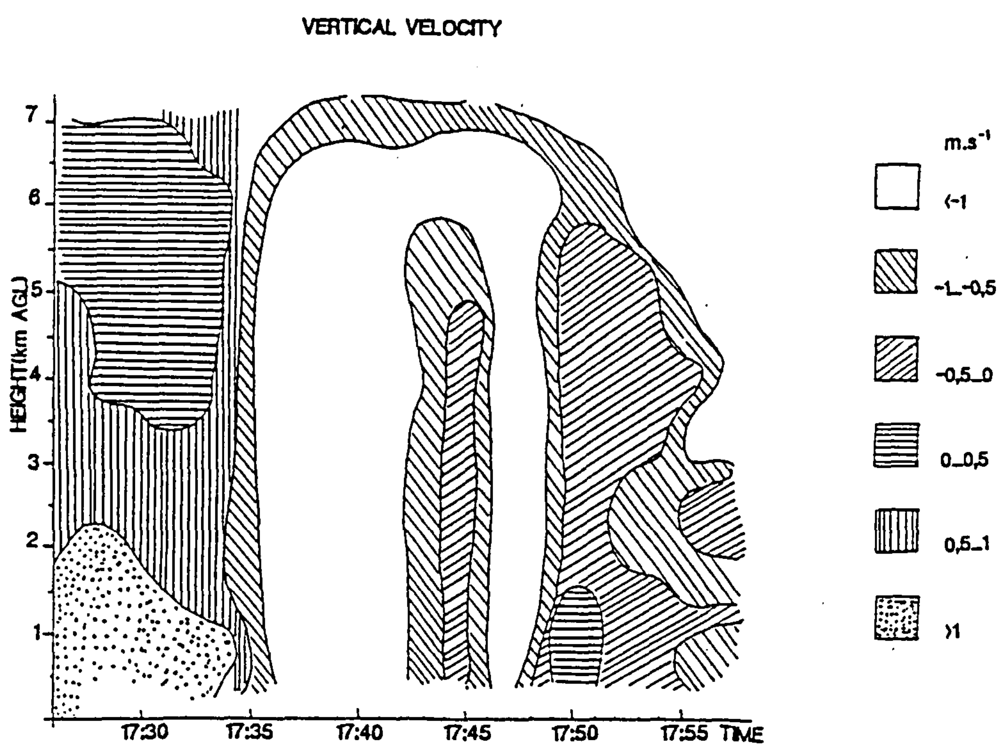

Figure 2.8: Vertical profile of vertical air velocity ($m.s^{-1}$), for the 21 November 1987 storm.

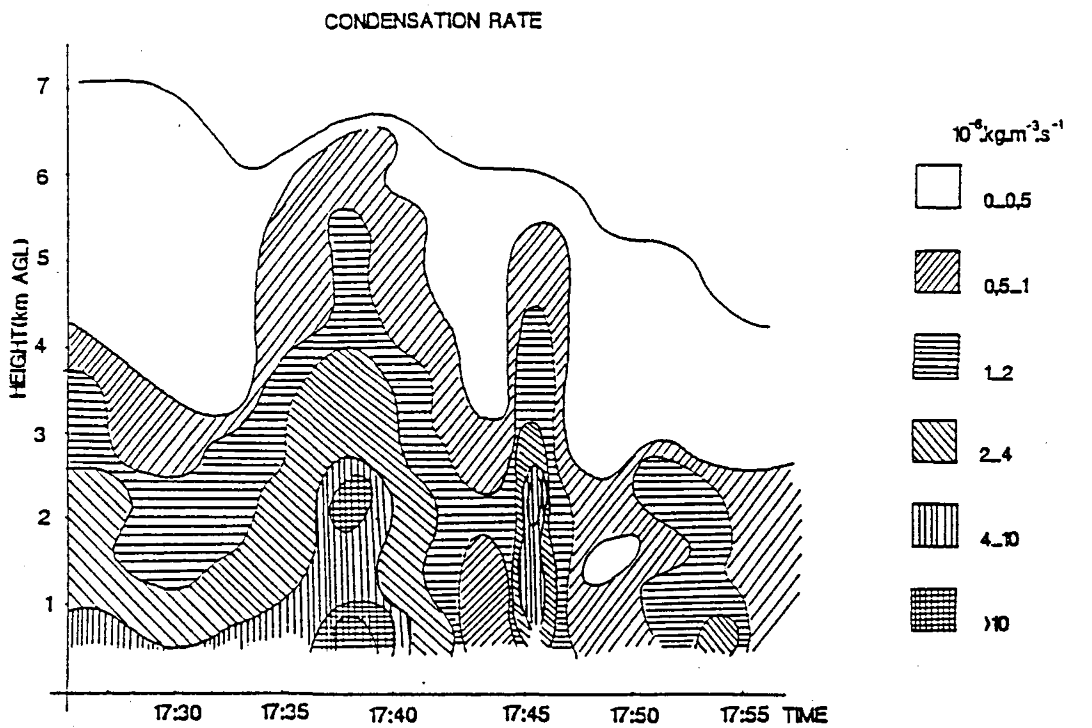

Figure 2.9: Vertical profile of condensation rate ($10^{-6}.kg.m^{-3}.s^{-1}$), for the 21 November 1987 storm.

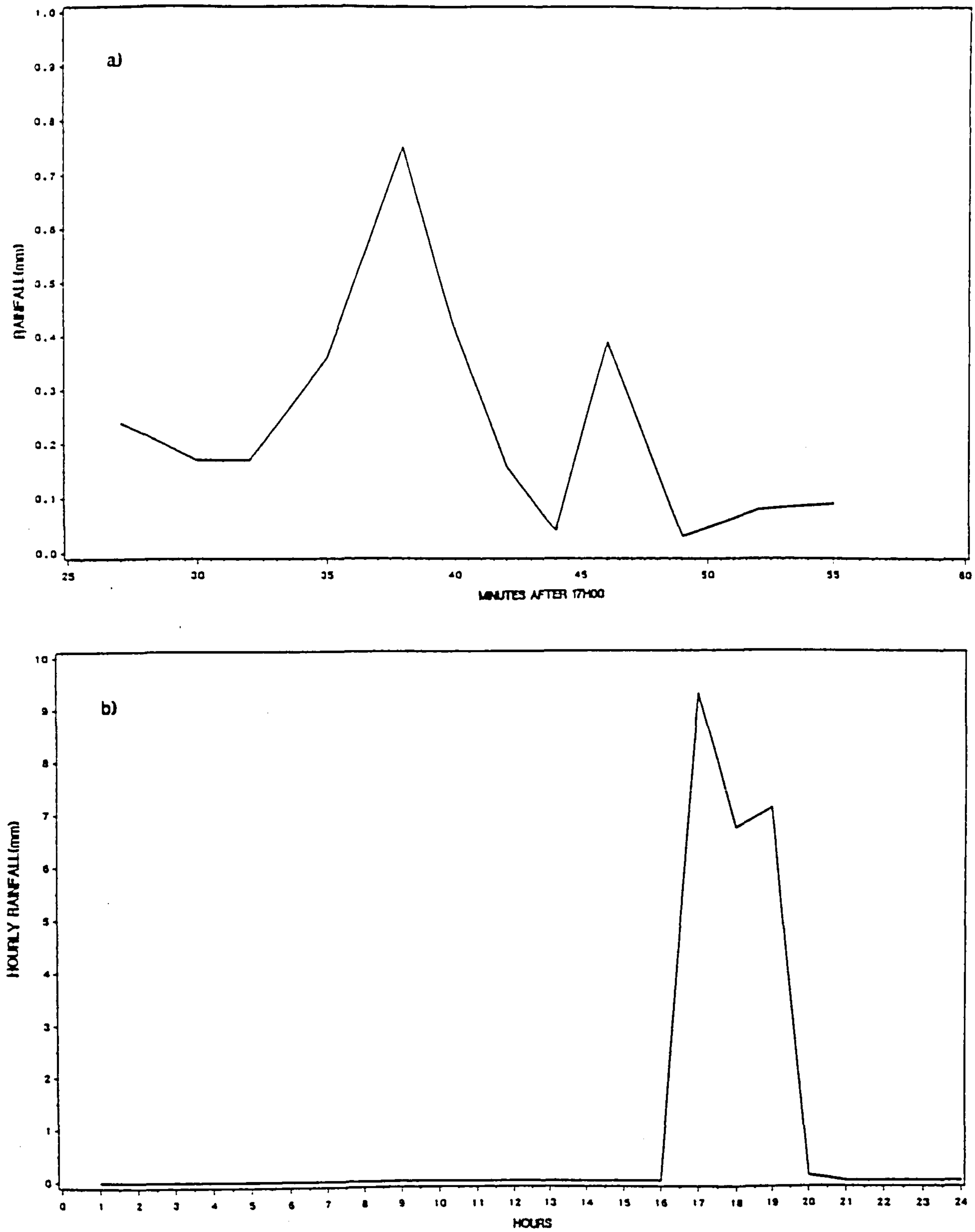

Figure 2.10: a) VAD derived rainfall during 17:27 and 17:55 on 21 November 1987.
b) Hourly rainfall at Jan Smuts Airport on 21 November 1987, which is located about 5 km outside the VAD circle in the east-southeast.

3. RAINDROP SIZE DISTRIBUTIONS AND Z-R RELATIONSHIPS

Sean O'Beirne

3.1 BACKGROUND

The study of drop size distributions (DSD) in rainfalls has a wide range of applications in the field of meteorology. Studies of changes in DSDs may hold important clues in understanding the processes of raindrop evolution. Quantifying pollutant scavenging and the erosional effects of drop impacts on soils requires detailed knowledge of DSDs (Zawadzki and de Agostinho Antonio, 1988). DSD studies having received the most research attention, however, have been those relating DSDs to radar reflectivity in order to realise accurate radar-measurement of rainfall. Indeed, radar reflectivity factor (Z), liquid water content (M) and rainfall rate (R) are all direct functions of a given DSD (Doviak and Zrnic, 1984). Improvements in accuracy of radar-measured rainfall are still dependent on a better understanding of DSDs (Hodson, 1986).

Studies of DSDs have utilised a variety of measurement approaches, from analysis of coloured prints left on dyed absorbant paper (Marshall and Palmer, 1948), through raindrop cameras (Fujiwara, 1965) to electromechanical devices such as spectropluviometers (Donnadieu, 1980) and disdrometers (Joss and Waldvogel, 1967). In addition a number of DSD studies have been based on data from vertically-pointing Doppler radars (Sekhon and Srivastava, 1971; Pasqualucci, 1976; Hodson, 1986). All these studies have pointed to a considerable degree of temporal variation of raindrop spectra which can be related to various physical processes such as drop-sorting, aggregation, coalescence and drop break-up (Joss and Waldvogel, 1988). The variations in raindrop spectra also have a profound influence on rain rates and the reflectivity factor. In the course of this section drop-size distributions measured during the 1989/1990 rainfall season and their implications for radar-measurement of rainfall will be presented.

3.2 THEORY

Although Wiesner (1895) made one of the first known sets of DSD measurements, the work of Marshall and Palmer (1948) has received widest acclaim as seminal work in the field. Using dyed filter paper to measure the distribution of raindrops with size, they proposed a general relation of the form

$$N_D = N_o e^{-\Lambda D} \qquad (1)$$

where D is the raindrop diameter, N_D is the number of drops of diameter between D and D+dD, N_o is the value of N_D for D = 0, and Λ is an empirically determined coefficient of rain intensity (Battan, 1973). In addition Marshall and Palmer (1948) found that N_o was a constant and equal to 0,08 cm^{-4} and that

$$\Lambda = 4{,}1R^{-0{,}21}$$

where R is rainfall rate in $mm.h^{-1}$ and Λ in cm^{-1}.

The general applicability of such a relationship was criticised by Mason and Andrews (1960) who showed that while the M-P distribution was suitably representative of DSDs in warm frontal rain, coalescence showers had DSDs that were entirely different.

DSDs measured at the ground were somewhat restrictive in application and attention became increasingly focused on comparisons between DSDs measured at ground level compared with the initial spectra aloft. The importance of DSDs aloft, besides being in the area likely to be measured by radar, had the potential to offer valuable clues as to factors influencing the evolution of raindrop spectra. An initial exponential DSD for example, with a large negative slope would be substantially modified by the effects of coalescence, accretion and evaporation whereas only small changes would be evident in an initial DSD of relatively small negative slope (Hardy, 1963). Hardy concluded that spectra observed at the ground must develop from a distribution aloft having fewer smaller drops and more larger drops than indicated by an M-P distribution.

Srivastava (1967) argued that an M-P distribution would change only slowly during fall and that narrow distributions would rapidly tend towards an exponential distribution. On the basis of this evidence he concluded that the exponential shape of a DSD is due to the coalescence process. The effects of drop break-up were included in subsequent work in which equilibrium distributions were shown to be the result of a balance between drop growth and drop disintegration processes. These equilibrium distributions would be realised more rapidly in situations of higher liquid water content, but it was unlikely that they would be realised in natural conditions of liquid water content and fall distance (Srivastava, 1971). Srivastava noted furthermore that observed distributions were distinctly steeper and limited to smaller sizes than the computed distributions, implying that other processes besides break-up and coalescence were responsible for shaping DSDs, but the omission of factors such as the effects of collisional break-up and condensation may also have played a part.

Making use of a vertically-pointing Doppler radar, Sekhon and Srivastava (1971) measured DSDs at heights below the 0°C-level. Most of the size distributions were found to be well approximated by an exponential distribution but with a steeper curve than that of M-P. Of the conclusions they drew the most profound was that N_0 in fact increases with increasing rain rate and is thus not constant. Joss and Waldvogel (1974) confirmed this finding using ground-based disdrometer measurements and pointing out that the pattern of temporal variation of N_0 may often exhibit a "jump" which appeared to indicate a change in rainfall regime from continuous to convective rain or vice versa.

Young (1975) expanded on the work of Srivastava by improving the computations of the condensation and break-up treatments as well as including the activation of cloud condensation nuclei (CCN). Young utilised two conceptually different models namely "collisional break-up" and "spontaneous disintegration". The spontaneous disintegration model generated an even flatter curve than that produced by Srivastava (1971) leading Young to conclude that it was unlikely that spontaneous break-up was the sole agent in shaping DSDs. The collisional break-up model on the other hand produced a "steady state" spectrum, exponential in form and in fair agreement with M-P. List and Gillespie (1976) modelled DSD evolution in still air assuming warm rain processes. They used only collisional break-up data to produce spectra which had virtually no drops larger than 2,5 mm in diameter but with high concentrations of smaller drops. On the basis of these results List and Gillespie (1976) concluded that the existence of large drops could be solely attributed to ice-phase precipitation mechanisms. Srivastava (1978) in formulating equations by which evolving DSDs could be paramaterised, showed that collisional break-up dominates over spontaneous break-up when the initial number concentrations (N_D) of small drops is within the commonly observed range. When N_D was some two orders of magnitude lower, spontaneous break-up was seen to play a significant role in shaping the observed DSDs.

Carbone and Nelson (1978) using airborne optical spectrometer measurements, together with 3 and 10 cm radars, showed that the temporal evolution of DSDs at cloud base is dominated by updraught sorting (sedimentation) effects where smaller drops do not have sufficient terminal velocity to fall through cloud base. Sedimentation leads to higher numbers of large drops and lower number densities of small drops during the cloud-growth stage. During this stage number densities are typically one order of magnitude lower than M-P at the 1 mm diameter size. During dissipation, drop spectra assume M-P characteristics but rarely achieve comparably high concentrations of small drops or comparably low concentrations of large drops. The agreement found between their own results and those of Srivastava (1971; 1978), suggests that the spontaneous break-up process may be important for rainfall rates in excess of 30 $mm.h^{-1}$ when liquid water content values are greater than 1 $g.m^{-3}$. High variability of drop-spectra precludes the reliable use of conventional radar rainfall (Z-R) estimation techniques in convective precipitation unless some allowance is made for spatial and temporal change. On intensely studied storm days where large quantities of precipitation were produced, early radar echoes resulted from both liquid and ice-phase processes. In particular the question arises as to whether an ensemble of drops will evolve to a unique equilibrium if given enough time. Carbone and Nelson (1978) argued that the findings of their work cast doubt on the concept of a unique equilibrium in the presence of strong vertical air motions.

Hodson (1986) using a vertically pointing Doppler radar as well as data from Pasqualucci (1982a; 1982b) showed that the M-P distribution is entirely inappropriate for rain rates exceeding 25 $mm.h^{-1}$. At rain rates exceeding 25 $mm.h^{-1}$ the slope of the distribution, Λ, will tend towards a constant value between 2,1 and 2,3 mm^{-1}. A Z-R relationship computed from these values gives Z=939R and indicates that attenuation is also proportional to rain rate when the vertical wind velocity is nil. When the rain rate is greater than 25 $mm.h^{-1}$, the M-P distribution applies for drops greater than 3 to 3,5 mm in diameter, but larger drops have decreasing values of Λ arising from drop break-up. Drop break-up data from Low and List (1982) indicate that a large number of drops in the 3 to 3,5 mm size range are generated by drop break-up effects.

Srivastava's (1971) idea of equilibrium drop size distributions, in which drop growth effects were balanced out by drop disintegration effects received considerable attention in the 1980's. Srivastava found that natural levels of liquid water content would not allow realisation of equilibrium in the time or fall distance normally available. List *et al.* (1987) agreed with this claim showing model results of equilibrium DSDs to be trimodal with peaks at drop diameters of 0,268, 0,790 and 1,760 mm. Equilibrium distributions were shown to take time to evolve especially at rain rates of less than 10 $mm.h^{-1}$. In natural, steady rain spectra deviations from equilibria are indicative of a number of features. These features include not yet developed equilibria, changes in rain processes with height and whether rain origin is related to warm or cold cloud processes (List *et al.*, 1987). Using a time-dependent rain shaft model and assuming a M-P distribution with a rain rate of 50 $mm.h^{-1}$, List *et al.* showed that the largest drops would reach the ground first with the onset of rain. As more drops appear the drop spectrum widens rapidly as a result of collisional drop break-up. At high rain rates equilibrium is reached after some 3 km of fall. Results of the model runs showed that small drops measured at the ground do not originate at cloud base but occur rather as a result of collisional break-up effects amongst the larger drops during their fall. Although this specific work was based on assumptions pertaining to warm rain processes, List *et al.*, argued that the results may also represent cold cloud processes where warm rain develops parallel to the ice particles. List (1988) showed that any DSD will develop with time into an equilibrium DSD regardless of the initial spectrum. All equilibrium distributions have the same shape with observed differences being related to a factor proportional to rain rate.

3.3 INSTRUMENTATION

Drop-size distributions were measured using a Joss-Waldvogel raindrop disdrometer (Joss and Waldvogel, 1967) which was operated on the roof of the Atmos Building within the CSIR campus. The principle of operation of the disdrometer is that a voltage is induced into a sensing coil by the downward displacement of a styrofoam body. This signal is amplified and applied to another coil within the transducer to counteract the movement of the body and return it to its rest position (Figure 3.1). Thus, the instrument retains a high recovery rate and is capable of measuring several hundred drops a second (Waldvogel, 1974; Kinnel, 1976). The disdrometer was housed in a polystyrene-lined box to dampen extraneous noise from the drops hitting the roof and covered with foam rubber to prevent splashing effects. The disdrometer was operated in close proximity to a tipping-bucket rain gauge allowing appraisal of the disdrometer in measuring rainfall. Unfortunately some teething troubles with installing the disdrometer meant that continuous measurement was only effected from the end of November. The disdrometer was subsequently operational for the duration of the 1989/1990 rainfall season.

Rainfall totals measured using the disdrometer compared reasonably well with totals measured using the tipping-bucket rain gauge with a mean difference between the two instruments for 26 rain episodes of -0,097 mm. Significant departures for individual rain episodes are apparent, however, of which underestimates by the disdrometer during periods of high rain rate are most significant (Figure 3.2). The underestimation appears to be related to an instrument deficiency in that smaller drops are not always registered during high rain rates due to instrument dead-time. Various authors have reported this problem including Joss and Gori (1978) and List (1988). List in particular compared DSDs measured by disdrometer with those measured using a laser spectrometer. Small drops measured by the spectrometer were not recorded by the disdrometer in high rainfall rates. The deficiency should not detract too much from the usefulness of the instrument. Although rain rates may be underestimated on some occasions, calculation of the reflectivity factor will not be significantly affected by drops of less than 1 mm in diameter.

3.4 Z-R RELATIONSHIPS

There are a number of ways by which average DSD patterns can be represented. Of these the most widely used remains an average Z-R relationship. Radar reflectivity factor (Z) is given by the summation of the sixth power of drop diameters

$$Z = \int_0^\infty N_D D^6 dD \qquad (2)$$

and is expressed in units of $mm^6.mm^{-3}$. Rainfall rate is given by

$$R = \frac{\pi}{6}\int_0^\infty N_D D^3 Vt_D dD \qquad (3)$$

assuming the terminal velocity of drops (Vt) is constant (Wilson and Brandes, 1979). The relationship between Z and R is usually expressed in an empirically-determined equation of the form

$$Z = aR^b \qquad (4)$$

with values of a and b most commonly following those proposed by Marshall and Palmer (1948), viz. a = 200 and b = 1,6. Using the above equations to determine values of Z and R from the disdrometer data, a least squares regression fit with coefficients a = 300 and b = 1,4 was computed (Figure 3.3).

The general applicability of an average Z-R relationship has received criticism from as far back as 1965, however, when Fujiwara (1965) using a drop size camera indicated the need for different Z-R relationships for different rain types. Wide-ranging values for the coefficients a and b have been mooted from all over the world. Not only do Z-R relationships differ from place to place but also from storm to storm in the same place and even during the same storm event. Z-R variability is probably best summarised by the much-quoted example of Battan (1973) having documented over 65 different Z-R relationships. Carbone and Nelson (1978) showed that it was necessary to use different Z-R relationships depending on whether the storm was growing or dissipating and Hodson (1986) contended that the widely used M-P relationship is inappropriate at rainfall rates which exceed 25 $mm.h^{-1}$.

Significant Z-R variability is evident in convective storms over the Transvaal Highveld. By computing Z-R relationships for individual rain episodes during the 1989/1990 rainfall season, wide ranging values of the coefficients a and b are seen to exist (Figure 3.4). A series of Z-R relationship calculations at 5 $mm.h^{-1}$ intervals indicated that 25 $mm.h^{-1}$ is in fact a threshold above which the Z-R relationship differs significantly from the Z-R for all rainfall rates. A Z-R relationship of the form $Z = 638\ R^{1,28}$ was thus calculated for rain rates exceeding 25 $mm.h^{-1}$ on the Transvaal Highveld (Figure 3.5). Hodson's (1986) Z-R relationship for rain rates exceeding 25 $mm.h^{-1}$ is $Z = 939\ R$. Hodson based his Z-R computation on the assumption that the slope of the DSD, Λ, will become constant at 2,2 mm^{-1} in rain rates exceeding 25 $mm.h^{-1}$. A scatter plot of the relationship between rain rate and Λ determined from DSDs measured by disdrometer (Figure 3.6) indicates that although there is a definite trend towards a constant value of Λ, the constancy is only realised at rainfall rates exceeding 100 $mm.h^{-1}$ as Willis and Tattleman (1989) also suggest. In addition, Hodson shows how Pasqualucci's (1982a; 1982b) data from a vertically pointing Doppler radar indicates a constant value of Λ for liquid water content values exceeding 1,2 $g.m^{-3}$. A scatter plot of the relationship between liquid water content and lambda determined from the disdrometer data shows a similar pattern (Figure 3.7).

3.5 DROP SIZE DISTRIBUTIONS

Marshall and Palmer's (1948) investigation of the distribution of raindrops with size was based on time-averaged DSDs. Average DSDs for individual rain episodes over the Transvaal Highveld as measured by the disdrometer tend to be flatter than M-P curves with fewer small drops and more large drops (Figure 3.8). The temporal variation of DSDs is not represented in either a time-averaged DSD or an average Z-R relationship, however. The extent of the temporal variability of DSDs is clearly evident in a three-dimensional drop size distribution field (Figure 3.9). In order to quantify temporal variability in drop size spectra, Waldvogel's (1974) parameterisation method was used. Waldvogel based his technique on the assumption that a DSD averaged over one minute would be adequately described by an exponential distribution. The exponential distribution could be described in turn by the intercept value, N_o, and the slope, Λ. N_o and Λ are obtained by substituting for the number of drops N_D (Eqn. 1) in the equations for calculating liquid water content (W) and radar reflectivity factor (Z) as follows:

$$W = \frac{\pi}{6}\int_0^\infty N_D D^3 dD = \frac{\pi}{6} N_o \int_0^\infty e^{-\Lambda D} D^3 dD \tag{4}$$

$$Z = \int_0^\infty N_D D^6 dD = N_o \int_0^\infty e^{-\Lambda D} D^6 dD \tag{5}$$

N_o and Λ can now be calculated from Eqs. (4) and (5)

$$N_o = \frac{1}{\pi}\left(\frac{6!}{\pi}\right)^{4/3}\left(\frac{W}{Z}\right)^{4/3} W = 446\left(\frac{W}{Z}\right)^{4/3} W \tag{6}$$

$$\Lambda = \left(\frac{6!}{\pi}\right)^{1/3}\left(\frac{W}{Z}\right)^{1/3} = 6{,}12\left(\frac{W}{Z}\right)^{1/3} \tag{7}$$

Changes in rain rate, liquid water content and radar reflectivity factor can then be related to changes in the drop size spectra. In Figure 3.10, N_o, Λ and rain rate have been plotted as functions of time. At 16:30 (marked "a" in Figure 3.10), a pattern of moderately decreasing values of N_o and a considerable decrease in Λ are associated with a significant increase in rainfall rate. A flat slope and a low intercept value imply that the DSD is dominated by large drops with relatively few smaller drops. Such a pattern is similar to patterns derived from theoretical studies such as those of List (1988) who used a time dependent rain shaft model to show that the cloud base spectrum would be significantly modified by drop-sorting (sedimentation) effects. Drop sorting is the process by which only large drops have sufficient terminal velocity to fall through an updraught. The resultant DSD at ground level would thus be characterised by an initial scattering of large drops. As the numbers of the large drops increase, smaller drops would begin to appear in the spectra. These small drops would originate as a result of collisional break-up effects, rather than having originated at cloud base. Such a pattern can be seen at 16:35 (marked "b" in Figure 3.10) where an increase in the numbers of small drops is evidenced by a significant increase in N_o and a moderate increase in Λ.

The effect is even more pronounced in a storm of 22 December 1989 at 18:18 (Figure 3.11). There is an initial, parallel decrease in N_o and Λ. Both increase marginally in conjunction with a slight decrease in rainfall rate before Λ decreases again while N_o remains relatively low as the rainfall rate increases. Between 18:24 and 18:25 (marked "a" in Figure 3.11), N_o exhibits a "jump" similar to that described by Waldvogel (1974), of slightly more than one order of magnitude. At the same time Λ steepens and rainfall rate continues to increase. Λ subsequently decreases and the rainfall rate peak of 46,5 $mm.h^{-1}$ coincides with high values of N_o and low values of Λ (marked "b" in Figure 3.11). Stratiform rain on the other hand, without significant drop-sorting effects shows an entirely different pattern. On 4 March 1990 a convective storm system passed over the disdrometer site trailing an extensive region of stratiform rain. Rain fell intermittently for some 6 hours. After an initial downpour with the passing of the leading edge of the storm, rain had stopped falling by 21:59 and very gradually began to fall again after 22:00. The parallel increase in N_o and Λ implies that drop size spectra had no large drops (marked "a" in Figure 3.12). The pattern prevails for about 10 minutes before decreases in both N_o and Λ indicate an influx of large drops (marked "b" in Figure 3.12). Whether the influx of large drops is related to processes of rain drop evolution at cloud base or whether they have arisen from drop coalescence effects cannot be resolved.

In order to consider the effects of changing drop spectra on rain rate and reflectivity factor, the storm of 8 December 1989 is once again considered. In Figure 3.13b, the variation of the rain rate with time is compared with that of the reflectivity factor. Radar reflectivity exceeds rain rate at "a" whereas rain rate exceeds radar reflectivity at "b" and at "c". At "d" radar reflectivity changes from exceeding rain rate to underestimating rain rate in response to a changing DSD while rain rate remains reasonably constant.

Individual analyses are restrictive to an extent in considering seasonal patterns and trends. Values of Z and R were thus plotted as functions of N_o and Λ in order to summarise the relationship between changes in DSD and changes in rain rate and radar reflectivity (Figure 3.14). Of particular interest is the wide range of possible DSD spectra for each of the four groups of rain rate. Each plot is further divided into two groups of four blocks. The solid lines indicate seasonal median values of N_o and Λ. Median values were decided on as the most likely representation of an equilibrium DSD in which drop growth effects are balanced out by drop disintegration effects (Srivastava, 1971; Zawadzki and de Agostinho Antonio, 1986; List, 1988). The dashed lines indicate median values for the individual rain episodes. In the case of 4 March 1990 (Figure 3.14c), in which initial convective activity was followed by a prolonged period of stratiform rain, the median values are very close to equilibrium. Both 8 December and 22 December 1989 have much flatter median slopes implying greater numbers of large drops and the likelihood that smaller drops evident in the spectrum occurred as a result of drop break-up effects.

Data from the entire season was subsequently summarised in this way. A variety of combinations of N_o and Λ are evident from individual analyses and therefore all possible combinations were considered. These combinations are summarised in Table 3.1.

Table 3.1: Possible combinations of N_o and Λ and related characteristics of the DSD

N_0	Λ	Characteristics of the distribution
Median	Median	Equilibrium distribution
Median	Above median	Few large drops. Possible drop break-up effects
Median	Below median	More large drops. Drop coalescence and/or large drops originating at cloud base
Above median	Median	Higher numbers of drops across the spectrum High rain rates
Above median	Above median	Large numbers of small drops. Considerable drop break-up effects
Above median	Below median	Higher numbers of drops across the spectrum, but with relatively more larger drops
Below median	Median	Few drops across the entire spectrum
Below median	Above median	No large drops. Few small drops
Below median	Below median	Scattering of larger drops. Drop-sorting or coalescence effects

Each of the categories from Table 3.1 was incorporated into the N_o - Λ plot by adding the 25 and 75% quartiles from the entire data set. The divisions were then labelled A1 to D4 (Figure 3.15). Divisions within the quartiles (i.e. C1 to C4, B1 to B4, D2, D3, A2 and A3) are interpreted as the equilibrium values referred to in Table 3.1. Block A1 would thus represent below median values of N_o and below median values of Λ whereas block D1 would represent above median values of N_o with below median values of Λ. For each of the 16 blocks, rainfall rate measured by disdrometer was compared to rain rate as computed using the average Z-R relationship. The results are summarised in Table 3.2. It can be seen from the table that the maximum rain rate in block A1 was overestimated by the average Z-R relationship by about 55%. The maximum rain rate on this occasion was 116 $mm.h^{-1}$. In block D1 on the other hand, the maximum rain rate of 196 $mm.h^{-1}$ was underestimated by 36% using the average Z-R relationship. Similarly in blocks A4 to D3 in which similar rain rates were measured, the average Z-R relationship can both overestimate and underestimate the rain rate depending on the drop-size distribution.

Table 3.2: Differences between rain rate as measured and rain rate computed using an average Z-R relationship of $Z = 300\ R^{1.41}$

		1	% contribution *	2	% contribution	3	% contribution	4	% contribution
A	Mean	11,24%	13,2	-16,67%	9,6	-17,65%	9,3	-16,67%	4,9
	Min	-74,00%		-71,43%		-75,00%		-50,00%	
	Max	-54,69%		-25,12%		-18,33%		-15,79%	
B	Mean	24,00%	7,6	-3,75%	6,9	4,00%	6,8	8,33%	3,5
	Min	-65,00%		-24,19%		-9,09%		-8,33%	
	Max	-40,80%		-6,41%		9,09%		11,90%	
C	Mean	26,06%	3,9	19,77%	6,6	23,26%	7,0	24,00%	3,0
	Min	-4,23%		3,82%		10,20%		8,33%	
	Max	-12,92%		21,40%		23,22%		28,87%	
D	Mean	36,66%	2,3	39,64%	5,0	44,67%	7,6	47,77%	2,8
	Min	19,89%		25,73%		28,71%		32,79%	
	Max	36,19%		46,39%		53,63%		57,24%	

* refers to the percentage of values in each sector.
\+ indicates that measured rain rate is greater than the calculated one.
\- indicates that measured rain rate is less than the calculated one.

3.6 CONCLUSIONS

In the course of this section raindrop size distributions as measured at ground level using a raindrop disdrometer were discussed. An average Z-R relation of the form $Z=300R^{1.4}$ was calculated. The considerable degree to which DSDs may vary over time was highlighted and the effects of changing DSDs on rain rate and radar reflectivity factor were considered. Variations in DSDs were shown to cause both underestimation and overestimation of rain rate when using an average Z-R relation at both high and low rain rates depending on the shape of the drop spectra.

The results must be seen in the context of the limitation of this study. These include the fact that data from only one season was utilised in the study and that only ground-based measurements were considered. The degree to which DSD variability at the ground reflects that at cloud base needs more detailed investigation. The results do give some ideas though as to the sort of processes that act upon DSDs and how these effects are likely to influence the accuracy of radar-measured rainfall. What is clear from the results is that an average Z-R relation, although fundamental to radar-rainfall measurement should not be used without regard to the processes mentioned above.

3.7 REFERENCES

BATTAN L J, 1973. *Radar Observations of the Atmosphere*, University of Chicago, Chicago.

CARBONE R E and NELSON L D, 1978. The evolution of raindrop spectra in warm-based convective storms as observed and numerically modelled, *J. Atmos. Sci.*, 35, 2302-2314.

DONNADIEU G, 1980. Comparison of results obtained with the VIDIAZ spectropluviometer and the Joss-Waldvogel raindrop disdrometer in "rain of a thundery type", *J. Appl. Meteor.*, 19, 593-597.

DOVIAK R J and ZRNIC D S, 1984. *Doppler Radar and Weather Observations*, Academic Press, Orlando.

HARDY K R, 1963. The development of raindrop size distributions and implications related to the physics of precipitation, *J. Atmos. Sci.*, 20, 299-312.

HODSON M C, 1986. Raindrop size distributions, *J. Climate Appl. Meteor.*, 25, 1070-1074.

FUJIWARA M, 1965. Raindrop size distributions from individual storms, *J. Atmos. Sci.*, 22, 585-591.

JOSS J and GORI E G, 1978. Shapes of raindrop size distributions, *J. Appl. Meteor.*, 17, 1054-1061.

JOSS J and WALDVOGEL A, 1967. Ein Spektrograph fur Niederschlagstropfen mit automatischer Auswertung, *Pure Appl. Geophysics*, 68, 682-688.

JOSS J and WALDVOGEL A, 1988. Precipitation measurement and hydrology, in ed Atlas, D, *Radar in Meteorology*, Amer. Meteor. Soc., Boston, 557-606.

KINNEL P I A, 1976. Some observations of the Joss-Waldvogel rainfall disdrometer, *J. Appl. Meteor.*, 15, 499-502.

LIST R, 1988. A linear radar reflectivity-rainrate relationship for steady tropical rain, *J. Atmos. Sci.*, 45, 3564-3572.

LIST R and GILLESPIE J R, 1976. Evolution of raindrop spectra with collision-induced break-up, *J. Atmos. Sci.*, 33, 2007-2013.

LIST R, DONALDSON N R and STEWART R E, 1987. Temporal evolution of drop spectra to collisional equilibrium in steady and pulsating rain, *J. Atmos. Sci.*, **44**, 362-372.

MARSHALL J S and PALMER W McK, 1948. The distribution of raindrops with size, *J. Meteor.*, 5, 165-166.

MASON B J and ANDREWS J B, 1960. Drop size distributions for various types of rain, *Quart. J. Roy. Meteor. Soc.*, 86, 346-353.

PASQUALUCCI F, 1975. Low altitude Doppler radar measurements of precipitation at vertical incidence, *16th Radar Meteorology Conf.*, Houston, American Meteorological Society, 415-420.

PASQUALUCCI, F 1982a. Drop size distribution measurements in convective storms with a vertically pointing 35 GHz Doppler radar. Multi-Parameter measurement of precipitation, *U.R.S.I. Open Symposium*, Bournmouth, U.K., U.R.S.I. and I.E.E., 139-144.

PASQUALUCCI F, 1982b. The variation of drop size distribution in convective storms: A comparison between theory and measurement, *Geophys. Res. Lett*, 9, 839-841.

SEKHON R S and SRIVASTAVA R C. 1970. Doppler radar observations of drop-size distributions in a thunderstorm, *J. Atmos. Sci.*, 28, 983-994.

SRIVASTAVA R C, 1967. On the role of coalescence between raindrops in shaping their size distribution, *J. Atmos. Sci.*, 24, 287-292.

SRIVASTAVA R C, 1971. Size distributions of raindrops generated by their break-up and coalescence, *J. Atmos. Sci.*, 28, 410-415.

SRIVASTAVA R C, 1978. Parameterisation of raindrop size distributions, *J. Atmos. Sci.*, 35, 108-117.

WALDVOGEL A, 1974. The N_0 jump of raindrop spectra, *J. Atmos. Sci.*, 31, 1067-1078.

WIESNER J, 1895. Beitrage zur Kenntnis des tropischen Regens, *Bericht Math. Nat.Kl.*, Wien, 104.

WILLIS P T and TATTLEMAN P, 1989. Drop-size distributions associated with intense rainfall, *J. Appl. Meteor.*, 28, 3-15.

WILSON J W and BRANDES E A, 1979. Radar measurement of rainfall - a summary. *Bull. Amer. Meteor. Soc.*, 60, 1048-1058.

YOUNG K C, 1975. The evolution of drop spectra due to condensation, coalescence and break-up, *J. Atmos. Sci.*, 32, 965-973.

ZAWADZKI,I and DE AGOSTINHO ANTONIO M, 1988. Equilibrium raindrop size distributions in tropical rain, *J. Atmos. Sci.*, 45, 3452-3459.

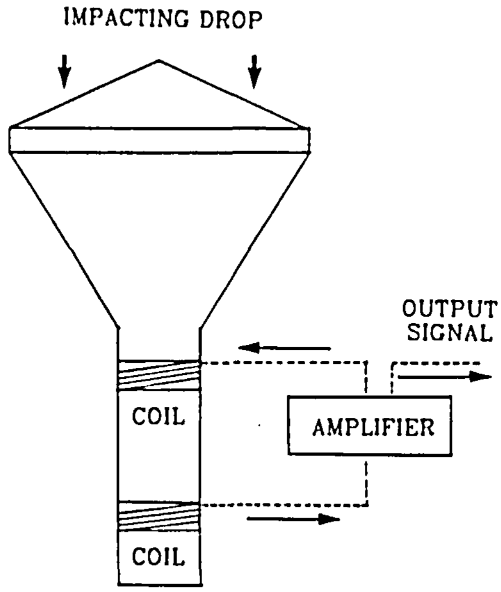

Figure 3.1: Schematic illustration of the principle of operation of the raindrop disdrometer.

Please note that in the following figures the variables R, Z, N_D and N_0 are plotted against logarithmic axes. All other variables are plotted against linear axes.

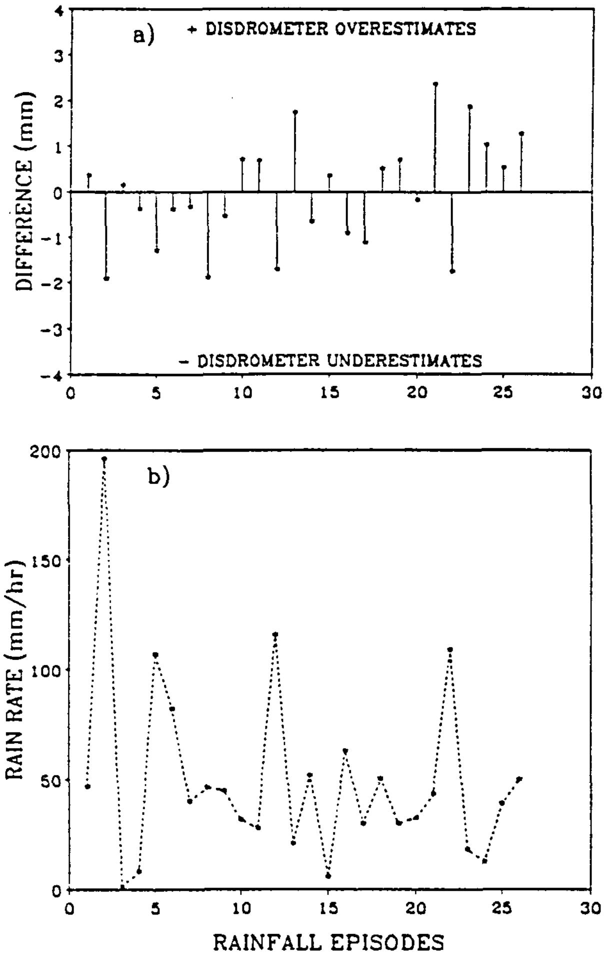

Figure 3.2: a) Differences between rain totals measured by disdrometer and those measured by tipping-bucket rain gauge for 26 consecutively numbered rain episodes during the 1989/90 rainfall season.
b) Maximum rainfall rates per minute for the rain episodes used in the above gauge/disdrometer comparison.

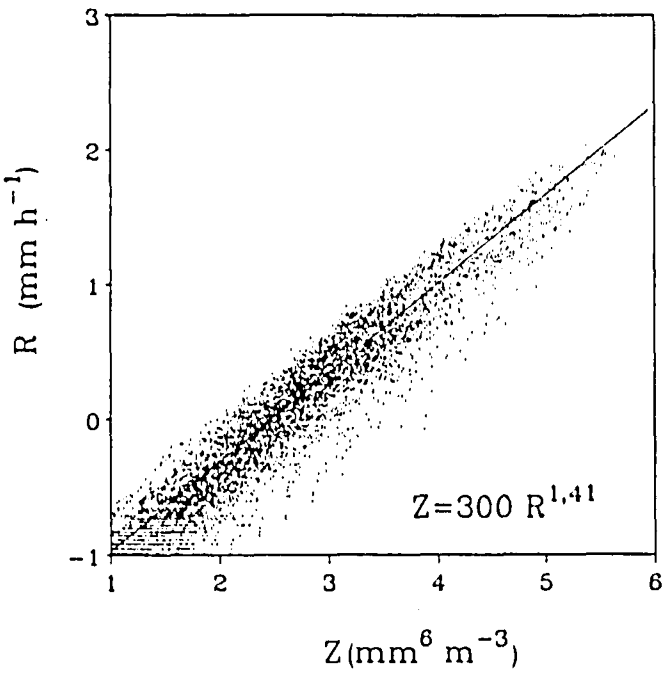

Figure 3.3: Scatter plot of the relationship between Z and R computed from disdrometer data recorded in Pretoria during the 1989/90 season.

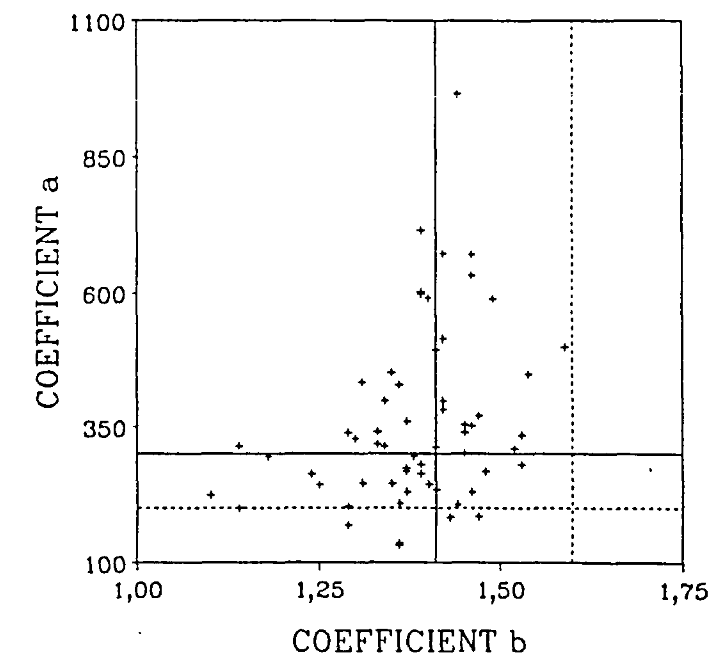

Figure 3.4: Distribution of coefficients a and b in the relationship $Z=aR^b$ calculated from individual rain episodes between November 1989 and May 1990.

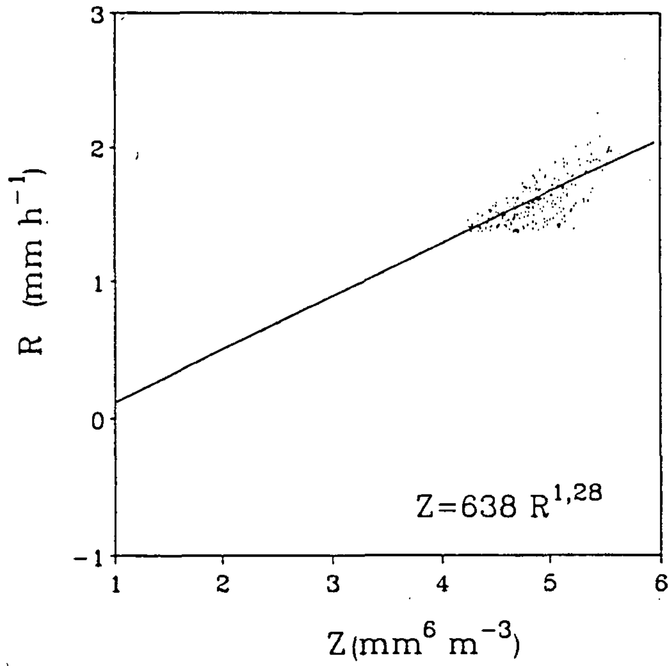

Figure 3.5: Scatter plot of the relationship between Z and R computed from disdrometer data for rain rates exceeding 25 mm.h^{-1}.

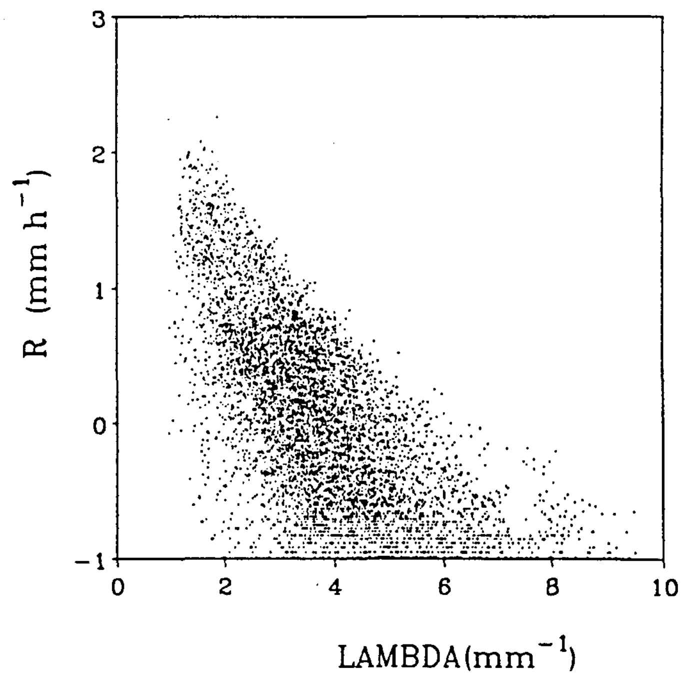

Figure 3.6: Scatter plot of the relationship between Λ and R computed from disdrometer data for the entire 1989/90 season.

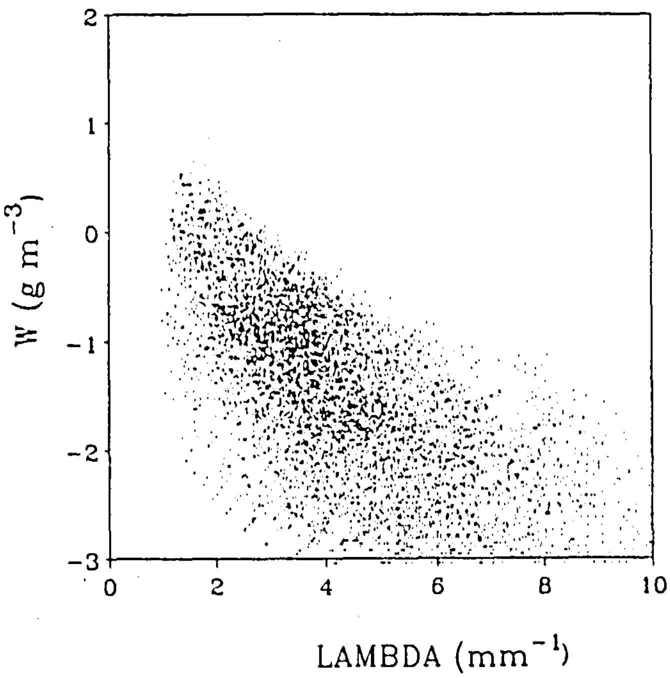

Figure 3.7: Scatter plot of the relationship between Λ and liquid water content computed from the disdrometer data for the entire 1989/90 season.

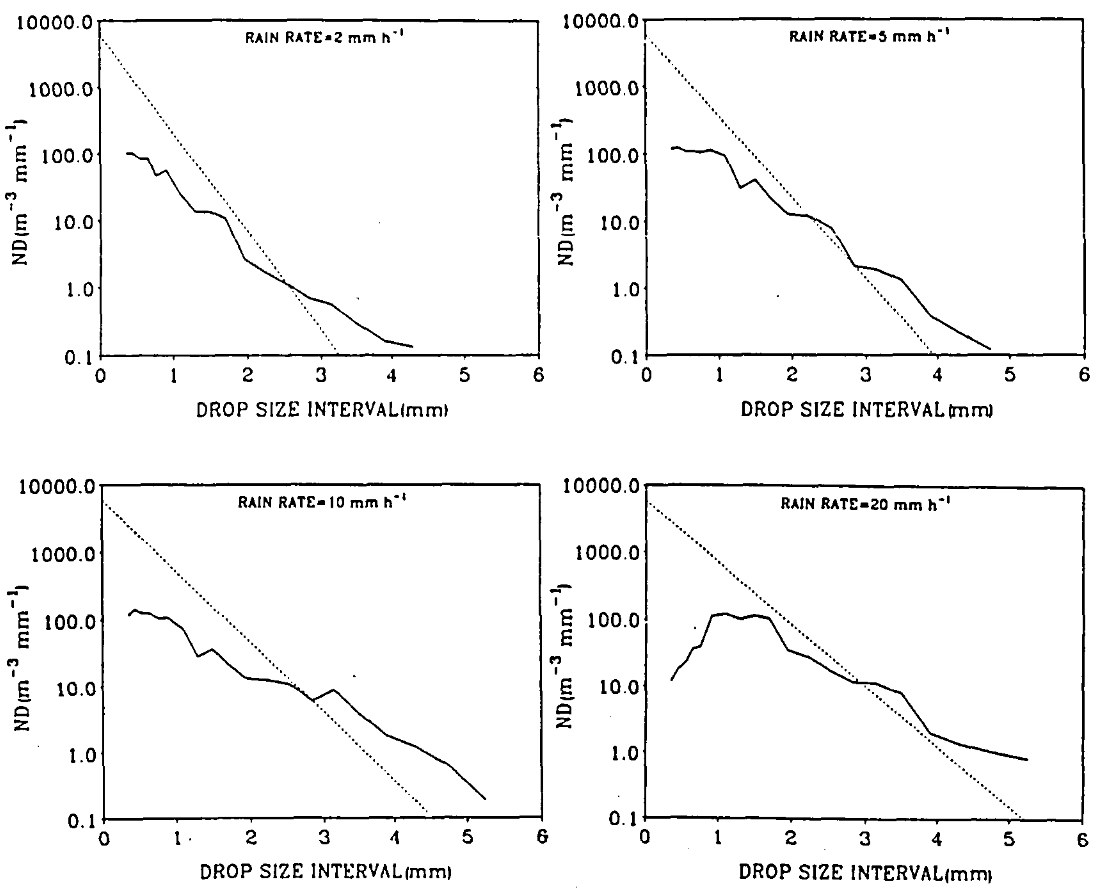

Figure 3.8: Plots of drop size distributions for rain events with differing average rain rates (solid lines), compared with Marshall and Palmer (1948) (dashed lines).

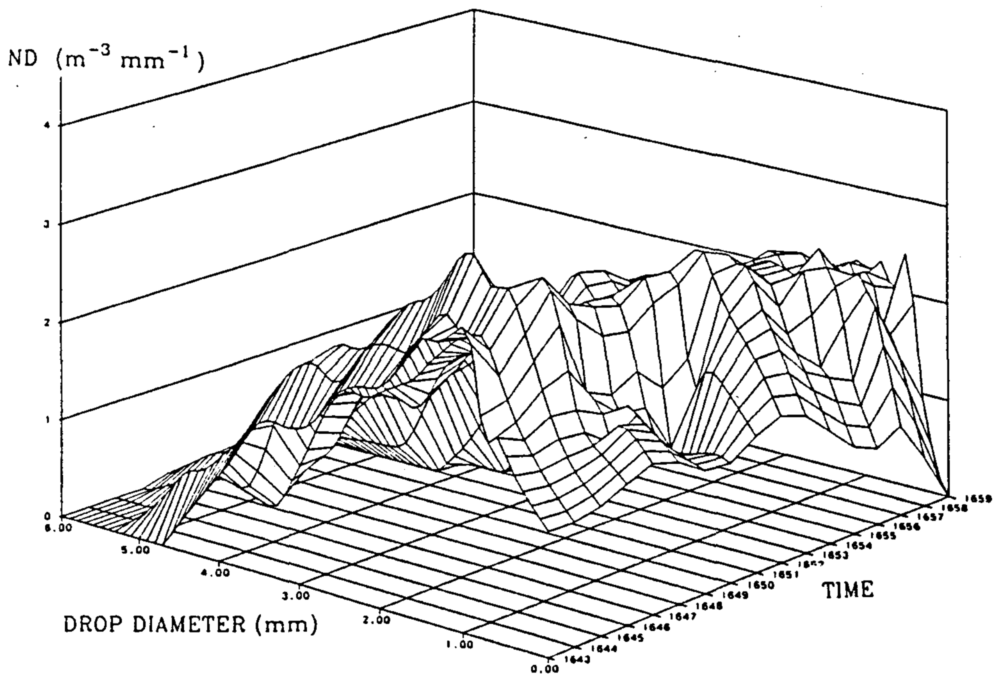

Figure 3.9: Three-dimensional drop size distribution field from 16:43 to 16:49 on 8 December 1989.

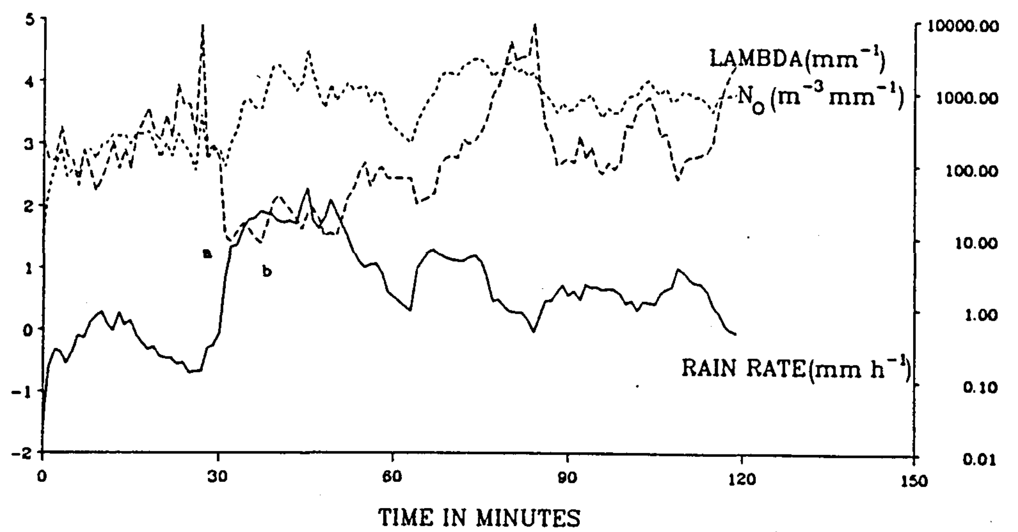

Figure 3.10: N_o, Λ and rain rate plotted as functions of time for 8 December 1989, 16:00 to 17:59. N_o and rain rate are plotted against a log scale on the right hand axis, Λ against a linear scale on the left hand axis. The letters a and b denote points of interest discussed in the text.

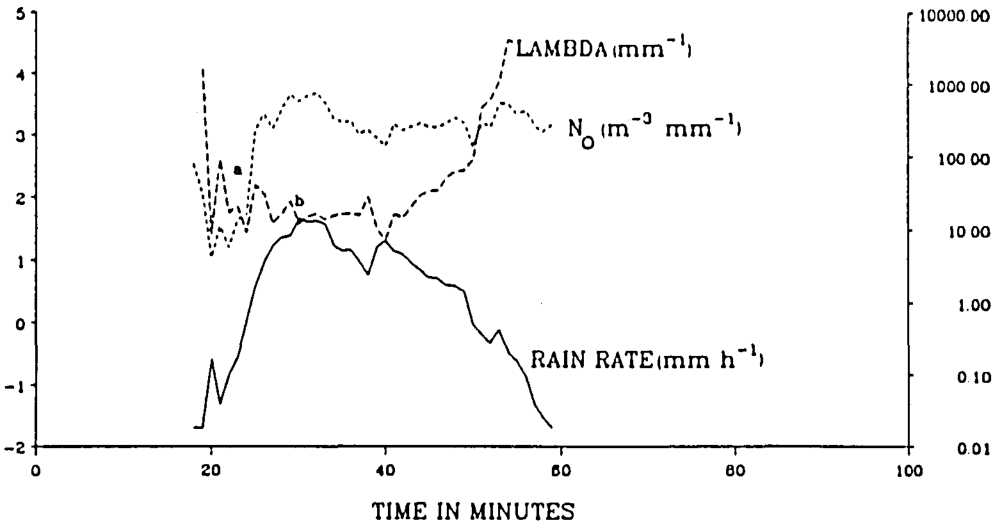

Figure 3.11: N_o, Λ and rain rate plotted as functions of time for 22 December 1989, 18:18 to 18:59. N_o and rain rate are plotted against a log scale on the right hand axis, Λ against a linear scale on the left hand axis. The letters a and b denote points of interest discussed in the text.

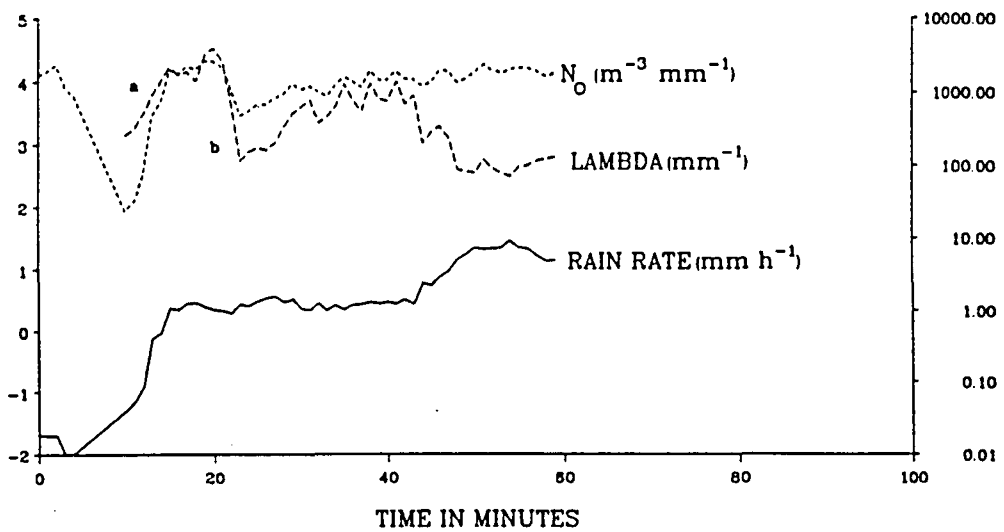

Figure 3.12: N_o, Λ and rain rate plotted as functions of time for 4 March 1990, 22:00 to 22:59. N_o and rain rate are plotted against a log scale on the right hand axis, Λ against a linear scale on the left hand axis. The letters a and b denote points of interest discussed in the text.

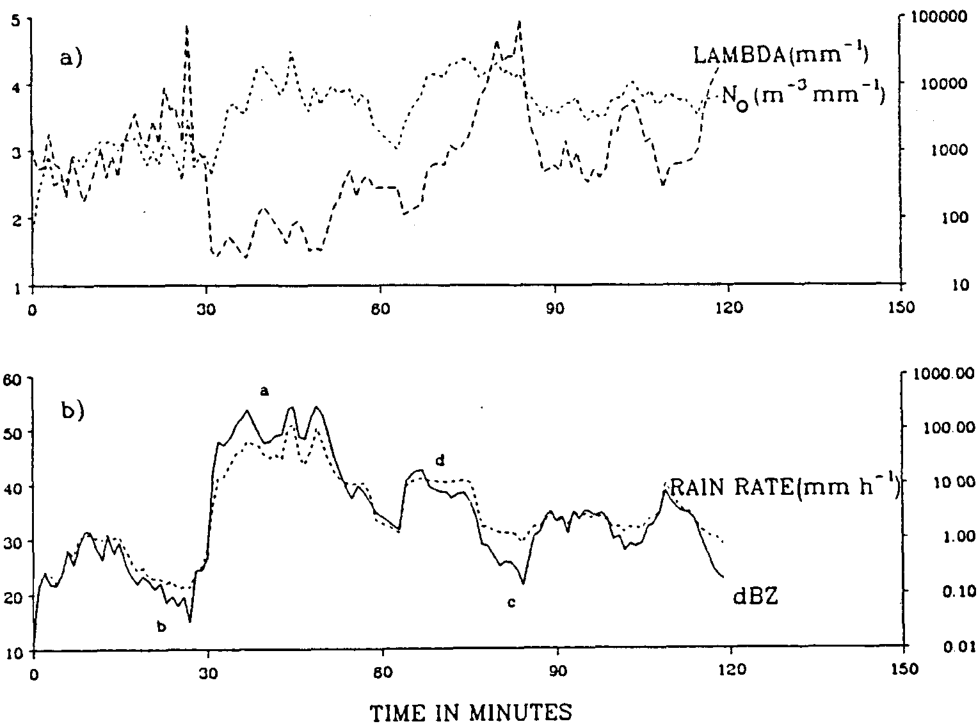

Figure 3.13: a) N_o and lambda plotted as functions of time for 8 December 1989, 16:00 to 17:59.
b) Rain rate and radar reflectivity factor for the same period. The letters a,b,c and d denote points of interest discussed in the text.

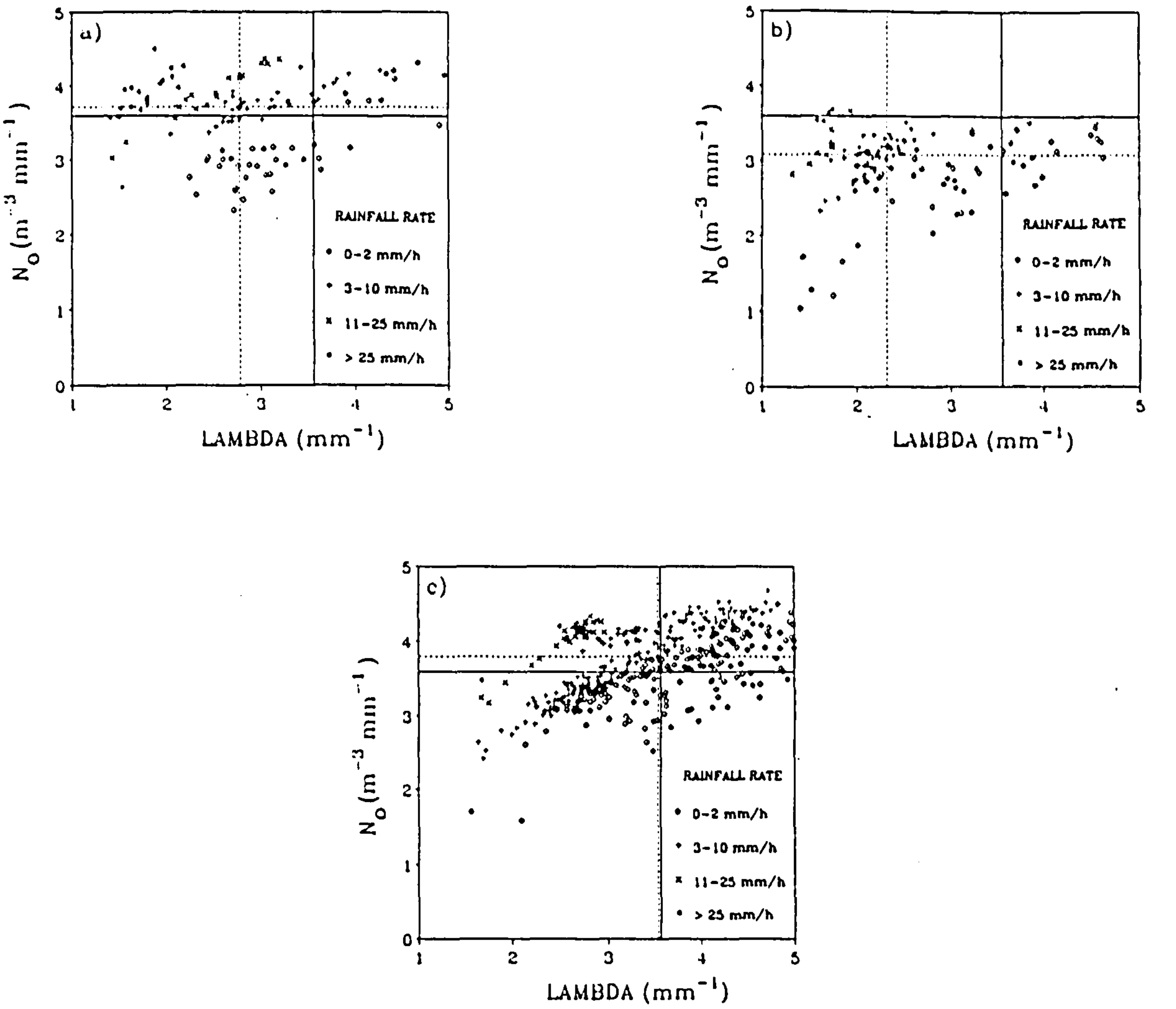

Figure 3.14: Rain rate as a function of N_o and Λ. Solid lines indicate median values for the entire season, dashed lines median values for the individual rain episode.

a) 8 December 1989, 16:00 to 17:59
b) 22 December 1989, 18:06 to 21:20
c) 4 March 1990, 19:14 to 05:21.

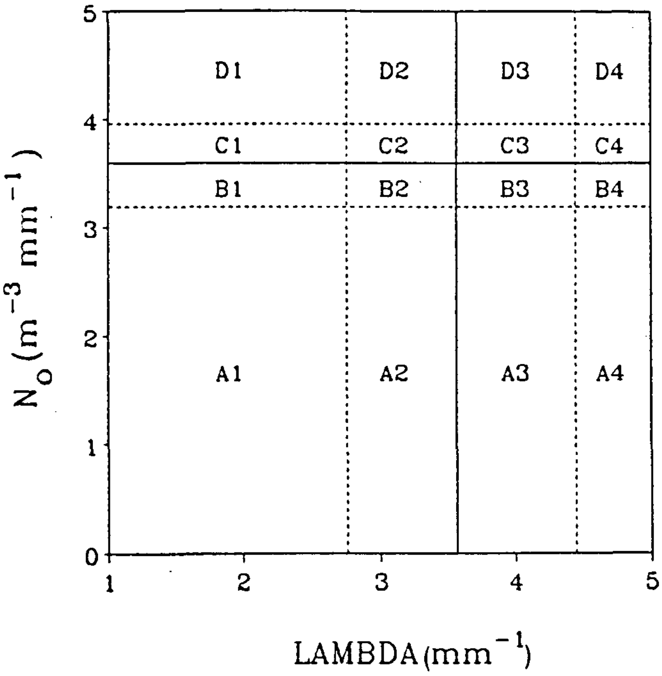

Figure 3.15: All possible combinations of N_o and Λ for rainfall rates exceeding 0,01 $mm.h^{-1}$. Solid lines indicate the median values, dashed lines the 25 and 75% quartiles respectively.

4. THE AREA-TIME-INTEGRAL METHOD OF RADAR-RAINFALL MEASUREMENT

Sean O'Beirne

4.1 BACKGROUND

The use of weather radar in measuring rainfall has a number of advantages over a rain gauge network. Firstly, as the equivalent of an infinitely dense rain gauge network, a 360° sweep of the radar accurately maps the areal extent of differing rainfall intensities within a precipitation field and secondly, rain information is assimilated in real-time. In an area such as the Transvaal Highveld where convective rain systems produce precipitation highly variable in space and time, radar measurement of rainfall becomes a necessity. Radar cannot be used to measure rainfall rate directly. However, the backscattered energy from varying raindrop distributions is measured and then related to rain rate. Inaccuracies in radar-measured rainfall thus may arise from variations in the Z-R relationship (see previous Section) or from anomalous propagation of the radar signal (Wilson and Brandes, 1979). In addition, precipitation may change considerably from the height of the radar beam to the ground (Austin, 1981).

The Area-Time-Integral (ATI) method of volumetric rainfall measurement has been proposed as a means of circumventing many of the above-mentioned problems (Doneaud, *et al.*, 1981; 1984a; 1988). The method is based on the principle that rain volume is dependant to a greater degree on storm area than on rainfall rate because the distribution of rainfall rates from one convective storm to the next is quite similar (Lopez, *et al.*, 1983) i.e. the probability density function (p.d.f.) of rainfall rates from one storm to the next is essentially constant (Atlas, *et al.*, 1990). In the previous progress report (Gomes *et al.*, 1989) the ATI technique was briefly examined and some preliminary results for convective storm systems over the Transvaal Highveld were presented. These results were based on hourly integrations over a 1° longitude by 0,5° latitude grid square and were used to suggest that a reflectivity threshold of 26,6 dBZ would be suitable for ATI computations over the Transvaal Highveld. For the purposes of the present report, an alternative method of defining the area over which to integrate echo area was used. This was simply to include all the echo area within a 100 km radius of the radar in the case of standard radar data and a 75 km radius in the case of data recorded in Doppler mode due to range limitations for short pulse operation. In the course of this Section, several different methods of determining a V-ATI relationship will be investigated in order to find an optimal relationship suitable for use in convective rainfall measurement by radar in storm systems over the Transvaal Highveld.

4.2 THEORY

The background to radar-measurement of rainfall and the ATI method in particular was reviewed in the previous progress report (Gomes *et al.*, 1989). Some of the more important aspects of that review are repeated here for continuity's sake.

The ATI technique of volumetric rainfall measurement is based on the relationship between storm size and rainfall volume in convective storm systems. Rain volume V over an area A during time t is given by

$$V = \int_t^{\infty}\int_A^{\infty} R\,da\,dt \qquad (1)$$

Assuming rainfall rate R to be constant Eqn. 1 could be rewritten as

$$V = R \int_t^{\infty}\int_A^{\infty} da\,dt \qquad (2)$$

It is the double integral that is referred to as ATI, a value which may be approximated for by summation i.e.

$$ATI = \int_t^{\infty}\int_A^{\infty} da\,dt \approx \sum_{i=1}^{\infty} A_i \Delta t_j \qquad (3)$$

An important part of the calculation of the ATI is determining an appropriate reflectivity threshold. Echo below this threshold is then not included in the ATI. There are a number of factors that need to be considered in selecting an appropriate threshold value. A threshold value set too high would exclude echo area that is significant in terms of precipitation produced. On the other hand, a threshold set too low would include echo area that is unlikely to produce significant amounts of precipitation (Doneaud, *et al.*, 1984a). This latter point is also important in reducing the need for an evaporation correction between the height of the radar beam and the ground (Doneaud, *et al.*, 1981). It was the determination of a suitable reflectivity threshold for ATI calculations on the Transvaal Highveld that was discussed in the 1989 progress report. An improvement in the correlation coefficient between ATI and radar-estimated rainfall volume was noted from the 23,3 dBZ to the 26,6 dBZ threshold. In addition Doneaud, *et al.*, (1981; 1984a) selected a 25 dBZ threshold in their ATI computations. On the - basis of the above mentioned considerations, a reflectivity threshold of 26,6 dBZ was considered suitable for ATI computation on the Transvaal Highveld.

Using an appropriate reflectivity threshold radar-estimated rain volume can be related to ATI in a power-law of the general form

$$V=K(ATI)^b \qquad (4)$$

where K and b are coefficients determined by the regression analysis. The average rain rate $\overline{R}$ in $mm.h^{-1}$ can then be ascertained from the ratio of the ATI in $km^2.h$ to the rain volume in $km^2.mm$. From Eqn. 2

$$\overline{R}=V/(ATI) \qquad (5)$$

By substituting (4) into (5)

$$\overline{R}=K(ATI)^{b-1} \qquad (6)$$

As the ATI decreases with increasing threshold value, the value of K must increase in order to maintain the volumetric rain accumulation (Doneaud, *et al.*, 1984a; Atlas, *et al.*, 1990).

4.3 DATA

Data used in the present study were obtained from an S-Band weather radar situated at Houtkoppen. Characteristics of the radar are to be found in the first progress report on the Precipitation and Airflow (PRAI) Project (Gomes and Held, 1988). Radar data in plan-position-indicator (PPI) format was used at minimum elevation angle (approximately 2°). Any echo area within a 100 km radius of the radar in the case of standard radar data and 75 km when the radar was operated in Doppler mode was included in the area integrations. A computer program was used to calculate the areas of echo clusters for different reflectivity thresholds (i.e. 23,3 dBZ; 26,6 dBZ; 30,0 dBZ and 33,3 dBZ). The corresponding rain volume for each echo area was computed using a Z-R relationship of $Z=300R^{1,41}$ which was calculated from data measured by the raindrop disdrometer. Data from the 1987/1988 and the 1988/1989 rainfall seasons, some 29 storm days in total, was used in the analysis.

4.4 RESULTS OF V-ATI CALCULATIONS FOR THE TRANSVAAL HIGHVELD

Pioneering work on V-ATI relationships was done by Doneaud, *et al.* (1981). Using data from convective storm systems over North Dakota, they proposed two alternative methods of computing a V-ATI relationship. The first of these was to use the maximum echo coverage of any one scan for each hour and the second to use the average echo coverage for each hour. Doneaud *et al.* (1981) found that the maximum echo coverage method had a better correlation coefficient (r=0,91) than the average echo coverage method (r=0,86) when regressed against radar-estimated rainfall volume, and therefore the former was recommended as the better approach. Regression parameters for radar-estimated rain volume versus ATI for the maximum echo coverage approach and the average echo area for convective storms over the Transvaal Highveld are given in Table 4.1 and Table 4.2, respectively.

In the case of the maximum echo area coverage, the highest correlation coefficient is evident at the 23,3 dBZ threshold. The correlation coefficient decreases from 23,3 to 26,6 dBZ and then increases marginally to the 33,3 dBZ threshold. On the strength of the correlation coefficient,

Table 4.1: Radar-estimated rain volume versus ATI regression parameters for differing reflectivity thresholds. RERV and ATI are calculated from maximum hourly echoes.

Threshold values in dBZ	23,3	26,6	30,0	33,3
Equivalent rainfall rate ($Z=300R^{1,41}$) in $mm.h^{-1}$	0,79	1,35	2,35	3,83
Coefficient K	3,27	10,04	11,85	14,28
Exponent b	1,15	1,03	1,05	1,07
Correlation coefficient	0,95	0,91	0,92	0,93
Log standard error of the estimate	0,13	0,17	0,15	0,14
Average rain rate calculated from the V-ATI relationship	9,58	12,40	16,58	22,30

Table 4.2: Radar-estimated rain volume versus ATI regression parameters for differing reflectivity thresholds. RERV and ATI are calculated from hourly echo area averages.

Threshold values in dBZ	23,3	26,6	30,0	33,3
Threshold rainfall rate ($Z=300R^{1,41}$) in $mm.h^{-1}$	0,79	1,35	2,35	3,83
Coefficient K	3,06	8,13	10,21	12,23
Exponent b	1,14	1,05	1,06	1,08
Correlation coefficient	0,96	0,93	0,94	0,94
Log standard error of the estimate	0,11	0,14	0,12	0,14
Average rain rate calculated from the V-ATI relationship	7,95	10,80	13,44	19,69

23,3 dBZ would appear to be a suitable reflectivity threshold and therefore for the maximum echo area method a V-ATI relationship of the form $V=3,27(ATI)^{1,15}$ at the 23,3 dBZ threshold appears to be most suitable (Figure 4.1). The fact that the exponent b exceeds 1 agrees with intuitive reasoning that larger storms are likely to have higher average rain rates.

When V-ATI relationships were calculated using hourly echo area averages a pattern of decreasing correlation coefficients with increasing threshold is evident. The higher correlation coefficient in the case of hourly echo area averages (r=0,96) and the lower standard error of the estimate (s=0,11) implies that this technique is possibly more accurate than the hourly maximum area technique. The average rain rates included in the tables were calculated using Eqn. 6 in which the average value of ATI for the various reflectivity thresholds was used as ATI value in the calculation. It is clear that the average rain rates generated by the V-ATI relationship will ultimately govern both the choice of reflectivity threshold and the most suitable method of V-ATI computation. There are a number of facets of the average rain rates in the tables that need consideration.

The V-ATI relationship computed by Doneaud *et al.* (1984a), using a 25 dBZ threshold, gave an average rainfall rate for convective storm systems over North Dakota of 4,0 $mm.h^{-1}$ (Doneaud *et al.*, 1984b) with a standard deviation of 1,55 $mm.h^{-1}$. However, Doneaud *et al.* (1984b) found a 20% increase in average rainfall rate in a subsequent, wetter rainfall season. Although a single disdrometer is unlikely to be a satisfactory gauge of average rainfall rates for an entire region, average rainfall rates calculated from the disdrometer data gave some interesting results. An average rainfall rate of 4,4 $mm.h^{-1}$ was calculated for the 1989/1990 rainfall season. More interesting was the fact that average rain rates of 7,3 $mm.h^{-1}$, 8,9 $mm.h^{-1}$, 11,3 $mm.h^{-1}$ and 15,1 $mm.h^{-1}$ were calculated when each of the four equivalent rain rate thresholds in the V-ATI computations were used. These are seen to be quite similar to the rain rates computed using the V-ATI relationships. The similarity in average rain rates from disdrometer data and those calculated from an average V-ATI relationship would appear to suggest that the assumption of constant p.d.f. of rainfall rate implicit in the ATI method is reasonable. The results also appear to indicate that even the minimum threshold of 23,3 dBZ may in fact overestimate the average rainfall rate. Clearly these conclusions would need better verification but they do provide interesting avenues of investigation.

It is also interesting to note that the values of the coefficient K computed in the V-ATI relationship for the Transvaal Highveld are very similar to those computed by Doneaud *et al.* (1984a). The V-ATI relationship that he finally proposed for convective storms over North Dakota was of the form $V=3,7(ATI)^{1,08}$. The fact that the average rainfall rates for the Transvaal Highveld were higher than those for North Dakota is definitely attributable to the moderately steeper slopes of the V-ATI relationships for the Transvaal Highveld. Rosenfield and Gagin (1989) compared characteristics of convective storm systems for Israel with those over South Africa in order to identify factors influencing the total rainfall yield from these systems. One of their findings was the relationship between rainfall volume and the absolute humidity at cloud base. They found that increases in the absolute humidity at cloud base were proportional to increases in the rain volume to the power of 1,2 in Israel and 1,69 in South Africa. They suggested that the precipitation efficiency of continental storms increases with increasing cloud base temperature and that convective storm systems over South Africa frequently exhibit cloud base temperatures of 12-15°.

In a similar vein Rosenfield *et al.* (1990) determined instantaneous area average rain rates by measuring the ratio of the area of rain intensity above a given threshold to the total echo area ($F<\tau>$) and comparing it to the areal rain intensity (R). The point is not to dwell on the method but merely to consider the fact that a comparison of $R\text{-}F<\tau>$ relationships between South Africa, Texas, Australia (Darwin) and data from the GATE experiment showed the steepest $R\text{-}F<\tau>$ slope for convective storms over South Africa. Rosenfield *et al.* (1990) also showed that in areas where warm rain processes are dominant, there will be an increased frequency of small showers characterised by light rainfall. Kraus and Bruintjies (1985) showed that convective rain over central South Africa is initiated through ice-phase mechanisms with no evidence of any significant warm rain processes. Mather and Parsons (1990) computed a V-ATI relationship of the form $V=5,90(ATI)^{1,1}$ for convective storms over the eastern escarpment, a relationship indicating still higher average rain rates.

The above evidence suggests that higher average rain rates given by V-ATI relationships for convective storm systems over the Transvaal Highveld are not unreasonable. Disdrometer data suggests that average rainfall rates closer to 4,5 $mm.h^{-1}$ would be better approximations but it must be pointed out that the latter part of the 1989/1990 rainfall season was characterised by a number of episodes of sustained stratiform rain. Nonetheless, the average rainfall rate of 7,95 $mm.h^{-1}$ in the case of the hourly echo averages (23,3 dBZ threshold) appears to be a more realistic value than the 9,58 $mm.h^{-1}$ in the case of the hourly echo area maximums. In addition, the higher correlation coefficient and lower standard error of the estimate deem the hourly echo area average method the more accurate. This would suggest that a V-ATI relationship of the form $V=3,06(ATI)^{1,14}$ is most appropriate to the Transvaal Highveld (Figure 4.2). Although the threshold used is now lower than that initially proposed, it is relevant to consider a conclusion drawn by Rogers (1989) in calculating a suitable average rain rate to be used in a rain storm model. Rogers concluded that thresholds of greater than 25 dBZ in the ATI technique would not be appropriate because of the increasing dependence of average rain rate on the maximum rain rate as higher thresholds are used to define the echo area.

An obvious shortfall of the hourly average echo area method is that a minimum tracking time of one hour would be needed before volumetric rainfall totals could be estimated. This inhibits the operational versatility which is cited as the main advantage of the ATI technique. It was decided therefore to calculate a V-ATI relationship based on scan-by-scan integrations. The regression parameters are summarised in Table 4.3. When consulting the table it must be borne in mind that the coefficient K has been calculated from ATI in units of $km^2.min$. Although the correlation coefficient for the scan-by-scan integration techniques is slightly less ($r=0,94$) than the hourly echo average method, the average rainfall rate of 8,14 $mm.h^{-1}$ still appears to be a reasonable value. Proper verification of the rainfall rate still needs to be done but the results suggest that a V-ATI relationship of the form $V=0,04(ATI)^{1,18}$ (Figure 4.3) would be most appropriate when using a scan-by-scan integration technique of computing V-ATI for convective storm systems over the Transvaal Highveld.

Table 4.3: Radar-estimated rain volume versus ATI regression parameters for differing reflectivity thresholds. RERV and ATI are calculated from scan-by-scan integrations.

Threshold values in dBZ	23,3	26,6	30,0	33,3
Threshold rainfall rate ($Z=300R^{1,41}$) in $mm.h^{-1}$	0,79	1,35	2,35	3,83
Coefficient K	0,04	0,06	0,09	0,14
Exponent b	1,18	1,16	1,15	1,13
Correlation coefficient	0,94	0,96	0,97	0,97
Log standard error of the estimate	0,04	0,03	0,02	0,02
Average rain rate calculated from the V-ATI relationship	8,14	10,23	13,66	19,00

4.5 CONCLUSIONS

In the course of this section the Area-Time-Integral (ATI) method of volumetric rainfall measurements was considered. Three different methods for determining a Volume versus Area-Time-Integral (V-ATI) relationship were considered. Of these the hourly average area method was deemed to be the most accurate. Although the V-ATI relationship computed using this method appeared to give average rainfall rates that appeared high, consideration of other literature showed that higher average rainfall rates are not unusual for convective storms over South Africa. Operational aspects of the ATI technique of volumetric rainfall measurement meant computing a V-ATI relationship that can be used on individual scans. Although the V-ATI relationship calculated required verification, they do appear to indicate that the ATI technique is an operationally viable means of radar measurement of rainfall.

4.6 REFERENCES

ATLAS D, ROSENFIELD D and SHORT D A, 1990. The estimation of convective rainfall by area integrals 1. The theoretical and empirical basis. *J. Geoph. Res.*, 95, 2153-2160.

DONEAUD A A, SMITH P L, DENNIS A S and SENGUPTA S, 1981. A simple method for estimating convective rain volume over an area. *Water Resour. Res.*, 17, 1976-1682.

DONEAUD A A, IONESCU-NISCOV S, PRIEGNITZ and SMITH P L, 1984a. The area-time integral as an indicator for convective rain volumes. *J. Climate Appl. Meteor.*, 23, 555-561.

DONEAUD A A, IONESCU-NISCOV S and MILLER J R (Jnr), 1984b. Convective rain rates and their evolution during storms in a semiarid climate. *Mon. Wea. Rev.*, 112, 1602-1612.

DONEAUD A A, MAKARAU A and JOHNSON L R, 1988. A modified ATI technique for nowcasting convective rain volumes over areas. *J. Appl. Meteor.*, 27, 491-502.

GOMES A M and HELD G, 1988. *First Progress report: Precipitation and Airflow (PRAI) Project*. CSIR Report EMA-C 8885, Pretoria, 18pp.

GOMES A M, O'BEIRNE S and HELD G, 1989. *Second Progress report: Precipitation and Airflow (PRAI) Project*. CSIR Report EMA-C 89126, Pretoria, 42pp.

KRAUSS T W and BRUINTJIES R T, 1985. Physical properties of summertime convective clouds in the Bethlehem region of South Africa. *Preprints, Fourth WMO Conference on Weather Modification*, Honolulu, World Meteor. Org., 251-254.

LOPEZ R E, THOMAS J, BLANCHARD D O and HOLLE R L, 1983. Estimation of rainfall over an extended region using only measurements of the area covered by radar echoes. Paper presented at 21st Conference on Radar Meteorology, Am. Meteorol. Soc., Edmonton, Alberta, Canada, Sept. 19-23.

MATHER G K and PARSONS R, 1990. Radar measurements of rainfall - the area method. Paper presented at the Seventh Annual Conference of the South African Society for Atmospheric Sciences, Pretoria, Oct. 22 & 23.

ROGERS R R, 1989. Average rain rate in a model rain storm, *Proceedings, 24th Conference on Radar Meteorology*, Miami, American Meteorological Society, 652-653.

ROSENFIELD D and GAGIN A, 1989. Factors governing the total rainfall yield from continental convective clouds. *J. Appl. Meteor.*, 28, 1015-1030.

ROSENFIELD D, ATLAS D and SHORT D A, 1990. The estimation of convective rainfall by area integrals 2. The height-area rainfall threshold (HART) method. *J. Geoph. Res.*, 95, 2161-2176.

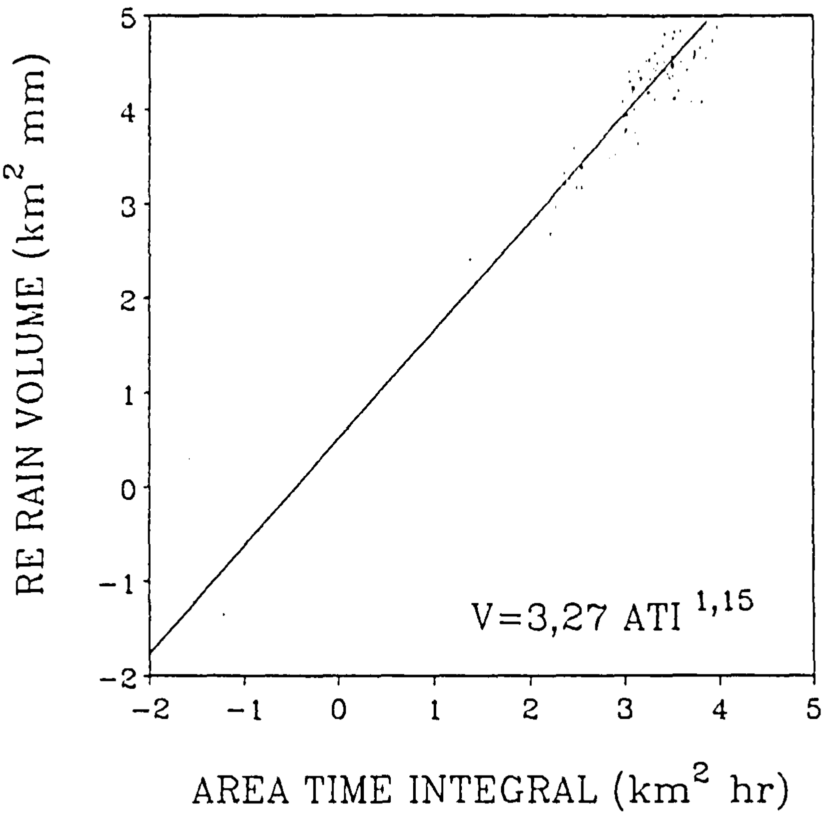

Figure 4.1 Scatter plot of the V-ATI relationship for convective storms over the Transvaal Highveld using the maximum hourly echo coverage method. The reflectivity threshold is 23,3 dBZ.

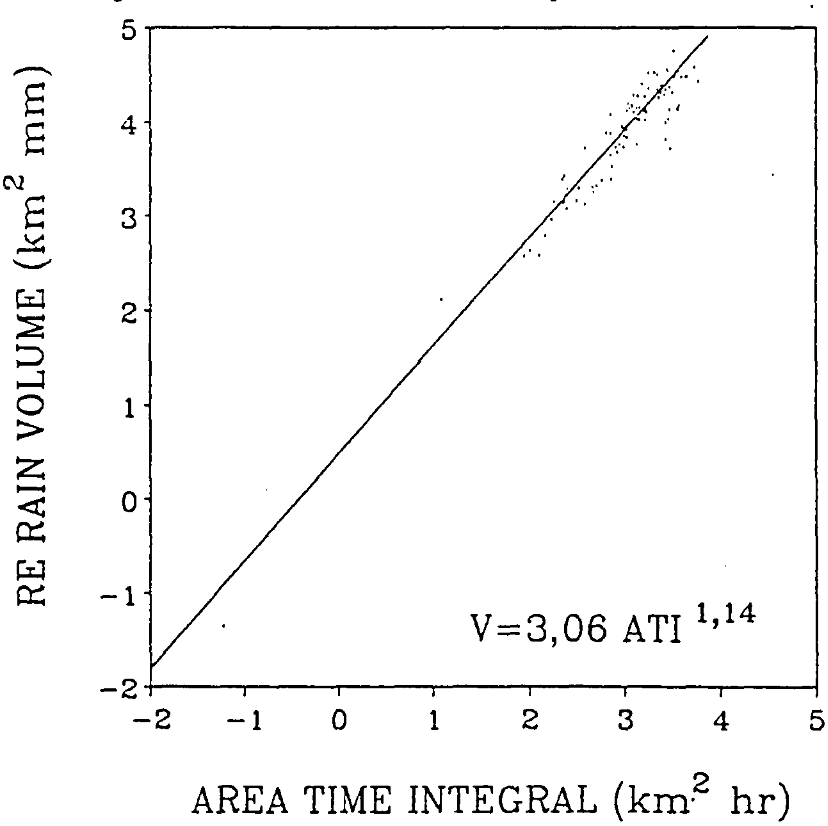

Figure 4.2 Scatter plot of the V-ATI relationship for convective storms over the Transvaal Highveld using the hourly average echo coverage method. The reflectivity threshold is 23,3 dBZ.

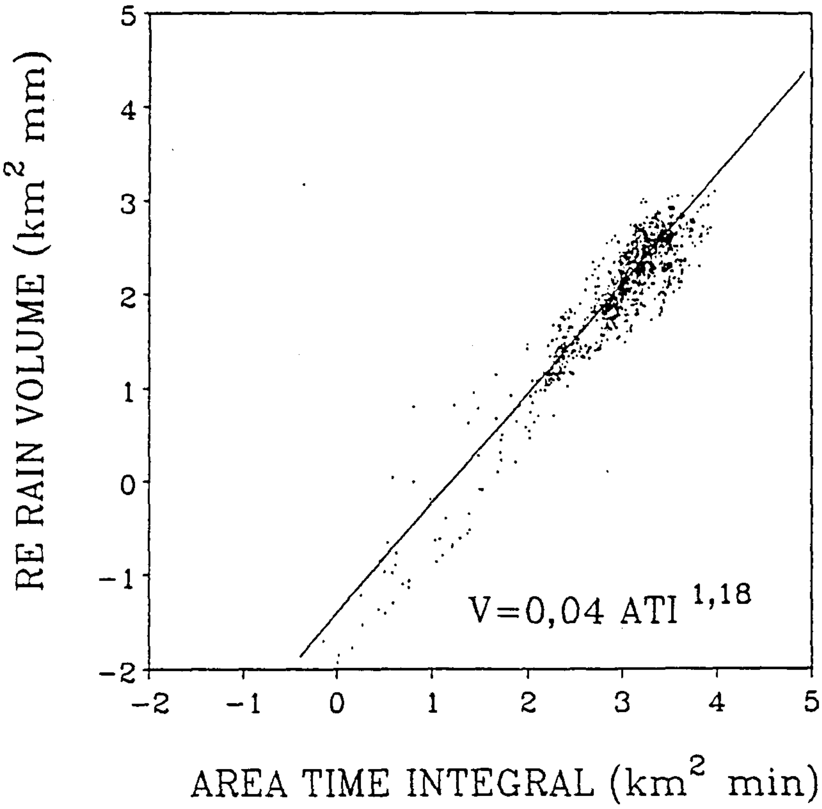

Figure 4.3 Scatter plot of the V-ATI relationship for convective storms over the Transvaal Highveld using a scan-by-scan integration technique. The reflectivity threshold is 23,3 dBZ.

5. DAUGHTER CELLS AND CLOUD SEEDING

Ronald C Grosh

5.1. BACKGROUND

Rain stimulation research in South Africa is expected to continue for a long time, as a water shortage is clearly developing in response to the pressure of population growth and the accompanying development of support industries. Rain stimulation research faces a variety of technical and practical problems which must be solved before an operational cloud seeding program can be expected to provide optimum results (e.g. Changnon *et al.*, 1975). In this Chapter, the way in which the characteristics of cloud regeneration mechanisms might affect the scientific and logistical considerations of a rain stimulation project utilising airborne dispersion of glaciogenic seeding material, are broadly discussed. Radar observations of multicellular storm growth provide the main basis for this discussion, as this type of storm has been the main focus of the promising Programme for Atmospheric Water Supply, PAWS (CSIR/CloudQuest, 1990).

Multi-cellular storms have been found to be suitable candidates for rain stimulation experiments in the eastern part of South Africa, both from the operational and scientific viewpoints. Towers on the edge of relatively isolated multiple cellular storms have been successfully penetrated repeatedly by the sturdy aircraft employed for seeding (a Learjet) with a negligible rate of failure to penetrate due to pilot judgement of overly severe convection. More importantly, early seeding results based on three years of data (approximately 85 cases) have been positive, on average, with radar observations indicating both statistically significant <u>and</u> physically logical rain enhancements following randomized seeding of growing turrets at the -10°C level with dry ice (CSIR/CloudQuest, 1990). Unfortunately, these storms are not the heaviest rain producers and the hydrologic significance of seeding them has yet to be quantified. Studies by Carte and Held (1978) of storm occurrences on the South African Highveld have shown that, although squall lines and similar well organised convective systems clearly will produce more rain on a case by case basis, they are naturally efficient, relatively infrequent (7% of storm days) and dangerous to penetrate as well. Fortunately, isolated thunderstorms occur on about 39% of Highveld storm days with scattered storms occurring on the other 54% of these days. Multi-cellular storms occur frequently (72%) on days with scattered storms, but less frequently on days with isolated storms. Nevertheless, multi-cellular storms are the dominate storm type on more than half of the storm days over the Witwatersrand region (Carte and Held, 1978). Thus, a large selection of cases is potentially available for modification.

Areal rain stimulation projects utilising set ground networks of a given areal extent may have severe logistic problems if large numbers of cells are present and must be treated for long periods. Some of the writer's previous research in this area was directed towards providing logistical information to be used for planning seeding logistics under a given type of weather situation (strong convection-hail) over a 5000 km^2 network in central Illinois (Changnon *et al.*, 1975). For example, it was found that, on average, five or six 40 dBZ radar cells would require treatment at one time and that (maximum gain) echoes would exist over the network for five and six hours with large (diameter ≈100 km) storms needing to be circumnavigated in that warm humid climate. However, the South African rain research is not yet in the network phase. Thus, the characteristics of individual cloud systems are examined without regard to a surface network. It is the building blocks of clouds that are of most interest here, but not just for logistic reasons. The characteristics of multicellular cloud mergers are of scientific importance as well, since natural cloud growth mechanisms will affect weather modification efforts.

5.1.1 Observational cloud merger studies

The most extensive cloud merger studies are all based on radar observations, primarily low elevation angle scans. Westcott (1977) examined 600 echoes on three summer days in Florida, Lopez (1976) analysed 6000 echoes from six tropical cloud clusters north-east of Barbados, and Houze and Cheng (1977) tracked 2000 GATE echoes using this procedure. However, the vertical radar structure of merging storm echoes has been analysed much less frequently, two studies in Illinois are discussed here (Changnon 1976, Grosh 1978a).

Westcott found that merged echoes were 5 (first order mergers) to 30 times (second order - or subsequent - mergers) larger in area than single echoes and produced 10 to 100 times as much rain. However, Lopez found that smaller echoes tended to grow as a result of merger, but that some initially large echo pairs would decrease in size after merging. A further scale dependence was quantified by Houze and Cheng. Only 5% of echoes smaller than 100 km^2 merged, but larger storms (up to 1000 km^2 and 10 000 km^2) were more likely to form by merger (22% and 59%, respectively). Changnon found that all 190 convective storm echoes he examined from a 19 day study period grew vertically after merging. About half of the mergers occurred during the first quarter of echo life time. Grosh studied the full three dimensional structure of six merging echoes and used radar and rain gauges to determine the rain flux from the echo areas over a dense surface network. Merged echoes were larger and produced more rain than unmerged echoes. However, feeder type merging dominated the small sample and impressive echo growth did <u>not</u> follow merging.

Gomes *et al.* (1989) report a cloud merger observed in South Africa by Doppler radar. In this case new cloud clusters were found to develop ahead of the large (30 km length) main cell, probably in the convergent area caused by its cold air outflow. In this case, the merging of two large storms was also observed to coincide with hail and heavy rain at the ground.

New cells tend to form near expected inflow regions, on the equatorward side (approximately 50%) and leading edge (approximately 25%), of multicellular storms on the Highveld (Carte and Held, 1978). This result compares reasonably well with the results of the American Thunderstorm Project (Beyers and Braham, 1949) where the distance dependency of new cell formation was also described (e.g. new cells are very likely to form between cells less than 10 km apart, but 11 times less likely when separated by over 14,5 km (Figure 5.1).

5.1.2 Feeder cells

Examples of storms with more organised inflow regions have been discussed by Dennis *et al.* (1970). Based on 22 Great Plains (USA) severe storms, they found that feeder cells formed close to the main cell (within 2 km) and rapidly merged. Large and steady severe storms had feeder cells forming in a line along the right rear flank (northern hemisphere). The feeder cell could become the main core of the storm in some cases. A related type of storm in the more humid Midwest (USA) has been described by Grosh (1978b), and Grice and Maddox (1984) state that these severe quasi-stationary rain storms occur frequently in other climates as well. In these last cases, the merging cell merges directly with the older core and becomes the dominant tower (Figure 5.2). These storms have some similarities with the more steady supercell storms which appear to evolve beyond this stage due to a slightly different environment. Supercell storms occur rarely in the mid latitude climates where they were discovered, and there was only one report of a supercell-like storm in the first seven years of the CSIR radar programme (Carte, 1981). Thus, they will be encountered infrequently and, because of their severity, would be avoided as a seeding target in any case.

5.1.3 Daughter cells

On the other hand, Chisholm and Renick (1972) have described the daughter cell type of repeating merger mechanism whereby a new cell appearing to the near right rear (northern hemisphere) grows to become the dominant cell as the older parent cloud fades *next* to them (Figure 5.3). This case is thought to minimise the effective spreading of seeding material compared with the feeder case where the new cells actually move into the same region the older parent cell occupies.

5.1.4 Weak evolution

In organised cases with reasonably proximal merging cells, Foote and Frank (1983) have applied the term "weak evolution" to distinguish cases in between the multicell model (where cores never merge, similar to the daughter cell case, for example) and the steady supercell model. If the updraught diameter (D) is small relative to the distance (L) between significant updraughts, the case can be categorised as multi-cellular (separate cores). When L is small compared with D, the supercell term is more appropriate. When L is intermediate, convection may approach the single supercell state more closely than the multiple cell case, but individual cell cores though merged can still be distinguished and convection is noticeably less steady (Figure 5.4). Obviously, some feeder cell storms have strong similarities to the weak evolution case, such as in the case of the quasi-stationary rain system.

5.1.5 Cloud model studies

Several groups have studied cloud mergers with numerical models (Orville *et al.*, 1980; Cheng, 1989; Turpeinen, 1982; Wilkens *et al.*, 1976; Hill, 1974; Wilhelmson and Chen, 1982; Farley and Orville, 1986). The models have a distinct advantage over the standard merger observation technique (radar) in that the nature of the merger can be more accurately described, e.g. there is no longer a need to speculate as to whether updraughts have merged along with rain areas, the model calculations can tell all. Wilkens *et al.* (1976) studied the most basic elements of cloud merging, thermals. Their 2-D model output revealed an important fundamental result; if the positive buoyancy fields of adjacent thermals mostly overlapped, the thermals would merge. Also, as expected, if the buoyancy fields did not overlap, merging did not follow, and, furthermore, the vertical motions damped.

Moving up to cells with scale of several kilometres, Hill (1974) described the formation of a storm which drew in smaller cells. After merger, the smaller storms developed *within* the larger circulation. At about the same scale Orville *et al.* (1980) studied mergers between feeder and mature type clouds with a 2-D model and found that mergers only occur if the clouds are in different growth stages and are sufficiently close to each other. In the output, pressure gradients were observed to occur which drove smaller cells (4 km diameter) toward the main cell (7 km).

Three-dimensional models have shown how two updraughts might merge (a dynamic merger) via the new updraught of the bridge cloud forming between the two initial clouds which first connect via "echo (rain) merger" (Turpeinen, 1982).

Also, a study of hailstorm feeder clouds was undertaken by Cheng (1989) via a 2-D model with high resolution. Ambient air flow and/or low-level cold outflows induced by evaporation led to wind shear generated gravity waves and the development of nearby feeder cloud formations. Moisture distribution was also found to play an important role in the development of the waves and clouds. The calculated cloud separations agreed with observations. New cells were found to form over or just behind the cold outflow boundary of previous cells (Wilhelmson and Chen, 1982; Farley and Orville, 1986). Also, Thorpe *et al.* (1980) and Droegemeir and Wilhelmson (1987) modelled the thunderstorm outflows and found they behave as cold density currents.

5.1.6 The nature of echo merging

Although there have been many studies of echo merging, some of the most basic features of merging are not well understood because of instrumental shortcomings (Westcott, 1984). In particular, when a rain area is observed to merge with another echo area observed by ordinary radar, it is not possible to specify whether the updraughts have merged as well. Obviously, this may have great impact on the dispersal of seeding material, not to mention storm dynamics. For example, the larger diameter of combined updraughts may increase their protection from entrainment and thereby lead to considerably enhanced storm energetics. Also, the role of larger scale dynamics in the merger process is usually poorly specified. Thus, the true cause of the subsequent cloud intensification and growth which is often observed (and is the reason for much of the interest in mergers) remains quite obscure. That is, what is more important to the post merger intensification, the local interaction of cloud elements or the larger scale forcing? Although the nature of larger scale forcing is unlikely to be resolved for some time, Doppler radar (Westcott and Kennedy, 1989) and/or in situ aircraft observations of updraught state and location (Malkus, 1954) have the potential for supplying some of the information necessary to clarify these issues. However, neither these observations nor cloud models are available to the present study. Although multiple level radar observations could be utilized to monitor some aspects of the dynamic state of the merging clouds, in the present study single level PPI observations were found to be adequate to support the conclusions.

5.2 DATA

CSIR archives of digital data from the S-band Houtkoppen radar covers about 10 years. This data bank served as the primary source of information for the merger study, primarily because of the convenient and relatively advanced in-house data display programs available at CSIR where the study was to be performed. Multiple cellular storm cases were selected from days with relatively isolated convection, as determined from the archive of occasional polaroid photographs of the PPI display on storm days as observed by the CSIR radar at Houtkoppen. Based on the PAWS results, special attention was focused on isolated multi-cellular storms during days with 40 dBZ echoes, warm cloud bases (cloud-base temperature >5°C) and moderate instability (ΔT at 500 hPa >0°C).

5.2.1 Sample size

Six selected multiple cellular merged storms from three days in 1987 were tracked on the radar imagery for this study, 3 November (1 storm), 16 November (4 storms) and 2 December (1 storm). The storms were chosen primarily because of their merged or multiple-cellular nature, and *relatively* isolated locations. Severe storms (producing hail) and those near the radar ground clutter pattern were avoided. Although the sample of storms used here is small, a wide range of cloud conditions were covered, including warm and cool bases and strong and weak translation (Table 5.1).

5.2.2 Synoptic and mesoscale conditions

However, on all three days the synoptic pressure patterns giving rise to the multiple cellular storms were rather similar (see Figures 5.5a, b and c). A trough was observed over the heart of the country and high pressure dominated the west coast with a high pressure centre also observed north of Maputo on either the east coast or some eastern inland location. The contour pattern was the most confused on 3 November 1987, as low pressure also extended from the south coast up to the northeast coast and the eastern high pressure centre was displaced inland. Noontime, upper-level winds at Irene were generally from the west-southwest on all three days.

However, only on 3 November 1987 were no northerly-component wind being reported near or below cloud base (Figure 5.5d). Peak winds were observed at 200 hPa and were 21 to 32 $m.s^{-1}$, with the weakest jet also occurring on 3 November 1987. Thus, single cell storms were not expected on these days, but multicell storms were clearly favoured and on the two days with distinct directional shear, the possibility of severe weather needed to be considered as these hodographs are approaching the supercell profiles described by Chisholm and Renick (1972). Cloud bases were moderate to warm and the atmosphere unstable (Table 5.1). On all three days, cloud top heights for boundary layer parcels (60 hPa averaging depth) could rise to above 200 hPa (about 12,4 km) and about 6 km above the seeding level at -10°C (Figures 5.5e, f and g).

Table 5.1. Atmospheric and cloud conditions over Irene at noon on the three study days in 1987 (60 hPa averaging depth).

Variables	3 Nov	16 Nov	2 Dec
1. Cloud Base Temp (°C)	9,5	6,7	13,0
2. 500 hPa Buoyancy (°C)	5,5	3,0	5,0
3. 1÷2	1,7	2,2	2,6
4. Mixing Ratio (g/kg)	11,0	9,4	12,9
5. Convective Temperature (°C)	29,5	30,4	27,5
6. Speedshear to jet peak (s^{-1})	$1,7*10^{-3}$	$2,1*10^{-3}$	$2,8*10^{-3}$
7. Cell Speed ($km.h^{-1}$)	~15	~50	~20

16 November 1987 was the day with the coldest cloud bases, while 2 December 1987 had the warmest cloud bases, the largest subcloud moisture content, and the greatest windshear.

5.3 MERGER CRITERIA

The following criteria were applied in analysing the radar observations.

i. Duration: any contact.

ii. Initial cell separation: all detectable separations (23 dBZ threshold was used).

iii. Size: multi-cellular storms were the main focus of attention, especially semi-isolated cases. Well organised storms (squall lines and heavy storms) are not the primary interest. 40 dBZ echoes were also required. At Nelspruit the horizontal extent of the multi-cellular storms passing the PAWS seeding criteria averaged at about 50 km^2 with peak areas being 117 km^2. Storm-top heights should also be able to reach the -10°C level (seeding level).

OTHER MONITORED CHARACTERISTICS

i. Wind, stability, cloud base temperature.

ii. Cell motion versus system motion.

iii. Storm orientation.

iv. Type of merger:
   a) Feeder versus daughter cells (versus weak evolution).
   b) Differential cell motion.
   c) Expansion merging.
   d) Bridging between pre-existing cells.
   [e) Updraught/downdraught merging as well as rain areas (in ideal conditions).]

5.4 ANALYSES

5.4.1 3 November 1987

On 3 November 1987 small, widely scattered echoes began to form after about 13:00 SAST (South African Standard Time). By 16:00 storms were beginning to show clearly multicellular form and were distributed in randomly located clusters about the Houtkoppen radar. Continued echo growth then followed, but the overall echo pattern remained essentially random until about 18:00 when some of the multiple cellular storms appeared to be forming a broad scattered line approximately 90 km north of Houtkoppen. A self propagating storm (echo C) which generated several new cells on its downwind edge was tracked using contoured plots of the digital radar data.

The digital radar data starting at 15:21 was examined. A more or less 60 km long line extended from the radar toward the southwest and there was also a large area of randomly distributed storm echoes centred about 30 km to the south. These two storm areas are not analysed here because they were associated with ground clutter contamination and known severe weather reports (hail).

At about 16:30, a rapidly growing and intense (50 dBZ) new echo (C) developed about 65 km northwest of the Houtkoppen radar and about 30 km from the northern end of the linear echo (Figure 5.6a). At about this time, two major new echoes (B and C) had appeared near an earlier cell (A) at the end of the line. Echoes A and B died shortly after this time. However, storm C went through a major growth phase and was still being tracked at the end of the examined data an hour and a half later. Thus, it was chosen for analysis.

Storm C quickly developed a small new 40 dBZ intensity centre, C2 (Figure 5.6b, 16:38) near the appendage sprouting northeastwards at 16:32 (Figure 5.6a). This was in turn quickly enveloped by the expanding 40 dBZ contour of the initial core C (Figure 5.6c, 16:41).

By 16:53 (the next available image, Figure 5.6d) three new 50 dBZ intensity centres had formed near the earlier bulges about the three leading edges of echo C (Figure 5.6c) and surrounded the old core which was still maintaining a 50 dBZ contour as well. However, the old core quickly dissipated as the three new 50 dBZ centres grew rapidly in area (Figure 5.6e, 16:59).

The forward cell (C4) appears to have become by far the dominant cell, e.g., at 17:19 (after some missing scans; Figure 5.6f) the other cells were greatly reduced in intensity.

Forward propagation continued as contiguous new 50 dBZ cells sprang to life, first to the right (C6; Figure 5.6f, 17:19) and then to the left (Figure 5.6g, 17:30) of the general echo motion.

Finally, the last two cells appeared to have merged through the expansion of the 40 dBZ contour as the cells themselves weakened (17:35; Figure 5.6h).

5.4.2 16 November 1987

On 16 November, several moderate sized (approximately 20 km in diameter) convective complexes occurred about the Houtkoppen radar site. At times the storms showed some evidence of an overall linear alignment pattern, but in general the situation was best described as a disorganised area of squalls. In the late afternoon, several storms approached the radar from the west-northwest. Four storms that could be easily tracked (i.e. not confused with ground targets) were studied.

The 16th November was the day with the strongest low-level (below 700 mb) winds, especially for northerly components. Thus, at the start of the radar data (15:41) examined for this day an intense (50 dBZ) nearly 50 km long linear cell approximately 50 km to the southwest of the radar was observed to be moving at about 50 $km.h^{-1}$ toward the east-southeast. This system appears to have consisted of two primary convective areas originally, with the more northerly cell probably developing as the southerly component maximized its intensity (Figures 5.7a and b).

This echo couplet appeared to be moving in parallel with a line which was very close to the radar and probably contaminated by ground return. Further convective developments to the north of the couplet were becoming apparent by 16:00 as several small cells started to appear and grow while the north cell (B) began to maximize its low-level rain flux (Figures 5.7b and c). However, another smaller associated echo couplet (C-D) a few kilometres to the south of cell A (Figure 5.7a) was also growing during this time and other new cells appeared nearby as well. At 16:18 the echo couplet A-B merged with the weaker southern echo couplet C-D apparently as a result of the expansion of C-D. Differential motion relative to the larger A-B couplet appears to have been non-existent (although a precise determination of the translation speed of evolving storms is rarely possible).

The cluster of five or so closely spaced echoes trailing to the immediate north of the merged system (A-B-C-D) at 16:00 will be referred to here as M-N-O-P-Q (Figure 5.7b). Some of these echoes also merged by expansion, first the weaker couplet M and N (Figure 5.7c) and then 10 minutes later the stronger cells O-P-Q (Figure 5.7d). The echo cores maintain their separation distances during this period. Two notable additional echoes form during this period (16:08-16:18), R and S. Echoes M, N and O dissipate during the next half hour (Figure 5.7f). However, M-N never merged with O-P-Q. Echo S pulsates between one and two cores during most of its lifetime, but then merged to the rear of P-Q by 16:49 just as the complex moved into heavy ground clutter (Figure 5.7h). Once again, differential storm speed is not the merger mechanism. The echoes S and P bridged at 16:49 with the core centres in about the same relative location they were in at 16:18.

Storm R grew rapidly. It was about 15 km long by 16:08 (Figure 5.7c), and based on its shape probably consisted of three major towers or cells at that time, although there is no separation in the 30 dBZ contour. This storm also moved rapidly (40 to 50 $km.h^{-1}$) eastward. By 16:18 (Figure 5.7d) it had a 50 dBZ core which was 4 km long and it was rapidly producing contiguous new cells along its north and south edges. The new northern convection (Rn) quickly developed a large (6 km diameter) clearly separate 50 dBZ centre (16:26, Figure 5.7e) as the consolidated southern core shrunk. At this time, a separate new cell (R3) can be seen about 3 km to the northwest of the northern core. This new cell and another separate cell, R4, to its northwest (Figure 5.7g) also rapidly grew and merged with the parent cell (Rn) (Figure 5.7h). The rapid intensification of the new convection (R4) was probably related to strong outflow from (Rn) which was just passing its intensity peak, and from R3 which had already started a rapid decline from its peak of 50 dBZ at 16:43. This storm provides the closest approach to the classical daughter cell example of Chisholm and Renick (1972), reproduced in Figure 3.

5.4.3 2 December 1987

On 2 December, an echo system which grew by a mechanism that appeared similar to the well-known 'daughter cell' pattern (Chisholm and Renick,

1972) was observed approxiamtely 50 km north-northwest of the Houtkoppen radar.

This system occurred between two older irregularly shaped lines of echoes. The longer line was about 200 km long and located some 90 km south of the radar. The shorter line (approximately 80 km long) was about 90 km to the west and nearly perpendicular to the west end of the longer line. As time passed, these two features became more cluster-like. The daughter cell variant developed between these more established systems about 40 km from the nearest echoes to the south.

Starting at about 15:54, radar observations were made of the newer convection. There were four main cells associated with the new daughter type system (Figure 5.8a). Three of the cells had intensities above 40 dBZ. The most intense of these was the cell furthest to the east (cell A), which intensified to more than 50 dBZ by 16:00 and had a diameter of about 10 km (Figure 5.8b). The somewhat larger cell to its north (cell B) was more complex and had a double core. The four cells were separated by about 5 km or less between cells.

These cells remained separate at the 23 dBZ level for about 10 minutes more and then at 16:04, shortly after the peak rain from cell A, the two northernmost cells merged at the 23 dBZ level as an area of weak echo bridged the gap between them (Figure 5.8c). Within nine minutes all four cells were linked at the lowest intensity level (23 dBZ), and by 16:20 (Figure 5.8d) a linear configuration was emerging along the northwest side of the complex from the alignment of the northernmost cell (B) with the two cells furthest to the west and the considerable expansion and thereby merging of their 30 dBZ core areas. 50 dBZ intensities were observed at two locations along the line, as well as in cell A. Cell A diminished soon after its peak rainout and the linear pattern to the north became dominant (Figure 5.8e). The complete system was in an advanced state of decay by 17:00.

Thus, a southern hemisphere version of the classic daughter cell merging seems to be occurring around 16:20. Actually, existing echoes are merging via expansion. Nevertheless, the intensification of the line after the peak rain from cell A indicates that its outflow air may have contributed to the enhancement of the new line. Since this is not the feeder cell pattern (there is little relative motion of the cells and there is also no sign of overwhelming growth by any of the cell cores), it is probably best to associate the expansion type of merging with the daughter cell pattern, as the central cores appear to remain relatively independent throughout the process and would all have to be treated separately by a seeding aircraft.

5.5 CONCLUSIONS

The merged cloud systems described in this study had dimensions of about 25 to 50 km (23 dBZ contour). Typical 40 dBZ cells were up to 5 to 15 km long, with 50 dBZ cores being roughly half that size. Thus, these storms are large but still likely treatment candidates. It also seems likely that up to four cells may often be present at about the same time in a multicellular system in the process of developing and more contiguous cells may appear later on during continued propagation.

Based on virtually all the storms studied here, it is quite clear that a very common type of echo pattern in multicell storms is for sequential cells to appear near each other but with cores (and towers) which do not merge. Instead, they remain remote at nearly constant spatial separations and echo merging is achieved primarily via the expansion of the weaker echo periphery of the discrete cells. Furthermore, over 20 years of experience with storm observations suggest that the expansion pattern is one of the most, if not the most, frequent types of cloud merging. Nearby cells may exist independently or may be initiated and/or influenced by the downdraughts or pressure pulses from neighbouring cells, but the actual mechanism of the cells linking together is related to the cells proximity rather than some explosive strongly interactive dynamic mechanism and thus, the merging often occurs in a relatively benign fashion. If isolated multiple cellular storms are to be focused on for the rain stimulation research activities, this type of merging will be encountered quite frequently. Expanding systems are probably not as likely to be hazardous for penetrating aircraft as those systems merging via mechanisms involving strong relative cell motions or the rapid systematic self generating propagation and incorporation of new cells. Nevertheless, expanding storm systems will still be relatively difficult to treat for rain stimulation purposes, as the storms may still be quite intense, and each cell must be treated individually.

5.6 REFERENCES

BEYERS H R and BRAHAM R R Jr, 1949. *The Thunderstorm: Report on The Thunderstorm Project*. US Government Printing Office, Washington DC, 287pp.

CARTE A, 1981. Morphology of persistent storms in the Transvaal on 16/17 October 1978. *Atmos. Phys.*, 54, 86-100.

CARTE A and HELD G, 1978. Variability of hailstorms on the South African plateau. *J. Appl. Meteor.*, 17, 365-373.

CHANGNON S A Jr, MORGAN G M, ACHTEMEIR G L, TOWERY N G and GROSH R C, 1975. Design of an experiment to suppress hail project for Illinois. *J. Appl. Meteor.*, 14, 771-782.

CHANGNON S A Jr, 1976. Effects of urban areas and echo merging on radar echo behaviour. *J. Appl. Meteor.*, 15, 561-570

CHENG L, 1989. Numerical simulations of hailstorm feeder-cloud initiation. *Atmos. Ocean.*, 27, 279-305.

CHISHOLM A J and RENICK J H, 1972. The kinematics of multicell and super-cell Alberta hailstorms. *Contribution to 6th Annual Conference of the Canadian Meteorological Society*, Toronto, 24-31.

CSIR/CLOUDQUEST, 1990. *Programme for Atmospheric Water Supply. Phase 2, 1987-1989, Volume 1: Executive Summary*. WRC Report No. 133/5/90, Pretoria, 8pp.

DENNIS A S, SCHOCK C A and KOSCIELSKI A, 1970. Characteristics of hailstorms in western South Dakota. *J.Appl. Meteor.*, 9, 127-135.

FARLEY R D and ORVILLE H D, 1986. Numerical modelling of hailstorms and hailstone growth. Part 1: Preliminary model verification and sensitivity test. *J. Clim. Appl. Meteor.*, 21, 2014-2035.

FOOTE G B and FRANK H W, 1983. Case study of a hailstorm in Colorado. Part III: Airflow from triple Doppler measurements. *J. Atmos.Sci.*, 40, 686-707.

GOMES A M, O'BEIRNE S and HELD G, 1989. *Second Progress Report: Precipitation and Air Flow (PRAI) Project*. CSIR, Pretoria, 42pp.

GRICE G K and MADDOX R A, 1984. Radar signatures associated with heavy rains. *Preprints: 22nd Conference on Radar Meteorology*, AMS, Boston, 182-187.

GROSH R C,1978a. Lightning and precipitation in the life history of isolated thunderstorms. *Preprints: Conference on Cloud Physics and Atmospheric Electricity*, AMS Boston, 617-624.

GROSH, R C, 1978b. A local severe rainstorm. *Preprints: Flash Floods Conference*, AMS,Boston, 70-79.

HILL G E, 1974. Factors controlling the size and spacing of cumulus clouds as revealed by numerical experiments. *J. Atmos. Sci.*, 31, 646-673.

HOUZE R A, Jr and CHENG C P, 1977. Radar characteristics of tropical convection observed during GATE. Mean properties and trends over the summer season. *Mon. Wea. Rev.*, **105**, 964-980.

LOPEZ R E, 1976. Radar characteristics of the cloud populations of tropical disturbances in the northwest Atlantic. *Mon. Wea. Rev.*, **104**, 268-283.

MALKUS J S, 1954. Some results of a trade-cumulus cloud investigation. *J. Meteor.*, 11, 220-237.

ORVILLE H D, KUO H, FARLEY R D and HWANG C S, 1980. Numerical simulation of cloud interactions. *J. Rech. Atmos.*, 14, 499-516.

PRESTON-WHYTE R A and TYSON P D, 1988. *The Atmosphere and Weather of Southern Africa*. Oxford U. Press., Cape Town.

TURPEINEN O, 1982. Cloud interactions and merging on day 261 of GATE. *Mon. Wea. Rev.*, 110, 1238-1254.

WESTCOTT N E, 1977. Radar characteristics of south Florida convective rainfall. *Proceedings, Sixth Conference on Planned and Inadvertent Weather Modification*. Champaign-Urbana, Ill. 10-13 October 1977, AMS, Boston, 190-191.

WESTCOTT N E, 1984. A historical perspective on cloud mergers. *Bull. Amer. Meteor. Soc.*, **65**, 219-226.

WESTCOTT N E and KENNEDY P C, 1989. Cell development and merger in an Illinois thunderstorm observed by Doppler radar. *J. Atmos. Sci.*, **46**, 117-131.

WILHELMSON R B and CHEN C S, 1982. A simulation of the development of successive cells along a cold outflow boundary. *J. Atmos. Sci.*, 39, 1466-1483.

WILKENS E M, SASAKI Y K, GERBER G E and CHAPLIN W H Jr, 1976. Numerical simulation of the lateral interactions between buoyant clouds. *J. Atmos. Sci.*, 33, 1321-1329.

01/28c/sgg

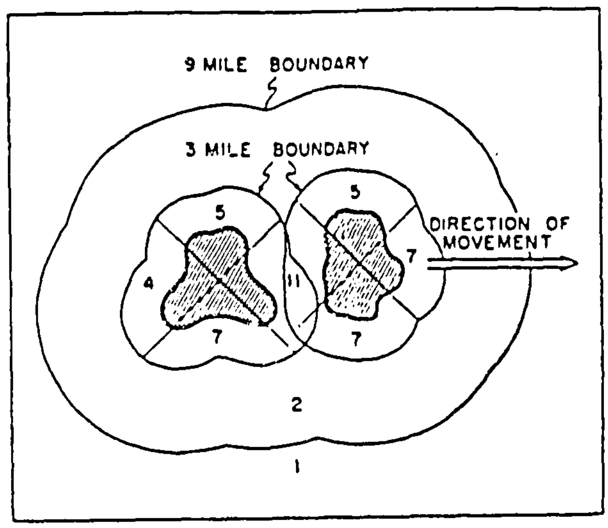

Figure 5.1 The relative probability for the formation of new thunderstorm cells in the vicinity of parent cells (northern hemisphere). The hatched areas represent the PPI radar echoes from the parent cells and the irregular closed curves represent the limits of the 3- and 9-mile (4,8 and 14,5 km) zones surrounding the echoes. The numbers indicate the relative probability of new echo (cells) formation in the zones and quadrants with the probability outside the 9-mile (14,5 km) zone being considered as unity. (After Byers and Braham, 1949; Westcott, 1984.)

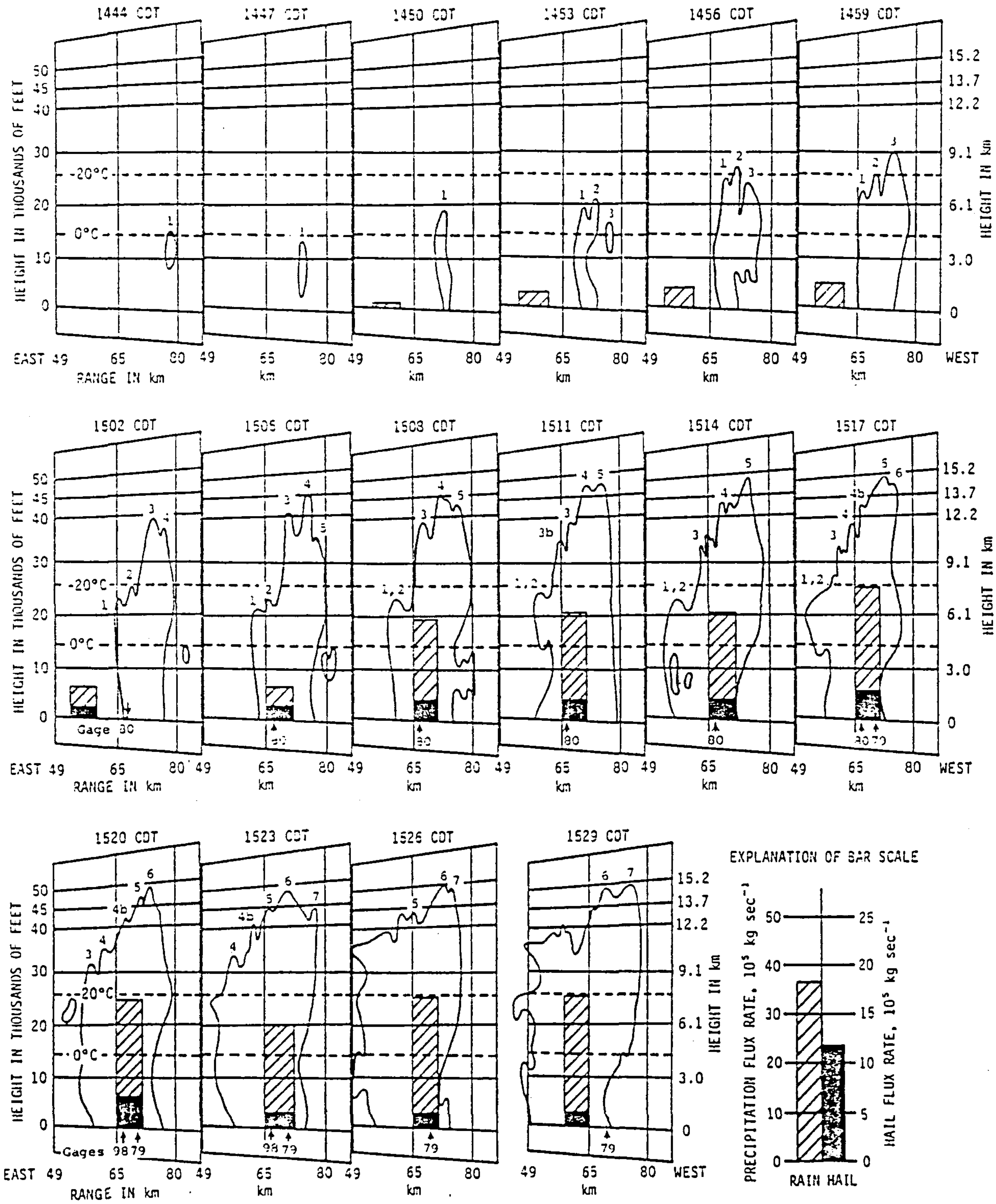

Figure 5.2 Feeder cells overtaking earlier cells and becoming the dominant cell in a heavy Illinois rain storm. (After Grosh, 1978b.)

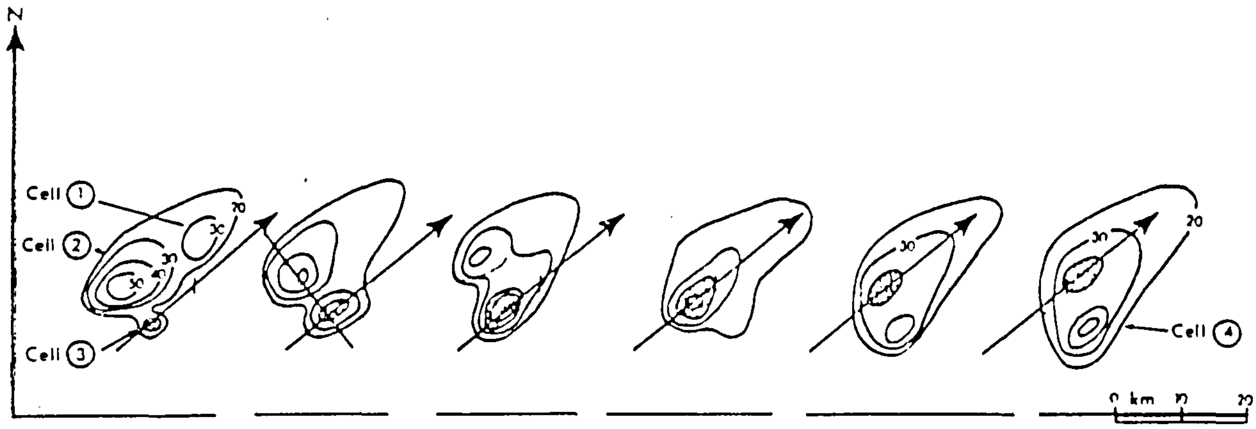

Figure 5.3 Schematic PPIs of evolution of multicellular Canadian storm over 21 minute period. (After Chisholm and Renick, 1972.)

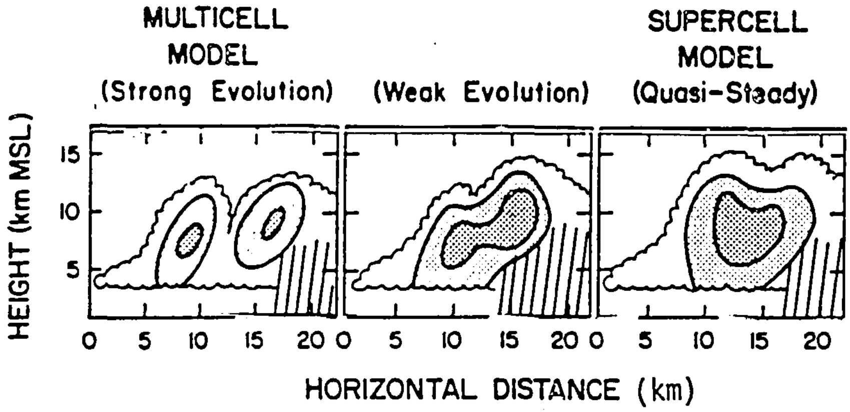

Figure 5.4 Schematic depiction of "weak evolution" of updrafts as seen in comparison with the structural difference between strongly evolved and steady storms. Contour lines represent 5 and 15 mps isotachs. (After Foote and Frank, 1983.)

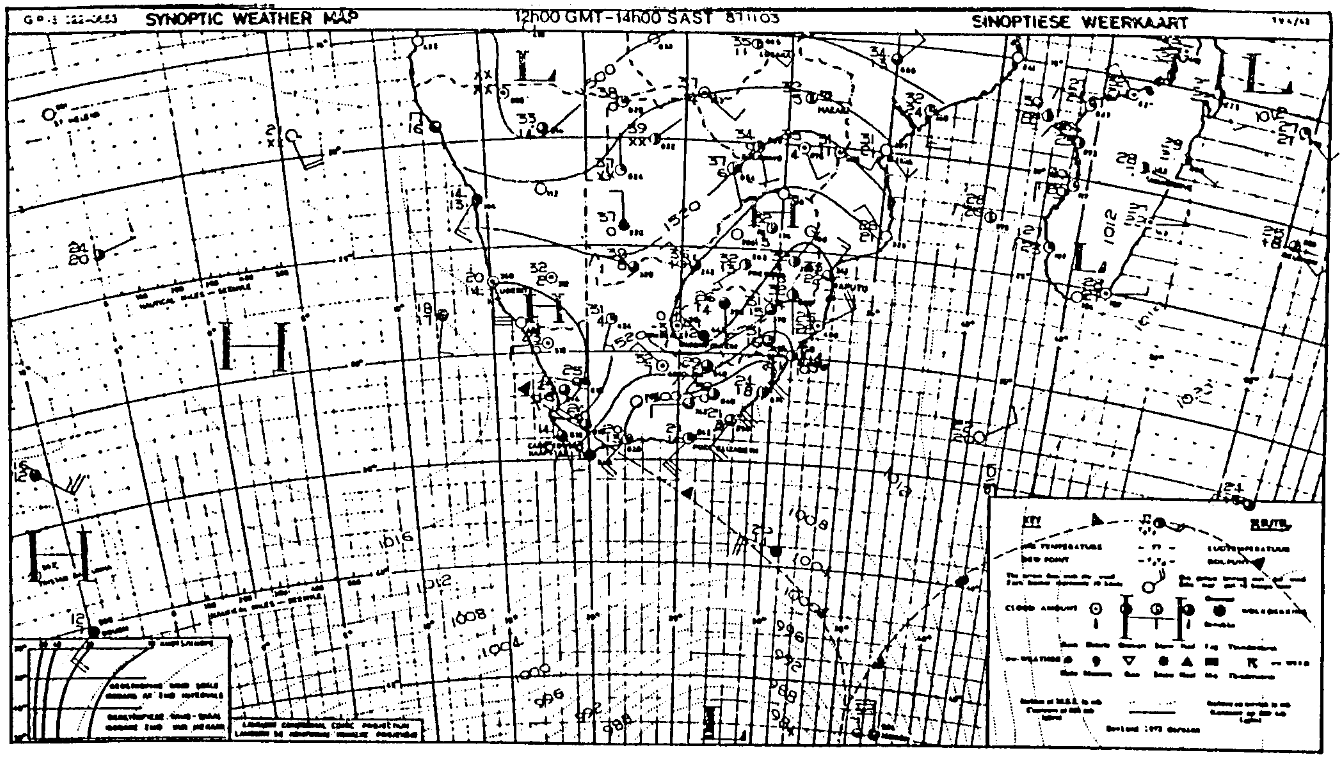

Figure 5.5a Synoptic weather chart for 3 November, 1987 (SA Weather Bureau).

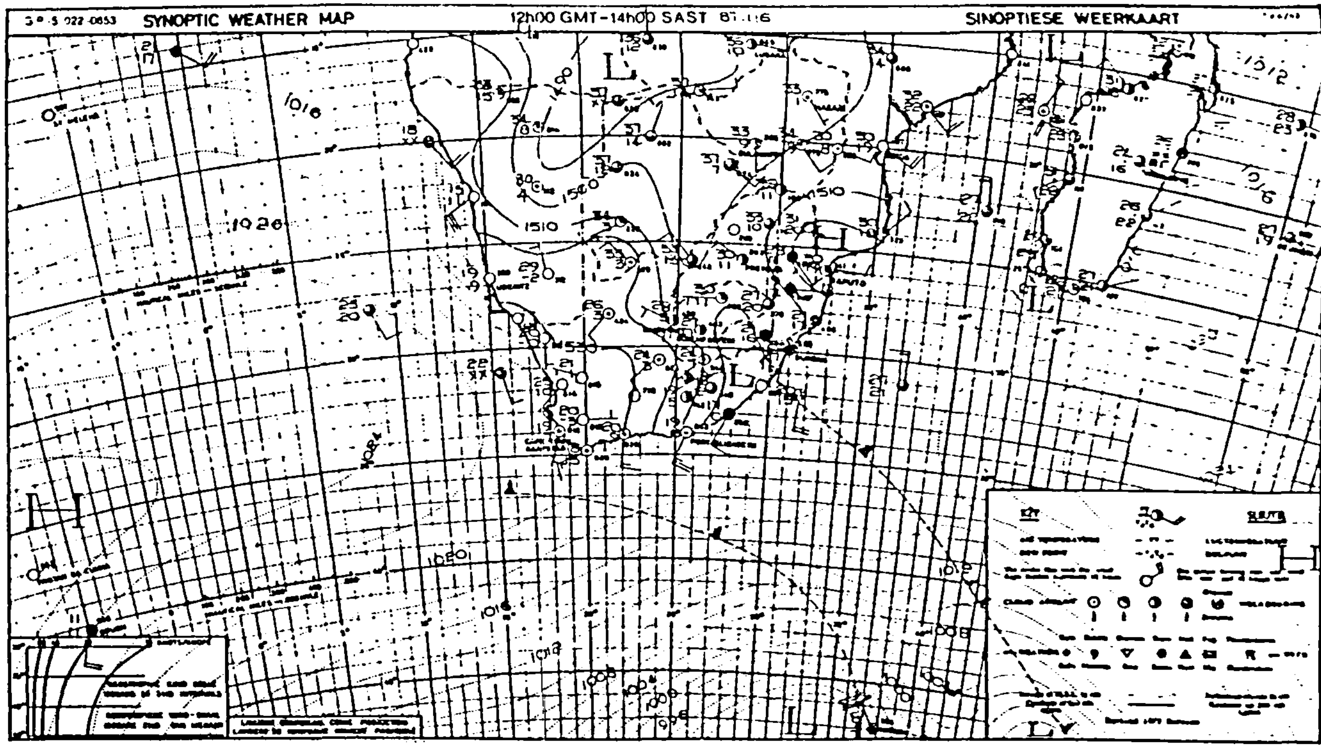

Figure 5.5b Synoptic weather chart for 16 November 1987 (SA Weather Bureau).

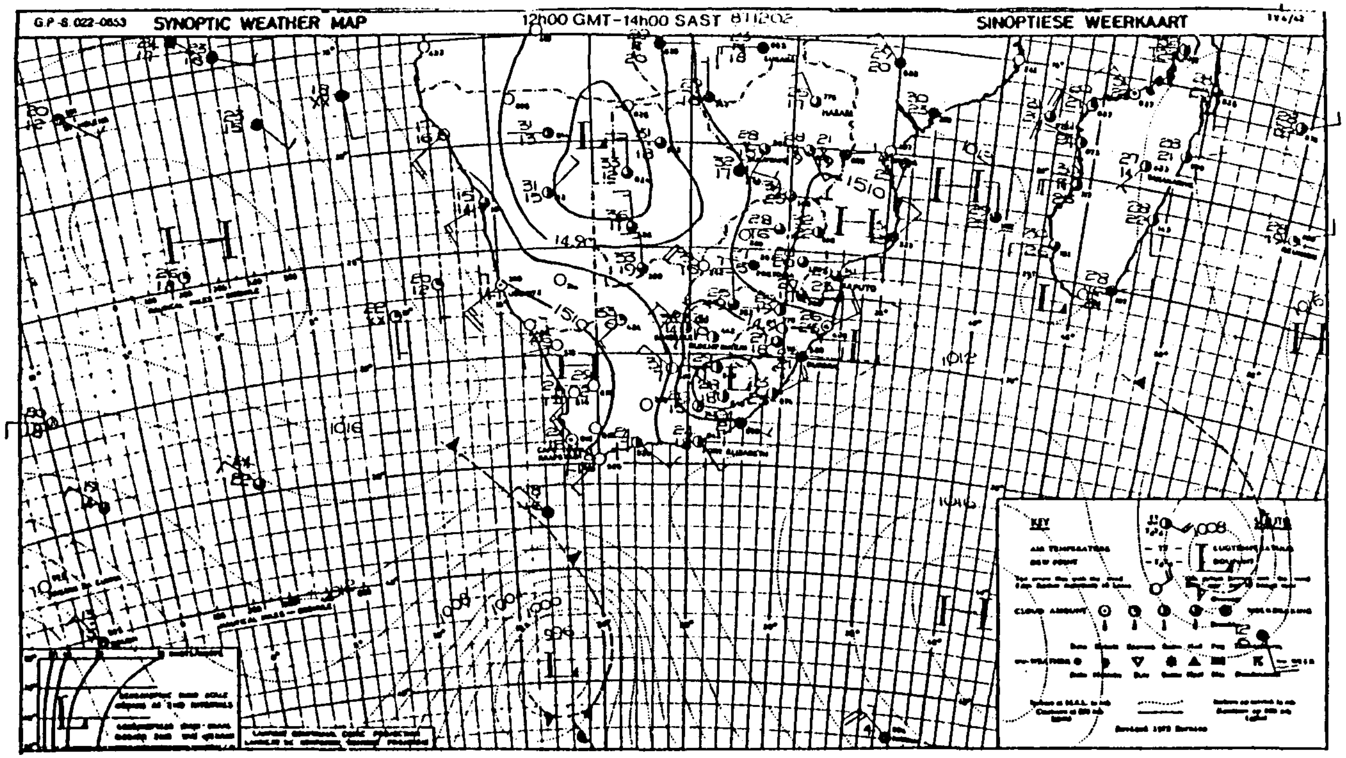

Figure 5.5c Synoptic weather chart for 2 December 1987 (SA Weather Bureau).

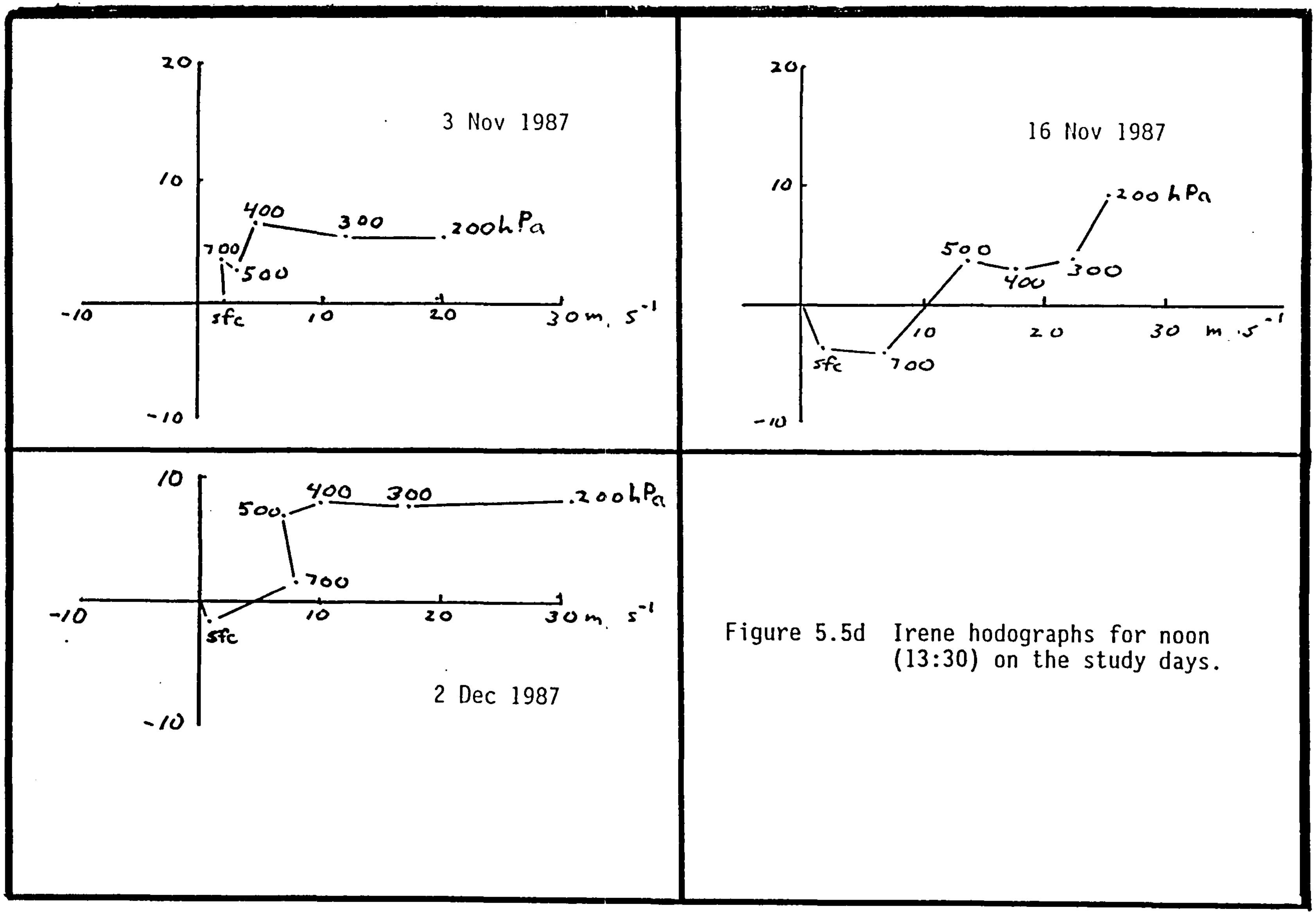

Figure 5.5d Irene hodographs for noon (13:30) on the study days.

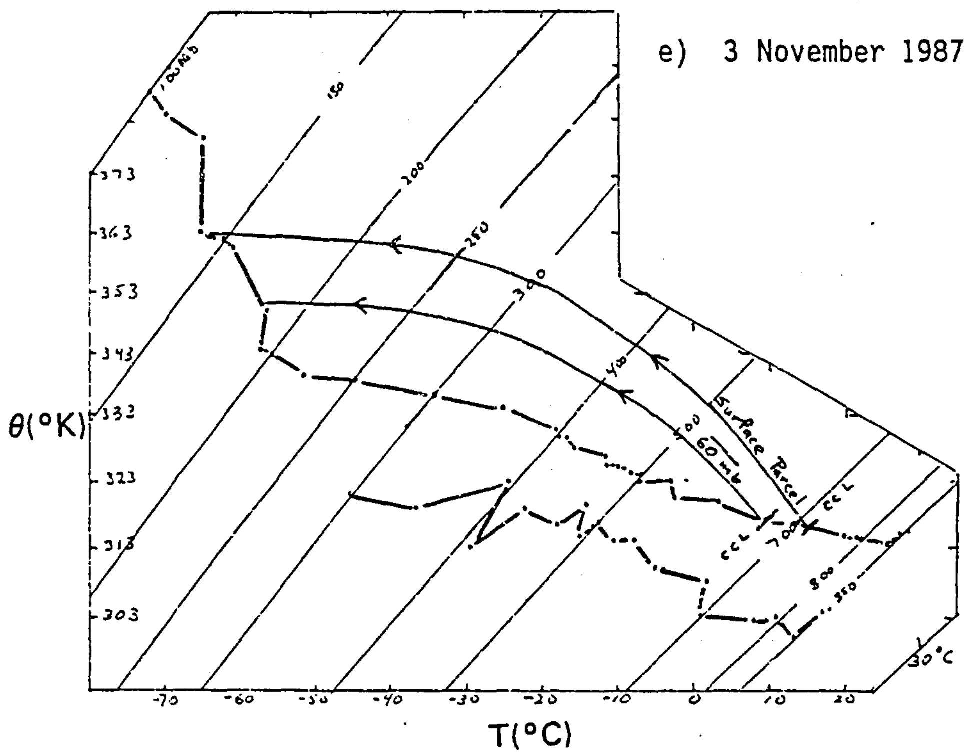

Figures 5.5e, f and g Noon soundings from Irene for the three study days. Thermodynamic "trajectories" are for surface conditions and a surface layer 60 hPa deep.

g) 2 December 1987

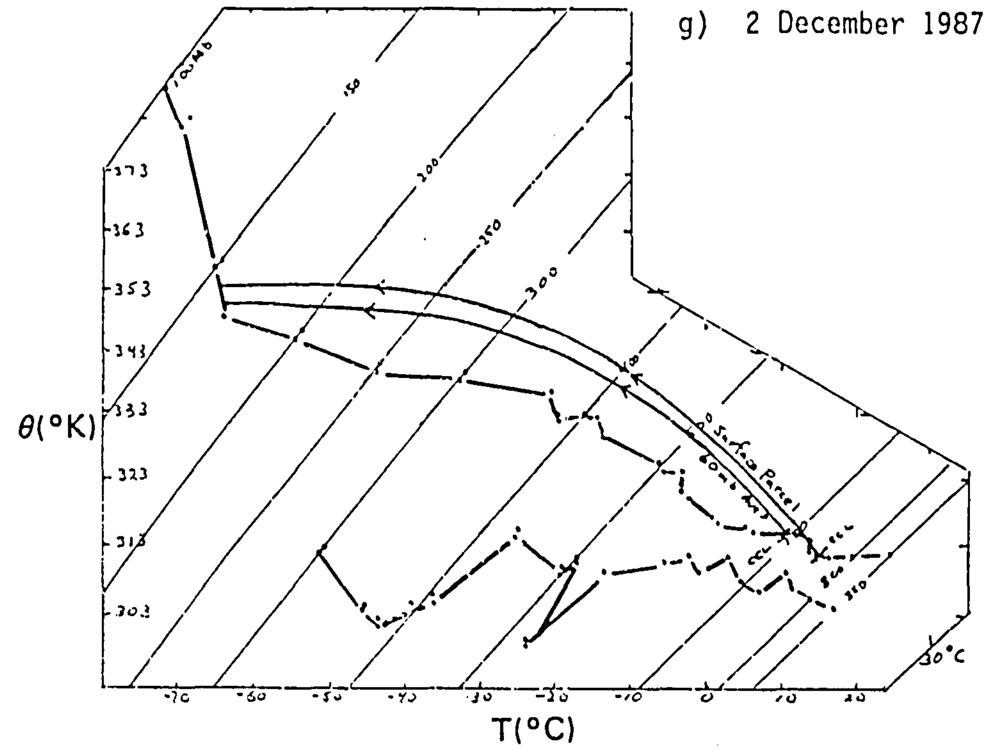

f) 16 November 1987

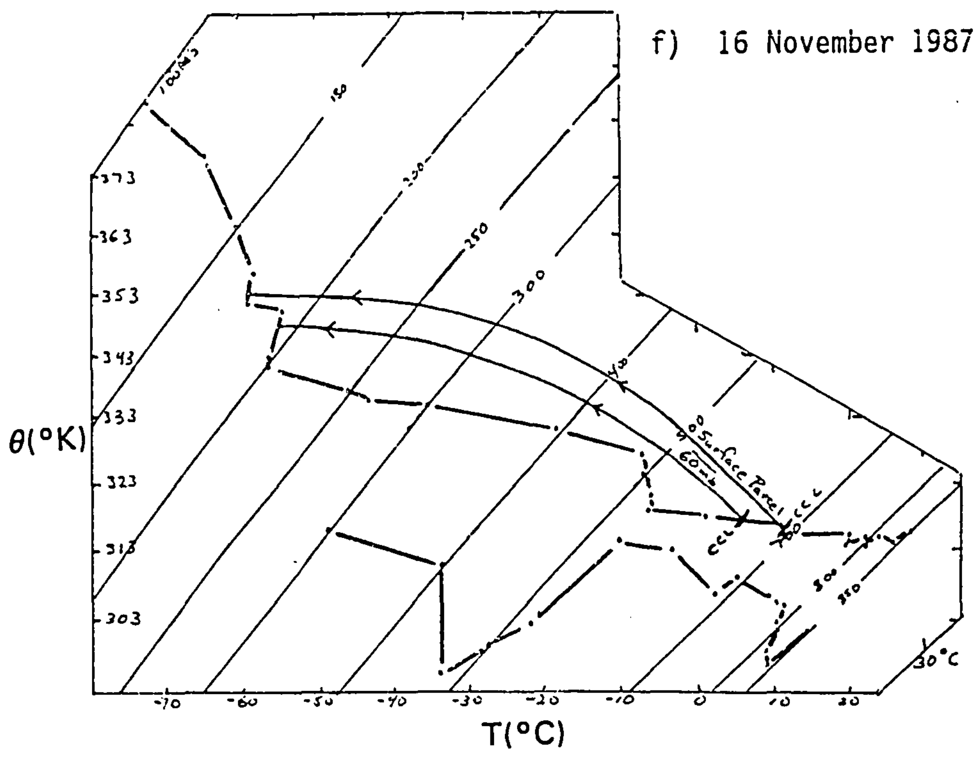

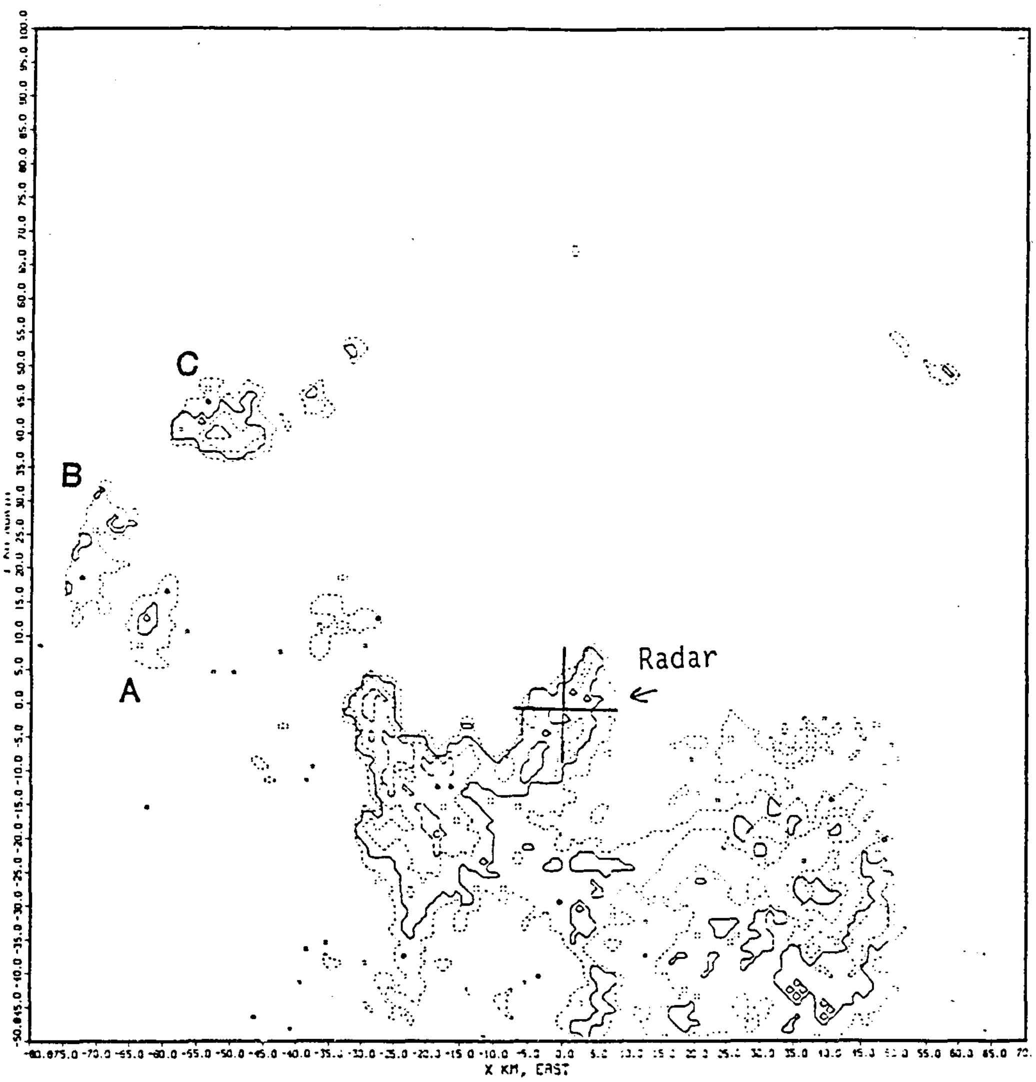

Figure 5.6 Radar PPI images for 3 November 1987 (antenna elevation 5°). Contours depict 23, 30, 40 and 50 dBZ intensities.
a) 16:32 SAST.

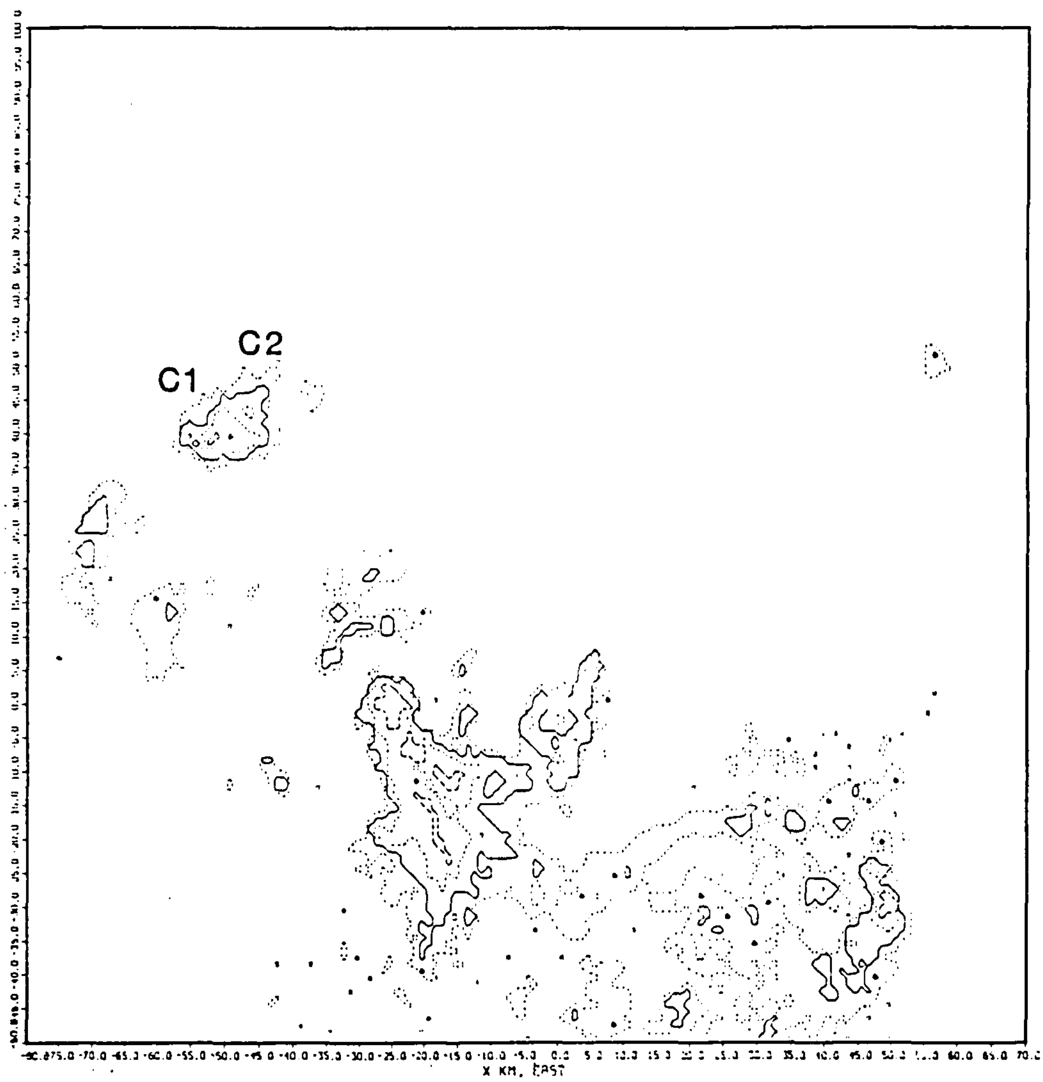

Figure 5.6b 16:38

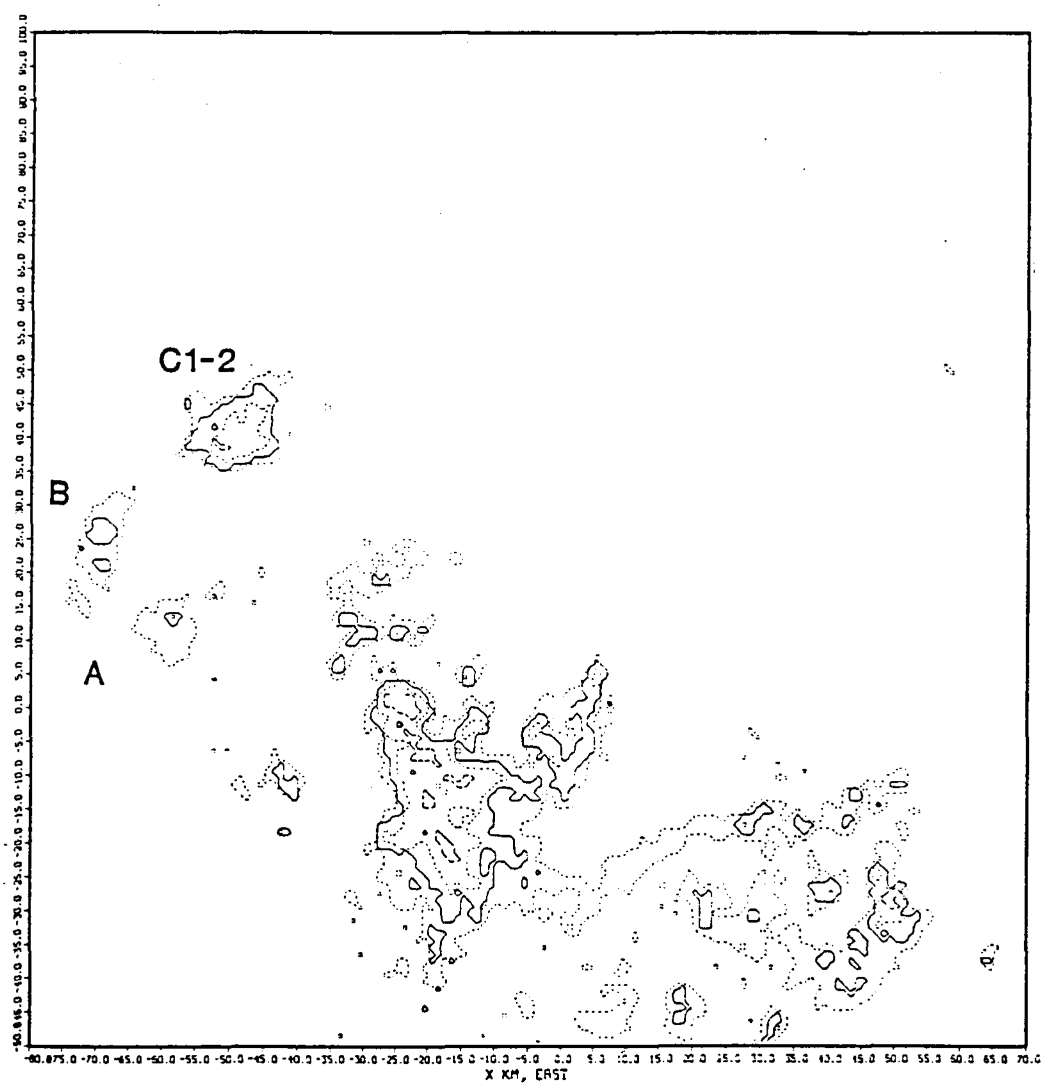

Figure 5.6c 16:41

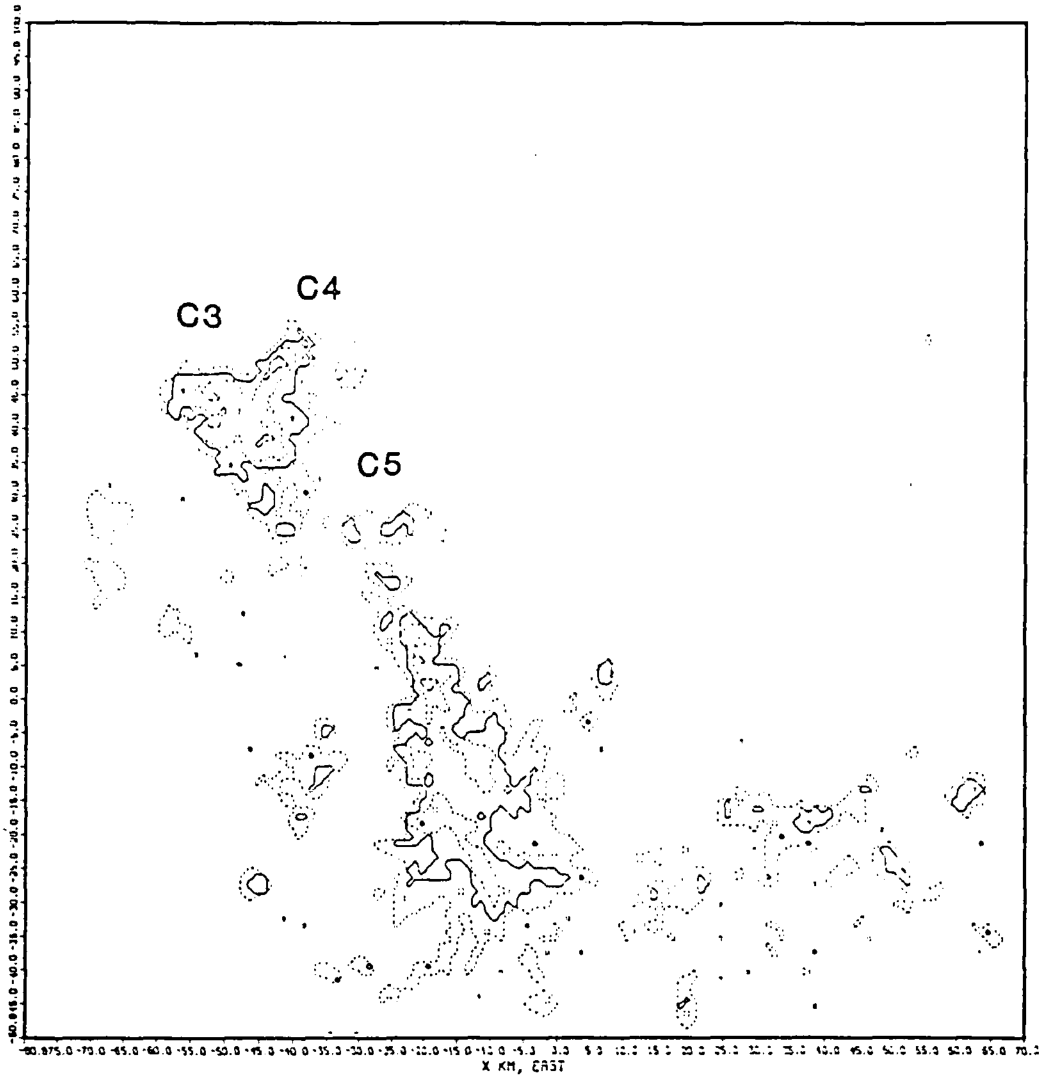

Figure 5.6d 16:53

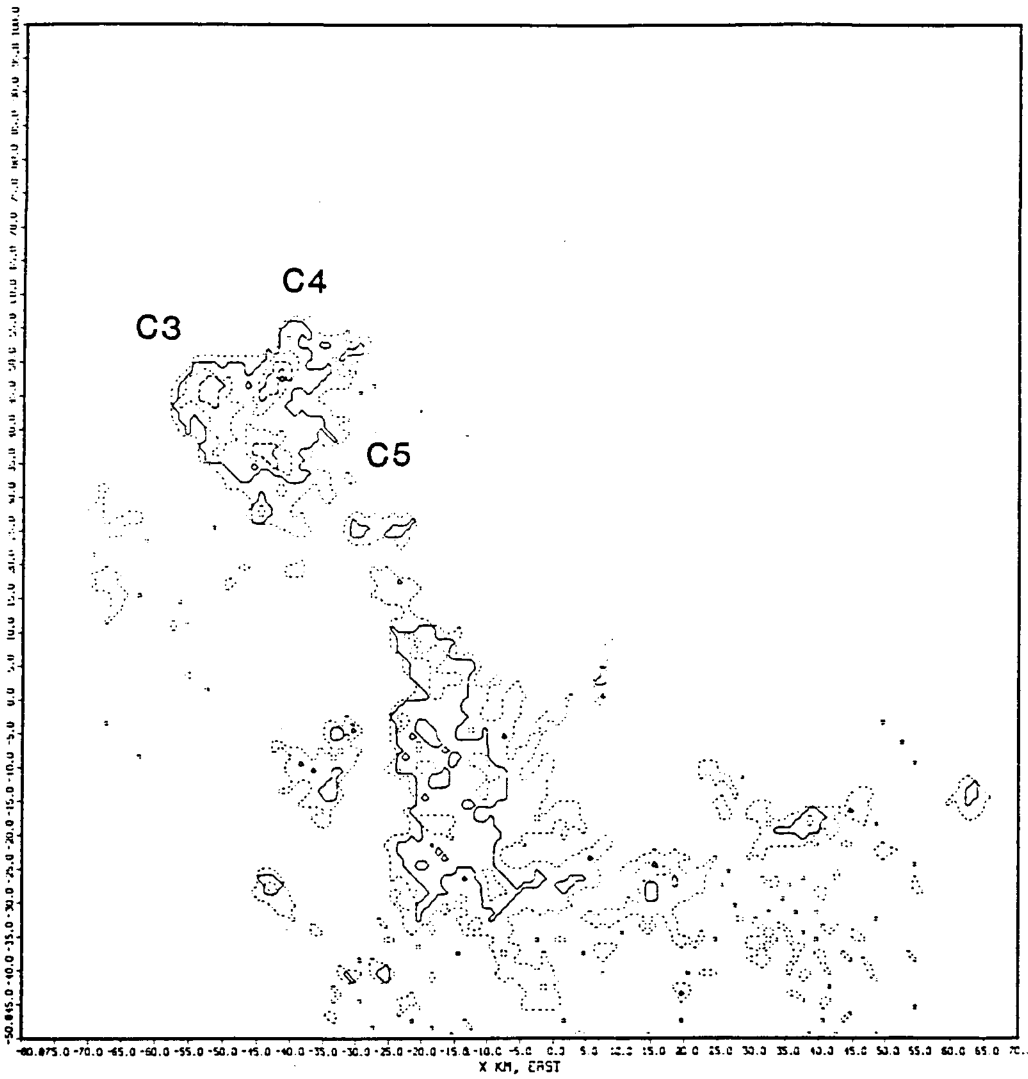

Figure 5.6e 16:59

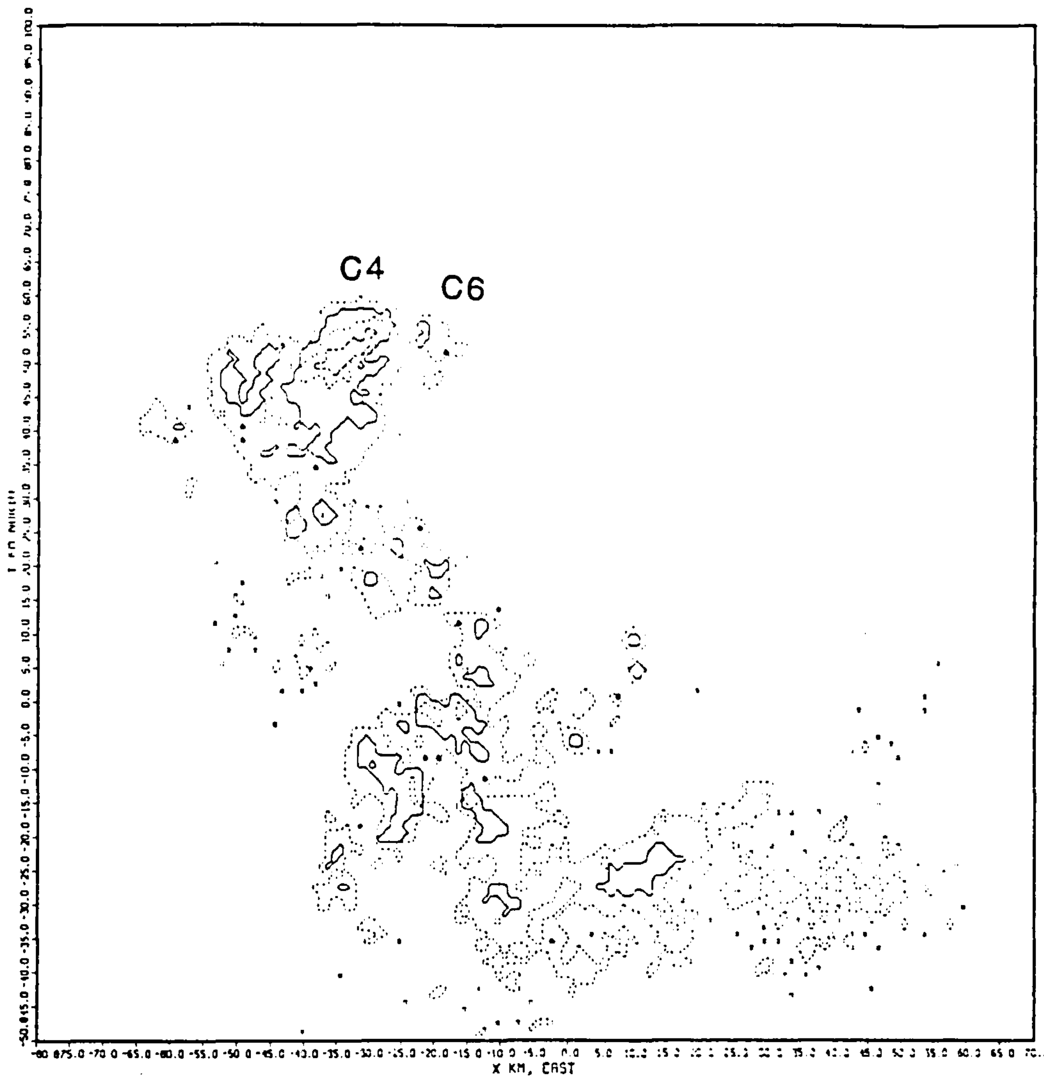

Figure 5.6f 17:19

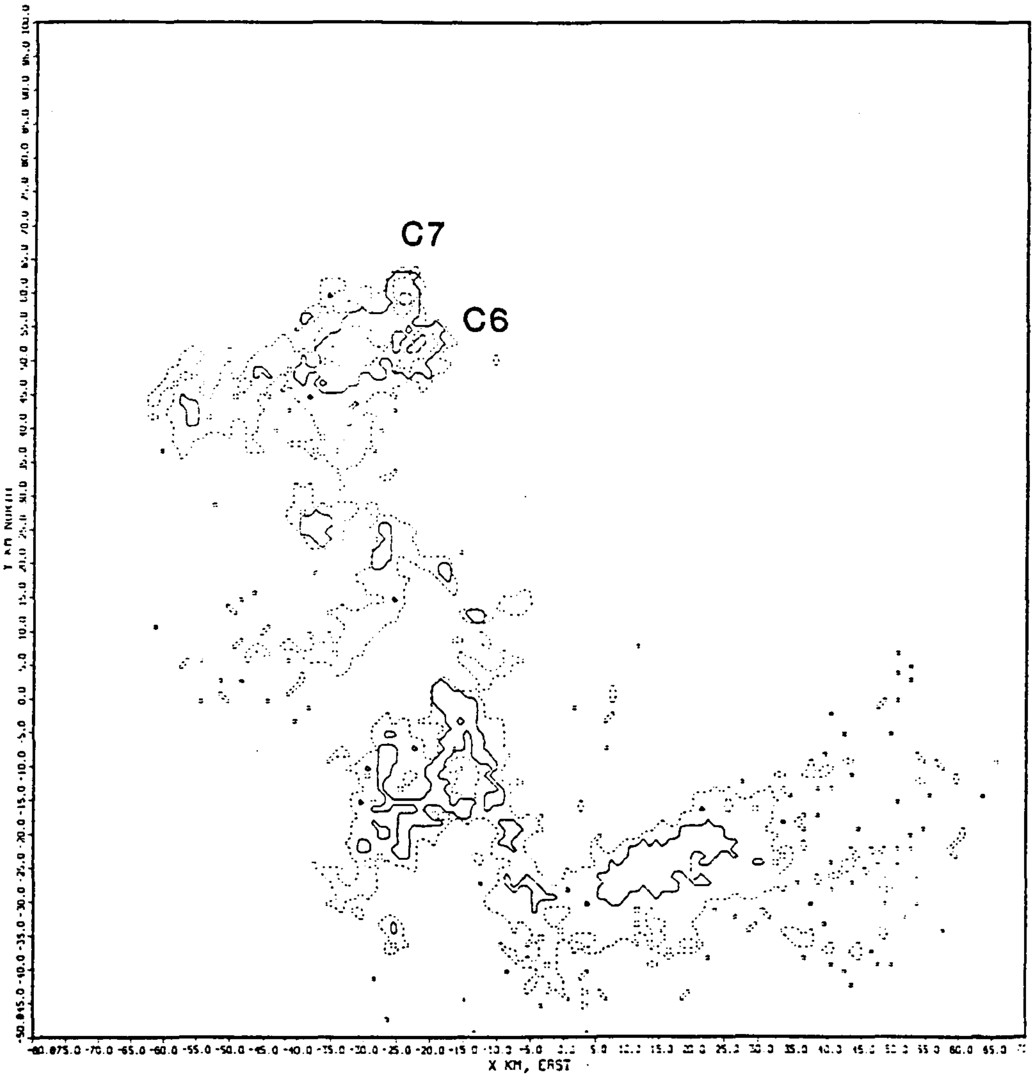

Figure 5.6g 17:30

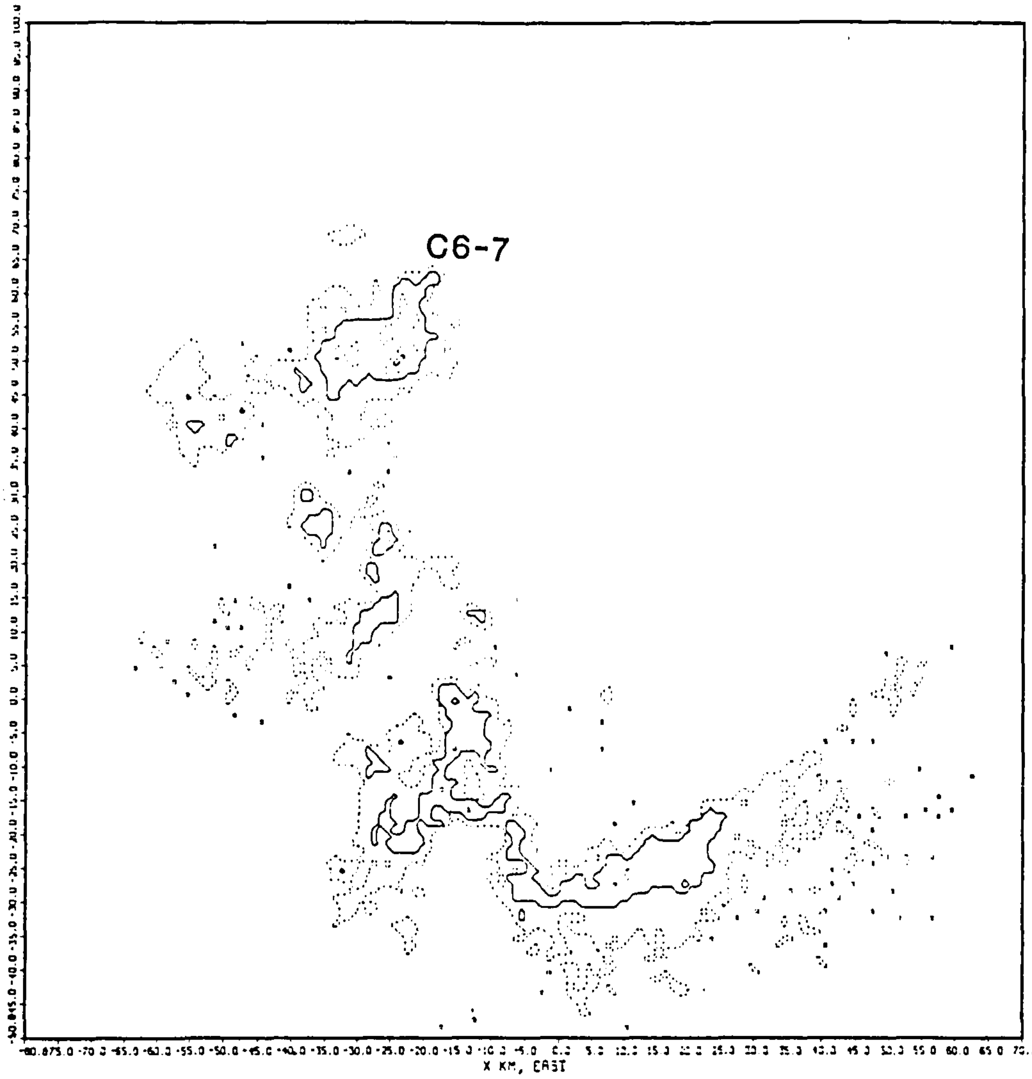

Figure 5.6h 17:35

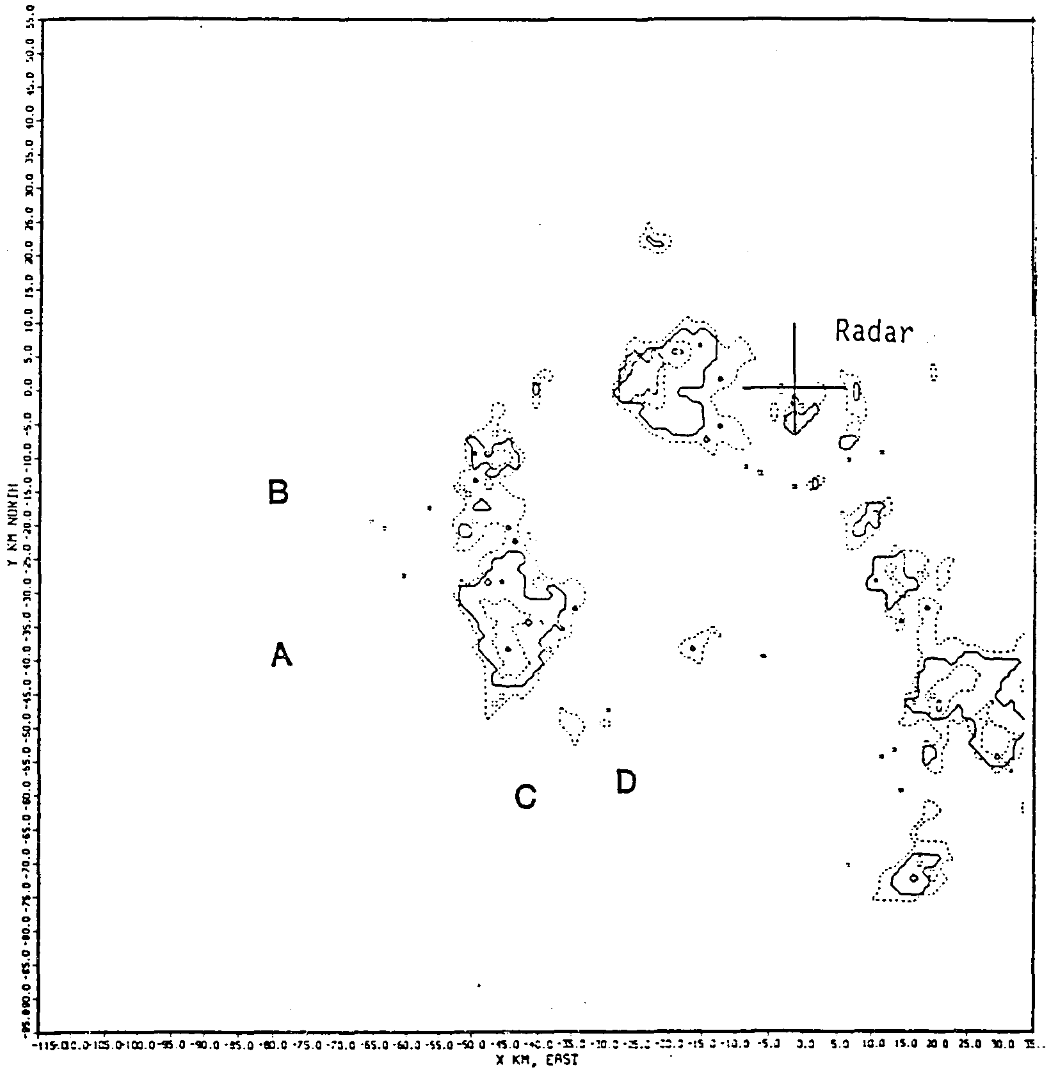

Figure 5.7 Radar PPI images for 16 November 1987 (antenna elevation 2°). Contours depict 23, 30, 40 and 50 dBZ intensities.
a) 15:41 SAST.

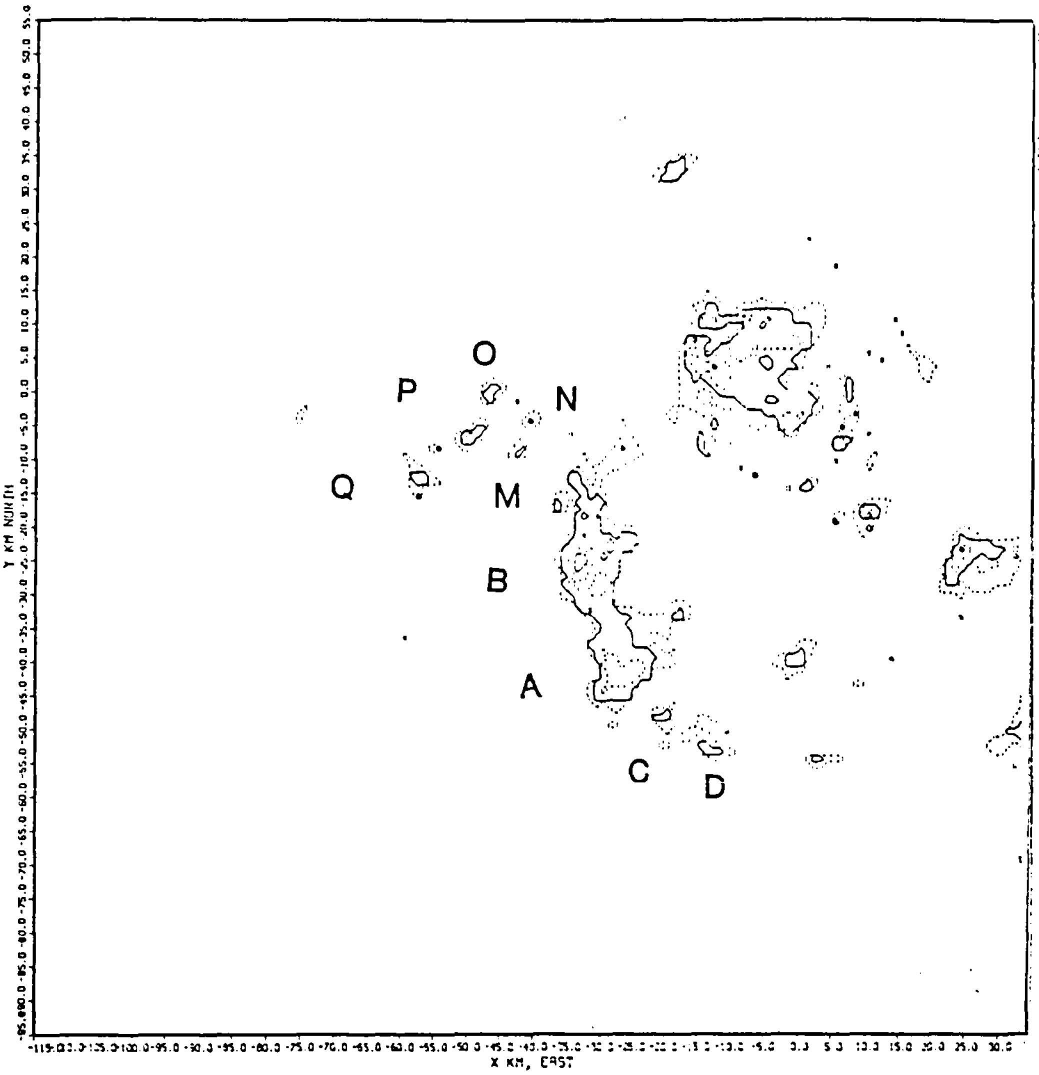

Figure 5.7b 16:00

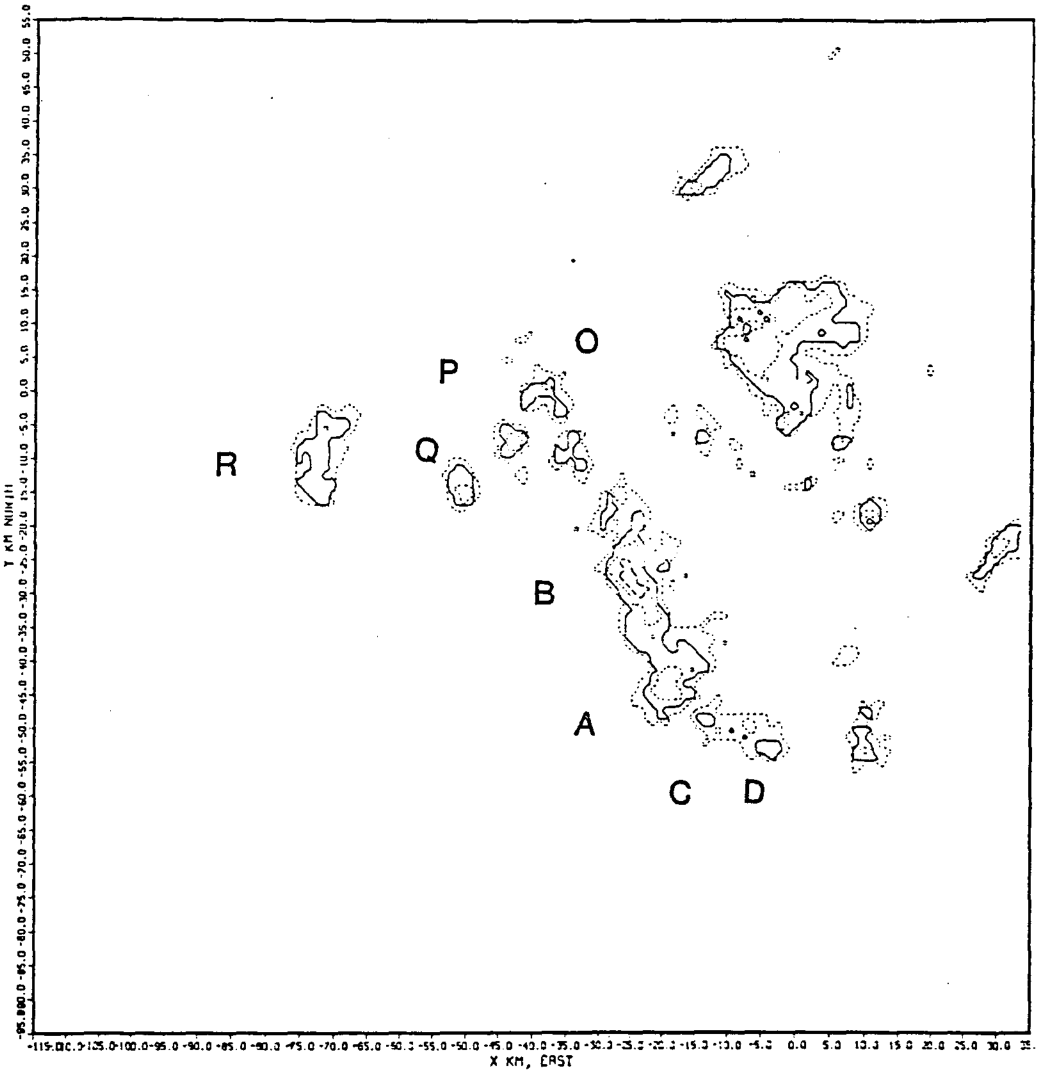

Figure 5.7c 16:08

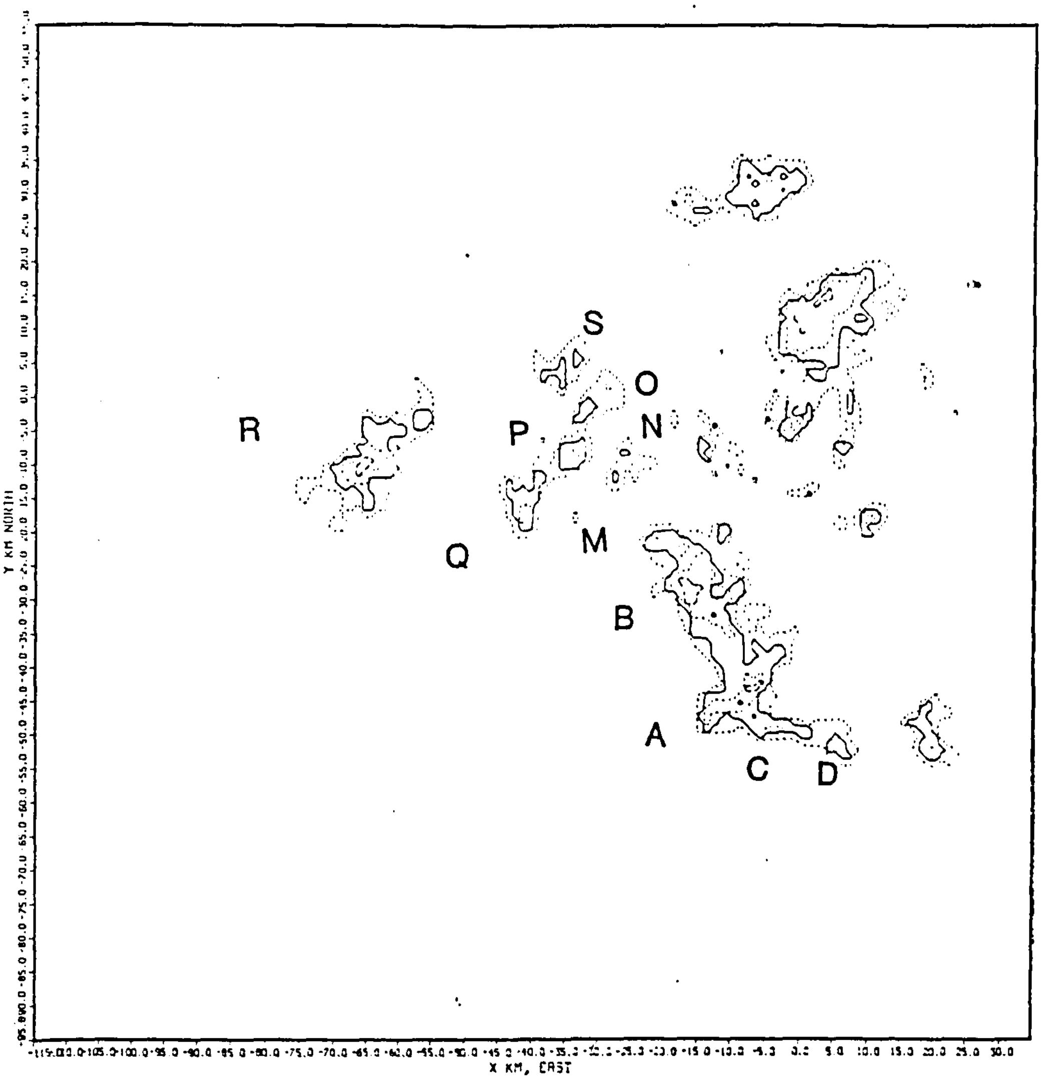

Figure 5.7d 16:18

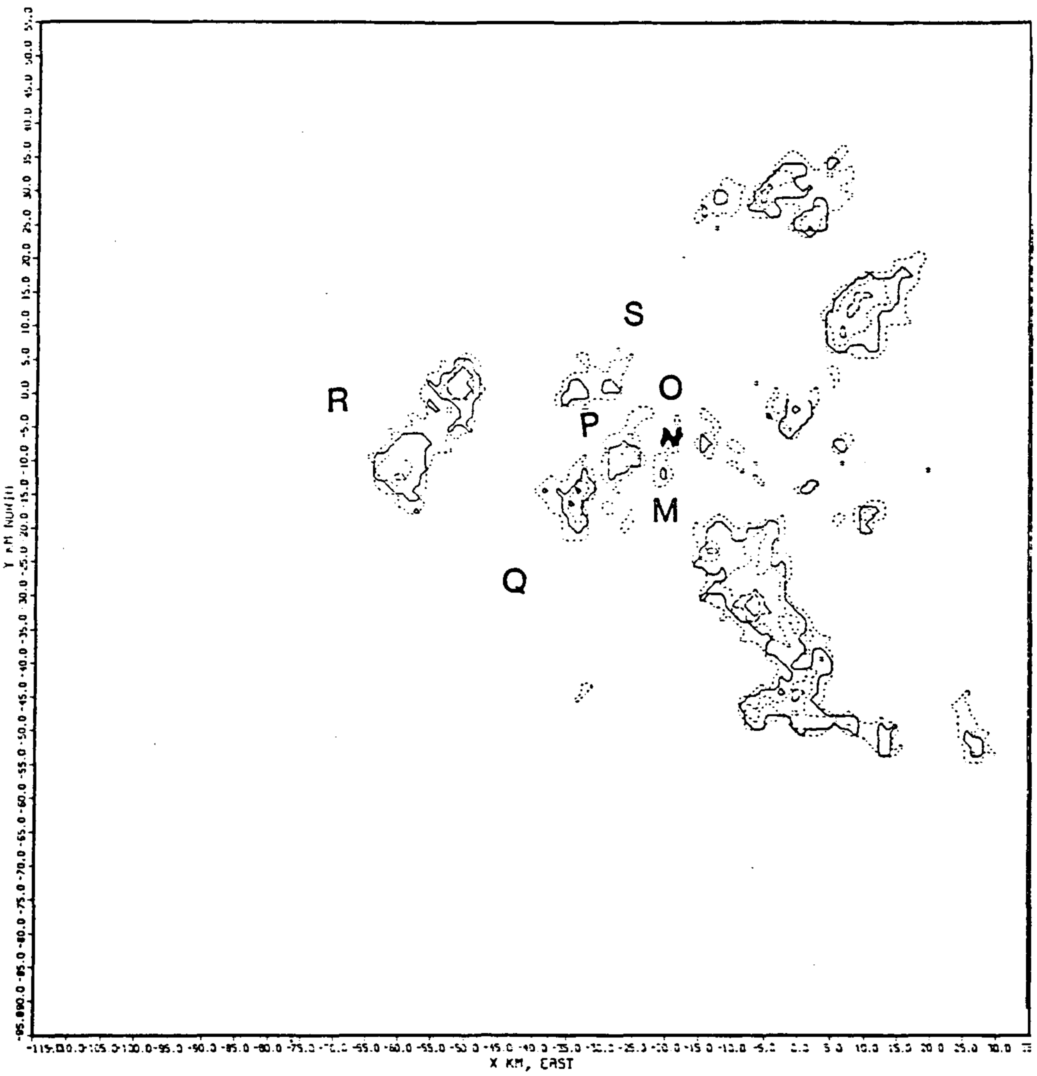

Figure 5.7e 16:26

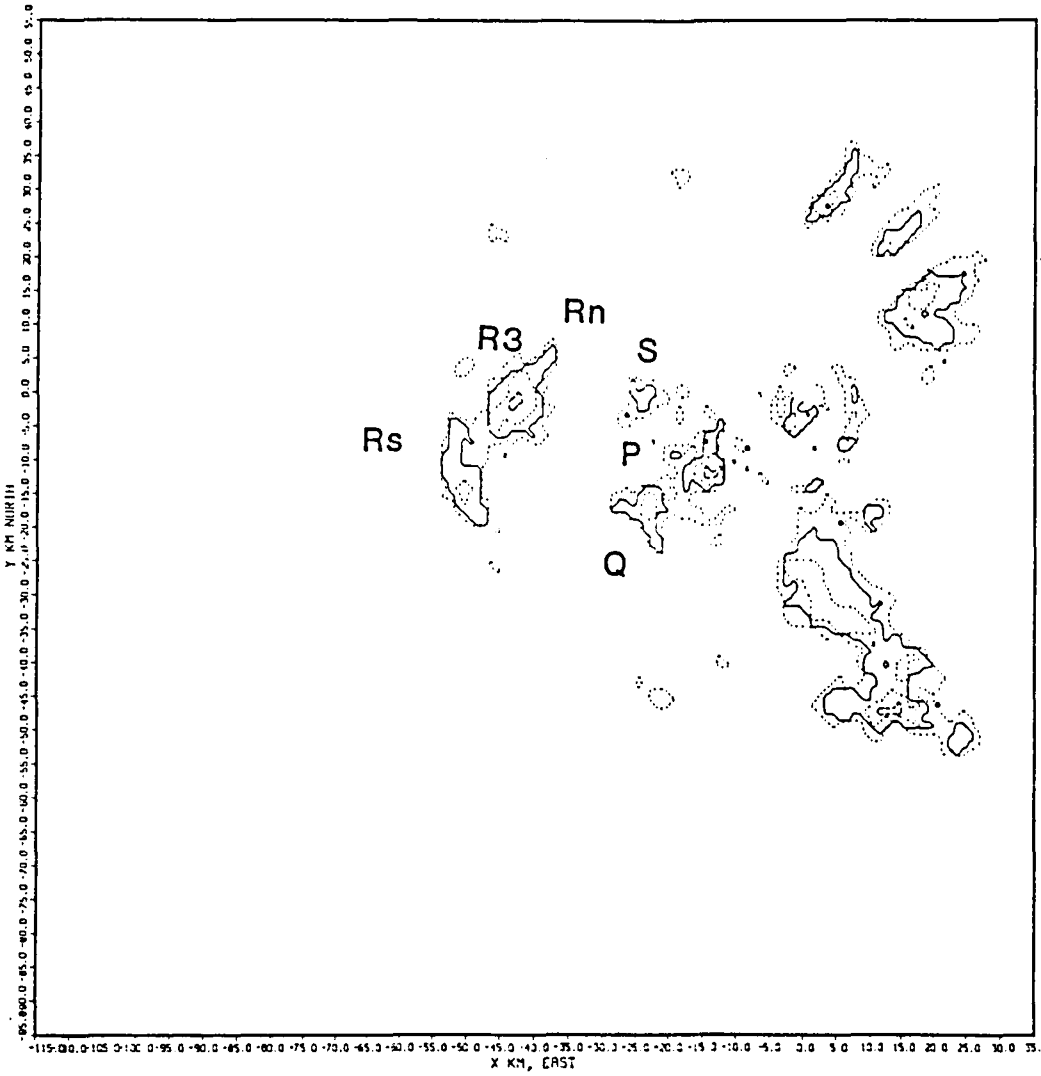

Figure 5.7f 16:39

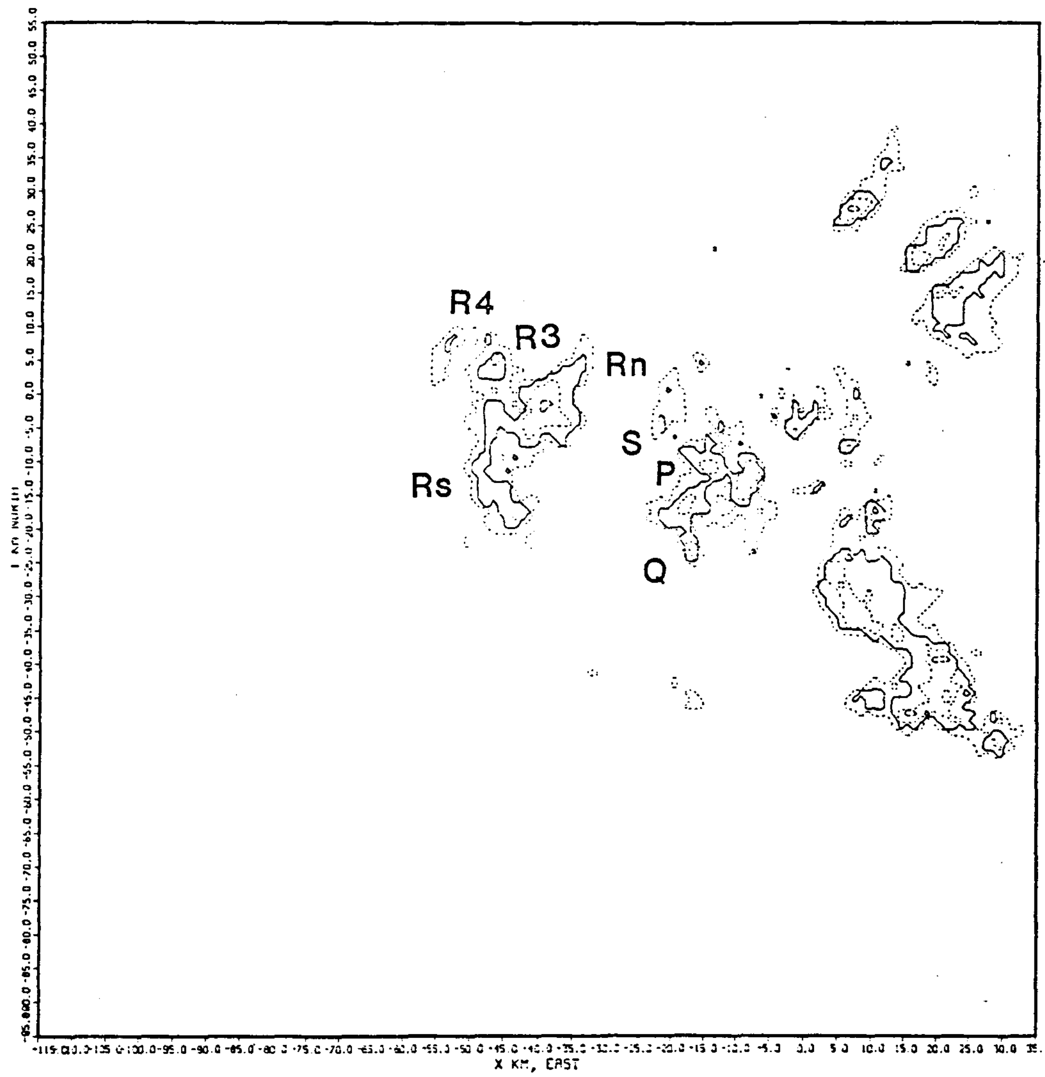

Figure 5.7g 16:43

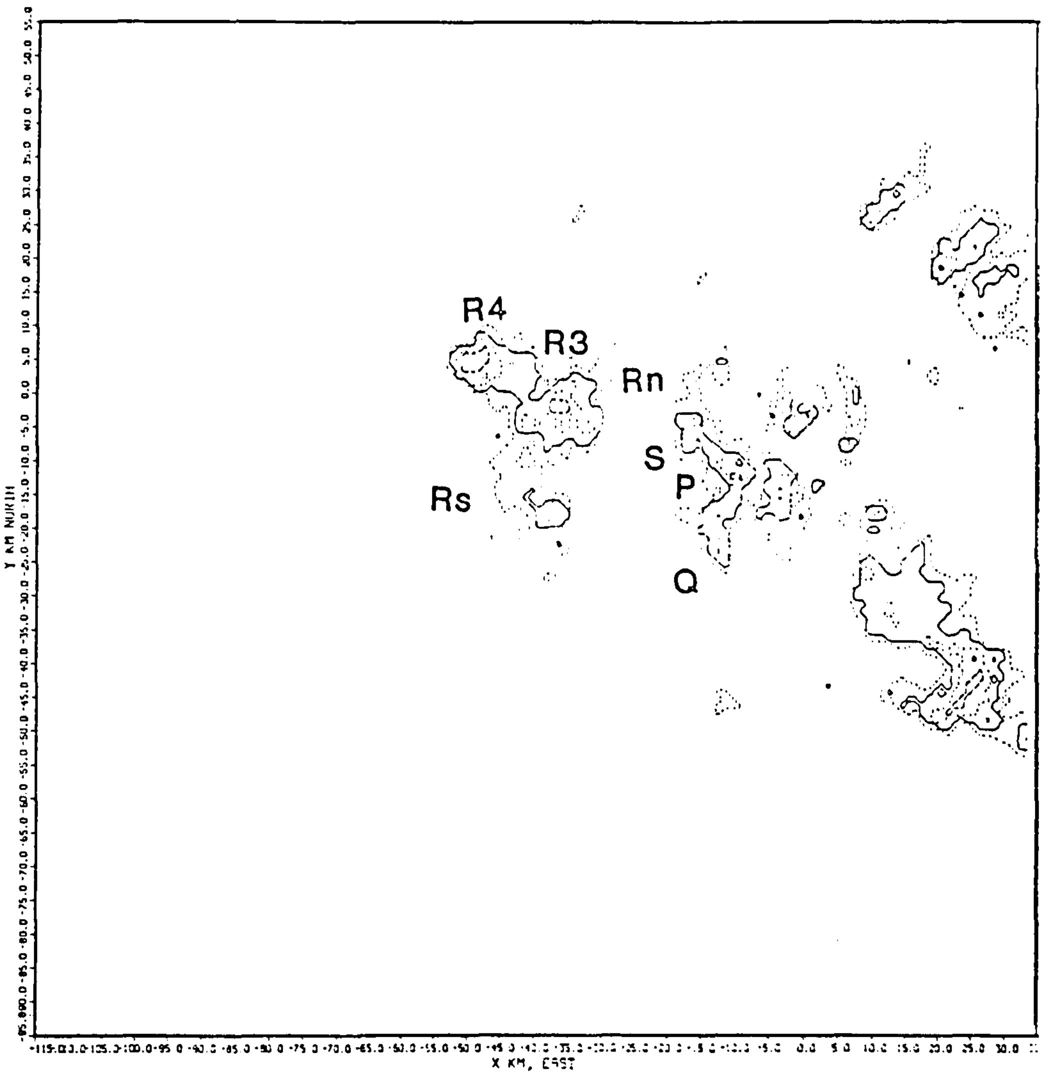

Figure 5.7h 16:49

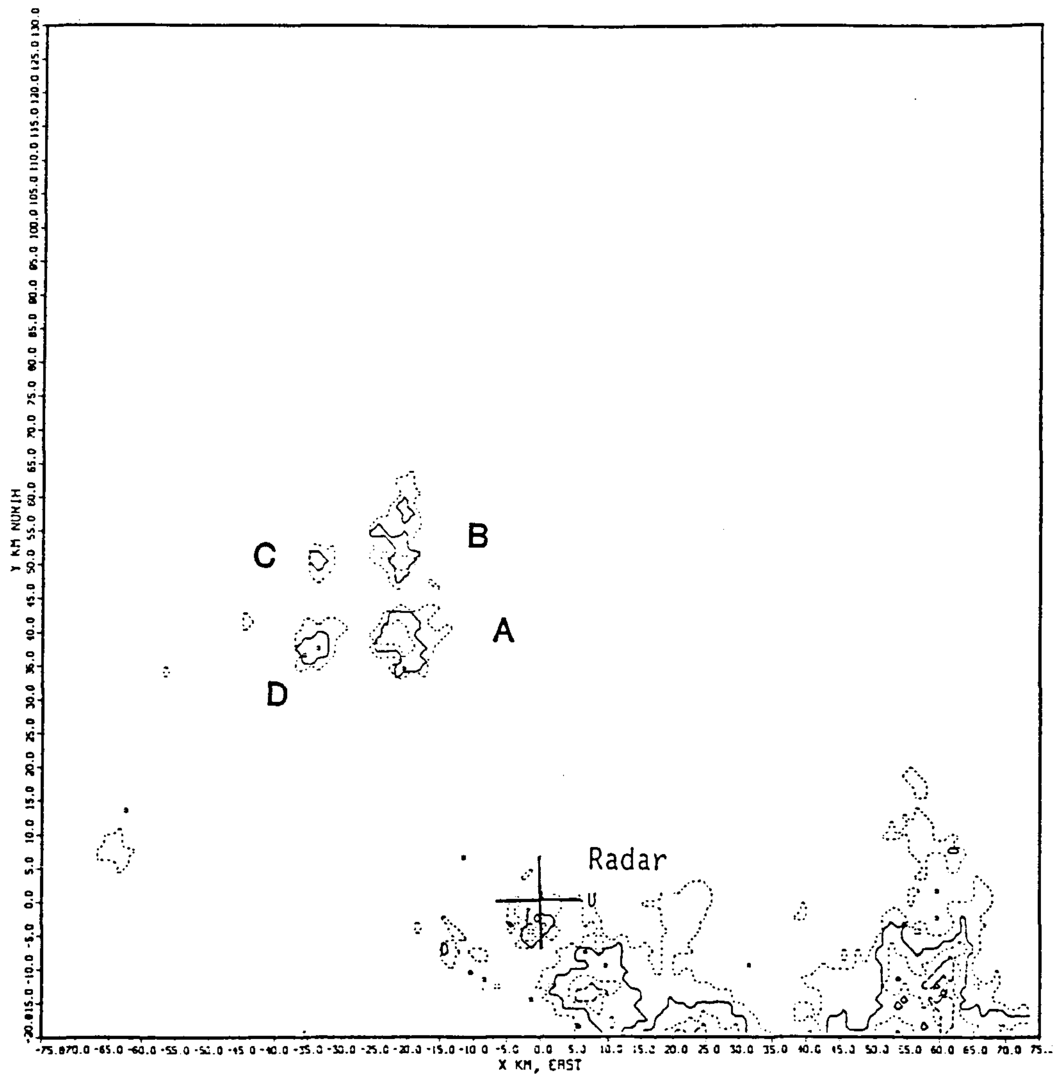

Figure 5.8 Radar PPI images for 2 December 1987 (antenna elevation 2°). Contours depict 23, 30, 40 and 50 dBZ intensities.
a) 15:54 SAST.

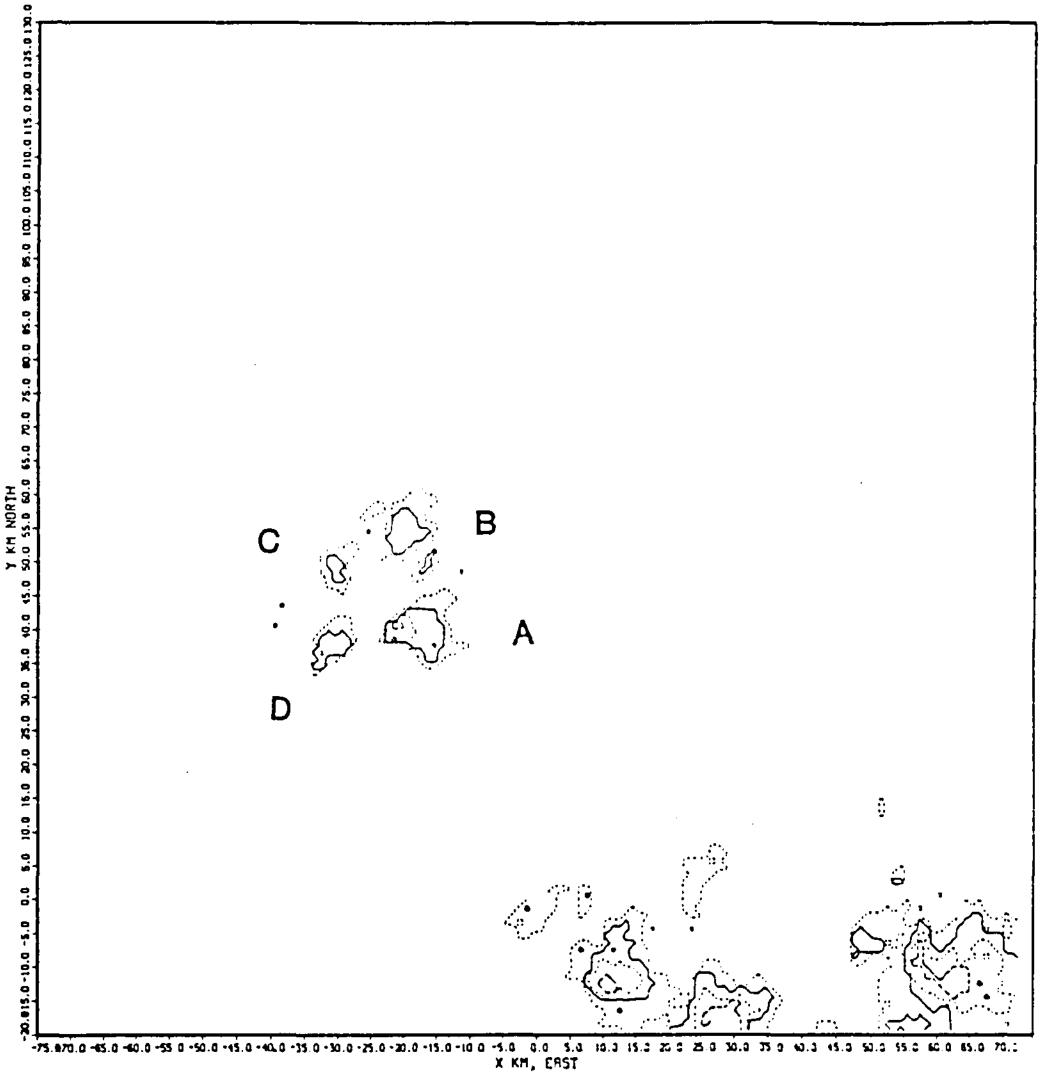

Figure 5.8b 16:01

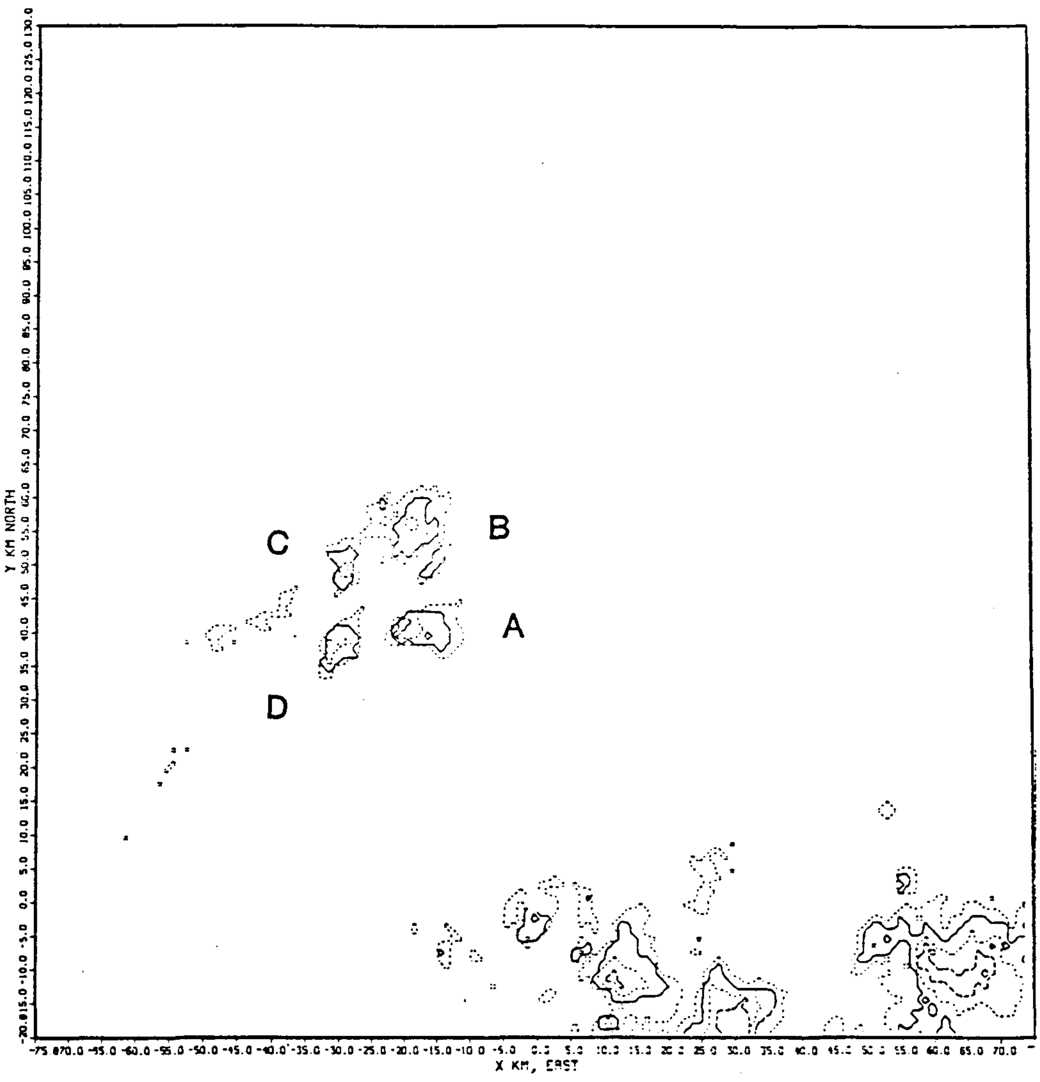

Figure 5.8c 16:04

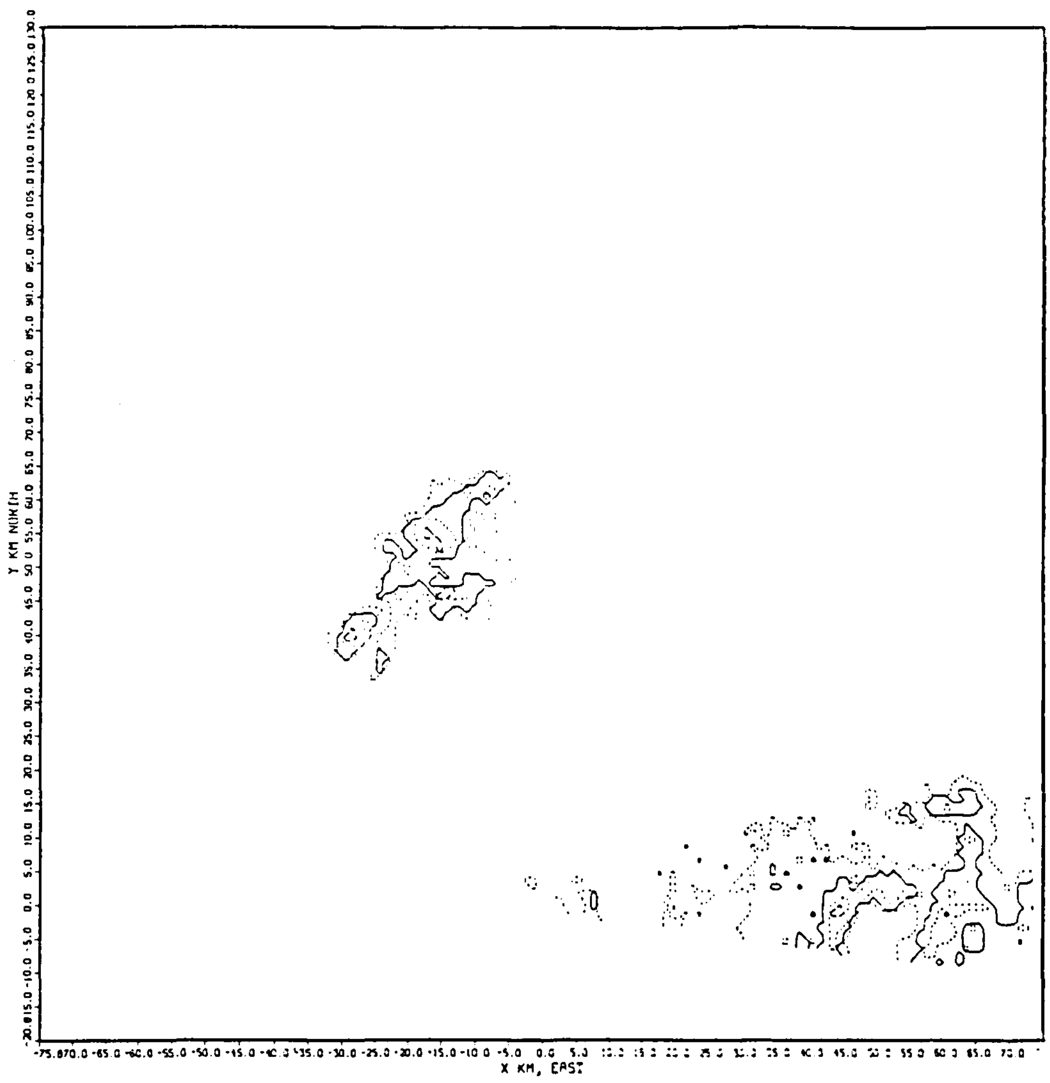

Figure 5.8d 16:20

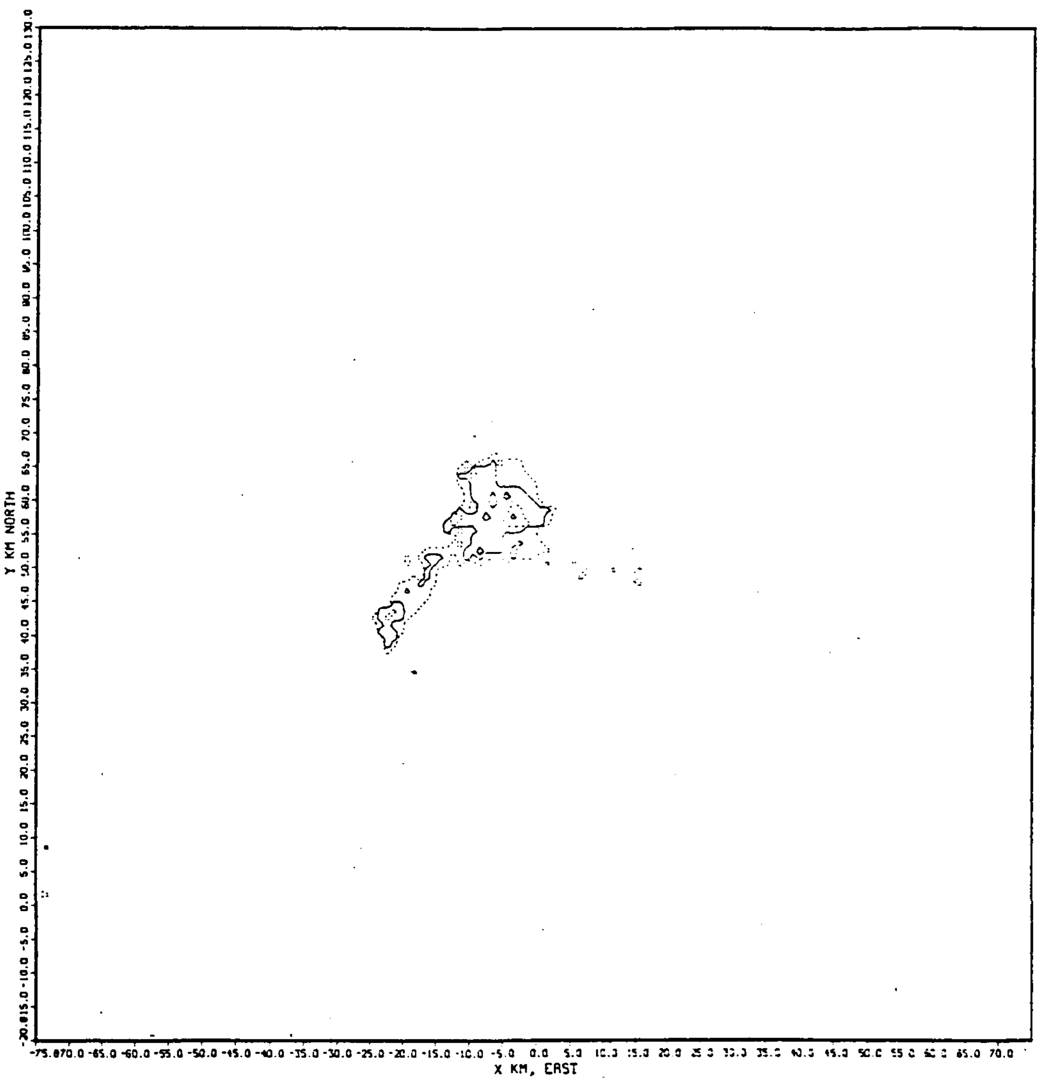

Figure 5.8e 16:39

6. EARLY STORM DEVELOPMENT AND CLOUD MERGERS: A SINGLE-DOPPLER RADAR CASE STUDY

Gerhard Held and Dawid J deV Swanepoel

The purpose of this study is to highlight the complexity of cell development and subsequent merging with either the parent storm (feeder-cloud mechanism) or with a quasi-independent cell (daughter-cell concept) by studying detailed radar reflectivity and radial air flow patterns in an isolated multicellular storm on the Transvaal Highveld.

The importance of cell mergers for successful cloud seeding experiments or operations, as well as for efficient cloud modelling has already been discussed in a lengthy introduction to the previous Section. Also, results from investigations of various cloud-merger mechanisms in other parts of the world have been dealt with in a brief literature study in Section 5. However, in order to put the findings of this detailed case study into proper perspective, it is thought that the most relevant research results from North America should be reiterated briefly.

Dennis *et al.*, (1970) described the feeder-cloud mechanism very neatly for a relatively large sample of hailstorms which were observed in western South Dakota. The term "feeder-cloud" was first used by Goyer *et al.* (1966) during a study of persistent hailstorms. According to Dennis *et al.* (1970) most of their case studies showed that new growth tended to be on the western or southwestern flank of storms, i.e. on the trailing edge of typical eastward-moving storms. The inflow region was often marked by lines of cumulus ("feeder") clouds which grew rapidly into new cells as they merged into the "mother storm". However, they also reported occasional cases where the inflow was on the southern or southeastern side of the storms, but in both cases the inflow region was on the equatorward side of the storms, which agrees well with findings from Highveld storms (Carte and Held, 1978), although in South Africa, the new development is more commonly found near the leading edge of the storms.

Cheng and Rogers (1988) also linked the occurrence of feeder clouds to the formation of hail. In their study of Alberta hailstorms, they found that feeder clouds formed approximately in a line parallel to the vertical ambient wind shear near cloud base level. The spacings between feeder clouds were almost equal and estimated to be 3 km and eventually manifested as distinct hail streak events at the surface. The persistent location of feeder clouds was speculated to be the result of interaction between the inflow and the low-level outflow of the storm.

The importance of the "weak-echo-region" (WER) was first stressed by Browning and Donaldson (1963). The existence of this echo-free region within the storm was attributed by them to adiabatic concentrations of water in the form of rather small cloud droplets which, owing to the high velocities within the core of the updraught, would not have sufficient time to attain radar-detectable sizes. Chisholm and Renick (1972) reported that combined radar, aircraft and photo observations have shown conclusively that cloud-filled WERs observed by radar are accompanied by extensive, smooth, uniform updraughts at cloud base of the order of 4 to 6 $m.s^{-1}$. Thus, the observation of a WER in a radar echo would indicate a major updraught into this particular storm.

The daughter-cell merging situation has been described by Chisholm and Renick (1972) for multicellular hailstorms occurring in Alberta. They found that new radar cells develop from cloud towers 3 to 5 km in diameter in a preferred region on the RH storm flank (i.e. equatorward side). The newly formed cell does not move into the storm complex, but rather grows rapidly and becomes the storm centre. Meanwhile, the original cell begins to decay while another new cell forms.

A slightly different concept of cell mergers was described recently by Westcott and Kennedy (1989) which is especially important for the current study because it relates to a non-severe thunderstorm. Two different cases of mergers are discussed, one of which is based on differential cell motion when one cell is decreasing in intensity while the other one is increasing. The second case is thought to be more relevant for our particular case study, because the development of a new cell between two existing cells produced the merger. Periods of significant intercell flow at 4 km coincided with the times when the mid-level reflectivity band linking the cell cores showed rapid intensification. Westcott and Kennedy (1989) suggested that the intercell flow is a result of radial outflow observed at heights above the maximum updraught level in the actively growing echoes. The strengthening of the reflectivity bridge may have been the result of both particle transfer and environmental modification due to radial outflow.

Before embarking on the detailed case study, it should be stressed that the above findings strictly apply to severe or hail-producing storms observed in the northern hemisphere. Only Westcott and Kennedy (1989) analysed a non-severe storm. Thus, significant deviations from those results might have to be expected, since Carte and Held (1978) already stressed the different behaviour pattern of thunderstorms occurring on the South African Highveld.

6.1 THE STORM IN GENERAL (27 April 1987)

The atmosphere over the interior, especially over the central, eastern and northern parts of the subcontinent was quite unstable (Figure 6.1) on 27 April 1987, with an upper level trough being undercut by a relatively strong High ridging in from the Indian Ocean across almost the entire subcontinent (Figure 6.2). Such conditions are very conducive for the development of thunderstorms on the Highveld.

A great variety of single and multicellular thunderstorms developed during the early afternoon in a band extending from about 120 km west of the radar to about 150 km east of it, with a width (north - south extent) of between 60 km in the west and 120 km in the east. The larger storm complexes occurred over the eastern Transvaal Highveld and the Witwatersrand region. The storm band as a whole moved slowly in a northerly direction.

An isolated, and for the Highveld, typical multicellular storm (Carte and Held, 1978) which had developed at 14:45 between 5 and 10 km southeast of the radar was chosen for the study. It moved at an average speed of 32 $km.h^{-1}$ to the northeast and consisted of a minimum of two cells at any time during its life cycle of two hours, with new cells developing on the left flank, while the storm decayed on the right flank (Figure 6.3). Individual cells moved at speeds of up to 40 $km.h^{-1}$. The storm reached maximum intensity between 15:24 and 15:38. Echo tops reached up to 12 km AGL and maximum reflectivities were 60 to 63,3 dBZ. At 15:39, radial velocities of 21 $m.s^{-1}$ were observed at 9 km AGL (PPI elevation 18°) in the updraught core. Six minutes later grape-size hail fell on the ground at which time the reflectivity near ground level increased to 66,6 dBZ.

For the purpose of studying the very early stages of storm development and the related radial velocity field, emphasis was put on the best resolution of the lower range of reflectivities. Therefore, all cross-sections depicting merger situations are contoured for 23,3, 30, 33,3, 36,6 and 40 dBZ, since a maximum of five different contours can be plotted at any one time. Three separate plots were made of every PPI in the volume scan in order to resolve all 15 levels from 23,3 to $\geq$60 dBZ at 3,3 dBZ intervals. However, due to a capacity problem of the VM mainframe computer, reflectivity contours from 50 dBZ upwards may have been plotted incorrectly at this stage (the problem will be rectified as soon as possible), but actual values can be verified by means of B-scans. The radial velocity field has not been corrected for storm movement, hence no actual speeds are quoted from the plots. The maximum unambiguous velocity is 25 $m.s^{-1}$. The length of the arrow indicating the direction and magnitude of the radial velocity at a particular point is proportional to the speed (see Figure 6.4: the arrow shown in the key corresponds to 25 $m.s^{-1}$; an arrow of half this length would thus represent 12,5 $m.s^{-1}$).

A total of approximately 420 PPI plots and 600 vertical cross-sections were generated for the storm period from 14:43 to 15:31 during which merger situations were studied.

6.2 EXAMPLE OF A DAUGHTER-CELL MERGING SITUATION

The first volume scan considered in this analysis was from 14:43:04 to 14:45:29, covering elevation angles between 2° and 22°. The radial air flow was almost exclusively towards the radar. No signs of new cell development in the vicinity of the storm could be found on any of the PPIs. However, clear evidence of a new cell is seen on the 18° PPI of the subsequent volume scan. The vertical cross-section through the storm shows that the cell had obviously developed very rapidly between 5 and 8 km AGL and 3-4 km to the northeast of the mature cell, with a maximum reflectivity of 33,3 dBZ at 6,4 km (Figure 6.4). The radial air flow is noteworthy in so far as it was light to moderate and away from the radar in the new cell (18°), whereas it was in the opposing direction in the old storm.

During the next volume scan, new development can also be seen just east of the mature cell, but being part of it and only in the lower levels (up to 8°). The radial flow in the mature cell is still towards the radar, while it is outwards in both regions of development. The new cell had grown significantly and also intensified as can be seen from the set of vertical cross-sections in Figure 6.5, which are parallel to each other and spaced at 1 km intervals. A slight bridging between the two cells can be seen above 6 km AGL at very low reflectivity levels (<26,6 dBZ). Figure 6.6 shows that the new cell had further grown and intensified and also moved away from the older cell, although still linked at low reflectivity aloft. It's precipitation still had not reached ground level. The radial air flow was increasing significantly with height from 8° to 18° elevation, indicating an updraught tilted away from the old cell. Precipitation from the new cell reached the ground at 14:55 (Figure 6.7). Airflow at the 2° elevation indicated strong convergence in the region of the new cell, while the radial component of the air flow at the old cell was now pointing away from the radar. Aloft, it was diverging in the old cell (5°-18° elevation), but in the new cell, radial flow was away from the radar, and still strongly increasing in speed with height, but slightly decreasing above 10 km AGL. It is noteworthy that the link between the old and the new cell had intensified slightly (26,6 dBZ) in some areas as can be seen from the 18° PPI and the cross-sections.

The volume scan commencing at 14:57:59 (Figure 6.8a) illustrates very nicely how two mature cells merge into one storm complex by expansion and intensification of radar reflectivities aloft. The 2° PPI indicates a

3 km separation of the 23,3° dBZ contour between the cells (5 km for 30 dBZ). The centres of the echo cores are approximately 11 km apart. The maximum reflectivity reached just more than 50 dBZ in the old cell, but was slightly above 53,3 dBZ in the new cell and was in both cases in the lower part of the echo (3-4 km AGL). It is noteworthy, that the 23,3 dBZ contours were just fusing on the 8° PPI with a predominantly outward air flow, except in the region where the bridging takes place. The 12° PPI shows that even the 30 dBZ contour has now merged. The air flow was still predominantly outwards, but a small convergence zone can be seen on the eastern flank of the new cell indicative of strong entrainment into the storm (the actual speeds would be much bigger since the cell was moving in an eastward direction and thus its speed would have to be *added* to the opposing radial component). A similar convergence was also observed on the 5° PPI. The 18° PPI showed a totally merged single cell with strong radially outward flow except in the centre where a small convergence area is observed. This volume scan is best documented by sets of west - east and north - south oriented, parallel vertical cross-sections (Figures 6.8b,c). The cross-section from southwest to northeast through the slowly collapsing old cell, the linking "accumulation zone" aloft and the new cell is probably the most characteristic picture of what is actually happening. Since this section is almost tangential, no inferences about the air flow in this plane can be made on the basis of the radial velocity components. However, it is quite safe to assume that a reasonably strong updraught is required to suspend the large volume of rainwater between about 4 and 6,5 km AGL between the two cells. This could be indicative of a possible mechanism how the old cell becomes entrained into the new one.

The next volume scan started at about 15:01 (Figure 6.9a). The 2° elevation PPI did not reveal any significant features, but the 23,3 dBZ contours of the two cells were now only 1,5 km apart (30 dBZ - 3 km). Strong convergence can be seen at the eastern edge of the old cell, while the new cell is characterised by radial outwards flow, except on the northeastern flank where there is an indication of light convergence. On the 5° PPI (not shown) the 23,3 dBZ contour is already merged between the two cells and the 30 dBZ is only 2 km apart; the radial flow pattern is mostly away from the radar. On the 8° PPI the 30 dBZ is still not joined, but the intensity of the new cell is already ≥50 dBZ while the old cell gradually decreases (maximum about 33,3 dBZ). The radial flow is still mostly outwards, except in the merging zone where there is a bit of convergence (southern part) as well as divergence (northern part). The next PPI at 12° shows only one cell with significant convergence on the southern flank and some divergence in the centre. In general, the radial speeds are light to moderate. The 18° PPI is unfortunately incomplete (not shown), but does indicate a strong shear of the radial component in the southern half of the new cell. The 25° PPI shows that the new cell (maximum 36,6 dBZ) and another nearby storm are coming quite close to each other. In both cases, one can see diverging radial air flow in the most intense cores. Strong flow towards the northern flank of the left storm can be observed, but this will be discussed in the next section on the first echo study. The last scan was at 35° elevation (not shown) and basically indicates a general outward flow from the left storm, especially strong on the northern flank. Figure 6.9b shows west - east cross-sections at one 1 km spacing (the base lines are indicated in Figure 6.9a). Strong convergence can be seen on the 8° and 12° PPI above an area which appears echo-free on the lower elevations (Figure 6.9a). The west - east cross-sections show very clearly how this then leads to a merger aloft. South - north sections through the same complexes (Figure 6.9b) show the development of first echoes some 6 km north of the older cells. Their history, however, will be discussed in the next section. The total merging of the original old and new cells is depicted in two southwest - northeast sections (right hand side of Figure 6.9c). The narrowing of the gap below the accumulated precipitation aloft can be seen very clearly. The old cell is now almost depleted. This process of final merging continues during the next volume scan which is not shown here. The final act can be seen in the scan commencing at 15:06 (Figure 6.10a) where the old cell is basically gone. Only a relatively insignificant 30 dBZ contour on the 2° PPI indicates where its remnant is. There is nothing left of it on the 5° PPI. The air flow in this region is very weak and generally away from the radar. All its former energy has obviously been absorbed into the new cell through the merging process aloft. Vertical sections 2 and 3 in Figure 6.10c depict the storm after the merging had been complete.

6.3 EXAMPLE OF A FEEDER-CELL MERGING SITUATION

The first time that an early echo near the multicellular storm, which was chosen as study object, was detected during the volume scan commencing at about 14:58 (Figure 6.8a). On the 12° PPI, only an area of about 1 x 1 km was covered by FE1 at that stage, but strong radial flow outwards was already noticed. It was about 5 km north of the parent echo. It is also noteworthy that the Doppler velocities indicated the presence of the echo on the 8° PPI, while the reflectivity was obviously too low and too patchy to produce a contoured echo. However, it can be seen in the B-scan as a very weak echo.

At about 15:01 (Figure 6.9a) FE1 can now be seen on the 5° PPI scan covering an area of about 2 x 1 km some 4-5 km north of other echoes and in an area of strong convergence, as one would expect. It should be pointed out that the radial air flow pattern on the 2° PPI was rather confused. Another first echo, FE2, was observed on the 8° PPI, about 6 km east of FE1, covering an area of 1 x 1 km and displaying strong outward flow. FE1 was approximately 3 x 1,5 km large with light inward flow. Both echoes were still observed on the 12° PPI, FE1 being 1 x 1 km with weak outward flow and FE2 2 x 3 km with divergence on the southeastern flank. The position of both echoes (FE1 and FE2) relative to the mother storm can be seen nicely in cross-sections 4 and 8, respectively, in Figure 6.9c.

The following volume scan (15:03:33 to 15:05:41) shows FE1 and FE2 in almost the same positions as in the previous scans. Only FE2 has slightly grown in size and intensified to 27 dBZ (8° PPI). However, a new cell, FE3, appeared between the original first echoes, extending from 3 to 6 km AGL, with a very small core of $\geq$27 dBZ. The radial velocities indicated an outward flow at all levels, mostly very light, except in the vicinity of the small cores of FE2 and FE3 where it was slightly stronger. It can be speculated that these first echoes are induced by a downdraught flowing from the mother storm in a northerly direction.

The next volume scan (15:06:22 to 15:08:16) depicted in Figure 6.10 seems to indicate fierce competition amongst the various first echoes, and the first one to have become radar-detectable need not necessarily be the one which has better chances to develop. FE1 has by now totally disappeared, while FE2 has grown significantly to about 4 x 3 km (5° PPI) with the 26,6 dBZ contour extending right down to ground level (Figure 6.10a). The air flow was light to moderate away from the radar at all levels. FE3 has also grown and intensified, but more at higher levels (12° and 18°, Figure 6.10b) than FE2, which can also be seen in the vertical sections in Figure 6.10c (cross-sections 7 and 5). The radial air flow in FE3 was mostly towards the radar and fairly strong up to 12° elevation. This led to a strong shear zone between FE2 and FE3 which can be seen on the 5° radial flow pattern. Also noteworthy is the shear on the northern flank of the mother storm, clearly visible on the 8° and 12° PPI. The 18° elevation scan is of particular interest because it shows the echo core of FE3 (30 dBZ between 5 and 6 km AGL; also see cross-section 7 in Figure 6.10c) and a strong outward flow in the radial velocity field. This created a very strong shear of the radial air flow with height between the 12° and 18° scans. FE3 does not appear on the 25° PPI any more; however, there is still a strong shear zone along the northern flank of the mother storm, extending up to 35° elevation (>10 km AGL).

Another interesting feature of this volume scan is brought to light in cross-sections 17 and 18 (Figure 6.10c) where the sudden development of a new cell in the immediate vicinity of an existing storm becomes evident. This storm, designated B, is east of the previously described mother storm (see cross-section 14). There was no sign in the previous volume scan of new development in this region. The core is centred around 8 km AGL and already has a reflectivity of 37 dBZ. A relatively strong convergence of radial velocities in this region is evident on the 12° PPI. Strong radial outflow can be seen on the 18° flow pattern, most likely being indicative of a northeastwards tilted updraught.

It had already been mentioned above that FE1 had ceased to exist, and that FE3 appears to have the better survival chances. This is confirmed by the observations of the next volume scan, starting at 15:09. FE2 only appears on the lowest two PPIs (2° and 5°) and has, in fact, already merged with FE3 (Figure 6.11a, 2° PPI). The radial air flow in both echoes is relatively weak and outwards, but its strength increases rapidly with height in FE3 and reaches a maximum where the reflectivity also indicates the echo core, viz. 12° and 18° elevation (>30 dBZ). As can be seen from the vertical sections in Figure 6.11b, the mother echo is strongly tilted towards the north (sections 6 to 8; left side) and northeast (sections 6 and 7; right side). Also shown in these sections is the beginning of a weak-echo-region (WER) on the northern flank of the mother storm, where FE3 tends to merge into the anvil (cross-section 9).

The radial air flow pattern in the mother storm (A) is quite noteworthy. Although it is generally outwards from the radar and moderate on all scans, the variation in strength along the northwestern flank is remarkable. A very strong component towards northeast can be seen on the lowest two scans (2° and 5°, Figure 6.11a) most likely indicating a strong downdraught. Above it, the radial velocities decrease significantly (8° and 12° elevation), but thereafter they increase rapidly with height (18° to 35°, Figure 6.11a), suggesting an overlying, strong updraught blowing into the anvil on the northern flank of the storm and capable of supporting large quantities of precipitation in this region. This would also explain the strong tilt of the northern echo depicted in Figure 6.11b.

Another interesting feature of this volume scan is the rapid entrainment of the newly developed cell, indicated in the previous volume scan, into storm B as shown in the south - north section no. 18 in Figure 6.11b. The radial velocities reached a maximum on the 18° PPI with a very strong eastward component in the central and southern portion of the echo.

The next volume scan commenced at 15:11:43. It is noteworthy that already on the 2° PPI the 23,3 dBZ contour of FE3 is shown to be linked to the mother storm (Figure 6.12a). Although FE3 can be identified as a separate entity on all scans, the vertical sections in Figure 6.12b indicate the already beginning entrainment into the mother storm at several levels. FE3 reached maximum reflectivity (37 dBZ) between 4 and 5 km AGL (see section 9 in Figure 6.12b). This section also indicates rapid intensification and expansion of the anvil on the northern flank of the mother storm. The radial air flow pattern in FE3 is still similar to the one in the previous volume scan. Noteworthy, however, are the extremely strong radial velocities in the mother storm on the 35° PPI, indicative of major developments aloft. The top of the storm is approximately 12 km AGL. The weak echo region underneath the vigorously growing anvil is clearly visible in the west-southwest - east-northeast section (no. 7) in Figure 6.12b. According to Browning and Donaldson (1963) and Chisholm and Renick (1972) a strong updraught can be anticipated in this region.

It is interesting to note that storms A and B are rather close together and linked by lower-intensity reflectivity-contours (generally 26,6 dBZ up to 12° elevation and 30 dBZ on 18° PPI). However, they do not appear to interfere with each other or show signs of a possible merger. Two cores of eastwards pointing radial velocity maxima in storm B can be distinguished on the 18° PPI (Figure 6.12a), resulting in a relatively strong tilt of its echo core into the same direction. The development aloft on the northern flank of storm B can still be distinguished clearly (sections 19 to 21 in Figure 6.12b). It is characterised by a light, converging air flow pattern on the 12° and 18° scans (Figure 6.12a).

FE3 is still steadily growing, both in size and intensity as shown in the following volume scan (15:14:23 to 15:16:43). It can be seen from the 2° PPI that FE3 now is about 5 km in diameter and the 30 dBZ contour has reached ground level (Figure 6.13a). The air flow is very weak away from the radar. The 5° PPI is extremely interesting in this case because of the air flow pattern, which indicates convergence where FE3 is progressively being entrained or merged with its mother echo. Also, the reflectivity has exceeded 36,6 dBZ which is reaching up to the 35° PPI (Figure 6.13a). The next scan at 8° elevation shows that the radial air flow was outward again and quite weak. Only from 18° upwards did the air flow again become stronger, reaching maximum radial velocities towards northeast on the 35° PPI. This is obviously the same updraught core already mentioned in the discussion of the previous volume scan (see north - south section no. 7 in Figure 6.13b). The west-southwest - east-northeast section discussed earlier has not changed much and still indicates a strong tilt of the echo towards northeast and an underlying

WER. The rapidly northwards expanding and intensifying anvil of storm A can also be seen in the west - east cross-sections 3 to 7. Storm B also has a significant anvil on its northern flank. The cell which developed aloft on its northern boundary has now been completely entrained in the main storm (B) and is hardly noticeable in the south - north section 23 in Figure 6.13b.

FE3 is continuing to expand, especially in the mid-levels (5° and 8° elevation) with the 36,6 dBZ contour extending to ground level as shown by the volume scan of 15:17. Maximum reflectivities are increasing steadily, viz. 43,3 dBZ on 5° PPI and 40 dBZ on 8°. From 12° elevation upwards FE3 becomes more and more incorporated into its mother echo (Figure 6.14a). The radial air flow pattern of FE3 is relatively weak and outwards directed in all levels. The convergence zone has not been detected in these scans. The mother storm (A) has moderate outwards directed radial air flow at all levels. Vertical cross-sections from west to east at 2 km intervals (Figure 6.14b) show the core of FE3 (cross-section 3), and going southwards, they also show the anvils of storms A and B which have intensified to such an extent that these storms have actually merged aloft (sections 7 to 11). The radial air flow in this region was quite strong towards the east. The section 8 (southwest - northeast) still indicates a very strong tilt of storm A towards northeast with an underlying WER. South - north sections (11A and 12A) illustrate the merging of FE3 into its mother echo.

The next volume scan (15:19:35 to 15:21:33) does not differ significantly from the previous one in both the reflectivity and air flow patterns, and is therefore not discussed in detail here. The tilt and the strongly developed anvil remain a very characteristic feature of storm A and FE3. Although the storm complex as a whole is steadily moving towards northeast, the relative positions of A and FE3 remain more or less the same throughout the intensification process. Very much the same applies to the subsequent volume scan (15:22:17 to 15:24:13). However, there are definite indications that FE3 and storm A have reached the early stages of dissipation. This is manifested in an increase of reflectivity near ground level (at 2° FE3 has 40-43 dBZ) while the height of the 26,6 dBZ contour of FE3 has dropped to below 4 km AGL. This is illustrated in

Figure 6.15a (2° PPI) and Figure 6.15b (section 13, south - north). The radial velocities have dropped significantly with the exception of two regions indicated on the 18° PPI. Three vertical sections from southwest - northeast and one from west to east through these regions show clearly that these are areas where development aloft is still very active, thus regenerating the storm complex while the older cells are collapsing. The new development aloft appears to be generated by the mechanism described in the previous Section (Chapter 6.2).

This gradual process of decay and regeneration between or near existing storms continues during the next three volume scans until the old storms and cells have virtually disappeared or were replaced by new ones by 15:30. As discussed in section 6.1, the storm complex continued to move in a northeasterly direction for another 75 minutes.

6.4 CONCLUSIONS

The detailed, three-dimensional case study of an isolated, and for the Highveld, typical multicellular storm illustrates very clearly the various mechanisms of cloud merging, cell development and regeneration, which sustain such storms for hours while they are traversing the Highveld. Since this case study is based on observations made before the 1989/90 season, the resolution of the reflectivity was only in steps of 3,3 dB with a lower threshold of 23,3 dBZ. (The more recent observations from the past two seasons could be resolved to fractions of a dB, but time was insufficient to incorporate such data.) However, in view of the results achieved in this Section, it is thought that the resolution of the reflectivity factor was sufficient for an initial investigation. Radial velocities of the air flow inside the storm were also carefully analysed and, whenever possible, interpreted in terms of updraughts or downdraughts.

Two main mechanisms were identified:

i) Daughter-cell merging situation.

A new cell had developed rapidly between 5 and 8 km AGL some 3-4 km northeast of a mature cell. As the new cell grew and intensified, the radial air flow was increasing significantly, indicating an updraught tilted away from the old cell. The two cells then merged into one complex by rapid expansion and intensification within a period of about 10 minutes. Seven minutes later, the original cell had been totally incorporated into the new structure and could no longer be identified.

ii) Feeder-cell merging situation.
Three very small cells of 1-2 km in diameter have been observed forming some 4-5 km north of mature echoes in an area of strong convergence within a period of about five minutes. It is noteworthy that the cell which had formed later than and between the existing two was the one to have developed to full maturity, by entraining the flanking cells quite rapidly. This process took less than six minutes. Once this cell had established itself as the survivor, it grew rapidly in height, area and intensity and moved together with its mother cell for a period of about 18 minutes. It eventually merged into the mother storm, but always remained identifiable during its whole life cycle of less than 25 minutes.

A *slightly different mechanism* of a feeder-cell merging situation was observed in parallel to the above case. A new cell had developed aloft on the perimeter of an existing storm rapidly growing in intensity and volume. Within a matter of five to seven minutes it had been totally incorporated in the leading edge of the old storm aloft, thus dramatically enhancing its anvil and tilt of the echo core.

It is noteworthy that these different cell merging mechanisms can occur sequentially or simultaneously during the same storm situation on one particular day. The main difference between daughter-cell and feeder-cell merging situations appears to be the reflectivity factor, and thus the cell intensity, which is much greater in the case of daughter-cell mergers than in feeder-cell merging situations (the feeder-cell is generally ≤ 40 dBZ). It should also be pointed out that features of all cell-merging mechanisms discussed in the introduction to this Section (Dennis *et al.*, 1970; Cheng and Rogers, 1988; Chisholm and Renick, 1972; Westcott and Kennedy, 1989) could be detected at one or other stage of the analysis.

Case studies of this nature are very time consuming, as can be seen from the fact that a total of approximately 420 PPI plots and 600 vertical cross-sections formed the basis of the analysis of a storm period lasting less than one hour! It is therefore impossible, at this stage, to estimate the relative frequency of the various storm merger situations.

It has also become very obvious that, in order to study storm or cell merger situations, one must have the three-dimensional reflectivity and air flow pattern available for making useful inferences. The latter should actually be derived from dual or triple Doppler radar observations rather than inferred from single Doppler radar observations, a fact which had also been stated by Cheng and Rogers (1988).

However, both types of merger mechanisms are very important for cloud-seeding experiments as the reaction to the introduction of seeding material might yield different results depending on the merger type.

6.5 REFERENCES

BROWNING K A and DONALDSON R J, 1963. Airflow and structure of a tornadic storm. *J. Atmos. Sci.*, 20, 535-545.

CARTE A E and HELD G, 1978. Variability of hailstorms on the South African plateau. *J. Appl. Meteor.*, 17, 365-373.

CHENG L and ROGERS D C, 1988. Hailfalls and hailstorm feeder clouds - an Alberta case study. *J. Atmos. Sci.*, 45, 3533-3545.

CHISHOLM A J and RENICK J H, 1972. The kinematics of multicell and supercell Alberta hailstorms. *Proceedings, 6th Annual Conference of the Canadian Meteoroloical Society*, Toronto, 24-31.

DENNIS A S, SHOCK C A and KOSCIELSKI A, 1970. Characteristics of hailstorms of western South Dakota. *J. Appl. Meteor.*, 9, 127-135.

GOYER G G, HOWELL W E, SCHAEFER V J, SCHLEUSNER R A and SQUIRES P, 1966. Project Hailswath. *Bull. Amer. Meteor. Soc.*, 47, 805-809.

WESTCOTT N E and KENNEDY P C, 1989. Cell development and merger in an Illinois thunderstorm observed by Doppler radar. *J. Atmos. Sci.*, 46, 117-131.

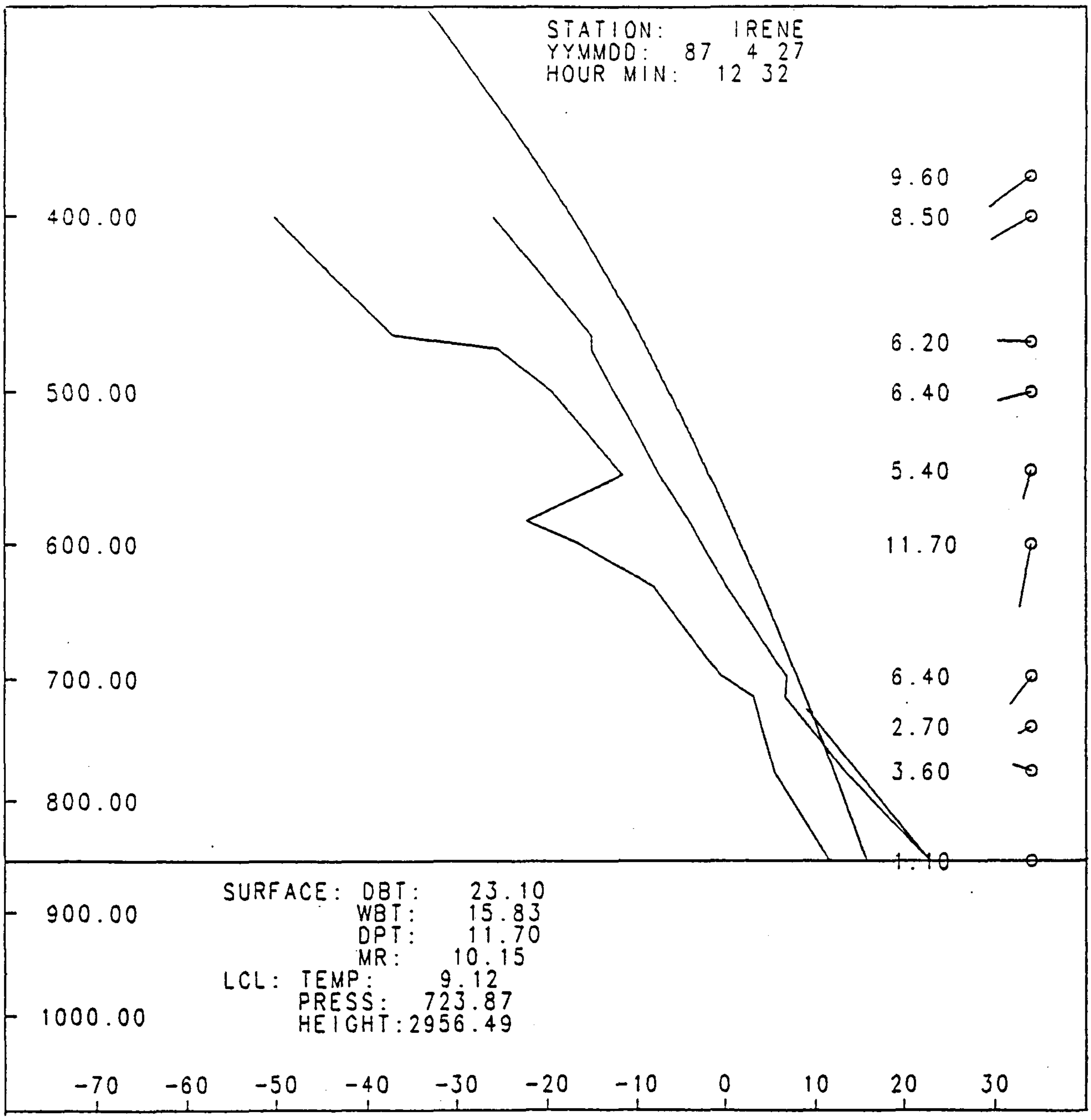

Figure 6.1: Midday (13:30 SAST) sounding from Irene (Pretoria) on 27 April 1987 (Stueve diagram).

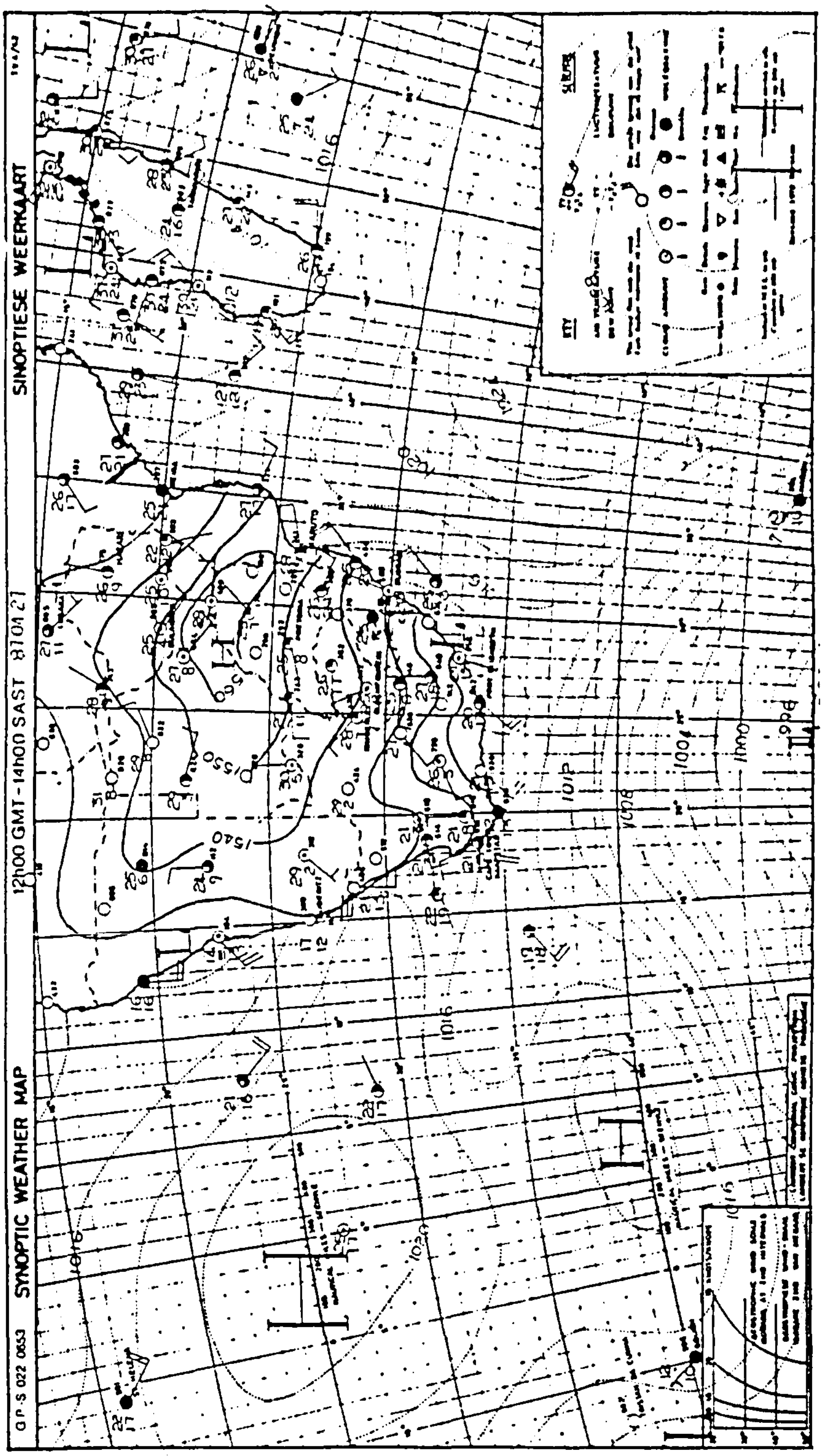

Figure 6.2: Synoptic weather map on 27 April 1987, 14:00, showing sea-level isobars (dotted) and 850 hPa contours over the continent (South African Weather Bureau).

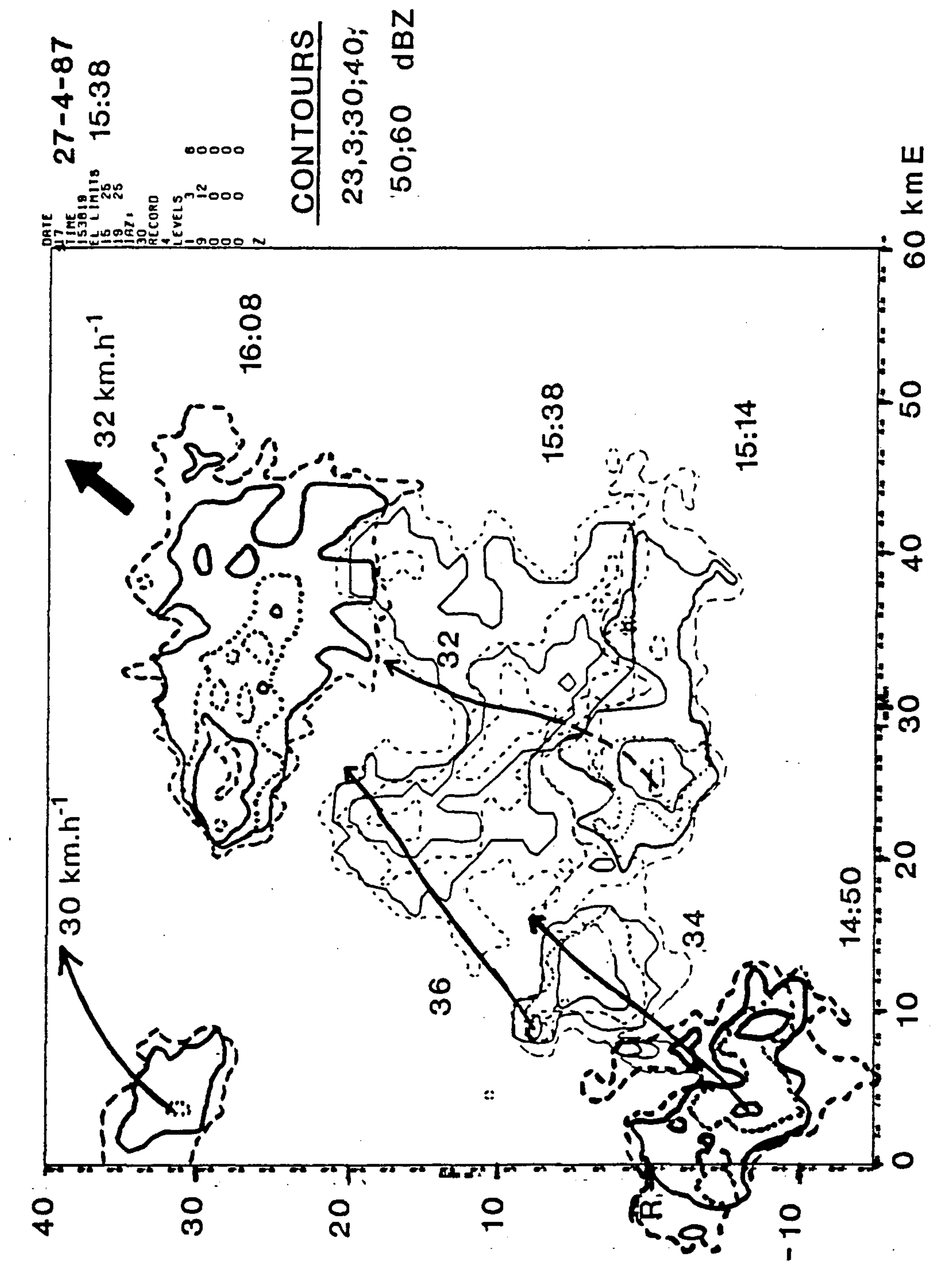

Figure 6.3: The multicellular storm of 27 April 1987 and its movement depicted at four different times. The position of the Houtkoppen radar is marked R.

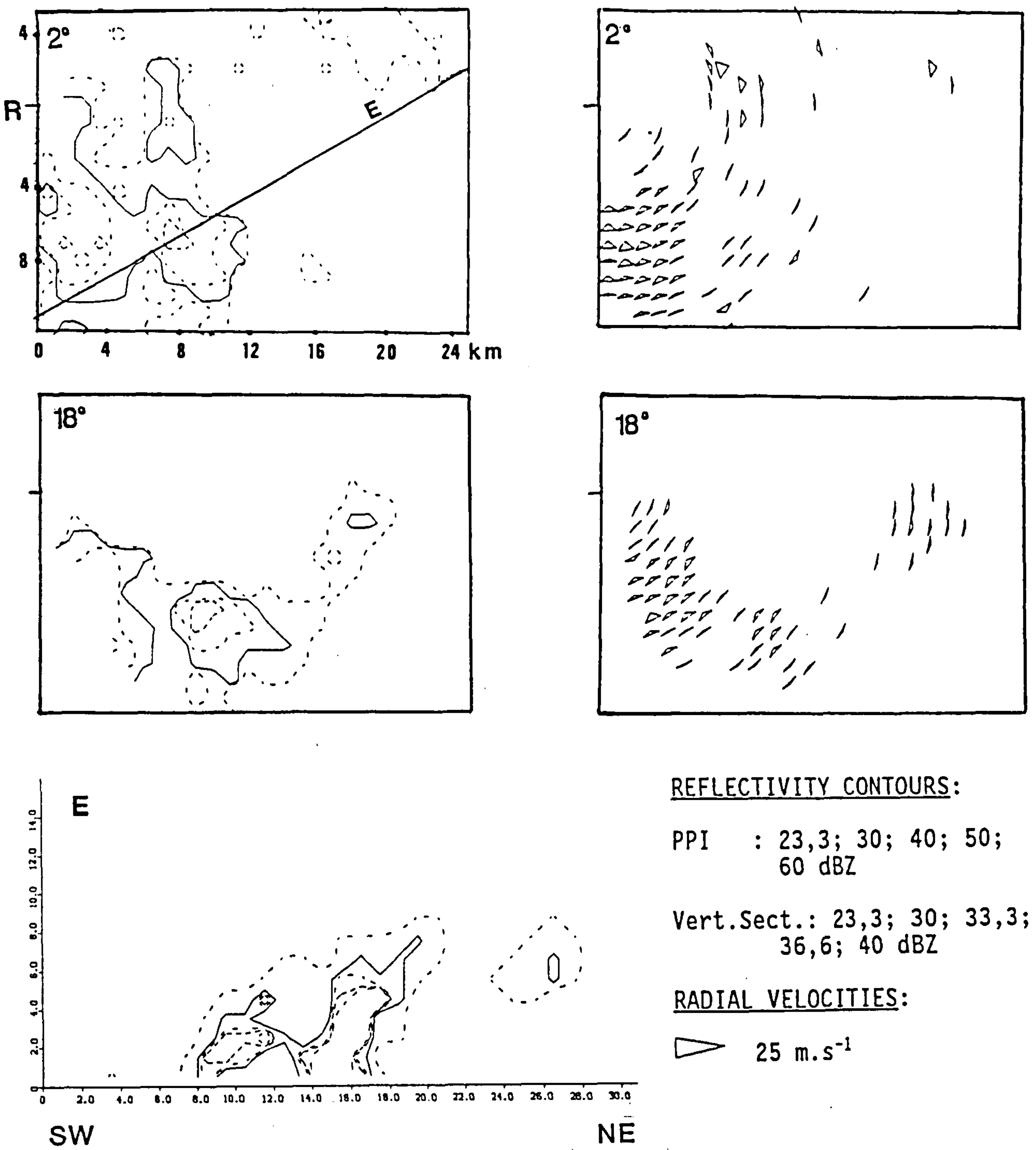

Figure 6.4: 14:46:48 - 14:48:30, showing the first echo of new development northeast of a mature storm (horizontal distance and height of vertical sections are indicated in km).

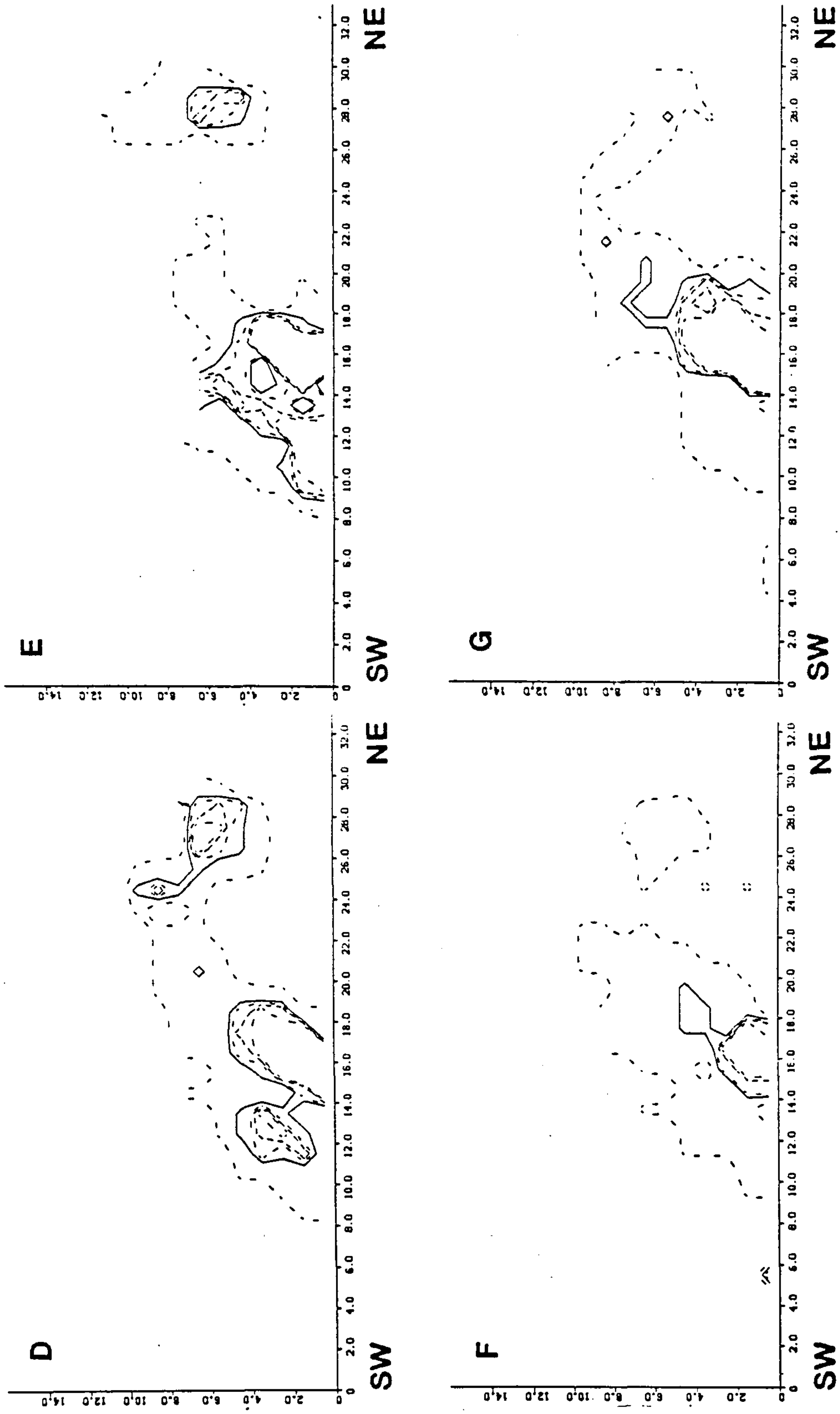

Figure 6.5: 14:49:38 - 14:51:59. Vertical cross-section, E, is along the same base line as in Figure 6.4. The base line for D is 1 km to the northwest, while F and G are 1 km apart to the southeast and all are parallel to E.

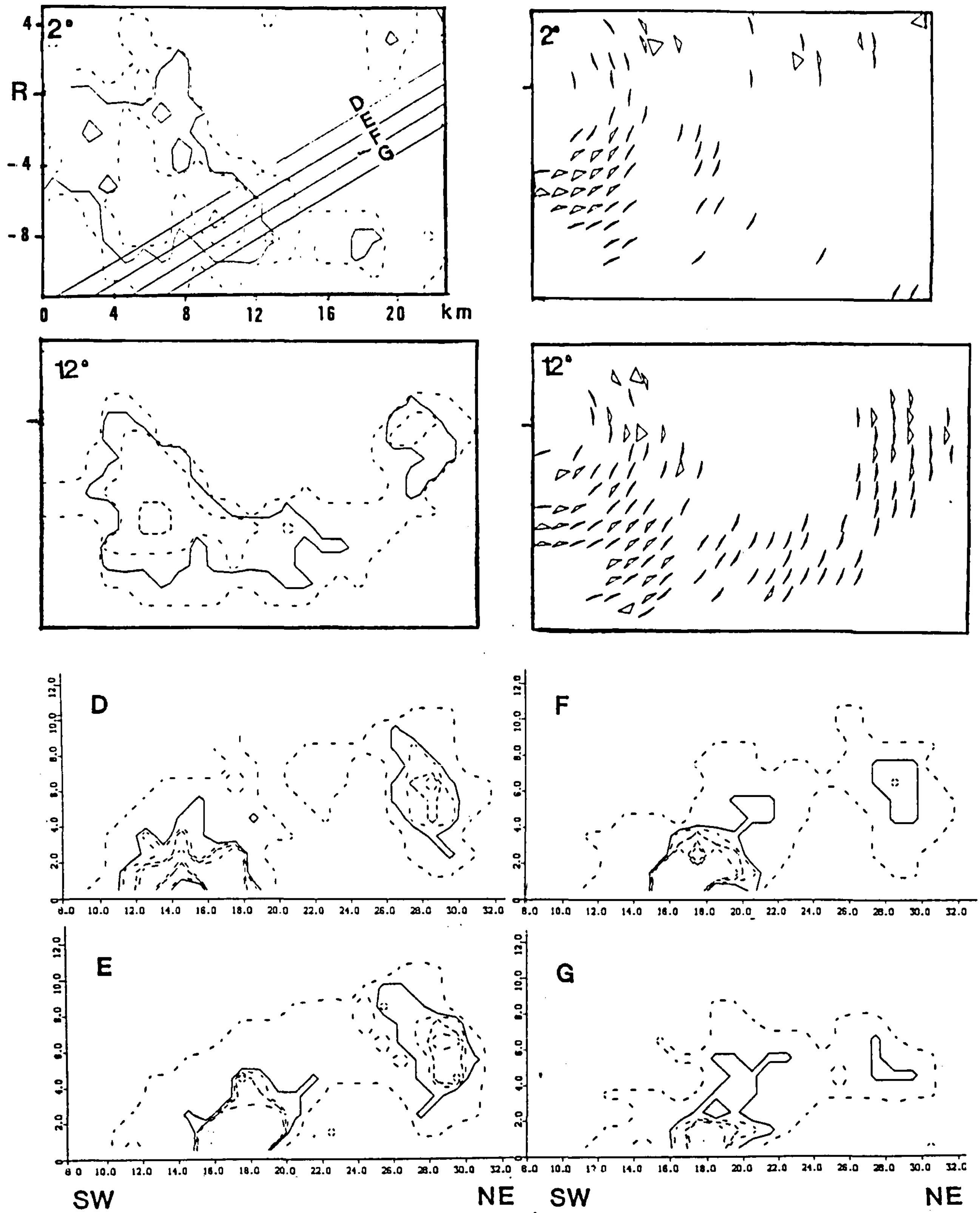

RADIAL VELOCITIES:

25 m.s^{-1}

Figure 6.6: 14:52:29 - 14:54:43 (see Figure 6.4 for key).

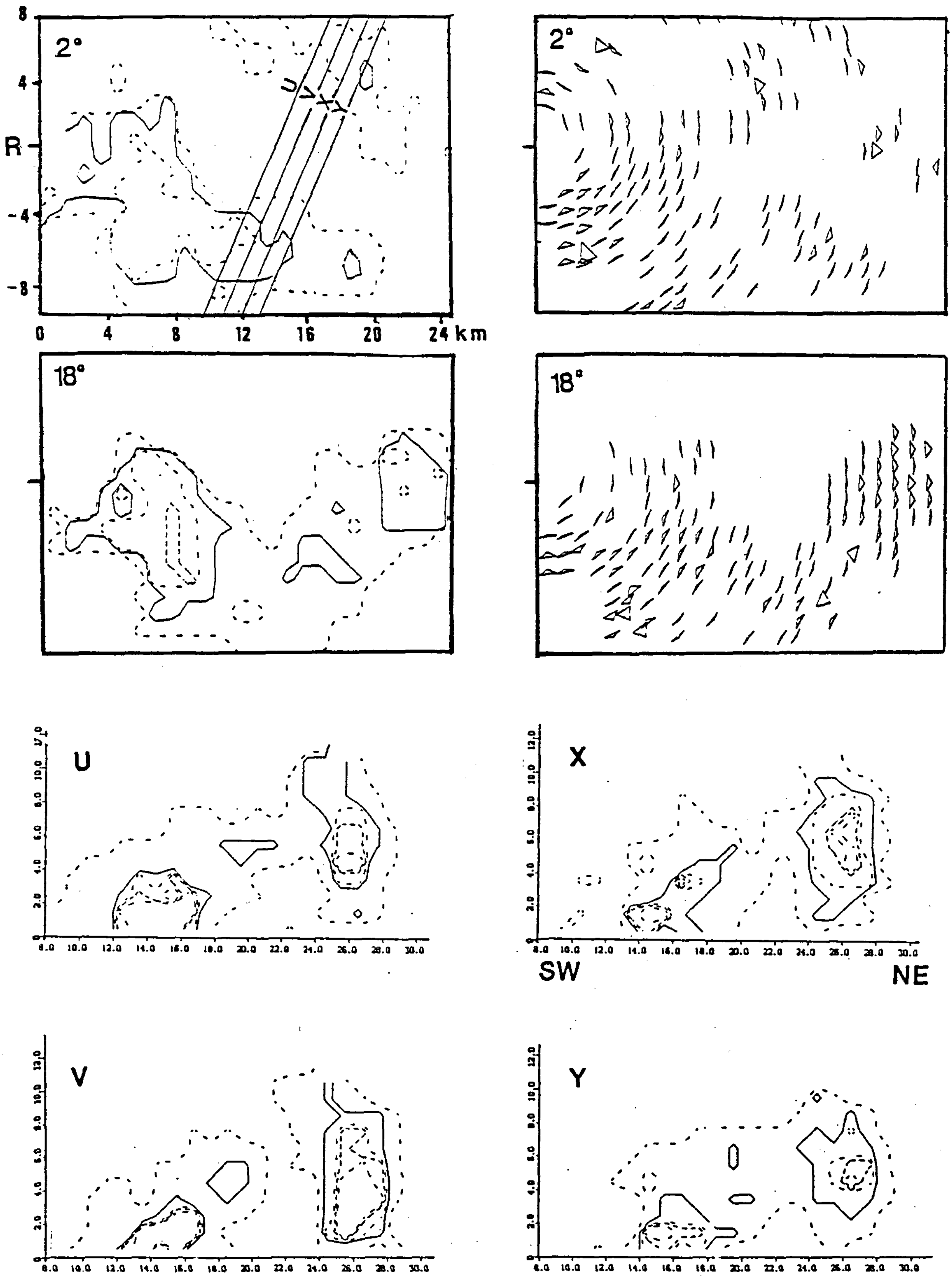

Figure 6.7: 14:55:23 - 14:57:20 (see Figure 6.6 for key).

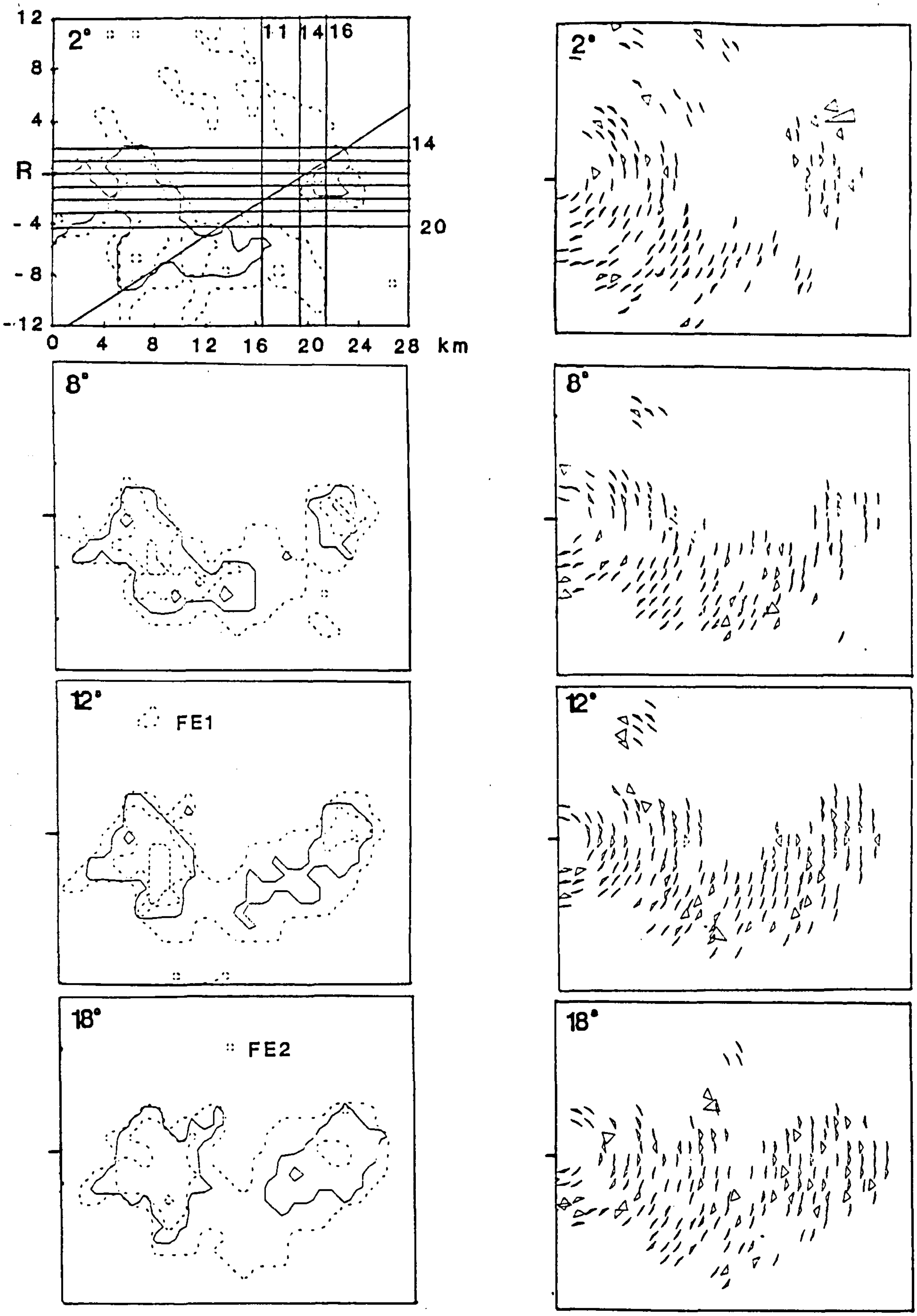

Figure 6.8a: 14:57:59 - 15:00:00. PPI contours and radial velocity field (see Figure 6.10a for key).

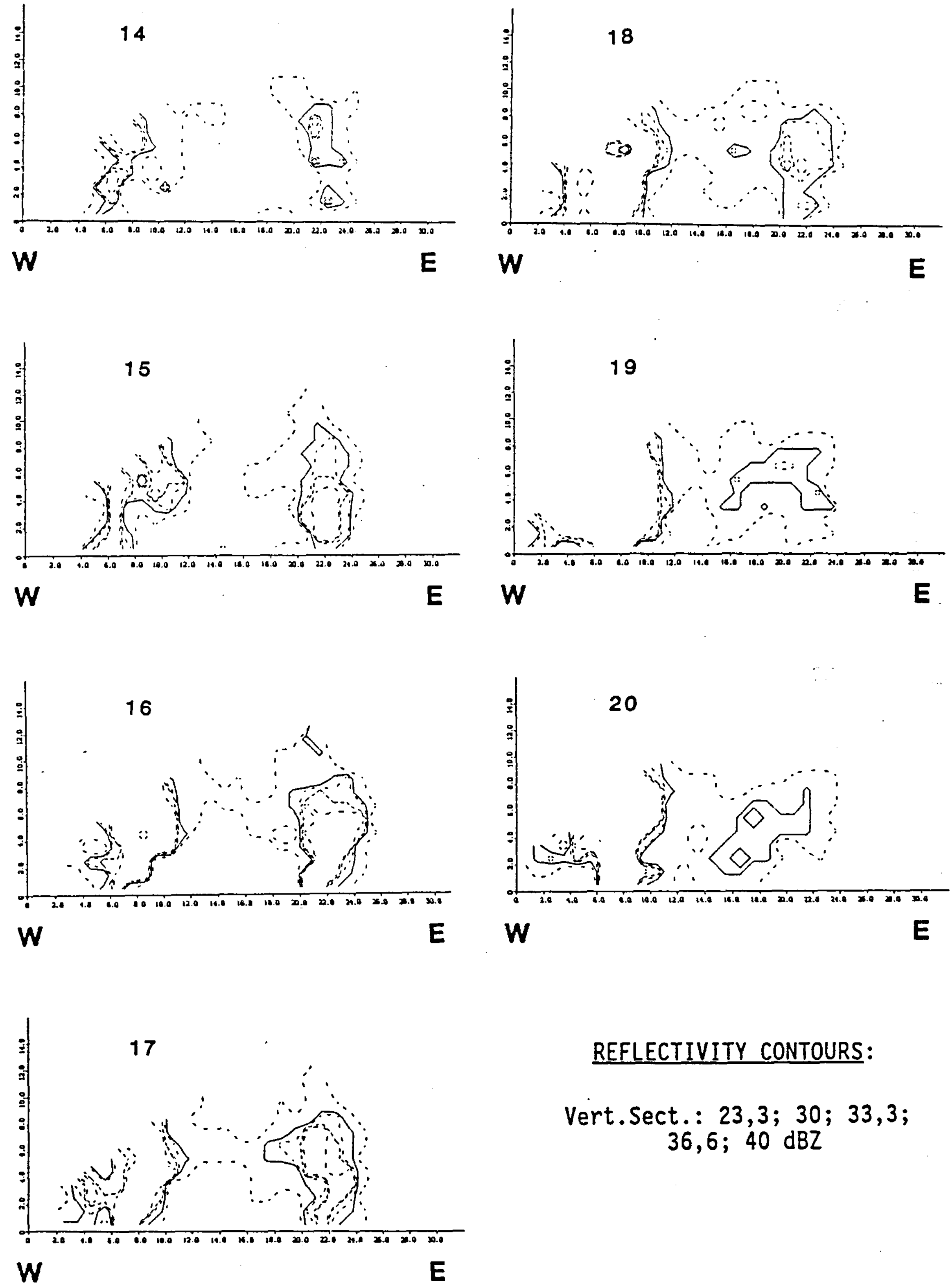

Figure 6.8b: 14:57:59 - 15:00:00. West - east vertical sections at 1 km spacing along base lines 14-20 marked in Figure 6.8a.

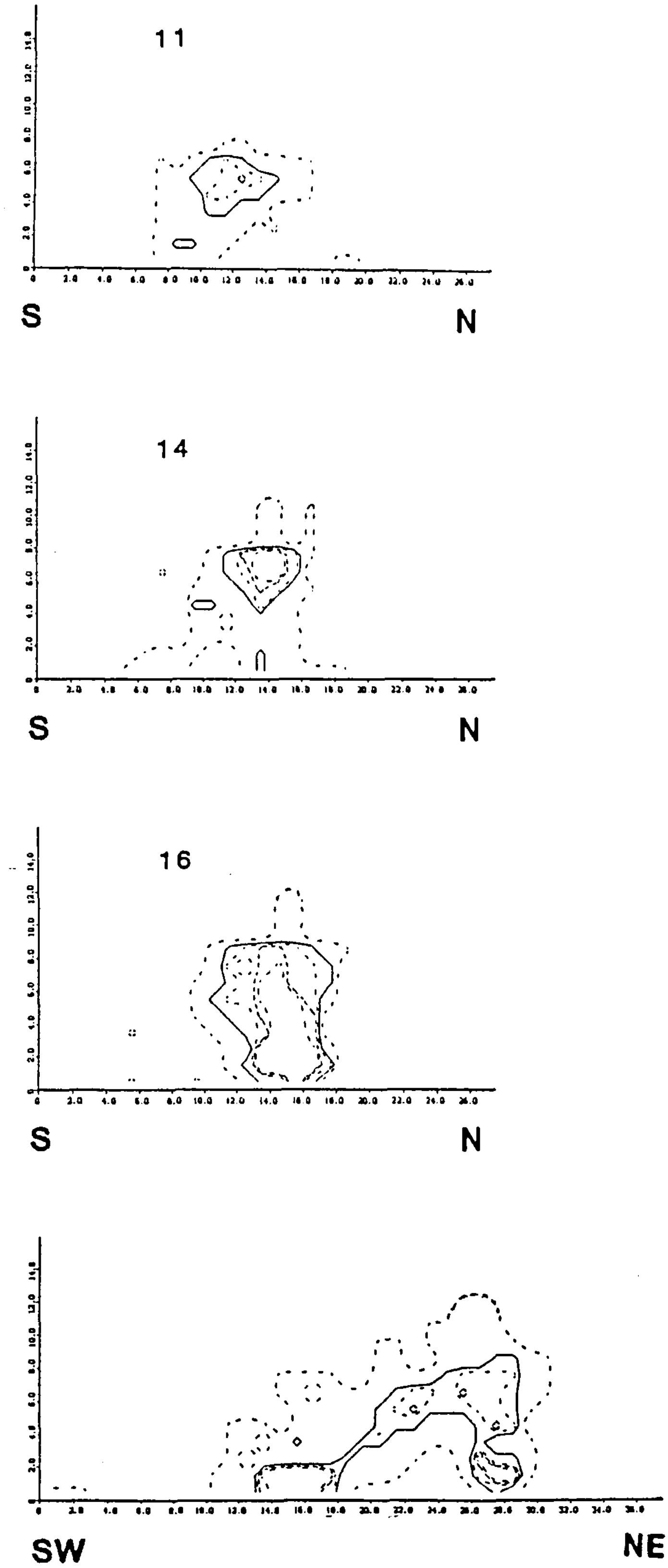

REFLECTIVITY CONTOURS:

Vert.Sect.: 23,3; 30; 33,3; 36,6; 40 dBZ

Figure 6.8c: 14:57:59 - 15:00:00. South - north and southwest - northeast vertical sections along base lines marked in Figure 6.8a.

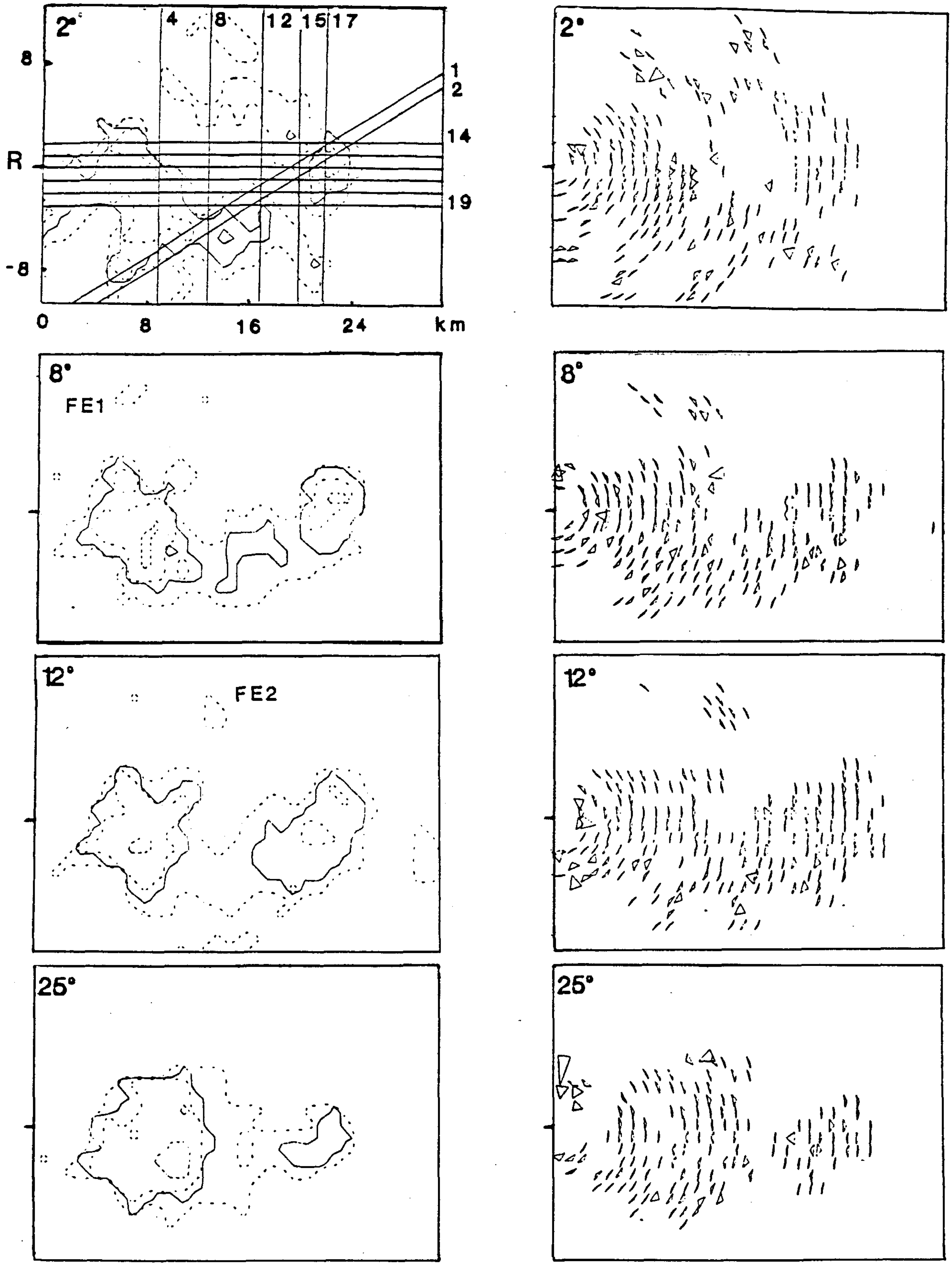

Figure 6.9a: 15:00:52 - 15:03:05. PPI contours and radial velocity field (see Figure 6.10a for key).

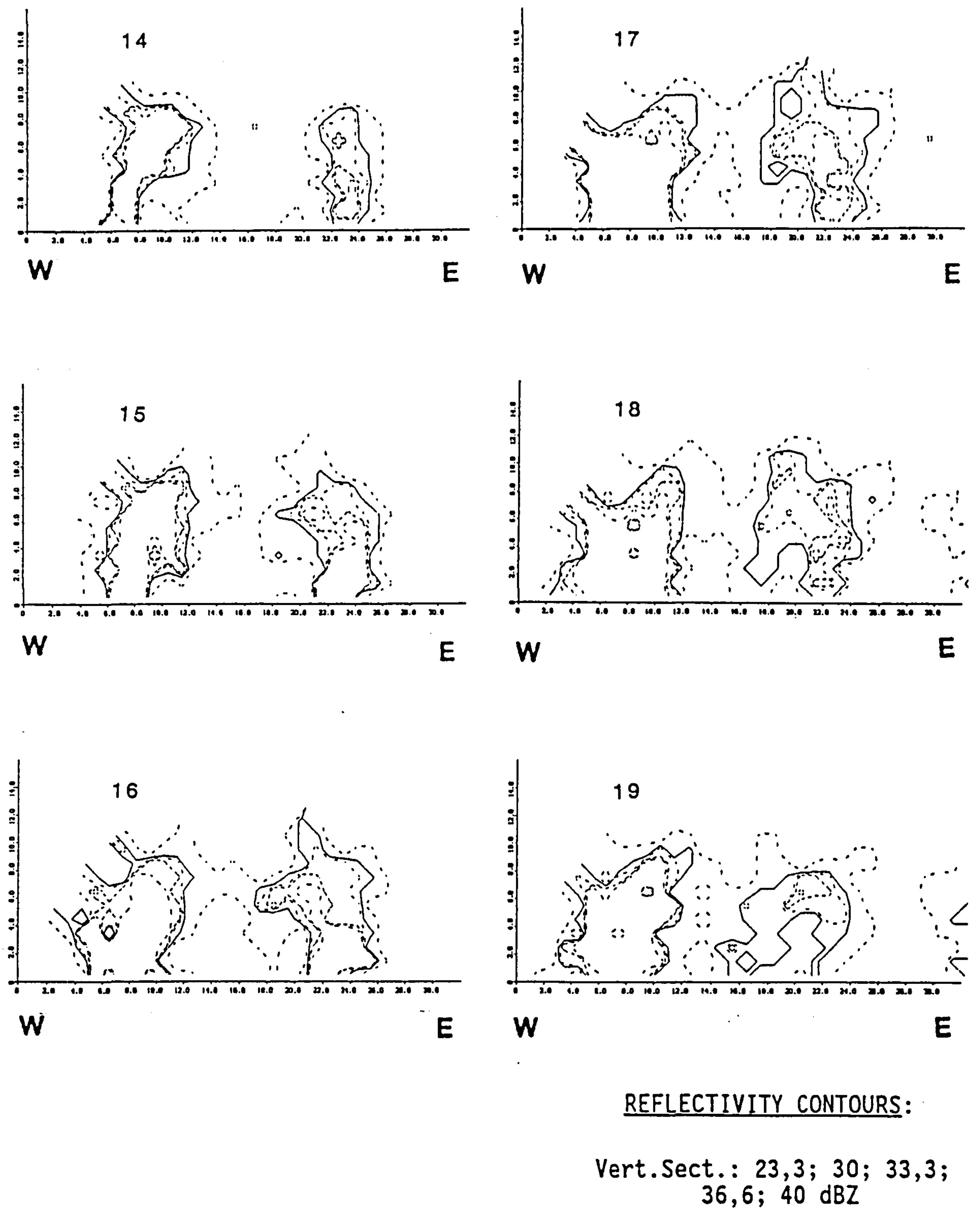

Figure 6.9b: 15:00:52 - 15:03:05. West - east vertical sections at 1 km spacing along base lines 14-19 marked in Figure 6.9a.

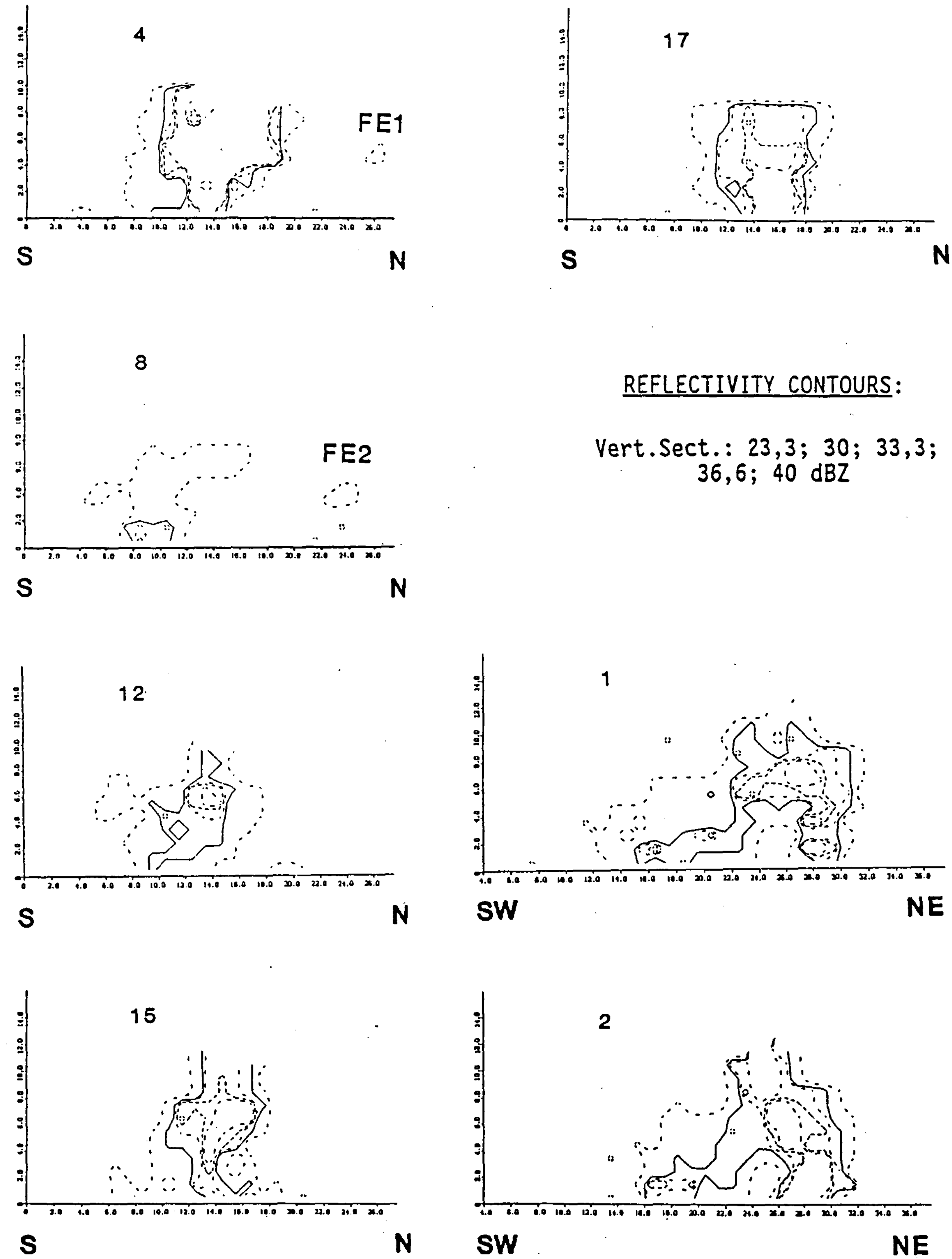

Figure 6.9c: 15:00:52 - 15:03:05. South - north and southwest - northeast vertical sections along base lines marked in Figure 6.9a.

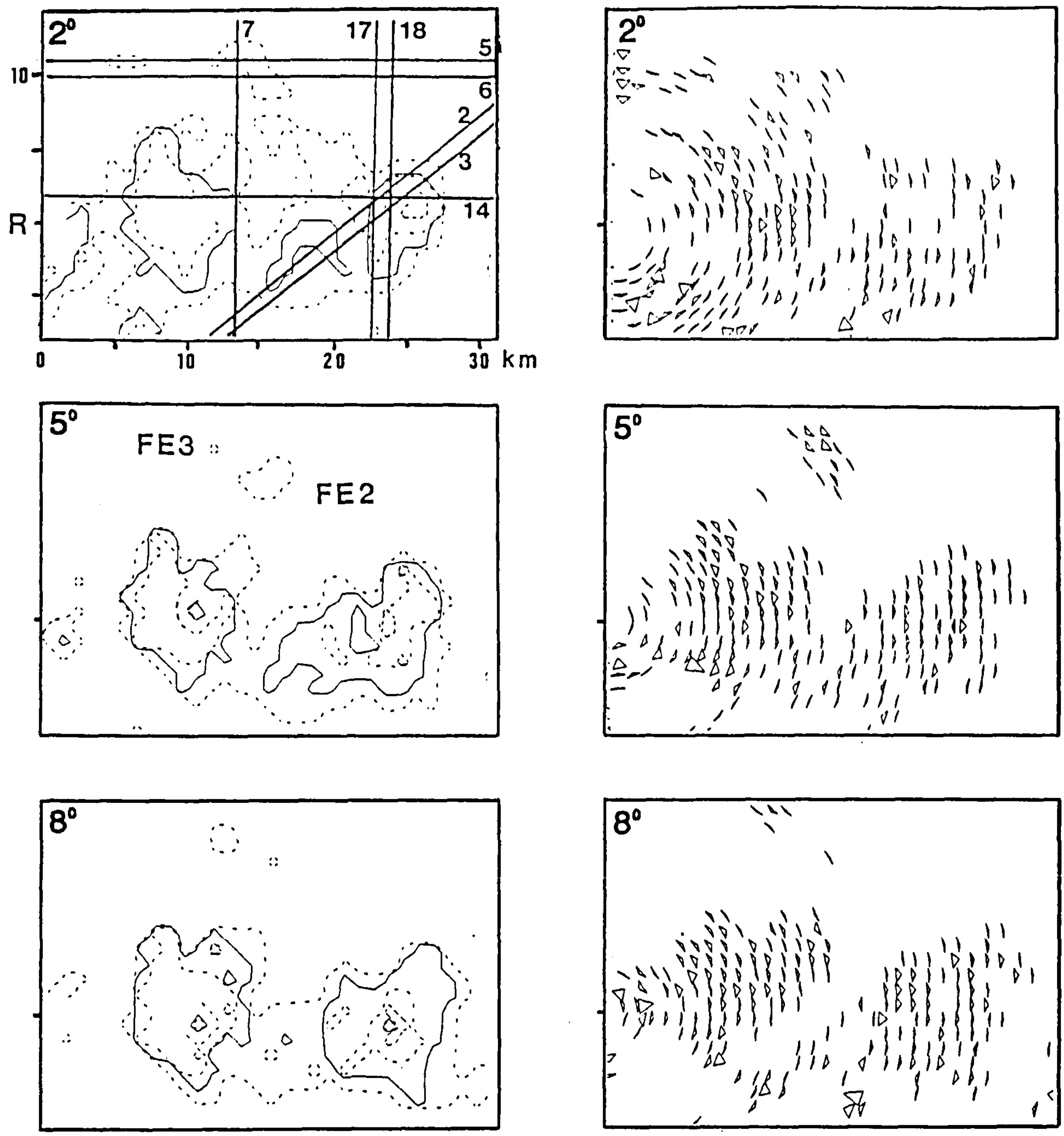

REFLECTIVITY CONTOURS:

PPI : 23,3; 30; 40; 50; 60 dBZ

Vert.Sect.: 23,3; 30; 33,3; 36,6; 40 dBZ

RADIAL VELOCITIES:

25 m.s^{-1}

Figure 6.10a: 15:06:22 - 15:08:16. PPI contours and corresponding radial velocity fields (2° to 8° elevation).

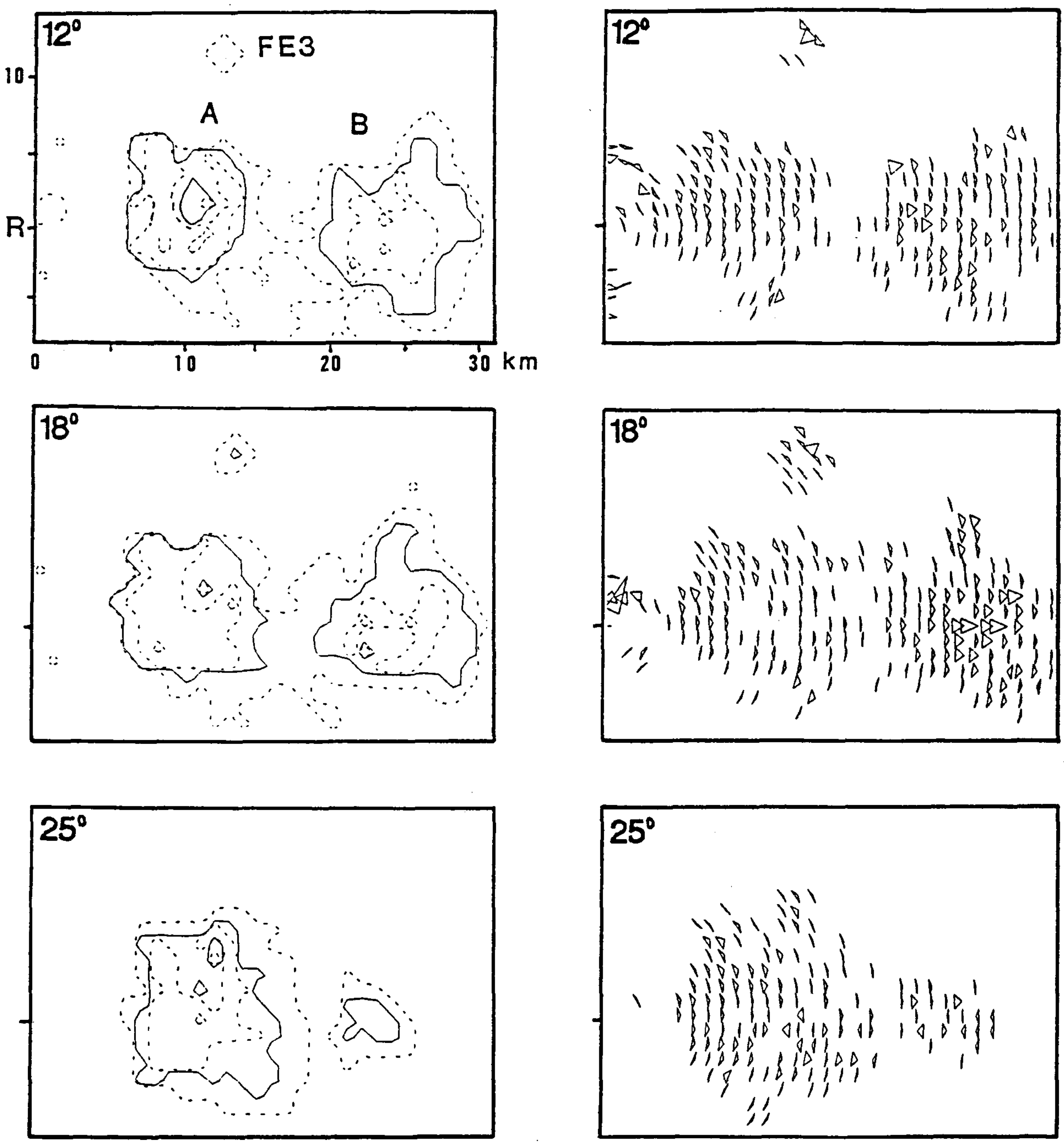

REFLECTIVITY CONTOURS:

PPI : 23,3; 30; 40; 50; 60 dBZ

Vert.Sect.: 23,3; 30; 33,3; 36,6; 40 dBZ

RADIAL VELOCITIES:

▷ 25 m.s^{-1}

Figure 6.10b: 15:06:22 - 15:08:16. PPI contours and corresponding radial velocity fields (12° to 25° elevation).

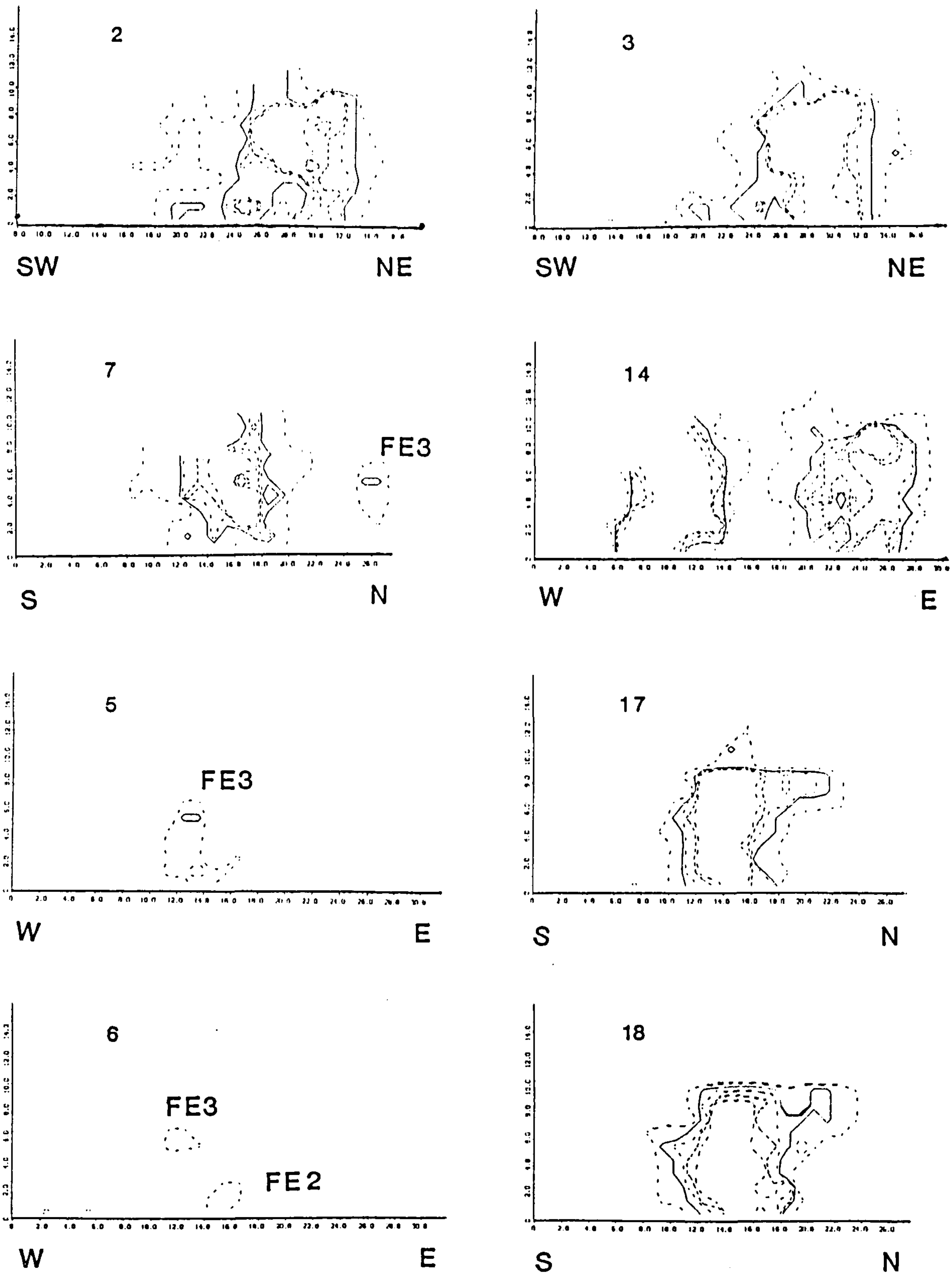

Figure 6.10c: Vertical sections along base lines marked in Figure 6.10a.

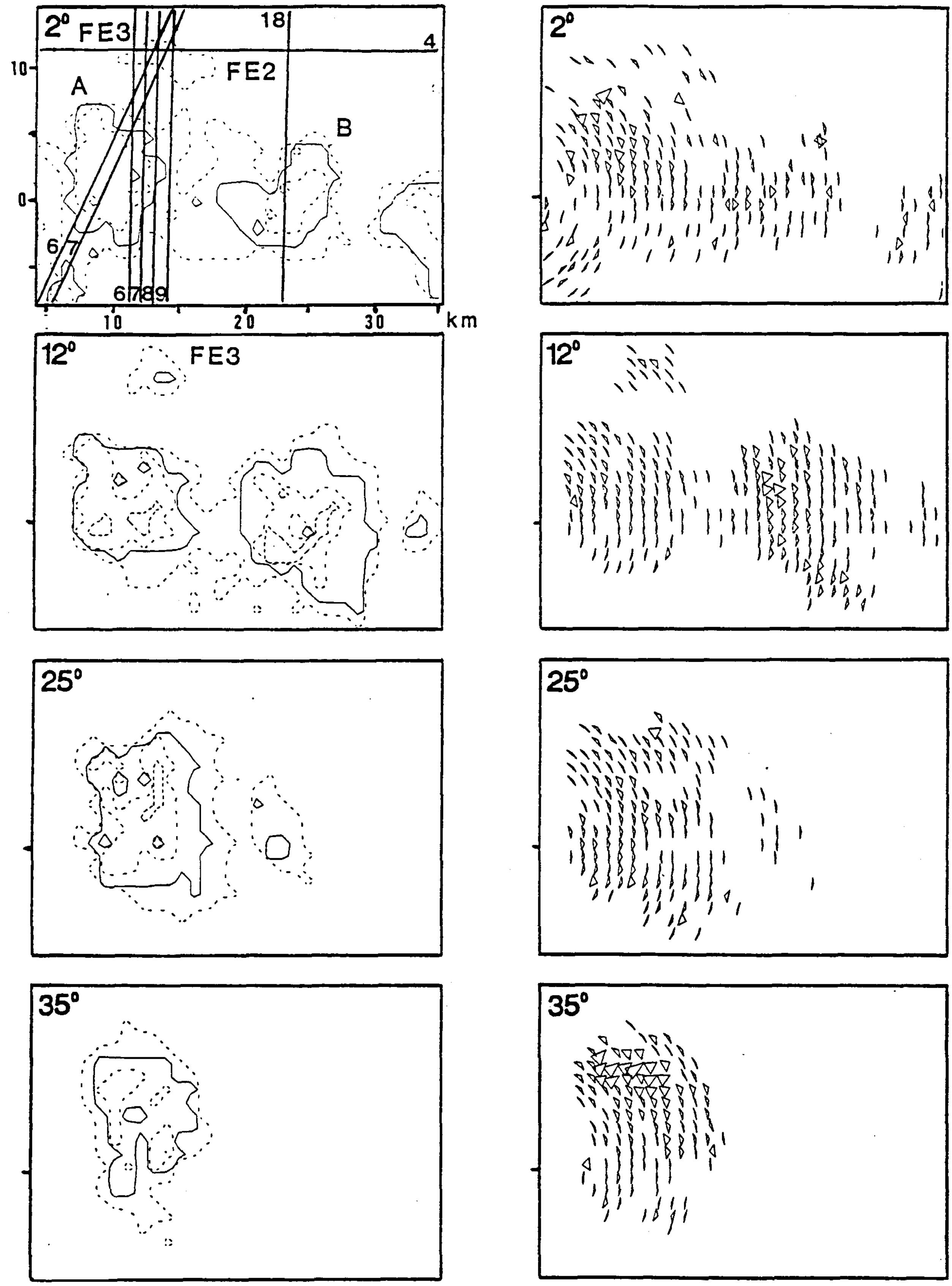

Figure 6.11a: 15:09:02 - 15:11:03. PPI contours and radial velocity field (see Figure 6.10a for key).

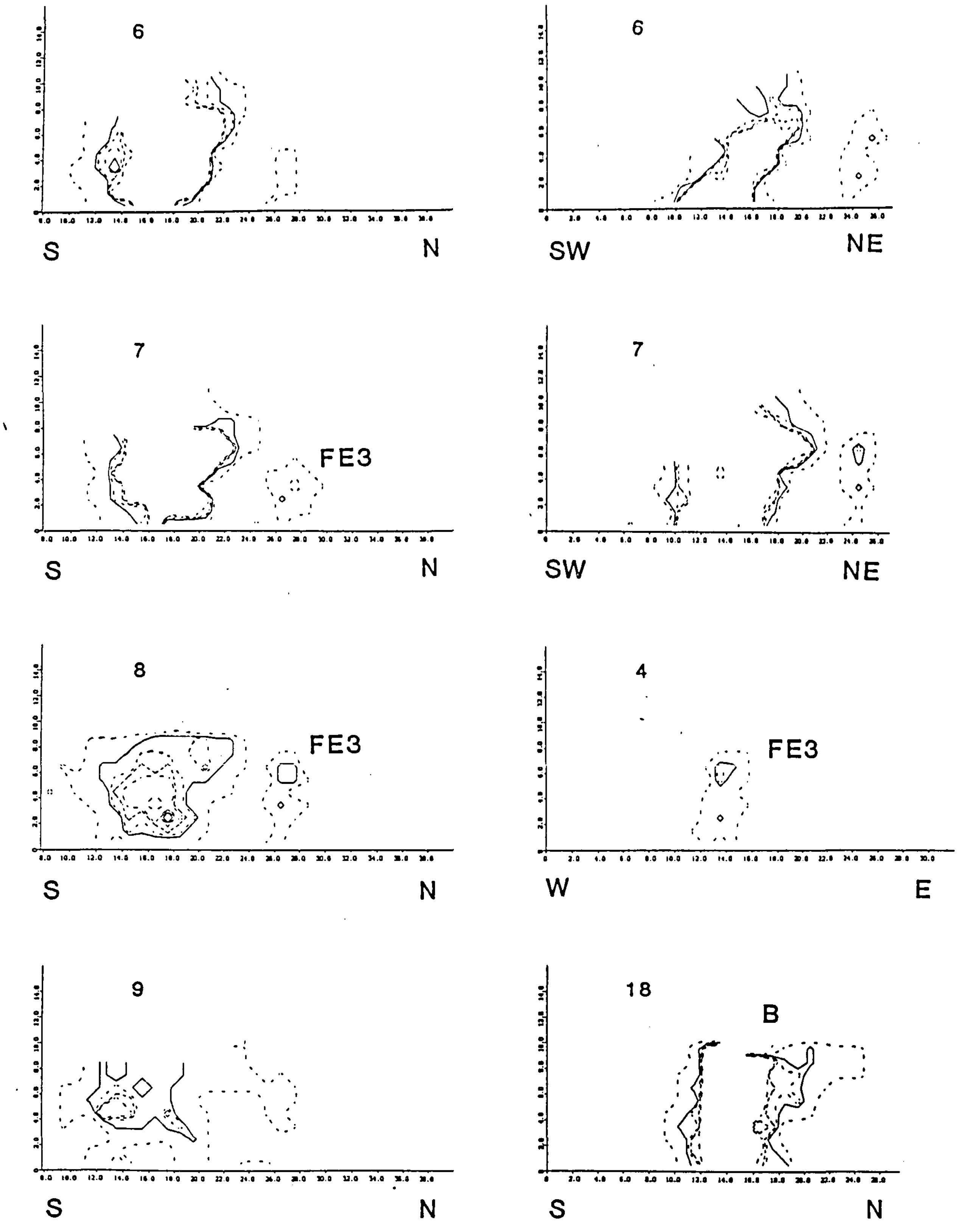

Figure 6.11b: 15:09:02 - 15:11:03. Vertical cross-sections along base lines shown in Figure 6.11a (see Figure 6.10a for key).

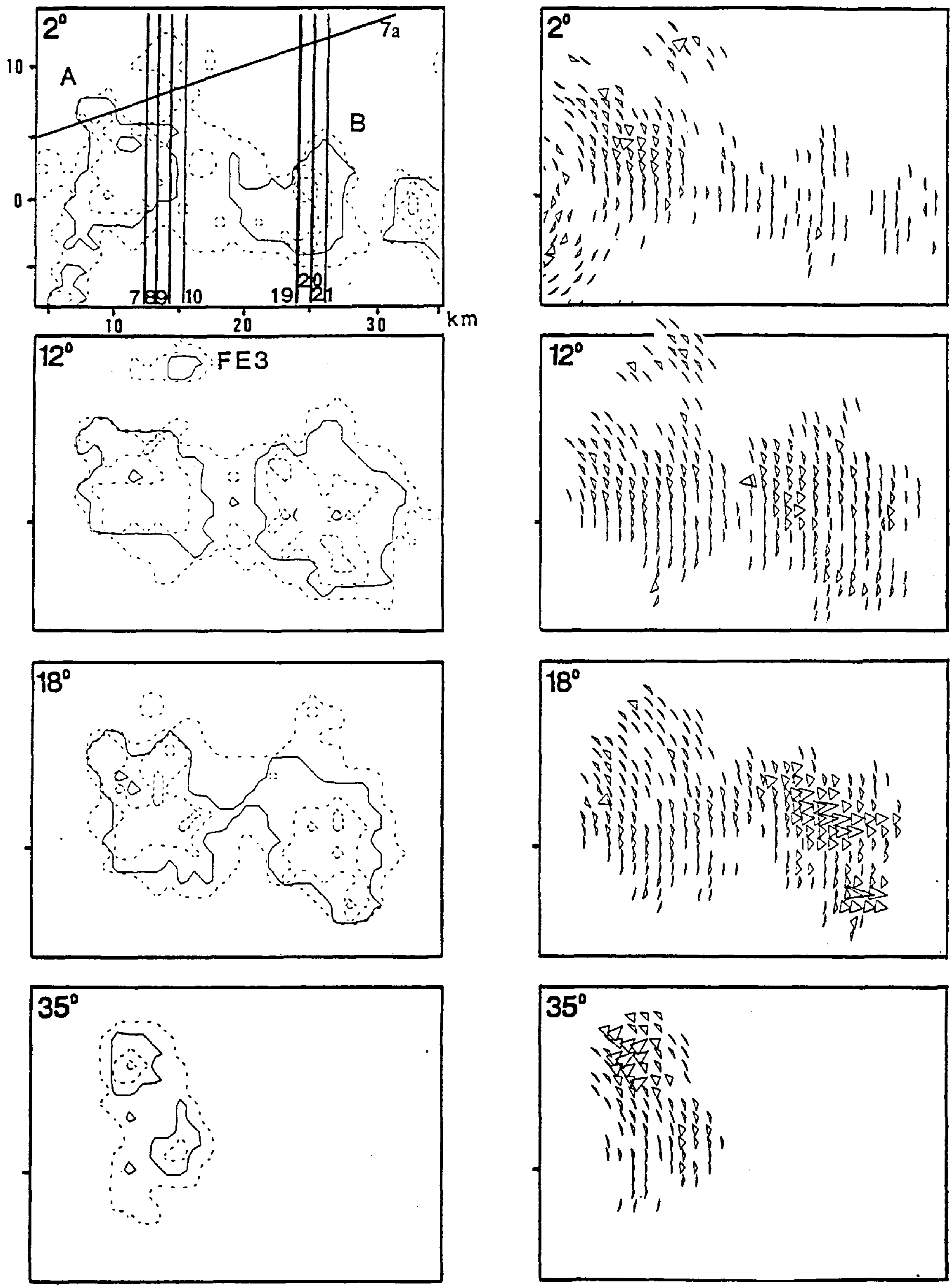

Figure 6.12a: 15:11:43 - 15:13:43. PPI contours and radial velocity field (see Figure 6.10a for key).

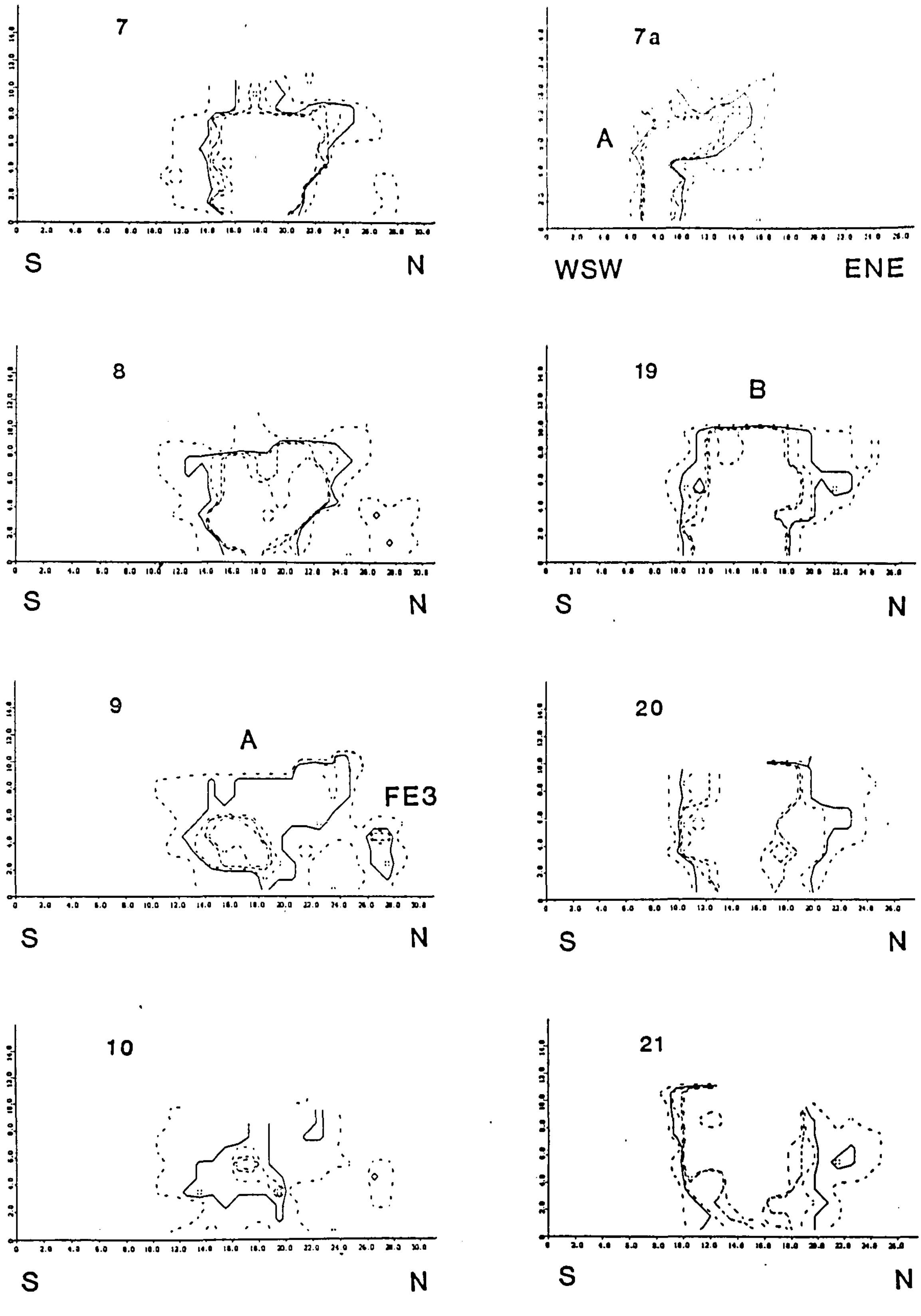

Figure 6.12b: 15:11:43 - 15:13:43. Vertical cross-sections along base lines shown in Figure 6.12a (see Figure 6.10a for key).

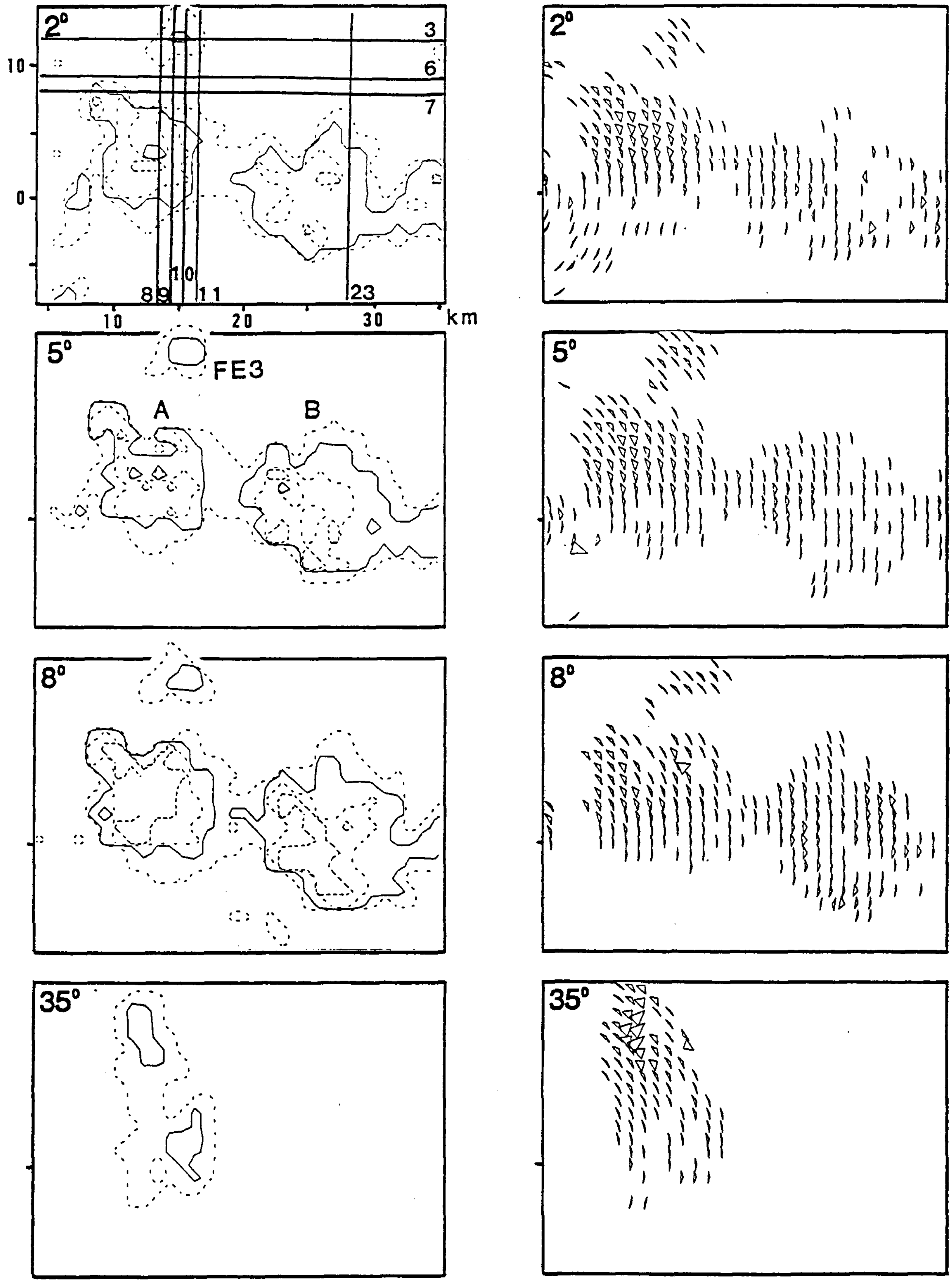

Figure 6.13a: 15:14:23 - 15:16:43. PPI contours and radial velocity field (see Figure 6.10a for key).

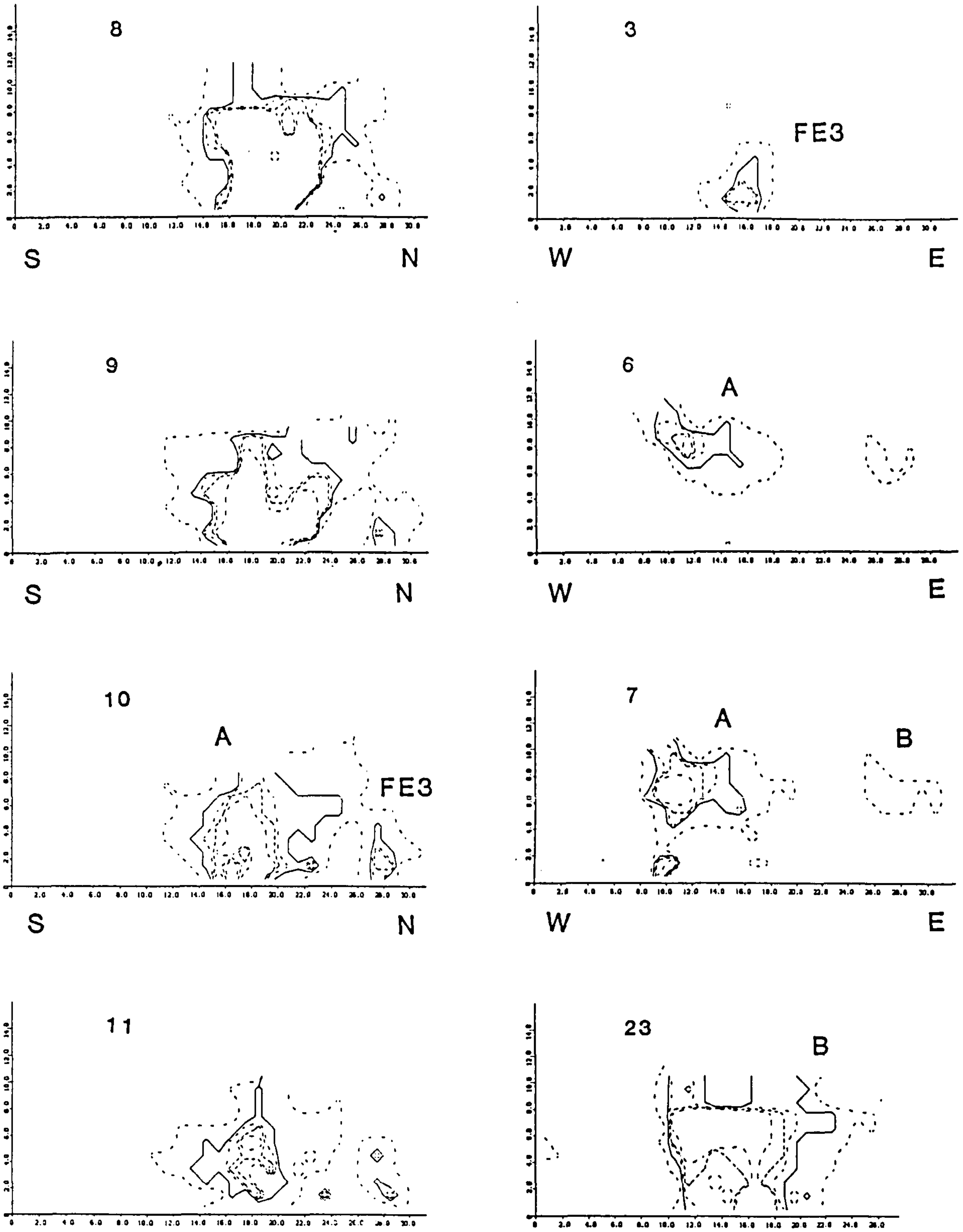

Figure 6.13b: 15:14:23 - 15:16:43. Vertical cross-sections along base lines shown in Figure 6.13a (see Figure 6.10a for key).

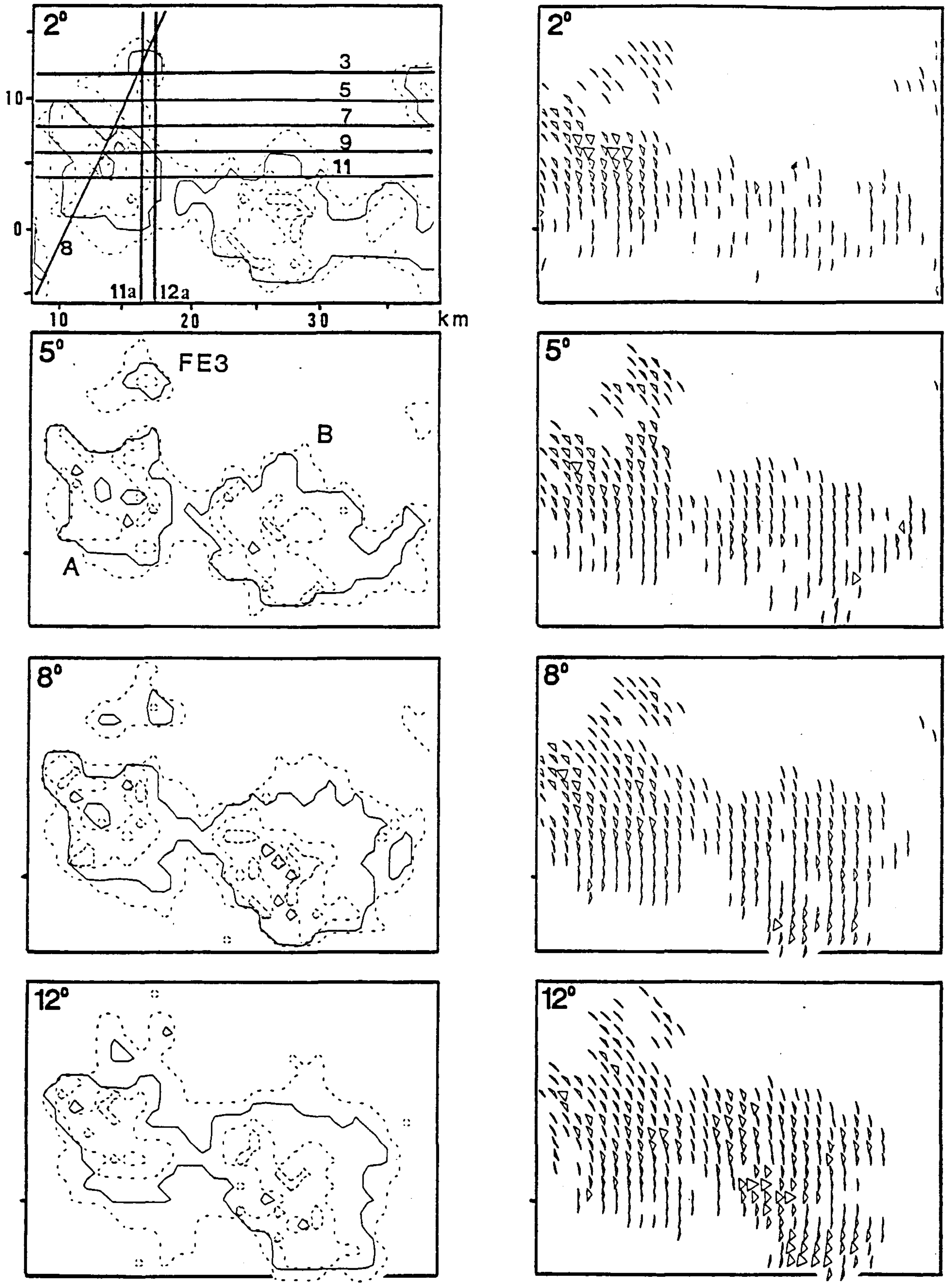

Figure 6.14a: 15:17:03 - 15:18:54. PPI contours and radial velocity field (see Figure 6.10a for key).

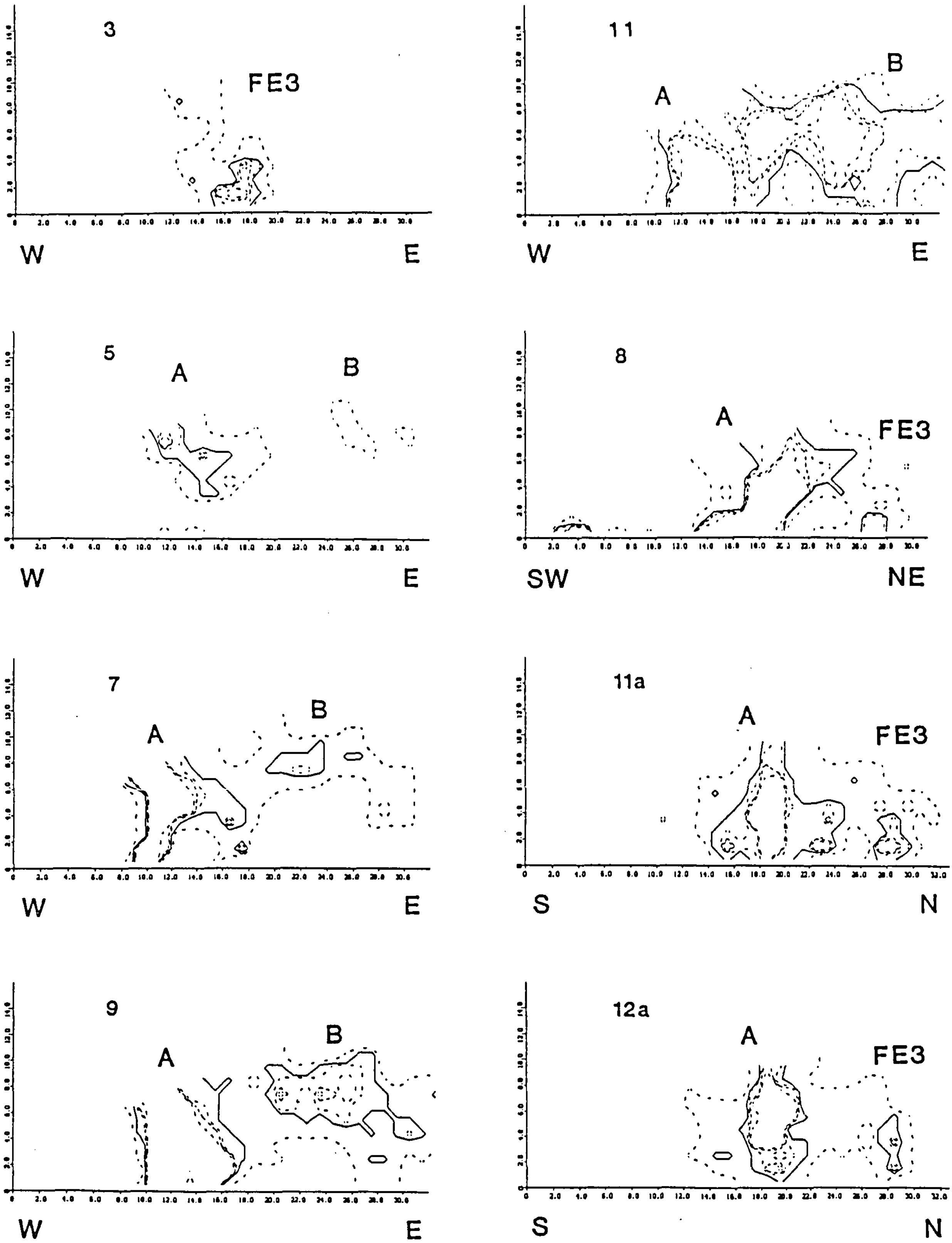

Figure 6.14b: 15:17:03 - 15:18:54. Vertical cross-sections along base lines shown in Figure 6.13a (see Figure 6.10a for key).

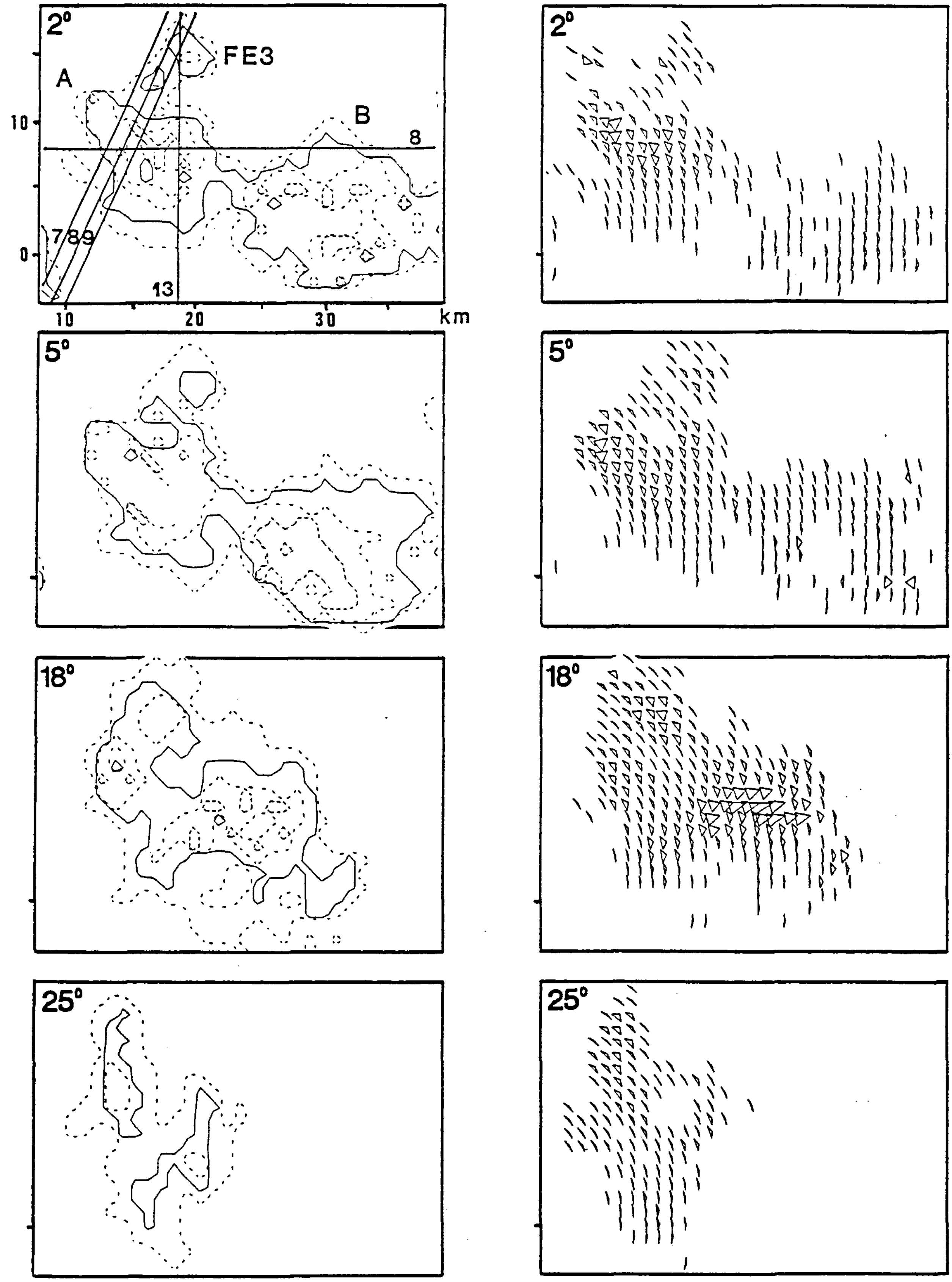

Figure 6.15a: 15:22:17 - 15:24:13. PPI contours and radial velocity field (see Figure 6.10a for key).

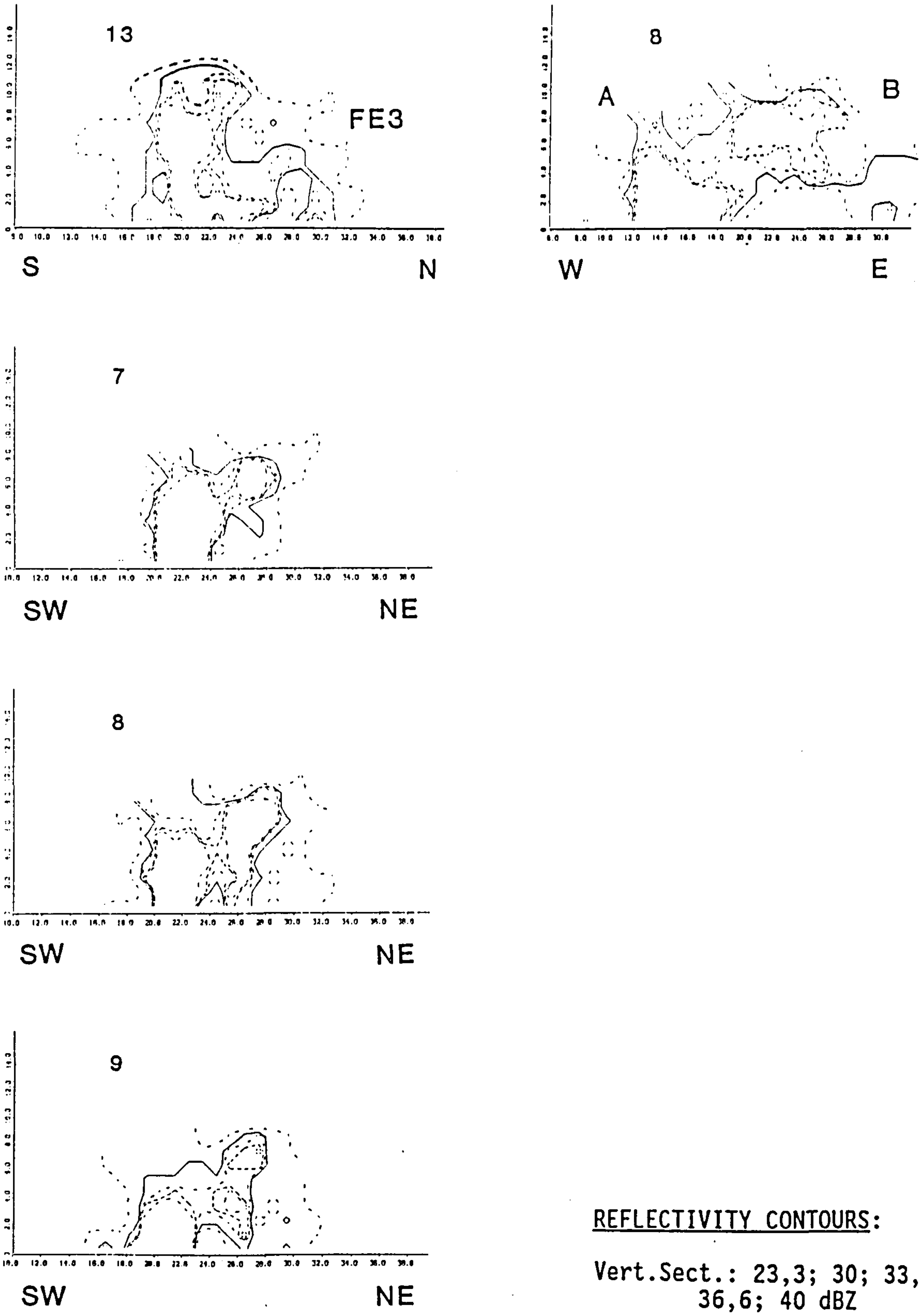

REFLECTIVITY CONTOURS:

Vert.Sect.: 23,3; 30; 33,3;
36,6; 40 dBZ

Figure 6.15b: 15:22:17 - 15:24:13. Vertical cross-sections along base lines shown in Figure 6.13a (see Figure 6.10a for key).

7. PROCESSING OF DOPPLER RADAR DATA

Gerhard Held and Ana Maria Gomes

Although it was initially envisaged that at least two Doppler radars (S-band at Houtkoppen and C-band at CSIR) would be operational during the 1989/90 season, this did, unfortunately, not materialise. Only the S-band radar at Houtkoppen was operated routinely, while test runs were made with the C-band radar on the CSIR campus. The reasons for this were manifold, but can mostly be traced back to interfacing problems between the hardware output from the modified EEC C-band radar and the Hewlett-Packard A600 computer which proved to be just too slow on some of its peripherals to accommodate the data stream in its entirety. In order to remedy the problems, certain hardware modifications and streamlining of the data acquisition program (which had been subcontracted to a private consultant) had to be undertaken. During the course of many test runs, several other difficulties had to be overcome which resulted from these latest modifications. Therefore, no useful data could be collected using more than one Doppler radar until March 1991.

However, the difficulties outlined above did certainly not deter from completing the implementation of the CRAY programs on the CSIR's VM mainframe computer and their final testing. These programs to process radar data from multiple Doppler radars were initially obtained through the courtesy of Dr Jay Miller from the National Center for Atmospheric Research (NCAR) where they ran on a CRAY 1-A supercomputer. EMATEK, at its own expense, subcontracted a specialist group from DATATEK to convert these programs and implement them on the VM mainframe computer. Final testing and fine tuning of the input data was then undertaken within the framework of the "DOPDATE" project as indicated in the Work Programme approved by the WRC for 1990.

In order to analyse radar data with the NCAR programs, two major steps have to be executed, viz. 'SPRINT' (Sorted Position Radar Interpolation) and 'CEDRIC' (Cartesian Space data processor). 'SPRINT' is designed to interpolate volumetric radar space measurements collected at constant elevation angles to a regularly spaced three-dimensional Cartesian grid

(Mohr *et al.*, 1981). 'CEDRIC' is used for the reduction and analysis of single and multiple Doppler radar volumes in Cartesian space. It provides a wide variety of commands for data manipulation coupled with significantly enhanced display capabilities (Mohr, 1985). The full capabilities of both program suites have been described in great detail by Mohr *et al.* (1981), Miller *et al.* (1986) and Mohr *et al.* (1986). Copies of these three papers are included in Appendix B.

After implementation of 'SPRINT', it was found that the Universal Radar Data Format, as specified by Barnes (1980), required more storage space on the VM mainframe computer than could be allocated. It was therefore decided to modify the input format of our radar data in order to facilitate speedy processing.

7.1 ANALYSIS OF SINGLE-DOPPLER RADAR OBSERVATIONS

All sections of 'SPRINT' and 'CEDRIC' have been thoroughly tested with Houtkoppen's single Doppler radar data. Typical examples of the output from 'SPRINT' are shown in Figures 7.1a, b, c, and d.

Now that 'SPRINT' has provided the matrix of reflectivity and radial velocity data, 'CEDRIC' will perform any analysis of these volume scans as required, including automatic (or specified) unfolding of radial velocities, remapping of data for vertical cross-sections, statistical analysis of data, filling of gaps in the data set, compensation of velocities for storm motion and algebraic manipulation of multi-dimensional Cartesian fields. A histogram indicating frequencies of specific reflectivities within a complete volume scan is shown in Figure 7.2. CAPPIS at 3 km AGL for the same volume scan display the radar reflectivity (Figure 7.3) and rainfall rate (Figure 7.4), respectively.

7.2 PRELIMINARY ANALYSIS OF DUAL DOPPLER RADAR OBSERVATIONS

On 4 March 1991, the first promising observation of a storm with both, Pretoria and Houtkoppen radars, was obtained. After a preliminary study of records from each radar individually was done, it was decided to analyse a small storm consisting of two cells and located approximately 25 km from both radars (Figure 7.5a). The single-Doppler radial velocity and reflectivity data were independently converted to a three-dimensional Cartesian coordinate system by SPRINT, using a successive linear interpolation algorithm described by Mohr and Vaughan (1979) and Mohr *et al.* (1981). The regular volume containing data in this case covers 80 x 50 km in the horizontal and 7,2 km in the vertical. The spacing of grid points was 1,0 km in the horizontal and 0,5 km in the vertical.

Preliminary single-Doppler analysis of records from both, Houtkoppen and Pretoria, has been completed and the dual Doppler analysis for the period 15:56:16 to 15:59:05 should be available soon. The three-dimensional wind field will be computed using the CEDRIC analysis package, developed at NCAR (Mohr *et al.*, 1986). The CEDRIC analysis scheme solves the three-dimensional wind field iteratively, utilising the geometrical relationships among the single-Doppler velocities measured by each radar, the Cartesian wind components and the location in space, and the vertical integration of the anelastic continuity equation.

The CAPPIs in Figure 7.5a have been generated for increments of 0,5 km in height, but only every other one is shown in the Figure. The maximum reflectivity value in each CAPPI is indicated by X and its value printed just above the key on the righthand side. Figure 7.5b shows the 5,2 km MSL CAPPI with the radial wind vectors. The strong divergence in cell A at this level, and actually extending from 4,7 to 6,2 km, is noteworthy.

Davis-Jones (1979) has noted from experience that a minimum beam intersection angle (difference in azimuth of the two radars when they are scanning identical volumes) of 30° is usually necessary for qualitatively reasonable dual Doppler analyses. This particular storm which occurred on 4 March 1991 seems, at a first approach, to be suitable for dual analysis, because it falls within the range mentioned above. Figure 7.6 shows the position of both radars. The full circles indicate the maximum range for each radar when operated in Doppler mode. The dashed circles outline the area for optimal dual Doppler radar observations. An even more suitable, isolated storm was observed on 26 March 1991 and the dual-Doppler observations have been used to demonstrate the application and versatility of the CRAY programs for synthesizing the storm and for calculating the three-dimensional air flow within it.

This particular storm initially consisted of several small cells between 7 and 27 km northeast of the Houtkoppen radar (12:37) as shown in Figure 7.7. These cells merged within a period of less than 20 minutes into one multi-cellular complex which moved from 210° at an average speed of 9,9 $m.s^{-1}$. It reached its peak intensity (> 50 dBZ) at approximately 13:14. This volume scan was therefore chosen for a detailed dual-Doppler analysis. The complex continued to move towards northeast but gradually dropped in intensity and decreased in size from 13:35 onwards (Figure 7.7).

The volume scan from 13:13:08 to 13:15:10 was then processed by SPRINT and CEDRIC with a horizontal grid of 1 km and a vertical resolution of 0,5 km. The CAPPIs showing the reflectivity contours from the Houtkoppen radar and the related horizontal wind field from 2,8 to 8,3 km MSL are depicted in Figures 7.8 and 7.9. Vertical cross sections along the baselines shown in Figure 7.8 show the reflectivity pattern with height and the air flow in terms of up- and downdraughts. Figure 7.10 shows vertical sections along south - north and west - east baselines. Figure 7.11a and b depict vertical sections along baselines from southwest to northeast and northwest to southeast, respectively. These sections were constructed by first rotating the storm around a new origin ("REMAPPING" facility) so that the new X-axis is pointing towards 146° from true north.

This is the very first time that the actual three-dimensional air flow has been observed in a South African thunderstorm and presented graphically in terms of up- and downdraughts related to the reflectivity pattern.

7.3 REFERENCES

BARNES S C, 1980. Report on a meeting to establish a common Doppler radar exchange format. *Bull. Amer. Meteor. Soc.*, 61, 1401-1404.

DAVIS-JONES R P, 1979. Dual-Doppler radar coverage area as a function of measurement accuracy and spatial resolution. *J. Appl. Meteor.*, 18, 1229-1233.

MILLER L J, MOHR C G and WEINHEIMER A J, 1986. The simple rectification to Cartesian space of folded radial velocities from Doppler radar sampling. *J. of Atmos. and Oceanic Techn.*, 3, 162-174.

MOHR C G, 1985. SPRINT - Sorted Position Radar Interpolation. User's Manual.

MOHR C G and VAUGHAN R L, 1979. An economical procedure for Cartesian interpolation and display of reflectivity factor data in three-dimensional space. *J. Appl. Meteor.*, 28, 661-670.

MOHR C G, MILLER L J and VAUGHAN R L, 1981. An interactive software package for the rectification of radar data to three-dimensional Cartesian coordinates. *Preprints of 20th Conference on Radar Meteorology*, Boston, Amer. Meteor. Soc., 690-695.

MOHR C G, MILLER L J, VAUGHAN R L and FRANK H W, 1986. The merger of mesoscale data sets into a common Cartesian format for efficient and systematic analysis. *J. of Atmos. and Oceanic Techn.*, 3, 143-161.

```
SUMMARY OF INPUT COMMAND
------- -- ----- -------

                 UNIT NUMBER:     21
                   TAPE NAME:  RAD52
                 REWIND TAPE:  NO
        NUMBER FILES TO SKIP:      0
             EXPERIMENT NAME:  MULDOP
                  RADAR NAME:  HOUT


>>>>>GRID    -40.    0.     -20.    10.    1.    2.    10.    1.        <<<<<

   SUMMARY OF CARTESIAN COMMAND
   ------- -- --------- -------

   CARTESIAN COORDINATE SYSTEM SPECIFICATIONS:

    AXIS    MINIMUM (KM)    MAXIMUM (KM)     DELTA (KM)    NO. OF PTS.
    ----    ------------    ------------     ----------    -----------

     X         -40.00            0.00           1.00           41
     Y         -20.00           10.00           1.00           31
     Z           2.00           10.00           1.00            9

    AXIS ORDER IS   X  Y  Z
    ANGLE OF THE X-AXIS RELATIVE TO NORTH:   90.0 DEGREES
    (X,Y)  AXES ARE SPECIFIED RELATIVE TO:  (0.00,0.00)

>>>>>PROCESS     20. 171349. 172123.                                   <<<<<

   SUMMARY OF PROCESS COMMAND
   ------- -- ------- -------

                          DATE (YYMMDD):      20
              BEGINNING TIME (HHMMSS): 171349
                 ENDING TIME (HHMMSS): 172123
    SPECIAL VOLUME PROCESSING PERFORMED:  NONE
  ELEVATION SCANS WILL BE DETERMINED BY: SWEEP NUMBER

++++++++++++++++++++++++++++++++++++++++++++++++++++++++++++++++++++++++++++++++++++++++++

      VOLUME FOUND   -   DAY :   20        BEGINNING TIME : 171349
```

SCAN		ELEVATION				AZIMUTH		SPACING			BEAMS	
NO	DIR	FIXED	MIN	MAX	MEAN	BEG	END	MIN	MAX	MEAN	GOOD	BAD
1	1	2.00	1.89	1.89	1.89	152.2	78.6	1.00	1.50	1.24	523	0
2	1	5.00	5.19	5.19	5.19	165.5	79.1	1.00	1.50	1.24	512	0
3	1	6.00	6.19	6.19	6.19	103.7	77.2	1.09	1.41	1.24	560	0
4	1	12.00	12.19	12.19	12.19	200.4	79.8	1.09	1.41	1.24	484	0
5	1	18.00	18.19	18.19	18.19	204.0	55.8	1.09	2.41	1.25	460	0
6	1	25.00	25.19	25.19	25.19	229.1	37.3	1.09	1.41	1.24	425	0
7	1	35.00	35.30	35.30	35.30	205.2	19.0	1.09	1.41	1.24	430	0
8	1	50.00	50.30	50.30	50.30	271.1	21.0	1.09	1.41	1.25	377	0

Figure 7.1a: Extracts from input commands and statistics of volume scan.

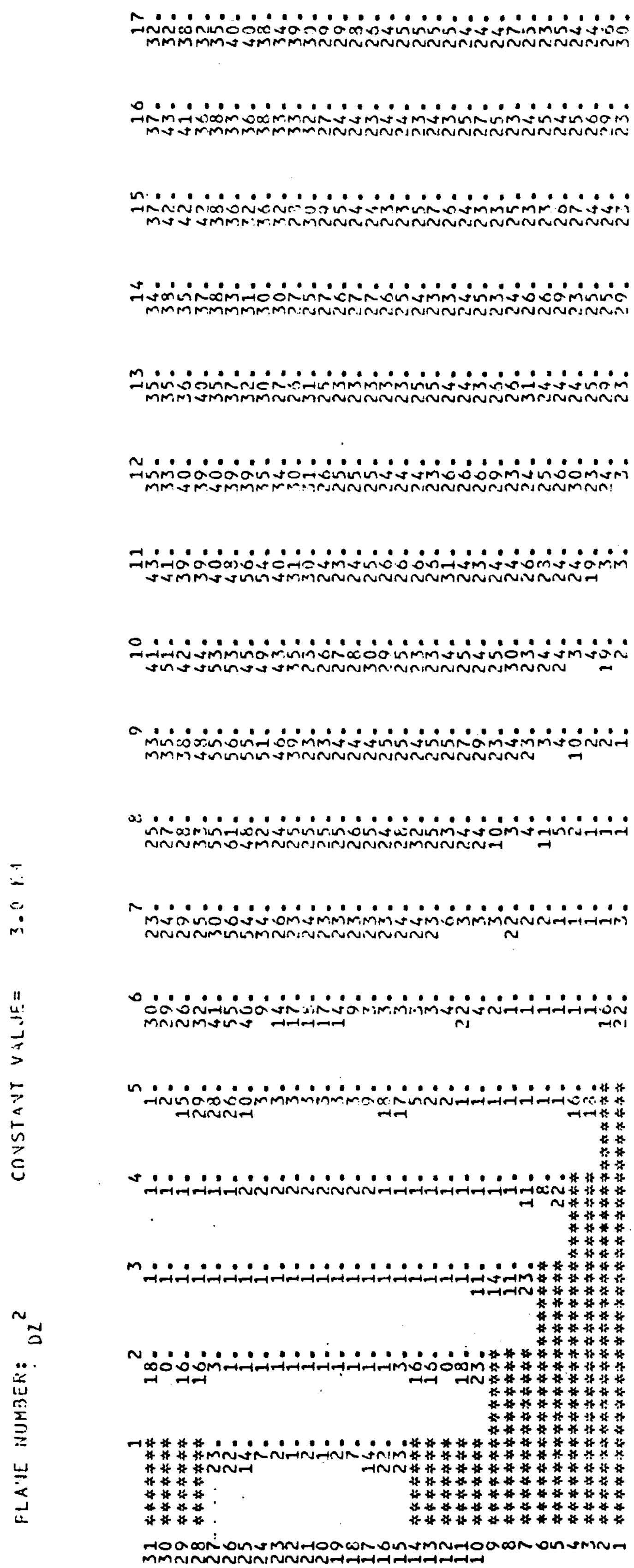

Figure 7.1b Radar reflectivity (dBZ) for CAPPI at 3,0 km AGL (only part of picture). The spacing of grid points is 1 km for both the x and y axis.

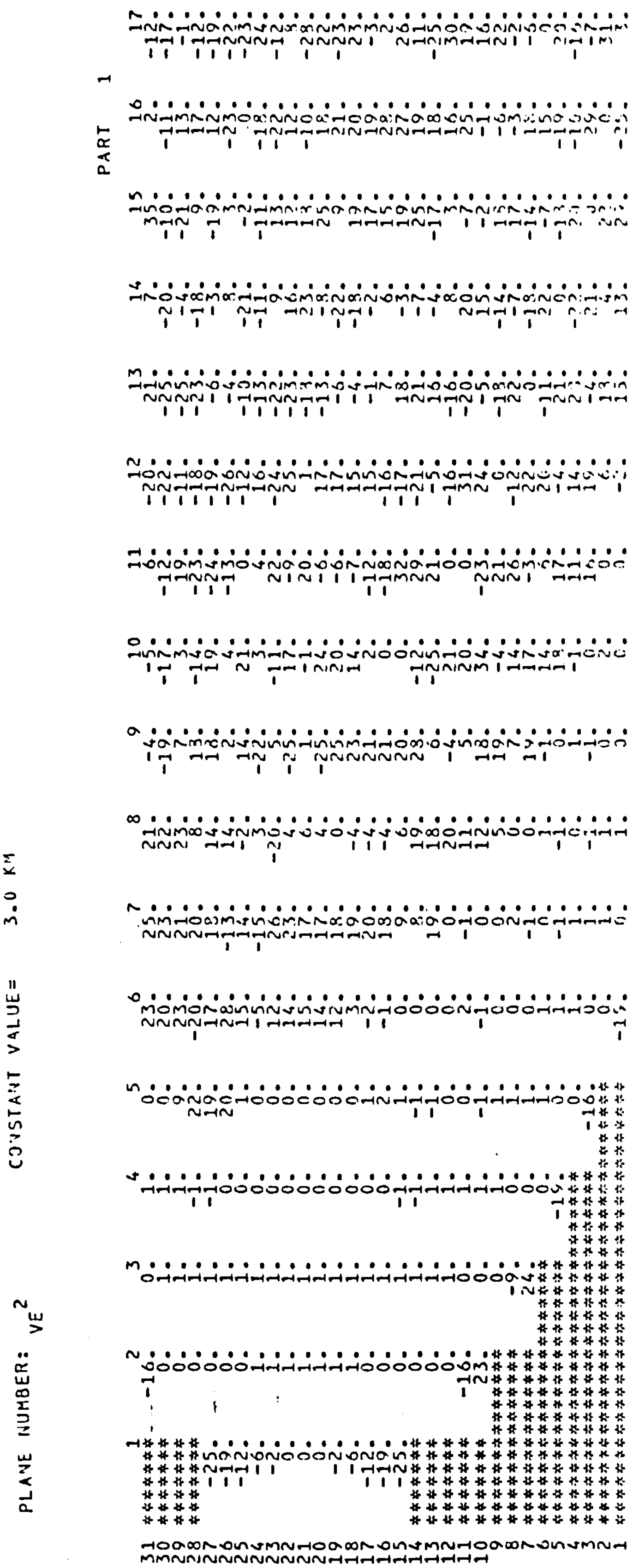

Figure 7.1c Velocity field ($m.s^{-1}$) for the CAPPI shown in Figure 7.1b

PLANE NUMBER: QU^2 CONSTANT VALUE= 3.0 KM

PART 1

	1	2	3	4	5	6	7	8	9	10	11	12	13	14	15	16	17
31	*******	61.	31.	32.	44.	15.	89.	99.	-81.	-13.	53.	3.	58.	68.	5.	-10.	10.
30	*******	61.	54.	24.	100.	15.	100.	48.	31.	-18.	1.	53.	-4.	8.	-51.	-28.	54.
29	*******	62.	54.	-49.	-12.	68.	100.	1.	-97.	-30.	29.	69.	48.	-25.	2.	15.	15.
28	*******	68.	46.	-49.	83.	27.	67.	30.	46.	-14.	35.	32.	81.	15.	6.	2.	30.
27	21.	68.	32.	44.	66.	-23.	49.	-7.	51.	-7.	-11.	58.	1.	-53.	-10.	-13.	2.
26	61.	31.	32.	44.	36.	32.	48.	30.	34.	9.	-16.	-35.	23.	52.	-16.	29.	-32.
25	61.	31.	24.	100.	-28.	41.	14.	-48.	65.	50.	-33.	-17.	18.	61.	94.	-75.	57.
24	61.	54.	24.	100.	39.	-11.	-47.	-63.	-9.	-38.	23.	-7.	27.	49.	13.	23.	3.
23	61.	54.	24.	100.	100.	17.	34.	40.	50.	46.	17.	49.	-14.	-16.	69.	75.	13.
22	62.	54.	24.	63.	100.	17.	63.	-80.	90.	-33.	42.	-19.	-20.	6.	-18.	-22.	28.
21	62.	54.	24.	63.	100.	17.	96.	-52.	-70.	-39.	49.	55.	73.	43.	10.	-75.	55.
20	62.	54.	24.	63.	100.	17.	96.	-52.	87.	14.	-52.	49.	27.	-14.	40.	29.	79.
19	61.	54.	24.	100.	100.	17.	91.	-52.	87.	14.	-54.	54.	47.	14.	20.	97.	41.
18	61.	54.	24.	100.	39.	-40.	91.	31.	87.	14.	36.	54.	47.	42.	100.	98.	95.
17	61.	31.	24.	100.	39.	45.	91.	31.	95.	-56.	36.	1.	47.	-79.	54.	22.	-42.
16	61.	31.	32.	44.	39.	45.	47.	31.	95.	101.	19.	6.	59.	-3.	54.	48.	-113.
15	21.	63.	32.	44.	-32.	45.	47.	-54.	43.	101.	19.	38.	97.	-3.	47.	41.	30.
14	*******	68.	46.	-49.	-32.	100.	29.	96.	23.	43.	35.	37.	97.	47.	89.	100.	39.
13	*******	62.	54.	-49.	63.	100.	17.	96.	-52.	87.	14.	-54.	54.	47.	42.	54.	26.
12	*******	61.	54.	24.	100.	39.	-40.	91.	31.	95.	101.	36.	6.	59.	-3.	47.	40.
11	*******	61.	31.	32.	44.	39.	45.	47.	-54.	43.	43.	19.	33.	97.	47.	39.	100.
10	*******	-43.	68.	46.	-49.	-32.	100.	29.	96.	22.	87.	14.	-54.	54.	47.	-79.	54.
9	*******	*******	62.	54.	24.	63.	100.	-40.	91.	31.	95.	101.	19.	38.	97.	47.	89.
8	*******	*******	61.	31.	32.	44.	39.	45.	47.	45.	23.	43.	36.	-54.	54.	47.	-79.
7	*******	*******	-43.	68.	45.	-49.	63.	100.	17.	96.	-52.	87.	-56.	19.	33.	97.	47.
6	*******	*******	*******	62.	54.	24.	100.	39.	45.	47.	-54.	43.	43.	36.	-54.	54.	47.
5	*******	*******	*******	61.	31.	32.	44.	-32.	100.	29.	[illegible]	31.	95.	101.	17.	38.	97.
4	*******	*******	*******	*******	62.	54.	24.	100.	39.	45.	47.	45.	23.	43.	14.	36.	6.
3	*******	*******	*******	*******	61.	31.	32.	44.	-32.	100.	17.	91.	31.	95.	43.	35.	-54.
2	*******	*******	*******	*******	*******	62.	54.	24.	100.	39.	45.	29.	96.	-52.	27.	101.	19.
1	*******	*******	*******	*******	*******	61.	68.	46.	-47.	63.	100.	45.	47.	45.	23.	37.	-55.

Figure 7.1d Quality field (percent) for the CAPPI shown in Figure 7.1b Data points with percentages between -60,0 and 60,0 should be carefully examined before accepting or discarding these data.

```
DZ           XY KM          MEAN      STDV        N     I1    I2    J1    J2          MIN      MAX
             VOLUME         26.31     9.24     3729      1    31     1     4          0.4     60.8
        HISTOGRAM          (SCALED BY    1.00)        1479 BAD POINTS
(         ,      0.00):                                                                       0.00
(     0.00,      5.00): ***                                                                   3.33
(     5.00,     10.00): ***                                                                   3.49
(    10.00,     15.00): **                                                                    1.56
(    15.00,     20.00): **                                                                    1.58
(    20.00,     25.00): ******************************************                           41.65
(    25.00,     30.00): **************************                                           25.85
(    30.00,     35.00): *********                                                             8.88
(    35.00,     40.00): ******                                                                6.01
(    40.00,     45.00): ***                                                                   3.22
(    45.00,     50.00): **                                                                    2.23
(    50.00,     55.00): **                                                                    1.80
(    55.00,     60.00):                                                                       0.40
(    60.00,     65.00):                                                                       0.03
(    65.00,     70.00):                                                                       0.00
(    70.00,     75.00):                                                                       0.00
(    75.00,     80.00):                                                                       0.00
(    80.00,     85.00):                                                                       0.00
(    85.00,     90.00):                                                                       0.00
(    90.00,     95.00):                                                                       0.00
(    95.00,      +    ):                                                                      0.00
      INTERVALS          ....+....+....+....+....+....+....+....+....+                        PER
                             5%  10%  15%  20%  25%  30%  35%  40%  45%                      CENT
```

Figure 7.2 Frequency distribution of reflectivity values within the volume scan on 16 November 1987, 17:13:49 - 17:16:17, generated by 'CEDRIC'.

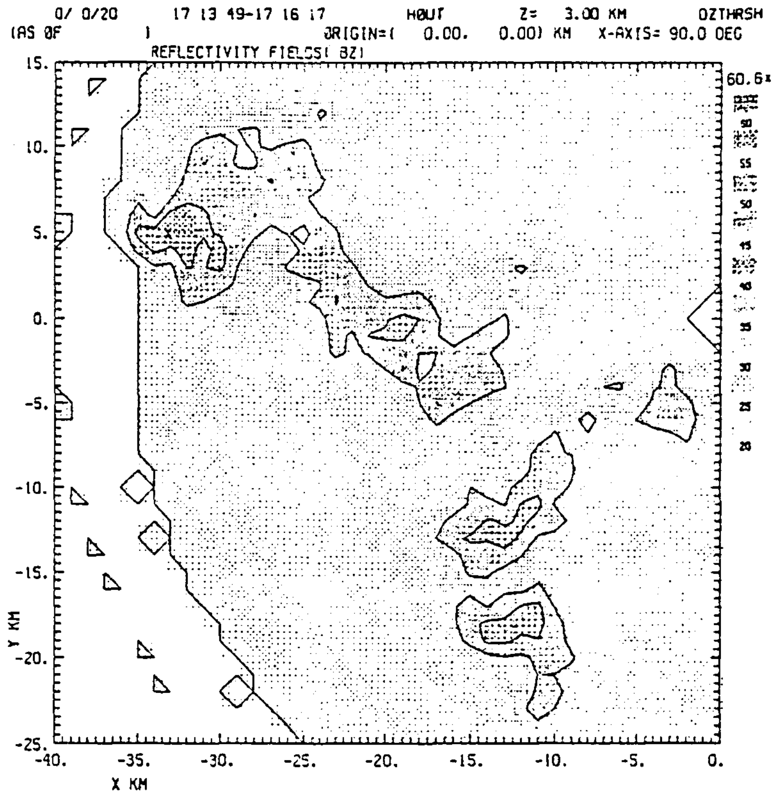

Figure 7.3 CAPPI at 3 km AGL showing radar reflectivities (dbZ) for part of the volume scan on 16 November 1987, 17:13:49 - 17:16:17, generated by 'CEDRIC'.

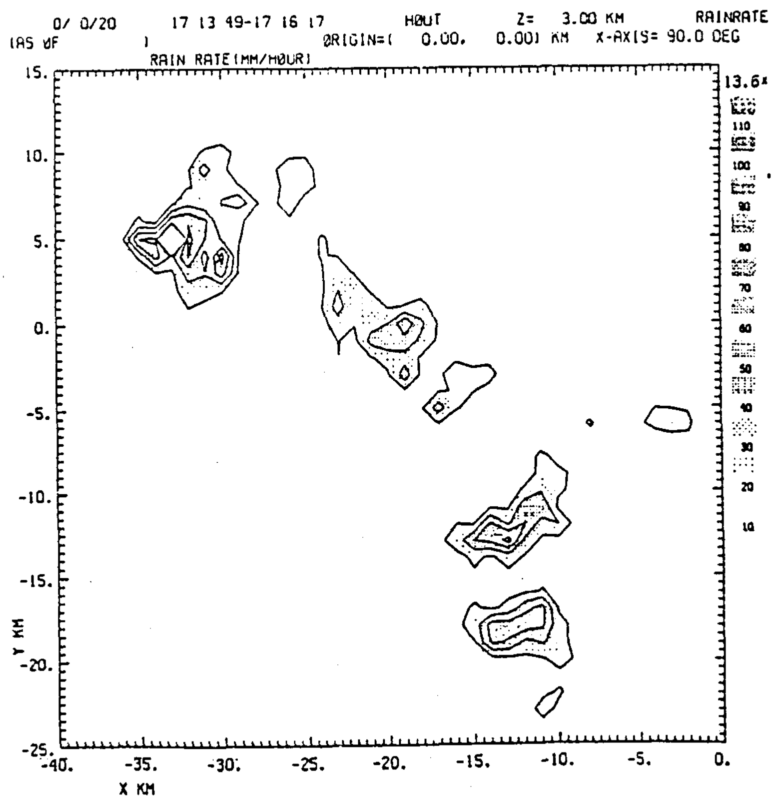

Figure 7.4 Rainfall rates ($mm.h^{-1}$) for above CAPPI, also generated by 'CEDRIC'.

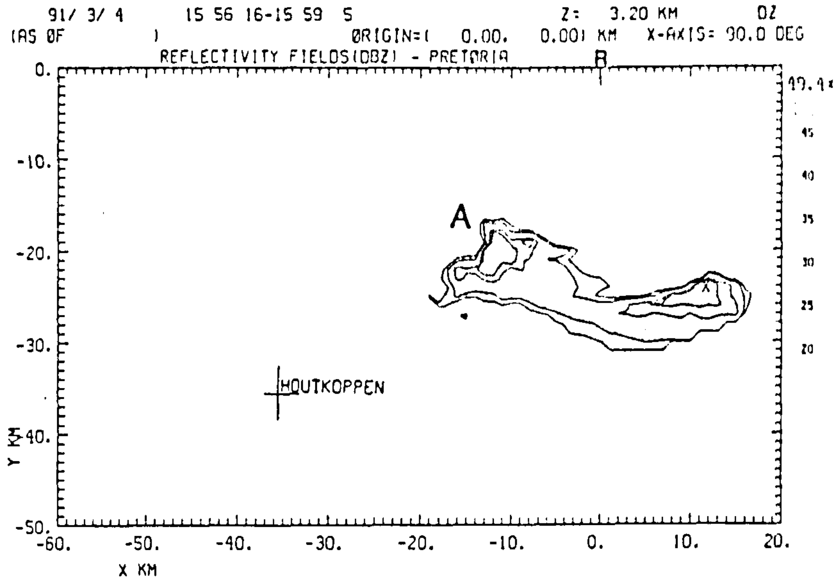

4,2 km

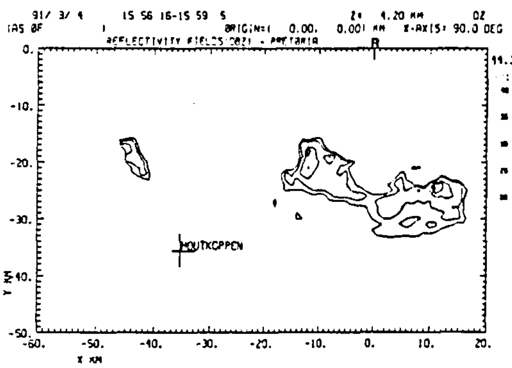

6,2 km

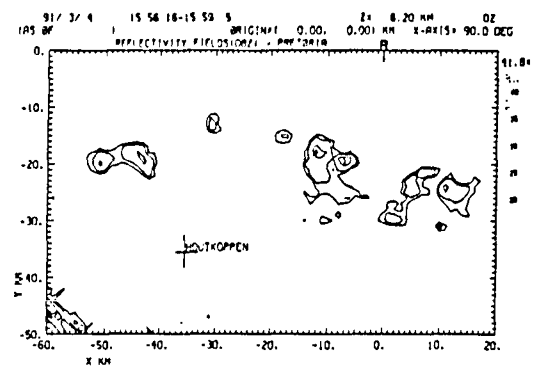

5,2 km

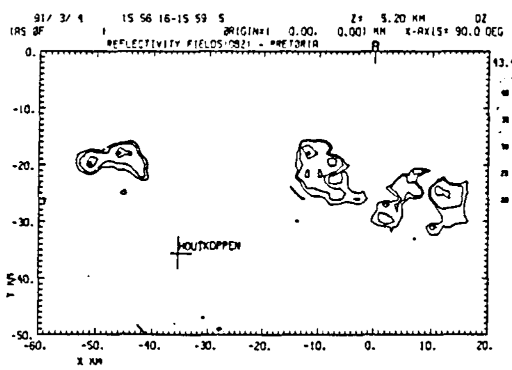

7,2 km

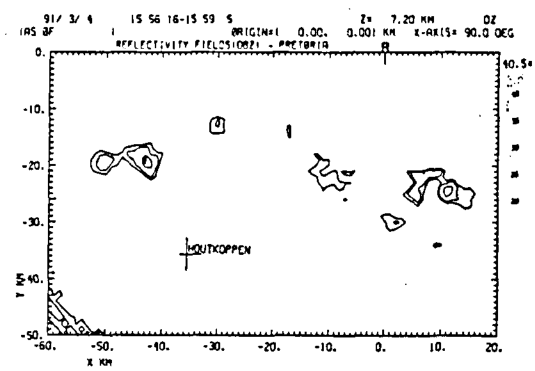

Figure 7.5a: CAPPIs generated by SPRINT and plotted by CEDRIC, showing reflectivity contours in dBZ of a storm observed by the Pretoria Doppler radar on 4 March 1991 at 15:56 at 3,2 km, 4,2 km, 5,2 km, 6,2 km and 7,2 km MSL (outer contour is 20 dBZ, contour interval is 5 dB, scale in km relative to the Pretoria radar R).

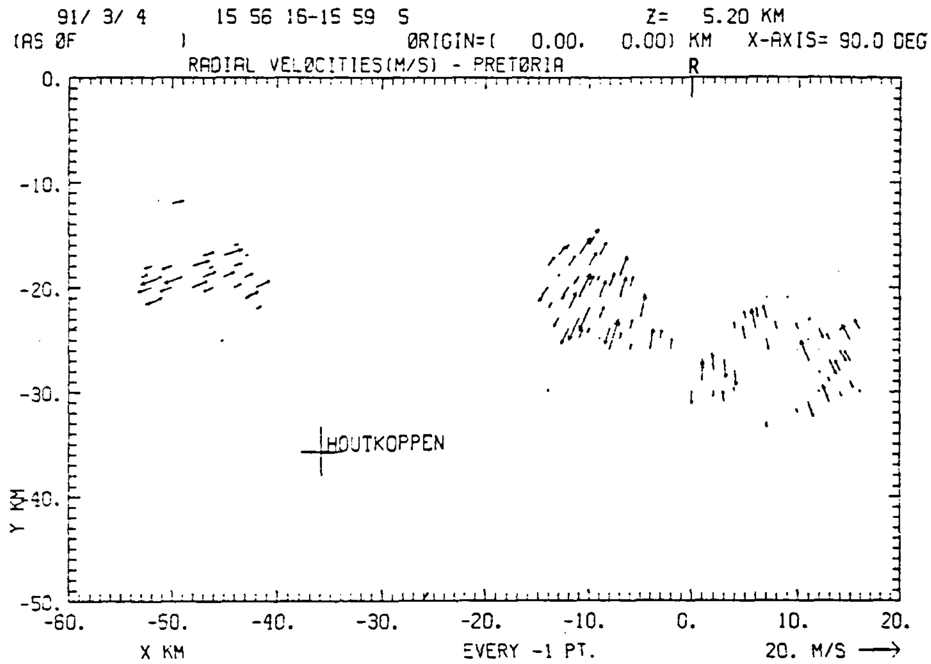

Figure 7.5b: CAPPI at 5,2 km MSL showing radial wind vectors for the same scan as in Figure 7.5a.

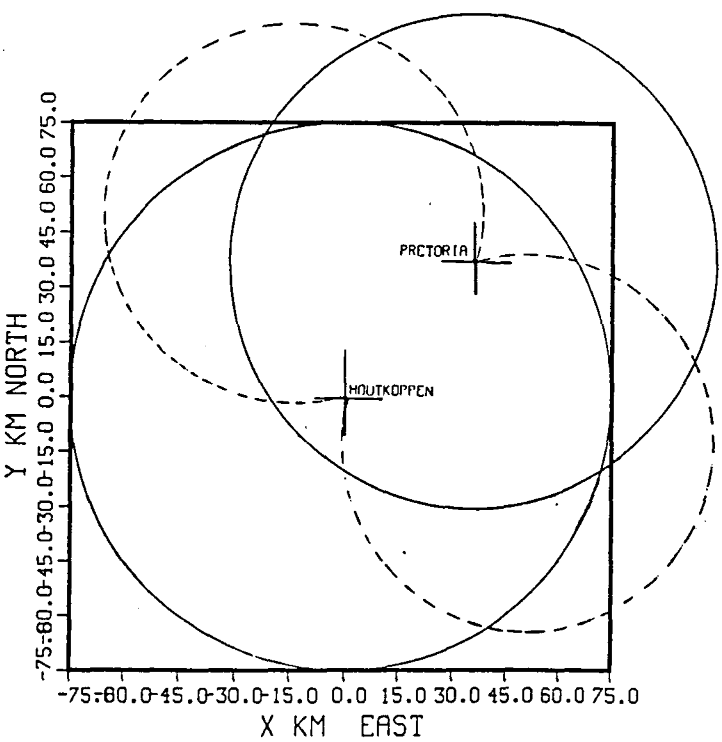

Figure 7.6: Maximum range of Doppler radars at Houtkoppen and Pretoria (full circles) and area of optimal dual Doppler radar coverage (dashed line).

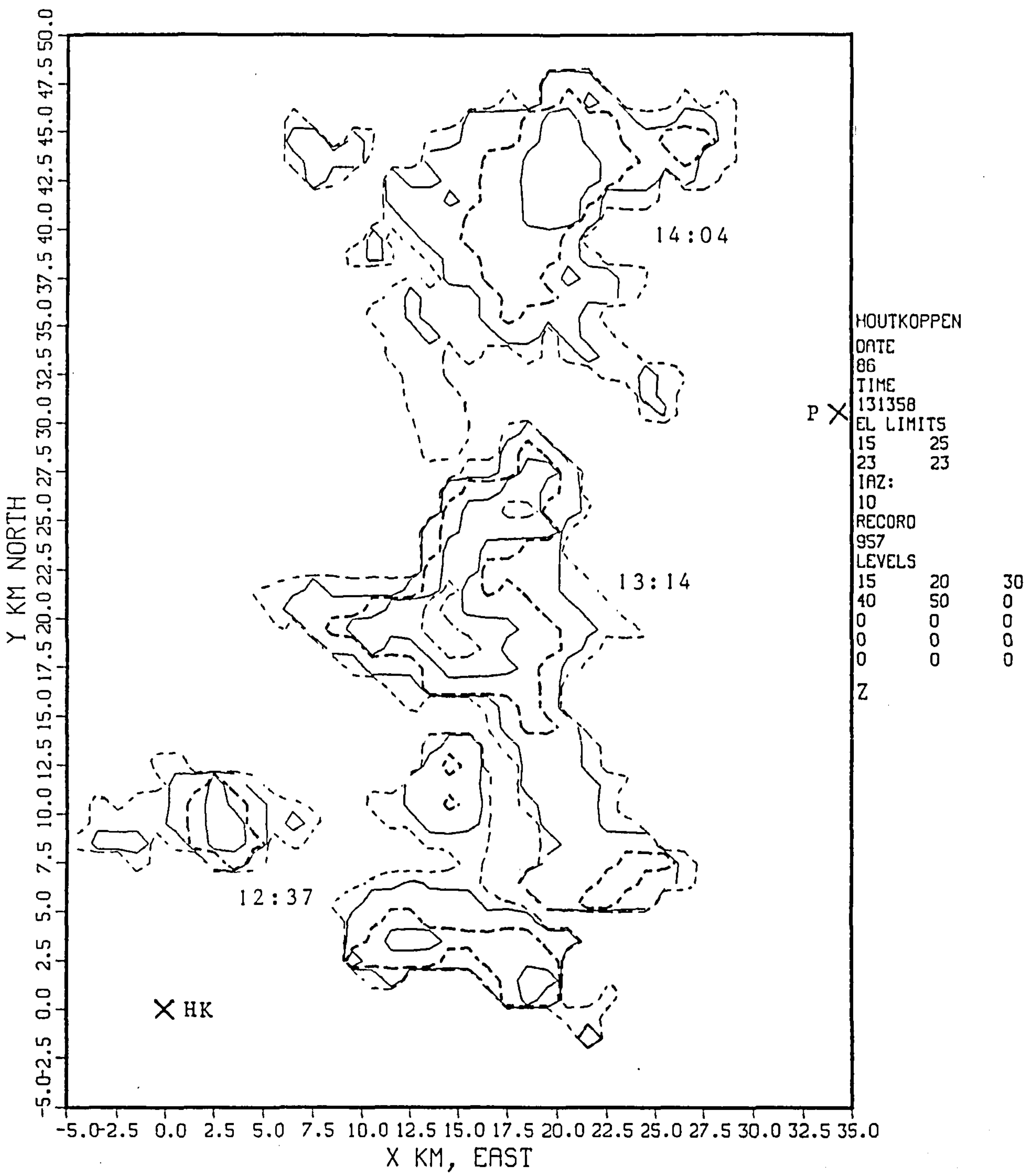

Figure 7.7: Schematic history of an isolated multi-cellular storm on 26 March 1991, based on 2° elevation PPIs as recorded at Houtkoppen. Reflectivity contours are 15, 20, 30, 40 and ≥ 50 dBZ, using the conventional CSIR PPI plotting routines. The positions of the radars are marked HK (Houtkoppen) and P (Pretoria).

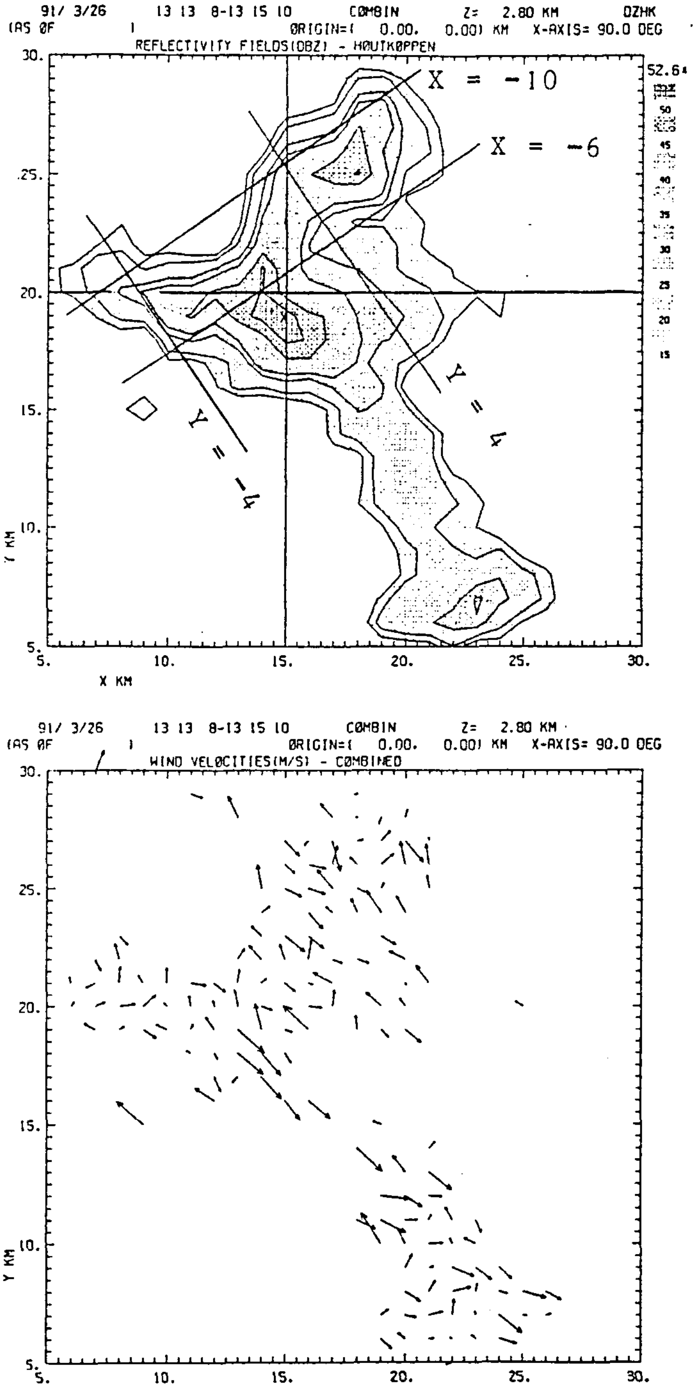

Figure 7.8: CAPPI at 2,8 km MSL (approximately 1,3 km AGL) of the storm on 26 March 1991 calculated by CEDRIC from a volume scan between 13:13:08 and 13:15:10.
Top: reflectivity contours in dBZ, intervals of 5 dB, observed by Houtkoppen radar.
Bottom: horizontal wind velocity field in m.s^{-1} synthesized from Houtkoppen and Pretoria Doppler radar observations.
The scale of these plots is the same as in Figure 7.7. The baselines of the vertical cross-sections are indicated.

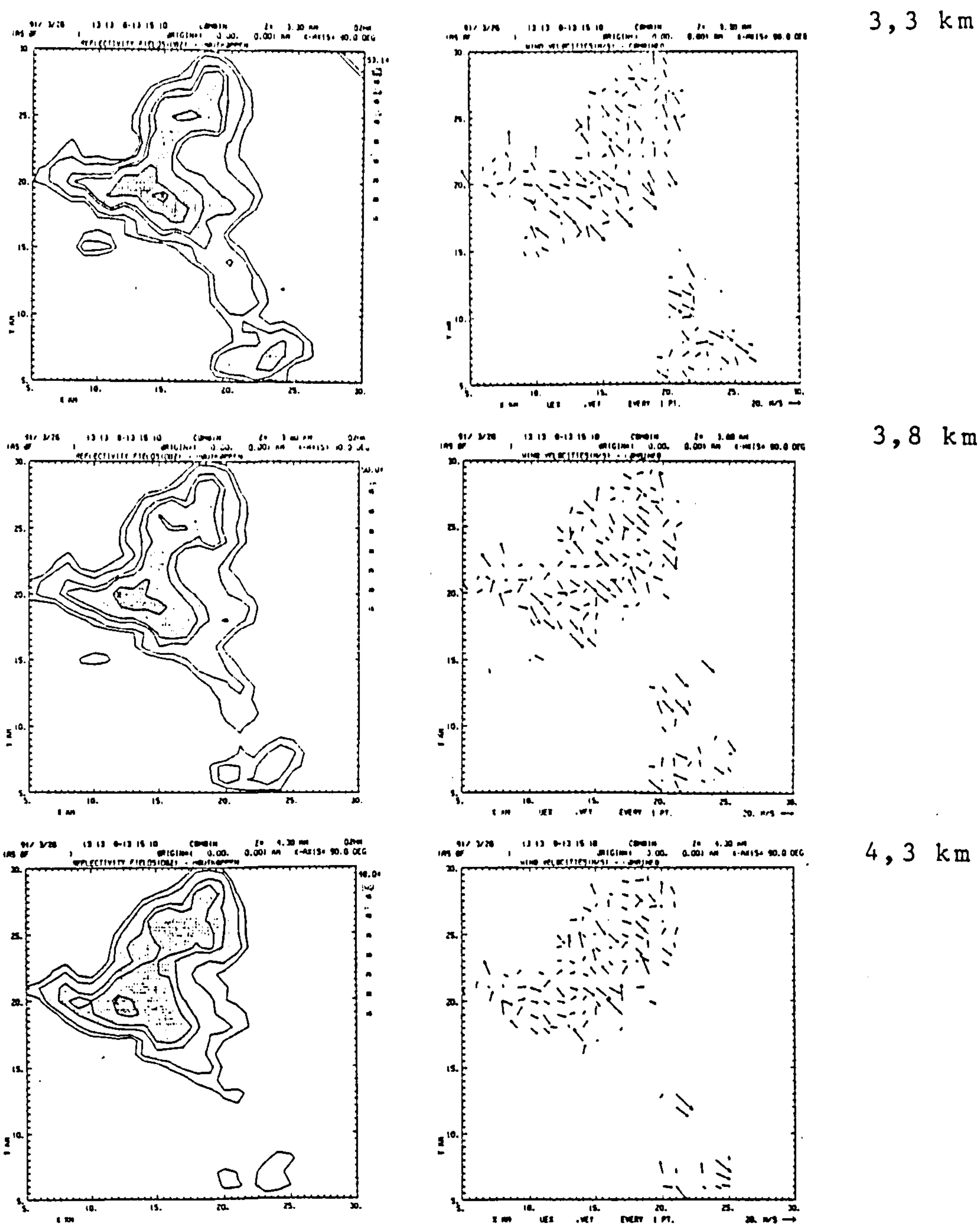

Figure 7.9: CAPPIs of the storm on 26 March 1991 (volume scan 13:13:08 - 13:15:10) at 500 m height intervals, showing reflectivity and horizontal air flow patterns.

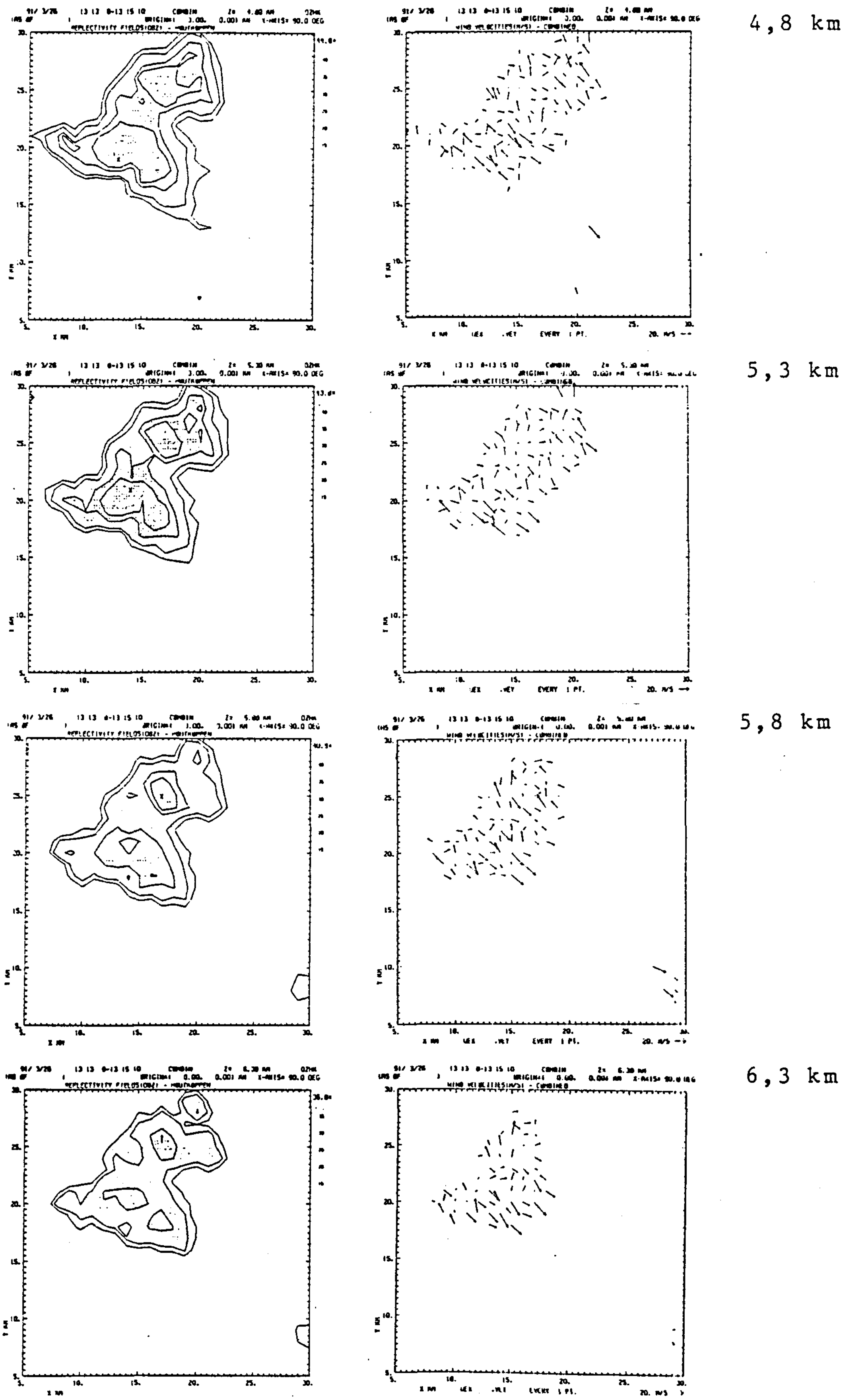

Figure 7.9: Continued

6,8 km

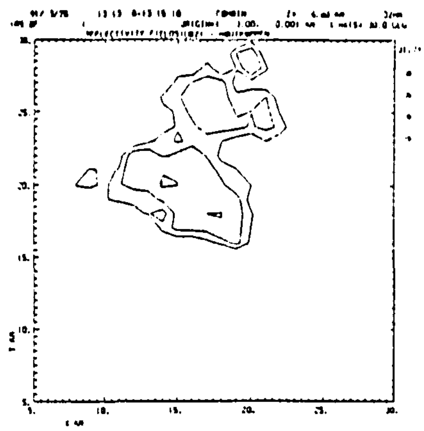

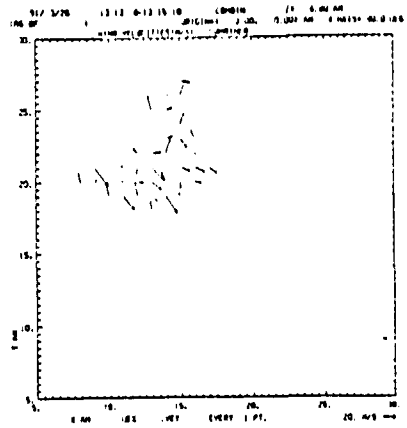

7,3 km

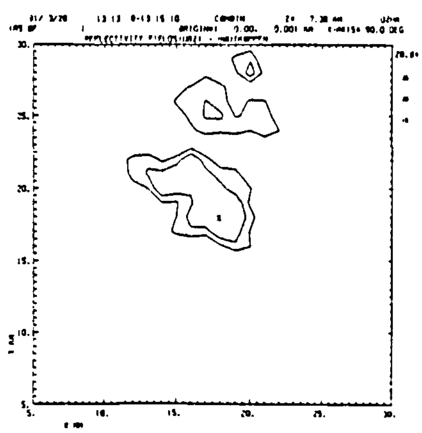

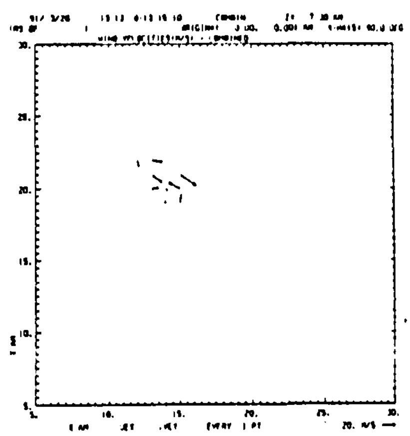

7,8 km

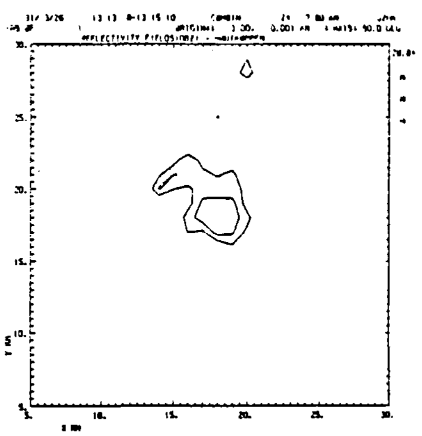

The air flow could not be calculated at this level because the echo is on the baseline between the two radars and therefore only spurious values are generated.

8,3 km

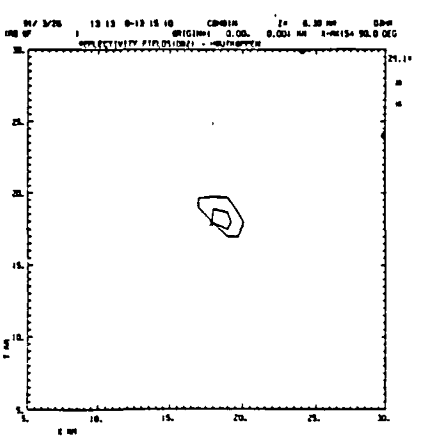

The air flow could not be calculated at this level because the echo is on the baseline between the two radars and therefore only spurious values are generated.

Figure 7.9: Continued

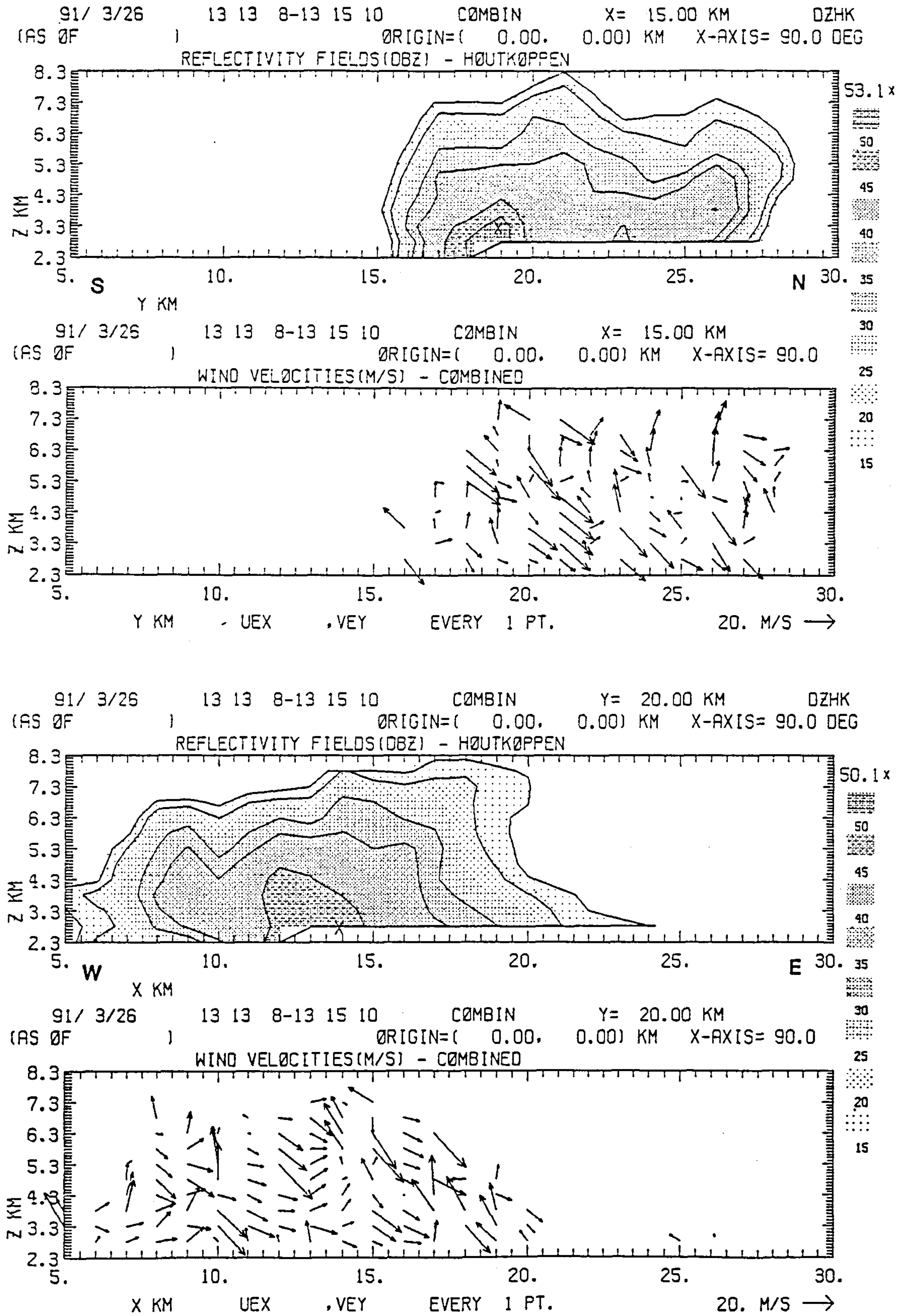

Figure 7.10: Vertical cross-sections through the storm shown in Figure 7.9 along baselines from south to north and west to east (see Figure 7.8 for exact position of baselines).

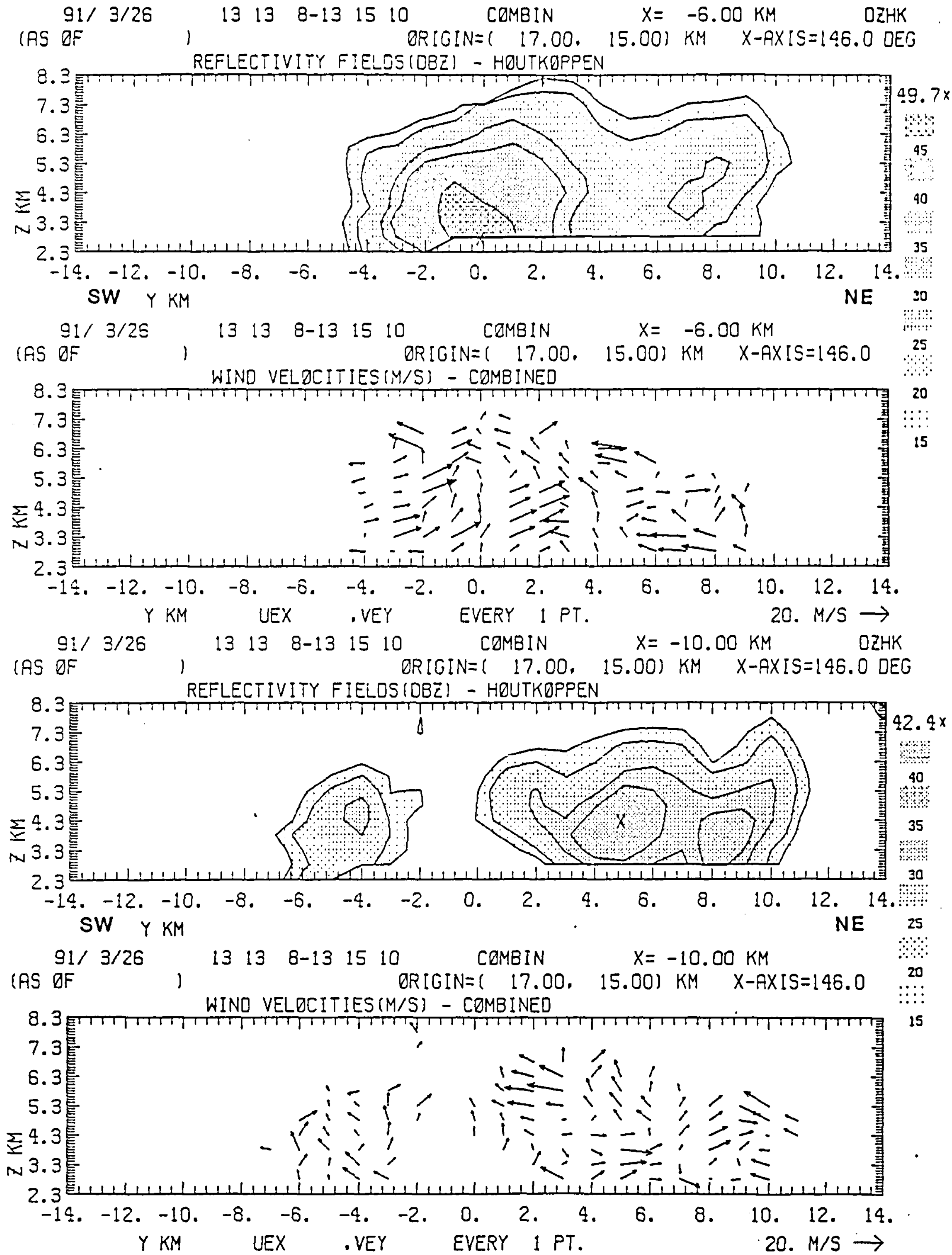

Figure 7.11a: Vertical cross-sections through the storm shown in Figure 7.9 along baselines from southwest to northeast (see Figure 7.8 for exact position of baselines).

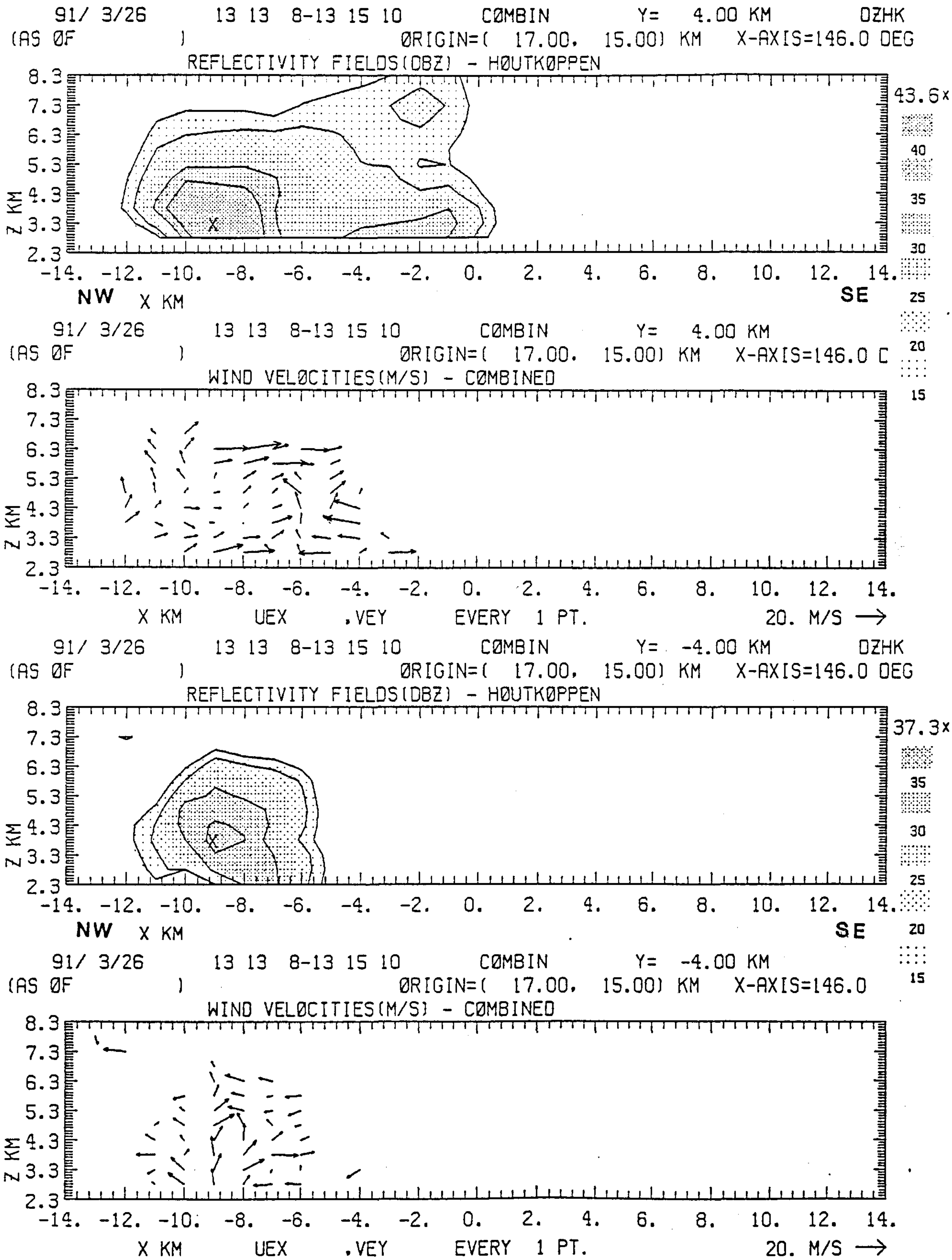

Figure 7.11b: Vertical cross-sections through the storm shown in Figure 7.9 along baselines from northwest to southeast (see Figure 7.8 for exact position of baselines).

8. CONCLUSIONS AND RECOMMENDATIONS

This Section is not intended to repeat any of the conclusions already made by the respective authors at the end of every Section, but rather to highlight the most significant findings on which the recommendations are based.

The original proposal for the three-year PRAI project was aimed at providing supplementary information on precipitation processes on the Highveld for on-going weather modification research projects which are being sponsored by the Water Research Commission (WRC) and the South African Weather Bureau. It had been realised that accurate measurement of total areal rainfall is of prime importance for precipitation enhancement projects. It was therefore proposed to establish relationships between:

- the spatial distribution of precipitation within clouds and the internal air flow in thunderstorms,

- the surface precipitation (rain and hail) patterns and the three-dimensional air flow in storms,

- rainfall intensities as measured by rain gauges and the reflectivity recorded by radar.

It was also proposed to verify or reject the hypothesis of accumulation zones above the main updraught region and to *possibly* identify storm systems which have a good potential for producing rain on the ground, but are inefficient in their mechanism and would therefore be more suitable for cloud seeding operations than naturally efficient clouds.

A request to appoint an additional climatologist for the second and third year of the PRAI project was approved by the WRC. Thus, the research proposal could be expanded to include detailed studies of raindrop-size distributions and Z-R relationships in an attempt to improve the accuracy of radar measurements of areal rainfall. In line with this objective was also the investigation of the V-ATI (Volume x Area-Time-Integral) of radar reflectivity. These research objectives were focused even sharper at the end of the second year, based on results achieved thus far, as well as on recommendations of the *Workshop on Rainfall Stimulation Research in South Africa*, which was held during August 1989.

The WRC also approved further funds for additional analysis work under the project name DOPDATE, which was to run concurrently with the PRAI project during 1990. The emphasis of the new project was on the selection and analysis of convective clouds at a very early stage in their life cycle, in order to verify and *possibly quantify* the daughter-cell and feeder-cell cloud merging concepts of storm mechanisms on the Highveld.

The joint execution of both projects resulted in a drastic improvement of the sensitivity of the Houtkoppen S-band radar; also the other two C-band radars were to have come on line during the 1989/90 rainy season; the CRAY computer programs should be verified and tested and the EVAD (Extended Velocity-Azimuth Display) method should be investigated as a means for extracting maximum information from existing single-Doppler radar data.

The objectives as summarised above and in detailed annual Work Programmes which were approved by the Steering Committee, have by and large been achieved. Unfortunately, the implementation of the multiple Doppler radar facility was delayed significantly, due to unforeseen reasons stated in Section 1 of this report. However, the facility is now operational (since February 1991) and examples of the horizontal and vertical air flow in an isolated storm have been included in this report in order to demonstrate the application and versatility of the CRAY programs which were adapated and installed on the CSIR VM mainframe computer.

For completeness of this final report it seems appropriate to extract some of the conclusions from the previous annual progress reports (Gomes and Held, 1988; Gomes, O'Beirne and Held, 1989; see Section 1 for full references).

In the first preliminary report, Gomes and Held (1988) presented a review of the characteristics related to severe weather phenomena with special emphasis on squall lines. These mesoscale systems have been found to be very effective in producing rain. The attention had been focused on observations made during the 1987/88 season. A 12-day period during November 1987 was investigated when several severe storms occurred (9 to

20 November 1987). Conserved parameters like the equivalent potential temperature were selected to represent the thermodynamic structure of the atmosphere, which is modified by large-scale downdraughts after the passage of a disturbance. Two particular days within the period (10 and 19 November 1987) were chosen for detailed analysis, because, on the first day, storms were very effective rain producers, while on the second severe hail storms occurred.

The similarities in the two storms which occurred during November 1987, with other case studies from earlier years could be emphasized as far as the multicellular structure is concerned and the penetration into the tropopause on one of the days. Certainly the key answer resides in the structure of the internal air flow characteristics of each particular storm. Considering differences and similarities between the two storms (10 and 19 November 1987) one could designate the apparent semi-stationary nature with individual cells moving at about the same speed as the complex as a whole in the first case and individual cells moving twice as fast as the complex in the second. Echo tops reached great heights in both cases, but they only penetrated the tropopause on 19 November. Maximum reflectivities during approximately 20 minutes were between 67 and 69 dBZ during the most intense phase of the storm on 10 November (Figure 8.1). At that stage the ascending core and subsequent descending core are observed in intense downdraught regions (Figure 8.2). Radar reflectivities of 67 dBZ were present in the storm on 19 November which were very persistent in time, filled a large volume and were of great vertical extent, indicating the presence of strong updraughts in the cloud, which can be highlighted by examining the corresponding radial velocity fields (Figures 8.3a and b).

Only minor differences in the three-dimensional radar reflectivity pattern were found between the two storm systems. The basic difference seems to reside in their air flow structure as can be seen from the resultant radial velocity fields recorded by the Doppler radar. Although these findings were preliminary, the potential to use Doppler radar to identify efficient rain producing systems and severe weather has been clearly demonstrated.

In the second Progress Report (Gomes *et al.*, 1989) more insight into the behaviour of storms has been gained by expanding the number of case studies that include Doppler radar data. Although generalisations concerning the exact patterns of air flow would have been premature, it was becoming increasingly obvious that answers to key issues concerning the structure and dynamics of thunderstorm development are to be found in the internal flow patterns of each particular storm.

The case study of 7 January 1988 presented by Gomes *et al.* (1989) exhibits some type of organisation during its mature stage, where rotation represented by some symmetry in the radial velocity field through the core of the storm suggests the presence of strong updraughts. This is in accordance with observations reported from North America.

If signatures of the radial velocity field observed in the storm of 19 November 1987 are compared with those for the 7 January 1988 storm, some significant differences in the air flow structure can be identified. On 19 November 1987, the presence of couplets of opposing radial velocities aligned azimuthally suggests a meso-cyclone signature not observed in the storm on 7 January 1988 (Figures 8.4 and 8.5). The first one did produce severe hail while no hailfall but good rain was reported from the second one while traversing the hail-reporting network.

The study of the storm that occurred on 27 December 1987 indicated that a relationship exists between air flow and dynamic interaction between storm cells and cloud complexes. The importance of such dynamic interaction is not to be overlooked, particularly in the light of the fact that the merging of the large multicellular complexes coincided with hail and heavy rainfall at the ground. The importance of understanding air flow conditions that lead to the development of feeder clouds is related to the ways in which these cells may contribute to the enhanced vigour of the storm system. The possibility of a synergistic effect as a result of the merging of the two multicellular complexes or of the incorporation of a feeder cell into the main cloud complex cannot be discounted.

Highlights from the third year of investigations are:

- Results achieved with applying the EVAD (Extended Velocity-Azimuth Display) method to derive precipitation efficiency from single-Doppler radar observations (Section 2.2 in this report).

- The investigation of raindrop size distributions and Z-R relationships, which showed that, based on the entire season's data, underestimation or overestimation of rainfall rate using an average Z-R relationship is a function of changes in the drop size distribution and not in rainfall rate (Section 3 in this report).

- Results based on the V-ATI (Volume versus Area-Time-Integral) which showed that average rainfall rates for convective storms over the Transvaal Highveld calculated using a V-ATI relationship were seen to be higher than those for other parts of the world but this is in keeping with characteristics of South African storms (Section 4 in this report).

- Preliminary findings from detailed case studies of storm merger mechanisms in South Africa, with special emphasis of reflectivity and air flow patterns in daughter-cell and feeder-cell merger situations (Sections 5 and 6 in this report).

Based on the findings of both the PRAI and the DOPDATE projects, the following recommendations are made:

- Following the recommendations of the *Workshop on Rainfall Stimulation Research in South Africa* (Berg-en-Dal Conference Centre, Kruger National Park, 21-23 August 1989) which was attended by all leading scientists in the field of cloud physics in South Africa and by four overseas experts, all available resources, both in manpower and hardware, should be coordinated in a National Research Project, in order to obtain the optimal benefit from such a unique set-up.

- Since the CSIR multiple Doppler radar facility is still the only one in South Africa which deploys S- and C-band Doppler radars for thunderstorm research, it seems only logical to maintain such a unique asset, especially now, since the first dual Doppler radar observations have become available. This had also been emphasized by the overseas consultants on many occasions.

  However, the CSIR cannot carry the full burden of maintaining and further developing the three Doppler radars without external support from either Government Departments or the Water Research Commission.

- At least one complete season of good dual or triple Doppler radar observations should be available to perform some important climatological investigations such as the frequency of occurrence of certain cloud merger situations in South Africa and their mechanisms and impact on rain stimulation efforts (e.g. daugher-cell versus feeder-cell cloud merger). A better understanding of the early cloud stages and of rapidly forming accumulation zones above a weak-echo-region would be equally important for cloud seeding experiments.

- Various improvements to the radar facility would be of great advantage, e.g.:

  - Addition of a polarisation facility for the detection of ice-phase precipitation aloft.

  - Real-time display of radial velocities at least at the Houtkoppen S-band radar.

- EVAD (Extended Velocity-Azimuth Display) method, based on a typical example, has been shown to be a suitable tool to derive precipitation efficiency from good single-Doppler radar observations of stratiform-type rainfall. Special scanning cycles should be incorporated in a Doppler radar research project in order to obtain a more representative sample of different synoptic situations conducive to uniform precipitation patterns from storms for which EVAD was applied to calculate precipitation estimates and efficiencies (more rain gauges, longer observational periods and a better time resolution would be required for fine-tuning EVAD in South African precipitation systems).

- Finally, it should be borne in mind that the above recommendations only address the most important issues, either in principle or in more detail for larger research components. There are numerous less spectacular suggestions inherent in the various individual conclusions contained in this report which should certainly not be neglected.

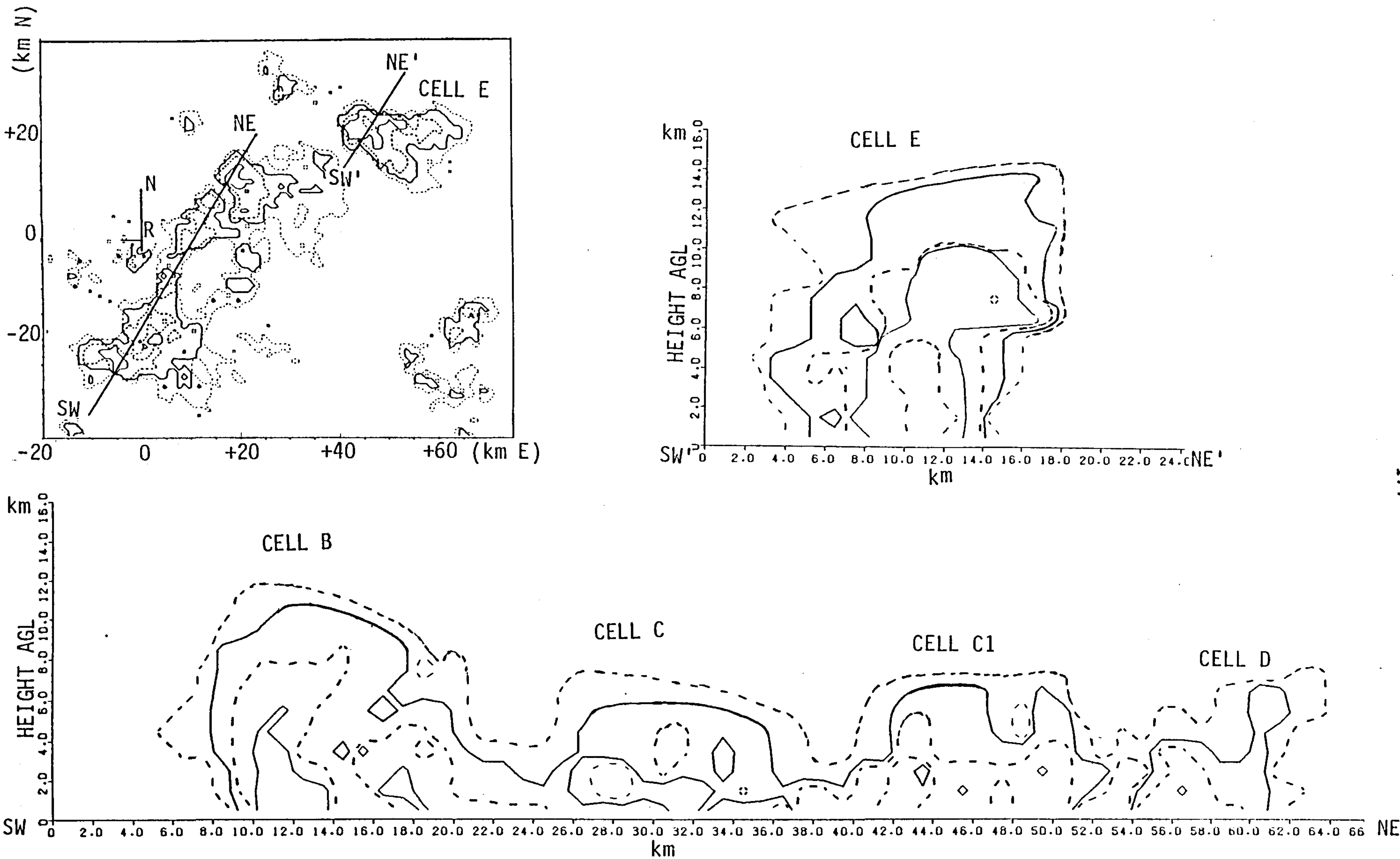

Figure 8.1: Computer plots of the squall line on 10 November 1987, 15h13. Top left: 2° PPI. Top right: Vertical cross-section through cell E from SW to NE as shown in the 2° PPI. Bottom: Vertical cross- section through the main storm as indicated by the base line.

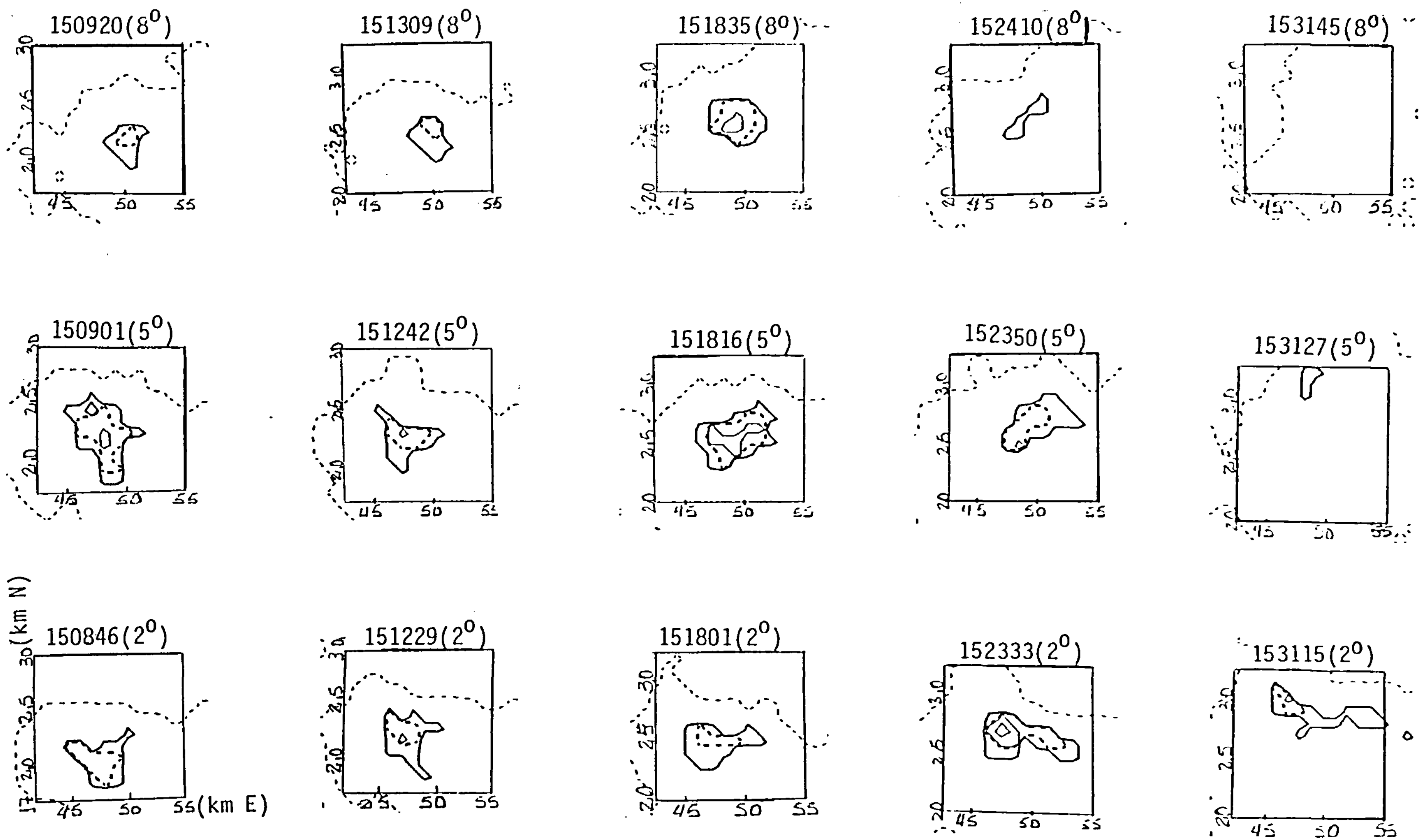

Figure 8.2: Radar signature associated with a downburst at the ground. Times in h:m:s; radar contours: 23, 47, 50, 53, 57 dBZ.

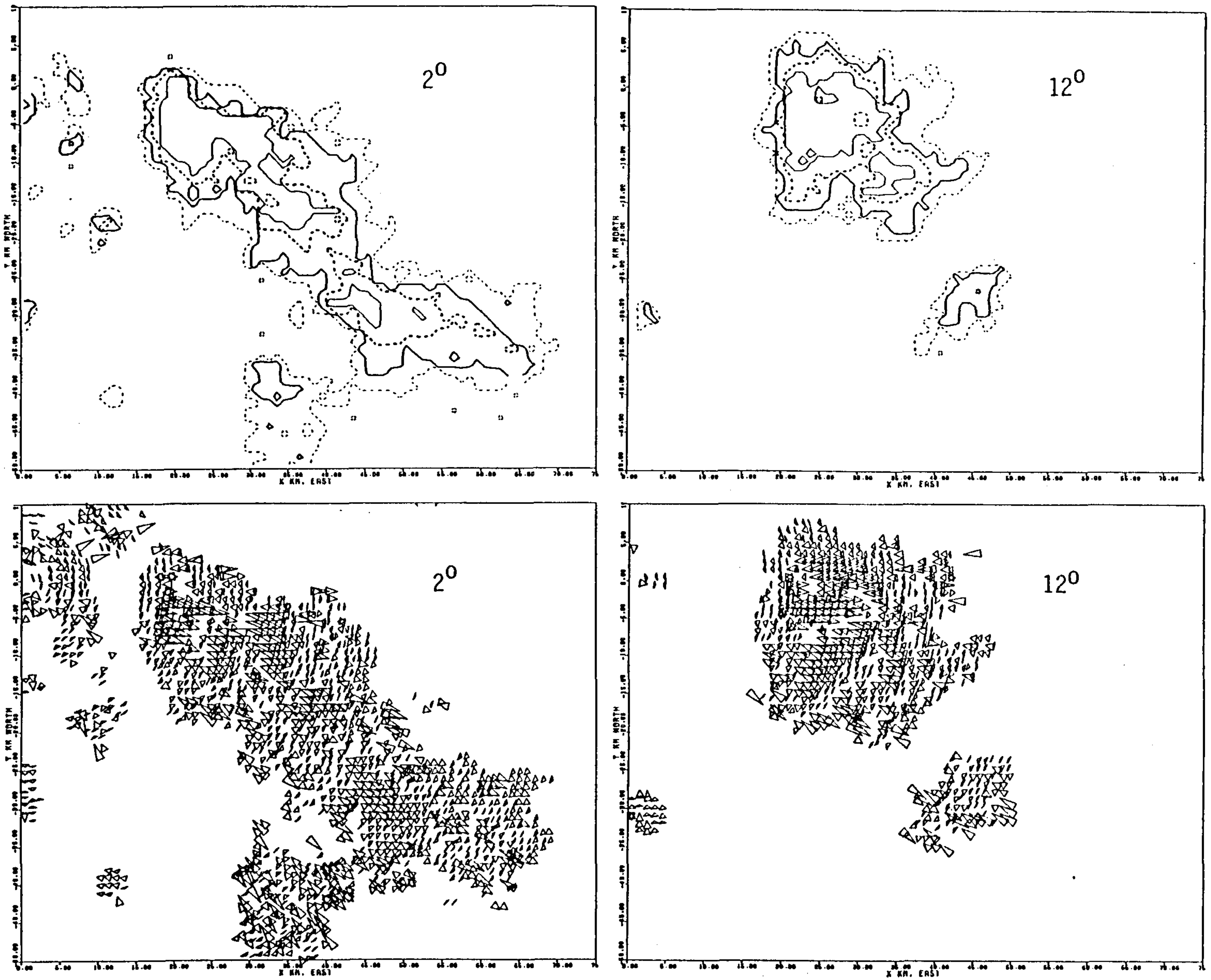

Figure 8.3a: 19 November 1987, 19h42: Radar reflectivity and airflow pattern at 2° and 12° elevation.

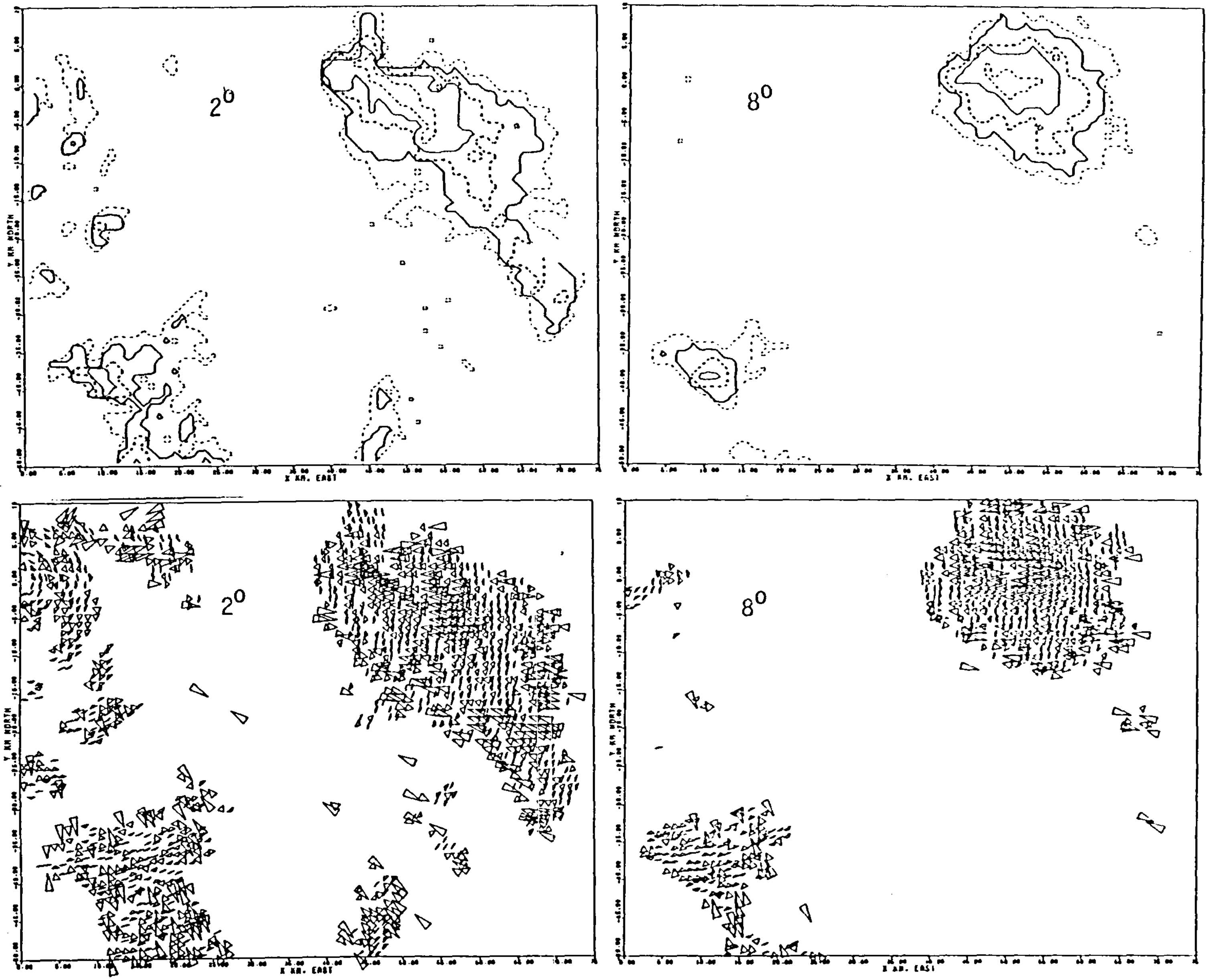

Figure 8.3b: 19 November 1987, 20h06: Radar reflectivity and airflow pattern at 2° and 8° elevation.

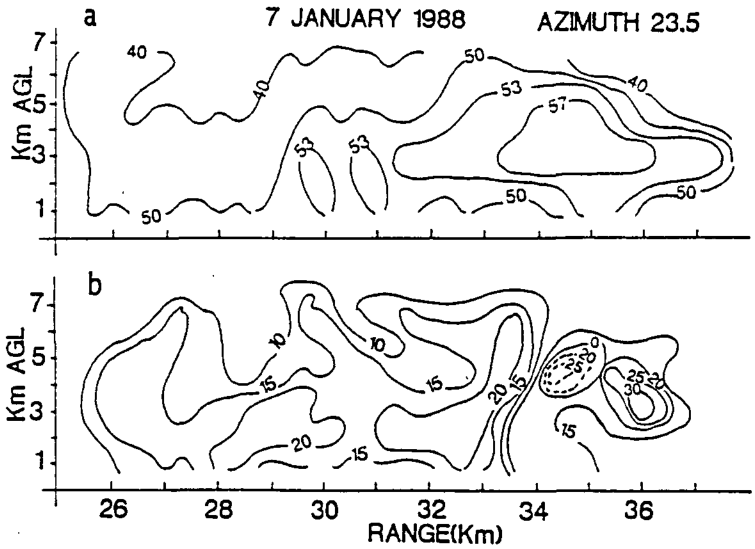

Figure 8.4: 7 January 1988, 22:05. RHI (Range Height Indicator) through azimuth 23,5°
(a) reflectivity contours in dBZ
(b) Doppler velocities in $m.s^{-1}$ (dashed lines: radial velocities away from the radar; solid lines: towards radar).

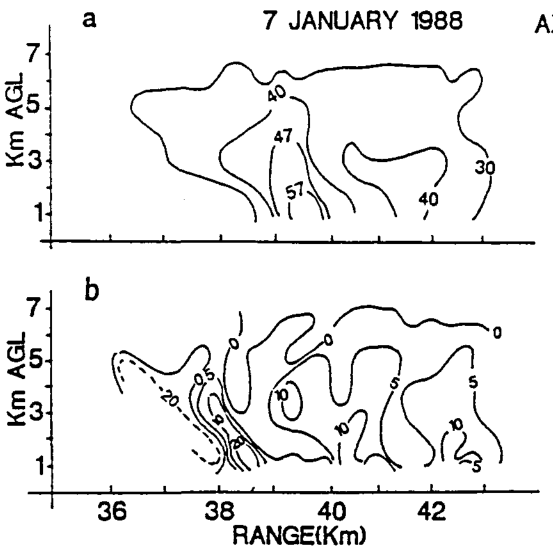

Figure 8.5: 7 January 1988, 22:27. RHI (Range Height Indicator) through azimuth 23,5°
(a) reflectivity contours in dBZ
(b) Doppler velocities in $m.s^{-1}$ (dashed lines: radial velocities away from the radar; solid lines: towards radar).

9. ACKNOWLEDGEMENTS

The *Precipitation and Air Flow (PRAI) Project* and the *Doppler Radar Data Processing (DOPDATE) Project* were financially supported by the Water Research Commission. However, research could not have been conducted without the vital support of the operational side of the project (hardware maintenance and data acquisition) by the CSIR Executive under the project MULDOP.

The staff of the radar facility provided the tools and the observations for the above research projects and their important contribution and dedication is gratefully acknowledged. A special word of thanks should go to Messrs M C Hodson, D J Dicks and G du Plessis for maintenance, development and radar observations.

Dr L J Miller of the National Center for Atmospheric Research in Boulder provided copies of the original CRAY programs, SPRINT and CEDRIC, which were then implemented on the CSIR's VM mainframe computer. He is sincerely acknowledged for this valuable contribution towards Doppler radar research in South Africa. Mrs E E Jacobs and Mrs R de Villiers are acknowledged for implementing the CRAY programs on the VM mainframe computer and for their assistance with the verification of these programs. Also, the staff of the CSIR Computer Centre is thanked for their patience and assistance in processing radar data tapes during the duration of the projects.

Certain meteorological data, mostly radiosonde observations, were supplied by the South African Weather Bureau and Mr J A Koch is thanked for his friendly assistance.

Miss Y Hong and Mrs L M Boatwright are thanked for assisting with the preparation of figures and the final report. The mammoth task of typing the manuscript was professionally handled by Mrs S G Good, who is wholeheartedly thanked for her part in completing this report.

10. APPENDIX A

Paper presented at the Sixth Brazilian Meteorological Congress, 19-24 November 1990, Salvador, Bahia, Brazil.

Proceedings of the 6th Brazilian Meteorological Congress.
19-24 November 1990.
Salvador-Bahia, Brazil
pp820-825

STRUCTURE OF A CONVECTIVE STORM ON THE SOUTH AFRICAN HIGHVELD BASED ON SINGLE-DOPPLER RADAR ANALYSIS

A M Gomes and G Held

Atmospheric Processes & Management Advice, EMATEK, CSIR
P O Box 395, PRETORIA 0001, South Africa

1. INTRODUCTION

The occurrence of deep convection in central and northeastern regions of South Africa is often accompanied by hail, producing extensive agricultural damage (Carte, 1977). Deep convective situations provide the major portion of rainfall on the South African plateau which is about 1500 m above MSL. The life cycle and dynamic characteristics of severe storm systems over the Transvaal Highveld have been studied extensively by Held (1982), Held and Carte (1979) and Held and van den Berg (1977), where mechanisms leading to the development of deep convection are highlighted, and the need for knowledge of the internal air flow structure of such storms is stressed.

The S-band radar is positioned approximately 22 km north-northwest of the centre of Johannesburg and 45 km southwest of Pretoria. Modifications to the radar and a locally developed pulse-pair processor allow the remote measurement of air flow inside clouds since 1987.

Considering severe storm types that occur on the Highveld, the squall line is the one which is characterised by its widespread areal coverage. Most squall lines are very efficient in producing rain and hail over large areas, but are significantly less frequent than isolated or scattered storms (Carte and Held, 1978). Analysis of two squall line systems that traversed the Johannesburg-Pretoria area in November 1987 (Gomes and Held, 1988) showed that the radial velocity field, as observed by the Doppler radar, exhibited well organised mesoscale features, such as couplets of radial velocities, indicative of strong convergence. Smull and Houze (1985, 1987) and Rutledge *et al.* (1988) focused their interpretation of single-Doppler radar images on the two-dimensional flow structure shown in RHI presentations of the squall line.

They indicated the presence of kinematic structures connecting the development of a trailing rain region to the leading convective rain band; there is a front to rear system relative flow aloft, overlying a rear to front flow which, in turn, overlies a rearward flow at low levels. These ideas are used in the interpretation of the case study presented in this paper. However, the precipitation system presented here, which occurred on 7 January 1988, does not show the development of a trailing rain region, because of its predominantly convective character.

2. VERTICAL STRUCTURE OF THE ATMOSPHERE PRIOR TO STORM DEVELOPMENT

Vertical profiles of the thermodynamic variables and the wind hodograph were obtained from radiosonde ascents made just south of Pretoria (Irene) at 12 GMT.

The vertical wind profile from the midday sounding (approximately six hours before the storm had passed through the radar surveillance area) showed that the subcloud winds were northeasterly, backing with height to westerly at cloud base, then to southwesterly in the mid-troposphere and thereafter veering to west-northwesterly remaining fairly constant in direction. The wind shear in the cloud layer, extending from 3.2 to 9.6 km MSL is $2.3 \times 10^{-3} s^{-1}$ with considerable directional shear in the lower levels.

Profiles of the potential temperature (θ), equivalent potential temperature (θ_e) and saturated equivalent potential temperature (θ_{es}) (Figure 1) show an atmosphere with high surface temperatures (θ_e and θ_{es}). A positive lapse rate of θ_e and θ_{es} below 3 km indicates that this layer was potentially and conditionally unstable. A shallow stable layer is found between 3 and 3.5 km. From there up to 5 km θ_e is relatively low, so evaporative cooling and downdraught formation are favoured in this layer (Riehl, 1969; Zipser, 1977). The 0°C level was located near 4.5 km MSL.

3. RESULTS AND DISCUSSION OF THE 7 JANUARY 1988 STORM

The discussion of the evolution of the 7 January 1988 storm is based on a series of PPI's. Radar echoes from 20:30 to 22:40 SAST (South African Standard Time) have shown intense convective activity spread throughout the 75 km range of the Doppler radar. The analysis concentrates on a period during which the major storm was approximately 20 km southwest of the radar, where isolated storms began to show a more organised structure. Like most of the storms occurring in this area, this one was also multicellular in structure. By 21:10, there were basically three major clusters located near the central area and to the east of the radar. During the following 25 minutes, the northern and eastern cells were moving southwards and westwards respectively, merging with the storm located southwest of the radar. By 21:46, a well-defined line of precipitation, approximately 60 km long and 25 km wide, could be observed. During this period, the system was already in its mature phase, with a well-developed leading convective rainband propagating northeastwards at an average speed of 30 $km.h^{-1}$. After 22:11, one could observe an interesting feature, where shallow cells began to appear in the northeastern part of the storm, probably as a result of the downdraught, undercutting and lifting the air ahead. Radar reflectivities and radial components of the air flow at 22:27 are shown in Figure 2a and b. Downdraughts penetrate the inflowing air, splitting and lifting it to the level of free convection and, in so doing, creating a new updraught region forward of the old cell (Wallace and Hobbs, 1977). By approximately 22:38, the area had been totally filled with precipitation.

Figure 2c illustrates the multicellular nature of the storm in a vertical cross-section along the line A-AA. It can be seen that the echo in the leading convective band extended to a height of 15 km AGL, with maximum reflectivities between 50 and 60 dBz. Also important to notice is the overhang on its northwestern flank together with a weak-echo-region (WER) most probably indicating the position of the updraught. The most striking aspect of the radial velocity images is the dominant flow towards the radar (Figure 2b). The radial velocities are much larger, 25-30 $m.s^{-1}$, in the area enclosed by the most intense reflectivity values. It is rather a complex pattern to physically interpret. The small wedge of radial flow velocities away from the radar in the northwestern part of the storm complex indicates most probably aliasing of velocities. The extensive area of relatively low radial velocities towards the radar in the southern rear of the storm (Figure 2b) could be interpreted in two ways. It could be a low velocity region, or it may be a region where the wind is almost tangential to the radar which would also result in small radial components of the velocity. Figures 3a and b show Z (reflectivity) and V (radial velocity) respectively, in cross-sections along the 23.5° azimuth in a plane, more or less in the direction of the storm movement. Storm overhang and strong reflectivity gradients on the leading edge suggest strong inflow into the storm. At 22:05 (Figure 3a) the dominant flow from low levels up to 7 km has a large positive component, with local extremes of up to 20 $m.s^{-1}$ maintained until it reached the core represented by the maximum values of reflectivity, where a sharper tilt was observed at a range of 33 to 37 km. Vertical cross-sections of the reflectivity and radial flow velocities at 22:27 (Figure 3b) illustrate a similar structure to that shown previously for 22:05. However, the air flow was somewhat weaker and the maximum radial velocities had descended to the lowest 2 km, following the collapse of the core.

It might be premature to draw conclusions at this stage of the analysis. However, radial convergence in the mid-levels appears to be characteristic during the stage of maximum storm intensity, indicative of organised updraught areas.

4. ACKNOWLEDGEMENTS

This research project was partially supported by the Water Research Commission. The radar operators are thanked for their dedication in collecting the Doppler radar data, and the South African Weather Bureau is acknowledged for making the radiosonde observations available.

5. REFERENCES

CARTE A E, 1977. Hail damage to agriculture and its prevention. South African Journal of Science, 73, 327-330.
CARTE A E and HELD G, 1978. Variability of hailstorms on the South African Plateau. J. of Appl. Met., 17, 365-373.
GOMES A M and HELD G, 1988. First progress report: Precipitation and air flow (PRAI) project. CSIR Report EMA-C 8885, Pretoria, 32pp.
HELD G, 1982. Comparison of radar observations of a devastating hailstorm and a cloud burst at Jan Smuts Airport. E M Agee and T Asai (eds), in Cloud Dynamics, Reidel Publ. Co., Dordrecht, 273-284.
HELD G and CARTE A E, 1979. Hailstorms in the Transvaal during January 1985. S A Geogr. J., 61, 128-142.
HELD G and VAN DEN BERG H J C, 1977. A pre-frontal squall line on 14 November 1975. Arch. Met. Geoph. Biokl., 26, 361-379.
RIEHL H, 1969. Some aspects of cumulonimbus convection in relation to tropical weather systems. Bull. Amer. Met. Soc., 30, 587-595.
SMULL G F and HOUZE R A, Jr, 1985. A mid-latitude squall line with a trailing region of stratiform rain: Radar and satellite observations. Mon. Wea. Rev., 113, 117-133.
SMULL G F and HOUZE R A, Jr, 1987. Dual-Doppler radar analysis of mid-latitude squall line with a trailing region of stratiform rain. J. Atmos. Sci., 44, 2128-2148.
RUTLEDGE S A, HOUZE R A, Jr, BIGGERSTAFF M I and MATEJKA T, 1988. The Oklahoma-Kansas mesoscale convective system of 10-11 June 1985: Precipitation structure and single-Doppler radar analysis. Mon. Wea. Rev., 116, 1409-1430.
WALLACE J M and HOBBS P V, 1977. Atmospheric science, an introductory survey. Academic Press, New York, (Chapter 5).
ZIPSER E J, 1969. The role of organized unsaturated convective downdrafts in the structure and rapid decay of an equatorial disturbance. J. Appl. Meteor., 8, 799-814.

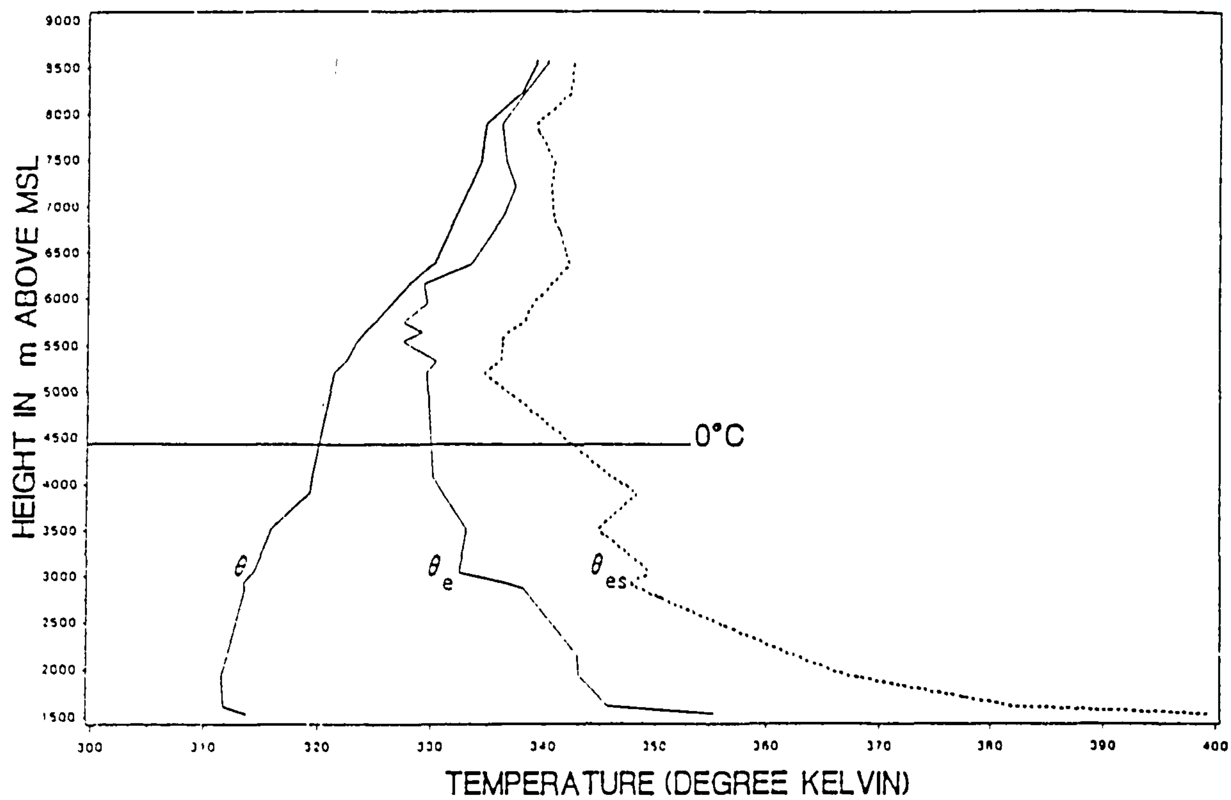

Figure 1: Vertical profiles of the potential temperature (θ), the equivalent potential temperature (θ_e) and the saturated equivalent potential temperature (θ_{es}) at Irene on 7 January 1988, 12:00 GMT.

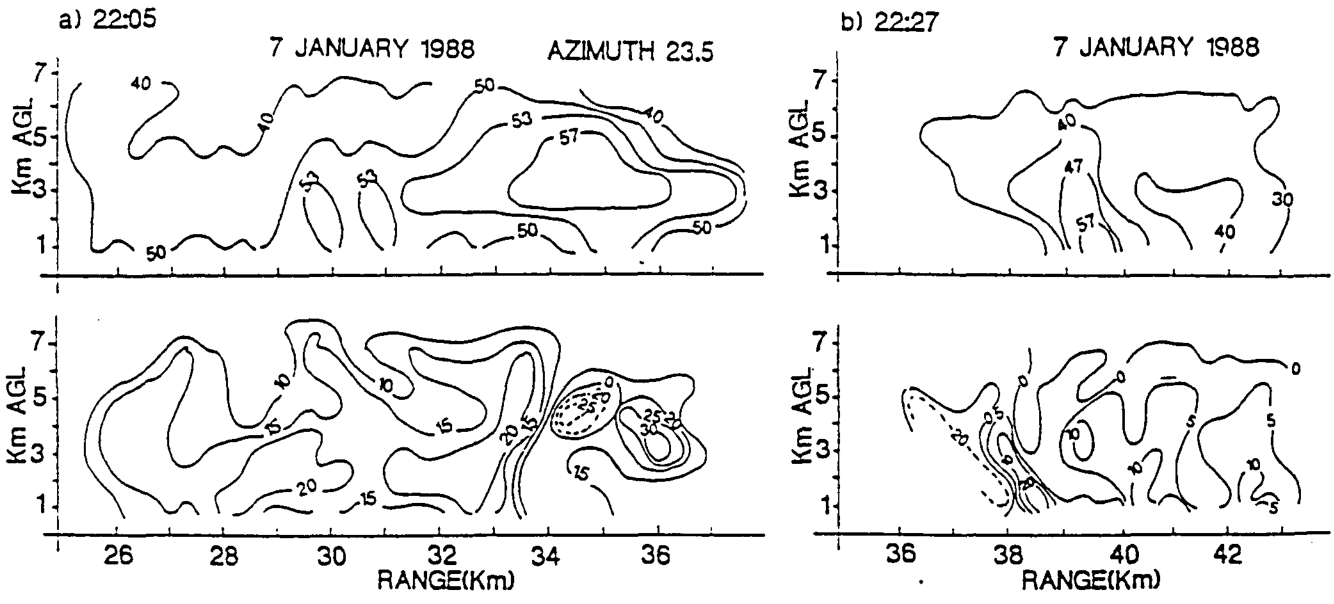

FIGURE 3: 7 January 1988. RHI (Range Height Indicator) section through azimuth 23.5°, indicating reflectivity contours in dBz (top) and Doppler velocities in $m.s^{-1}$ (bottom; dashed lines: radial velocities away from the radar, viz. negative velocities; solid lines: towards the radar, viz. positive velocities).

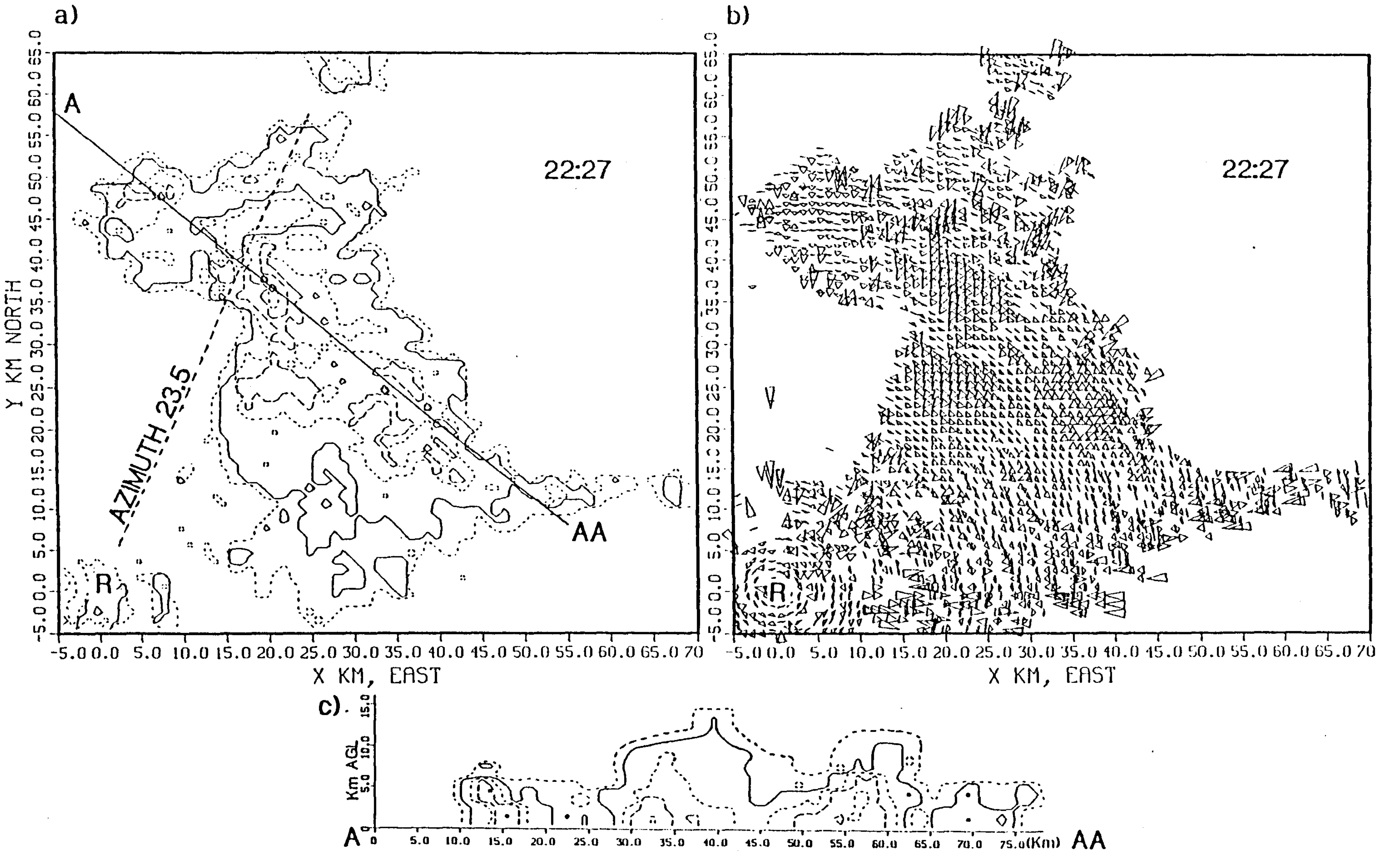

Figure 2: 7 January 1988. (a) PPI plot at 2° elevation (reflectivity contours: 23, 30, 40, 50, 60 dBz).
(b) Radial air flow pattern at 2° elevation.
(c) Vertical cross-section along the line A-AA.

11. APPENDIX B

Copies of publications describing the application of the programs 'SPRINT' and 'CEDRIC' for multiple Doppler radar analysis.

MILLER L J, MOHR C G and WEINHEIMER A J, 1986. The simple rectification to Cartesian space of folded radial velocities from Doppler radar sampling. *J. of Atmos. and Oceanic Techn.*, 3, 162-174.

MOHR C G, MILLER L J and VAUGHAN R L, 1981. An interactive software package for the rectification of radar data to three-dimensional Cartesian coordinates. *Preprints of 20th Conference on Radar Meteorology*, Boston, Amer. Meteor. Soc., 690-695.

MOHR C G, MILLER L J, VAUGHAN R L and FRANK H W, 1986. The merger of mesoscale data sets into a common Cartesian format for efficient and systematic analyses. *J. of Atmos. and Oceanic Techn.*, 3, 143-161.

appen/28c/sgg

Reprinted from JOURNAL OF ATMOSPHERIC AND OCEANIC TECHNOLOGY, Vol. 3, No. 1, March 1986
American Meteorological Society

The Simple Rectification to Cartesian Space of Folded Radial Velocities from Doppler Radar Sampling

L. JAY MILLER, CARL G. MOHR AND ANDREW J. WEINHEIMER

The Simple Rectification to Cartesian Space of Folded Radial Velocities from Doppler Radar Sampling*

L. JAY MILLER, CARL G. MOHR AND ANDREW J. WEINHEIMER

*National Center for Atmospheric Research*** *Boulder, CO 80307*

(Manuscript received 5 September 1984, in final form 8 July 1985)

ABSTRACT

Periodic sampling of the Doppler radar return signal at the pulse repetition frequency causes measured velocities to be ambiguous (folded) when true meteorological velocities along the radial direction exceed the Nyquist or folding value. Furthermore, mean radial velocity estimates become more uncertain as the spatial variability of velocity increases or the returned signal strength decreases. These data have conventionally been prepared for such uses as multiple-Doppler radar wind synthesis by unfolding and editing them in the sampling domain (range-azimuth-elevation spherical coordinates).

An alternative method of locally (to the output grid point) unfolding the *unedited* radial velocities during their linear interpolation to a regular Cartesian grid is presented. The method preserves the spatial discontinuities of order twice the Nyquist value associated with velocity folding. A nondimensional velocity quality parameter is also computed which serves to identify interpolated values that contain too much variance to be reliable. Editing of radar data is thereby postponed until all radar data are mapped to the analysis coordinate system. This allows for iterative global unfolding and multiple-Doppler synthesis of complicated convective storm flow patterns. The resolution of folding in such flow fields may require more information than is usually available from single radar radial velocity fields in spherical coordinates. Further, the amount of data that must be subsequently manipulated is reduced about ten-fold in the process of interpolation.

1. Introduction

Radial velocities measured by Doppler radars are often interpolated to a regular (x, y, z) grid, especially when they are used in the multiple radar synthesis of three-dimensional wind fields. Although the processing of multiple radar data involves other steps such as the actual synthesis of three-dimensional winds using measurements from several viewing directions (e.g., Carbone et al., 1980), we have restricted this paper to the transformation of data from radar space to analysis space (interpolation), the removal of velocity ambiguities (unfolding), and the elimination of spurious values (thresholding). Common practice is to edit and unfold individual radar velocity measurements in the sampling space (range-azimuth-elevation; R, A, E) before interpolating them (e.g., Ray and Ziegler, 1977; Oye and Carbone, 1981). However, this step can be done after interpolation provided the remapping method preserves the statistical characteristics of the measured radial velocities and does not introduce any biases in the interpolated values. Two especially important characteristics are the spatial discontinuities associated with folding of the radial velocities due to periodic sampling at the pulse repetition rate and the randomness of velocities when the backscattered signal strength indicates that only noise is present.

Most radar systems use the covariance or "pulse-pair" technique (e.g., Zrnić, 1977) to estimate the power-weighted average radial velocity within pulse volumes at several range locations along the pointing direction. When only noise is present in the backscattered return, this technique should give mean radial velocities that are uniformly distributed from $-V_n$ to V_n (the Nyquist co-interval) where V_n is the folding or Nyquist velocity. Unknown biases in the radial velocity processor can sometimes corrupt the noise distribution, but it is usually nearly uniform with a few preferential estimates occasionally occurring.

When the magnitude of the true meteorological radial velocity within a pulse volume exceeds V_n, sampling the return signal at the pulse repetition rate will cause estimates of Doppler velocity to be ambiguous or folded (e.g., Doviak et al., 1978). When this happens an integer multiple of twice the Nyquist velocity must be added to the measured pulse-volume average value to remove this ambiguity (Ray and Zeigler, 1977). Folding therefore represents an artificial and identifi-

* An earlier version of this paper appeared in the *Preprints of the 21st Radar Meteorology Conference*, Edmonton, Alberta, Canada, Sept. 1983, sponsored by the American Meteorological Society.

** The National Center for Atmospheric Research is sponsored by the National Science Foundation.

able spatial discontinuity of order $2V_n$ in the radial velocity. If the discontinuity is not handled properly when aliased data are transformed to a regular xyz-grid, the velocity estimates cannot be correctly unfolded after interpolation.

The three-dimensional interpolation scheme developed by Mohr and Vaughan (1979) has been modified to include range averaging and local velocity unfolding. They determined the grid point value by a three-dimensional linear interpolation of eight measured values from two consecutive range locations along the four beams (two azimuths from each of two elevation scans) surrounding the grid point. All these data are usually obtained within 10–15 s (30–40 s in extreme cases of large azimuthal sectors) even though the scan of the entire volume of interest may take 2–3 min. Radar data that contain ambiguous measurements can be interpolated with this method *without first unfolding them in radar sampling space* since the extension we propose preserves the original spatial discontinuities associated with folding. Further, this local unfolding technique applied to uniformly distributed noise estimates results in interpolated noise that remains nearly uniform with almost the same variability as the original distribution. The algorithm is discussed and the application of this procedure to a folded velocity field is presented. The advantages and cautions associated with this technique are also discussed.

2. Rectification of folded radial velocities

An example of radial velocities measured at an elevation angle of 9.5° by the NCAR/FOF (Field Observing Facility) CP-2 10-cm radar on 2 August during the 1981 Cooperative Convective Precipitation Experiment (CCOPE; Knight, 1982) in southeastern Mon-

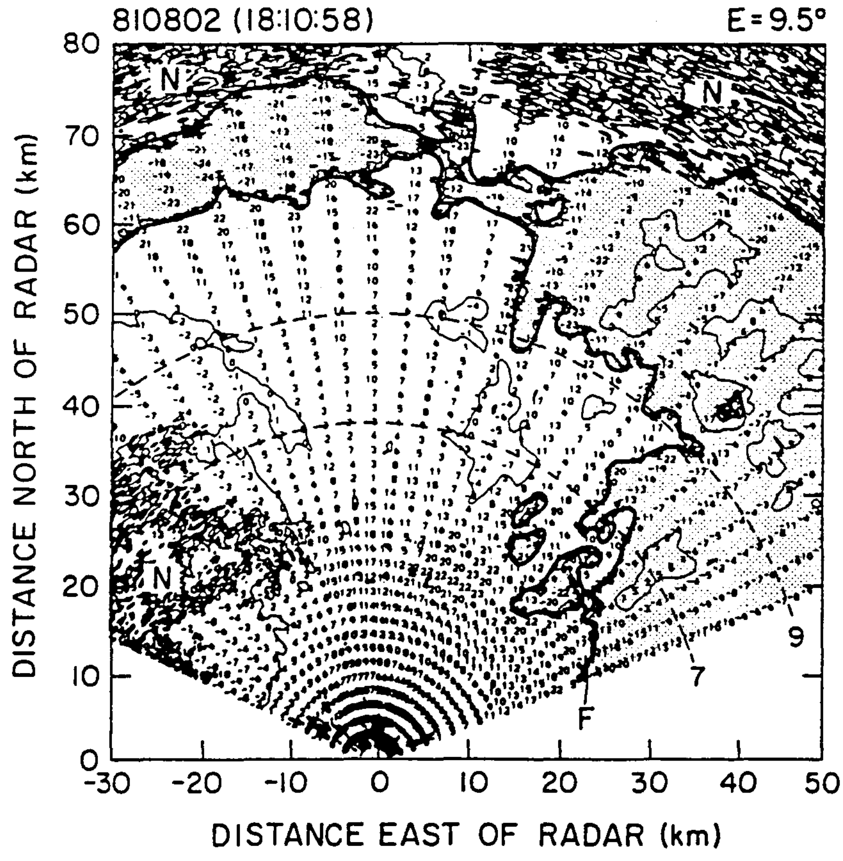

FIG. 1. Horizontal projection of measured radial velocities at an elevation angle of 9.5° from CP-2. These data were obtained on 2 August 1981 during the CCOPE field program in southeastern Montana. Numbers at every eighth gate along every sixth ray represent the magnitude of the radial velocity (positive values indicate motion away from the radar), with contours drawn at −25, 0 and 25 m s^{-1}. The bold line (F) indicates the position of the local discontinuity associated with folding. Regions of ambiguous or folded (about the Nyquist velocity of 25.6 m s^{-1}) velocities are shaded. Noisy estimates (N) exist to the northwest and also beyond about 70 km north of the radar. Ranges where the 7 and 9 km horizontal planes pass through this elevation surface are shown by dashed arcs.

tana is shown in Fig. 1. These data are part of the storm-volume scan from 1809:09 to 1812:32 (Mountain Daylight Time) that will be used to demonstrate the proposed technique. The storm was sampled every 200 m, 0.7° and 1° in range, azimuth, and elevation, respectively. The local discontinuity associated with folding is marked with a bold line. At locations away from the fold discontinuity the radial velocity field is again continuous, though perhaps ambiguous. Shaded regions in the figure contain ambiguous velocities while noise estimates exist beyond about 70 km to the north and in a patch northwest of the radar. Figure 2 shows these data after velocities have been unfolded in radar space using conventional methods (e.g., Oye and Carbone, 1981). In this example, noisy estimates (those mean values from low signal-to-noise power ratio regions or from broad velocity spectra) are retained though they could have been easily removed. In Section 4 we will compare interpolations of folded (Fig. 1) and unfolded (Fig. 2) values at 7 and 9 km (dashed arcs) to demonstrate that the same results can be obtained using the proposed alternative method.

Conventional editing and unfolding steps can be postponed until after interpolation so long as poor estimates of velocity and folding can still be identified. The idea is to designate a local velocity at each (x, y, z) point and to offset all velocities that affect this point so that they lie within the ambiguous velocity interval of this initial estimate prior to interpolation. This is done independently at each interpolation grid point and only represents a local resolution of velocity folding. Interpolated velocities which are folded must be subsequently de-aliased in Cartesian space using global techniques.

The true (unfolded) radial velocity U at a (R, A, E) measurement point is

$$U = V + \kappa V_a; \quad \kappa = 0, \pm 1, \pm 2, \cdots \qquad (1)$$

where V is the measured quantity which may be aliased and is subject to measurement error, $V_a = 2V_n$ is the ambiguous velocity interval, and κ is the integer factor needed to remove Nyquist folding ambiguities from V. When the measured velocity differs by more than V_n from the value expected at the grid point, the integer folding factor in Eq. (1) is nonzero and can be approximated by

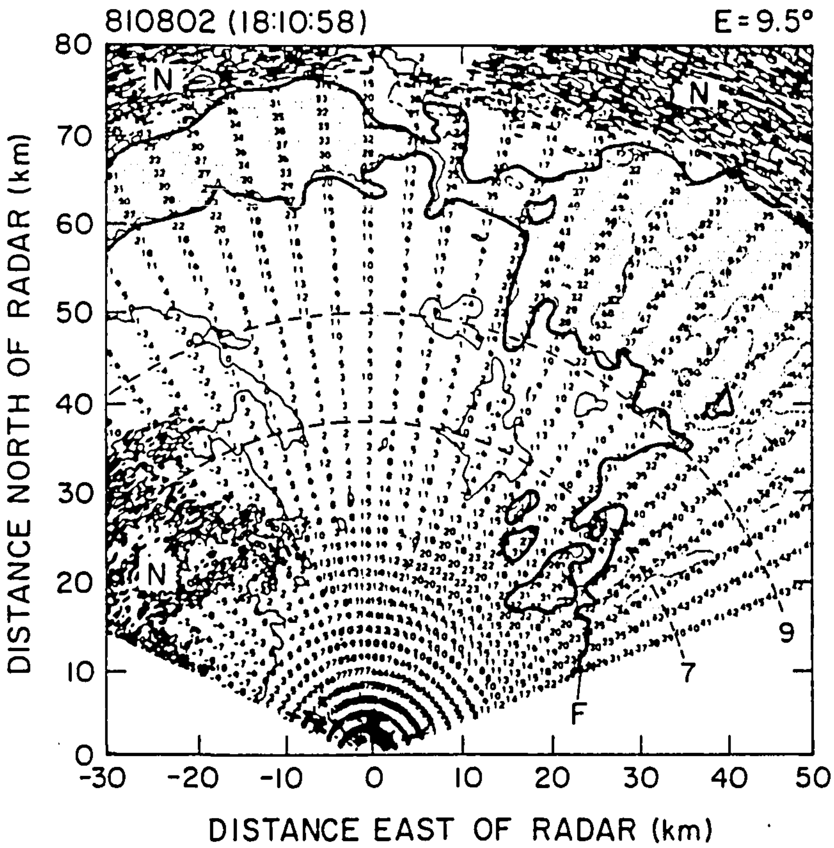

FIG. 2. Radial velocities shown in Fig. 1 after they have been unfolded in radar space. Areas where velocities have been de-aliased are shaded. An additional contour at 51.2 m s^{-1} has been added. This corresponds to the zero contour in the ambiguous zone in Fig. 1.

$$K = \frac{U_e - V}{V_a}, \tag{2a}$$

where U_e is a preliminary estimate of the true radial velocity (U) at the (x, y, z) point. The appropriate integer unfolding factor is determined by

$$\kappa = \begin{cases} \text{INT}(K + 0.5), & \text{if} \quad K \geq 0 \\ \text{INT}(K - 0.5), & \text{if} \quad K < 0, \end{cases} \tag{2b}$$

where INT represents truncation toward zero. The quantity U_e is arbitrarily set to one of the measured input values in the neighborhood of the (x, y, z) point, and the remaining contributing values are forced into the ambiguous velocity interval centered on U_e using Eqs. (1) and (2). Strictly this operation does not represent complete unfolding, but temporary removal of a discontinuity that would result in biased estimates when interpolation to grid points is performed. To completely unfold or de-alias the velocities, the addition or subtraction of another integer multiple of V_a may still be needed after interpolation. Henceforth, we will refer to the removal of the folding discontinuity within the population of input measurements contributing to the estimate at each (x, y, z) point as local unfolding or more simply as "unfolding."

Since U_e comes from the population of input samples which are contained within the Nyquist co-interval (unless they have been previously unfolded), the values of κ determined by Eq. (2) will be -1, 0, or $+1$. *It is assumed that no true velocity is more than V_n from the reference velocity.* This is equivalent to assuming that the largest possible physical gradients of radial velocity that can occur within the sampling cell surrounding the Cartesian grid point are $V_n/(M-1)\Delta R$ in range, $V_n/R\Delta A \cos E$ in azimuth, and $V_n/R\Delta E$ in elevation, where ΔR, ΔA and ΔE are the respective sampling increments. The sampling cell consists of M range (R) gates and four adjacent beams, two in azimuth (A) and two in elevation (E). Spatial gradients across the sampling cell larger than these will cause the true radial velocities to be spread over more than one V_a interval, leading to the requirement that some values of κ exceed unity. In this event, which is uncommon provided the Nyquist velocity is large (about 25 m s^{-1}) and radar (R, A, E) sampling locations are closely spaced (less than about 1 km), the algorithm will obviously fail to interpolate an unbiased velocity value.

Radar velocity measurements from a range slab of thickness M gates centered at slant range R to the interpolation xyz-grid point are range-averaged to obtain estimates at each of four azimuth-elevation locations surrounding the xyz-grid point:

$$\hat{U}(A_j, E_k) = \sum_{m=1}^{M} U_m/M,$$

where the U_m have been "unfolded" according to Eqs. (1) and (2). This step is done to approximately equalize the sampling increments in the range and cross-beam directions and is not intended to represent complete filtering that may be required. The quantities A_j and E_k represent the respective azimuth and elevation angles of the beams. A caret denotes either range-averaged or xyz-grid values, and quantities without a caret represent either measured or "unfolded" velocities at radar sampling locations. The geometry of the angular sampling cell at the range of the xyz-grid point and interpolation are illustrated in Fig. 3. Following Mohr and Vaughan (1979), these range-averaged data are bilinearly interpolated using

$$\hat{U}(A, E) = \left(\frac{E_{k+1} - E}{\Delta E}\right) \times \left[\hat{U}_j\left(\frac{A_{j+1} - A}{\Delta A}\right) + \hat{U}_{j+1}\left(\frac{A - A_j}{\Delta A}\right)\right]_k + \left(\frac{E - E_k}{\Delta E}\right) \times \left[\hat{U}_j\left(\frac{A_{j+1} - A}{\Delta A}\right) + \hat{U}_{j+1}\left(\frac{A - A_j}{\Delta A}\right)\right]_{k+1}, \tag{3}$$

where $\Delta E = E_{k+1} - E_k$, $\Delta A = A_{j+1} - A_j$. The terms in brackets represent linear interpolations along azimuth at the k and $k+1$ elevation levels. Combining Eqs. (1) and (3), in abbreviated form the "unfolded" and interpolated radial velocity becomes

$$\hat{U}(x, y, z) = \sum_{A,E} (wV)_{jk} + V_a \sum_{A,E} (w\kappa)_{jk}. \tag{4}$$

The first term on the right is the geometrically weighted sum of measured values, while the second term represents a weighted folding factor to correct for bias that would result if measured values were not locally unfolded before interpolation. The quantity w is the geometric weighting factor associated with each (A_j, E_k) location in Eq. (3). The values of κ in Eq. (4) are the

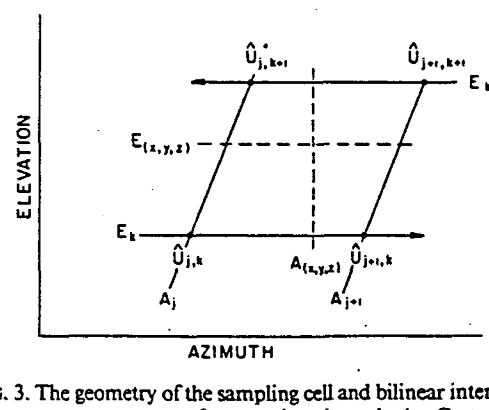

FIG. 3. The geometry of the sampling cell and bilinear interpolation along a constant range surface passing through the Cartesian grid point (x, y, z). The $\hat{U}_{jk}$ represent the averages of M range gate measurements centered at $R(x, y, z)$ and located at the four radar beams left and right, above and below the point $A(x, y, z)$, $E(x, y, z)$.

ones that must be used to remove the local discontinuity from the measured velocities.

The form of the weighting function to be used in Eq. (4) for interpolating radar information to a regular Cartesian grid is usually a matter of personal preference. We choose the linear weighting and range averaging presented in Eq. (3); other distance weighting schemes such as the Cressman method (e.g., Ray et al., 1975) could also be used. All such schemes assign a distance-weighted average value to the grid point, where the weight decreases rapidly as the distance from the grid point increases or else only estimates within some small radius of the grid point are used. It is not our intent to debate the virtues of all such schemes; however, if the method employed uses values only in proximity to the output grid point, the discontinuity associated with folding can be removed and then the weighting applied in the way we present. That is, they can be interpolated without prior radar-space editing.

Figure 4 illustrates the results of interpolating the folded radial velocity field (shown in Fig. 1) at two levels in the storm using the methodology that we propose. These horizontal planes at 7 (Fig. 4a) and 9 km (Fig. 4b) intersect the elevation plane in Fig. 1 at the dashed arcs. The boundary of folded radial velocities in the southeast portion of the grid is shown by a bold line, with shading indicating regions of ambiguous velocities as in Fig. 1. A zone of ambiguous velocities extends northward along the eastern portion of the grid as also seen in Fig. 1. The patch of noisy measurements northwest of the radar is also clearly replicated as evidenced by the many contours in the western portion of the domain. A time associated with each interpolation grid point is also obtained by applying the same linear interpolation scheme to the original observation times. In this way the multiple radar synthesis that includes advective corrections at Cartesian grid points as formulated by Gal-Chen (1982) can be utilized.

3. Quality of the interpolated velocities

Since the interpolation method is applied to all radar-measured velocities without prior editing, we need a way to determine the quality of the interpolated value. This measure can be used later in Cartesian space to reject unreliable velocities interpolated from radar measurements that are too noisy and to identify regions where local unfolding may have required a folding factor exceeding unity. When no signal is present covariance-measured radial velocities ideally have variance $\sigma_n^2 = V_n^2/3$, so that large local variability should tell us when interpolated values are coming from an input population dominated by noise. Further, large spatial gradients of the measured velocities should also lead to significant variability. When neither of these conditions exist, the spread of velocities should be much smaller. Thus we compare the sample variance var(U) of "unfolded" velocities to be used in the interpolation with the expected value of σ_n^2 for white noise to determine the reliability of the interpolated velocity. A nondimensional velocity quality parameter

$$Q(x, y, z) = 1 - \mathrm{var}(U)/\sigma_n^2 \qquad (5)$$

is calculated. All measurements affecting a grid point estimate are locally unfolded using Eqs. (1) and (2) and then their corresponding variance var(U) is obtained.

The nondimensional velocity quality parameter Q is close to zero when all radial velocities are noise (see Appendix for the expected value and variance of Q when a noise population is unfolded), and it approaches unity as the spatial variability of the measured velocities decreases. Further, Q can become negative when the distribution of "unfolded" measurements is more clustered toward its extreme values with fewer estimates near the center velocity. The parameter Q reflects variability from measurement errors in individual velocities as well as large spatial gradients in the true radial velocity field surrounding the interpolated grid point. It is, therefore, a better measure of the acceptability of grid point estimates than is the magnitude of the covariance function which is often used to determine reliability of individual measurements contributing to the interpolated estimate. More importantly, Q can be computed for all radar systems in the same way. Systems that do not record the magnitude of the covariance function instead flag the velocity as good or bad at the time of measurement (e.g., the bad data flag bit used in the NCAR/FOF 5 and 10 cm radars). Unfortunately, such procedures do not allow the data-user to decide if these values are acceptable for his purposes.

An example of the actual behavior of Q in a noise-only environment was determined by interpolating radial velocities from NCAR's CP-2 radar. The transmitter was intermittent for a short time on 11 July 1981 during CCOPE so that noise-only data could be recorded while the antenna was rotating and the processing system was still operating. This provided recorded data at spatial resolution typically associated with normal probing of severe convective storms. The frequency distribution of Q for interpolation at one horizontal level is shown in Fig. 5 (solid line histogram). It roughly obeys a Gaussian law with a nearly zero mean value and standard deviation of about 0.3 so that interpolated (signal) velocities appear to be acceptable when $Q > 0.6$. This can be seen also in the distribution of Q when both signal and noise are present (Fig. 5, dashed line histogram). The values to the right of 0.6 are definitely associated with signal since a value of $Q = 0.8$ corresponds to var(U) = 43.7 m^2 s^{-2} with noise variance σ_n^2 = 218.4 m^2 s^{-2} for this case. (The Nyquist velocity was 25.6 m s^{-1}).

A histogram of noise input velocities from a volume scan on 2 August 1981 (Fig. 1) is shown in Fig. 6a. The percent of the total number of values (3194) appearing

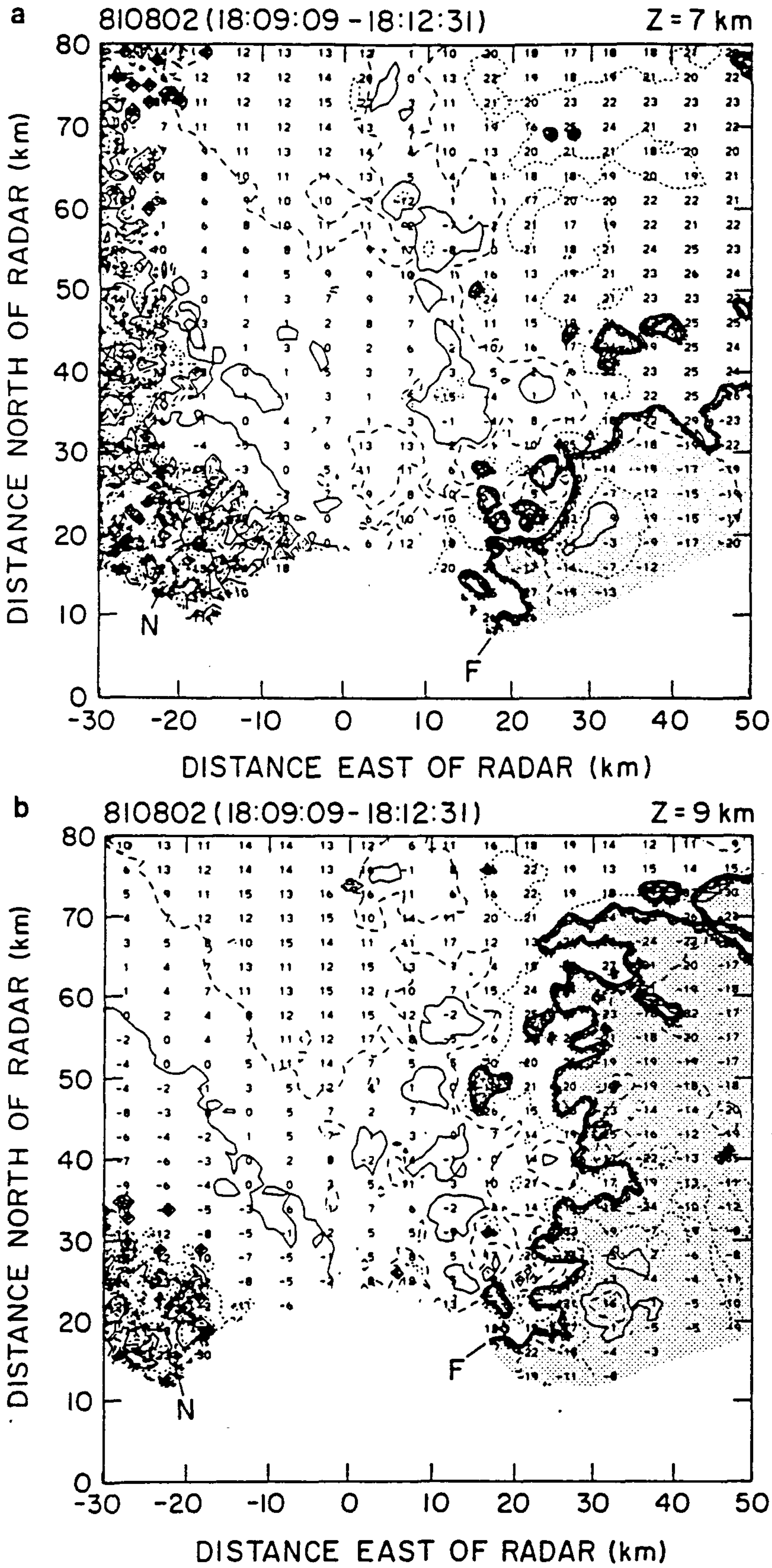

FIG. 4. Samples of unedited and interpolated (with local unfolding) radial velocities at (a) 7 km and (b) 9 km. These horizontal sections pass through the 9.5° elevation plane of Fig. 1 at the dashed arcs. Numbers represent the radial velocity at selected locations with contours drawn at 10 m s^{-1} intervals starting at -30 m s^{-1} in the repeating pattern: dashed, short-dashed and solid. The zero contour is solid. The bold line (F) marks the position of the local discontinuity caused by folding. The regions of ambiguous (folded) velocities are shaded. Noisy velocities (N) exist along the western portion of the grid.

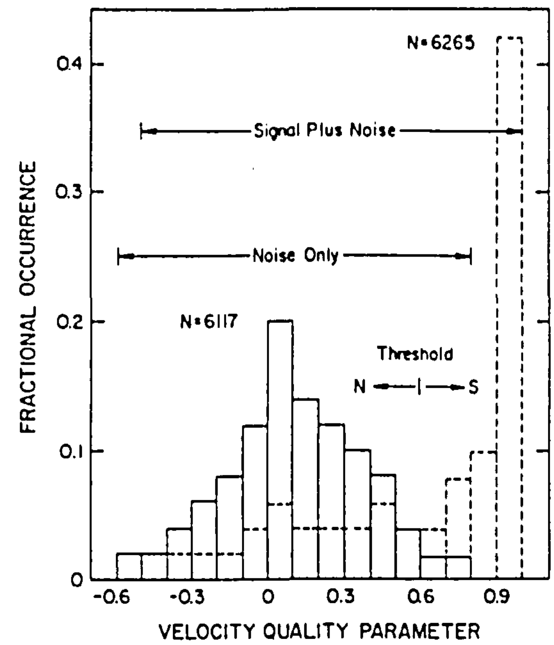

FIG. 5. Frequency distributions of velocity quality parameter for interpolated noise-only (solid) and signal-plus-noise (dashed) radial velocity fields. The numbers of values at this horizontal level (6 km above mean sea level) used to determine the distributions were 6117 and 6265, respectively. A value of 0.6 appears to adequately separate noise from signal.

in each of the bins of width 2 m s^{-1} is represented by the ordinate. The distribution is nearly uniform with sample mean of 0.01 m s^{-1} and standard deviation of 14.51 m s^{-1}, compared to theoretical values of 0.0 and 14.78 m s^{-1}, respectively. The distribution of interpolated (with local unfolding) velocities corresponding to the noise-only input velocities in Fig. 6a is shown in Fig. 6b. Since the reference velocity used for local unfolding is itself equally likely to occur anywhere within the ambiguous velocity interval, the effect of interpolation with unfolding is to create local Gaussian populations having an expected value of U_e and conditional variance equal to that of $\hat{U}$ for a given U_e. The distribution of $\hat{U}$ is then a convolution of this (relatively narrow) Gaussian with the original uniform distribution (Rohatgi, 1976). The tendency for more values to be concentrated near zero is mostly a result of convolving a Gaussian distribution whose width depends on the number of original measurements used in the interpolation with the *actual* distribution of velocities coming from the radar processor.

If no local unfolding were invoked the distribution of velocities would look like the one shown in Fig. 6c. If the radial velocities come from statistically similar populations having zero mean and equal variance σ_n^2, the variance of the grid point estimate is

$$\sigma^2(\hat{U}) = \sigma_n^2 \frac{\sum w_{jk}^2}{M},$$

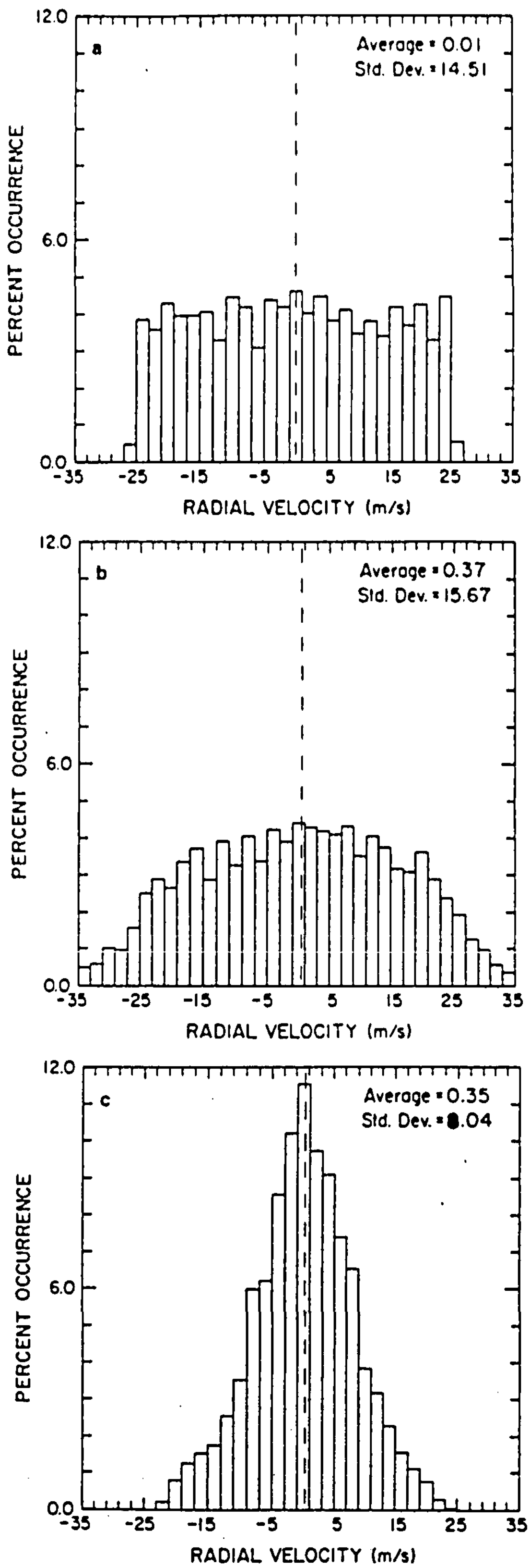

FIG. 6. Frequency distributions of radial velocities for "noise-only" (i.e., Q less than 0.5) portions of the 2 August radar scan volume presented in Figs. 1, 2 and 4: (a) input, (b) interpolated with local unfolding, and (c) interpolated without local unfolding. The average

where the quantities w_{jk} are the geometric weighting factors in Eq. (3). If the grid point should happen to coincide with an original sample location, all the weights except one are zero. If, however, the grid point is equidistant from all four sample locations (see Fig. 3), the sum of squares of weights is 0.25. Since all values of A, E are equally likely to occur, the expected value of $\Sigma\ w_{jk}^2$ is its areal average of 4/9. Three gates were used so the expected variance is $0.15\sigma_n^2$ or a standard deviation of 5.7 m s^{-1} compared to the observed value of 8.04 m s^{-1} (Fig. 6c). As can be seen the distribution of interpolated (with local unfolding, Fig. 6b) noise-only measurements is clearly "noiselike" and is similar to the one found in radar space (Fig. 6a). The importance of the local unfolding is further evidenced by noting the character of the contours in the western portion of Fig. 4a and contrasting that with what would happen if no local unfolding were invoked during interpolation (Fig. 6c). Some of the chaotic character would be lost.

4. Comparison with conventional methods

All radial velocities except noisy ones (as determined by the bad data flag bit) were carefully unfolded in radar space and then interpolated using the linear method with three-gate smoothing, but with no additional local unfolding. Examples of these data are shown in Fig. 7. Shaded regions in the eastern portion of the grid where velocities were originally ambiguous are now unfolded. Noisy estimates in the western portion were interpolated with local unfolding to replicate the effects discussed in Section 3.

For comparison, unedited original measurements such as those shown in Fig. 1 were interpolated with local unfolding and then unfolded in Cartesian space (Fig. 8), using global techniques described by Mohr and Miller (1983). These data were also thresholded on the velocity quality parameter ($Q > 0.6$) to eliminate the noisy portion. At grid locations outside regions of noise the average difference between velocity estimates derived by conventional methods and our method was 0.05 m s^{-1} with a standard deviation of only 0.11 m s^{-1}.

To further substantiate this equality of methods, we constructed several scatter plots to show point-by-point comparisons of velocities derived by conventional methods with those obtained by the proposed method. The following radial velocity fields were created:

VGUF—velocities were unfolded in radar space and then interpolated with no additional unfolding,

value is marked by a vertical dashed line. Each bin of width 2 m s^{-1} designates the percent of all velocities (total of 3194) that occurred within the bin. The average value and standard deviation of the distribution is shown in the upper right hand corner.

VNUF—unedited velocities were interpolated with local unfolding,

VLUF—the field VNUF was unfolded in Cartesian space,

VBIA—unedited velocities were interpolated without local unfolding,

VGTH—the field VGUF was thresholded on Q, and

VLTH—the field VLUF was thresholded on Q.

Figure 9a shows a scatter plot of the conventional method velocity (VGUF) along the abscissa versus the interpolated with local unfolding velocity (VNUF). There are two regression lines of VNUF that are offset by V_a = 51.2 m s^{-1} above and below (or right and left of) the one-to-one line. These represent values that need to be unfolded in Cartesian space, while values along the one-to-one line were never ambiguous in the first place. These velocities (VNUF) are shown in Fig. 9b after unfolding has been accomplished in Cartesian space. The few points that do not lie along the one-to-one line are from the noisy regions, as seen in Fig. 9c where these values have been eliminated by thresholding on Q. Note the small improvement in the correlation coefficient from $r = 0.998$ in Fig. 9b to $r = 1.000$ in Fig. 9c indicating that both methods are producing identical results in regions of usable data.

Contrast these results with the ones in Fig. 10 where unedited velocities were interpolated without local unfolding. The shaded area indicates regions where velocities cannot be unfolded by the addition or subtraction of any integer multiple of the ambiguous velocity. This is further demonstrated in Fig. 11 where these biased velocities (VBIA) are plotted against the conventional-method velocities (VGUF). The vertical scatter of VBIA near the Nyquist velocity typifies the amount of bias that occurred. The large scatter near the negative Nyquist is also from biasing as well as from noisy values. Although the bias in these velocities cannot be removed, all these interpolated velocity values can be eliminated by thresholding on the velocity quality parameter computed using unedited input measurements.

5. Concluding remarks

We have discussed a way of rectifying folded velocity measurements taken in radar sampling space to regular (x, y, z) analysis space. These locally unfolded and interpolated velocities can then be globally unfolded using techniques described by Mohr and Miller (1983). Noisy data are eliminated and remaining velocities are unfolded using the interactive software package CEDRIC (Mohr and Miller, 1983). This procedure has been shown to give results identical to those using more conventional approaches.

Two main advantages of not editing radial velocities until after interpolation are 1) the amount of radar data that must be subsequently manipulated is reduced by a factor of ten to twenty; and 2) all the data from

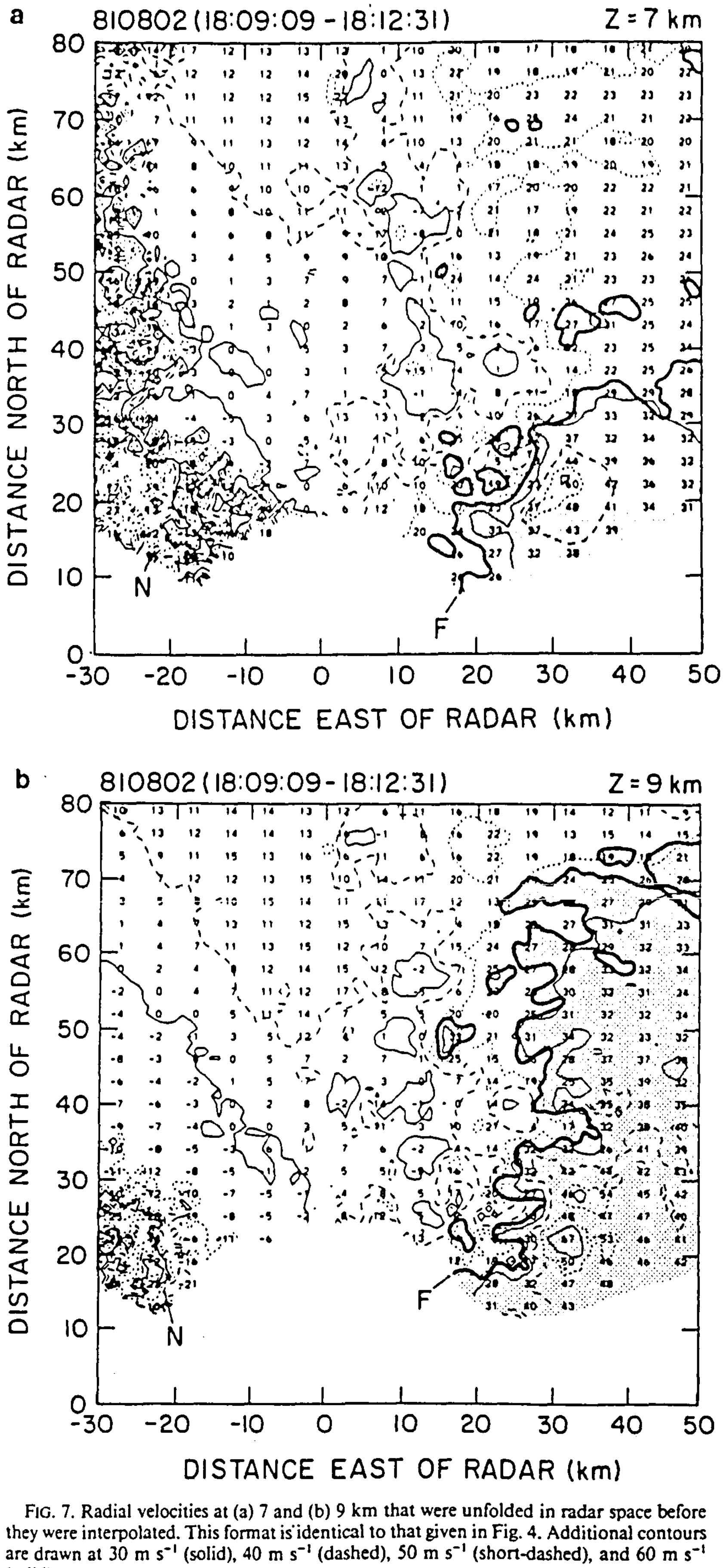

FIG. 7. Radial velocities at (a) 7 and (b) 9 km that were unfolded in radar space before they were interpolated. This format is identical to that given in Fig. 4. Additional contours are drawn at 30 m s^{-1} (solid), 40 m s^{-1} (dashed), 50 m s^{-1} (short-dashed), and 60 m s^{-1} (solid).

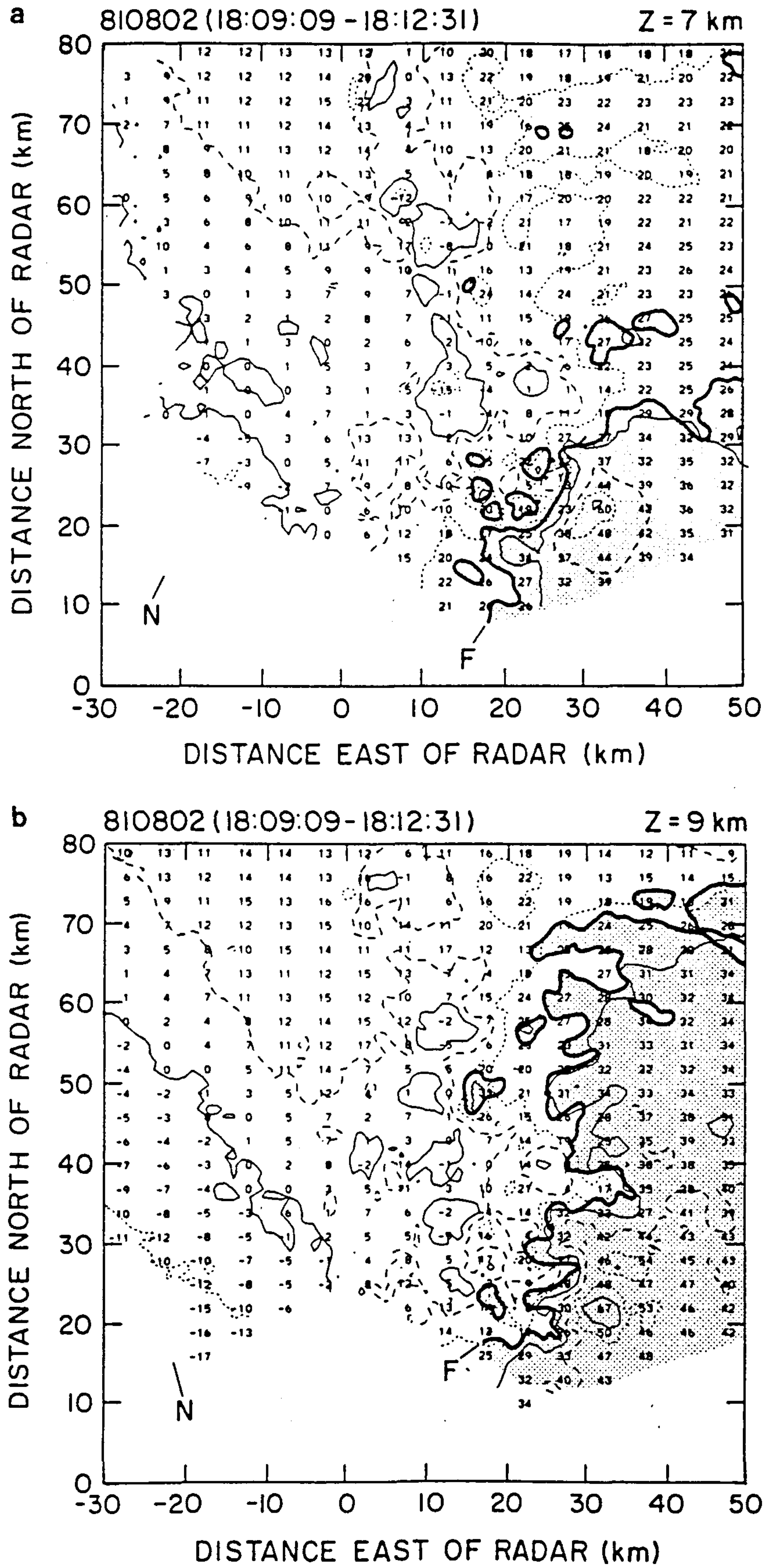

FIG. 8. Interpolated (with local unfolding) velocities shown in Fig. 4 that were unfolded in Cartesian space and thresholded on the quality parameter (Q greater than 0.6). Additional contours have been added as in Fig. 7. Compare these fields with those in Fig. 7.

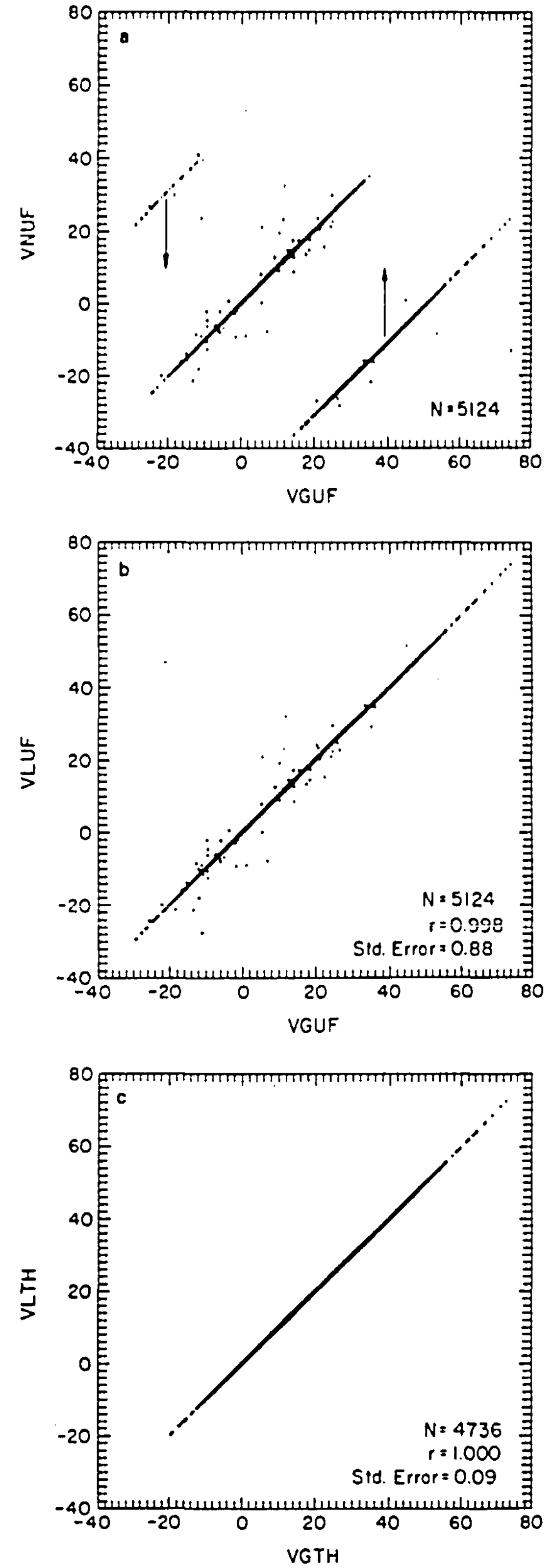

FIG. 9. Scatter plots of radial velocities that were unfolded in radar space and then interpolated (VGUF) versus (a) VNUF—locally unfolded during interpolation and (b) VLUF—unfolded VNUF in Cartesian space. The directions of movement of (VGUF, VNUF) pairs when VNUF is unfolded are marked by arrows in (a). VGTH was produced by thresholding VGUF on the velocity quality parameter and is plotted versus (c) VLTH—thresholded VLUF on quality parameter. The number of points (N), linear regression coefficient (r), and standard error [defined as $\sigma_y(1 - r^2)^{1/2}$, where σ_y is the ordinate] are marked in the lower right-hand corner.

different radars are located at common grid points, thereby facilitating interactive global unfolding and multiple radar wind synthesis attempts of difficult cases. When adjacent true velocity values differ by more than twice the Nyquist velocity, the local unfolding-interpolation scheme will fail to interpolate a correct grid point estimate. Application of Eqs. (1) and (2) would give a folding factor of one, rather than the required two or more. The interpolated value would therefore be incorrect.

For a large severe storm there may be as many as 500–1000 range gates per beam, 100–200 beams per elevation sweep and 15–20 sweeps per storm volume or about $1\text{–}4 \times 10^6$ original sampling points per storm volume. These are typically interpolated to about 100×100 grid points at 15–18 vertical levels, or 1.5–1.8 $(\times 10^5)$ values. Large radar data bases such as the one from the CCOPE Doppler radar network can be written to mass storage devices (e.g., the terabit memory system at NCAR) where they can be processed using a batch version of this interpolation procedure (Mohr et al., 1981) on the CRAY-1A computer. Most of these radar measurements can be interpolated without prior radar-space editing and written to tape for transport to smaller machines such as a VAX 11/780 computer where the results can be edited and synthesized in Cartesian analysis space. This means that about one-tenth as many magnetic tapes must be handled, and most if not all of the data needed for a case study can reside on disk in the smaller machine.

Many times there is insufficient information available from a single radar to unambiguously unfold all the measured velocities. If the computation-intensive step of interpolation does not have to be repeated, preliminary unfolding and synthesis can be attempted. Incompatibilities between radars will usually show up as physically impossible resultant vector winds so that the offending values of radial velocity can then be unfolded in a different way and resynthesized. Furthermore, since most meteorologists are more accustomed to working with data on constant height surfaces rather than constant elevation angle surfaces (radar spherical coordinates), Cartesian space is a more comfortable framework for manipulating the data base and arriving at believable results. Measurements can be transformed without radar space editing in most cases so that the majority of the data processing can be delayed until all radar estimates are organized onto a common (for all radars) grid where editing is less tedious and time-consuming.

Acknowledgments. The authors acknowledge the diligent efforts of the NCAR Field Observing Facility

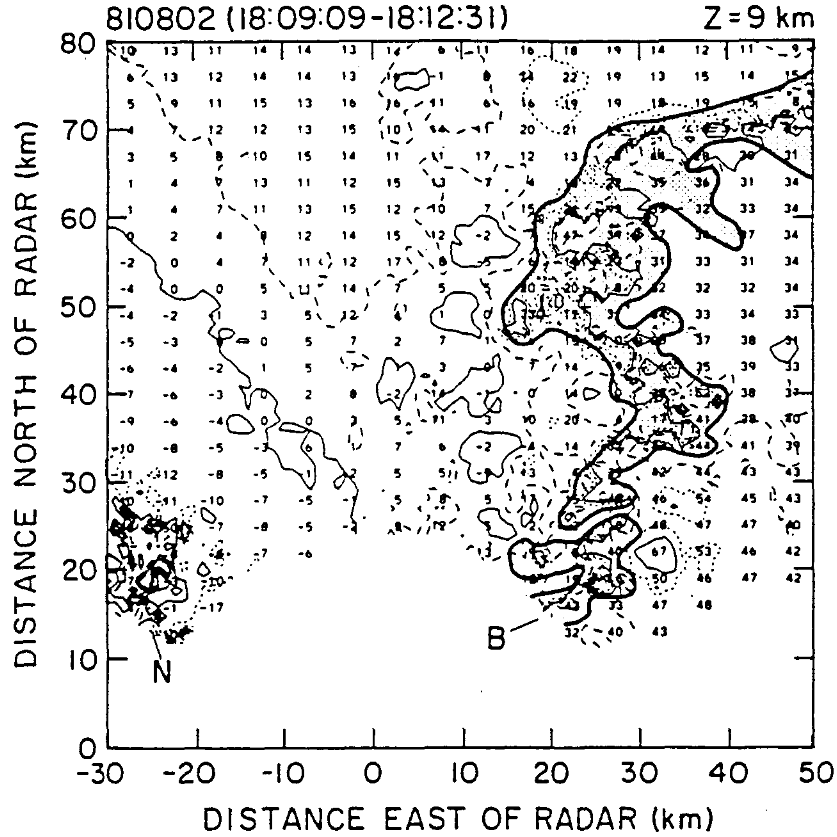

FIG. 10. Biased velocities that result when unedited and folded velocities are interpolated without invoking the local unfold algorithm. These data were then unfolded using the velocities in Fig. 7b as references. The shaded region surrounding the fold discontinuity contains biased velocities; that is, they cannot be unfolded to agree with Fig. 7b by the addition or subtraction of integer multiples of the ambiguous velocity, V_a.

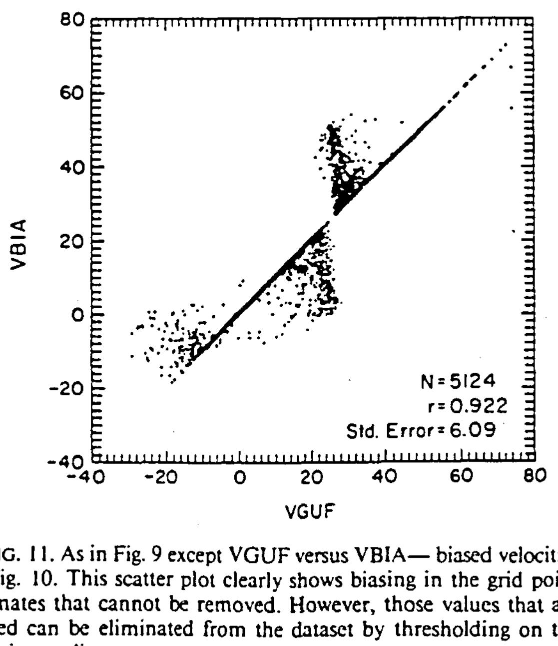

FIG. 11. As in Fig. 9 except VGUF versus VBIA— biased velocities of Fig. 10. This scatter plot clearly shows biasing in the grid point estimates that cannot be removed. However, those values that are biased can be eliminated from the dataset by thresholding on the velocity quality parameter.

technical staff in the maintenance and operation of the CP-2 radar. The success of the CCOPE experiment would not have been possible without the dedication of these technicians and engineers.

APPENDIX

Behavior of the Variance and Nondimensional Velocity Quality Parameter

In this appendix we consider the behavior of the variance [var(U)] and nondimensional velocity quality parameter (Q) in Eq. (5) when all radial velocity measurements are random noise. This is of fundamental importance since we calculate these statistics at each grid point and use their values to discriminate against interpolated velocities coming from regions of noise. The applicability of this exercise is limited, however, by the extent to which the pulse-pair processor is not ideal and does not yield a uniform distribution of output velocities in noise.

When no return signal is present, covariance-determined velocities will ideally be distributed uniformly from $-V_n$ to V_n, and thus will have a zero mean and variance $\sigma_n^2 = V_n^2/3$. However, the unfolding of such a distribution to a reference velocity that is a sample from the population results in a variance somewhat smaller than σ_n^2. The velocity notation used in the main body of the paper is retained: at radar sampling locations V_i and U_i represent measured and unfolded velocities, respectively. The local mean value of the unfolded velocities is

$$\bar{U} = \frac{\sum U_i}{I}, \tag{A1}$$

with variance [$Z = \mathrm{var}(U)$ in Eq. (5)]

$$Z = \frac{\sum (U_i - \bar{U})^2}{I - 1}. \tag{A2}$$

The expected value of Z for a uniform noise distribution is derived from the conditional probability density for the unfolded velocities U_i, given that a reference velocity $V_1 = v_1$ has been chosen. For $i \neq 1$, the U_i will be uniformly distributed over a range of $2V_n$ centered at v_1. The conditional probability density of the $U_i(i \neq 1)$ is

$$p_{U_i|V_1}(u_i|v_1) = \begin{cases} \dfrac{1}{2V_n}, & v_1 - V_n < u_i < v_1 + V_n \\ 0, & \text{otherwise.} \end{cases} \tag{A3}$$

Further, for $i = 1$ the unfolded velocity will certainly be v_1, given that $V_1 = v_1$:

$$p_{U_1|V_1}(u_1|v_1) = \delta(u_1 - v_1), \tag{A4}$$

where δ is the Dirac delta function. The conditional expectation or mean of each of the U_i is v_1:

$$\begin{aligned} E_c[U_i] &= \int du_i u_i p_{U_i|V_1}(u_i|v_1) \\ &= v_1. \end{aligned} \tag{A5}$$

The conditional expectation of Z may be expressed in terms of the conditional variances of the U_i given by

$$E_c[(U_i - v_1)^2] = \begin{cases} \sigma_n^2, & i \neq 1 \\ 0, & i = 1. \end{cases} \tag{A6}$$

Then by taking steps identical to those in the derivation of the expected value of a sample variance (e.g., Bendat and Piersol, 1971), it follows that

$$E_c[Z] = \frac{I-1}{I}\sigma_n^2. \tag{A7}$$

(This Z is actually not a sample estimate of variance in the usual sense, because the values of U_i do not constitute a random sample of a single random variable, U_1 being distributed differently than the other U_i.) From the definition of the velocity quality parameter in Eq. (5), the expected value of Q becomes

$$\begin{aligned} E_c[Q] &= 1 - E_c[Z]/\sigma_n^2 \\ &= \frac{1}{I}. \end{aligned} \tag{A8}$$

This will be near zero for most practical choices of I ($I = 12$ for 3-gate range averaging).

In order to distinguish between signal and noise using the parameter Q, it is important that the variance of Q in noise not be too large. Otherwise, a significant number of values of Q in noise, which are expected to be near zero, may actually be near unity, as they are for signal. The conditional variance of Q, $\mathrm{var}_c[Q]$, may be shown to be

$$\begin{aligned} \mathrm{var}_c[Q] &= \frac{4}{5(I-1)}\left(1 + \frac{1}{2I} - \frac{4}{I^2}\right) \\ &\approx \frac{4}{5I}. \end{aligned} \tag{A9}$$

This indicates that the reliability of Q as a discriminator against noise is increased by increasing the number of samples I going into each grid point estimate.

REFERENCES

Bendat, J. S., and A. G. Piersol, 1971: *Random Data: Analysis and Measurement Procedures*, Wiley-Interscience, 407 pp.

Carbone, R. E., F. I. Harris, P. H. Hildebrand, R. A. Kropfli, L. J. Miller, W. Moniger, R. G. Strauch, R. J. Doviak, K. W. Johnson, S. P. Nelson, P. S. Ray and M. Gilet, 1980: The multiple Doppler radar workshop, November 1979. *Bull. Amer. Meteor. Soc.*, **61**, 1169–1203.

Doviak, R. J., D. Sirmans, D. Zrnić and G. B. Walker, 1978: Considerations for pulse-Doppler radar observations of severe thunderstorms. *J. Appl. Meteor.*, **17**, 189–205.

Gal-Chen, Tzvi, 1982: Errors in fixed and moving frames of references: Applications for conventional and Doppler radar analysis. *J. Atmos. Sci.*, **39**, 2279–2300.

Knight, C. A. (Ed.), 1982: The Cooperative Convective Precipitation Experiment (CCOPE), 18 May–7 August 1981. *Bull. Amer. Meteor. Soc.*, **63**, 386–398.

Mohr, C. G., and L. J. Miller, 1983: CEDRIC—A software package for Cartesian space editing, synthesis and display of radar fields under interactive control. *Preprints, 21st Conf. on Radar Meteorology*, Boston, Amer. Meteor. Soc., 569–574.

——, and R. L. Vaughan, 1979: An economical procedure for Cartesian interpolation and display of reflectivity factor data in three-dimensional space. *J. Appl. Meteor.*, **18**, 661–670.

——, L. J. Miller and R. L. Vaughan, 1981: An interactive software package for the rectification of radar data to three-dimensional Cartesian coordinates. *Preprints, 20th Conf. on Radar Meteorology*, Boston, Amer. Meteor. Soc., 690–695.

Oye, R., and R. Carbone, 1981: Interactive Doppler editing software. *Preprints, 20th Conf. on Radar Meteorology*, Boston, Amer. Meteor. Soc., 683–689.

Ray, P. S., and C. Ziegler, 1977: De-aliasing first-moment Doppler estimates. *J. Appl. Meteor.*, **16**, 563–564.

———, R. J. Doviak, G. B. Walker, D. Sirmans, J. Carter and B. Bumgarner, 1975: Dual-Doppler observations of a tornadic storm. *J. Appl. Meteor.*, **14**, 1521–1530.

Rohatgi, V. K., 1976: *An Introduction to Probability Theory and Mathematical Statistics*, Wiley and Sons, 684 pp.

Zrnić, D. S., 1977: Spectral moment estimates from correlated pulse pairs. *IEEE Trans. Aero. Elec. Sys.*, **AES-13**, 344–354.

AN INTERACTIVE SOFTWARE PACKAGE FOR THE RECTIFICATION OF RADAR DATA TO THREE-DIMENSIONAL CARTESIAN COORDINATES

C. G. Mohr, L. J. Miller and R. L. Vaughan
National Center for Atmospheric Research*
Boulder, Colorado 80307

1. INTRODUCTION

Interactive mini-computer systems have become an indispensable medium for the acquisition, editing, display, and archival of digital radar data. The usefullness of interactive systems in an operational environment is well documented (see Silver and Geotis, 1976) and today most research radar processors incorporate a minicomputer as a major component in the acquisition system. In the laboratory environment, there exists a number of post-processing facilities which have been designed for the editing and display of archived data sets. Interactive systems at Alberta (Ramsden *et al.*, 1976), Air Force Geophysics Laboratory (Glover, 1980), and at the National Center for Atmospheric Research (Brown and Borgogno, 1980) have all proven themselves to be indispensable for the initial reduction and interpretation of digital radar data.

In forecasting developments for the 1980's Serafin and Lhermitte (1980) anticipated the evolution of even more elaborate interactive systems that would provide all the functions necessary for the synthesis and display of vector wind fields from multiple Doppler radars. As a modest step toward that goal we, at NCAR, have developed an interactive software package for the rectification of digital radar fields to a three-dimensional Cartesian coordinate system.

Aside from the obvious necessity for transforming multiple Doppler velocities to common coordinates, there are numerous advantages to be gained by replicating radar fields onto a regular Cartesian grid. The resultant data structure contains fewer data points, is easier to manipulate, facilitates the construction of more meaningful displays, and lends itself more readily to interpretation.

2. INTERACTIVE VS. BATCH INTERPOLATION

It is reasonable to question whether there are any advantages to be gained by implementing the task of Cartesian rectification as an interactive function. Characteristically, it is a time comsuming I/O intensive process best performed on a large general purpose computer. However, as experience has shown, this transformation is also a highly parameterized and occasionally unpredictable procedure often requiring numerous trial and error iterations before the radar data is satisfactorily replicated in Cartesian coordinates.

Unknowns to be resolved prior to final interpolation include 1) size, resolution, placement and orientation of the Cartesian grid; 2) identification of "noise" and how it should be handled; 3) fields to rectify and their attendent idiosyncrasies (i.e., Z vs. dBZ, velocity fields and the folding problem); and 4) the selection of an appropriate method for interpolation.

Consequently, there is an obvious need for observing the results of a particular interpolation in a timely fashion so that potential errors can be avoided prior to the archival of a permanent output file.

3. GENERAL OUTLINE OF THE SYSTEM

3.1 Hardware

The interactive package was developed for use on the Digital Equipment Corporation VAX family of minicomputers. The particular configuration upon which this package has been implemented is a VAX 11/780 processor with 2-160 megabyte disk drives, two magnetic tape transports and a 300 line per minute matrix printer with graphics capabilities. Users have access to the machine through a variety of alphanumeric and vector graphics terminals located in a common area. Although digital imaging hardware with color capability could certainly be supported it is not a requirement in this system.

Burgess *et al.* (1976) have shown that even in an operational environment, concise displays of Doppler data are possible without the need for sophisticated digital imaging equipment. For this reason, and in the interests of portability, we have taken some care not to inexorably link the interactive software in any way to specialized hardware or system-dependent features.

3.2 Software

As indicated in the previous section, emphasis was placed on making the basic software package portable from one system to another. It is written according to FORTRAN-77 standards and with the exception of the NCAR graphics software

* The National Center for Atmospheric Research is sponsored by the National Science Foundation.

(documented by Wright, 1978), the package does not require any resident or system-dependent routines.

All data structures and buffers are parameterized in the main program so that the package can be configured according to the size and nature of the radar data as well as the computer system upon which it is run. Program speed depends on a variety of factors including characteristics of the input data, buffer sizes, number of fields, and machine load. Nevertheless, a conservative timing estimate can be obtained based upon the number of grid locations in the Cartesian coordinate system by using 30,000 points per minute as a reference.

3.3 System Configuration

Figure 1 illustrates the major hardware and software components of the interactive Cartesian rectification system. Data flow paths indicate the relational structure among these components.

Transfer of data between magnetic tape and disk storage is handled by a separate program designed to process tapes generated in the common Doppler radar data exchange format. (See Barnes, 1980, for the specifications of this format.) Cartesian coordinate data is written to output

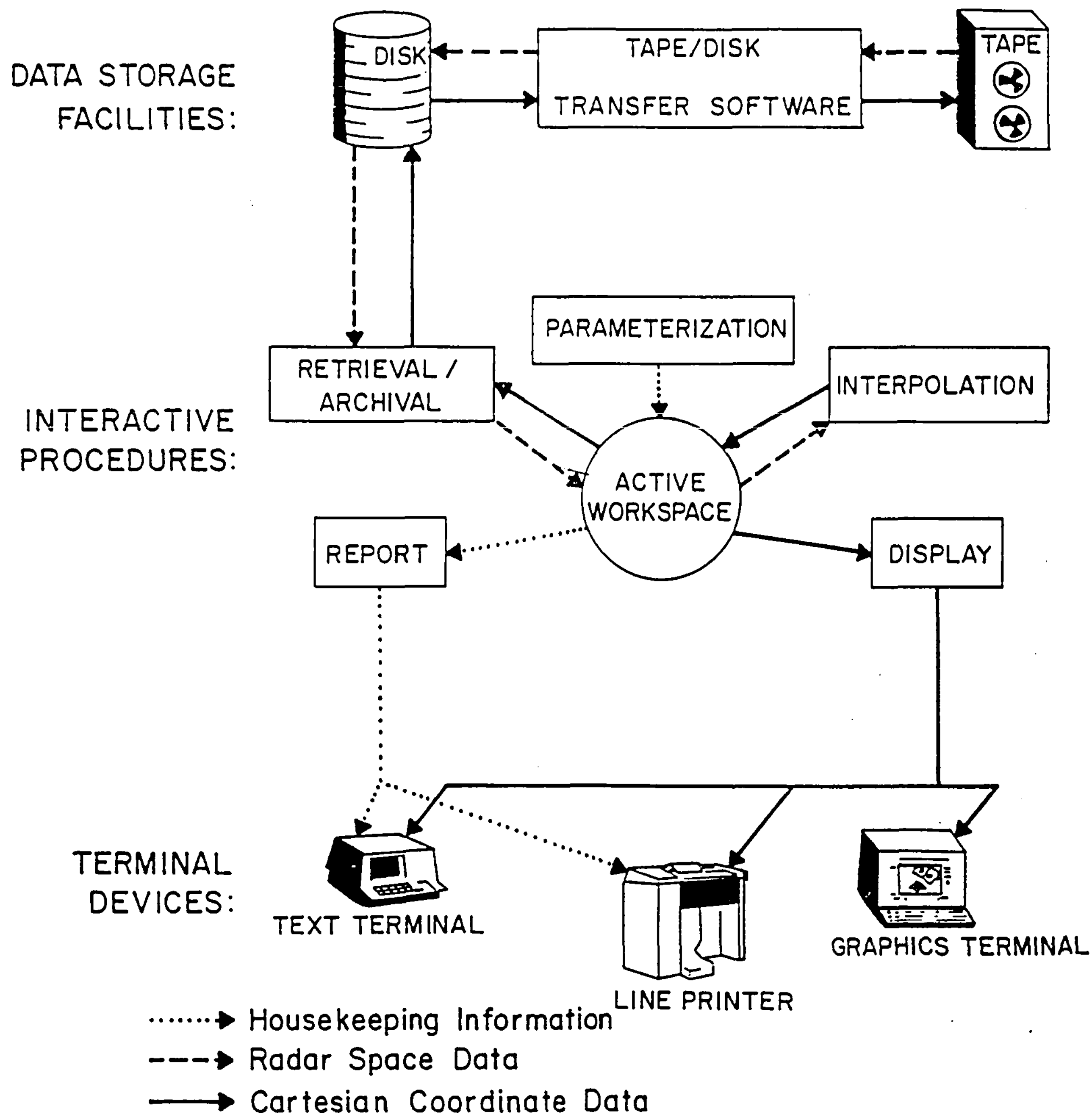

Fig. 1. Major hardware and software components of the interactive Cartesian rectification system. Relationships among components are indicated by data flow paths.

tapes in a standard format used within NCAR that is compatible with the batch mode Multiple Doppler Radar Analysis System (MUDRAS) described by Kohn *et al.*, 1978.

Interactive command procedures available to the user fall into five general categories:

1) Retrieval/archival of radar space and Cartesian data to and from disk;
2) Parameterization of the Cartesian coordinate system and rectification method;
3) Initiation of the actual interpolation;
4) Report on current parameterization and input/output data structures; and
5) Display by means of alphanumeric products and vector graphics.

Reports may be sent to either the text terminal at which the user is situated, a line printer, or both. Alphanumeric displays are disposed of similarly. If terminal devices with graphics capabilities are available, plots may be generated.

4. INTERACTIVE COMMANDS DESCRIPTION

4.1 Retrieval/Archival Commands

INPUT: This command connects a radar space data set residing on disk to the active workspace. It permits the user to process data from more than one radar without having to reenter the program.

VOLUME: This command selects an input volume scan from the connected radar space data set and activates it for input to the interpolation procedure.

MUDRAS: Once an acceptable Cartesian output volume has been generated (it may be one of several trial and error iterations), this command archives the result on disk storage as a permanent data set.

4.2 Parameterization Commands

CARTESIAN: This command allows the user to specify the characteristics of the destination Cartesian coordinate system. Size, resolution, orientation and placement are all defined by the user. In addition, the axis to be held constant (i.e., Z, Y, or X) and the spatial units of the axes (i.e., kilometers, miles, feet, etc.) may also be selected. The Cartesian grid may consist of up to 64 levels, each containing a maximum of 16,000 points.

METHOD: This command specifies the constraints under which the radar space data is to be converted to a Cartesian coordinate system. The purpose of the rectification procedure is to replicate the radar fields in X, Y, Z space with a minimum of alteration. Mueller (1977) has observed that small scale features, exemplified by high reflectivity gradients, appear less often as the sampling volume increases. Analogous results can be expected when "sampling down" to the Cartesian grid. For this reason we have elected to use as small a sample volume as possible in our rectification method; namely the volume defined by the eight original values surrounding each Cartesian location in space.

Figure 2 illustrates this sample volume and the basic method employed for Cartesian rectification. Wherever possible, bilinear interpolation is performed at the projection point on each of 2 successive elevation planes. A final estimate at the Cartesian location is computed using the interpolated values at the projection points. Mohr and Vaughan (1979) have shown this to be an effective method when applied to reflectivity data from severe storms. Miller and Strauch (1974) and Pytlowany *et al.* (1979) have also successfully employed similar interpolation procedures in the conversion of radar space data to CAPPI planes.

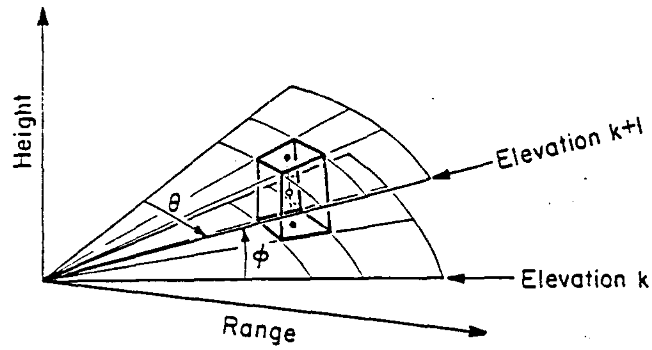

Fig. 2. Illustration of sampling volume used for Cartesian rectification. Volume is defined by the eight adjacent radar space samples surrounding a Cartesian location in space. Solid dots indicate projection points of the Cartesian grid location (shown as an open dot) on consecutive elevation scan planes k and k+1.

Within the framework outlined above, any one of three rectification methods may be specified:

1) *Closest point,* which selects the original radar value nearest the destination Cartesian location as the best estimate;

2) *Successive bilinear interpolation,* (described earlier); or

3) *Hybrid interpolation* whereby method 2 is performed whenever all eight values satisfy user-defined threshold criteria; otherwise the closest point (method 1) is selected. This hybrid method ensures that "noisy" data is replicated without significant alteration in weak signal regions.

When methods 2 or 3 are employed the user is asked to designate a threshold field and a minimum value upon which the validity of data points in all fields can be determined. For all methods, thresholds may also be set for each rectified field prior to output.

As mentioned earlier, certain problems are encountered when attempting to rectify reflectivity and velocity data. With respect to reflectivity data, some analysts choose to interpolate the intensity field while others prefer the computations to be performed on the logarithmic quantities dBM and/or dBZ. All three field types are recognized by the software and options exist for deriving dBM from intensity and dBZ from dBM after rectification has been completed.

Rectification of unedited velocity data is, of course, compounded by the aliasing problem. Potential ambiguities in the rectified velocity field estimates are avoided by ensuring that all eight radar values are in the same unambiguous nyquist velocity interval prior to interpolation. This optional de-aliasing technique is similar to the one described by Ray and Ziegler (1979) in which all velocities within a specified region are folded into the same interval according to some reference velocity. In our implementation the region consists of the eight points defining the three-dimensional sampling volume and the radial velocity value associated with the strongest returned power among the eight points is used as a reference. Should it become necessary, dealiasing of rectified estimates can be subsequently performed in Cartesian space without compromising the original radial velocity data.

4.3 Interpolation Command

The *INTERPOLATION* command transforms the data contained in the radar space volume to the designated Cartesian coordinate system according to the constraints specified by the user in the *METHOD* command. It may be invoked at any time provided that all relevant data structures and parameterization have been previously defined. That being the case, the user is able to make minor adjustments to the parameterization followed by re-interpolation until a satisfactory result is obtained. By the same token, once the proper parameterization has been established for a particular radar volume, subsequent rectification of similar cases may proceed without delay.

This command invokes a one-pass algorithm through the original radar data based upon the retrieval strategy prescribed by Mohr and Vaughan (1980). The current implementation has been modified to accommodate 360 degree scanning as well as Cartesian coordinate systems in which the radar position is embedded. There are no limits on the size of the input data set and a maximum of 10 radar fields may be processed at a time.

4.4 Report Command

The function of the *REPORT* command is to supply general information upon request and to maintain a permanent record of activity during an interactive session. Figure 3 contains an example of hard copy output generated for a single volume by the *REPORT* command. Summaries of the radar space data set, the Cartesian output file and the method employed for rectification all appear in this report. The insertion of user-supplied comments is also illustrated.

Although not included in this example, parameterization of the Cartesian coordinate system and header information associated with any archived data sets may also be examined. Any report which the user wishes to retain may be diverted to a permanent text file for future reference.

4.5 Display Command

Figure 4 contains examples of output generated by the DISPLAY command. These display products fall into two distinct categories.

4.5.1 Symbolic displays

Symbolic displays represent the data by means of alphanumeric symbols and are designed for use with inexpensive text terminals and line printers.

Whenever a symbolic display cannot be viewed completely within the area provided by a particular terminal, the display is automatically subdivided according to the characteristics of the device.

```
RADAR (.RAD)  VOLUME HEADER      PINTST
  DATE: 78/ 7/28        TIME: 14: 9: 2--14:18:32        PTS/RECORD:  384
  TAPE: E1677      RADAR: NOAA-C     PROGRAM: PULSIN.0     PROJECT: PINTST
  NO. OF FIELDS:  3

  FIELD NAME       SCALE FACTOR
     VEL                100
     VAR                100
     DBZ                100

  RADAR HEIGHT (KMSL):    1.500
  GATES/SCAN: 120   FIRST GATE (KM): 21.000      GATE SPACING (KM):  0.300
  NYQUIST VELOCITY (M/S): 16.10

  SCAN SUMMARY
   SCAN      ELEVATION        DIRECTION  (+1: CW, -1:CCW)
     1          0.50             -1
     2          1.50              1
     3          2.50             -1
     4          3.50              1
     5          4.50             -1
     6          5.50              1

INTERPOLATION METHOD SUMMARY

  METHOD:  DOPPLER HYBRID WITH OPTIONAL VELOCITY UNFOLDING

  INPUT FIELDS
   NO.    NAME      SCALE FACTOR       INTERPOLATE      RESET VALUE      FOLDING
    1     VC           100.0              YES                           FOLDED
    2     SW           100.0              YES
    3     DI           100.0              YES

  OUTPUT FIELDS
   NO.    NAME      SCALE FACTOR       INTERPOLATION    RESET VALUE      FOLDING
    1     VC           100.0              DIRECT                        UNFOLDED
    2     DZ           100.0              DERIVED           0.00
    3     SW           100.0              DIRECT

  THRESHOLDING
   FIELD: DI         MINIMUM ACCEPTABLE VALUE:     5.00
   NYQUIST (M/S):    16.10

CARTESIAN (.CAR)  VOLUME HEADER      TPOC            INTERPOLATION METHOD: 3
  DATE: 78/ 7/28        TIME: 14: 9: 2--14:18:32      PTS/RECORD:  512
  TAPE: E1677      RADAR: NOAA-C     PROGRAM: TERPOC.1     PROJECT: PINTST
  NO. OF FIELDS:  3
  FIELD NAME      SCALE FACTOR
   VE                 100
   DZ                 100
   SW                 100

  AXIS      MINIMUM (KM)       MAXIMUM (KM)       DELTA (KM)     NO. OF PTS.
    X          -45.00              -5.00              0.50            81
    Y          -30.00              10.00              0.50            81
    Z            2.00              10.00              1.00             9

     AXIS ORDER IS   X  Y  Z

  RADAR HEIGHT (KMSL):    1.500



  (X,Y) LOCATION OF THE RADAR (KM): (   0.00,   0.00)
  ANGLE OF X-AXIS REL. TO NORTH:   90.00


     *****   THIS IS AN EXAMPLE OF USER SUPPLIED TEXT   *****

     THE PRECEEDING INFORMATION IS A REPORT ON ...
       1- INPUT VOLUME IN RADAR SPACE,
       2- INTERPOLATION METHOD PARAMETERIZATION, AND
       3- CARTESIAN SPACE OUTPUT FILE.

            - END OF MESSAGE -
```

Fig. 3. Summary of an interpolated volume as generated by the REPORT command. Information regarding the input data set, Cartesian output file and transformation criteria are presented in this report.

When a text terminal is used, an interrupt (awaiting user response) is initiated after the generation of each subsection, so that the information remains frozen on the screen until it is no longer needed. Similar subsectioning, determined by the maximum number of characters per line, is performed without interruption when displays are disposed to a line printer.

Three symbolic products are currently available:

1) *Digital Display* - Fig. 4a is a digital display of reflectivity data from a 41 x 41 CAPPI plane. The number of digits is selectable and any datum which cannot be properly encoded according to the number of digits specified is represented instead by its sign.

2) *Coded Display* - Fig. 4b is a coded display of the same CAPPI. Individual symbols for each reflectivity estimate are generated according to a user-controlled symbol table. As in the previous display, periods indicate Cartesian estimates below threshold or for which no data exists.

3) *Statistical Summary* - Fig. 4d contains reflectivity field statistics for

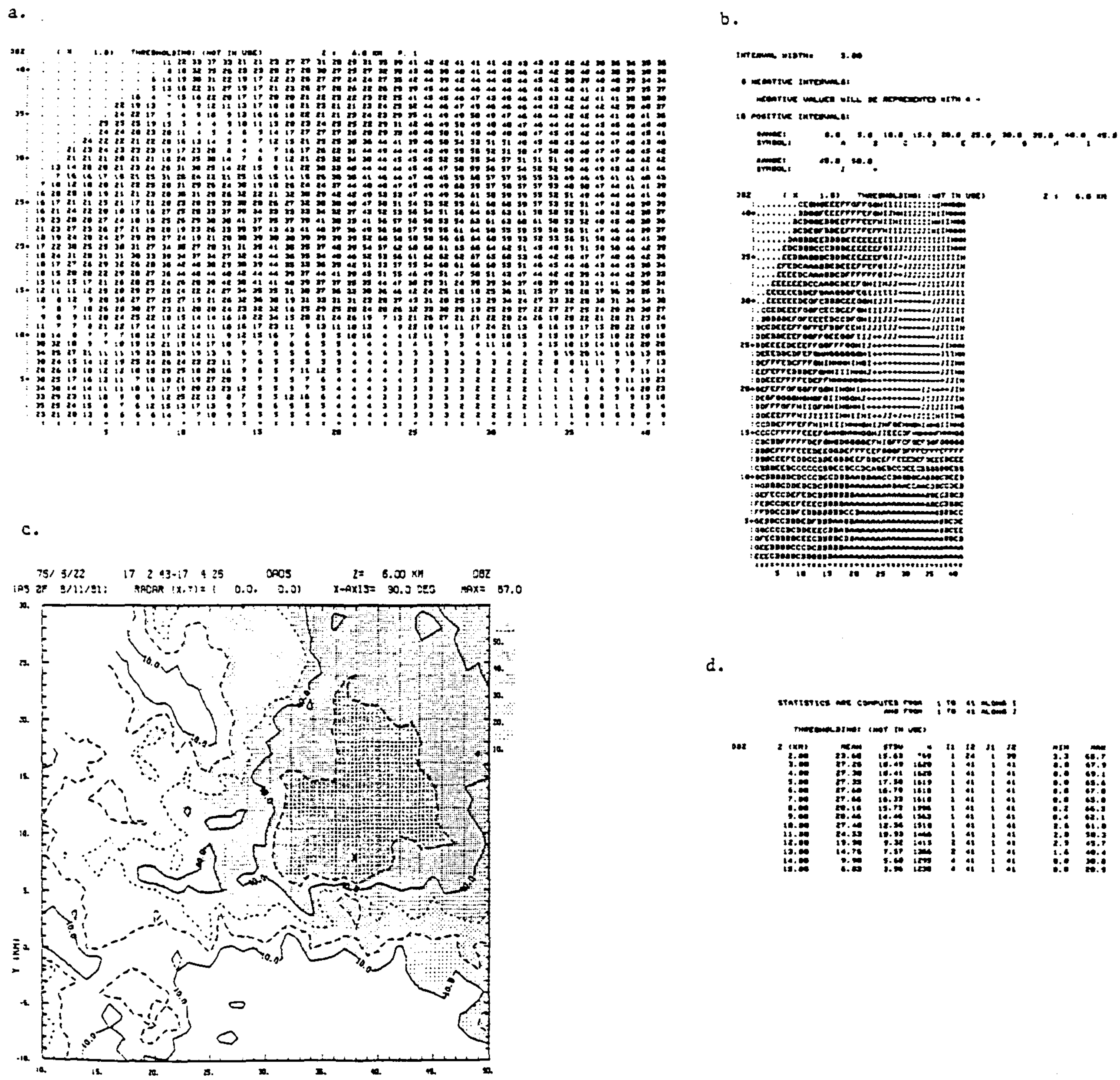

Fig. 4. Sample products generated by the DISPLAY command. In these examples the reflectivity field (dBZ) from a 41 by 41 CAPPI at 6 km is shown. Figure 4a contains a digital display of dBZ values. Periods indicate Cartesian locations below threshold or for which no data exists. Figure 4b contains a coded display, 4c contains a contour/grayscale plot and 4d contains a statistical summary for the entire volume. Annotation describes these displays in further detail.

every CAPPI in the volume. Statistics may be generated for any or all planes and radar fields.

For all presentations, the user is permitted to specify regions of interest and threshold criteria. Whenever digital and coded displays are produced, scaling factors may also be employed.

4.5.2. Graphics displays

These products can only be generated on terminal devices with graphics capabilities. Figure 4c contains a contour/grayscale plot of the same CAPPI presented in the digital and coded displays. Contour levels and grayscale tones may be generated separately or, as in this example, in conjunction with one another. Options permit the selection of a viewing window, contour levels, and annotation features.

More sophisticated displays, such as perspective illustrations of the data, have not been incorporated into the rectification software. Although the effort required to do so would be minimal, it is felt that such products best belong in a separate package designed specifically for the manipulation and display of archived data sets.

5. SUMMARY

The Cartesian rectification package has been operating experimentally for approximately six months. During that time a variety of modifications and embellishments (most of which are described in this manuscript) have been incorporated into the software. As discussed earlier, it is primarily intended for use in the reduction of Doppler radar data. The utility of this software will be examined in the fall of 1981 when it will be enlisted in the analysis of radar data collected during the 1981 CCOPE[1] field season. This interactive package has been developed as a supplement to the batch processing facilities already available on the large NCAR computers through the existing MUDRAS software.

Future plans call for the implementation of an interactive synthesis program and eventually the development of analysis software capable of editing, manipulating, and displaying Cartesian fields interactively. Throughout this effort we shall have a unique opportunity to examine which, if any, radar analysis functions should be performed in batch mode on a large computer and which, if any, belong in an interactive environment.

6. ACKNOWLEDGMENTS

The authors wish to acknowledge the efforts of Ray Bovet in establishing and maintaining the excellent facilities available on the MRS/VAX 11/780 which were used to develop and test the software. We also wish to acknowledge Karen Miller (CSD/NCAR) for her software support in the development of the tape to disk transfer programs and the report generator. Finally we wish to commend Will Garcia for his figure drafting and Carol Brown and Sue Stippich for preparing the manuscript.

[1] CCOPE is an acronym for the Cooperative Convective Precipitation Experiment conducted near Miles City, Montana, during the summer of 1981.

7. REFERENCES

Barnes, S. L., 1980: Report on a meeting to establish a common Doppler radar data exchange format. *Bull. Amer. Meteor. Soc.*, *61*, 1401-1404.

Brown, B. C., and V. F. Borgogno, 1980: A laboratory radar display system. *Preprints 19th Conf. on Radar Meteorology*, Miami Beach, Amer. Meteor. Soc., 272-285.

Burgess, D. W., L. D. Hennington, R. J. Doviak and P. S. Ray, 1976: Multimoment Doppler display for severe storm identification. *J. Appl. Meteor.*, *15*, 1302-1306.

Glover, K. M., 1980: On the automation of weather radar information for air and ground operations. *Preprints 19th Conf. on Radar Meteorology*, Miami Beach, Amer. Meteor. Soc., 118-124.

Kohn, N. M., A. L. Johnston and C. G. Mohr, 1978: MUDRAS - Multiple Doppler radar analysis system. *NOAA Tech. Memo. ERL/WPL-35*, Wave Propagation Laboratory, Boulder, 170 pp.

Miller, L. J., and R. G. Strauch, 1974: A dual-Doppler radar method for the determination of wind velocities within precipitation weather systems. *Remote Sens. Environ.*, *3*, 219-235.

Mohr, C. G., and R. L. Vaughan, 1979: An economical procedure for Cartesian interpolation and display of reflectivity factor data in three-dimensional space. *J. Appl. Meteor.*, *18*, 661-670.

_____ and _____, 1980: A proposed algorithm for the real-time interpolation of reflectivity factor data in three-dimensional space. *Preprints 19th Conf. on Radar Meteorology*, Miami Beach, Amer. Meteor. Soc., 294-300.

Mueller, E. A., 1977: Statistics of high radar reflectivity gradients. *J. Appl. Meteor.*, *16*, 511-513.

Pytlowany, P. J., F. P. Richards and M. D. Hudlow, 1979: GATE radar CAPPI derivation for three-dimensional reflectivity analysis. *NOAA Tech. Memo. EDIS-27*, Environmental Data and Information Service, Washington, D. C., 28 pp.

Ramsden, J., M. R. Johnson, R. G. Humphries and B. L. Barge, 1976: Interactive computer-generated displays of radar data. *Preprints 17th Conf. on Radar Meteorology*, Seattle, Amer. Meteor. Soc., 468-473.

Ray, P. S., and C. Ziegler, 1977: De-aliasing first-moment Doppler estimates. *J. Appl. Meteor.*, *16*, 563-564.

Serafin, R. J., and R. M. Lhermitte, 1980: Meteorological radar developments in the 1980's. *Prep. 19th Conf. on Radar Meteor.*, Miami Beach, Amer. Meteor. Soc., 679-685.

Wright, T., 1978: NCAR Graphics software (Fourth Preliminary Edition). Prepared by the Atmospheric Technology Division of the National Center for Atmospheric Research, Boulder, Colorado.

Reprinted from JOURNAL OF ATMOSPHERIC AND OCEANIC TECHNOLOGY, Vol. 3, No. 1, March 1986
American Meteorological Society

The Merger of Mesoscale Datasets into a Common Cartesian Format for Efficient and Systematic Analyses

CARL G. MOHR, L. JAY MILLER, ROBIN L. VAUGHAN AND HAROLD W. FRANK

National Center for Atmospheric Research, Boulder, CO 80307*

(Manuscript received 3 March 1985, in final form 8 July 1985)

ABSTRACT

During the 1981 summer season within a 70 000 km² area surrounding Miles City, Montana, researchers from approximately twenty institutions participated in the Cooperative Convective Precipitation Experiment (CCOPE). The measurements collected during this project comprise one of the most comprehensive datasets ever acquired in and around individual convective storms on the high plains of North America. Principal data systems utilized during CCOPE included 8 ground-based radars (7 of which had Doppler capability), 12 instrumented research aircraft, and a network of 123 surface stations.

A major data processing goal has been to combine these independently acquired mesoscale measurements into a numerical description of observed atmospheric conditions at any point in time. Using the CCOPE data archive as an example, this paper describes the procedures used to reduce these high resolution observations to a common spatial and temporal framework. The final product is a digital description of the environment similar to that employed by most modelers—a three-dimensional Cartesian coordinate system containing fields that represent the instantaneous state of the atmosphere at discrete times across the period of interest. A software package designed to facilitate the construction and analysis of these composite data structures will also be discussed.

1. Introduction

One of the fundamental purposes of the Cooperative Convective Precipitation Experiment (CCOPE) was to assemble a comprehensive dataset on convective clouds using the fullest possible array of available meteorological measurement systems. Efforts were focused on acquiring and later reconstructing complete descriptions of the atmospheric conditions related to three phases of thunderstorm activity: prestorm, early storm, and mature storm. During the three-month period of operation, approximately 300 billion bits worth of information were recorded on computer tape for later reduction and analysis. A complete summary of the 1981 CCOPE field program along with a list of all the organizations and individuals responsible for the various instrument systems is provided by Knight (1982).

The challenge from a data processing standpoint was to reduce this large body of measurements as efficiently as possible and to make it accessible for analysis by any and all participants. A considerable number of software systems have been developed for the purpose of compositing meteorological observations. Most are designed to be used interactively on minicomputers and each can be identified with respect to some area of specialization. PROFS (Reynolds, 1982) assimilates real-time information for use in regional-scale forecasting; McIdas III (Suomi et al., 1983) and GEMPAK (desJardins and Petersen, 1985) provide excellent facilities for the analysis of conventional and satellite measurements; PCDS (Treinish and Ray, 1985) processes climatological datasets; and RADPAK (Heymsfield et al., 1983) contains highly accurate algorithms for remapping satellite data and edited radar observations to common display coordinates.

The procedures and software described in this article have been developed for use in a batch environment and their primary purpose is to reduce high resolution measurements from different field observation systems to a large multidimensional data structure (>100 000 grid locations). The batch computing environment at NCAR consists of two Cray-1A processors, an AMPEX terabit mass storage device, and a Dicomed camera system with 4096^2 resolution. This environment is ideal for processing data from mesoscale field experiments such as CCOPE for the following reasons:

Accessibility. A large segment of the atmospheric community has access to the computing facilities at NCAR and all the datasets and programs are readily available on the system.

Computing power. The vectorizing architecture and speed of the Cray-1A processor permits the use of multidimensional editing and analysis algorithms that cannot be supported on smaller machines.

Throughput. Multiple datasets representing hours of observations can be analyzed by a single job.

* The National Center for Atmospheric Research is sponsored by the National Science Foundation.

Hard copy capability. Publication quality displays can be produced in large quantities quickly and inexpensively.

The algorithms utilized for reducing and analyzing these field measurements are, for the most part, well known and are documented in the literature. Our strategy has been to organize them together in a fashion so that major decisions regarding the final form of the composite storm description can be postponed until reports from all sources have been converted to Cartesian coordinates. By way of illustration, a unified digital description of a mature storm observed during CCOPE on 1 August 1981 at 1640 local time will be constructed from independent Doppler radar, aircraft, and surface instrument network (i.e., mesonet) measurements. A software package called CEDRIC that contains a comprehensive set of analysis tools for manipulating the information in these data structures will also be discussed.

2. Data collection and archival

The successful reconstruction of a mesoscale event from multiple data sources is directly related to how well the information is organized. Analysis efforts in the past have been needlessly complicated by the diversity of formats produced by independent instrument systems. In recognition of this problem common archive formats for Doppler radar and mesonet observations were informally adopted by the meteorological community at the beginning of the decade (Barnes, 1980). These formats were utilized in CCOPE, and as a direct result we were able to avoid costly reformatting and maintenance of redundant software systems for those datasets. Similar benefits were realized for the set of airborne measurements through the use of generalized input routines.

Figure 1 contains a schematic diagram depicting a typical CCOPE mature storm study and the roles of the principal data systems in the investigation. A detailed summary of the entire archive along with the technical specifications of each system can be found in the 1981 CCOPE Data Inventory (1982).

a. Radar

Seven Doppler radars participated in coordinated scanning of the target volume while an eighth conventional radar maintained surveillance over the entire region. Each Doppler radar recorded reflectivity and radial velocity and, at two of the sites, dual wavelength reflectivity measurements were acquired at wavelengths of 10 and 3 cm. Approximately 2–4 min were required to scan a mature storm, and during that time each radar collected upwards of one million individual pulse volume samples. The life cycle of most storms was embodied in 10–20 of these coordinated three-dimensional scans. In accordance with the CCOPE operations

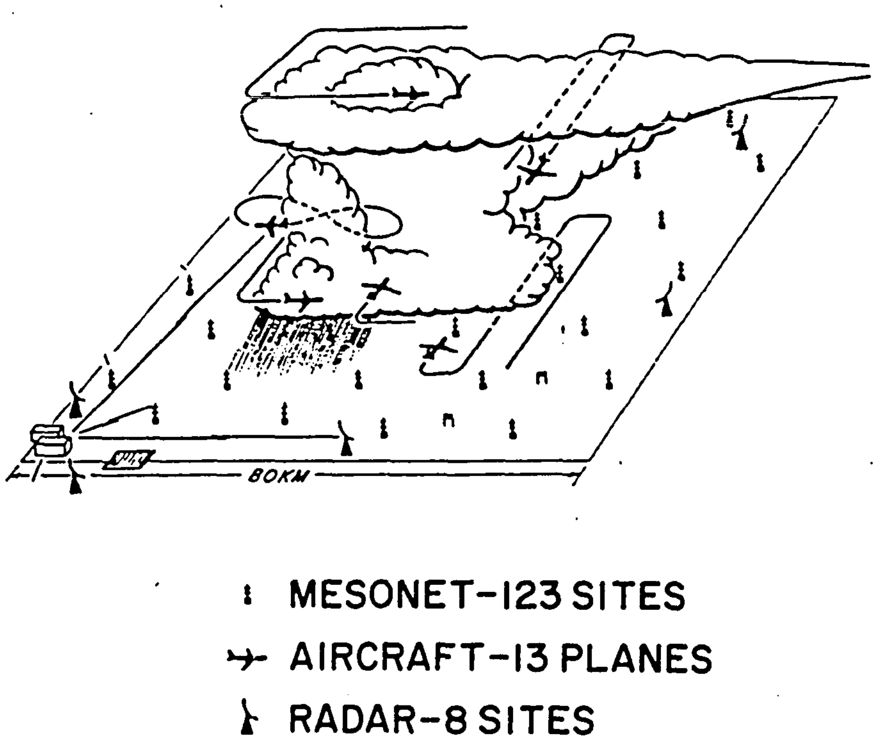

FIG. 1. Schematic depiction of a typical CCOPE mature storm study illustrating the principal data collection systems and their roles in the investigation. (Courtesy Water and Power Resource Service, U.S. Dept. of Interior.)

plan (1981), the organizations responsible for the individual radars provided their data in the common Doppler radar exchange format described by Barnes (1980). An obvious benefit of this requirement was that it shifted the burden of reformatting from the analysts to the suppliers of the data. As a result, the problems associated with imposing a logical structure onto the volume scans were solved by those persons who were best equipped to deal with the idiosyncrasies of their respective datasets. In general, this "universal radar format" is an excellent medium for the archival and exchange of radar space information. Although inconsistencies were later detected in some of the tapes, appropriate corrections could usually be made in the access software. Only on rare occasions was it necessary to rewrite any of the original archive tapes.

b. Aircraft

As many as 12 instrumented aircraft ranging from a motorless Schweizer 2-32 sailplane to a multi-engine Convair 990 jet collected in situ measurements throughout various regions of the thunderstorm. Typical missions included coordinated updraft mapping near cloud-base (propeller-driven aircraft), penetrations into developing cloud turrets (propeller and sailplane), and systematic probing of the storm top and surrounding environment (jet aircraft). Independent onboard data acquisition and display systems generated digital time series of pressure, temperature, moisture, wind, and hydrometeor occurrences along with related navigational information. These reports were recorded directly onto magnetic tape at a basic rate of one sample per second. The duration of most research flights was from two to four hours.

The aircraft data base, like the radar data base, consisted of reduced and calibrated measurements archived on magnetic tapes that were provided by the same institutions that collected the data. Since no "common format" existed for aircraft data, the programs that read these tapes had to be made flexible enough to accommodate time series reports from any source. The program best exemplifying this particular approach is the GENPRO processor (Lackman and Friesen, 1983) which was used to generate standard plots of common parameters for all participating aircraft.

c. Mesonet

A fixed network of 123 automated surface stations was deployed over a region 120 km on a side. Ninety-six of these stations (PROBE)[1] were spaced at 20 km intervals over the entire area while 27 sites (PAM)[2] were nested within the larger array at 7 km intervals in a more densely-spaced network whose dimensions were 60 by 50 km. The PROBE system telemetered 5 min averages of pressure, temperature, moisture, and wind via satellite to a central computer in Denver, Colorado where the reports were transferred to magnetic tape for subsequent processing. PAM stations transmitted similar information at 1-min resolution via radio link to a nearby communications center, which was responsible for real-time display and archival of the measurements. Except for an occasional instrument failure, both systems operated 24 hours a day.

Magnetic tapes containing measurements from the PROBE (5 min) and PAM (1 min) networks were provided separately in the common mesonet exchange format. By agreement no editing was performed on these archive datasets other than to identify events associated with instrument malfunctions. Data from the two networks were reassembled on the mass storage system at NCAR and reports from all 123 sites were subsequently calibrated using systematic procedures developed by Wade and Engle (1985).

The existence of common formats (radar and mesonet) and the design of flexible input algorithms (aircraft) meant that only one access routine was needed to read any or all reports from a given dataset. As a result, basic archival tasks specific to each system such as intercomparison of independent instruments, incorporation of improved calibrations, and the generation of standard graphic products were all greatly simplified. For example, if an additional display of airborne measurements was requested, the changes only had to be made in a single program instead of a dozen (one per aircraft) potentially different places! Similar savings in software development and maintenance costs were realized for the radar and mesonet systems.

3. Building the composite data structure

Once well-calibrated, internally consistent, and complete datasets have been constructed for each of the systems, the reports can be remapped to Cartesian coordinates. Identified with each grid location are all available meteorological parameters, or fields, describing the atmospheric parcel that it represents in space and time. Fields of interest include pressure, temperature, moisture, reflectivity, and the (u, v, w) components of the vector signifying the instantaneous motion of the parcel. The advantages of this destination data structure are obvious. It is simple enough so that fields from any measurement system can be incorporated and the data at any location can be readily accessed, manipulated, altered, and displayed.

Figure 2 illustrates our data processing scheme. Reports from the radar, aircraft, and mesonet datasets are converted to the destination Cartesian coordinate structure using specialized interpolation routines called SPRINT, ACANAL, and SMANAL, respectively.

[1] Portable Remote OBservations of the Environment system operated by the Montana Department of Natural Resources and Conservation.

[2] Portable Automated Mesonet system operated by the Atmospheric Technology Division of the National Center for Atmospheric Research.

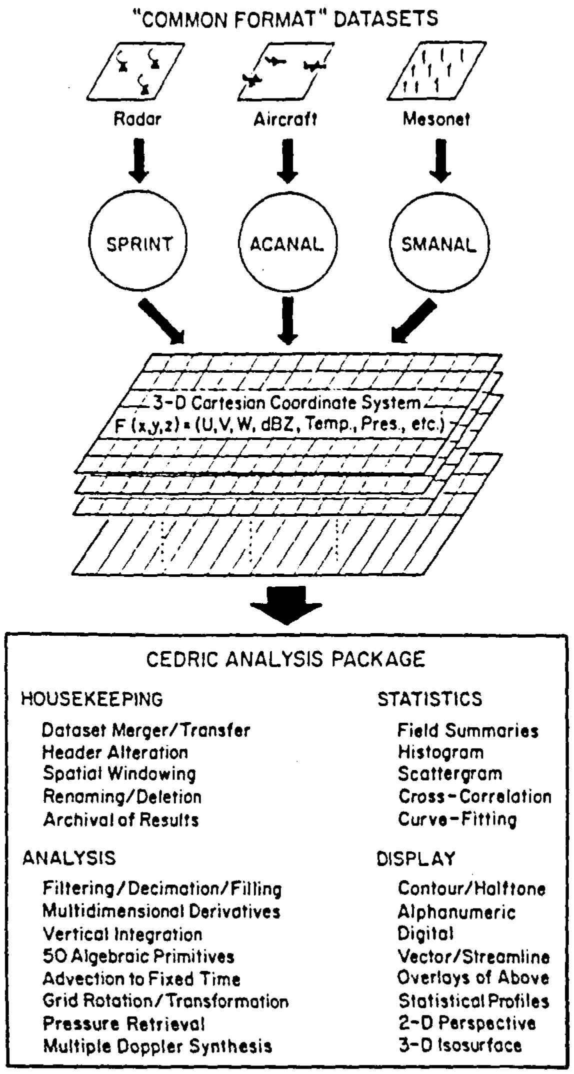

FIG. 2. Processing diagram illustrating the flow of information from the common format datasets to the multi-parameter Cartesian coordinate structure. Specialized transformations specific to each dataset perform the remapping. Additional manipulation of the Cartesian space reports is conducted using CEDRIC.

These remapping procedures utilize existing techniques and have been designed to provide the user with a broad range of options for preconditioning the input reports, parameterizing the transformations, and examining the interpolated fields. Researchers may freely manipulate these options in order to generate gridded products that satisfy their personal preferences and scientific requirements. Unlike some software systems (e.g., Koch et al., 1983) no constraints are imposed on the selection of values affecting either the weighting function or the placement and resolution of the output grid.

Each interpolation procedure is also capable of transferring input reports without alteration to the nearest destination Cartesian grid location. This additional capability has proven useful for making point comparisons of independent observations such as radar parameters versus in situ aircraft measurements. These kinds of studies and other analyses are performed on the resultant Cartesian data structures using the CEDRIC (Custom Editing and Display of Reduced Information in Cartesian Space) software package.

a. Radar

Ground-based radar measurements are converted to a three-dimensional Cartesian coordinate system by SPRINT, using a successive linear interpolation algorithm described by Mohr and Vaughan (1979) and Mohr et al. (1981). Each field selected for interpolation is independently converted using original radar measurements from the four beams (two on either side, above and below) surrounding each destination Cartesian location in space. This procedure is illustrated in Fig. 3. The open dot indicates a destination grid point. Solid dots appear at its projection point along an arc of constant range on adjacent elevation planes k and $k + 1$. Radar space input reports are denoted by the corners of the box. Estimates at each projection point are computed using bilinear interpolation—first along range and second across azimuth. A final linear interpolation is performed along elevation using the estimates at these projection points in order to produce a resultant value at the Cartesian location.

Whenever there is an insufficient number of reliable (that is, not flagged as missing or "bad") radar space values to perform a bilinear interpolation at the projection point on an elevation plane, the closest input report whether it be "good" or "bad" is selected instead. If either or both elevation planes have been assigned a closest point value, the Cartesian location will receive its final estimate from the nearer of the two. This is done to ensure that "noisy" data are replicated without significant alteration in the weak signal regions, particularly along the edges of the storm.

When using this hybrid technique, the user must specify a maximum distance past which a "closest" point value should not be trusted as being represen-

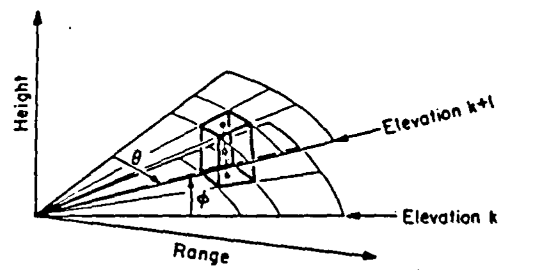

FIG. 3. Illustration of sampling volume used for Cartesian transformation of radar data. Volume is defined by the eight adjacent radar space samples surrounding a Cartesian location in space. Solid dots indicate projection points of the Cartesian grid location (shown as an open dot) on consecutive elevation scan planes k and $k + 1$. The quantity θ is the angular direction along azimuth and Φ is the elevation angle above the horizon (after Mohr et al., 1981).

tative. If this distance is exceeded along any one axis (range, azimuth, or elevation), the Cartesian location will be flagged as missing. The user may also attempt to equalize the spatial resolution in the range and azimuth directions by requesting that a fixed number of gates be averaged along each beam. Certain field types receive specialized treatment in SPRINT:

1) *Velocity*. The finite interval over which a uniformly pulsed Doppler radar measures radial velocities is from $-V_n$ to $+V_n$ where V_n is the Nyquist velocity expressed as a function of the pulse repetition frequency (PRF) and transmitted wavelength (λ):

$$V_n = (\text{PRF})\lambda/4. \tag{1}$$

Whenever the true velocity exceeds the magnitude of the Nyquist value for a given radar the measured velocity is ambiguous or "folded." Velocity fields are conventionally unfolded one elevation plane at a time in radar space using, for example, the interactive Doppler editing software (IDES) developed by Oye and Carbone (1981). An alternative technique proposed by Miller et al. (1985) demonstrates how unfolding can instead be performed in Cartesian space provided that the input velocities contributing to the estimate at each grid location are forced into the same unambiguous Nyquist interval during the interpolation. SPRINT has been designed to support either approach.

2) *Quality*. Whenever a velocity field is interpolated, SPRINT generates a corresponding field called QUAL that contains a measure of the quality of the Cartesian space velocity estimates. This nondimensional parameter is derived at every grid location using:

$$Q(x, y, z) = 1 - \text{var}(U)/(V_n^2/3) \tag{2}$$

where var(U) is the spatial variance of the unfolded input velocities contributing to the estimate. The discriminating properties of Q are described by Miller et al. (1985).

3) dBZ and dBM. Fields whose estimates are in logarithmic units may be optionally converted to linear units before any calculations are performed. If no reflectivity (dBZ) field is present, it may be derived from the received power (dBM).

4) *Time*. SPRINT does not adjust for storm motion when it remaps radar space reports to Cartesian coordinates. Instead, the time in seconds relative to the beginning of the scan is calculated from the header information associated with the four beams surrounding each Cartesian grid location and saved as an additional parameter in a field called TIME. The presence of this field enables us to interpolate observations from the individual radars without having to deal with the problem of storm advection at this step of the data reduction. Although some accuracy is lost (the four beams contributing to each grid estimate may be as much as 15 s apart), advecting in Cartesian space offers more flexibility in the later stages of the analysis, particularly when determining which analysis time and combination of radars produces the most representative wind field.

SPRINT provides a description of the input and output characteristics of every volume that it processes along with a statistical summary of the interpolated fields.

b. Aircraft

Aircraft measurements acquired at a constant altitude are remapped by ACANAL to a two-dimensional Cartesian grid that is structurally compatible with the synthesized radar observations. Complete details of the procedure are given in Fankhauser et al. (1985). An important region of the storm that contains insufficient reflectors to be adequately observed using radar is the inflow sector just below cloud base. Constant altitude flight patterns designed to map this region were flown every 15 to 20 min by one or more research aircraft. Figure 4a contains the ground-relative track flown by an instrumented Beechcraft Queen Air (304D) during a 16 min period of inflow observation on 1 August 1981. The symbol (+) is plotted at 12-s intervals along the track. Circles appear every whole minute. In order to generate an instantaneous picture of the region under investigation, it is necessary to select a fixed analysis time (1640 MDT) and to reposition each 1-s input report either forward or backward in space with respect to the moving storm. The result of this time normalization using the observed storm motion of 263° at 8.3 m s^{-1} is given in Fig. 4b. Vectors emanating from the repositioned track denote direction and speed of the ground-relative horizontal (u, v) winds measured by the aircraft.

Given an airplane ground speed of ~80 m s^{-1}, the spatial separation of the 1-s reports is approximately 80 m. Information at this resolution is considerably denser than both the intertrack distances (2.5 km) and the typical spacing of the Cartesian grid locations (1 km). These differences are resolved by applying a low pass filter to the time series of all original measurements and extracting the filtered samples at intervals consistent with those larger scales for input to the interpolation algorithm. In this case a 12-s interval was chosen which corresponds to a distance of ~1 km. The locations of these input reports are denoted by the (+) symbols appearing in Fig. 4a, b.

The Barnes objective analysis scheme (Barnes 1964; 1973) is utilized for interpolating the irregularly spaced input values to Cartesian coordinates. The weight assigned to an input datum at distance D from a specific grid location is given by the exponential function:

$$W = \exp[\ln(c)(D^2/R^2)], \tag{3}$$

where R is a user-selectable "radius-of-influence" at which W is equal to c. All input values are weighted

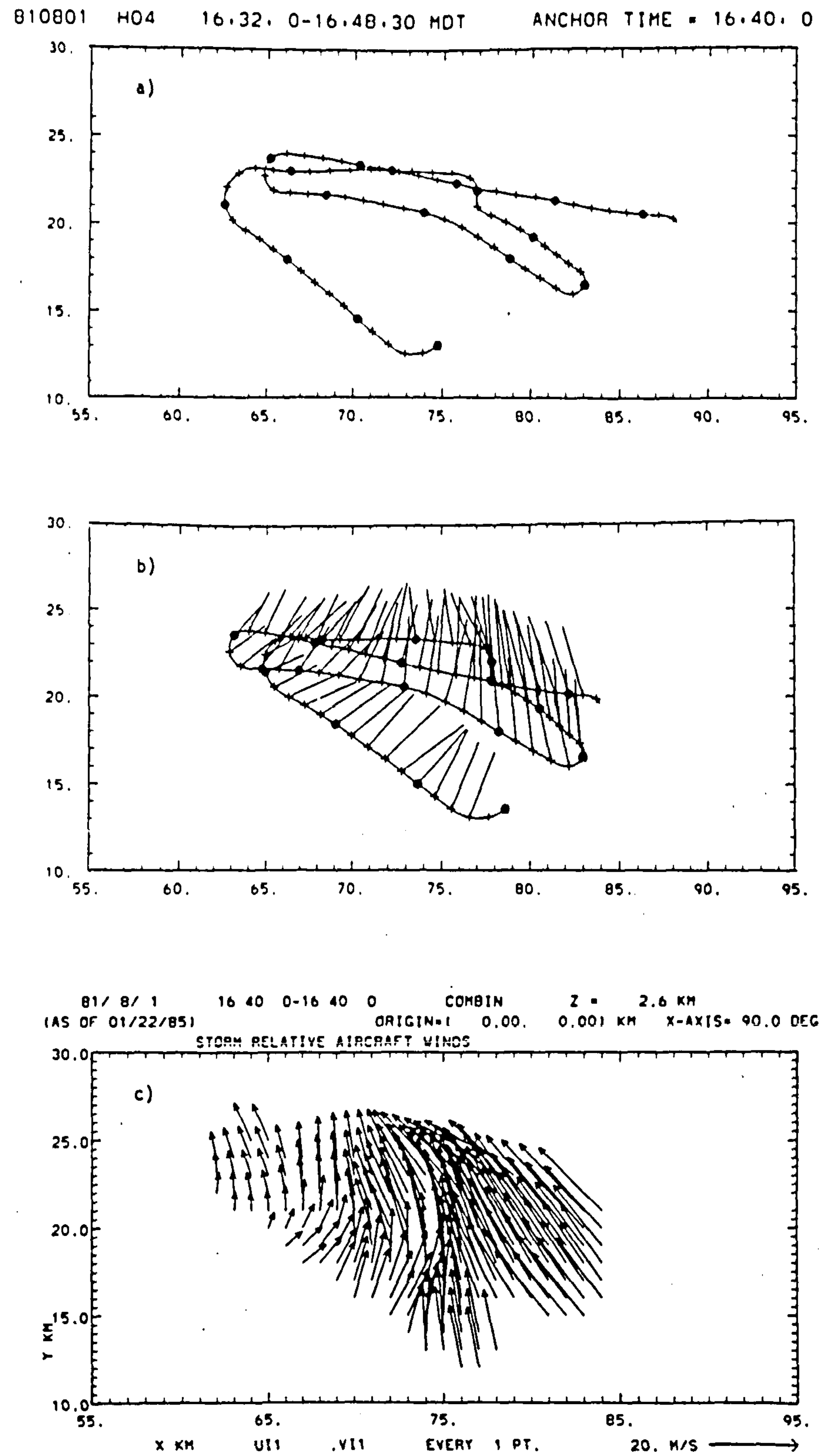

FIG. 4. (a) Ground relative flight track for NCAR Queenair Hiplex-4 (H04) flown near cloudbase (2.6 km MSL) in the inflow sector of a large thunderstorm on 1 August 1981 during the indicated time period. Track begins at (x, y) grid location (75, 13). Circles indicate 1 min positions. (b) Flight track in (a) repositioned with respect to observed storm motion of 263° at 8.3 m s^{-1} and an analysis time of 1640 MDT. Horizontal wind vectors plotted at 12 s intervals along the track are ground relative and are scaled so that 5 km = 20 m s^{-1}. (c) Storm relative horizontal airflow interpolated to a 1-km resolution grid using input from (b) and subtracting out the storm motion. Reference vector appears at lower right. Axes are labeled in km relative to the primary research radar, CP-2, located near Miles City, Montana (after Fankhauser et al., 1985).

using this relationship and the resultant normalized estimate is assigned to the grid location. The constant c has been set to 0.1 so that R uniquely determines the shape of the function. Using simulated data fields Caracena et al. (1984) have shown that the ideal value for λ_0 in the generalized Gaussian weighting function

$$W = \exp[-D^2/\lambda_0^2] \tag{4}$$

can be determined by:

$$\lambda_0 = 1.366\Delta X,$$

where ΔX is the spacing of the input reports. Accounting for the natural logarithm of 0.1 which we have incorporated into our formulation, this result translates to an optimal value of $R \approx 0.9\Delta X$ in Eq. (3). Since the distance between input reports is almost never uniform, the coarsest spatial resolution in any direction through the advected data generally determines our choice of ΔX and subsequently R as well. Another user-selectable parameter is the number of iterative improvement passes to apply to the grid of interpolated estimates. Each pass reduces the difference between the original input values and their Cartesian space counterparts by applying the same remapping function to the current set of residuals.

The resultant horizontal wind field is illustrated in Fig. 4c. An influence radius of 3 km with 5 iterative passes was used to perform the remapping, and storm relative vectors have been computed by subtracting the storm motion vector from the interpolated (u, v) components. Interpolated fields that are routinely produced from constant altitude aircraft observations include the components of air motion (u, v, w), pressure, temperature, and mixing ratio. Display products generated by ACANAL include profiles of the input time series (filtered and unfiltered) as well as two-dimensional plots (as in Fig. 4) of the constant altitude observations before and after interpolation.

c. *Mesonet*

Surface mesonet reports are remapped by SMANAL to a structurally compatible two-dimensional Cartesian grid in another region of the storm where the radar cannot provide accurate meteorological observations—near the ground. The mesonet input dataset consists of average values from all 123 sites at a uniform resolution of 5 minutes. Figure 5a contains a map showing every operational station inside a 90 by 90 km section of the surface network on 1 August 1981. Data from these sites are to be interpolated to a Cartesian grid with 1 km spacing whose boundaries are delineated by the dashed box in the center of the figure. Figure 5b shows the relocated horizontal wind measurements that are used as input to the remapping. In order to increase the number of input measurements and to preserve any transient features in the airflow that happen to be situated between stations at the analysis time (1640 MDT), provisions are made for the inclusion of as many as six additional off-time reports. This advective procedure is similar to that prescribed by Barnes (1973) where the relative weight of the relocated reports may, at the analyst's discretion, be lessened as a function of time. In the example shown, fully-weighted observations from 1635 and 1645 MDT have been displaced downstream and upstream respectively according to the same observed storm motion (from 263° at 8.3 m s^{-1}) used to reposition the aircraft track.

The same formulation (Eq. 3) that was utilized for interpolating the aircraft observations is also applied to the input surface mesonet reports. Optional variations that are available to the analyst for dealing with the unevenly-spaced network include:

(i) specifying two different radii-of-influence—one for the PROBE network and the other for the more densely spaced region embedded within it;

(ii) designating a minimum and maximum radius-of-influence and permitting the algorithm to compute a value between the two at each individual grid location based upon the spatial distribution of the surrounding input reports; and

(iii) removing all the PAM sites from the interpolation in order to work with a network of stations (PROBE) that is uniformly spaced.

For the remapping demonstrated in Fig. 5, all sites were included and a fixed radius of 25 km with two iterative passes was used in order to maintain uniform resolution across the entire output grid. Although there is a considerable loss of detail in the western half of the network, the position of the storm in our example required that we compromise the analysis with this seemingly large radius-of-influence so that the surface observations could be remapped to the area shown without any distortion effects in the data sparse regions. The results of interpolating the horizontal wind field (depicted in Fig. 5b) and subtracting out the storm motion vector are presented in Fig. 5c. Every third vector is plotted. The pressure, temperature, and moisture fields are routinely generated in a similar fashion. The surface topography field shown in Fig. 5d is constructed using a bilinear interpolation method, which ensures that the height above sea level at a given (x, y) location will be identical on all output grids created by the program. Displays produced by SMANAL include the preceding figures as well as contour plots and statistical summaries of the interpolated fields.

All of the software described in this section has been developed for use in batch mode on the Cray-1A computer system at NCAR. Two of the programs, SPRINT and CEDRIC, have also been adapted for interactive use on Digital Equipment Corporation VAX minicomputers with VMS operating systems. User guides are available containing all the necessary information for understanding and running these programs, including sample decks and dataset descriptions. The lo-

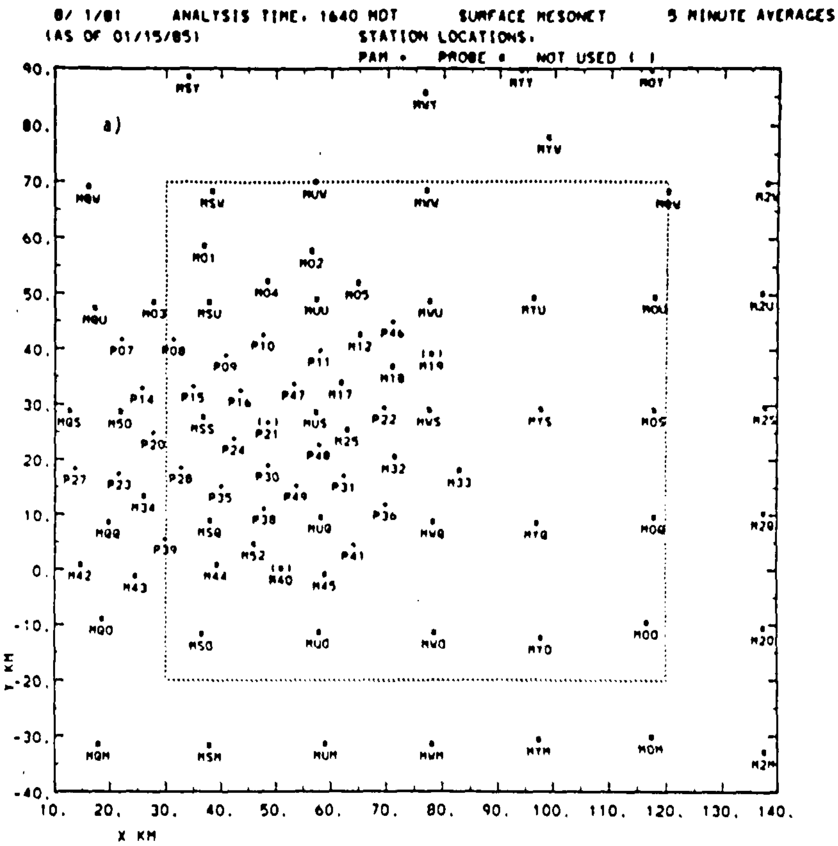
8/ 1/81 ANALYSIS TIME, 1640 MDT SURFACE MESONET 5 MINUTE AVERAGES
(AS OF 01/15/85) STATION LOCATIONS,
PAM • PROBE • NOT USED ( )
a)
Y KM
X KM

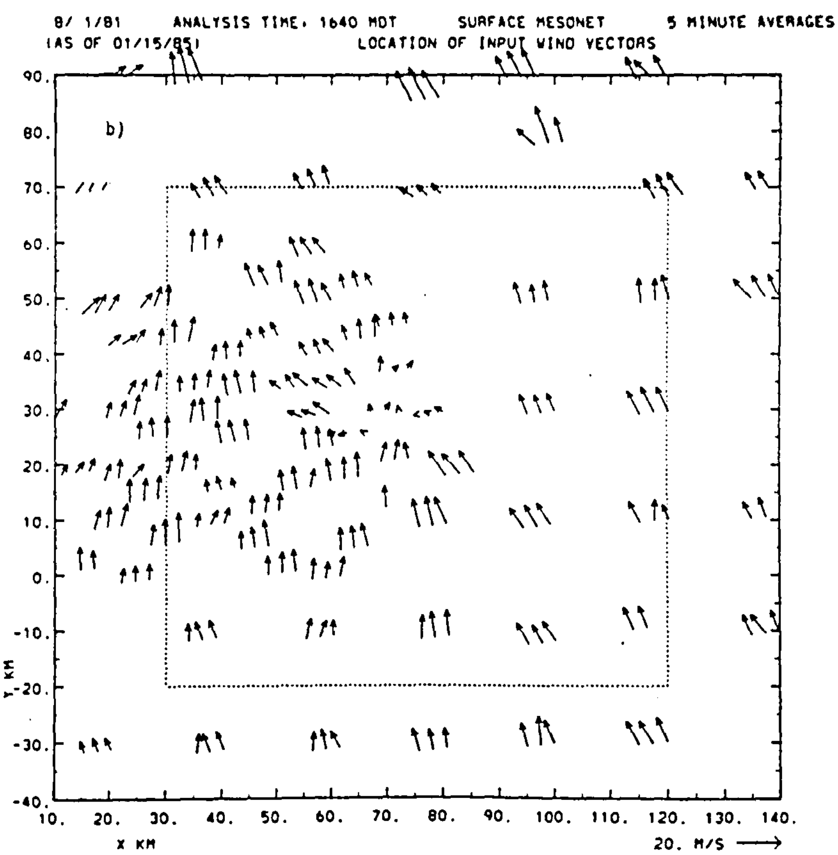
8/ 1/81 ANALYSIS TIME, 1640 MDT SURFACE MESONET 5 MINUTE AVERAGES
(AS OF 01/15/85) LOCATION OF INPUT WIND VECTORS
b)
Y KM
X KM
20. M/S

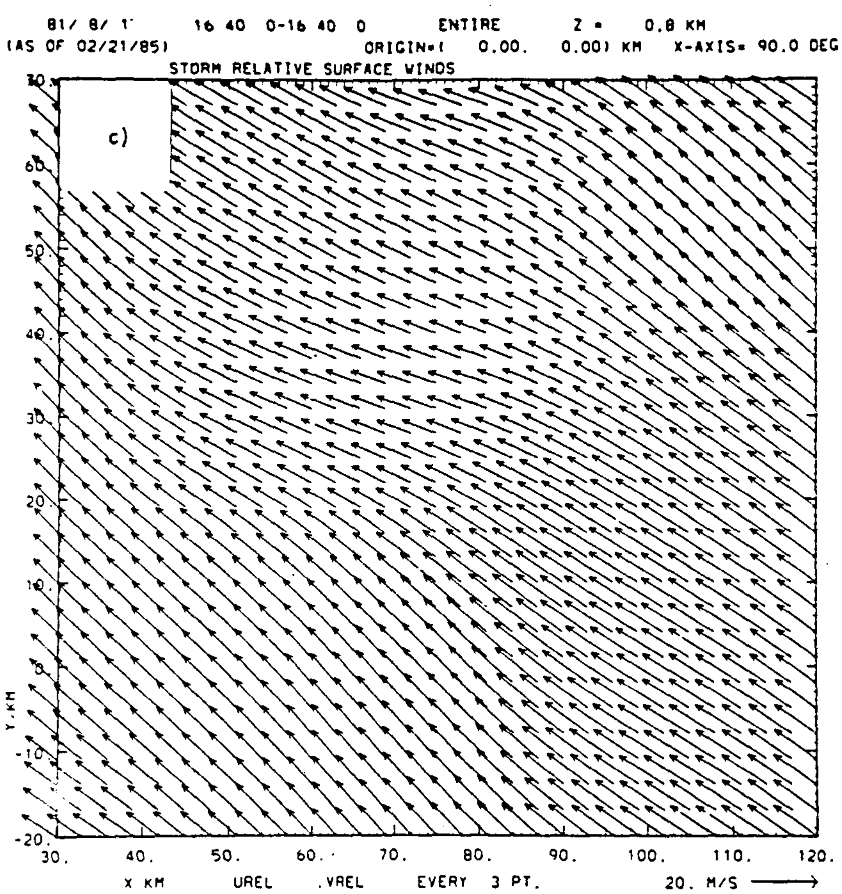
81/ 8/ 1 16 40 0-16 40 0 ENTIRE Z = 0.8 KM
(AS OF 02/21/85) ORIGIN=(0.00, 0.00) KM X-AXIS= 90.0 DEG
STORM RELATIVE SURFACE WINDS
c)
Y KM
X KM UREL ,VREL EVERY 3 PT. 20. M/S

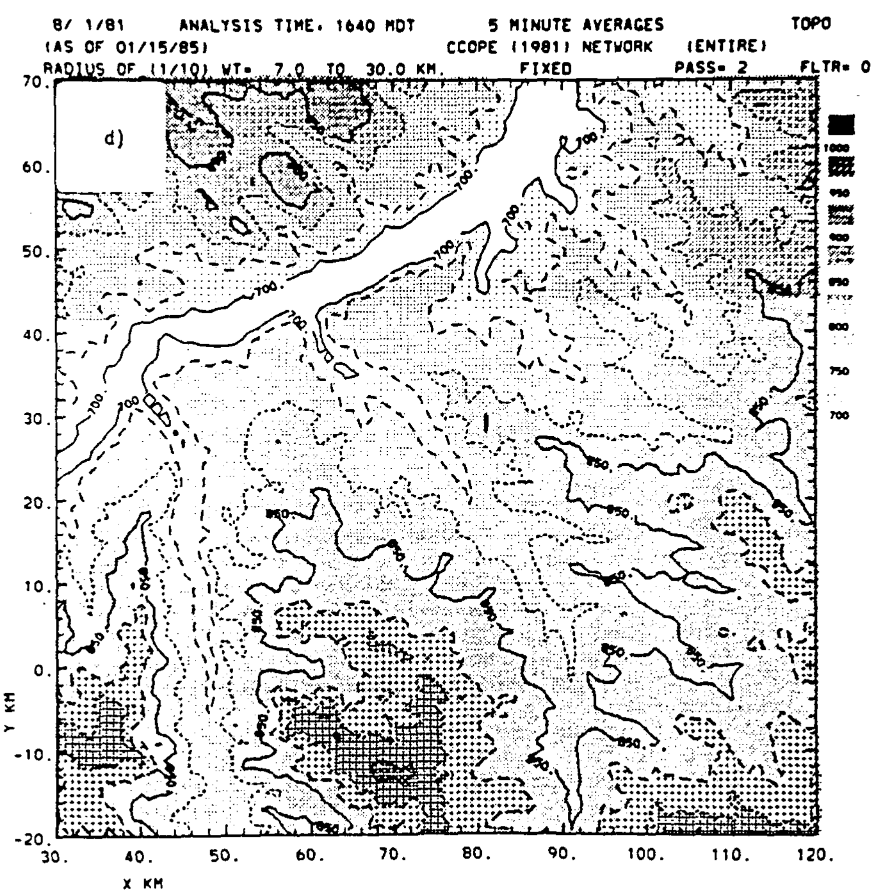
8/ 1/81 ANALYSIS TIME, 1640 MDT 5 MINUTE AVERAGES TOPO
(AS OF 01/15/85) CCOPE (1981) NETWORK (ENTIRE)
RADIUS OF (1/10) WT= 7.0 TO 30.0 KM. FIXED PASS= 2 FLTR= 0
d)
Y KM
X KM
1000
950
900
850
800
750
700

cation, size, axes spacings, and contents of the Cartesian coordinate system may be arbitrarily defined by the user as long as the subsequent dimensions of the structure do not exceed (127 × 127 × 63) and that it does not contain more than 25 interpolated fields.

4. Analyzing the composite data structure

The CEDRIC analysis package contains a comprehensive set of commands for combining, editing, analyzing, and displaying the interpolated data fields. Many of the concepts embodied in CEDRIC had their origins in the MUDRAS (Multiple Doppler Radar Analysis System) software developed by Kohn et al. (1978). Virtually all of the operations are multidimensional and may be performed on any subset of the data with either the x, y, or z coordinate held fixed. Results can be archived at any stage of the analysis.

In the early stages of analysis when an overall strategy is still being developed for investigating an unfamiliar dataset, the interactive version of the program can be an invaluable aid. However, once the strategy has been established it becomes far more expedient to move from the minicomputer to a large batch processing environment. This is particularly true when dealing with datasets from CCOPE and other large mesoscale field experiments where the sheer bulk of information readily overwhelms the capacity of anything less than a supercomputer such as the Cray-1A at NCAR and its supporting facilities. With this in mind, our discussion of CEDRIC proceeds in the context of a batch environment where the data processing functions described below are most often used.

The batch mode command syntax of CEDRIC was designed to be as simple as possible. Commands consist of 80 character card image formats beginning with a keyword starting in column 1. Each card image is divided into 10 (8-col) groups referred to as P1 through P10. The keyword always occupies P1. Groups P2–P10 contain parameters relevant to the command. Commands are processed in the order in which they appear and may be repeated as often as desired. Default values (given in the user documentation) are used whenever a required parameter is left blank or if the information supplied is erroneous.

Any sequence of CEDRIC commands which must be repeated more than once during a run can be defined as a separate entity and subsequently executed using a single statement. Symbolic names can be used in place of the parameters in these command sequences and replaced with appropriate values just prior to execution. This facilitates the construction of commonly utilized procedures which, with a few minor alterations, can operate on multiple datasets in the same run. User-supplied comments may appear anywhere in the deck so long as they are bracketed by special delimiting statements. This construct is particularly useful for temporarily de-activating certain procedures without having to remove them from the command stream.

The remainder of this section contains a description of the principal functions available to the analyst in the CEDRIC software.

a. Retrieval and archival of Cartesian datasets

CEDRIC reads an existing Cartesian dataset from some external medium (disk, tape, or mass store) into the active workspace where the contents of the dataset can be altered and displayed. The active workspace takes on the spatial characteristics of the input volume most recently acquired unless the destination coordinates have been predefined by the user. Whenever a predefined Cartesian structure exists the input dataset is mapped to the user-specified coordinates so long as the two systems have grid locations in common. Missing data flags are supplied at destination locations that do not exist in the input volume and transferred reports that have no home in the target coordinates are discarded. After a Cartesian volume has been read into the active workspace, additional fields may be brought in from other datasets residing on external media. It is through the use of these procedures that complementary observations from the aircraft and mesonet systems are merged together with the Doppler radar products. Once the active workspace has been established, a three-dimensional rectangular region may be designated through which all reports will be accessed. This permits all algebraic operations to be performed on a subsection of the current (x, y, z) grid without disturbing the surrounding values and for displays to be generated on any coordinate background. The contents of the active workspace may be written to external storage in the same standard format as the input datasets at any stage of the analysis.

FIG. 5. (a) Surface mesonet sites contributing input measurements to the Cartesian space remapping on 1 August 1981 at an analysis time of 1640 MDT. Crosses and asterisks mark the locations of PAM and PROBE sites, respectively.
(b) Input horizontal wind reports from 1635, 1640, and 1645 recording times repositioned with respect to storm motion of 263° at 8.3 m s^{-1}.
(c) Storm relative horizontal winds interpolated to a 1-km grid with storm motion removed. Boundaries of this grid correspond to the dashed box shown in the interiors of (a) and (b).
(d) Surface topography in meters MSL mapped to the same 1 km grid as depicted in (c). Contours are drawn every 50 m and computer generated gray-scale shading has been added for emphasis. The Yellowstone River Valley appears as the unshaded region in white. Coordinate origin is the same as in the aircraft remapping (Fig. 4).

b. Filtering and data filling

Two-dimensional spatial filtering may be performed along any axis using either fixed weights over a local (3 × 3) region, a scale-telescoped filter developed by Leise (1981) or a linear least-squares approximation over a selectable ($n \times n$) region of influence (Bevington, 1969). Regions of missing data in observed fields would, if ignored, prevent the use of many routine analysis functions—filtering included. This situation can be remedied by replacing the missing values in a plane (either temporarily or permanently) using one of two available techniques. Leise's data filling algorithm (1981) is generally used to extend the entire dataset globally while the constrained local area linear least-squares approximation is better suited to the elimination of isolated data voids surrounded by good reports. Facilities also exist that allow the user to decimate data fields containing questionable reports. Outlyers are identified and removed from the field depending upon their deviation from the mean value of either a global or a local population.

c. Algebraic manipulation

By far the most popular and powerful analysis tool, the algebraic manipulation command (FUNCTION), enables users to construct customized algorithms for manipulating and altering data fields. The printer-file report given in Fig. 6 illustrates the use of this facility. Statements furnished by the analyst are delineated by angle brackets (⟩⟩⟩⟩⟩). The initial directive invokes the FUNCTION command and contains two parameters. The first (Z) specifies that the z-axis is to be held fixed, and the second (WINDOW) confines the calculations to a previously defined subset of the full (x, y, z) structure. Following this directive the program displays the requested axis configuration, the remaining user-supplied FUNCTION statements, and the spatial dimensions of the current subset region or "editing window." In this example three algebraic operations are grouped together to combine a pair of existing data fields in the following manner:

1) Aircraft (W-AIRC) and radar (W-RADAR) vertical velocity estimates are averaged together wherever both exist to produce a temporary field called W-MEAN;

2) A preliminary composite field (W-COMP) is then constructed by taking the average values from W-MEAN wherever they exist and filling in with the values from W-AIRC otherwise;

3) Finally, the radar estimates are blended in with the existing values of W-COMP to produce the combined vertical velocity field, W-STORM.

Information presented in the bottom portion of the figure verifies the successful execution of these operations and the addition of W-STORM to the active workspace. Similar operations are used to construct composite u and v component fields over the full volume of the storm. Customized functions that are frequently used in the analysis of mesoscale datasets include converting radar reflectivity to equivalent rainfall, adjusting vertical velocity estimates with variational schemes, and deriving the terms of the vorticity equation from the kinematic fields.

```
>>>>>FUNCTION                                              Z        WINDOW <<<<<

AXIS CONFIGURATION:                         +
                                          Y +
                         Z (FIXED)          +++
                                             X

>>>>>        W-MEAN  T        +       W-AIRC  W-RADAR 0.5      0.5
>>>>>        W-COMP  T        ORELSE  W-MEAN  W-AIRC
>>>>>        W-STORM P        ORELSE  W-COMP  W-RADAR
>>>>>END

EDITING WINDOW LOOKS LIKE THIS:
                 INDICES                       DISTANCES
AXIS  POSN.    MIN      MAX            MIN      MAX     UNITS
  X     1       1        51            55.0    105.0     KM
  Y     2       1        51             0.0     50.0     KM
  Z     3       4         4             2.6      2.6     KM

 0 CONSTANT FIELD PLANES W/INITIALIZATION INFO

FUNCTION STACK...

F (OUT)  TYPE   FUNCTION      F1      F2           C1      C2      C3      C4
W-MEAN   /T    C1*F1+C2*F2   W-AIRC  W-RADAR     0.500   0.500
W-COMP   /T    F1.ORELSE.F2  W-MEAN  W-AIRC
W-STORM  /P    F1.ORELSE.F2  W-COMP  W-RADAR

DIRECTION THROUGH THE Z-PLANES:  1
    W-STORM  WILL BE CREATED AND SAVED AS A PERMANENT EDIT FIELD SCALED BY   64

 7 EDIT FIELDS EXIST AT PRESENT:
    W-AIRC   W-STORM  DZ-CP2   DZ-CHILL W-RADAR  COUNT    WREL
```

FIG. 6. Sample CEDRIC output illustrating the use of the FUNCTION facility. Commands entered by the user are preceded by ⟩⟩⟩⟩⟩. Remaining text is generated by the program.

d. Velocity unfolding

Although radial velocity estimates may have already been unfolded in radar space prior to Cartesian transformation, areas containing ambiguities might not be evident until the data has been examined in horizontal and vertical cross-sections or until a preliminary air motion synthesis has been attempted. Returning to radar space to perform additional unfolding after these velocities have already been interpolated is an unnecessary and cumbersome step backwards. By comparison Cartesian space unfolding offers the following advantages:

- the number of velocity estimates is considerably smaller;
- automated unfolding procedures which take advantage of the orthogonality of the data structure can be used to produce an internally consistent three-dimensional velocity field; and
- the radial velocity field from any radar can be directly compared and brought into agreement with the other radars in the network before it is incorporated into an existing synthesis.

Ambiguous radial velocity measurements in Cartesian space can be corrected using any one of the following techniques:

Automatic 2-D unfolding. Questionable radial velocities are identified and temporarily removed based upon their deviation from the mean of a local ($n \times n$)

region surrounding each grid point. Estimates are generated at the missing locations using Leise's data extension algorithm and saved in a separate array. Suspect velocities are then unfolded using the corresponding estimates as their reference and returned to the original velocity field.

Automatic template unfolding. A template field containing reference velocities is specified and used as a "seed" to initiate the procedure at any designated horizontal or vertical plane. The radial velocities in that plane are unfolded using the corresponding values in the template field as a reference. The unfolded array is saved and subsequently data-filled for use as the template for unfolding the two adjacent planes. Once those planes have been processed, the point-by-point slope of the unfolded velocity field is also taken into account when generating the templates for the next pair of planes to be operated upon. This procedure continues outward in both directions until the entire windowed region has been unfolded.

Forced unfolding. All velocities within the designated spatial window and either inside or outside of an arbitrary velocity range are forced to be within the same Nyquist interval of a user-specified reference velocity.

Forced template unfolding. A template field is specified and the velocity information in it is used as a reference for unfolding the measurements in another velocity field at each corresponding location in the volume. One method of generating the template field for use with this scheme has been to resample the (u, v, W) components from an existing particle motion synthesis at the location of a radar which has not yet been included in that synthesis. The resultant field of computed radial velocities can then be used as a reference for unfolding the actual measurements from the radar. This technique has proven to be particularly useful for incorporating additional estimates from Doppler radars which have acquired their velocities under extreme conditions within a narrow Nyquist interval.

e. Coordinate transformation

Before any time or space transformations are performed in Cartesian coordinates, it is first necessary to determine the storm displacement from one time period to the next. This may be accomplished objectively using a procedure that computes the array of linear cross-correlation coefficients between the horizontal planes of a pair of fields which are lagged with respect to one another along each axis of the plane. When the fields being correlated contain identical quantities from two consecutive volumes and no substantial temporal evolution has occurred, the speed and direction of a moving phenomenon can be readily deduced. Once this information is available, commands can be invoked for remapping the data to a new user-specified coordinate system and for advecting reports with temporal inconsistencies to a common time-of-day.

The remapping procedure is generally used to relocate a sequence of volumes to storm-relative coordinates (translation) and for generating vertical sections along the direction of storm motion (rotation). The destination coordinate system must be identical to the old one along the z-axis but may vary in placement and orientation along the x and y axes. Bilinear interpolation is used to remap the reports in regions where the two structures intersect, elsewhere missing data flags are supplied.

Cartesian space reports can be advected to a common time-of-day position provided that every grid location has a discrete acquisition time associated with it. Acquisition times are expressed in seconds relative to the beginning time of the volume and may be either constant for all points, constant within each z-level, or unique to each grid location. In conjunction with a designated storm motion, these acquisition times are used to differentially advect the data within each horizontal level to locations consistent with a fixed reference time. Values are then redistributed to (x, y) grid points using the same bilinear method that is employed in the remapping. This advection scheme is also available as an automated feature in the multiple Doppler synthesis.

f. Air motion synthesis

This procedure combines radial velocity reports from as many as six ground based Doppler radars. Options also exist for incorporating airborne Doppler measurements into the synthesis and are discussed by Mueller and Hildebrand (1985). The orthogonal components of target motion are computed using a least-squares solution of the system of over-determined equations whenever four or more input values are available, an exact solution if three are present, and a dual-radar approximation of the horizontal winds if only two exist. The formulations used to derive these orthogonal components (u, v, W) from multiple Doppler measurements at each (x, y, z) location are provided by Ray et al. (1978).

Prior to synthesis, all incoming data fields are automatically advected in the manner described above with corrections made to the input radial velocities and the transformation coefficients as prescribed by Gal-Chen (1982). Different size datasets may be combined so long as their coordinate structures are compatible. A Cartesian space output volume is created that contains the following fields:

U, V, W	orthogonal components of target motion;
USTD, VSTD, WSTD	normalized standard deviation associated with the estimate of each component;
CT	bit map of the radars contributing usable radial veloc-

ities to the synthesis at each grid location.

In addition, any original data fields associated with the contributing radars may also be included.

After a Cartesian space volume has been constructed containing kinematic observations from all available sources, a field of vertical air motions (w) can be obtained either by subtracting out the particle fall speeds from W (using an empirical velocity-reflectivity relationship) or by integrating the equation of mass continuity in either an upward or downward direction along the z-axis. When this latter technique is employed, the horizontal divergence is calculated using a centered-differencing scheme and supplied as the integrand. Boundary conditions may be either a constant, a fraction of the integrand, or values taken from another field. The resultant set of vertical velocities can be subsequently adjusted to conform with independent aircraft and ground-based measurements using the facilities available in FUNCTION. In addition to these air motion applications, this procedure can also be used as a general integrator to compute, for example, the total water in the atmosphere above each (x, y) grid location.

g. Pressure retrieval

An estimate of the pressure perturbation field at every z-level can be obtained using an algorithm described by Gal-Chen and Hane (1981). This algorithm solves, in a least-squares sense, the momentum equations rewritten in the form:

$$\left.\begin{aligned} \partial P/dx &= F \\ \partial P/dy &= G \end{aligned}\right\} \qquad (5)$$

where dx and dy are the grid spacings along the x and y axes respectively. The input fields, F and G, can be constructed from the composite wind components using the algebraic operators available in FUNCTION. The output field, P, contains an estimate of the difference between the pressure at every grid location and the mean value of the horizontal plane. Details regarding the methodology of pressure retrieval from observed kinematics are provided by Gal-Chen (1978).

5. Displaying the composite data structure

A diverse selection of printed and plotted outputs is available in CEDRIC for examining the data fields. Options permit the user to view any region of interest by specifying an arbitrary window prior to display. In addition, the axis to be held constant when generating two-dimensional products may be altered at any time and the Cartesian dataset will be accessed accordingly. Plotted displays are produced using a device-independent vector graphics package developed at NCAR by Wright (1978).

Figure 7 presents a summary of the header information associated with the Cartesian space dataset

```
CEDRIC (.CED)  VOLUME HEADER                      HF7F07
 GENERAL INFORMATION...
  DATE:          8/ 1/81     SOURCE:   HF7L02     SCIENTIST: FRANK
  BEG TIME:    16:40: 0      RADAR:    COMBIN     SUBMITTER: FRANKH
  END TIME:    16:40: 0      PROGRAM:  CEDR.8     DATE RUN:  01/02/85
  VOL. NAME:  COMPOS1        PROJECT:  CART       TIME RUN:  02:09:13
  SCAN MODE:  CRT            TAPE:     HF7F07     SEQUENCE:  111087

 DATA CHARACTERISTICS...
  COMPUTER:        C1     RECS/FIELD:        1     PTS/FIELD:     2601
  BITS/DATUM:      16     RECS/PLANE:        5     NO. PLANES:      23
  BLOCK SIZE:    3200     RECS/VOLUME:     139     BAD DATA:    -32768
  WORDS/PLANE:    651     WORDS/FIELD:   14973     MAX FIELDS:      25

 FIELDS PRESENT:  5 ...
   NO.   NAME        SCALE FACTOR
    1    UREL            64
    2    UREL            64
    3    DZS(CP2)       100
    4    WDOP            64
    5    WAIR            64

 LANDMARKS PRESENT:  3     ( 2 RADAR) ...
   NO.   NAME      X (KM)     Y (KM)     Z (KM)
    1    ORIGIN     0.00       0.00      0.000
    2    CP-2       0.00       0.00      0.788
    3    CHIL      26.54      52.20      0.815

 ORIGIN  LATITUDE:       46 DEG    25 MIN    55.60 SEC
         LONGITUDE:     105 DEG    56 MIN    10.50 SEC

 CARTESIAN COORDINATE SYSTEM SPECIFICATIONS...
  AXIS      MINIMUM (KM)      MAXIMUM (KM)        DELTA (KM)     NO. OF PTS.
   X           55.00             105.00              1.00            51
   Y            0.00              50.00              1.00            51
   Z            0.00              14.00              0.60            23

  AXIS ORDER IS   X  Y  Z
  ANGLE OF THE X-AXIS RELATIVE TO NORTH:      90.00     DEG.
  (X,Y)  AXIS ARE SPECIFIED RELATIVE TO:  (   0.00,    0.00)
```

FIG. 7. Standard summary of the pertinent header information associated with each Cartesian space dataset. General information, data characteristics, fields, landmarks, and coordinate structure are all provided in this easy-to-read format whenever a dataset is transferred to or from the active workspace.

containing a description of the storm under investigation at 1640 MDT on 1 August 1981. The fields in this dataset are:

- UREL, VREL — storm relative horizontal wind components;
- DZS (CP2) — S-band reflectivity from the NCAR CP-2 radar;
- WDOP — vertical component of target motion (including particle fall speeds);
- WAIR — vertical air motion (excluding particle fall speeds).

The composite set of air motions (UREL, VREL, WAIR) were constructed from mesonet, aircraft, and Doppler radar measurements in the following manner. Wherever multiple radar observations were available (those regions where the reflectivity exceeded ~15 dBZ), UREL and VREL were derived from a storm relative synthesis using six Doppler radars. At ground level (0.8 km) horizontal winds were supplied by the surface mesonet remapping in section 3c. Aircraft remappings provided additional estimates of UREL and VREL at 2.6 and 8.0 km. Coincident data values were averaged and isolated voids in the UREL and VREL fields were eliminated using the least-squares data filling algorithm. Finally, with the exception of the surface reports, both fields were smoothed along all three axes using the Leise filter. The vertical air motion field, WAIR, was obtained by integrating the horizontal divergence (∂UREL/∂x + ∂VREL/∂y) along the z-axis and adjusting the estimates to satisfy the constraint that WAIR be equal to zero at the bottom and top of the domain.

a

```
STATISTICS ARE FROM (  1 TO  51)  (  55.0 TO  105.0 KM  ) ALONG I
                    (  1 TO  51)  (   0.0 TO   50.0 KM  ) ALONG J
                    (  1 TO  23)  (   0.0 TO   14.0 KM  ) ALONG K
```

DZS(CP2) Z KM	MEAN	STDV	N	I1	I2	J1	J2	MIN	MAX
0.8	0.00	0.00	0	0	0	0	0	0.0	0.0
1.4	0.00	0.00	0	0	0	0	0	0.0	0.0
2.0	7.09	18.37	1895	6	34	1	40	-6.9	60.7
2.6	9.07	17.26	2213	6	51	1	50	-7.6	61.9
3.2	9.07	16.90	2257	6	51	1	50	-7.7	60.4
3.8	8.20	16.94	2254	6	51	1	50	-8.3	61.0
4.4	7.45	17.33	2254	6	51	1	50	-9.6	63.8
5.0	7.07	17.72	2252	6	51	1	50	-9.9	64.2
5.6	7.11	17.86	2252	6	51	1	50	-10.1	62.9
6.2	7.14	17.90	2253	6	51	1	50	-10.5	65.0
6.8	7.26	17.80	2256	6	51	1	50	-10.6	64.6
7.4	7.71	17.58	2241	5	51	1	50	-11.1	62.6
8.0	8.57	17.20	2212	5	51	1	50	-10.9	62.0
8.6	9.09	16.82	2177	5	51	1	50	-11.2	61.3
9.2	11.30	16.17	2190	5	51	1	50	-11.2	60.4
9.8	12.57	15.51	2227	5	51	1	50	-11.3	59.5
10.4	12.78	14.63	2270	5	51	1	50	-10.8	57.1
11.0	11.71	13.61	2299	5	51	1	50	-11.3	54.9
11.6	8.06	12.33	2309	5	51	1	50	-11.8	58.3
12.2	4.42	10.81	2309	5	51	1	50	-11.2	48.2
12.8	0.10	9.04	2272	5	51	1	50	-11.1	41.6
13.4	-2.54	7.29	2199	5	51	1	50	-10.6	38.8
14.0	-3.61	5.53	2182	5	51	1	50	-9.8	31.9
VOLUME	7.28	15.97	45893	5	51	1	50	-11.3	65.0

b

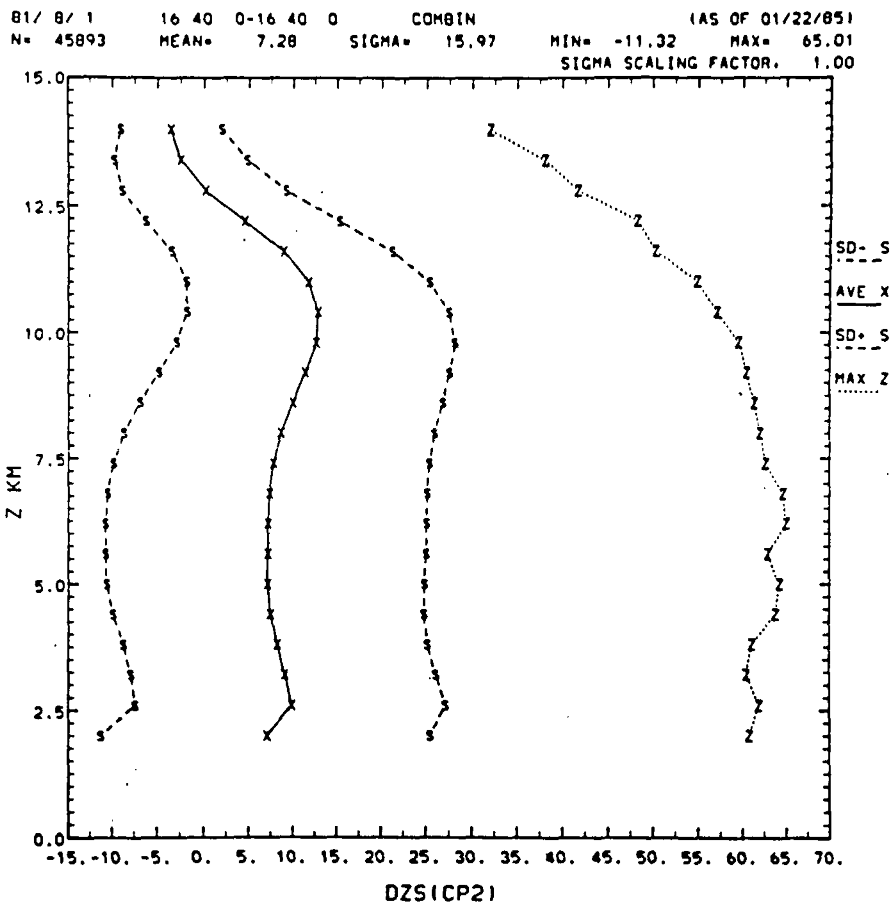

FIG. 8. Selected examples of statistical presentations available in CEDRIC:
(a) Statistics by plane and by volume in a tabular form for reflectivity field DZS (CP-2). Z-axis is held fixed. No data exists for levels below 2.0 km.
(b) Selected statistics from (a) plotted as a function of height. Mean value at each level, mean +/− sigma and maximum reflectivity are included in this display. Volume statistics are provided in the labeling at top of figure.

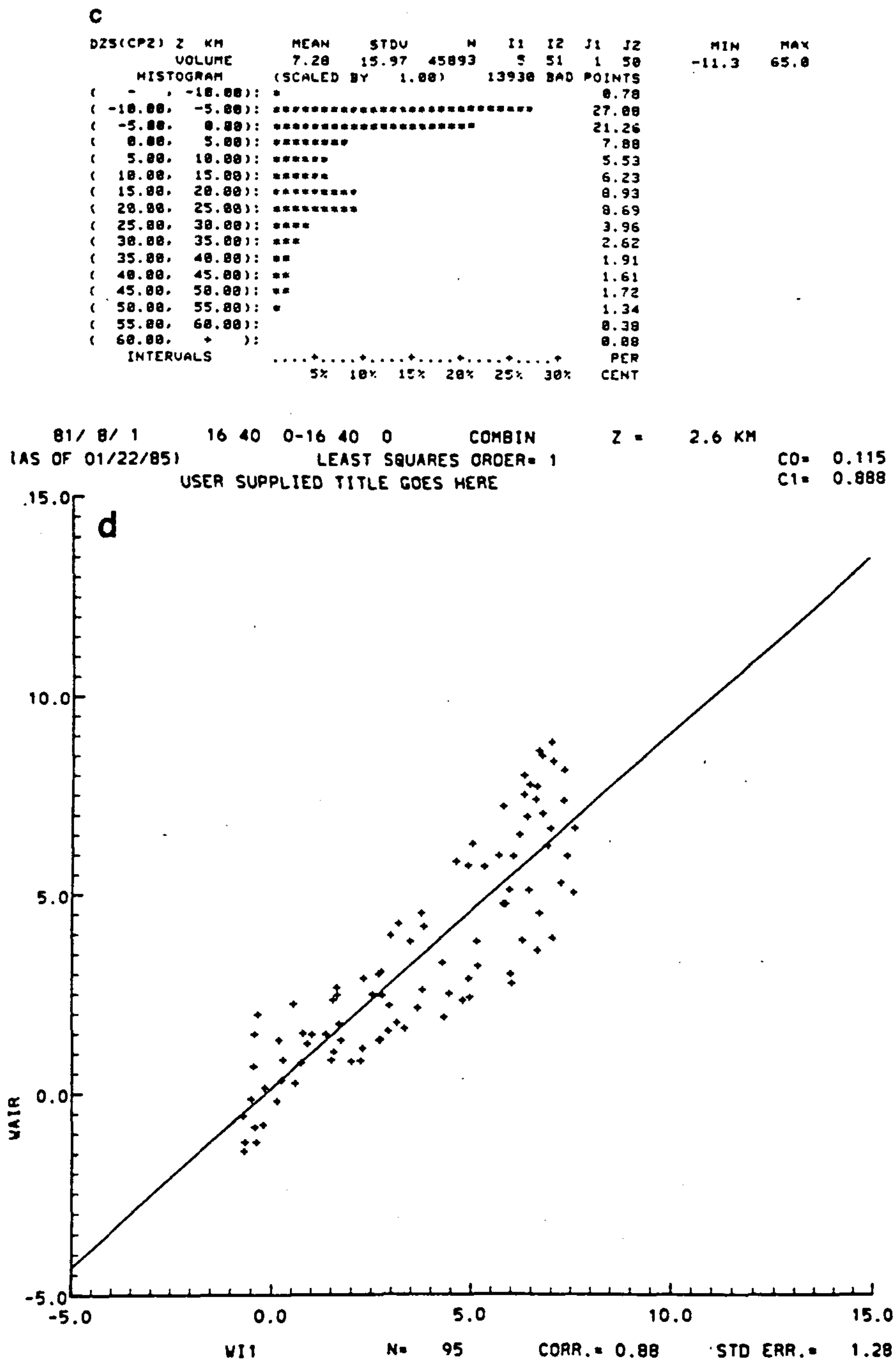

FIG. 8. (c) Frequency distribution of the entire volume of reflectivity values. Statistics for the population appear at the top. The term "bad points" refers to grid locations at which no reports were present.
(d) Scatter diagram of vertical air motion reports from Doppler analysis (WAIR) versus horizontal aircraft mapping (WI1) at height of 2.6 km. Equation of "best fit" line through the data is given at upper right. Number of pairs, correlation coefficient, and standard error of estimate appear below the horizontal axis.

As discussed earlier, the location of the analysis grid dictated the use of a large radius-of-influence in the surface mesonet remapping. Consequently, the wind patterns associated with the lowest level (0.8 km) have been preserved at larger scales than those retained in the Doppler radar and aircraft interpolations. Nevertheless, the surface data provided a sufficiently representative divergence field to enable us to use it as the lower boundary in the integration procedure. Had the storm been located above the dense network, surface observations would have been remapped at a resolution comparable to the other instrument systems and tech-

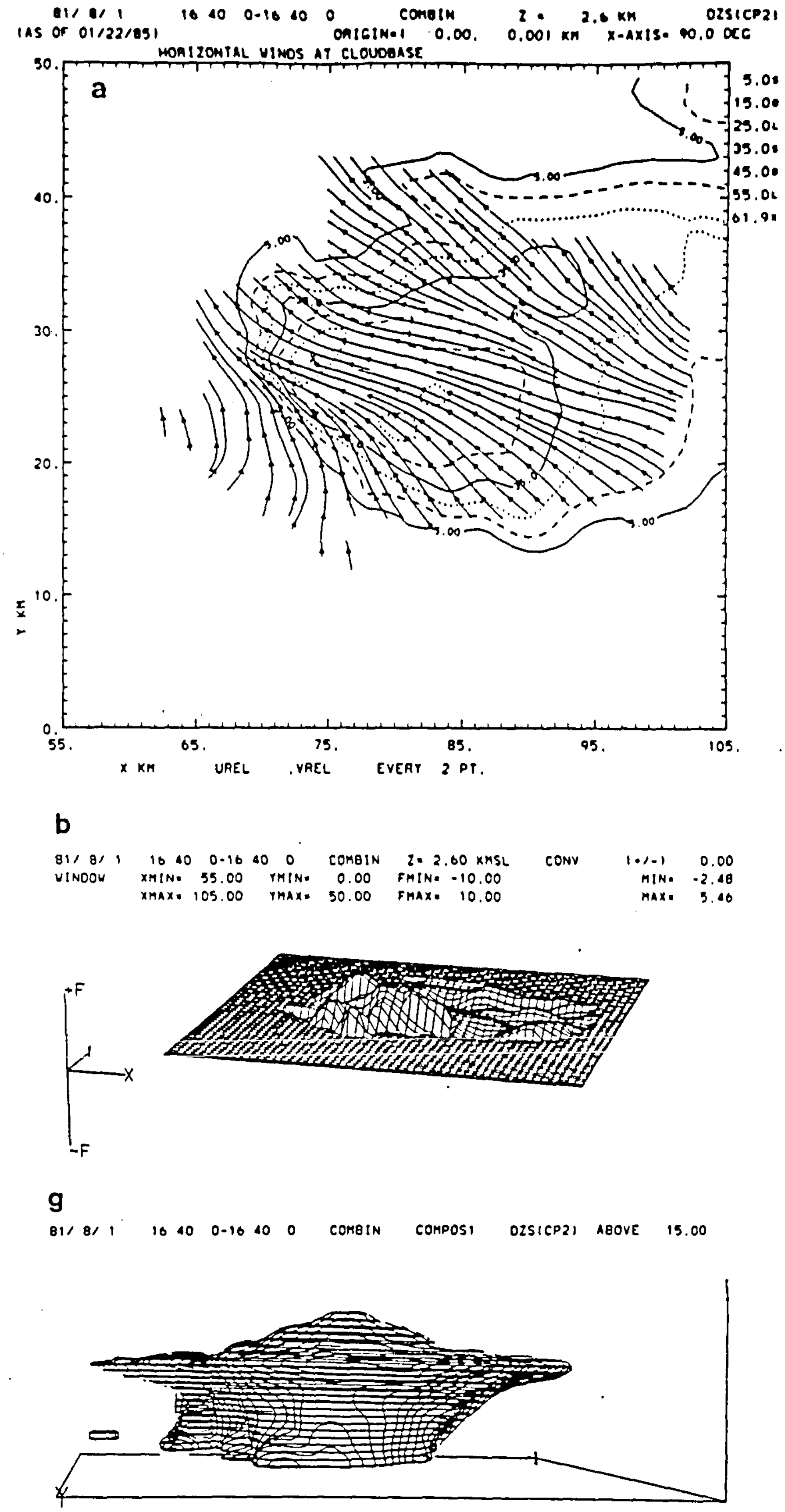

FIG. 9. Selected examples of two and three-dimensional displays produced by CEDRIC:

(a) Contoured reflectivity near cloudbase (2.6 km). Horizontal winds are depicted as streamlines in the overlay. Doppler winds have been extended at southwest flank using aircraft measurements.

(b) Two-dimensional perspective of the horizontal convergence using the winds shown in (a).

(g) Three-dimensional perspective of the entire reflectivity field DZS (CP-2). Values in excess of 15 dBZ are visible.

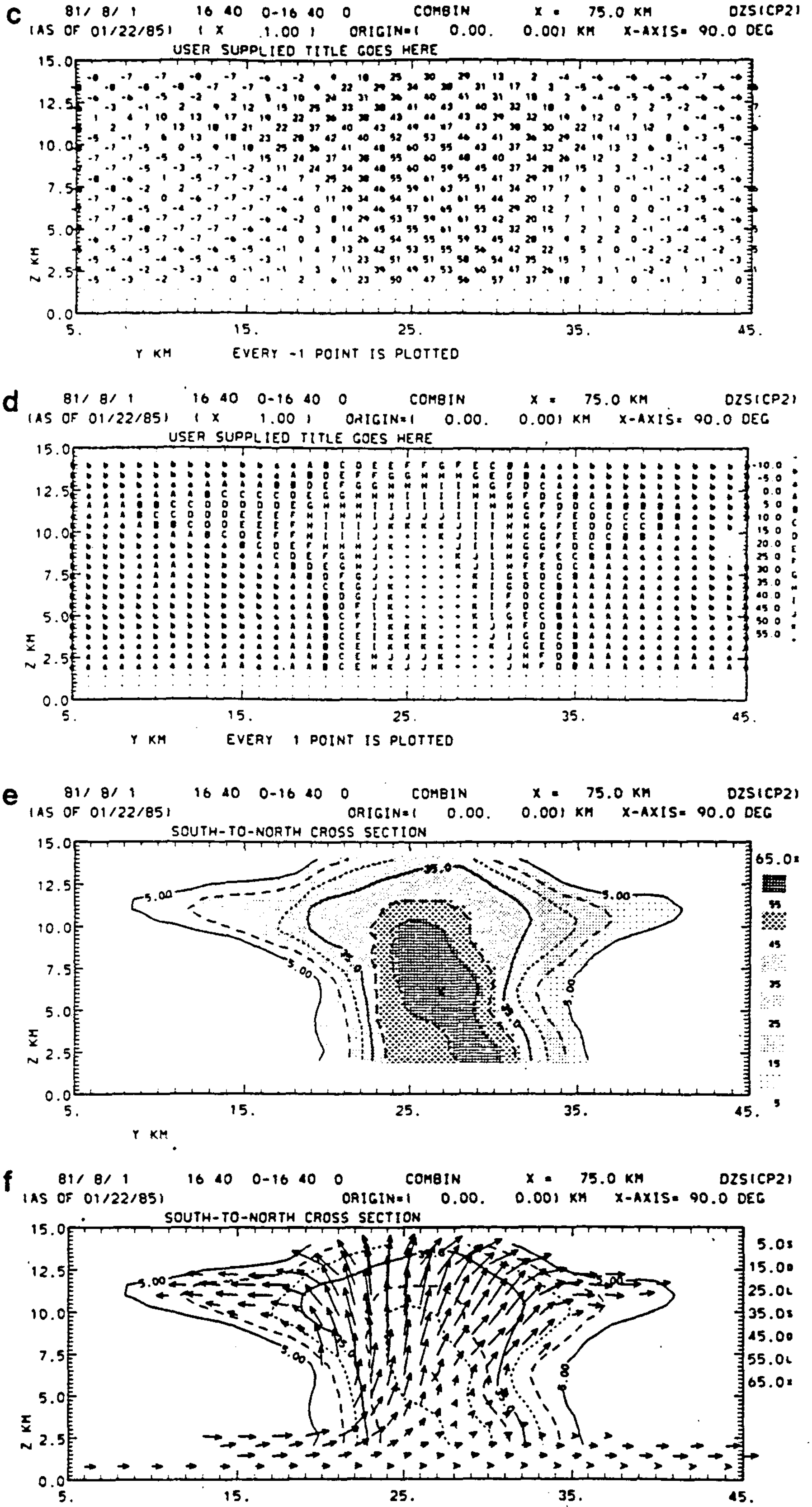

(c) Digital display of the reflectivities in a vertical south-to-north cross-section through the core of the storm.
(d) Coded display of the same reflectivity field and cross-section as in (c). User-specified reference table appears at right of figure.
(e) Contour plot with standard alternating dash pattern, line labeling, and termination of contours at missing data locations. Maximum value (65 dBZ) is indicated by an (X). Optional computer generated gray-scale shading has also been added.
(f) Simple contour plot with vectors depicting the composite air motion deduced from Doppler, aircraft, and mesonet observations included as an overlay. Reference vector is given at lower right.

niques incorporating the topography field in Fig. 5d could have been used to establish a more accurate lower boundary condition.

The resultant three-dimensional Cartesian space volume is the principal source for the displays presented in the remaining figures. Altitudes (z) are given in kilometers above sea level, x and y distances are in kilometers east and north with respect to the primary research radar CP-2. Figure 8 contains some examples of statistical products that are commonly used to examine the Cartesian space fields. Figure 8a is a tabular summary of the S-band reflectivity from CP-2, DZS (CP-2), at levels of constant altitude. The columns in this presentation are (from left to right): height of the cross-section, mean, standard deviation (σ), number of "good" estimates, the beginning and ending indices of the rectangular region surrounding the "good" estimates, and the minima and maxima of the population. Statistics over the entire volume are given in the last line. Figure 8b illustrates some statistical properties of the same field as plotted profiles. The four profiles included in this display are: mean $- \sigma$, mean, mean $+ \sigma$, and maximum value. User-specified symbols (S, X, and Z) corresponding to these profiles are digitized at the location of every z-level in the Cartesian volume. Figure 8c is a frequency distribution partitioned into intervals of 5 dBZ for the same reflectivity field. In this example, every report in the volume has been included. The term "bad points" refers to Cartesian grid locations for which no data are available. The percent contribution from each interval appears in the right-hand column of the display. Figure 8d is a scatter diagram of the vertical velocity field (WAIR) obtained by integrating the horizontal divergence versus vertical velocities at coincident locations (WI1) obtained from the constant altitude aircraft remapping presented earlier in section 3b. Correlation coefficient, standard error of estimate, and the equation of the least-squares line fit are included in the labeling. This particular comparison indicates that, within the context of the Cartesian space data structure, these independent estimates of vertical air motion are in satisfactory agreement.

Figure 9 demonstrates the facilities that exist for examining data fields in two and three dimensions. Figure 9a contains a contour plot of the reflectivity field at cloud base (2.6 km) with streamlines depicting the storm relative horizontal airflow superimposed. Horizontal winds measured by the cloud base aircraft (shown earlier in Fig. 4c) have been merged with Doppler results to extend the observations into the "echo free" inflow region at the southwest flank of the storm. Figure 9b is a perspective display of the convergence field (CONV) at the same altitude computed using the horizontal winds depicted in Fig. 9a. Viewing window and minimum-maximum values are provided in the titling.

Figures 9c through 9f present four different displays of the reflectivity field along a vertical cross section taken through the core of the storm at $x = 75$ km. In Fig. 9c the actual reflectivity values are digitized at their respective locations in the display. For purposes of readability the user has specified that every other point be plotted. Periods indicate grid locations for which no reports exist. In Fig. 9d each reflectivity value is represented by a symbol that has been assigned according to the user-defined table at the right. In this example positive reflectivities are denoted by capital letters; lower case letters are used for negative values. Reports in excess of the table limits are indicated by their signs (+ or −).

Figure 9e contains a contour plot of the data. Display characteristics over which the user has control include the levels to be contoured, line patterns and labels, designation of relative highs and lows, and whether or not contouring should be suppressed when values below threshold are encountered. The maximum value (65 dBZ) is indicated on the figure and in the labeling by an X. Both this feature and the supplementary gray-scale shading are optional.

Vectors depicting the storm relative airflow in the plane (VREL, WAIR) appear as an overlay in Fig. 9f. Winds beyond the boundary of the echo have been resolved using surface mesonet and low level aircraft observations. In general, any pair of the two-dimensional plot types illustrated in Figs. 9c through 9e may be combined together in a single display with either streamlines or vectors superimposed. The final display (Fig. 9g) is a three-dimensional isosurface plot of the total reflectivity surface in excess of 15 dBZ. This particular image has been generated with respect to a viewing angle directly west of the storm at a height of 10 km. Any field in the dataset can be depicted in a similar fashion.

6. Concluding remarks

This paper has presented an effective strategy for combining mesoscale observations from independent surface network, aircraft and radar data acquisition systems. The approach outlined has been successfully applied to the CCOPE data archive and as a result, information from any day of interest can be readily reduced to a common Cartesian coordinate system for analysis and display. Our experience with these procedures has led us to the following conclusions:

1) The common radar and mesonet formats save an enormous amount of data processing effort and should always be used for the exchange of such information after the completion of all field experiments. There should be similar formats for all major data collection systems.

2) Reports within each individual dataset should be carefully examined before any attempt is made to merge them with information from the other data systems. Although CEDRIC contains a full complement of tools for editing in Cartesian coordinates, problems such as poorly calibrated sensors, nonlinear biases and mislocated reports are best resolved before any time-space transformations or remappings are performed.

3) Provided that calibrated datasets are available and (x, y, z) space is the eventual destination, conversion to Cartesian coordinates at the earliest opportunity can significantly expedite the analysis effort. This is particularly true of radar measurements which, using proper precautions, can be processed almost entirely in an orthogonal coordinate system (Miller et al., 1985).

Now that established mechanisms exist for dealing with the high resolution datasets (radar, aircraft, and mesonet), we intend to focus our efforts toward incorporating as many of the remaining measurements as resources permit. Well-documented procedures exist for remapping rawinsonde (Fankhauser; 1969, 1974) and satellite observations (Hambrick and Phillips, 1980) to Cartesian coordinates. Time resolved cloud-to-ground lightning strokes (Orville and Rosentel, 1983) will most probably be assigned to the nearest grid locations in the lowest horizontal level. Plans also include the development of reformatting software to convert the output fields generated by mesoscale models to the CEDRIC format, thus enabling direct comparisons between observed and predicted conditions.

Acknowledgments. Mr. Thomas Engle (Cray Industries) deserves credit for setting up the CCOPE mesonet database on the mass storage system at NCAR. We also acknowledge the efforts of the part-time student programmers who have contributed either directly or indirectly to the success of this undertaking: Doug Rhoades (now with General Dynamics), Patti Cochran (now with GTE), Paul Poulsen (now with Ball Research), and Marta Oryshchyn and Jose Alvistur (still at NCAR). Special thanks also to Sudie Kelly for preparing the manuscript.

REFERENCES

Barnes, S. L., 1964: A technique for maximizing details in numerical weather map analysis. *J. Appl. Meteor.*, **3**, 396–409.

——, 1973: Mesoscale objective map analysis using weighted time-series observations. NOAA Tech. Memo. ERL NSSL-62, 60 pp. [NTIS COM-73-10781].

——, 1980: Report on a meeting to establish a common Doppler radar exchange format. *Bull. Amer. Meteor. Soc.*, **61**, 1401–1404.

Bevington, P. R., 1969: *Data Reduction and Error Analysis for the Physical Sciences.* McGraw-Hill, 336 pp.

Caracena, F., S. L. Barnes and C. L. Doswell, III, 1984: Weighting Function Parameters for Objective Interpolation of Meteorological Data. *Preprints, 10th Conf. on Weather Forecasting and Analysis,* Clearwater Beach, Amer. Meteor. Soc., 109–116.

CCOPE Operations Plan, 1981: Convective Storms Division, NCAR, 250 pp.

1981 CCOPE Data Inventory, 1982: Bureau of Reclamation, U.S. Dept of Interior Report, 451 pp.

desJardins, M. L., and R. A. Petersen, 1985: GEMPAK: A meteorological system for research and education. *Preprints, Int. Conf. on Interactive Information and Processing Systems for Meteorology, Oceanography, and Hydrology,* Los Angeles, Amer. Meteor. Soc., 313–319.

Fankhauser, J. C., 1969: Convective processes resolved by a mesoscale rawinsonde network. *J. Appl. Meteor.*, **8**, 778–798.

——, 1974: The derivation of consistent fields of wind and geopotential height from mesoscale rawinsonde data. *J. Appl. Meteor.*, **13**, 637–646.

——, C. J. Biter, C. G. Mohr and R. L. Vaughan, 1985: Objective analysis of constant altitude aircraft measurements in thunderstorm inflow regions. *J. Atmos. Ocean. Technol.*, **2**, 157–170.

Gal-Chen, T., 1978: A method for the initialization of the anelastic equations: Implications for matching models with observations. *Mon. Wea. Rev.*, **106**, 587–606.

——, 1982: Errors in fixed and moving frame of references: Applications for conventional and Doppler radar analysis. *J. Atmos. Sci.*, **39**, 2279–2300.

——, and C. E. Hane, 1981: Retrieving buoyancy and pressure fluctuations from Doppler radar observations: A status report. *Atmos. Technol.*, R. Carbone, Ed., Vol. 12, NCAR, 98–104.

Hambrick, L. N., and D. R. Phillips, 1980: Earth locating image data of spin-stabilized geosynchronous satelites. NOAA Tech. Memo. NESS 111, 49 pp.

Heymsfield, G. M., K. K. Gnosh and L. C. Chen, 1983: An interactive system for compositing digital radar and satellite data. *J. Climate Appl. Meteor.*, **22**, 705–713.

Knight, C. A., 1982: The Cooperative Convective Precipitation Experiment (CCOPE), 18 May–7 August 1981. *Bull. Amer. Meteor. Soc.*, **63**, 386–398.

Koch, S. E., M. desJardins and P. J. Kocin, 1983: An interactive Barnes objective map analysis scheme for use with satellite and conventional data. *J. Climate Appl. Meteor.*, **22**, 1487–1503.

Kohn, N. M., A. L. Johnston and C. G. Mohr, 1978: MUDRAS—Multiple Doppler radar analysis system. NOAA Tech. Memo. ERL/WPL-35, Wave Propagation Lab, Boulder, 170 pp.

Lackman, R. L., and R. B. Friesen, 1983: General purpose data processing software for scientific data sets. *Preprints, Fifth Symposium Meteor. Observations and Instrumentation,* Toronto, Amer. Meteor. Soc., 231–238.

Leise, J. A., 1981: A multidimensional scale-telescoped filter and data extension package. NOAA Tech. Memo. ERL/WPL-82, Wave Propagation Lab, Boulder, 20 pp.

Miller, L. J., C. G. Mohr and A. J. Weinheimer, 1986: The simple rectification to Cartesian space of folded radial velocities from Doppler radar sampling. *J. Atmos. Oceanic Technol.*, **3**, 162–174.

Mohr, C. G., and R. L. Vaughan, 1979: An economical procedure for Cartesian interpolation and display of reflectivity factor data in three-dimensional space. *J. Appl. Meteor.*, **18**, 661–670.

——, L. J. Miller and R. L. Vaughan, 1981: An interactive software package for the rectification of radar data to three-dimensional Cartesian coordinates. *Preprints, 20th Conf. on Radar Meteor.*, Boston, Amer. Meteor. Soc., 690–695.

Mueller, C. M., and P. H. Hildebrand, 1985: Evaluation of meteorological airborne Doppler radar. Part II: Triple-Doppler analyses of air motions. *J. Atmos. Ocean. Technol.*, **2**, 381–392.

Orville, R. E., and E. Rosentel, 1983: Ground-strike lightning locations in CCOPE. *Trans. AGU*, **64**, 666.

Oye, R., and R. Carbone, 1981: Interactive Doppler editing software. *Preprints, 20th Conf. on Radar Meteorology,* Boston, Amer. Meteor. Soc., 683–689.

Ray, P. S., K. K. Wagner, K. W. Johnson, J. J. Stephens, W. C. Bumgarner and E. A. Mueller, 1978: Triple-Doppler observations of a convective storm. *J. Appl. Meteor.*, **17**, 1201–1212.

Reynolds, D. W., 1982: Prototype workstation for mesoscale forecasting. *Bull. Amer. Meteor. Soc.*, **64**, 264–273.

Suomi, V. E., R. Fox, S. S. Limaye and W. L. Smith, 1983: McIDAS III: A modern data access and analysis system. *J. Climate Appl. Meteor.*, **22**, 766–778.

Treinish, L. A., and S. N. Ray, 1985: An interactive information system to support climate research. *Preprints, Int. Conf. on Interactive Information and Processing Systems for Meteorology, Oceanography, and Hydrology,* Los Angeles, Amer. Meteor. Soc., 72–79.

Wade, C. G., and T. M. Engle, 1985: A technique for correcting humidity errors in mesometeorological data. *Proc., Int. Symp. on Moisture and Humidity: Its Measurement and Control in Science and Industry.* Washington, DC, Instrument Soc. Amer., 121–131.

Wright, T., 1978: *NCAR Graphics Software.* (4th preliminary ed.), Prepared by Atmospheric Technology Div., NCAR, Boulder.